Materials Science-Poland

an
Interdisciplinary Journal of
Physics, Chemistry and
Technology of Materials

Vol. 26, No. 3, 2008

ISSN 0137-1339
Index No. 375675

Wrocław
University
of Technology

PMS SOCIETY

CENTRE OF
ADVANCED MATERIALS AND
NANOTECHNOLOGY

Wrocław University of Technology
Centre of Advanced Materials and Nanotechnology

Materials Science-Poland

Vol. 26 • No. 3 • 2008

Oficyna Wydawnicza Politechniki Wrocławskiej

Materials Science is an interdisciplinary journal devoted to experimental and theoretical research into the synthesis, structure, properties and applications of materials.

Among the materials of interest are:

- glasses and ceramics
- sol-gel materials
- photoactive materials (including materials for nonlinear optics)
- laser materials
- photonic crystals
- semiconductor micro- and nanostructures
- piezo-, pyro- and ferroelectric materials
- high-T_c superconductors
- magnetic materials
- molecular materials (including polymers) for use in electronics and photonics
- novel solid phases
- other novel and unconventional materials

The broad spectrum of the areas of interest reflects the interdisciplinary nature of materials research. Papers covering the modelling of materials, their synthesis and characterisation, physicochemical aspects of their fabrication, properties and applications are welcome. In addition to regular papers, the journal features issues containing conference papers, as well as special issues on key topics in materials science.

Materials Science is published under the auspices of the Centre of Advanced Materials and Nanotechnology of the Wrocław University of Technology, in collaboration with the Institute of Low Temperatures and Structural Research of the Polish Academy of Sciences and the Wrocław University of Economics.

All accepted papers are placed on the Web page of the journal and are available at the address:
http://MaterialsScience.pwr.wroc.pl

Materials Science is abstracted/indexed in: Chemical Abstracts, Materials Science Citation Index, Science Citation Index Expanded.

The Journal is supported by the State Committee for Scientific Research

Editorial Office

Daniel Davies
Krzysztof Małecki

Printed in Poland

Drukarnia Oficyny Wydawniczej Politechniki Wrocławskiej
Zam. nr 621/2008.

Materials Science-Poland, *Vol. 26*, *No. 3*, *2008*

Electrical properties of $0.90Pb[(Mg,Zn)_{1/3}Ta_{2/3}]O_3$–$0.10PbTiO_3$ relaxor

S. PRASAD[1*], K. PRASAD[1**], S.N. CHOUDHARY[1], T.P. SINHA[2]

[1] Materials Research Laboratory, University Department of Physics, T. M. Bhagalpur University, Bhagalpur 812 007, India

[2] Department of Physics, Bose Institute, 93/1 A.P.C. Road, Kolkata 700 009, India

Polycrystalline $0.90Pb[(Mg_{2/3}Zn_{1/3})_{1/3}Ta_{2/3}]O_3$–$0.10PbTiO_3$ having a tetragonal perovskite type structure was prepared by the high temperature solid-state reaction method. Dielectric studies showed the relaxor behaviour with a diffuse phase transition. A high value of ε_{max} (> 10 000) was achieved with the temperature T_m of maximum permittivity around room temperature at 1 kHz. The frequency dependence of T_m was modelled using the Vogel–Fulcher law. The dielectric relaxation in the material investigated here was found to be analogous to the magnetic relaxation in a spin-glass system. The shape of the complex impedance curve indicated that the system exhibited almost the Debye type dielectric relaxation at 350 °C, where as a non-Debye profile was observed at temperatures below 325 °C. Furthermore, the relaxation frequency was found to shift towards higher frequencies upon increasing temperature.

Key words: *relaxor ferroelectrics; dielectric property; diffuse phase transition; dielectric relaxation*

1. Introduction

Relaxor ferroelectrics such as $Pb(Mg_{1/3}Nb_{2/3})O_3$, $Pb(Zn_{1/3}Nb_{2/3})O_3$, $Pb(Ni_{1/3}Nb_{2/3})O_3$, $Pb(Mg_{1/3}Ta_{2/3})O_3$, $Pb(Sc_{1/2}Ta_{1/2})O_3$, $Pb(Fe_{1/2}Nb_{1/2})O_3$, etc. have been extensively studied for their use in multilayer capacitors (MLCs) and for electrostrictive applications. Among these $Pb(Mg_{1/3}Nb_{2/3})O_3$ (PMN) and its solid solutions with other compounds like $PbTiO_3$, $BaTiO_3$, etc. are the most widely studied. These compounds are generally characterized by their frequency dependent broad maximum in the temperature dependence of dielectric permittivity. However, $Pb(Mg_{1/3}Ta_{2/3})O_3$ and its solid solutions have been given comparatively little attention. As $Pb(Mg_{1/3}Ta_{2/3})O_3$ also exhibits disordered perovskite structure and typical relaxor ferroelectric properties, its preparation in pure or modified form and subsequent characterization deserve further investigation.

---

[*]Permanent address: Department of Physics, B.N. College, Bhagalpur 812 007, India.
[**]Corresponding author, e-mail: k_prasad65@yahoo.co.in; k.prasad65@gmail.com

Lead magnesium tantalate $Pb(Mg_{1/3}Ta_{2/3})O_3$ (PMT) is a well known relaxor ferroelectric having anomalously large electric permittivity and a broad diffuse phase transition [1] near – 98 ºC. On the other hand, lead titanate $PbTiO_3$ (PT) is a normal ferroelectric exhibiting a sharp peak in the electric permittivity and its Curie temperature is around 490 ºC. As PMT has a highly tolerant ABO_3 structure, it provides enough scope for modification either at the *A*- or *B*-site. It has been observed that the electrical properties and the temperature of the maximum of permittivity T_m of PMT can be controlled effectively by proper doping at *B*-site. Also, the addition of PT in PMT offers an advantage to shift the phase transition temperature to the higher temperature side [2, 3].

To the best of our knowledge, even after having made an extensive literature survey, there has been no report so far on the polycrystalline $0.90Pb[(Mg_{2/3}Zn_{1/3})_{1/3}Ta_{2/3}]O_3$ $–0.10PbTiO_3$ (PMZT-PT (90/10)). We recently studied a similar relaxor system, namely $0.80Pb[(Mg_{2/3}Zn_{1/3})_{1/3}Ta_{2/3}]O_3–0.20PbTiO_3$, which showed good dielectric properties. The value of T_m was found to be 57 ºC with $\varepsilon_{max} = 8412$ at 1 kHz [4]. Furthermore, in order to bring T_m near to room temperature, the percentage of added PT was reduced in this work. Accordingly, the present study considers the dielectric response of PMZT-PT(90/10) ceramic prepared through the columbite precursor method over a wide range of frequencies and temperatures. Impedance spectroscopy and Cole –Cole formalism were employed in order to investigate the dielectric relaxation in PMZT-PT(90/10) ceramic. Despite earlier investigations, the mechanism responsible for freezing processes in relaxor ferroelectrics is yet to be completely understood. A similar system, PMN, was earlier found to have analogies with the spin-glass system in which thermally activated polarization fluctuations occurred above a static freezing temperature T_f. Based on this fact, it is considered that the relaxor ferroelectric behaves much like a polar-glassy system, which can be modelled through the Vogel–Fulcher law [5, 6]:

$$f = f_0 \exp\left(-\frac{E_a}{k_B\left(T_m - T_f\right)}\right) \tag{1}$$

where f is the operating frequency, f_0 – the pre-exponential factor, k_B – the Boltzmann constant and E_a is the activation energy. Accordingly, to understand the mechanism responsible for the freezing process in PMZT-PT(90/10), dielectric data were modelled using the Vogel–Fulcher relation in the present investigation.

2. Experimental

$0.90Pb[(Mg_{2/3}Zn_{1/3})_{1/3}Ta_{2/3}]O_3–0.10PbTiO_3$ ceramic was prepared by the standard dry route, using a two-stage process. First, a columbite ($Mg_{2/3}Zn_{1/3}Ta_2O_6$) precursor was prepared at 1000 °C for 5 h using $MgCO_3$, ZnO and Ta_2O_5, according to the thermochemical reaction:

$$\frac{2}{3}\mathrm{MgO}+\frac{1}{3}\mathrm{ZnO}+\mathrm{Ta_2O_5}\xrightarrow{\Delta}\mathrm{Mg_{2/3}Zn_{1/3}Ta_2O_6}$$

This was then recalcined with PbO at 900 °C for 4 h to yield Pb[($Mg_{2/3}Zn_{1/3}$)$_{1/3}$ $Ta_{2/3}$]O_3. The chemical reaction taking place was as follows:

$$\mathrm{PbO}+\frac{1}{3}\mathrm{Mg_{2/3}Zn_{1/3}Ta_2O_6}\xrightarrow{\Delta}\mathrm{Pb[(Mg_{2/3}Zn_{1/3})_{1/3}Ta_{2/3}]O_3}$$

The purity of chemicals used was higher than 99%. Finally, 10 wt. % of PT was mixed with PMZT to obtain the desired compound: 0.90Pb($Mg_{2/3}Zn_{1/3}$)$_{1/3}Ta_{2/3}O_3$ –0.10$PbTiO_3$. Further cylindrical pellets of 0.90 mm in diameter and 1.52 mm thick were prepared under an isostatic pressure of 6×10^7 N·m^{-2}. Polyvinyl alcohol was used as a binder. The pellets were then sintered at 1200 °C for 2 h. The formation of the compound was checked by X-ray diffraction (XRD) using an X-ray diffractometer (Phillips PW1710, Holland) with CuK_α radiation λ = 1.5443Å over a wide range of Bragg angles ($20° \le 2\theta \le 80°$). To study the electrical properties, both flat surfaces of the pellets were electroded with a fine silver paint, and subsequently dried at 200 °C for 1 h before conducting the experiment. Electrical impedance Z, phase angle θ, capacitance and the dissipation factor of the sample were measured both as a function of frequency (0.1 kHz–3 MHz) as well as of temperature (20–350 °C) using a computer controlled LCR-Hightester (HIOKI 3532, Japan).

3. Results and discussion

3.1. Structural studies

A standard computer program (POWD) was used for the XRD-profile (Fig. 1) fitting. There was good agreement between the observed and calculated inter-planer

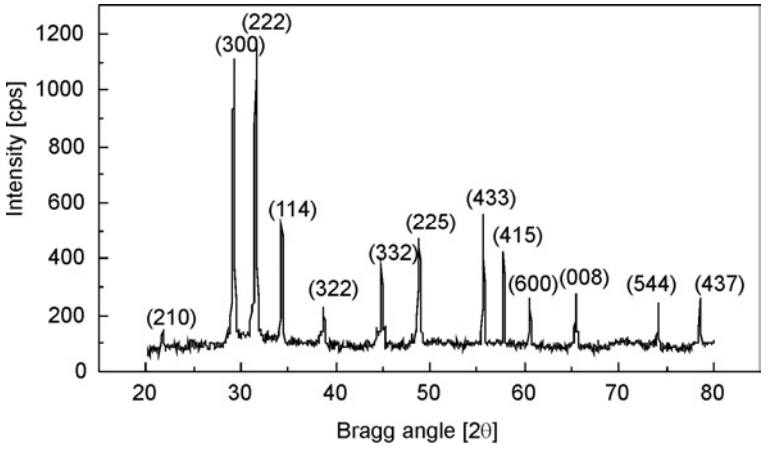

Fig. 1. X-ray diffraction pattern of 0.90Pb[($Mg_{2/3}Zn_{1/3}$)$_{1/3}Ta_{2/3}$]O_3–0.10$PbTiO_3$ at room temperature

spacing (d-values). There was no trace of any extra peaks due to constituent oxides which suggests the compound has a single-phase tetragonal structure. The lattice parameters were found to be: a = 9.159Å and c = 11.412Å, with an estimated error of $\pm 10^{-3}$Å. The criterion adopted for evaluating the correctness, index reliability, and the structure of PMZT-PT was the sum of differences between observed and calculated d-values (i.e., $\sum | d_{obs} - d_{cal} |$ to be a minimum. The tetragonal axial ratio (c/a) and unit cell volume (a^2c) have been estimated to be 1.246 and 957.32 Å^3, respectively. Hence, decreasing the percentage of PT reduces both the tetragonal axial ratio as well as the unit cell volume [4].

3.2. Dielectric studies

Figure 2 illustrates the temperature dependence of the electric permittivity ε and the dissipation factor tan δ at various frequencies. The plots show a broad maximum (diffuse phase transition, denoted as DPT) around 10 °C, and show strong frequency dispersion which indicates the relaxor behaviour of PMZT-PT. It was observed that the temperature T_m of maximum permittivity shifted to higher temperatures (from 29 ºC at 1 kHz to 35 °C at 1 MHz) while ε_{max} decreased (from 10 426 at 1 kHz to 6923 at 1 MHz) (inset of Fig. 2) and tan δ_{max} increased (from 0.067 at 1 kHz to 0.098 at 1 MHz) (inset of Fig. 2) upon increasing frequency. One can therefore see that lowering the percentage of added PT in PMZT caused a downward shift by 28 ºC in T_m, and caused ε_{max} to increase by 2014 with a decrease in dielectric loss [4].

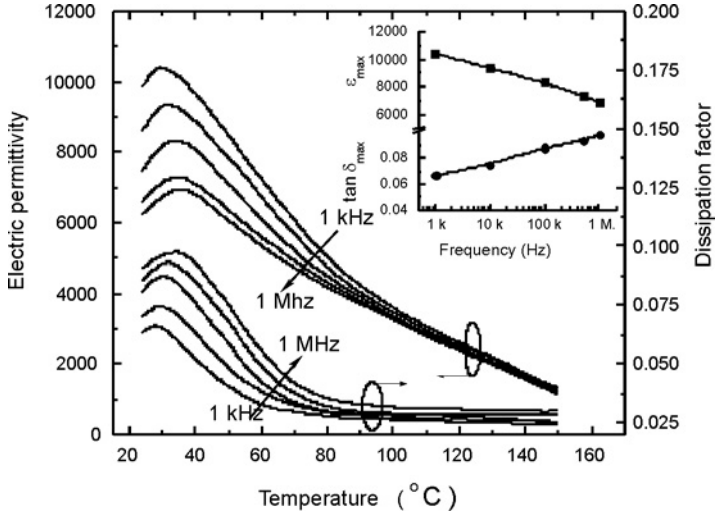

Fig. 2. Temperature dependence of electric permittivity of $0.90Pb[(Mg_{2/3}Zn_{1/3})_{1/3}Ta_{2/3}]O_3$–$0.10PbTiO_3$ at 1 kHz, 10 kHz, 100 kHz, 500 kHz and 1 MHz. The inset shows the variation of maximum value of ε and tanδ upon frequency

The results obtained in PMZT-PT(90/10) thus makes it a potential candidate for applications in devices. The sharp decrease in the electric permittivity as a function of increasing frequency can be explained in terms of the interfacial polarization. Contribution from interfacial polarizability comes due to the presence of two layers of materials of different conductivity. Here the motion of the charge carrier occurs readily in the higher conductivity phase, but is interrupted at the phase boundary due to the lower conductivity of the second phase [7]. In the case of polycrystalline ceramics, this is commonly observed if the grains are semiconducting and the grain boundaries are insulating. The semiconductive grains in PMZT-PT ceramics are believed to be caused by oxygen loss during firing at higher temperatures, in accordance with the reaction [8]:

$$\mathrm{O_0} \longleftrightarrow \frac{1}{2}\mathrm{O_2} \uparrow + \mathrm{V_0^{\bullet\bullet}} + 2\mathrm{e^-}$$

where all the species conform to the Kröger–Vink defect notation. These defects affect impedance and capacitance in the formation of barrier layers at the grain–grain boundary interface. During cooling after sintering, the reverse reaction occurs, but, due to the insufficient time available during cooling, reoxidation takes place and is restricted only to grain boundaries. This results in a difference between the resistance of grain boundary and grain, giving rise to a barrier [9]. The build-up of charges at the grain –grain boundary interface causes large polarization, resulting in a high electric permittivity at lower frequencies. Also, analogous to many other dipolar glassy systems, PMZT-PT(90/10) ceramic exhibits pronounced dispersion peaks in $\tan\delta$ (Fig. 2), which shift to lower temperatures (from 33 °C at 1 MHz to 27 °C at 1 kHz) as frequency decreases.

In order to examine the diffuse phase transition and relaxor more closely, the relationship between ε and T above T_m can be expressed by the modified Curie–Weiss law [10]:

$$\frac{1}{\varepsilon} - \frac{1}{\varepsilon_m} = \frac{\left(T - T_m\right)^\gamma}{C'} \tag{2}$$

where $C' = 2\varepsilon_m\delta^\gamma$ is the modified Curie–Weiss constant, δ is the diffusivity parameter, and γ is the diffuseness exponent, which can vary from 1, for normal ferroelectrics, to 2 for relaxor ferroelectrics. Equation (2) can be solved graphically using a log-log plot, as shown in Fig. 3. The slope of the curve represents the value of the critical exponent, while the intercept gives the diffuseness parameter according to the following equation:

$$\delta = \left(\frac{\mathrm{e}^{-\mathrm{intercept}}}{2\varepsilon_m}\right)^{1/\gamma} \tag{3}$$

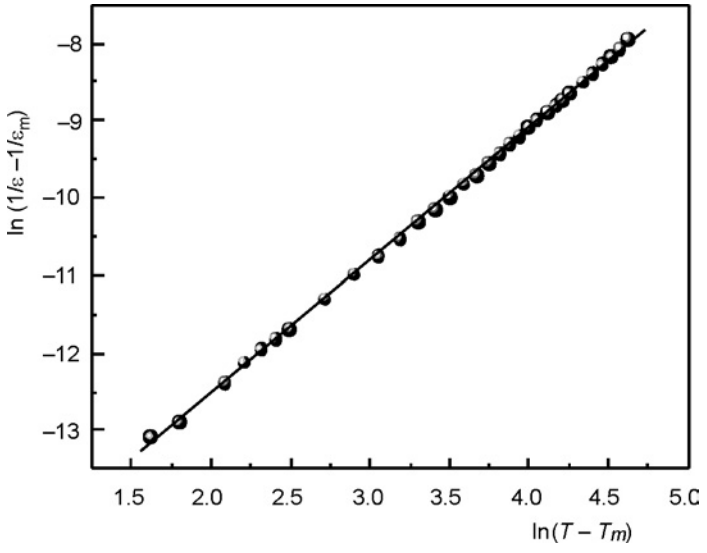

Fig. 3. Dependence of $\ln(1/\varepsilon - 1/\varepsilon_m)$ on $\ln(T - T_m)$ for $0.90Pb[(Mg_{2/3}Zn_{1/3})_{1/3}Ta_{2/3}]O_3$–$0.10PbTiO_3$ at 1 kHz

Linear regression analysis established $\gamma = 1.71$, $\delta = 32.36$ and $C' = 79.01\times10^5$ °C at 1 kHz which clearly indicates the DPT, and is found to increase with increase in frequency. It is expected that some disorder in the cation distribution (compositional fluctuations) causes the DPT where the local Curie points of different microregions are statistically distributed around the mean Curie temperature [11]. The non-equality of phase transition temperature obtained from ε–T and tan δ–T measurement also confirms the DPT.

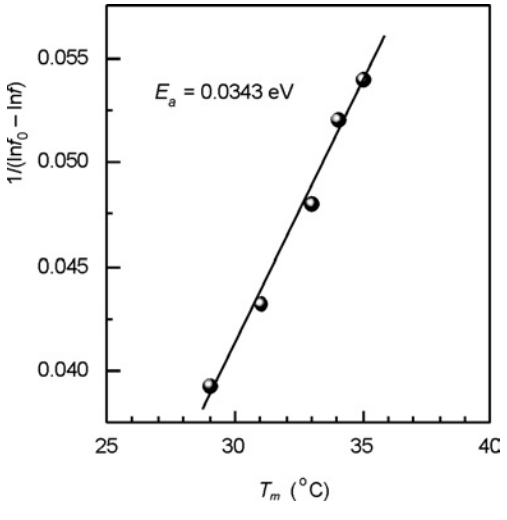

Fig. 4. Verification of the Vogel–Fulcher equation

Figure 4 shows the variation of $1/(\ln f_0 - \ln f)$ against the inverse of temperature T_m. Solid circles represent the experimental data. A linear least-squares fit of dielectric data, as in Eq. (1), calculates the values of E_a, f_0 and T_f as 0.0343 eV, 1.104×10^{14} Hz and 13.54 ºC, respectively. These values are also consistent with earlier reports on similar systems [4, 12–17]. The value of f_0 is found to lie in the optical frequency range of lattice vibrations. An excellent fit of the Vogel–Fulcher law with the experimental data constitutes strong evidence for a static freezing temperature of thermally activated polarization fluctuations in PMZT-PT. Therefore, dielectric relaxation in PMZT-PT may be considered as analogous to the magnetic relaxation in spin-glass system with polarization fluctuations above a static freezing temperature.

The polydispersive nature of dielectric relaxation can be checked through the Cole–Cole plots [18]. For pure monodispersive Debye relaxation, one expects semicircular plots, with the centre located on the ε' axis. However, for polydispersive relaxation, these Argand plane plots are close to circular arcs with end-points on the real axis, and with the centre lying below this axis. The complex electric permittivity is known to be described by the empirical relation:

$$\varepsilon^*(\omega) = \varepsilon' - i\varepsilon'' = \varepsilon_\infty + \frac{\Delta\varepsilon}{1+(i\omega\tau)^{1-\alpha}} \tag{4}$$

where $\Delta\varepsilon = \varepsilon_s - \varepsilon_\infty$ is the contribution of the relaxator to static permittivity ε_s, ε_∞ is the contribution of higher frequency polarization mechanism, τ (= $1/2\pi f$) is the mean relaxation time of the relaxators. The parameter characterizes the distribution of relaxation times, and it increases as the number of internal degrees of freedom of relaxators becomes larger.

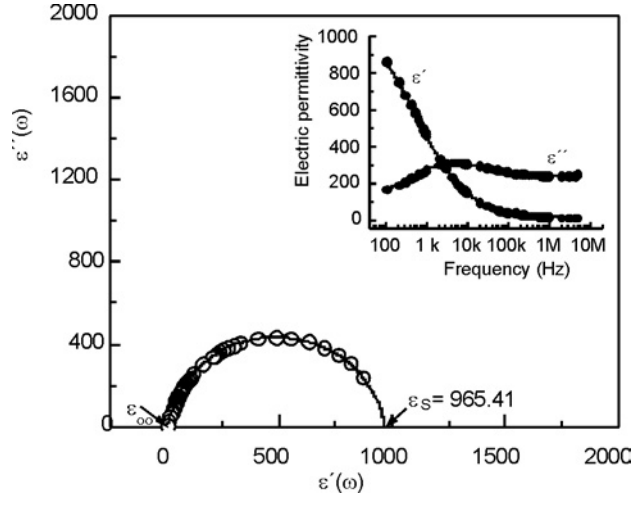

Fig. 5. Cole–Cole diagram for 0.90Pb[$(Mg_{2/3}Zn_{1/3})_{1/3}Ta_{2/3}$]$O_3$–0.10$PbTiO_3$ at 350 °C.
The inset shows the variation of real and imaginary parts of ε with frequency at 350 °C

The parameter α provides a measure of departure from an ideal Debye condition. It can, however, be determined from the location of the centre of the Cole –Cole circles: Figure 5 depicts a representative plot for PMZT-PT at 350 ºC. When α tends to zero (i.e., $(1 - \alpha) \rightarrow 1$), Eq. (4) reduces to a classical Debye's formalism. It can be inferred from this plot that the relaxation process is of polydispersive non-Debye type ($\alpha \cong 0.011$). The parameter α was determined from the angle subtended by the radius of the circle with the ε' axis passing through the origin of the ε'' axis. The value of $\Delta\varepsilon$ is estimated to be 961. Also, as can be seen from the inset in Fig. 5, the value of ε' decreases as frequency increases, while ε'' shows a peak at 3 kHz. The value of τ comes to be 5.305×10^{-5} s.

3.3. Impedance studies

The inset in Figure 6 shows the real and imaginary parts, Z' and Z'' respectively, of impedance variation at frequencies corresponding to the temperatures 300 ºC, 325 ºC and 350 ºC. It can be seen that the magnitude of Z' decreases as a function of increasing frequency and increasing temperature. The Z' values for all temperatures converge above 100 kHz. This may be attributable to the release of space charges. The curves

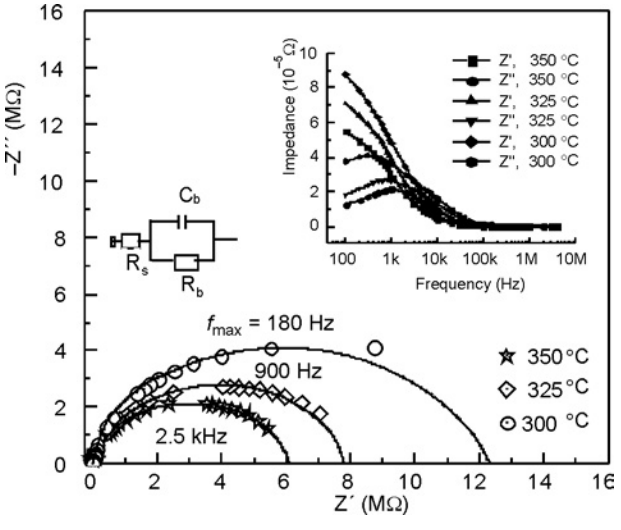

Fig. 6. Complex impedance of $0.90Pb[(Mg_{2/3}Zn_{1/3})_{1/3}Ta_{2/3}]O_3$–$0.10PbTiO_3$ at various temperatures. The inset shows dependence of Z' and Z'' on frequency at 300 °C, 325 °C and 350 °C

also display a single relaxation process, indicating an increase in a.c. conductivity upon increasing temperature and frequency. From the profile of the curves it can be inferred that the complex impedance of the electrode/ceramic/electrode capacitor is the sum of the single RC-circuit (Debye relaxators) in a parallel combination. Therefore,

$$Z^*(\omega,T) = Z_o(T)\int_0^\infty \frac{g(\tau,T)d\tau}{1+i\omega\tau} \tag{5}$$

which gives

$$Z'(\omega,T) = Z_o(T)\int_0^\infty \frac{g(\tau,T)d\tau}{1+\omega^2\tau^2} \tag{6}$$

$$Z''(\omega,T) = Z_o(T)\int_0^\infty \frac{\omega T\ \ g(\tau,T)d\tau}{1+\omega^2\tau^2} \tag{7}$$

where $\tau = RC$ is the relaxation time, $g(\tau,T)$ is the distribution function: this determines the distribution of relaxation times. In the case of a broad spectrum, i.e. $\tau_{min} \le \tau \le \tau_{max}$, Z'' can be approximated as (see [19])

$$Z'' \cong KZ_0(T)g(\tau,T) \tag{8}$$

where K is a constant. Therefore, $Z''(\omega,T)$ should provide the information about the distribution function $g(\tau,T)$. The curve for Z'' vs. frequency shows that the Z'' values reach a maximum (Z''_{max}) which shifts to higher frequencies as temperature increases. This also indicates a single relaxation process in the system. The variation profile of Z' and Z'' vs. frequency resembles the variation of ε' and ε'' vs. frequency (Fig. 5, inset). Figure 6 shows the plot of Z' vs. Z'' for PMZT-PT ceramic at three different temperatures. A semicircle could be traced from 300 °C onwards. All these curves start almost at the origin ($R_\infty \sim 20\ \Omega$) and hence there should be a series resistance (R_s) of 20 Ω for the LCR circuit representation of the sample. The high frequency semicircle may be ascribed to the parallel combination of bulk resistance (R_b) and capacitance (C_b) of PMZT-PT. The appropriate equivalent circuit comprising of R_s, R_b and C_b is shown in the inset in Fig. 6. The value of R_b can be directly obtained from the intercept on the Z' axis, the frequency at which the inflection point occurs in Z'' yields the measure of the relaxation time (τ_b), since at this point $\omega\tau_b = 1$ and the value of C_b can be calculated using the relation:

$$2\pi f_{max} R_b C_b = 1 \tag{9}$$

where f_{max} is the frequency at the maximum of the semicircle. It is observed that the peak maxima of the plots decrease, and f_{max} shifts to higher values when temperature increases. Furthermore, the values for R_b, C_b and τ_b decrease as temperature increases (Table 1). The decrease in the value of R_b upon increasing temperature reveals a negative temperature coefficient of resistance (NTCR) in PMZT-PT. It can also be noticed that the complex impedance plots are not represented by full semicircles; rather, the semicircular arcs are depressed and the centres of the arcs lie below the real (Z') axis, similarly to the Cole–Cole plot (Fig. 5). The complex impedance in such situations has been described by the Cole–Cole formalism [20]:

$$Z^*(\omega) = Z' + iZ'' = \frac{R}{1 + \left(\frac{i\omega}{\omega_0}\right)^{1-n}} \tag{10}$$

where n represents a measure of how much the electrical response deviates from an ideal condition (i.e., $(1 - n) \rightarrow 1$ in Eq. (10) gives rise to a classical Debye formalism).

Table 1. Parameters obtained from the complex impedance plots at various temperatures

Parameter	Temperature [°C]		
	300	325	350
R_b [Ω]×10^{-5}	12.425	7.808	6.104
C_b [F]×10^{10}	7.113	2.264	1.043
τ_b [s]×10^4	8.842	1.768	0.637
n	0.033	0.022	0.011

Fitting the complex impedance data to Eq. (10) gives a non-zero value of n which decreases when temperature rises (Table 1), and hence confirms the polydispersive nature of dielectric relaxation in PMZT-PT. This may be due to the presence of distributed elements in the material–electrode system [18]. It is also noticed that as temperature increases $n \rightarrow 0$, following the classical Debye type relaxation. At 350 ºC, an almost full semicircle is observed ($n = 0.011$). Therefore, one can deduce that with the temperature increasing, the complex impedance data approaches the Debye type relaxation.

Hence, the relaxor ferroelectrics at high temperature could be considered as an ensemble of uncorrelated Debye-like relaxators with some relaxation times. As the temperature is lowered, the correlation among the Debye relaxators becomes stronger through the formation of nanopolar clusters [19]. Since the relaxation times of the relaxators within polar clusters are distributed over a wide spectrum at lower temperatures, their response to external fields are in a different time domain. This results in the deviation from the Cole–Cole plot with partial semicircular arcs. It is clear from Fig. 6 that as the measuring temperature decreases, the centre of the Cole–Cole semicircles shifts below the Z' axis, inferring a possible average profile of various Cole–Cole semicircles. This cannot arise due to any other secondary factor such as interfacial capacitance or defects whose relaxation times are assumed to be superimposed with the actual ceramic response. If we assume that the interfacial capacitance also exhibits a similar type of dielectric dispersion, the high temperature in the Cole–Cole plots would have been split into two discrete semicircles, not observed in the present case. The value of R^2 (regression coefficient) for all the data fits, quoted in this paper, is ≥ 0.9992.

4. Conclusion

Polycrystalline samples of PMZT-PT having cubic structure were prepared by the coulombite precursor method. The compound showed a relaxor behaviour with a diffuse phase transition. A high value (> 10 000) for the electric permittivity was obtained at 1 kHz, with the temperature of maximum permittivity near room temperature. Modelling the dielectric data using the Vogel–Fulcher law constitutes strong evidence for a static freezing temperature of thermally activated polarization fluctuations in PMZT-PT. Therefore, dielectric relaxation in PMZT-PT may be considered as analogous to the magnetic relaxation in spin-glass systems having polarization fluctuations above a static freezing temperature. Cole-Cole analysis indicated the relaxation to be of non-Debye type and the relaxation frequency shifting to the higher side with an increase in temperature. The deviation from a Debye profile in the present system may be attributed to the formation of the nanopolar clusters.

Acknowledgement

The authors (SNC and KP) acknowledge the financial support of the Department of Science and Technology (DST), New Delhi (Ref. No.: SP/S2/M-15/97).

References

[1] BOKOV V.A., MYL'NIKOVA I.E., Sov. Phys. Tech. Phys., 2 (1961), 2428.
[2] CHOI S.W., JUNG J.M., J. Kor. Phys. Soc., 29 (1996), S672.
[3] LEE S.H., JUNG J.M., CHOI S.W., J. Korean Phys. Soc., 32 (1998), S1013.
[4] PRASAD S., PRASAD K., CHOUDHARY S.N., SINHA T.P., Physica B: Cond. Matter, 364 (2005), 206.
[5] VOGEL H., Z. Phys., 22 (1921), 645.
[6] FULCHER G., J. Am. Ceram. Soc., 8 (1925), 339.
[7] SINGH S.P., SINGH A.K., PANDEY D., J. Mater. Res., 18 (2003), 2677.
[8] LEE S.B., LEE K.H., KIM H., Jpn. J. Appl. Phys., 41 (2002), 5266.
[9] CHEN D.R., GUO Y.Y., Electron. Element. Mater., 1 (1982), 25.
[10] UCHINO K., NOMURA S., Ferroelectr. Lett., 44 (1982), 55.
[11] PRASAD K., Ind. J. Eng. Mater Sci., 7 (2000), 446.
[12] VIEHLAND D., LI J.F., JANG S.J., CROSS L.E., WUTTING M., Phys. Rev. B, 46 (1992), 8013.
[13] TAGANTSEV A.K., Phys. Rev. Lett., 72 (1994), 1100.
[14] VIEHLAND D., JANG S.J., CROSS L.E., WUTTING M., J. Appl. Phys., 68 (1990), 2916.
[15] BOKOV A.A., LESHCHENKO M.A., MALITSKAYA M.A., RAEVSKI I.P., J. Phys: Cond. Matter., 11 (1999), 4899.
[16] KUMAR A., PRASAD K., CHOUDHARY S.N., CHOUDHARY R.N.P., Matter. Lett., 58 (2004), 3395.
[17] TU CHI-SHUN, CHAO F.-C., YEH C.-H., TSAI C.-L., Phys. Rev. B, 60 (1999), 6348.
[18] MACDONALD J.R., *Impedance Spectroscopy Emphasizing Solid Materials and Systems*, Wiley, New York, 1987.
[19] BONNEAU P., GARNIER O., CALVARIN G., HUSSON E., GAVARRI J.R., HEWAT A.W., MORREL A., J. Solid State Chem., 91 (1991), 350.
[20] COLE K.S., COLE R.H., J. Chem. Phys., 9 (1941), 341.

Received 6 September 2006
Revised 7 June 2007

Materials Science-Poland, *Vol. 26*, *No. 3*, *2008*

Biomimetic growth of apatite on titania nanotube arrays fabricated by titanium anodization in NH_4F/H_2SO_4 electrolyte

TIAN TIAN, XIAO XIU-FENG, SHE HOU-DE, LIU RONG-FANG*

College of Chemistry and Material Science, Fujian Normal University, Fuzhou 350007, China

Titania nanotube arrays were fabricated by anodizing titanium in NH_4F/H_2SO_4 electrolyte. The crystal structure and apatite-forming ability of the titania nanotube arrays were investigated. The samples were examined by ESEM, XRD and FT-IR. The results indicate that the crystal structure of the titania nanotube arrays transformed from amorphous to anatase and rutile ones upon rising the temperature of annealing. The surface structure of the nanotube arrays could enhance the bioactivity of titania. The bioactivity of titania nanotube arrays depends on their crystal structure, diminishing in the following series: mixture of anatase and rutile structure > anatase > amorphous.

Key words: *titania; nanotube array; apatite; bioactivity*

1. Introduction

Titanium and its alloys are used as a common material for bone implants under biomechanical loading conditions due to their excellent mechanical properties and biocompatibility [1, 2] despite their poor bonding ability. In order to improve the bone bonding ability of titanium implants, many attempts have been made to modify the chemistry composition and structure of titanium surfaces. These methods include dip coating [3], plasma spraying [4,5], magnetron sputtering [6], ion implanting [7], electrocrystallization [8], electrophoretic deposition [9], hydrothermal electrodeposition [10], anode oxidation [11], acid etching [12], oxidation with hydrogen peroxide [13], sol-gel methods [14,15], alkali-heating procedure [16], acid-alkali or precalcification procedure [17,18], and surface-induced mineralization [19]. Plasma spraying is one of the most widely investigated methods for titanium coating but the major problem is that it is a line of sight process, and the coating is nonuniform and heterogeneous.

*Correponding author, e-mail: rfliu@vip.sina.com

Another problem is that the HA powder is heated at extremely high temperature and deposited with very high velocity on the metal surface. Furthermore, the composition and crystallinity of HA are difficult to control. Naturally, it is believed that an ideal bioactive method, simple and cost-effective, should be employed.

Recently, it has been reported that bioactive titanium surface can be prepared by fabricating a titania nanotube array layer on the surface of titanium [29]. Tsuchiya et al. [29] reported that the presence of the titania nanotube arrays on a titanium surface enhanced the apatite formation. In this paper, a layer of titania nanotube arrays was obtained *via* anodic oxidation on titanium in NH_4F/H_2SO_4 electrolyte. The bioactivities of the layers annealed at various temperatures with various crystal structures were studied by soaking 1.5 times simulated body fluid (1.5 SBF).

2. Experimental

Titanium foils (99.5% pure) were purchased from the Northwest Institute For Non-Ferrous Metal Research (China). Prior to anodization, the titanium foils were ultrasonically cleaned in acetone and distilled water for 5 min, respectively, and then eroded in 4 wt. % HF–5 M HNO_3 for 30 s followed by ultrasonic cleaning in distilled water for 5 min and dried in air at 40 °C. A two-electrode arrangement with a graphite cathode was used. 1.75 M H_2SO_4 solutions with 0.5 wt. % NH_4F were used as an electrolyte. The anodizing voltage was kept constant at 20 V during the entire process with a DC power supply (GOA, China). The whole course of anodization was conducted at room temperature (25 °C) with magnetic agitation. The samples were dried at 40 °C in air, and then annealed at various temperatures (from 300 °C to 600 °C) for 4 h in a furnace with air.

The bioactivity study was carried out by inserting the as-prepared sample into culture vials containing simulated body fluid (1.5 SBF) for 9 days at 37 °C without stirring. The composition of the 1.5 SBF was reported as Kukobo [20] but the quantity of Ca and P added was 1.5 times greater to shorten the period of the bioactivity study. The samples were taken out, washed with distilled water and dried in air at 40 °C before coating characterization.

Philips XL30 ESEM was employed for the structural and morphological characterization of the sample. X-ray diffraction measurements were performed on Philips X'Pert MPD diffractometer with CuK_α radiation, the X-ray generator operated at 40 kV and 40 mA. Data sets were collected over the range of 5–90° with a step size of 0.02° and a count rate of 4.0 °/min. Identification of phases was achieved by comparing the diffraction patterns of the samples with ICDD (JCPDS) standards. FT-IR spectra were obtained by using an Nicolet Avatar 360 spectrometer at the resolution of 4 cm^{-1}.

3. Results and discussion

Figure 1 shows the surface morphology and cross-sections of the titania nanotube arrays fabricated by anodizing titanium in 1.75 M H_2SO_4 solutions with 0.5 wt. %

NH_4F. It is clear that the surface of the titania nanotube layer is flat and smooth with discrete, hollow, cylindrical, tubular features. The nanotubes of the arrays possess the inner diameter of about 120 nm and the length of ca. 300 nm. This structure possesses larger surface areas and is different from the nonporous TiO_2 layers formed from other electrolytes, such as sulfuric acid [21, 22]. In fluoride-containing electrolytes, the anodization of titanium is accompanied with its chemical dissolution due to the formation of TiF_6^{2-}. Highly uniform nanotube arrays, instead of nonporous structure, were formed [23, 24].

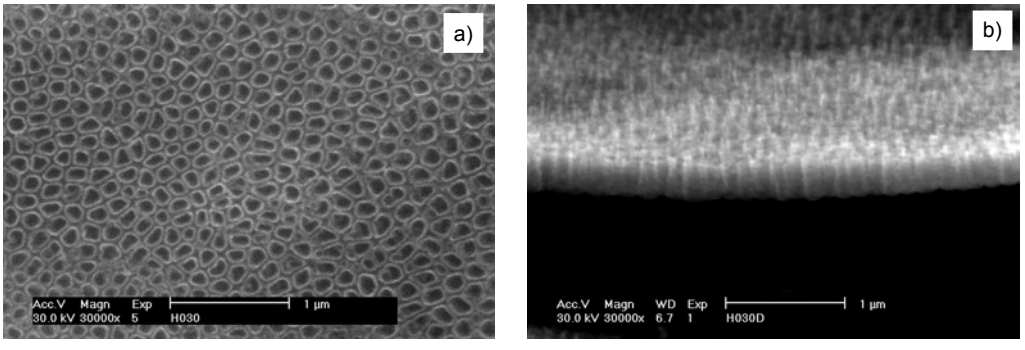

Fig. 1. The surface morphology (a) and cross-section (b) of the titania nanotube arrays

To evaluate the potential use of the titania nanotube layers as coatings for biomedical implants, the as-prepared titania nanotube layers were annealed at various temperatures and then soaked in 1.5 SBF. The microstructures of the nanotube arrays annealed from 300 °C to 600°C were observed by ESEM. There were no discernible changes in the tube diameters or wall thicknesses after annealing at 300 °C for 4 h. A little diminishing of the tube diameter occurred at 500 °C. As temperature raised to 600°C, obvious breakage occurred as shown in Fig. 2.

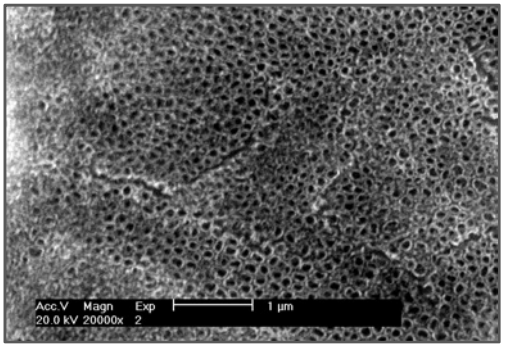

Fig. 2. The surface morphology of the nanotube arrays after annealing at 600 °C

Figure 3 shows the XRD patterns of the sample annealed at different temperatures. The as-prepared titania nanotube arrays were found to be amorphous (curve e). It is clear that the sample crystallized in the anatase phase at the temperature close to

300 °C (curve b). The diffraction peak of anatase phase is enhanced at 500 °C (curve c). When the temperature approaches 600 °C (curve d), the rutile phase emerges in the X-ray diffraction pattern. The same heat treatment was performed on pure titanium without titania nanotube arrays. There is only Ti peak appearing on the pattern at 500°C. The rutile phase emerges in the X-ray diffraction pattern straightly at 600°C (curve a).

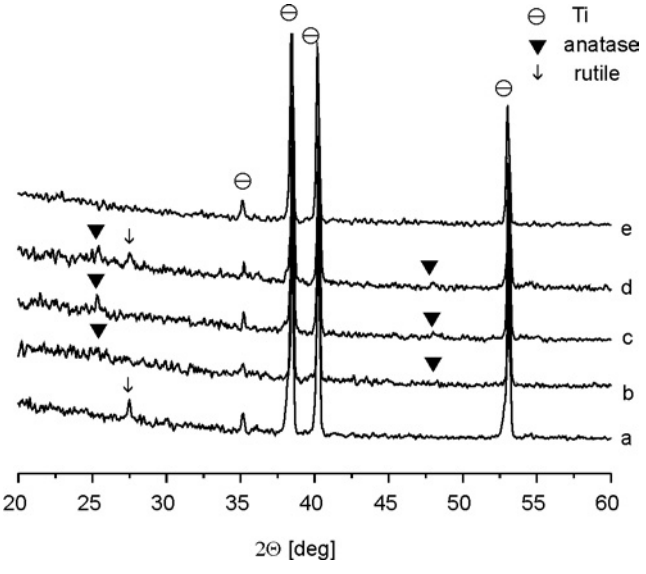

Fig. 3. XRD patterns of unanodized titanium (a) and the titania nanotubes arrays annealed at: b) 300 °C c) 500 °C, d) 600 °C, e) unannealed

The results indicate that the crystallization of titania nanotube arrays changes as the annealing temperature rises. The changes in morphologies of the titania nanotube arrays at high temperatures are the result of crystallization of titania nanotube arrays and oxidation of titanium substrate. Anatase and rutile are two ordinary phases of titania; both belong to tetragonal structures but there are four TiO_2 molecules in the unit cell of anatase, two in that of rutile. Oxygen octahedra are joined together *via* face in anatase, *via* culmination in rutile. According to the third principle of Pauling [20], the presence of shared polyhedral edges and especially shared polyhedral faces decreases the stability of the crystal structure. Thus the crystal phase of titania nanotube arrays could transform from anatase to rutile as the temperature is increased.

The surface morphologies of the annealed titania nanotube arrays after soaking in 1.5 SBF are shown in Fig. 4. There are no obvious changes on the surface of the unannealed titania nanotube arrays (Fig. 4a), and the mouths of the nanotubes are clearly visible. For the samples annealed at 300 °C (Fig. 4b), only a small amount of particles formed sparsely scattered on the surface of the sample and could only be detected with ESEM. The morphology is very similar to that of the deposited apatite on a substrate

through biomimetic processing utilizing SBF [26]. These particles were thus regarded as apatite. For the samples annealed at 500 °C (Fig. 4c) and 600 °C (Fig. 4d), a new layer formed on the surface of the titania nanotube arrays. The new layer formed at 600 °C is more compact than that formed at 500 °C.

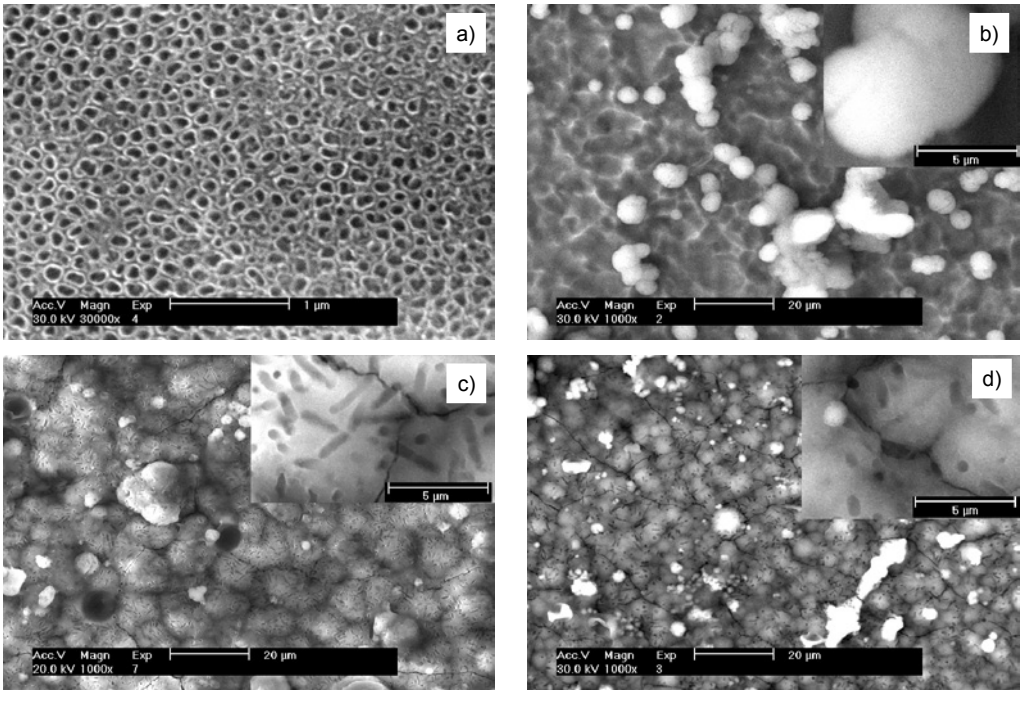

Fig. 4. SEM images of the samples soaked in 1.5 SBF unannealed (a) and annealed at 300 °C (b), 500 °C (c) and 600 °C (d)

The XRD pattern of the layer is shown in Fig. 5 and compared with the standard card (JCPDS 09-432), indicating that the layer formed on the surface of titania nanotubes is an apatite layer. The FT-IR spectra of the new layer formed on the nanotube surface annealed at 500 °C and 600°C are shown in Fig. 6. The new formed layer exhibited sharp P–O asymmetric stretching mode of PO_4^{3-} group at 1027 cm^{-1}, triple and double degenerated bending modes of phosphate O–P–O bands at 607, 568, and 470 cm^{-1} and modes of CO_3^{2-} group at 1458, 1418, and 871 cm^{-1}. A broad absorption band at 3451cm^{-1} and the bending mode at 1652 cm^{-1} are the bands of H_2O. The results indicate that the apatite formed on the nanotube arrays layer is B-type carbonated apatite, in which PO_4^{3-} groups are partly substituted by CO_3^{2-}.

Based on the above analyses, the bioactivity of titania nanotube arrays layer was ranked in the following series: annealed at 600°C > annealed at 500°C > annealed at 300°C > unannealed. The apatite deposition on titania has been reported by Healy and

Ducheyne [27]. They have suggested that titanium was subjected to passive dissolution in SBF and within a soaking period up to 400h, the passive dissolution was governed by the hydrolysis of titania, which resulted in the formation of OH^- and $Ti(OH)_n^{(4-n)+}$. The OH^- ions were adsorbed on the oxide surface forming Ti–OH groups, and subsequently promote the nucleation of apatite on the surface of titanium.

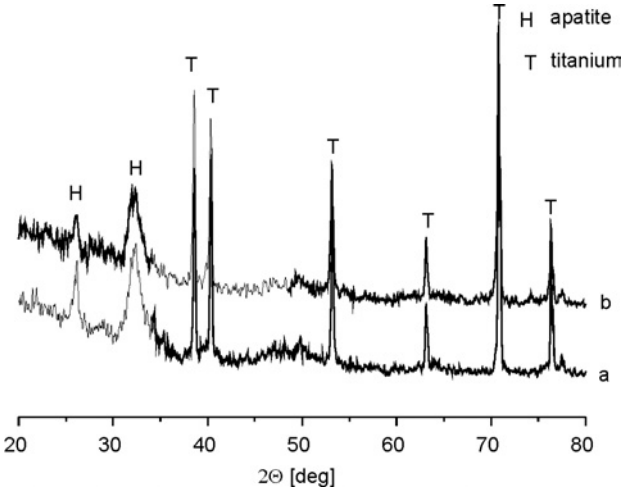

Fig. 5. XRD patterns of the samples soaked in 1.5 SBF annealed at 500 °C (a), and 600 °C (b)

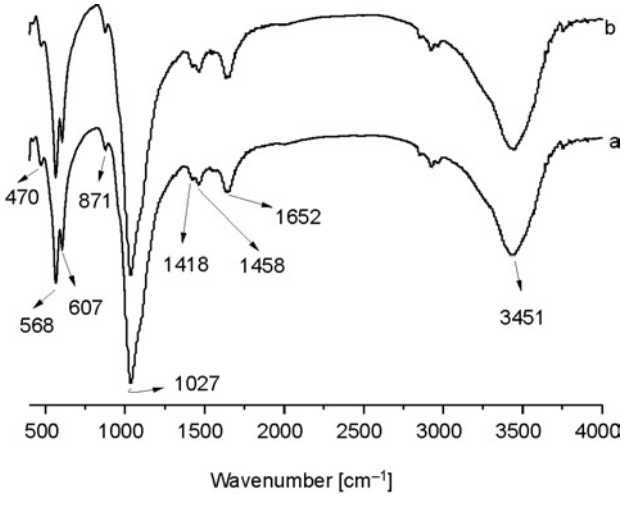

Fig. 6. FT-IR spectra of the new formedlayer after soaking in SBF for 9 days:
a) the nanotube arrays with anatase phase annealed at 500°C,
b) the nanotube arrays with a mixture of anatase and rutile phase annealed at 600 °C

The forming of the Ti-OH groups is the key factor for the nucleation of apatite. However, the bioactivity of the titania nanotube arrays is distinguished due to different

crystal structure at present. The results imply that not all Ti-OH groups, but certain type of Ti-OH groups in a specific structural arrangement, are effective in inducing apatite nucleation. The amorphous structure cannot induce apatite formation on their surface in SBF, whereas the anatase structure is able to induce apatite formation. However, the mixture of anatase and rutile structure possesses a better capability for the formation of apatite than the former structure. This phenomenon has been reported by Uchida [28] who found that the titania gels with an amorphous structure did not induce apatite formation on their surfaces in SBF, whereas gels with an anatase or rutile structure induced apatite formation on their surfaces. Thus the bioactivity of the titania nanotube arrays lies on the crystal structure, mixture of anatase and rutile structure > anatase > amorphous.

The control experiment has been carried out by Tsuchiya et al. [29]. They reported that on the compact anodic titania layer, which was obtained in H_2SO_4 solutions and annealed at 550 °C, there is no apatite layer formed after soaking in the 1.5SBF. The result implied that the porous structure of the titania nanotube arrays layer is advantageous to the nucleation of apatite because the porous nature of the titania nanotue arrays layer enhances the anchorage of the nucleation of apatite and opened up the possibility of the incorporation on the titanium.

4. Conclusions

The titania nanotube arrays were fabricated by titanium anodization in NH_4F/H_2SO_4 electrolyte. The crystal structure of the arrays was transformed from amorphous to anatase and rutile after annealing at various temperatures. The bioactivity study was carried out by soaking the samples in 1.5 SBF. The results show that the titania nanotube arrays with a mixture of anatase and rutile structure possess a high apatite forming ability, implying that titania nanotube arrays with a specific crystal structures such as anatase, mixture of anatase and rutile, are effective for apatite formation. These results suggest the bioactive titanium to be used as an implant material may be obtained by anodic oxidation and subsequent annealing.

Acknowledgements

The authors express their gratitude to the National Nature Science Foundation of China (30600149), the Science Research Foundation of Ministry of Health and United Fujian Provincial Health and Education Project for Tackling the Key Research, P.R. China (WKJ 2005-2-008) and Fujian Development and Reform Commission of China (No. 2004 [477]).

References

[1] LONG M., RACK H.J., Biomater., 19 (1998), 1621.

[2] BRUNETTE D.M., TENGVALL P., TEXTOR M., THOMSEN P., *Titanium in Medicine*, Springer Verlag Berlin, 2001, p.13

[3] LEE J., AOKI H., Biomed. Mater. Eng., 5 (1995), 49.
[4] GROOT K.D., GEESINK R., KLEIN C., SEREKIAN P., J. Biomed. Mater. Res., 21 (1987), 1375.
[5] CHEN J., TONG W., CAO Y., FENG J., ZHANG X., J. Biomed. Mater. Res., 34 (1997), 15.
[6] OZEKI K., YUHTA T., AOKI H., NISHIMURA I., FUKUI Y., Biomed. Mater. Eng., 10 (2000), 221.
[7] PHAM M.T., MAITZ M.F., MATZ W., REUTHER H., RICHTER E., STEINER G., Thin Solid Films, 379 (2000), 50.
[8] SHIRKHANZADEH M., J. Mater. Sci. Mater. Med., 6 (1995), 90.
[9] ZITOMIRSKY I., GOL-OR L., ISRAL I., J. Mater. Sci. Mater. Med., 8 (1997), 213.
[10] XIAO X.F., LIU R.F., ZHENG Y.Z., Mater. Lett., 59 (2005), 1660.
[11] ISHIZAWA H., OGINO M., J. Biomed. Mater. Res., 34 (1997), 15.
[12] MORRA M., CASSINELLI C., BRUZZONE G., CARPI A., DI SANTI G., GIARDINO R., FINI M., Int. J. Oral. Maxillofac Implants, 18 (2003), 40.
[13] TENGVALL P., ELWING H., LUNDSTROM I., J. Colloid Inter. Sci., 130 (1989), 405.
[14] LI P., OHTSUKI C., KOKUBO T., NANKANISHI K., SOGA N., GROOT K.D., J. Biomed. Mater. Res., 28 (1994), 7.
[15] PELTOLA T., PATSI M., RAHIALA H., KANGASNIEMI I., YLI-URPO A., J. Biomed. Mater. Res., 41 (1998), 504.
[16] KIM H.M., MIYAJI F., KOKUBO T., NAKAMURA T., J. Biomed. Mater. Res., 38 (1997), 121.
[17] WEN H.B., WOLKE J.G.C., WIJN J.R.D, LIU Q., CUI F.Z., GROOT K.D., Biomater., 18 (1997), 1471.
[18] WEN H.B., LIU Q., WIJN J.R.D., GROOT K.D., J. Mater. Sci. Mater. Med., 8 (1998), 121.
[19] BUNKER B.C., RIEKE P.C., TARASEVICH B.J., CAMPBELL A.A., FRYXELL G.E., GRAFF G.L., SONG L., LIU S., VIRDEN J.W., MCVAY G.L., Science, 264 (1994), 48.
[20] KOKUBO T., KUSHITANI H., SAKKA S., KITSUGI T., YAMAMURO T., J. Biomed. Mater. Res., 24 (1990), 721.
[21] YANG B.C., UCHIDA M., KIM H.M., ZHANG X.D., T KOKUBO., Biomater., 25 (2004), 1003.
[22] SUL Y.T., JOHANSSON C.B., JEONG Y., ALBREKTSSON T., Med. Eng. Phys., 23 (2001), 329.
[23] GONG D., GRIMES C.A., VARGHESE O.K., HU W., SINGH R.S., CHEN Z., DICKEY E.C., J. Mater. Res., 16 (2001), 3331.
[24] MOR G.K., VARGHESE O.K., PAULOSE M., MUKHERJEE N., GRIMES C.A., J. Mater. Res., 18 (2003), 2588.
[25] ROHRER G.S., *Structure and Bonding in Crystalline Materials*, Cambridge University Press, Cambridge, 2001, p. 365
[26] KOKUBO T., Biomater., 2 (1991), 155.
[27] HEALY K.E., DUCHEYNE P., J. Biomed. Mater. Res., 26 (1992), 319.
[28] UCHIDA M., KIM H.M., KOKUBO T., FUJIBAYASHI S., NAKAMURA T., J. Biomed. Mater. Res., 64A (2003), 164.
[29] TSUCHIYA H., MACAK J.M., MULLER L., KUNZE J., MULLER F., GREIL P., VIRTANEN S., SCHMUKI P., J. Biomed. Mater. Res., 77A (2006), 534.

Received 31 October 2006

Materials Science-Poland, *Vol. 26*, *No. 3*, *2008*

Modelling of tribological behaviours of composite PEEK-CF30 using BP neural networks

X. LIUJIE[1], R. CARDOSO[2], J. P. DAVIM[2*]

[1]Henan Engineering Research Center for Wear of Material,
Henan University of Science and Technology, Louyang 471003, China

[2] Department of Mechanical Engineering, University of Aveiro,
Campus Santiago, 3810-193 Aveiro, Portugal

A high performance of advanced composite PEEK-CF30 enables it to be utilized in many of the most critical areas in general industry such as automotive, electronics, medical and aerospace. In the present paper, a back propagation (BP) neural network was used to study the effects of the *pv* factor and sliding distance on the friction and wear behaviour of 30 wt. % carbon fibre reinforced poly(ether)–ether –ketone advanced composite (PEEK-CF30) at the contact temperature of 120 ºC. An experimental plan was performed on a pin-on-disc machine for obtained experimental results under unlubricated conditions. By the use of BP neural network, nonlinear relationship models of the friction coefficient (μ) and weight loss (W) of PEEK-CF30 vs. the *pv* factor and sliding distance (S) were built based on the experimental data. The test results show that the well-trained BP neural network models can precisely predict the friction coefficient and wear weight loss according to the *pv* factor and sliding distance. A new method of predicting wear behaviours of composite PEEK-CF30 has been provided by the authors.

Key words: *BP neural network; friction and wear; advanced composite (PEEK-CF30)*

1. Introduction

Preliminary investigations of neural networks techniques to predict tribological properties have been presented by Hutching's group at the University of Cambridge [1] and Jones et al. [2]. Subsequently, Friedrich et al. [3, 4] investigated the potential of artificial neural network techniques to predict and analyze the wear behaviour of short fibre reinforced plastics. Using multiple-layer feed-forward artificial neural network, the coefficient of friction and the specific wear rate have been predicted based on the measured data base for polyamide 4.6 composites. The predictive quality of the artificial neural network increased when enlarging the datasets and by optimising the net work construction.

*Corresponding author, e-mail: pdavim@mec.ua.pt

30 wt. % carbon fibre reinforced poly(ether)–ether–ketone (PEEK-CF30) is a relatively new semicrystalline polymer with high melting and glass transition temperatures |(T_m = 340 ºC and T_g = 143 ºC) [5]. The composite exhibits outstanding wear resistance and relatively low friction for several ranges of pressure, sliding velocity and contact temperature. The tribological behaviour of PEEK-CF30 composite/steel pair was extensively investigated in function of contact parameter and contact conditions (unlubricated or lubricated) [6–16]. Zhang et al. [10] tested PEEK composites blended with various contents of polytetrafuorethylene and/or graphite and reinforced with various amounts of short carbon fibres, against steel, using a block-on-ring tribometer under unlubricated conditions. According to these authors, the wear resistance of PEEK can be significantly improved by the use of various reinforcements (in particular, short carbon fibres, graphite flakes and PTFE particles), but at the cost of deterioration of some other mechanical properties in some degrees, e.g. toughness and strength. Davim et al. [15, 16] studied the friction and wear behaviour of PEEK-CF30 under dry conditions using statistical techniques.

The objective of the present study was the prediction of tribological behaviour (friction and wear) of PEEK-CF30 with the *pv* factor and sliding distance *S* using back propagation (BP) neural networks.

2. Algorithm and architecture of neural network models

In engineering, the BP algorithm is a kind of a generalized form of the least-mean-squares algorithm [17, 18]. The BP algorithm used in this work has been described elsewhere [19].

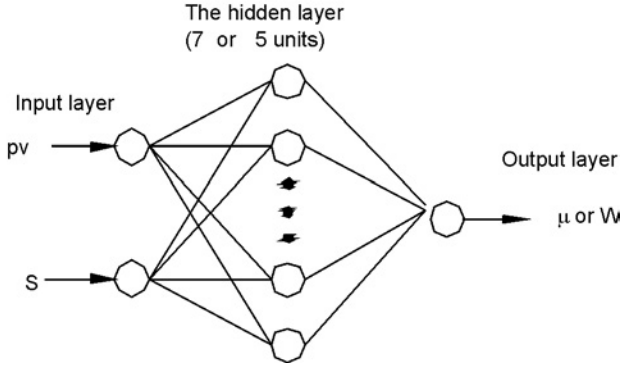

Fig. 1. Scheme of the BP network

The target of the research was to establish non-linear relationships between the input parameters (*pv*, *S*) and the output parameters (μ, *W*) using BP neural networks. Two three-layer neural networks were built and used for predicting the friction coefficient and wear weight loss, respectively, via the neural-network toolbox of Matlab 6.5® [18]. The quantity of nodes of hidden layers was determined by the trial-and-error

method. After trial-and-error computation for many times by the artificial neural network program, the perfect topologies ({2, 7, 1}, {2, 5, 1}) of the two neural networks were obtained (Fig. 1). Sigmoid and pureline transfer functions were employed for hidden layers and output layers, respectively.

3. Training and verifying

3.1. Experimental data

The experimental tests were conducted on a pin-on-disc tribometer. The pin was fixed to the load arm with a chuck. The pin stayed over the disc with two degrees of freedom: a vertical one, which allows normal load application by a pneumatic system, causing direct and permanent contact with the surface of the disc, and a horizontal one, for friction measurement. The temperature on contact was measured in steel disc boundary with an optical pyrometer. All experimental tests were performed with contact temperature of 120 °C. The composite tested in this investigation was the PEEK reinforced with 30 wt. % of carbon fibres (PEEK-CF30) manufactured by Erta®. The counterfaces tested were made of carbon steel Ck45K (DIN) with the arithmetic mean roughness value *Ra* of ca. 0.5 μm. All pins were weighed in a balance with 0.1 mg precision.

To ensure a reasonable distribution and a sufficient information content of the dataset, 30 experimental values of the friction coefficient and wear weight loss were collected, respectively, corresponding to various *pv* factors and sliding distances. Among these, 25 data were selected as training data of neural network, and the residuals were used to verify the predicted results.

3.2. Normalization

In order to relieve the training difficulty and balance the importance of each parameter during the training process, the examination data were normalized. It is recommended that the data be normalized between slightly offset values such as 0.1 and 0.9. One way to scale input and output variables in interval [0.1, 0.9] is

$$P_n = 0.1 + (0.9 - 0.1) \times \frac{P - P_{\min}}{P_{\max} - P_{\min}} \tag{1}$$

P_n is the normalized value of P, and $P_{\max}$ and $P_{\min}$ are the maximum and minimum values of P, respectively.

After the neural network was trained, tested and simulated, it is necessary for the simulating data to be unnormalized in the way corresponding to the normalization. The unnormalizing method is

$$P = \frac{(P_n - 0.1)(P_{\max} - P_{\min})}{0.9 - 0.1 + P_{\min}} \tag{2}$$

where P is the unnormalized value of P_n.

3.3. Training and verifying

After about 10 and 12 cycles of training, the training errors of two networks attained stabilization, reaching about 0.064 and 0.097, respectively, as shown in Figs. 2 and 3.

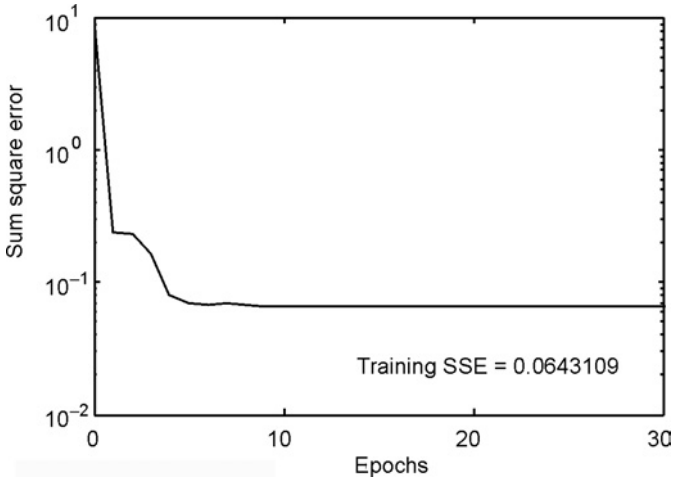

Fig. 2. The training error curve of friction coefficient network

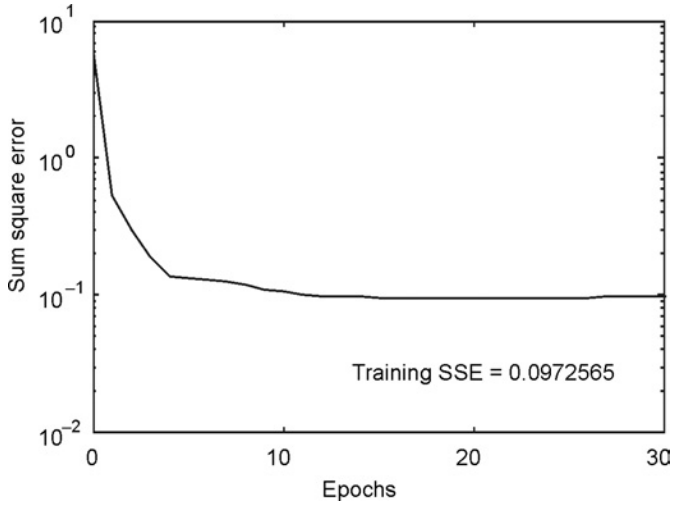

Fig. 3. The training error curve of wear weight loss network

The verifying results of trained data are shown in Figs. 4 and 5. The test results are shown in Table 1; the relative error of all the test data is lower than 15%.

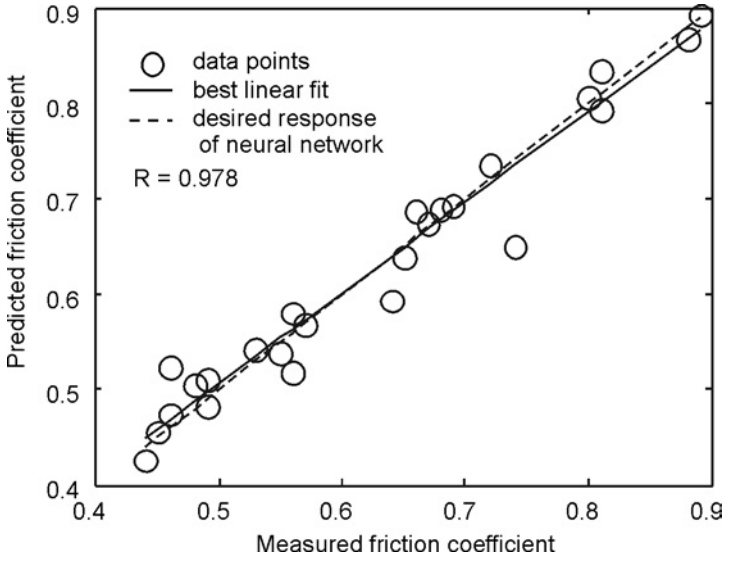

Fig. 4. Verifying results of the friction coefficient of training specimens using the BP neural network

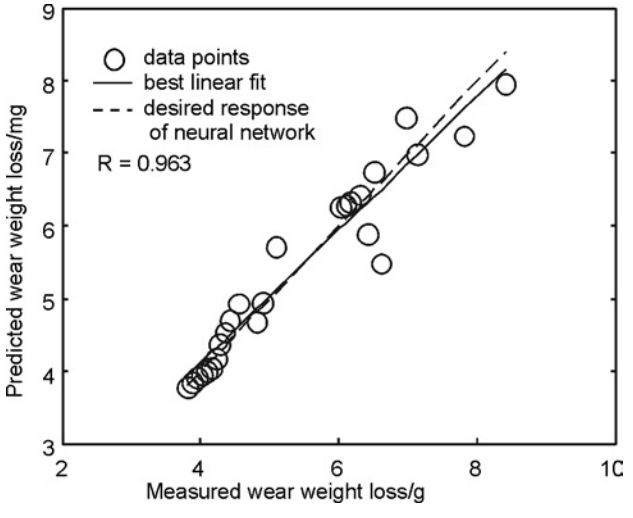

Fig. 5. Verifying results of wear weight loss of training specimens using the BP neural network

These results show that a well-trained network model takes on optimal generalization performance, and has a great accuracy in predicting the friction coefficient and wear weight loss.

Table 1. The tested data, predicted values of BP neural network and error

Inputs		Friction coefficient			Wear weight loss /mg		
pv /MPa·m·s^{-1}	Sliding distance/m	Tested data	Predicted values	Relative error/%	Tested data	Predicted values	Relative error /%
0.5	8000	0.83	0.83	0	6.4	6.5	1.8
1.0	3500	0.60	0.59	–2.5	4.5	4.8	7.9
1.5	8000	0.76	0.78	2.1	6.2	6.4	2.3
2.0	5000	0.59	0.62	4.9	5.0	5.2	5.6
2.5	10000	0.77	0.75	–3.1	6.9	7.7	12.2

4. Prediction and discussion

After neural networks have been successfully trained, all domain knowledge extracted out from the existing samples is stored as digital form in weights associated with each connection between neurons. Results shown in Figs. 6–9 were obtained making a full use of the domain knowledge stored in the trained networks. The figures show the dependences of tribological properties (friction coefficient and weight loss) on the *pv* factor and sliding distance.

4.1. Friction coefficient analysis

Figures 6–8 show the prediction of the coefficient of friction of PEEK CF30 against steel in function of the *pv* factor and sliding distance. The friction coefficient increased upon increasing the sliding distance and decreased upon increasing the *pv* factor. It is important to refer that all the results were obtained for temperatures below the glass transition temperature (T_g = 143 ºC) of the PEEK matrix of the composite. At the contact temperature, approximately 120 ºC, the increase of the *pv* factor facilitates

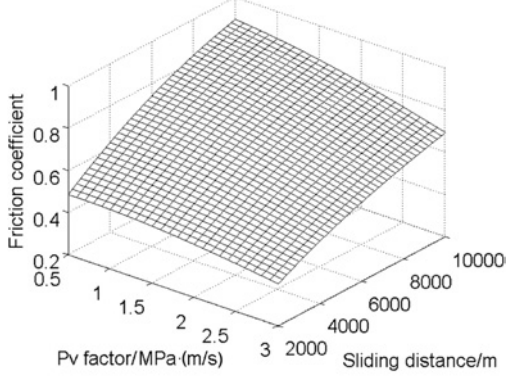

Fig. 6. Prediction for the relationship of the friction coefficient vs. *pv* and sliding distance using the BP neural network

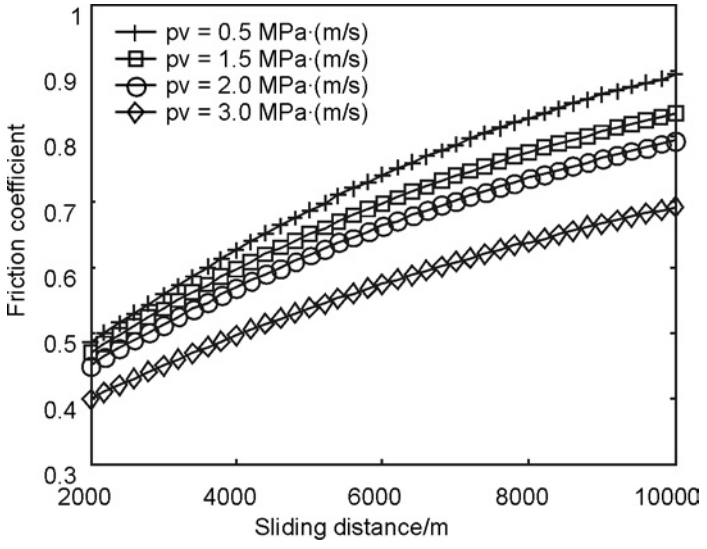

Fig. 7. Prediction for the effect of sliding distance
on the friction coefficient using the BP neural network

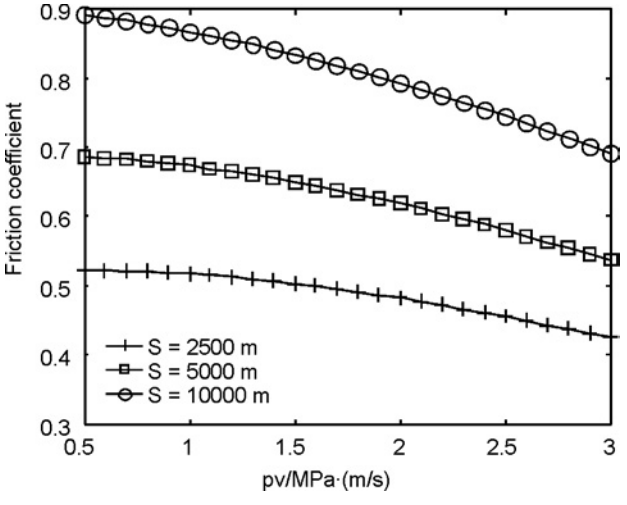

Fig. 8. Prediction for the effect of *pv* factor
on the friction coefficient using the BP neural network

the transference of the PEEK film for the steel counterface. With the increase of the *pv* factor this transfer film formed a uniform and continuous layer on the steel track. In general the increase of sliding distance damages the contact surface, resulting in increasing the friction coefficient. The friction coefficient is highly influenced by sliding distance and in a smaller degree by the *pv* factor.

4.2. Wear analysis

Figures 9 and 10 show the prediction of weight loss of PEEK CF30 against steel in function of the *pv* factor and sliding distance.

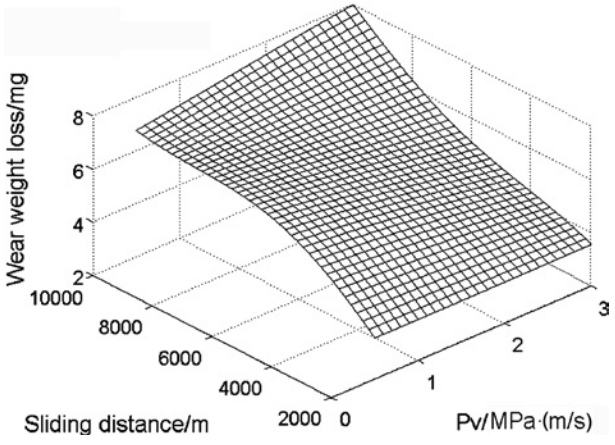

Fig. 9. Prediction for the relationship of wear weight loss vs. *pv* factor and sliding distance using BP neural network

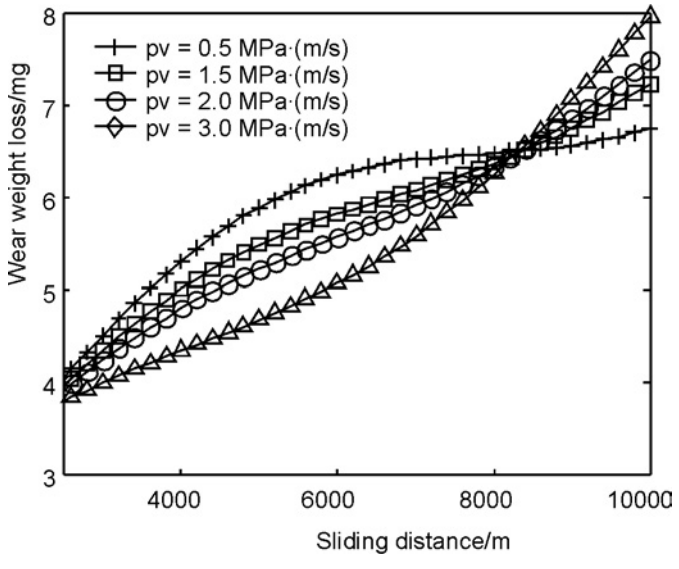

Fig. 10. Prediction for the effect of sliding distance on wear weight loss using neural network

At a small *pv* factor (0.5), the weight loss increases slowly above the sliding distance of 5000 m. On the other hand, at high *pv* values (1.5; 2.0 and 3.0), the increase of the weight loss is slower and nearly linear at small sliding distances, and much

steeper above ca. 7000 m. SEM examinations of the worn surface of PEEK CF30 revealed an increase of fibre breakage and fibre removal from PEEK matrix with the increasing of mechanical action *pv* factor (Fig. 11). The weigh loss is highly influenced by the sliding distance.

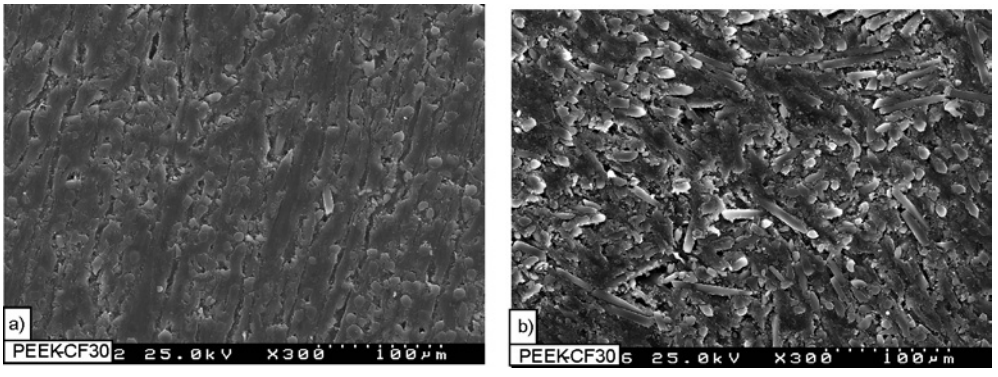

Fig. 11. Worn surface examples of PEEK-CF30 (sliding distance 10 km):
a) $pv = 0.5$ MPa·m·s^{-1}; b) $pv = 3$ MPa·m·s^{-1}

5. Conclusions

The following conclusions can be drawn from friction and wear behaviour of PEEK-CF30 using BP neural networks:

- Non-linear models of the friction coefficient and weight loss of PEEK-CF30 vs. the *pv* factor and sliding distance have been built. The test results show that the well-trained BP neural network models can precisely predict the friction coefficient and wear weight loss according to the *pv* factor and sliding distance.
- The friction and wear is highly influenced by sliding distance and in a smaller degree by the *pv* factor.
- The BP neural networks should be used for modelling the behaviour of the friction and wear in complex tribological systems with care and enough data. The degree of complexity of the investigated material and number of the factors affecting its properties do not allow considering the present results as generally true for all PEEK-based systems.

References

[1] RUTHERFORD K., HATTO P., DAVIES C., HUTCHINGS I.M., Surf. Coat. Techn., 86–87 (1996), 472.
[2] JONES S.P., JANSEN R., FUSARO R.L., Tribology Trans., 40 (1997), 312.
[3] VELTEN K., REINICKE R., FRIEDRICH K., Tribology Int., 33 (2000), 731.
[4] ZHANG Z., FRIEDRICH K., VELTEN K., Wear, 252 (2002), 668.
[5] RAE P.J., BROWN E.N., ORLER E.B., Polymer, 48 (2007), 598.

[6] VOSS H., FRIEDRICH K., Wear, 116 (1987), 1.
[7] FRIEDRICH K., KARGER-KOCSIS J., LU Z., Wear, 148 (1991), 235.
[8] LU Z.P., FRIEDRICH K., Wear, 181–183 (1995), 624.
[9] ELLIOTT D.M., FISHER J., CLARK D.T., Wear, 217 (1998), 288.
[10] ZHANG Z., BREIDT C., CHANG K ., FRIEDRICH K., Tribology Int., 37 (2004), 271.
[11] ZHANG G., LIAO H., LI H., MATEUS C., BORDES J.M., CODDET C., Wear, 260 (2006), 594.
[12] JACOBS O., JASKULKA R., YAN C., WU W., Tribology Lett., 18 (2005), 359.
[13] DAVIM J.P., MARQUES N., Tribology Lett., 11 (2001), 91.
[14] MARQUES N., DAVIM J.P., Key Eng. Mater., 230–232(2002), 487.
[15] DAVIM J.P., CARDOSO R., Ind. Lubr. Tribology, 10 (2005), 181.
[16] DAVIM J.P., CARDOSO R., Mater. Des., 27 (2006), 338.
[17] LIUJIE X., DAVIM J.P., CARDOSO R., J. Mater. Proc. Techn., 189 (2007), 374.
[18] GUO JING YANG ZHANGYU, *Analysis and Design of Neural Network Based on Matlab6.5*, Publishing House of Electronic Industry, Beijing, 2003, 313–319.
[19] LIUJIE X., JIANDONG X., SHIZHONG W., YONGZHEN RUI L., Mater. Des., 28 (2007), 1425.

Received 25 April 2007
Revised 16 November 2007

Materials Science-Poland, *Vol. 26*, *No. 3*, *2008*

Morphology expression and proliferation of human osteoblasts on bioactive glass scaffolds

Z. ZHOU[1*], L. CHEN[2]

[1]College of Chemistry and Chemical Engineering, Hunan University of Science and Technology, Xiangtan 411201, P.R. China

[2]Department of Orthopedics, the Second Xiangya Hospital, Central South University, Changsha 410011, P.R. China

Bioactive glass was designed as a scaffold to be used for bone reconstruction or regeneration. Bioactive glass scaffold with pore sizes ranging from in 100 μm to 400 μm in diameter was fabricated by the sol-gel method, and the biocompatibility evaluation of bioactive glass scaffolds was also performed by culture *in vitro* models. Cells cultured in the extracts of bioactive glass appeared to show normal morphology. The scaffolds supported osteoblast growth and induced differentiation within the 21 day culture period. Confocal laser scanning microscopy demonstrated a normal cell distribution and proliferation on porous biomaterials. Osteoblasts attached and proliferated on the scaffold as demonstrated by scanning electron microscopy (SEM). Nodule formation and multilayer structures were observed on the scaffold surface and in the pores of the glass. The relationship between seeding density and viability of human osteoblasts cultured on the porous bioactive glass were measured.

Key words: *bioactive glass scaffold; morphology; proliferation; human osteoblasts; biomaterials*

1. Introduction

Bioactive glass and ceramic materials have been given a lot of attention as candidates for implant materials since they possess certain highly desirable characteristics for some clinical applications of human skeleton substitution, heart values renewing, dental crown repairing [1, 2]. An ideal scaffold for bone tissue engineering applications should fulfil several criteria. First, the scaffold should be biocompatible (non toxic) and act as a three-dimensional (3D) template for *in vitro* and *in vivo* bone growth [3]. It therefore must consist of an interconnected macroporous network with a modal interconnected pore diameter of at least 100 μm to allow cell migration, bone

* Corresponding author, e-mail: zhou7381@sohu.com

ingrowth and eventually vascularization [4, 5]. The scaffold material should be the one that promotes cell adhesion and activity and ideally stimulates osteogenesis at the genetic level [6] so that a tissue engineered construct can be grown *in vitro*, ready for implantation. This construct should have mechanical properties matching those of the host bone. The scaffold should bond to the host bone, creating a stable interface and the scaffold should then resorb at the same rate as the bone is regenerated, with non-toxic degradation products.

Bioactive glass material used to repair and substitute human hard tissue is a new branch of material field and is to be gradually noticed in the field of medicine and clinic. Bioactive glass was chosen as a scaffold material because bioactive glasses bond to bone and stimulate bone growth (osteoinduction) [6]. Bioactive glass may meet biological requirements for its composition and microstructure should be similar to those of hard tissue of human beings. Even though the mechanical performance of bioactive glass cannot be matched to human hard tissue (bone and tooth), bioactive glass can be used as scaffolds to allow cell growth and be helpful to promote bone reconstruction or regeneration in the way of tissue engineering. In many cases, mechanical properties are much less important compared with biological features [7]. For example, due to excellent mechanical properties, metallic implants or prostheses are used to connect broken bones. However, stress that must be transformed by bone is impaired by the metallic implants, consequently, there is no stress to stimulate tissue growth at the broken bone ends, and the bone reconstruction would stop soon. On the other hand, if biodegradable implants such as bioactive glass are used as scaffolds, cellular tissue can grow into the pores in the scaffolds and partial stress will pass through the broken ends which may result in a stimulation action to accelerate bone reconstruction. In the present paper, biodegradable bioactive glass scaffolds were fabricated and modulated by cell culture before the scaffolds are moved into human body [8]. The initial response of human osteoblasts to bioactive glass scaffolds was investigated. Some biological performances related to both material feature and cell characters are revealed in this study.

2. Experimental

Fabrication of bioactive glass scaffolds and their characterization. The composition of porous glass is: SiO_2 (60 mol %), CaO (35 mol %), and P_2O_5 (5 mol %). First, bioactive glass powder was prepared by the sol-gel method [9]. Sol was prepared from tetraethylorthosilicate (TEOS), deionized water as a solvent, hydrochloric acid as a catalyst, and calcium nitrate and TEP as CaO and P_2O_5 precursors. The synthesis was carried out at a low pH causing a spontaneous gelation owing to hydrolysis of TEOS and subsequent condensation of formed Si–OH groups. The sol was kept 3 days at room temperature, to allow the hydrolysis and polycondensation reactions, until the gel was formed. For aging, the gel was heated at 60 °C for 3 days. The dried gel was heated at 160 °C for 2 days, then was ground for 8 h. Then the bioactive glass powder

was blended with foams and polyvinyl solution to obtain slurry, which was soaked by a porous organic material [10]. Finally, the specimen was sintered at 700 °C for 3 h. Pore size in specimen was controlled by pore size in the porous organic material.

Scanning electron microscopy (SEM) on gold-coated specimen was used to examine the morphological and textural features of the sample, using an accelerating voltage of 15 kV. X-ray diffraction (XRD) trace was obtained of the sample using a Philips PW1700 series automated XRD spectrometer, using a step scanning method with CuK_α radiation in Θ–2Θ scans and grazing incidence 2Θ scans. Macropore size distributions were determined by intrusion mercury porosimetry (Poresizer 9320, Micromeritics, U.S.A.). The mesopore diameter distribution was calculated by the BJH method [11] applied to the desorption curves, and micropore analysis was determined by the Horvath and Kawazoe method [12].

Proliferation and morphology of cell cultured in the extract. The cytotoxicity of the scaffold was assessed by preparing aqueous extracts according to the recommended method of International Standards Organisation (ISO) [13]. Stroma osteoblastic cells were obtained from the marrow of young adult male. The tissue culture plastic polystyrene was used as non-toxic negative control material and tin-stabilised (tributyltin) polyvinylchloride was used as the positive toxic control material. Before preparing the aqueous extracts, the bioactive glass discs were sterilized in an autoclave. The control material discs were immersed in 70% (volume fraction) ethanol for 1 h prior to treatment with PBS containing 100 units/cm^3 penicilin and 100 μg/cm^3 streptomycin for 1 h. Then all the discs were immersed in the extracting media for preparation of the extracts. The extract media were Dulbecco's modification of eagles medium (DMEM) supplemented with 10% foetal calf serum (FCS), 50 units/cm^3 penicillin and 50 μg/cm^3 streptomycin for cells. The ratio of the volume of the extractant to the surface area of the material was 1 cm^3/cm^2. The extraction process was carried out in a water bath at 37 °C in 75 cm^3 flasks which were shaken at a speed of 60–65 rev/min. After extracting for 48 h, the extracts were passed through a 0.22 μm filter, then stored at –20 °C. Cell attachment and cell morphology were observed under the reverse microscope.

Cell culture and proliferation on the scaffolds. For cell culture studies, scaffold samples were cut to 8×8×4 mm^3 and fixed to 24-well polystyrene culture plates using 2% agar (to prevent floating). The entire well plates were then sterilized under ultraviolet (UV) light for 1 h. The samples were then incubated in DMEM, supplemented with 1% (v/v) penicillin/streptomycin, at 37 °C for 72 h (preconditioning). Cell seeding was performed by addition of a concentrated cell suspension in a drop-wise manner to ensure cell loading directly onto the foams. After 10 days, other unattached cells were removed from the flasks by repeatedly washing with PBS. With confluent monolayers reached, cells were enzymatically lifted from the flasks by trypsin.

Aliquots of 50 mm^3 of cell suspensions with cell seeding densities of 5×10^3, 1×10^4, 5×10^4, 1×10^5, 1×10^6 and $5\times10^6/cm^2$ were seeded on the top surface area of the bioactive glass scaffolds (specimen) which were mounted in the 24 well polystyrene culture plats, respectively. The scaffolds were left undisturbed in an incubator for 45 min to allow the cells to attach to the scaffolds，after which time an additional 2 cm^3 culture medium containing 20 mm^3 dexamethasone was added to each well. Medium was changed every 2 days. At time intervals of 1, 2, 3, 4, 5, 6 weeks, cells in the scaffolds were washed three times by PBS，and deattached by trypsin solution. Cell numbers were determined both by heamocytometer counter and by a fluorometric quantification of DNA by an assay adapted from West. Cells were visualized in the confocal laser scanning microscope (CLSM) studied by staining the sample with ethdium and phalloidin.

For SEM observation, the specimens cultured for 21 days were dehydrated in a graded series of methanol prior to critical-point drying. The disks with the cultured cells were mounted on the aluminium stubs and coated with gold in a sputtering apparatus, and finally the specimens were examined at 15 kV under a scanning electron microscope.

Total protein determination of cells cultured on materials. To investigate cell proliferation and colonization rate on the materials, osteoblastic cells were cultured on the materials placed in 24 well plates with cell seeding densities of $5\times10^4/cm^2$. After seeding 1 h, 1.5 cm^3 culture medium was added to each well and the samples were incubated as before. At 24 h intervals the medium in the each row (4 wells) was removed and the cells washed with PBS to remove all the traces of the culture medium. On the 8th day, the final row was taken, and the cell protein in all the wells was solubilised using 1 cm^3 0.5mol/dm^3 NaCl and total protein content determination by the modified Lowry assay. Briefly, to each well, 100 mm^3 of 0.1 M NaOH was added and the plates were then covered with mylar film. The plates were swirled gently over night before 50 mm^3 of the cell lysates were transferred to a new 24 well plate together with bovine serum albumin (50 mm^3 of 0.063–1.0 μg/cm^3) as a standard. 200 mm^3 of the solution containing 50 cm^3 of 2% Na_2CO_3 dissolved in 0.1 M NaOH mixed with 0.5 cm^3 of 1% $CuSO_4$ and 0.5 cm^3 of 2% Na-K-tartrate was added to each well and the plates were swirled for exactly 10 min. 50 mm^3 of the Fohlin–Ciocalteu phenol reagent (diluted 1:5) was then added to each well and the plates were again left to swirl for 30 min. Absorbance was monitored at 690 nm using a Labsystems iEMS Reader MF. For comparison, a control group of cells was cultured in the 24 well plates (made of polystyrene) without materials.

Statistical analysis. All measurements were collected and expressed as mean standard deviations. Single factor analysis of variance was employed to assess the statistical significance of results for all biological experiments.

3. Results

3.1 Materials characterization

The XRD study of the bioactive glass confirms that the material is amorphous (Fig. 1) because no diffraction maxima are observed and only a broad band for 2Θ between 10° and 50° is detected for the gel bioactive glass.

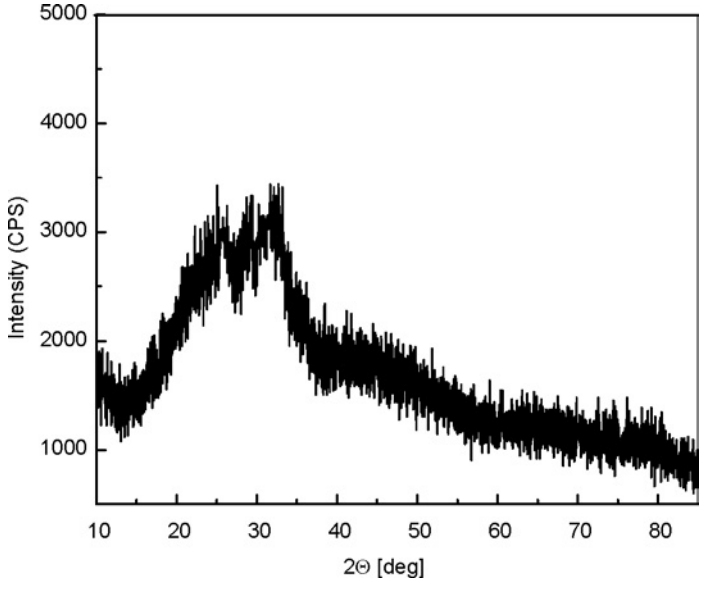

Fig. 1. XRD of bioactive glass

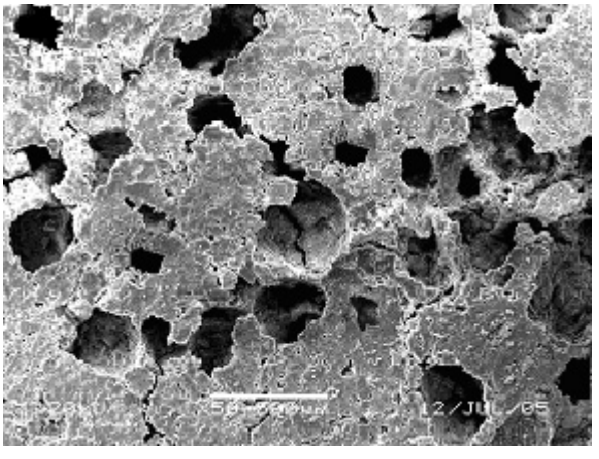

Fig. 2. SEM of bioactive glass scaffold obtained by the sol-gel method

SEM in Fig. 2 shows typical macroporous structure of the bioactive glass scaffolds with pore size ranged within 100–400 μm, which is 10–20 diameters of human osteoblast. The average pore size diameter is 55.75 μm and the pore volume is 0.435 cm^3/g measured by low pressure mercury intrusion porosimetry. Porous glass has a narrow and small pore size distribution in mesoporous scale with diameters in the range of 2–50 nm. The micropores in samples are mostly between 0.5 and 1 nm and the distributions are almost identical. Macropore size in scaffold is very important because cell growth in pores requires enough nutrition and metabolism. Too small pore size will limit cellular metabolism and also limit the cells to move into the pores. For cell growth in the pores, cell number must be sufficient because the environmental condition must be met for cell proliferation which depends on cell communication each other. The lower the cell density, the less information, the lower proliferation rate [14].

3.2. Cell morphology cultured in the extracts

Figure 3 shows the morphological observation of osteoblastic cells cultured in the extracts and the control. Cells appeared to show normal morphology in both the negative control (Fig. 3b) and extracts (Fig. 3c) with cell sizes ranging from 10 to 20 μm in diameter. Cells attached to the culture plate, and cells round in shape were in state of

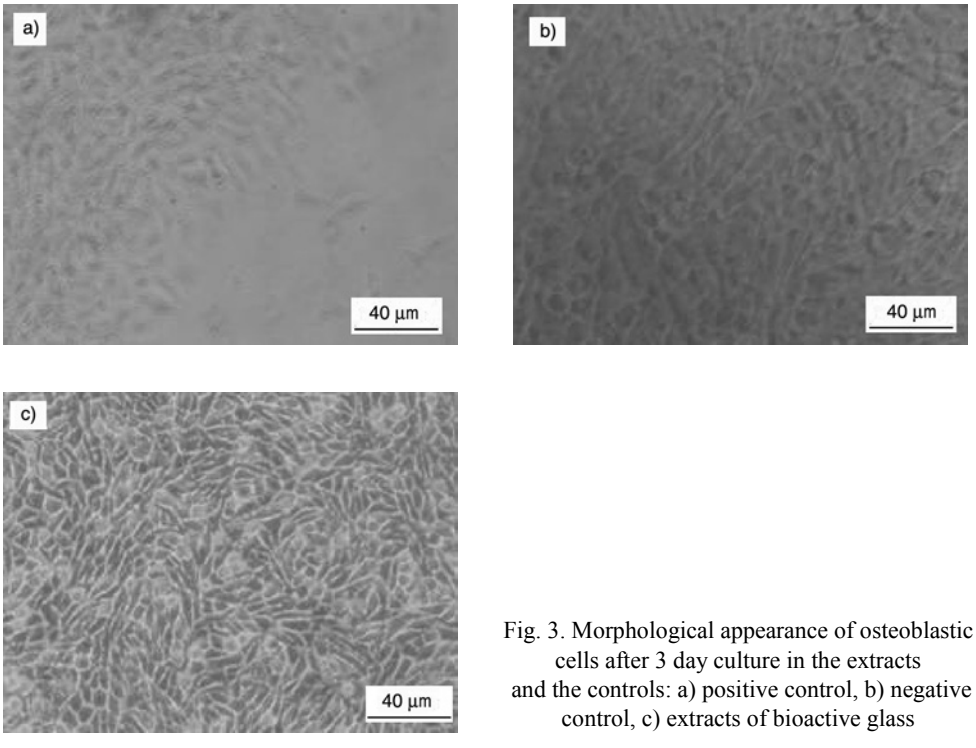

Fig. 3. Morphological appearance of osteoblastic cells after 3 day culture in the extracts and the controls: a) positive control, b) negative control, c) extracts of bioactive glass

synthesis of DNA (cell mitosis) which indicated that cells had strong generation abilities. However, it is apparent that the number of cells was increased in glass extract more than that in negative control. This indicated that bioactive glass extracts can promote cell growth and differentiation. After 3 day exposure to the positive control, almost all of the cells died and detached of the bottom of the culture plate (Fig. 3a). These results showed no toxicity was present in bioactive glass materials, and the positive control was severely toxic and caused a marked detachment and death in cell culture.

3.3. CLSM and SEM observation

As a result observed by CLSM (Fig. 4), after stained with ethdium and phalloidin, human osteoblast cells with the nucleus in the colour of red grew well on the surface of materials. Cells were observed to attach and spread on the scaffold structures. Cell morphology image showed elongated ellipses, with long processes extending from the cell body. In porous materials, cells grew along the walls of the pores and penetrated down to the bottom of many pores. There were some changes in the cell morphology depending on the shape of the pore wall.

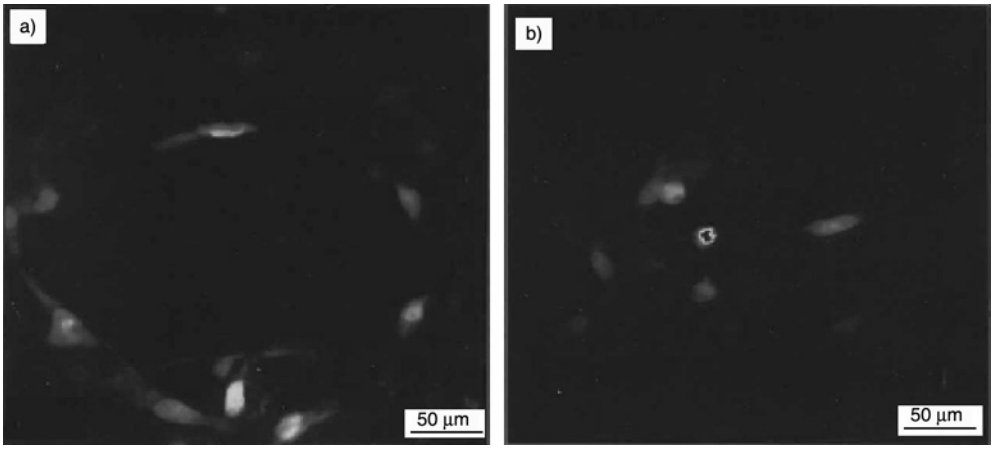

Fig. 4. CLSM images of cells in pores: a) 20 µm from the surface, b) 40µm from the surface

Mineralized nodule formation is basically considered to be the final result of differentiation and function of the osteoblasts. Figure 5 shows the osteoblasts morphology on the bioactive glass scaffold, where cells have been cultured for 21 days. Cells formed multilayer structures on surfaces of the materials (Fig. 5a), and nodule structures where mineralization occurs can be observed. The nodules were connected to the cell surface by extracellular fibres. The same multilayer structures and nodules were formed in scaffold pore, and cells attach and spread as shown in Fig. 5b. We found many nodules of various sizes and shapes on the cell multilayer. Cells surrounded collagenous matrix, matrix vesicles, and minerals. The rough surface of the porous

material may result in an uneven distribution of cells. Also some cells may migrate into and grow in the deep pores. Therefore, the cell distribution on the porous material surface is different from place to place.

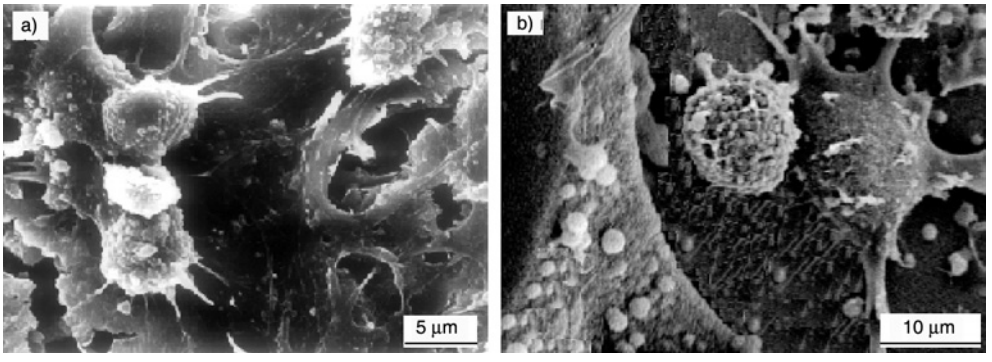

Fig. 5. SEM of human osteoblasts cultured on bioactive glass scaffold surface (a) and within a pore (b) for 21 days

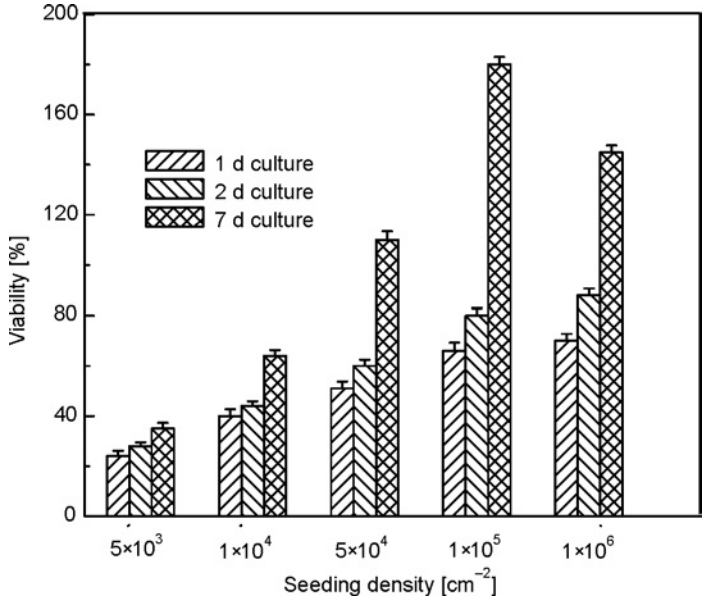

Fig. 6. Viability of human osteoblasts cultured on a bioactive glass

Cell proliferation at the surface of bioactive glass was measured by determining the increase in DNA content up to 7 days (Fig. 6). The proliferation results indicate a correlation between culture time and cell proliferation. Cell viability increased with the increase of culture time, there were statistically significant differences in cell viability between 7 day culture and fresh ones when seeding density exceeded $1\times10^4/cm^2$. On the other hand, cell viability was significantly influenced by seeding den-

sity, as shown in Fig. 6. For cell healthy growth, seeding density at least of $1\times10^4/cm^2$ is required; otherwise, cells in pores will die due to less information among cells.

3.4. Total protein determination of cells culture on materials

Proliferation of the human osteoblasts was measured quantitatively in terms of protein content on the materials (Fig. 7). Our results showed that total protein increased gradually in all cultures from day 1 up to day 6, then decreased, thereafter increased again after day 8. During the early stages of culture (days 1-4), no differences was noted between the bioactive culture and the control. However, on day 6 the total protein was significantly higher in the bioactive culture when compared to control cultures. From the results of protein assay, osteoblasts proliferation is more rapid on bioactive glass than on polystyrene, which indicates bioactive glass has the stimulating effects to promote cell proliferation rate.

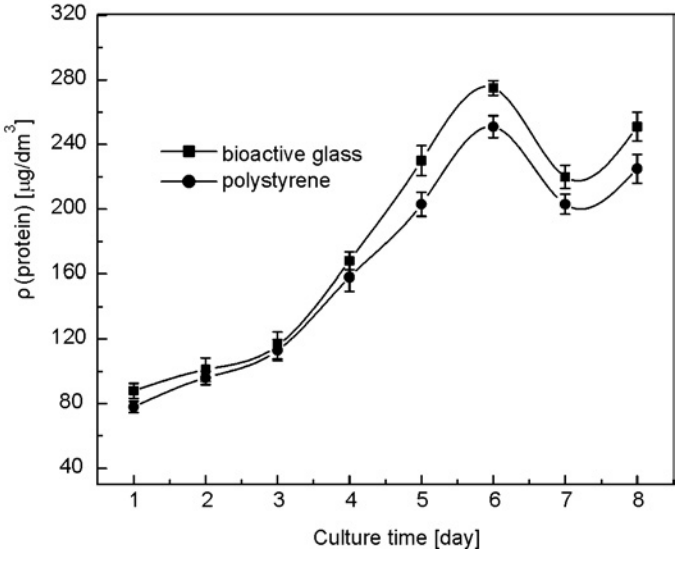

Fig. 7. Proliferation in terms of total protein of cells on bioactive glass compared with the cell culture on polystyrene culture plates

4. Discussion

An ideal scaffold would be the one that mimics the extracellular matrix of the tissue that is to be replaced so that it can act as a template in three dimensions onto which cells attach, multiply, migrate and function. The biological characteristics of bioactive glass based materials when used as implants depend on many factors such as

material composition, microstructure, porosity, and pore structure (morphology and size) [10].

Bioactive glasses are amorphous silica based materials that are biocompatible, bioactive, osteoconductive, and even osteoproductive [15]. Their bone bonding ability has been attributed to the formation of a hydroxycarbonate apatite (HCA) layer in the surface of the glass on contact with body fluid [16]. The composition and structure of the HCA layer is similar to that of bone mineral, hence a strong bond can be formed. An important discovery for the development of regenerative medicine is that dissolution products from bioactive glasses exert a genetic control over osteoblast (bone progenitor cells) cell cycle and rapid expression of genes that regulate osteogenesis and the production of growth factors [17, 18]. Silicon has been found to be a major contributor to the mineralization of bone and gene activation, which leads to the substitution of silicon for calcium into synthetic hydroxyapatite. *In vivo* results showed that bone ingrowth in silicon substituted HA granules was significantly greater than that into phase pure HA granules [16].

In the present investigation, an excellent biocompatibility of bioactive glass has been demonstrated by the *in vitro* cell growth on the material. Normal morphology of cells was retained after culture on material, and the cells were able to attach and grow on the material surface as well in deep pores within the materials. Primary human osteoblasts were observed to attach, spread, proliferate and form mineralized nodules when cultured on bioactive glass materials. Extensive nodule formation on the scaffolds was observed by SEM.

CLSM is an important method in many areas of biological and medical research. By confocal scanning, the out-of-focus-blur can be eliminated. The illumination is restricted to a single point and almost all the light emission from regions above and below the focal plane of a CLSM is physically prevented. A clear image can be obtained. Compared with SEM observation, CLSM is more favourable to observe cells in situ and to investigate the cell biological components and cell substructure by using staining. Specially, by CLSM the cells on different layers behind the first layer can be clearly observed and their shape measured. Therefore, the cells attached to the pore wall in the porous material could be scanned step by step down to the deep pore and numbers of cells at precise depths throughout the substratum could be estimated. A difficulty in our research was that neither CLSM nor SEM is able to observe cells which have moved into the lateral pores within the material.

During bone regeneration by autogenous osteoblast sterilized from stem marrow cells, the scaffolding materials used in this approach must allow the attachment of osteblasts because they are anchorage-dependent cells that require a supportive matrix in order to survive and proliferate. This approach shows that osteoblast can attach to the bioactive glass scaffolds. Subsequently, human osteoblasts populated the constructs by the proliferation of the transplanted cells and the migration of cells into the construct from the surrounding tissue while the bioactive glass gradually degrades or

partly degrades. Eventually, the construct is filled with calcified extracellular matrix secreted by the osteoblasts and is devoid of the synthetic biodegradable bioactive glass.

Cell proliferation on the materials was assessed by measuring total protein content by the Lowry method. Previous studies [17, 18] have shown that measurement of the total cell protein in proliferating cell cultures correlates well with cell numbers throughout the log phase of growth. As the osteoblasts approach confluence, they produce extracellular matrix on the materials. This is composed predominantly of type I collagen and, although it will contribute to the overall protein content of the cultures, it will not be detected by the Lowry assay. This method detects tyrosine, trytophan, and phenylalanine amino acid residues on protein molecules, whereas collagen, being mainly composed of glycine, praline and hydroxyproline, is not detected. The protocol used for the Lowry assay ensures that only attached cells are measured, and it is assumed that to remain attached to the materials the cells must be viable. Thus, the protein content is equivalent to the number of viable cells.

Cell viability was significantly influenced by seeding density. We failed to culture cells at low seeding densities on porous materials if the material had not been immersed in culture medium. We believe that there are two factors producing this effect. One is related with the cells themselves. Growing cells need to communicate with each other, and at low density due to lack of communication, cell colonization in deep pores would be impaired. The other factor results from the material surface. Higher bioactivity of material surface will induce acute inflammation by metabolism and secretion will impair after cells phagocyte the materials.

5. Conclusions

Bioactive glass scaffolds support the attachment, proliferation and mineralized nodule formation of human primary osteoblasts. It provides an appropriate environment for the proliferation and differentiation of osteoblasts and allows the ingrowth of vascular tissue to ensure the survival of the transplanted cells. During short culture term, cells displayed normal morphology features and migrated into deep pore. Multilayer structures and nodules were formed on the scaffold surface and in the pores of the glass. The result of total protein assay reviews that bioactive glass has the stimulating effects to promote cell proliferation rate. This scaffold therefore has potential in bone tissue regeneration.

Acknowledgements

This project has been financially supported by the National Natural Science Foundation of China (No. 50174059).

References

[1] TAKEZAWA T. A., Biomater., 24 (2003), 2267.
[2] HENCH L.L., POLAK J.M,. Science, 295 (2002), 1014.

[3] JONES J.R., POOLOGASUNDARAMPILLAI G., ATWOOD R.C., BERNARD D., LEE P.D., Biomater., 28 (2007), 1404.
[4] OKII N., NISHIMURA S., KURISU K., TAKESHIMA Y., UOZUMI T., Neur. Med-Chir., 41, (2001), 100.
[5] FREYMAN T.M., YANNAS I.V., GIBSON L.J., Prog. Mater. Sci., 46 (2001), 273.
[6] HENCH L.L., POLAK J.M., Science, 295 (2002), 1014.
[7] JONES J.R., TSIGKOU O., COATES E.E., STEVENS M.M., POLAK J.M., HENCH L.L., Biomater., 28 (2007), 1653.
[8] VITALE-BROVARONE C., VERNE E., ROBIGLIO L., APPENDINO P, BASSI F., MARTINASSO G., MUZIO G., CANUTO R., Acta. Biomater., 3 (2007), 199.
[9] ZHOU Z.H., RUAN J.M., ZOU J.P., ZHOU Z.C., SHEN X.J., J. Cent. South Univ. Technol., 3 (2007), 301.
[10] JONES J.R., HENCH L.L., J. Biomed. Mater. Res., 68 B (2004), 36.
[11] BARRETT E.P., JOYNER L.G., HALENDA P.P., J. Amer. Chem. Soc., 73 (1951), 373.
[12] HORVATH G., KAWAZOE K., J. Chem. Eng. Japan, 16 (1983), 470.
[13] ZHANG K., WASHBUN N.R., SIMON J.C.G., Biomater., 26 (2005), 4532.
[14] JONES J.R., EHRENFRIED L.M., HENCH L.L., Biomater., 27 (2006), 964.
[15] ANDRADE Â.L, VALÈRIO P., GOES A.M., LEITE M.F., DOMINGUES R.Z., J. Non-Cryst. Solids, 352 (2006), 3508.
[16] PATEL N., BEST S.M., BONFIELD W., GIBSON I.R., HING K.A., J. Mater. Sci: Mater. Med., 13 (2002), 199.
[17] XYNOS I.D., EDGAR A.J., BUTTERY L.D.K., HENCH L.L, POLAK J.M., Biochem. Biophys. Res. Commun., 276 (2000), 461.
[18] XYNOS I.D., EDGAR A.J., BUTTERY L.D.K., HENCH L.L, POLAK J.M., J. Biomed. Mater. Res., 155 (2000), 151.
[19] GOUGH J.E., JONES J.R., HENCH L.L., Biomater., 25 (2004), 2039.
[20] PADILLA S., ROMAN J., SANCHEZ-SALCEDO S., VALLET-REGI M., Acta. Biomater., 2 (2006), 331.

Received 30 April 2007
Revised 14 November 2007

Materials Science-Poland, *Vol. 26*, *No. 3*, *2008*

Synthesis, characterization, and visible-light photocatalytic activity of Fe_2O_3/SnO_2 nanocomposites

H. S. ZHUANG[1*], H. L. XIA[2], T. ZHANG[1], D. C. XIAO[1]

[1]College of Environmental Science and Engineering, Donghua University, Shanghai, 201620, P. R. China

[2]Research Institute of Quality and Technical Supervision and Inspection, Taizhou, 318000, P. R. China

A novel, visible-light-activated Fe_2O_3/SnO_2 photocatalyst was prepared by the co-precipitation method, and characterized by X-ray diffraction (XRD), transmission electron microscopy (TEM), N_2 adsorption–desorption measurement and UV-Vis diffuse reflectance spectroscopy. The phase composition, crystallite size, BET surface area and optical absorption of the sample were found to vary significantly with the calcining temperature. The photocatalytic activities of Fe_2O_3/SnO_2 photocatalysts were evaluated based on the photodegradation of acid blue 62 as a probe reaction. Experimental results indicated that the Fe_2O_3/SnO_2 photocatalyst calcined at 400 °C for 3 h (the molar ratio of Fe to Sn is 2:1) exhibited maximum photocatalytic activity due to the sample with a smaller particle size of 15 nm and a higher surface area of 28.8 $m^2 \cdot g^{-1}$. Under visible light ($\lambda > 400$ nm) irradiation, the degradation rate of acid blue 62 reached 98.0% in 60 min, which is about 3.6 times higher than that of the standard P25 photocatalyst. Additionally, the efficient electron–hole separation at the Fe_2O_3/SnO_2 photocatalyst interface may play another important role in photodegradation.

Key words: *photocatalysis; Fe_2O_3/SnO_2; acid blue 62; visible light*

1. Introduction

Semiconductor photocatalysis, as one of the advanced physicochemical processes, has been extensively studied for solving existing environmental problems such as wastewater treatment [1]. The process may proceed at ambient conditions, with the use of solar light as the energy source and atmospheric oxygen as oxidant [2]. Many organic compounds have shown to be oxidized to CO_2, water and mineral acids by this method [3]. Among various oxide semiconductor photocatalysts, TiO_2 was intensively investigated because of its biological and chemical inertness, strong oxidizing power, nontoxicity and long-term stability against photo and chemical corrosion [4, 5]. How-

*Corresponding author, e-mail: huishengzhuang@126.com

ever, there is still a problem that TiO_2 is effective only under ultraviolet irradiation ($\lambda < 380$ nm) due to its large band gap (3.2 eV) [6, 7]. Furthermore, fast recombination of photogenerated electron–hole pairs hinders the commercialization of this technology [8, 9]. Therefore, it is of great interest to separate the electron–hole pairs effectively to increase the photon efficiencies and develop new visible-light-activated photocatalysts to extend the absorption wavelength range into the visible light region. In this sense, an interesting approach to deal with the issue is carried out by a coupled semiconductor technique.

In recent works, there has been a number of studies related to the photocatalytic activity of coupled semiconductor photocatalysts, such as TiO_2/CeO_2 [10], TiO_2/WO_3 [11], TiO_2/SnO_2 [12], ZnO/SnO_2 [13]. These coupled semiconductor photocatalysts may increase the photocatalytic efficiency by increasing the charge separation and extending the photo-responding range. In addition, they also exhibit fine optical properties compared with the corresponding bulk ones due to the quantum confinement effects [14].

In this study, a novel visible-light-activated coupled Fe_2O_3/SnO_2 photocatalyst was synthesized by co-precipitation. In order to optimize the preparation for the photocatalyst, a series of Fe_2O_3/SnO_2 nanocomposites with various calcination temperatures and molar ratios of Fe to Sn were prepared, and their photocatalytic activities were evaluated using the indigoid dye, acid blue 62 (AB62), as a model organic compound. Furthermore, physical and optical properties of the Fe_2O_3/SnO_2 nanocomposites have been explored. To the best of our knowledge, the Fe_2O_3/SnO_2 photocatalyst has not been reported, and it shows significantly high photocatalytic activity in degradation aqueous AB62 solution under visible light irradiation ($\lambda > 400$ nm).

2. Experiment

Reagents. All chemicals used in this study were received from the Shanghai Chemical Reagent Factory of China and used without further purification. $NH_3 \cdot H_2O$, $SnCl_4 \cdot 5H_2O$ and $FeCl_3 \cdot 6H_2O$ were the analytical reagents. The intensity of AB62 is 200%.

Preparation of photocatalysts. Fe_2O_3/SnO_2 nanocomposite powders were prepared by co-precipitation. $SnCl_4 \cdot 5H_2O$ and $FeCl_3 \cdot 6H_2O$ were used as the starting materials, and ammonia (1:1) was used as the precipitator. $SnCl_4 \cdot 5H_2O$ and $FeCl_3 \cdot 6H_2O$ were mixed at various molar ratios and dissolved in a minimum amount of deionized water. The mixed solution was stirred at room temperature and added drop-wise with the ammonia until it transformed to precipitate completely. The precipitate was filtered and washed with deionized water until no Cl^- was found in the filtrates **(**the absence of Cl ions in the filtrate was checked using aqueous $AgNO_3$ solution**).** Then the wet powder was dried at about 100 °C in air to form the precursor of the coupled Fe_2O_3/SnO_2 photocatalyst. Finally, the precursors were calcined for 3 h at varuious temperatures in air to prepare the photocatalyst powders.

Characterization of photocatalysts. To determine the crystallite size and identity of the Fe_2O_3/SnO_2 nanocomposite powders, X-ray powder diffraction (XRD) analysis was carried out using a Rigaku D/max-2550PC diffractometer with unmonochromatized CuK_α radiation (λ = 0.15406 nm), over the 2θ collection range of 0–80°. The particle sizes and shapes of the samples were tested using a Hitachi H-800 Transmission Electron Microscone(TEM). The Brunauer–Emmett–Teller (BET) surface areas were determined using a Micromeritics ASAP 2010 N_2 adsorption apparatus. UV-Vis diffuse reflectance spectra (UV-Vis DRS) were recorded in air at room temperature in the 200–800 nm wavelength range, using a PE LAMBDA35 spectrophotometer with an integrating sphere.

Photocatalytic activity measurements. A 1000 W Xe lamp positioned over the quartz glass reactor was used as the light source and visible-light-activated photocatalytic activity of Fe_2O_3/SnO_2 photocatalyst was tested with all irradiation below 400 nm removed by using a cutoff filter. The distance between the light source and the surface of the solution was 50 cm. In all experiments, the photocatalytic reaction was kept at room temperature, which was achieved by a circulating water jacket (Pyrex).

A set of photocatalytic degradation experiments in aqueous AB62 solution was performed with the following procedure: 0.25g photocatalyst powders were added into 250 ml AB62 solution with an initial concentration of 50 $mg \cdot dm^{-3}$; prior to photoreaction, the aqueous mixture was magnetically stirred in the dark for 30 min to reach adsorption–desorption equilibrium; then the reaction mixture, still stirred, was irradiated by visible light vertically from the top; during the photoreaction, the samples were drawn from the reaction suspension at 10 min time intervals; the collected samples were centrifuged at 10 000 rpm for 10 min, and then filtered through a 0.2 μm millipore filter to remove the particles; The AB62 concentrations of the filtrates were analyzed by UV-Vis spectroscopy (TU-1810) at its maximum absorption wavelength of 595 nm.

3. Results and discussion

3.1. Catalyst characterization

The XRD patterns of the Fe_2O_3/SnO_2 photocatalyst calcined at various temperatures for 3 h are shown in Fig. 1. It can be seen that the XRD pattern of the sample calcined at 300 °C (Fig. 1a) only contains broad reflections of SnO_2 indicating poorly crystallized material. While calcined at 400 °C, the diffraction peaks clearly show that the SnO_2 and Fe_2O_3 nanocrystals co-existed in the samples. With the increase of calcining temperature (at 500 °C), the phase composition is still a mixture of SnO_2 and Fe_2O_3 phases but the diffraction peak intensity obviously increases due to the growth of crystallites and enhancement of crystallization. The average grain size estimated

from the highest intensity diffraction peaks of SnO_2 (2Θ = 33.92) using Scherrer's equation were 6.8 nm, 15.0 nm and 23.7 nm for samples a, b and c, respectively. It is obvious that the crystal sizes of the samples improved with the increase of calcining temperature, while the BET surface areas decreased. These processes are summarized in Table 1.

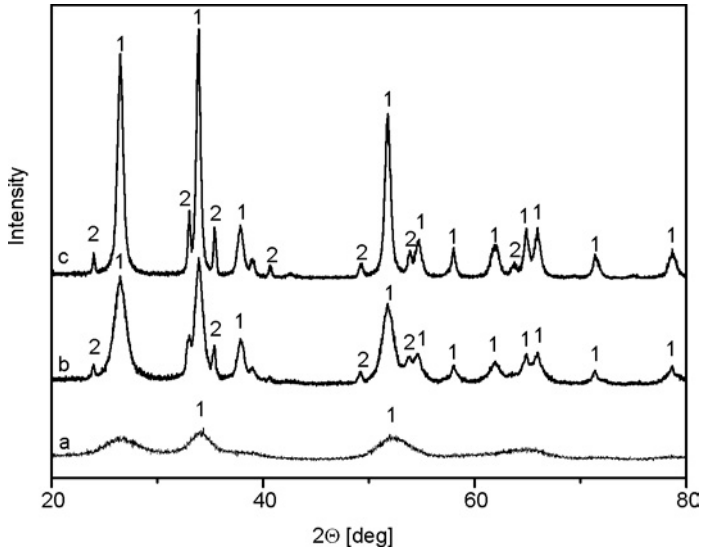

Fig. 1. XRD patterns of the Fe_2O_3/SnO_2 photocatalysts calcined at: a) 300 °C, b) 400 °C, c) 500 °C; 1 – SnO_2, 2 – Fe_2O_3

Table 1. Effect of calcination temperature on the average crystallite size and the BET surface area of the Fe_2O_3/SnO_2 samples

Calcination temperature [°C]	BET surface area[a] [$m^2 \cdot g^{-1}$]	Crystallite size[b] [nm]
300	–	6.8
350	37.4	–
400	28.8	15.0
500	16.0	23.7
600	5.6	36.2

[a]Surface area of the composite Fe_2O_3/SnO_2 photocatalyst powder.
[b]Average crystallite size calculated by applying the Scherrer formula to the highest intensity diffraction peaks of SnO_2(2Θ = 33.92).

The grain size of the Fe_2O_3/SnO_2 nanocomposite varied with calcining temperature, which has been confirmed in the TEM patterns (as shown in Fig. 2). It can be seen that the sample calcined at 300 °C appeared amorphous because of its weak crystallization. The grain edge of the sample was slightly dim (Fig. 2a). The TEM images also indicated that the grain size was homogenous and fairly small (about 15 nm)

when the sample was calcined at 400 °C. By contrast, the sample calcined at 500 °C displayed greater particle size, which is estimated to be about 25 nm due to the enhancement of crystallization or sintering between smaller particles. An increase in the calcining temperature caused the Fe_2O_3/SnO_2 photocatalyst particles to become larger. The result was in agreement with that of XRD.

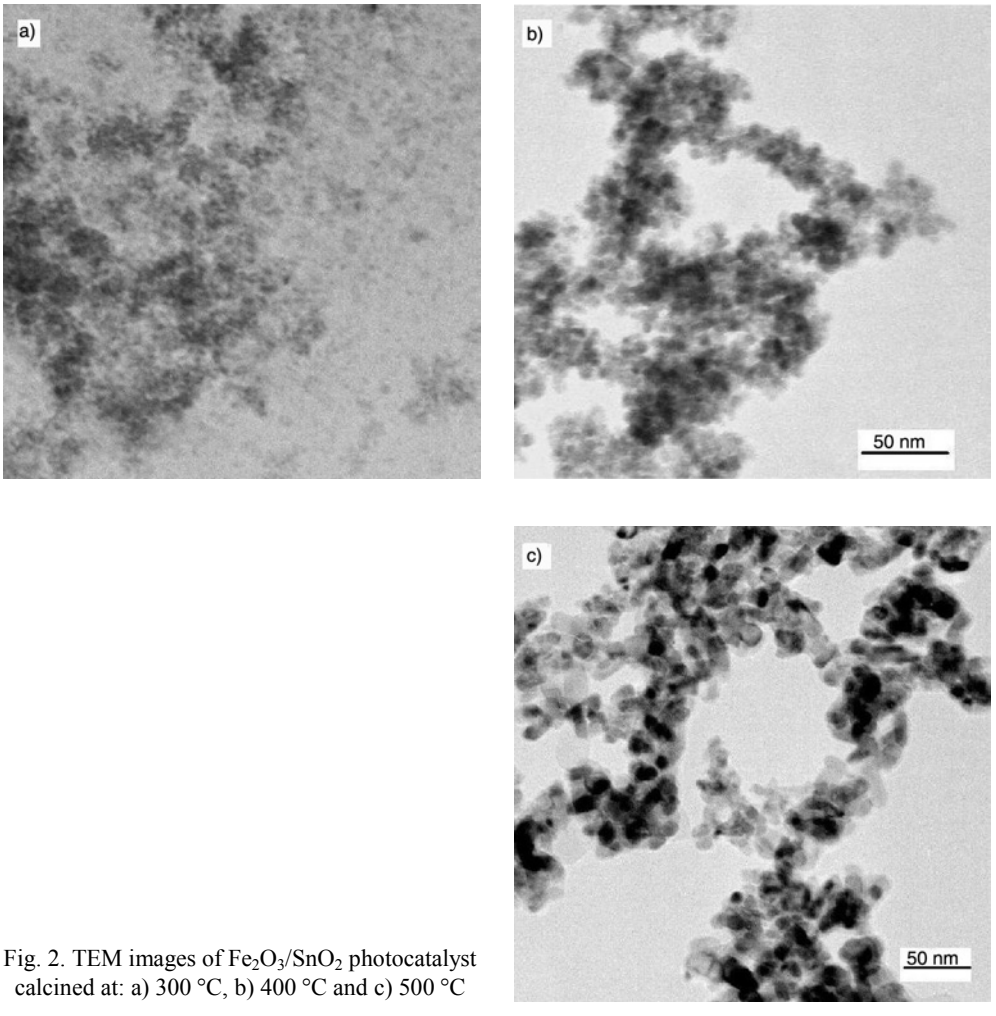

Fig. 2. TEM images of Fe_2O_3/SnO_2 photocatalyst calcined at: a) 300 °C, b) 400 °C and c) 500 °C

Figure 3 gives the UV-Vis-DRS of the Fe_2O_3/SnO_2 photocatalysts calcined at 300, 400 and 500 °C, respectively. It can be seen clearly that the intensity of reflectance is reduced with the increase of calcination temperature. This implies that the absorption edges of the samples shift to the longer wavelength range [15]. The wavelengths of absorption edges were determined by extrapolating the horizontal and sharply rising portions of the curve and defining the edge as the wavelength of the intersection [16]. When calcined at 300 °C, the sample has a little absorption in the range of visible light

and the absorption edge is about 460 nm. With the increase of calcining temperature (reached 400 °C), the absorption edge of the sample has a red-shift of about 20 nm.

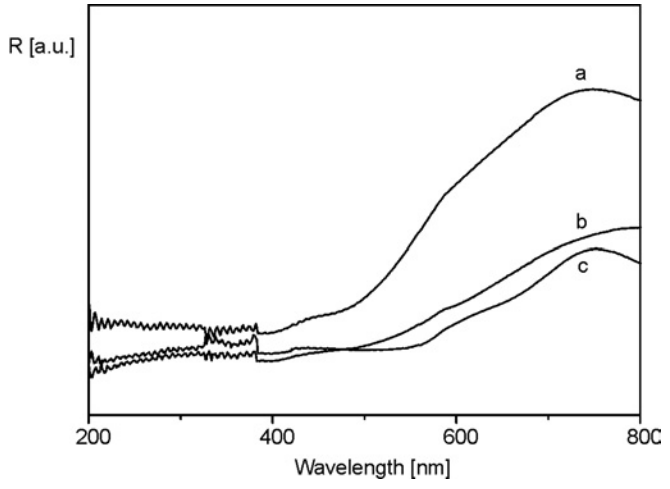

Fig. 3. UV-Vis-DRS of the Fe_2O_3/SnO_2 photocatalys calcined at: a) 300 °C, b) 400 °C and c) 500 °C

The red shift is presumably ascribed to the formation of the fairly homogenous Fe_2O_3 nanocrystals. The bandgap energy of Fe_2O_3 is 2.2 eV and it can be activated by the light below 563 nm [17], when it couples with SnO_2 semiconductor, the conduction band of SnO_2 acts as a sink for photogenerated electrons. The photogenerated holes move in the opposite direction, accumulate in the valence band of Fe_2O_3 particles, which leads to an increase in charge separation efficiency and extends the photo-responding range to visible light.

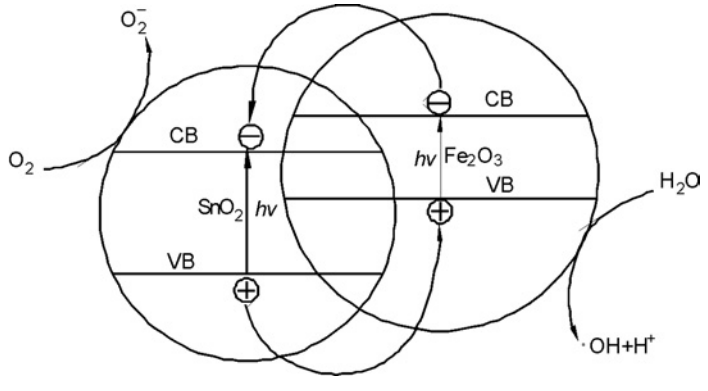

Fig. 4. Sketch map of photocatalytic mechanism of the coupled Fe_2O_3/SnO_2

The sketch map of photocatalytic mechanism of the coupled Fe_2O_3/SnO_2 is shown in Fig. 4. When the calcining temperature reaches 500 °C, the crystallite size becomes

larger, the sample shows more red shift (the absorption edge is about 530 nm) which is consistent with the result obtained by Yu et al. [18].

3.2. Photocatalytic activity studies

3.2.1 Effect of the preparation condition

It is well known that calcining temperature has a significant effect on the activity of the catalysts. Figure 5 shows the dependence of visible light photocatalytic activity on calcining temperature. It is displayed that the Fe_2O_3/SnO_2 nanocomposites calcined at 300 °C, 400 °C and 500 °C for 3 h showed higher photocatalytic activity, respectively. In the range of calcining temperature, the sample calcined at 400 °C reaches the highest photocatalytic activity with AB62 solution almost completely degradation in 60 min which may be attributed to the sample with good crystallization and high surface area. However, the photocatalytic activity of the photocatalyst decreased slightly when the calcining temperature decreased from 400 °C to 200 °C due to the weak crystallization. On the other hand, the photocatalytic activity decreased significantly when the calcining temperature increased from 500 °C to 700 °C: probably because of the decrease of surface area or occurrence of some sintering, although it had better crystallinity.

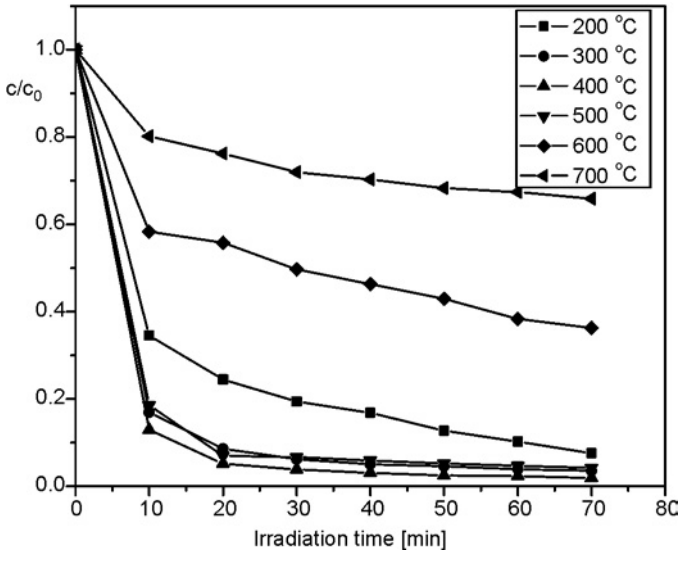

Fig. 5. Photocatalytic activity of the Fe_2O_3/SnO_2 photocatalysts calcined at various temperatures

The photocatalytic activities of the Fe_2O_3/SnO_2 nanocomposites with different molar ratios of Fe to Sn calcined at 400 °C for 3 h is shown in Fig. 6. It can be seen from Fig. 6 that pure SnO_2 showed lower photocatalytic activity compared to pure Fe_2O_3.

Therefore, the SnO_2 content should be an important factor affecting the photocatalytic activity of the Fe_2O_3/SnO_2 nanocomposite. It is obvious that the coupled Fe_2O_3/SnO_2 photocatalyst displayed higher photocatalytic activity than pure Fe_2O_3 and SnO_2, and the photocatalytic activity changed with the different molar ratio of Fe to Sn. The optimum molar ratio of Fe to Sn was 2:1, at which the photocatalytic activity of the coupled Fe_2O_3/SnO_2 photocatalyst was about 1.6 times that of the Fe_2O_3, and 5.5 times that of the SnO_2. The enhancement in the photocatalytic activity may be explained in terms of synergetic effect on the specific adsorption property and efficient electron–hole separation at the Fe_2O_3/SnO_2 interface.

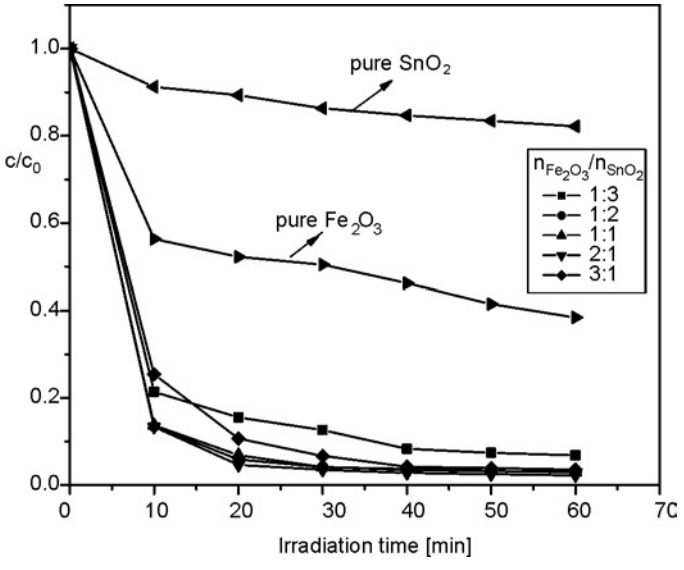

Fig. 6. Photocatalytic activity of the Fe_2O_3/SnO_2 photocatalyst with various molar ratios of Fe to Sn

Further increase in the SnO_2 or Fe_2O_3 content led to a decrease in the photocatalytic activity of the coupled Fe_2O_3/SnO_2 photocatalyst because of the lower photocatalytic activity of SnO_2 or the weaker crystallization of Fe_2O_3 at the same conditions. Therefore, for the Fe_2O_3/SnO_2 photocatalyst, the optimum photocatalytic activity in the range of our experiments appeared when the molar ratio of Fe to Sn is 2:1. A detailed theoretical explanation is in progress.

3.2.2. Comparison of photocatalytic performance

In order to explore the photocatalytic activity and stability of the Fe_2O_3/SnO_2 photocatalyst calcined at 400 °C for 3 h (the molar ratio of Fe to Sn being 2:1) under visible light ($\lambda > 400$ nm), the photocatalytic behaviour of the standard photocatalyst Degussa P25 was also measured as a reference. The result is shown in Fig. 7. The AB62 removal on the Fe_2O_3/SnO_2 photocatalyst reaches 98.0% in 60 min, obviously

higher about 3.6 times than the value of 27.4% over Degussa P25. The enhancement may be explained in terms of the synergetic effect on the specific adsorption property and efficient electron–hole separation at the Fe_2O_3/SnO_2 nanocomposites catalyst interfaces**.**

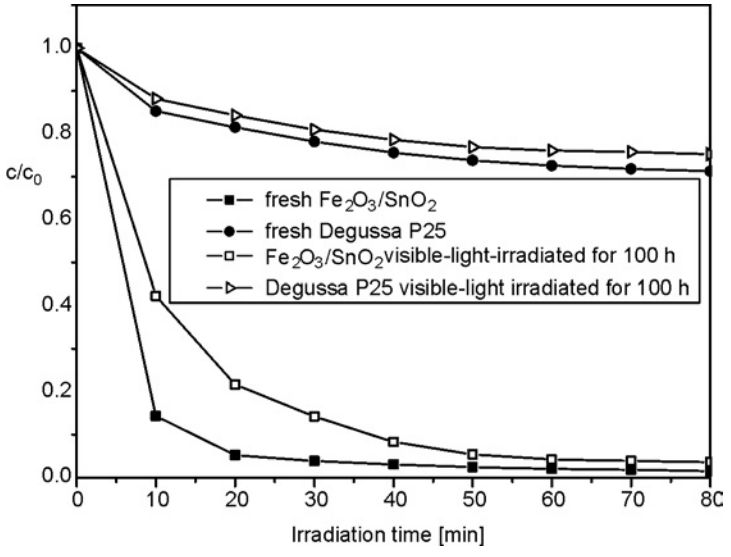

Fig. 7. Comparison for the photocatalytic activity and stability of the Fe_2O_3/SnO_2 photocatalyst with P25

It also can be seen from Fig. 7 that the photocatalytic activities became lower after the photocatalysts are irradiated for 100 h under visible light, and the long term stability of the Fe_2O_3/SnO_2 photocatalyst is poorer than that of P25. The XRD analysis indicates no changes in the phase composition of the photocatalyst after 100 h visible-light-irradiation (not shown). But the XRD results cannot rule out the possibility of the formations of some amorphous products, such as amorphous $Fe(OH)_3$, $SnO_2{\cdot}nH_2O$, Fe and Sn with no photocatalytic activity under the visible-light irradiation. It is possible that these amorphous products formed under the visible-light irradiation, which led to the decrease in the photocatalytic activity. A further study on the mechanism of deactivation is needed on this issue.

4. Conclusion

The visible-light-activated coupled Fe_2O_3/SnO_2 photocatalysts were prepared by co-precipitation. The characteristic patterns of XRD, BET, TEM and UV-Vis diffuse reflectance displayed that the sample calcined at 400 °C for 3 h (the molar ratio of Fe to Sn equal to 2:1) has better crystallinity, smaller crystal sizes and stronger response to visible light. The photocatalyst showed remarkable photocatalytic activity under

visible light ($\lambda > 400$ nm), 98.0% AB62 can be degraded in 60 min. A study on how to keep high photocatalytic activity and long term stability after many cycles of using the Fe_2O_3/SnO_2 photocatalyst is in progress. In a sense, the effective photodegradation of the dye by Fe_2O_3/SnO_2 photocatalyst under visible light is a very exciting research topic in photocatalytic area, and this work may provide new insights into the development of novel sunlight photocatalysts.

Acknowledgements

This work was supported by the National Natural Science Foundation of China (20677008) and the Innovation Foundation of Donghua University for Ph D candidates.

References

[1] RODRIGUEZ M., SARRIA V., ESPLUGAS S., PULGARIN C., J. Photochem. Photobiol. A: Chem., 151 (2002), 129.
[2] STYLIDI M., KONDARIDES D.I., VERYKIOS X.E., Appl. Catal. B: Environ., 47 (2004), 189.
[3] COLÓN G., HIDALGO M.C., NAVÍO J.A., Appl. Catal. A: Gen., 231 (2002), 185.
[4] KOSOWSKA B., MOZIA S., MORAWSKI A.W., GRZMIL B., JANUS M., Sol. Energy Mater. Sol. Cells., 88 (2005), 269.
[5] KOHTANI S., TOMOHIRO M., TOKUMURA K., NAKAGAKI R., Appl. Catal. B: Environ., 58 (2005), 265.
[6] HONG X.T., WANG Z.P., CAI W.M., LU F., ZHANG J., YANG Y.Z., MA N., LIU Y.J., Chem. Mater., 17 (2005), 1548.
[7] KUMAR S., FEDOROV A.G., GOLE J.L., Appl. Catal. B: Environ., 57 (2005), 93.
[8] YU J.G., YU J.C., CHENG B., HARK S.K., IU K., J. Solid State Chem., 174 (2003), 372.
[9] WANG C., ZHAO J.C., WANG X.M., MAI B.X., SHENG G.Y., PENG P.A., FU J.M., Appl. Catal. B: Environ., 39 (2002), 269.
[10] LIU B.S., ZHAO X.J., ZHANG N.Z., ZHAO Q.N., HE X., FENG J.Y., Surface Sci., 595 (2005), 203.
[11] TENNAKONE K., BANDARA J., Appl. Catal. A: Gen., 208 (2001), 335.
[12] LI X.Z., LI F.B., YANG C.L., GE W.K., J. Photochem. Photobiol. A: Chem., 141 (2001), 209.
[13] WANG C., WANG X.M., MAI B.X., ZHAO J.C., MAI B.X., PENG P.A., SHENG G.Y., FU J.M., J. Photochem. Photobiol. A: Chem., 168 (2004), 47.
[14] YU X.D., WU Q.Y., JIANG S.C., GUO Y.H., Mater. Charact., 57 (2006), 333.
[15] JANUS M., INAGAKI M., TRYBA B., MORAWSKI A.W., Appl. Catal. B: Environ., 63 (2006), 272.
[16] PROVENZANO P.L., JINDAL G.R., SWEET J.R., WHITE W.B., J. Lumin., 92 (2001) 297.
[17] KARUNAKARAN C., SENTHILVELAN S., Electrochem. Commun., 8 (2006), 95.
[18] YU J.G., XIONG J.F., CHENG B., YU Y., WANG J.B., J. Solid State Chem., 178 (2005), 1968.

Received 6 May 2007
Revised 4 March 2008

Materials Science-Poland, *Vol. 26*, *No. 3*, *2008*

Influence of nickel ions on dielectric and other physical properties of $PbO–MoO_3–B_2O_3$ glass system

P. SYAM PRASAD, V. RAVI KUMAR, G. NAGA RAJU, N. VEERAIAH*

Department of Physics, Acharya Nagarjuna University P.G. Centre, Nuzvid-521 201, A.P. India

$PbO–MoO_3–B_2O_3$ glasses containing various proportions of NiO (ranging from 0 to 1.0 mol %) have been prepared. A number of methods viz., differential thermal analysis, spectroscopic (IR and UV-Vis optical absorption, and ESR spectra) and dielectric properties (ε', $\tan\delta$, a.c. conductivity σ_{ac} over a range of frequencies and temperatures) of these glasses has been employed in studies. The results of differential thermal analysis suggest a high glass forming ability for the glass containing 0.6 mol % of NiO. The studies of UV-Vis and IR spectra show that nickel ions occupy both tetrahedral and octahedral positions in the glass network with the dominance of the tetrahedral positions when the concentration of NiO is below 0.6 mol % in the glass matrix. The analysis of the results of studies of dielectric properties reveals that there is an increase in the rigidity and the dielectric breakdown strength of the glass when the concentration of NiO is around 0.6 mol %.

Key words: *$PbO–MoO_3–B_2O_3$ glass; Ni^{2+} ions; DTA pattern; dielectric properties; ESR spectra; optical absorption*

1. Introduction

Molybdenum borate based glasses have been the subject of many investigations due to their catalytic properties. Molybdenum ions inculcate high activity and selectivity in a series of oxidation reactions of practical importance in glass matrices [1, 2]. Molybdenum ions exists at least in two stable valence states, viz., Mo(V) and Mo(VI) in a glass network. They act both as network formers with MoO_4^{2-} structural units and alternate with BO_4 structural units; these ions may also act as modifiers depending upon their concentration and nature of the host network. ESR studies on the glasses containing molybdenum ions have identified the presence of octahedrally coordinated Mo(V) ions along with distorted octahedrons approaching tetragons. Further, Mo–O bond in molybdenum hexavalent oxide is identified as significantly covalent [3, 4].

*Corresponding author, e-mail: nvr8@redifmail.com

Results of a number of recent studies on various physical properties viz., spectroscopic, ionic conductivity, dielectric properties etc., of variety of glass systems containing molybdenum ions are available [5–13].

Divalent nickel ions are interesting paramagnetic ions to probe in glass systems. Nickel ions are reported to occupy both tetrahedral and octahedral positions in glass matrices. A number of recent studies on diversified inorganic glass systems containing Ni^{2+} ions are available [14–19]. Attempts have also been made to detect the lasing action of these ions in certain crystal and glass systems since they possess several strong absorption bands in the visible and NIR regions where the pumping sources are easily available [20]. Octahedrally positioned Ni^{2+} ions are expected to exhibit eye safe laser emission of wavelength 1.56 μm ($^3T_2 \rightarrow {}^3A_2$) even at room temperature with low threshold energy which is of great importance in telecommunication [21]. The concentrations of ions in tetrahedral or octahedral positions depend on the quantitative properties of modifiers and glass formers, size of the ions in the glass structure, their field strength, mobility of the modifier cation, etc. Further, the investigation on the coordinate chemistry of Ni^{2+} ions in molybdenum–borate glass network is of interest in itself, because these ions are expected to influence physical properties of the glasses to a large extent. Hence, it is felt worthwhile to throw some light on the structural aspects of $PbO–MoO_3–B_2O_3$ glasses containing small proportion of nickel ions by studying some of their physical properties viz., dielectric properties (the electric permittivity, ε', the loss, tanδ, a.c. conductivity σ_{ac}, in the frequency range 10^2–10^6 Hz and in the temperature range 30–300 °C and the dielectric breakdown strength in air), spectroscopic properties (optical absorption in IR and UV-Vis regions, and ESR).

2. Experimental

Within the glass forming region of $PbO–MoO_3–B_2O_3$ glass system, a particular composition $30PbO–4MoO_3–66B_2O_3$ is chosen for NiO doping in the present study. The details of the composition are:

N_0: $30PbO–4MoO_3–66.0B_2O_3$; N_2: $30PbO–4MoO_3–65.8B_2O_3$: 0.2NiO;

N_4: $30PbO–4MoO_3–65.6B_2O_3$: 0.4NiO; N_6: $30PbO–4MoO_3–65.4B_2O_3$: 0.6NiO;

N_8: $30PbO–4MoO_3–65.2B_2O_3$: 0.8NiO; N_{10}: $30PbO–4MoO_3–65.0B_2O_3$: 1.0NiO.

Appropriate amounts (all in mol %) of reagent grades of PbO, MoO_3, H_3BO_3 and NiO powders were thoroughly mixed in an agate mortar and melted in a thick-walled platinum crucible in the temperature range 950–1050 ºC in an automatic temperature controlled furnace for about 1 h until a bubble free transparent liquid was formed. The resultant melt was then poured in a brass mould and subsequently annealed from 300 °C with a cooling rate of 1 ºC/min. The amorphous state of the glasses was checked by X- ray diffraction.

The samples were then ground and optically polished. The final dimensions of the samples used for dielectric and optical studies were about $1\times1\times2$ cm^3. The densities d

of the glasses were determined to the accuracy of 0.001 by the standard principle of Archimedes using *o*-xylene (99.99% pure) as the buoyant liquid. Differential thermal analysis was carried out using STA 409C model DTA-TG instrument with a programmed heating rate of 10 °C/min, in the temperature range 30–1000 ºC to determine the glass transition temperature and other glass forming ability parameters. The optical absorption spectra of the glasses were recorded at room temperature in the wavelength range 350–1400 nm up to the resolution of 0.1 nm using Shimadzu UV Vis-NIR spectrophotometer model 3101. The ESR spectra of fine powders of the samples were recorded at room temperature on E11Z Varian X-band (ν = 9.5 GHz) ESR spectrometer. Infrared transmission spectra were recorded on a Bruker IFS 66 V – IR spectrophotometer with a resolution of 0.1 cm^{-1} in the range 400–2000 cm^{-1} using potassium bromide pellets (300 mg) containing pulverized glass (1.5 mg). These pellets were pressed in a vacuum die at ca. 680 MPa. A thin coating of silver paint was applied (to the larger area faces) on either side of the glasses to serve as electrodes for dielectric measurements. The painted samples were then dried with a hot blower for about 10 minutes on either side. The details of dielectric measurements were similar to those reported in earlier papers from our laboratory [22, 23].

3. Results

Based on the glass density d and calculated average molecular weight $\bar{M}$, various physical parameters such as nickel ion concentration N_i, mean nickel ion separation r_i are evaluated for understanding the physical properties of these glasses using the conventional formulae [24] and the values obtained are presented in Table 1.

Table 1. Physical parameters of $PbO–MoO_3–B_2O_3$ glasses doped with NiO

Glass	Density d [g/cm^3]	Average mol.wt. M	Total nickel ion concentration [10^{21} ions/cm^3]	Interionic distance of Ni ions r_i [Å]
N_0	4.650	118.66	–	-
N_2	4.665	118.67	4.735	5.95
N_4	4.676	118.68	9.495	4.72
N_6	4.682	118.69	14.25	4.12
N_8	4.695	118.70	19.057	3.74
N_{10}	4.702	118.71	23.85	3.47

Figure 1 shows typical differential thermal analysis traces of $PbO–MoO_3–B_2O_3$glasses doped with NiO of various concentrations. The curves exhibit an endothermic effect due to glass transition temperature T_g; the value of T_g is evaluated from the point of inflection of this feature. At still higher temperatures an exothermic peak T_c due to the crystal growth followed by an endothermic effect due to the melting effect T_m are also observed. The values of T_g, T_c and T_m obtained for all the glasses are given in Table 2.

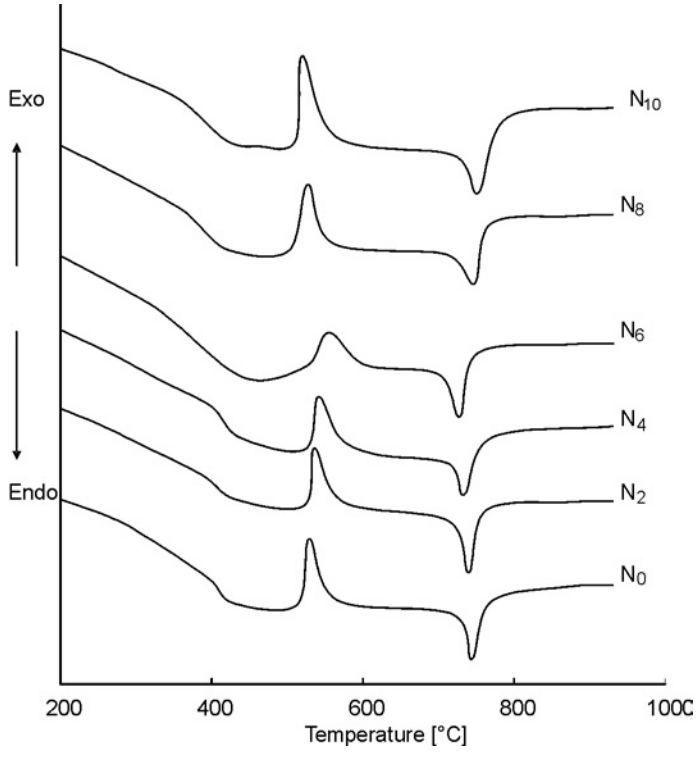

Fig. 1. DTA patterns of NiO-doped PbO–MoO_3–B_2O_3 glasses

Table 2. Results of differential thermal analysis of PbO–MoO_3–B_2O_3: NiO glasses

Glass	T_g	T_c	T_m	T_g/T_m	$(T_c-T_g)/T_g$	$(T_c-T_g)/T_m$	K_{gl}
N_0	701	802	1017	0.689	0.144	0.099	0.469
N_2	705	809	1013	0.695	0.147	0.102	0.509
N_4	710	814	1007	0.705	0.146	0.103	0.538
N_6	717	828	1001	0.716	0.154	0.110	0.641
N_8	697	800	1020	0.683	0.147	0.100	0.468
N_{10}	692	793	1025	0.675	0.145	0.098	0.435

The appearance of a single peak due to the glass transition temperature in DTA pattern of all the glasses indicates the homogeneity of the glasses prepared. Upon increasing concentration of NiO in the glass matrix, the difference $T_c - T_g$, which is proportional to glass forming ability, is found to increase whereas the difference $T_m - T_c$ which is inversely proportional to glass forming ability is found to decrease, with the increase in the concentration of NiO up to 0.6 mol %. From the measured values of T_g, T_c and T_m, the parameters T_g/T_m, $(T_c - T_g)/T_g$, $(T_c - T_g)/T_m$ and glass forming ability parameter K_{gl}, known as the Hruby parameter given by $(T_c - T_g)/(T_m - T_c)$, are evaluated; the value of these parameter exhibits maximum at $x \approx 0.6$ (Table 2, Fig. 2).

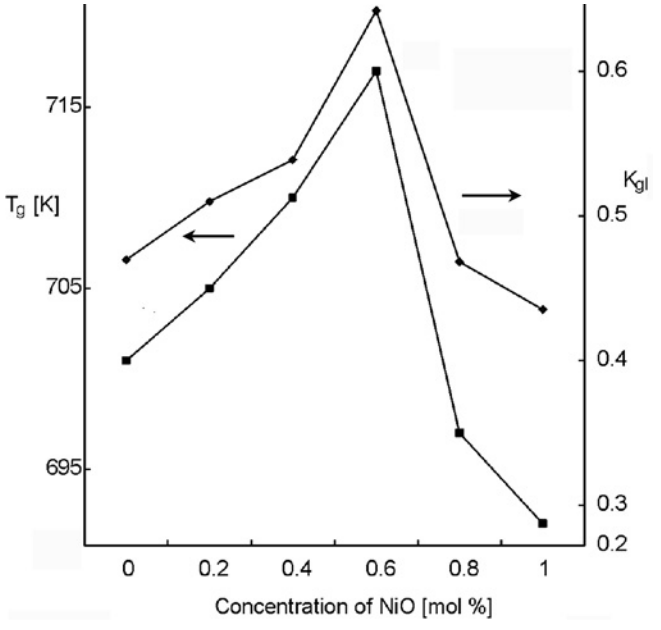

Fig. 2. Dependences of T_g and K_{gl} on the concentration of NiO

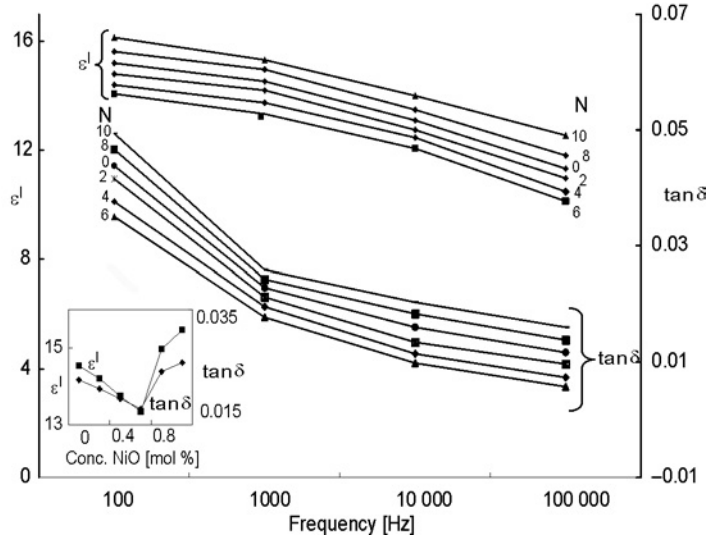

Fig. 3. Dependences of electric permittivity (ε^l) and loss ($\tan\delta$) on frequency at room temperature for $PbO–MoO_3–B_2O_3$ glass containing various amounts of NiO. The inset shows dependences of ε^l and $\tan\delta$ on concentration of NiO at 1 kHz

The electric permittivity ε' and loss $\tan\delta$ at room temperature (30 °C) of nickel free $PbO–MoO_3–B_2O_3$ glasses at 100 kHz are measured to be 11.32 and 0.0116, respectively; the values of ε' and $\tan\delta$ are found to increase considerably upon decreasing

frequency (Fig. 3). The dependence of these parameters with the concentration of NiO showed a decreasing trend in the composition range $0 \leq x \leq 0.6$, whereas beyond 0.6 mol % the parameters were found to increase (inset of Fig. 3).

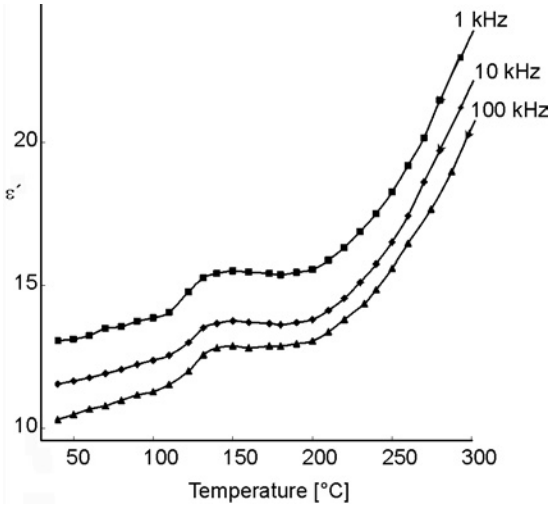

Fig. 4. Temperature dependences of electric permittivity of glass N_2 at various frequencies

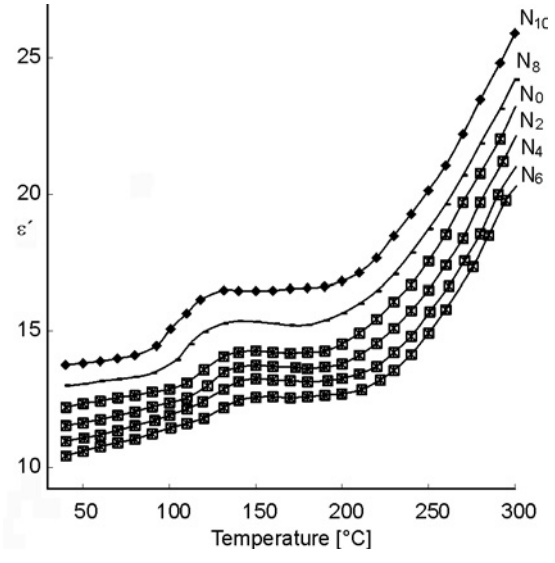

Fig. 5. Temperature dependences of electric permittivity at 10 kHz of $PbO–MoO_3–B_2O_3$ glasses doped with NiO of various concentrations

The temperature dependence of ε' at various frequencies of the glass N_2 (containing 0.2 mol % of NiO) and of the glasses containing various proportions of NiO at 10 kHz are shown in Figs. 4 and 5, respectively; the value of ε' is found to exhibit a con-

siderable increase at higher temperatures especially at lower frequencies for all the glasses maintaining the lowest value for glass N_6 at any frequency and temperature.

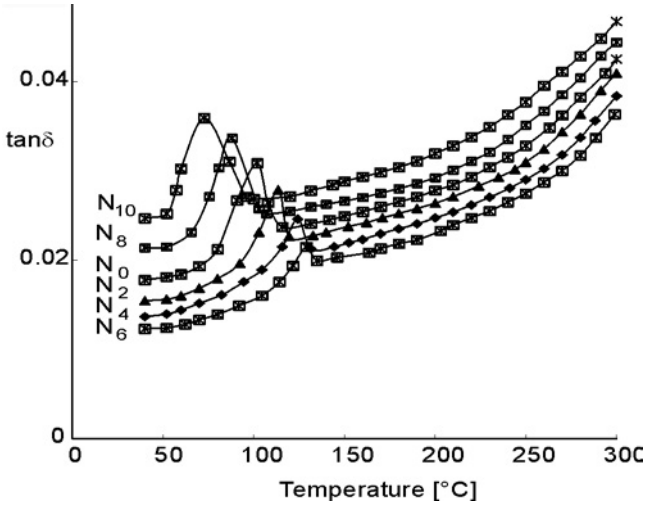

Fig. 6. Temperature dependences of dielectric losses at 1 kHz for $PbO–MoO_3–B_2O_3$ glasses doped with NiO of various concentrations

The temperature dependence of $\tan\delta$ of all the glasses at 1 kHz is presented in Fig. 6. The loss curve (of pure and NiO doped glasses) exhibited distinct maxima; upon increasing frequency, the temperature maximum shifts towards higher temperatures, and upon increasing temperature the frequency maximum shifts towards higher frequencies, indicating the relaxation character of dielectric losses of $PbO–MoO_3–B_2O_3$: NiO glasses. The observations on dielectric loss variation with temperature for various concentrations of NiO further indicate a gradual increase in the broadness and $(\tan\delta)_{max}$ of relaxation curves beyond 0.6 mol % of NiO. The Cole–Cole diagrams drawn between ε' and ε'', corresponding to 120 °C in the relaxation region showed that the dielectric relaxation in these glasses is a Debye-type relaxation with a certain set of relaxation times τ. From these diagrams, low- and high-frequency electric permittivities (ε_s and ε_∞, respectively) have been determined for samples doped with various amounts of NiO. The obtained average values of ε_s and ε_∞ for each concentration are presented in Table 3.

Table 3. Data on dielectric loss of $PbO–MoO_3–B_2O_3$: NiO glasses.

Glass	$(\tan\delta)_{max}$	Temperature range of relaxation [°C]	ε_s	ε_∞	Activation energy for dipoles [eV]	α
N_2	0.027	79–108	12.2	5.8	1.81	7
N_4	0.024	84–106	10.8	5.35	1.99	5
N_6	0.021	88–104	10.2	5.15	2.20	3
N_8	0.032	80–109	16.8	9.6	1.92	9
N_{10}	0.036	74–114	17.9	11.7	1.88	10

The parameter α characterizing the distribution function τ does not show any considerable change with temperature for a particular concentration; however, for different concentrations, the values are appreciably different (Table 3). The effective activation energy W_d for the dipoles is calculated for different concentrations of NiO and presented also in Table 3. The activation energy is found to be the highest for glass N_6.

The a.c. conductivity σ_{ac} may be calculated at various temperatures from the equation:

$$\sigma_{ac} = \omega\varepsilon'\varepsilon_0 \tan\delta \tag{1}$$

where ε_0 is the vacuum electric permittivity for different frequencies. The dependences of $\log\sigma_{ac}$ on $1/T$ for all the glasses at 100 kHz are given in Fig. 7.

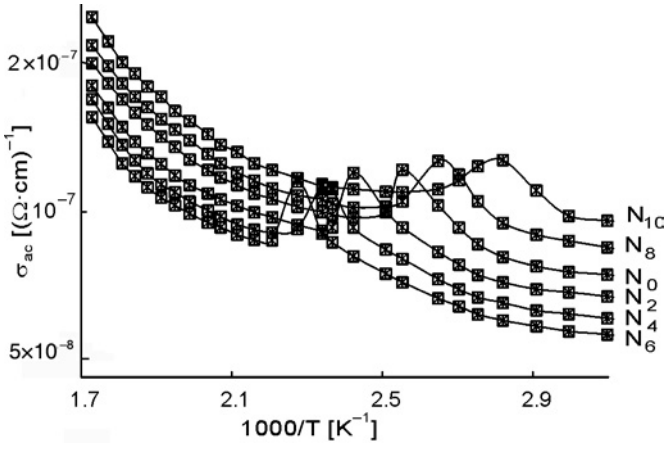

Fig. 7. Dependences of σ_{ac} on $1000/T$ for $PbO–MoO_3–B_2O_3$ glasses doped with NiO of various concentrations

Table 4. Data on a.c. conduction of $PbO–MoO_3–B_2O_3$: NiO glasses (See Sect. 4 for the discussion of $N(E_F)$)

Glass	$N(E_F)$ [$eV^{-1}\cdot cm^{-3}$]			Activation energy for conduction [eV]
	Austin and Mott [45]	Butcher and Hyden [51]	Pollak [52]	
N_2	8.91	3.72	9.06	0.251
N_4	8.33	3.47	8.46	0.265
N_6	7.77	3.24	7.90	0.284
N_8	10.50	4.38	10.7	0.258
N_{10}	11.40	4.75	11.6	0.248

The conductivity is found to decrease upon increasing concentration of NiO (at any given frequency and temperature) up to 0.6 mol % and beyond that it is found to increase. From these plots, the activation energy for conduction in the high tempera-

ture region over which a near linear dependence of $\log\sigma_{ac}$ on $1/T$ could be observed, is evaluated and presented in Table 4; activation energy is found to be the maximum for glass N_6 and minimum for glass N_{10}.

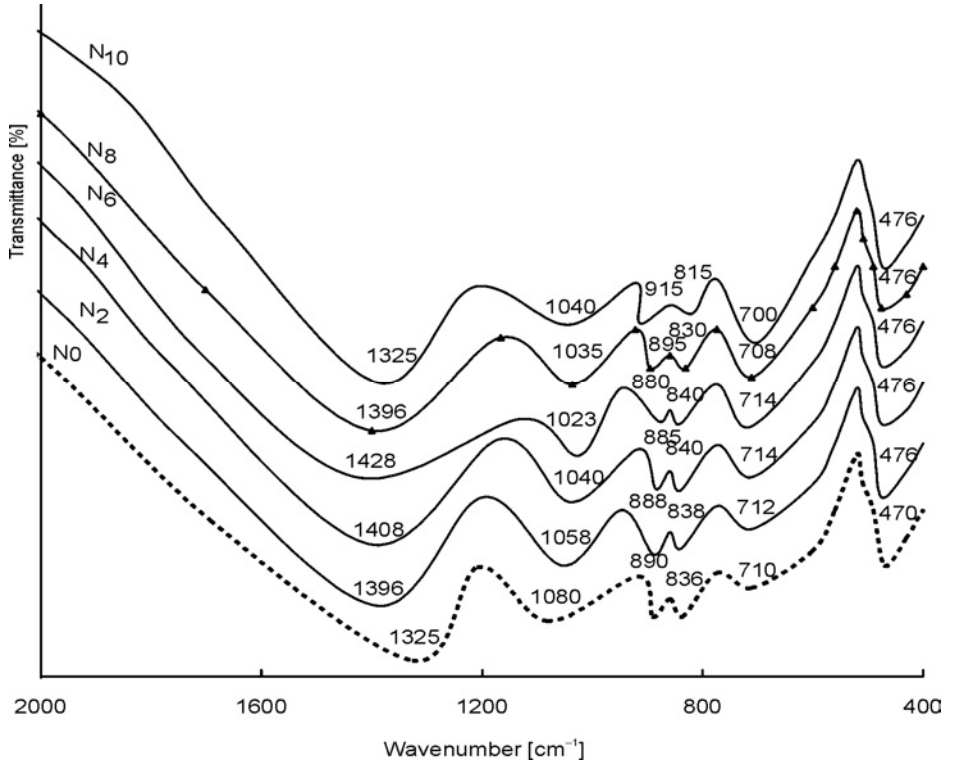

Fig. 8. IR spectra of $PbO–MoO_3–B_2O_3$: NiO glasses

The IR spectra of these glasses exhibited prominent bands in the regions 1300 –1400 cm^{-1}, 1000–1200 cm^{-1} and another band at about 710 cm^{-1} (Fig. 8); these bands are identified as due to the stretching relaxation of B–O bonds of the trigonal BO_3 units, vibrations of BO_4 structural units and due to the bending vibrations of B–O–B linkages, respectively [25]. Additionally, the band due to the vibrations of PbO_4 structural units is also located at about 470 cm^{-1} in the spectra of all the glasses. Yet, the spectra exhibit two well resolved bands at about 890 and 836 cm^{-1}; based on the earlier reported data [26, 27], these two bands have been attributed to ν_1 and ν_3 vibrational modes of MoO_4^{2-} tetrahedral units, respectively. Upon increase in the concentration of the dopant NiO, beyond 0.6 mol %, the following changes have been observed in the spectra: (i) the intensities of the bands due to MoO_4^{2-} tetrahedral units is observed to decrease and the band at 890 cm^{-1} is found to be shifted towards slightly higher frequency side whereas the band at 836 cm^{-1} is observed to be shifted towards

lower frequency (Table 5); (ii) the intensity of the band due to BO_3 structural units is observed to increase at the expense of the band due to BO_4 units.

Table 5. Band positions (in cm^{-1}) in the IR spectra of $PbO–MoO_3–B_2O_3$: NiO glasses

Glass	Borate groups			PbO_4	MoO_4 units	
	BO_3	BO_4	B–O–B			
N_0	1325	1080	710	470	890	836
N_2	1396	1058	712	476	888	838
N_4	1408	1040	714	476	885	840
N_6	1428	1023	714	476	880	840
N8	1400	1035	708	476	895	830
N_{10}	1389	1043	700	476	915	815

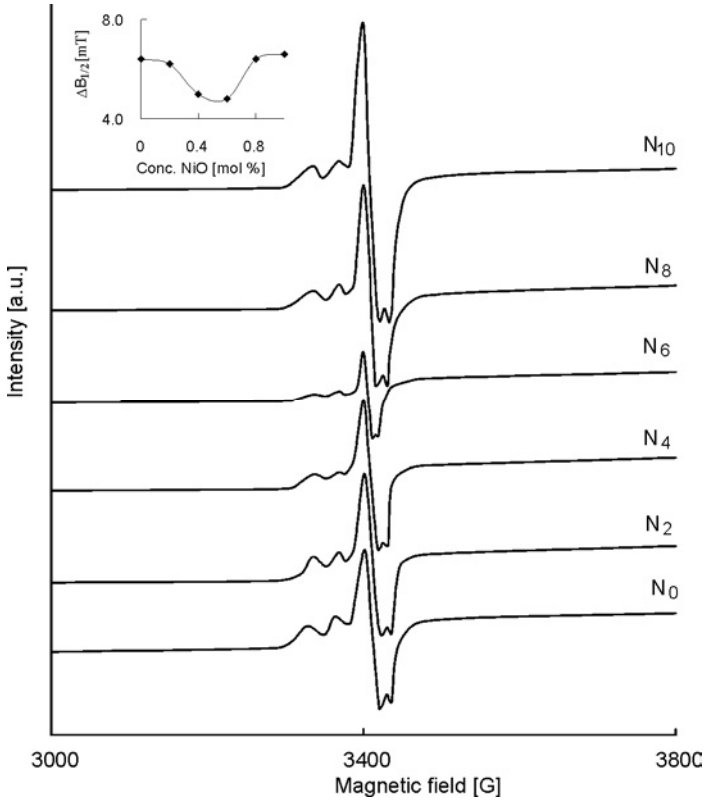

Fig. 9. ESR spectra of $PbO–MoO_3–B_2O_3$: NiO glasses recorded at room temperature; the inset gives the dependence of the half width $\Delta B_{1/3}$ on concentration of NiO

The ESR spectra (Fig. 9) of $PbO–MoO_3–B_2O_3$: NiO glasses recorded at room temperature exhibit a signal consisting of a central line surrounded by smaller satellites at about $g_\perp$ =1.943 and g_{ll} =1.886. The intensity and the half width $\Delta B_{1/2}$ of the central

line are observed to increase considerably when the concentration of NiO is increased beyond 0.6 mol % in the glass matrix (inset of Fig. 9).

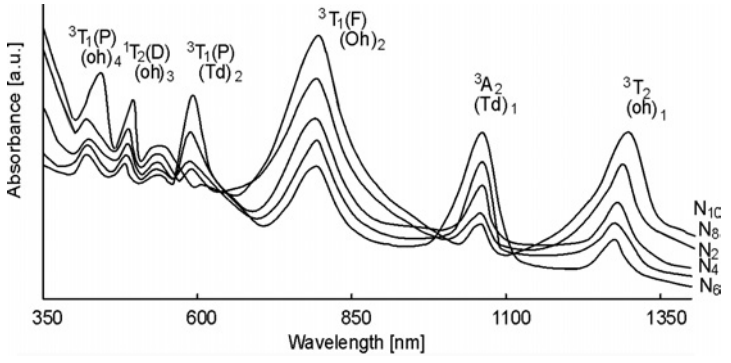

Fig. 10. Optical absorption spectra of $PbO–MoO_3–B_2O_3$: NiO glasses

The optical absorption spectra of $PbO–MoO_3–B_2O_3$: NiO glasses recorded at room temperature in the wavelength range 350–1400 nm are shown in Fig. 10. The spectrum of NiO free glasses exhibited an absorption band at about 550 nm (not shown in the figure). The intensity of this band is observed to be the largest in the spectrum of glass N_{10} and the lowest in the spectrum of glass N_6. Additionally, with the NiO doping the spectra exhibited several absorption bands due to Ni^{2+} ions. The spectrum of the glass (N_2) exhibited six clearly resolved intense absorption bands in the visible and NIR regions at 1282 nm (O_{h1}), 1061 nm (T_{d1}), 794 nm (O_{h2}), 590 nm (T_{d2}), 488 (O_{h3}) and at 422 nm (O_{h4}). As the concentration of NiO is increased up to 0.6 mol %, the intensity of the octahedral bands (O_h bands) is observed to decrease with a shift towards slightly lower wavelengths; in this concentration range the intensity of the two tetrahedral bands (T_d bands) is observed to increase with no considerable shift in the band positions. With the increase in the concentration of NiO from 0.6 to 1.0 mol %, the positions of the octahedral bands are shifted towards slightly higher wavelengths with increasing intensity at the expense of T_{d1} and T_{d2} bands. The summary of the data on the positions of various absorption bands is given in Table 6.

Table 6. Summary of the data on optical absorption spectra of NiO doped $PbO–MoO_3–B_2O_3$ glasses

Transition of nickel ions	Band positions [cm^{-1}]				
	N_2	N_4	N_6	N_8	N_{10}
Octahedral transitions					
$^3A_2$ (F) → $^3T_2$ (F)	7800	7824	7849	7745	7692
$^3A_2$ (F) → $^3T_1$ (F)	12589	12594	12666	12626	12562
$^3A_2$ (F) → $^1T_2$ (D)	20491	20618	20790	20491	20242
$^3A_2$ (F) → $^3T_1$ (P)	23640	23696	23809	23690	22376
Tetrahedral transitions					
$^3A_2$ (F) → $^3A_2$ (F)	9433	9433	9433	9433	9433
$^3A_2$ (F) → $^3T_1$ (F)	17543	17543	17543	17543	17543

4. Discussion

$PbO–B_2O_3$-MoO_3: NiO glasses have complex compositions being mixtures of network formers, intermediates and modifiers. It is a well known fact that B_2O_3 is a network former with BO_3 and BO_4 structural units. The presence of such BO_3 and BO_4 units in the $PbO–MoO_3–B_2O_3$: NiO glasses is evident from infrared spectral studies. PbO, which is $[PbO_{2/2}]$, tends to become four-connected to oxygens as $[PbO_{4/2}]^{2–}$ by acquiring this additional coordination. The band observed in the IR spectra at about 470 cm^{-1} suggests that there is a possibility for PbO to participate in the glass network with PbO_4 structural units. But at certain concentrations of PbO it also acts as a modifier. As a modifier, PbO enters the glass network by breaking up the B–O–B, B–O–Mo bonds (normally the oxygens of PbO break the local symmetry while Pb^{2+} ions occupy interstitial positions) and introduces coordinate defects known as dangling bonds along with non-bridging oxygen ions. In this case lead ions are octahedrally positioned. If NiO acts as a modifier in the glass network, additional non-bridging Pb–O bonds are expected to be formed at the expense of the bridging B–O–B and B–O–Pb linkages and may also introduce more non-bridging oxygen ions.

Molybdenum ions are expected to exist mainly in Mo^{6+} state in the $PbO–MoO_3–B_2O_3$ glass network; these ions are expected to participate in the glass network with tetrahedral $MoO_4^{2–}$ structural units and may alternate with BO_4 structural units. As the concentration NiO is increased (especially beyond 0.6 mol %), the colour of glasses becomes increasingly brown, indicating the reduction of molybdenum ions from Mo^{6+} state in to Mo^{5+} state. These Mo^{5+} (d^1) ions are quite stable and occupy octahedral positions with distortion due to the Jahn–Teller effect [28, 29].

The Ni^{2+} ions seem to exist in both four-fold and in six-fold coordination in the present glass network. In general, tetragonally positioned Ni^{2+} ions do not induce the formation of any non bridging oxygen ions but octahedrally positioned ions may act as modifiers [30].

Upon increasing concentration of NiO up to 0.6 mol %, the values of the glass transition temperature T_g and glass forming ability parameter K_{gl}, increase. The augmented cross-link density of various structural groups and closeness of packing are responsible for such an increase of these parameters. These results apparently suggest that there is a growing presence of tetrahedrally positioned nickel ions which increase the cross-link density and enhance the mean bond strength.

Using the Tanabe–Sugano diagrams for $Ni^{2+}(d^8)$ ion, the optical absorption spectra have been analyzed and the bands O_{h1}, O_{h2} and O_{h3} are assigned to the transitions from the $^3A_2$ ground state of octahedrally positioned Ni^{2+} ions to $^3T_2(F)$, $^3T_1(F)$ and $^3T_1(P)$ excited states, respectively. The bands with barycentres at about 1060 nm (T_d1) and 570 nm (T_d2) nm are attributed to the transitions $^3T_1(F) \rightarrow {}^3A_2(F)$ and $^3T_1(F) \rightarrow {}^3T_1(P)$ of Ni^{2+} ions in tetrahedral sites [31]; the band at about 420 nm represents a spin forbidden octahedral transition $^3A_2 \rightarrow {}^1T_2$ [21, 32]. Thus, the measurements of the optical absorption of $PbO–B_2O_3–MoO_3$: NiO glasses indicate that Ni^{2+} ions exist both in octa-

hedral and tetrahedral sites in the glass network. Further, the way the intensity of these bands varies with the concentration of NiO suggests that at smaller concentrations ($\leq$ 0.6 mol %), Ni^{2+} ions prefer to occupy tetrahedral positions whereas at larger concentrations, these ions occupy octahedral sites also in the glass network.

From these spectra it is also evident that the ratio, Ni^{2+}(oct)/Ni^{2+}(tet), increases with increase in the concentration of NiO beyond 0.6 mol %; further, the d–d transitions of the tetrahedral complexes are electric dipole allowed whereas those of octahedral complexes are electric dipole forbidden and are mainly due to static or dynamic distortions from the regular octahedral geometry of the glass network and they can also be magnetic dipole allowed.

Additional absorption band observed in the region 500–570 nm in the optical absorption spectra of these glasses is attributed to the excitation of Mo^{5+} ($4d^1$) ion [33]. In fact, for this ion, two optical excitations were predicted starting from b_2 (d_{xy}) ground state to ($d_{xz–yz}$) and ($d_{x^2-y^2}$) with δ = 15 000 cm^{-1} and Δ = 23 000 cm^{-1} [33]. Perhaps, due to intercharge transition transfer ($Mo^{5+} \longleftrightarrow Mo^{6+}$) in the glass network, the resolution of these transitions could not be observed. The highest intensity of this band observed in the spectrum of glass Mo_5 points out that the presence of the highest concentration of Mo^{5+} ions in these glasses. Such Mo^{5+} ions may form $Mo^{5+}O^{3-}$ molecular orbital states and are expected to participate in the depolymerisation of the glass network [33, 34] creating more bonding defects and non-bridging oxygens (NBO's) similar to octahedrally positioned Ni^{2+} ions.

The existence of molybdenum ions in Mo^{5+} state in these glasses is further confirmed by ESR spectral studies. The ESR spectrum of these glasses consists of a main central line surrounded by less intense satellites. The central line arises from even molybdenum isotopes (I = 0) whereas satellite lines correspond to the hyperfine structure from odd ^{95}Mo and ^{97}Mo (I = 5/2) isotopes [35]. The intensity of the signal is observed to increase gradually with the increase in the concentration of NiO beyond 0.6 mol %; this is an indicative of larger concentration of $Mo^{5+}O_3^-$ complexes in the glasses N_8 and N_{10}. The values of $g_\perp$ and g_{ll} from these spectra have been evaluated as 1.943 and 1.886; the structural disorder arising from the site-to-site fluctuations of the local surroundings of the paramagnetic Mo^{5+} ions can be accounted for the two components of the g values. The variation of NiO content seems to have no influence on the values of g even though the intensity of the signal is considerably affected. Further, the g values obtained for these glasses are found to be consistent with the reported values for many other glass systems (phosphate, borate, arsenate, etc.) containing molybdenum ions [36, 37]. The increase in the intensity and the half width $\Delta B_{1/2}$ of the signal with increase in the concentration of NiO (beyond 0.6 mol %) also supports the view point that in these glasses molybdenum ions exists largely in Mo^{5+} state.

In the IR spectra of $PbO–MoO_3–B_2O_3$: NiO glasses, the intensity of the bands due to more ordered BO_4 and MoO_4^{2-} tetrahedral units, is observed to be the highest for the glass N_6; with the increase of NiO content beyond 0.6 mol %, the intensity of the band due to BO_3 structural units is observed to build up at the expense of tetrahedral

bands. Further, the band due to ν_1 vibrational mode of MoO_4^{2-} tetrahedral units located at about 880 cm^{-1} (in the spectrum of the glass N_6) is observed to be shifted to the region of higher wavenumbers (915 cm^{-1}); in this region, the band due to partially isolated Mo–O bonds of strongly deformed MoO_6 groups is expected [38]. Similarly the ν_3 vibrational band of MoO_4^{2-} units observed at about 840 cm^{-1} in the spectrum of the glass N_6 is shifted towards the region of antisymmetric stretching vibrations of a Mo–$_{short}O_{long}$–Mo bridge associated with MoO_6 octahedral containing Mo=O bond (lower wavenumbers) [38]. These observations confirm that in the glasses containing NiO beyond 0.6 mol %, nickel ions mostly occupy octahedral positions, act as modifiers and are responsible for the increase in the degree of disorder in the glass network.

Among various electrical polarizations (viz., electronic, ionic, orientation and space charge), the space charge polarization depends on the purity and perfection of the glasses. With a gradual increase in the concentration of NiO in the glass matrix beyond 0.6 mol %, the values of ε', $\tan\delta$ and σ_{ac} are found to increase at any fixed frequency and temperature and the activation energy for a.c. conduction is observed to decrease. Obviously, this is because of an increasing concentration of octahedrally positioned Ni^{2+} and Mo^{5+} ions (evidenced from ESR and optical absorption measurements); these ions act as modifiers and generate bonding defects. The defects thus produced create easy pathways for the migration of charges that would build up space charge polarization leading to an increase in the dielectric parameters as observed [39]. When the concentration of NiO is increased up to 0.6 mol % in the glass matrix, the values of ε', $\tan\delta$ and σ_{ac} exhibit a decreasing trend (at any frequency and temperature) while the value of the activation energy for a.c. conduction exhibits an opposite trend; such a variation of these parameters may be ascribed to the presence of the cross linking of borate groups to form B–O–B and Pb–O–B bonds in the glass network as mentioned before. The presence of higher concentration of tetrahedral MoO_4^{2-} and NiO_4 units that take part network forming positions are also responsible for such low values of dielectric parameters in these samples.

The ascending values of $(\tan\delta)_{max}$, broadening of relaxation peaks and decrease in the value of activation energy for dipoles (Table 3) with increase in NiO concentration beyond 0.6 mol % in the glasses suggest an increase of freedom for dipoles to orient in the filed direction. This is also an indicative of decrease in the rigidity of the glass network. The observed dielectric relaxation effects may be attributed to the association of octahedrally positioned Ni^{2+} ions with a pair of any cationic vacancies in analogy with the mechanism-association of divalent positive ion with a pair of cationic vacancies – in conventional glasses, glass ceramics and crystals [40, 41].

If it is assumed that the electrical field in the glasses is the Lorenz field, the connection between the number N of the dipoles per unit volume, the electrical dipole moment μ and the low- and high-frequency electric permittivities ε_s and ε_∞ can be written according to the Clausius–Mossotti–Debye relation later modified by Guggenheim [42] as

$$\frac{\varepsilon_s - \varepsilon_\infty}{(\varepsilon_s + 2)(\varepsilon_\infty + 2)} T = \frac{4\pi N\mu^2}{27K} \tag{2}$$

Due to the fact that in the present glasses, ions and electric dipoles can be approximately regarded as mere points and the concentration of dipoles is not abnormally high, the applicability of the above equations for these glasses should be undoubted.

The quantity $N\mu^2$ in the right hand side of Eq. (2) represents the strength of dipoles. Substituting the values of ε_s and ε_∞, the quantity $4\pi N\mu^2/27K$ is calculated at 393 K for various concentrations of NiO and its dependence on the concentration of NiO is shown in the Fig. 11. The curve is observed to decrease up to 0.6 mol % of NiO and there after it is found to increase. Such a behaviour indicates an increase in the degree of spreading of relaxation times when the glasses are doped with NiO beyond 0.6 mol %. This result points out that in addition to Ni^{2+} ions, other type of dipoles also participating in relaxation effects. The other possibility is that Mo^{5+} (d^1) ions may form $Mo^{5+}O^{3-}$ complexes and may contribute to the relaxation effects [7, 35].

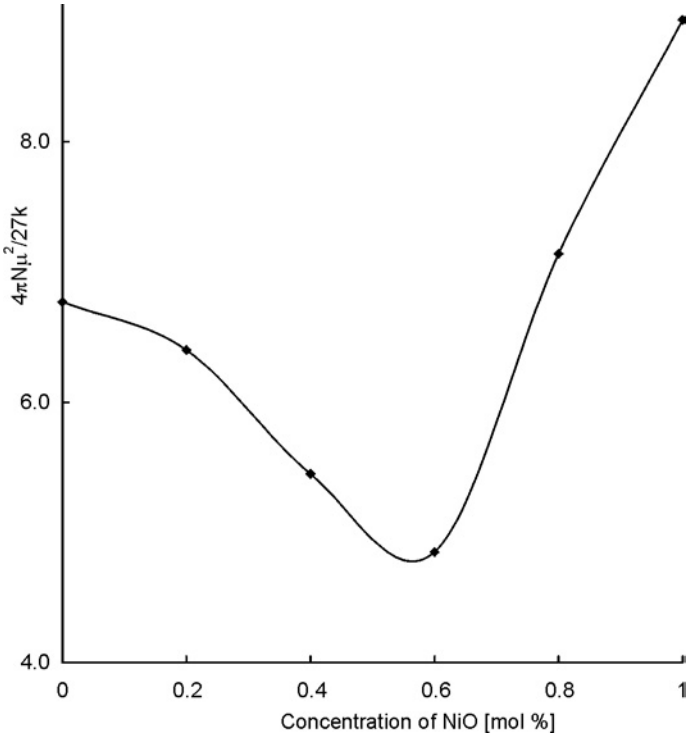

Fig. 11. Dependence of $4\pi N\mu^2/27k$ on concentration of NiO

In the plot $\log\sigma(\omega)$ vs. activation energy for conduction (in the high temperature region), a nearly linear relationship is observed (inset of Fig. 12); this observation

suggests that the conductivity enhancement is directly related to the thermally stimulated mobility of the charge carriers in the high temperature region [43]. Figure 12 represents the conductivity isotherms in function of NiO concentration; the curves pass through a minimum at approximately x = 0.6 mol %. The figure obviously suggests a kind of transition from predominantly electronic to ionic conductivity [44]. In the inset of the same figure, the activation energy for conduction is plotted in function of x. The plot is found to exhibit a maximum at x = 0.6 mol %.

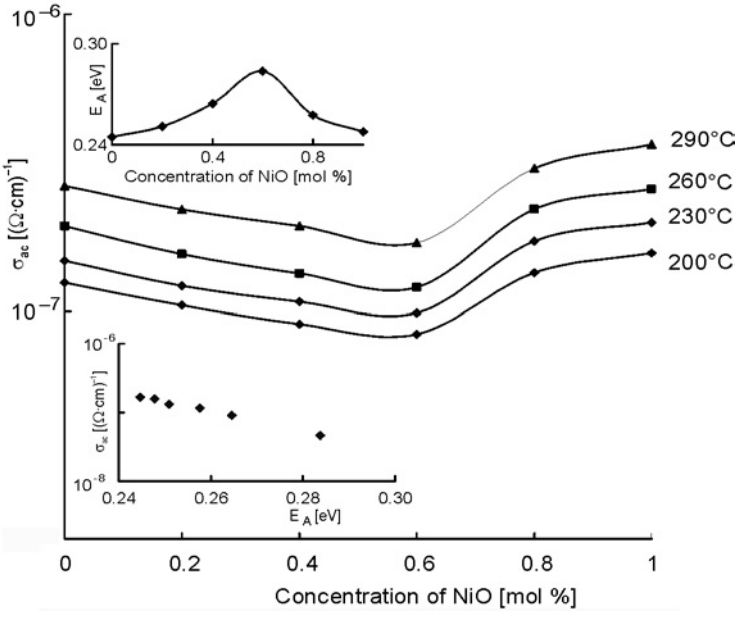

Fig. 12. Dependences of ac conductivity at 10 kHz on the concentration of NiO for $PbO–MoO_3–B_2O_3$ glasses. The upper inset shows dependence of activation energy on concentration of NiO, the lower one – dependence of ac conductivity on activation energy

Thus Figure 12 and its insets suggest the existence of two zones for conduction in the high temperature region viz., zone I, for x < 0.6 mol % and zone II for x > 0.6 mol %. In zone I, the electronic conduction seems to be dominant while in zone II, the ionic conductivity seems to be more significant. The possible explanation for this behaviour of conduction is as follows: With the entry of Ni^{2+} ions into the glass network, the electronic paths are progressively blocked causing an inhibition of the electronic current with a simultaneous increase in the ionic transport. The hopping polarons from $Mo^{5+} \longleftrightarrow Mo^{6+}$ responsible for conduction are attracted in pairs by the oppositely charged divalent nickel ions. This cation–polaron pairs move together as neutral entities. As expected, the migration of these pairs is not associated with any net displacement of the charge and thus does not contribute to electrical conductivity, as a result, a decrease in the conductivity up to 0.6 mol % of NiO.

The low temperature part of the conductivity (a nearly temperature independent part, as in the case of present glasses up to ca. 70 °C) can be explained based on the quantum mechanical tunnelling model [45] similar to many other glass systems reported recently from our laboratory [46–49]. The value of $N(E_F)$, i.e. the density of the defect energy states near the Fermi level, is evaluated using the equation [50]

$$\sigma(\omega) = \eta e^2 KT \left(N\left(E_F\right)\right)^2 \alpha^{-5} \omega \left(\ln\left(\frac{\nu_{ph}}{\omega}\right)\right)^4 \tag{3}$$

where η according to various authors is equal to: $\pi/3$ [45], $3.66\pi^2/6$ [51] or $\pi^4/96$ [52], for the frequency ($\omega = 2\pi r$) of 10^5 Hz at $T = 343$ K, taking $\alpha = 0.50$ $(Å)^{-1}$ (electronic wave function decay constant, obtained by plotting $\log\sigma_{ac}$ against R_i) and $\nu_{ph} \sim 5\times10^{12}$ Hz and in Table 4. The value of $N(E_F)$ is found to decrease with increasing concentration of NiO up to 0.6 mol % (indicating a decreasing disorder in the glass network, within this concentration range of NiO) and thereafter, it is observed to increase.

When a dielectric is placed in the electric field, the heat of dielectric loss is liberated. If the applied field is an alternating field, the specific dielectric loss, i.e., the loss per unit volume of the dielectric is given by [53]:

$$\rho_l = E^2 \omega \varepsilon' \varepsilon_0 \tan\delta \quad [\mathrm{W/m^3}] \tag{4}$$

This equation indicates that the lower the values of $\varepsilon'\tan\delta$ of a glass at a given frequency, lower are the values of ρ_l. The dielectric breakdown strength is in fact inversely proportional to the specific dielectric loss represented by Eq. (4). Our observations on dielectric parameters of $PbO–B_2O_3–MoO_3$: NiO glasses, as mentioned earlier, indicate that the rate of increase of $\varepsilon'\tan\delta$ with temperature is gradually decreased with increase in the concentration of NiO up to 0.6 mol %. Thus the experiments on dielectric properties of $PbO–B_2O_3$-MoO_3: NiO glasses also reveal that there is an increase in the dielectric breakdown strength of the glasses with increase in the concentration of NiO up to 0.6 mol % indicating the high rigidity of the glass network.

5. Conclusions

The analysis of DTA results suggests that the glass forming ability is the highest for the glasses containing 0.6 mol % of NiO. The spectroscopic investigations point out that the nickel ions occupy both tetrahedral and octahedral positions in the glass network. The octahedral positions seem to be dominant when the content of NiO is higher than 0.6 mol % in the glass. The dielectric parameters, ε', $\tan\delta$ and σ_{ac} are found to decrease and the activation energy for ac conduction is found to increase with the increase in the concentration of NiO up to 0.6 mol%; a considerable increase in the ac conductivity is also observed when the concentration of NiO is increased from 0.6 to 1.0 mol % in the glass matrix. The analysis of dielectric relaxation effects exhibited

by these glasses indicates that there is a spreading of relaxation times. The conduction in the high-temperature region seems to be connected with both electronic and ionic; more specifically, up to 0.6 mol % of NiO, the electronic conduction seems to be dominant while in the higher concentration range, the ionic conduction seems to prevail.

References

[1] DEL NERY S.M., PONTUSUCHKA W.M., ISOTANI S., ROUSE C.G., Phys. Rev. B, 49 (1994), 3760.
[2] DA ROCHA M.S.F., PONTUSUCHKA W.M., BLAK A.R., J. Non-Cryst. Solids, 321 (2003), 29.
[3] MOGUS- MILANKOVIC A., SANTIC A., GAJOVIC A., DAY D E., J. Non-Cryst. Solids, 325 (2003), 76.
[4] SIMON S., NICULA A.C., J. Non-Cryst. Solids, 57 (1983), 23.
[5] LYNEH J.F., SAYER M., SEGEL S.L., ROSENBLATT G., J. Appl. Phys., 42 (1971), 2587.
[6] CHOWDARI B.V.R., TAN K.L., LING F., Solid State Ionics, 113 (1998), 711.
[7] BOUDLICH D., HADDAD M., KLIAVA J., J. Non-Cryst. Solids, 224 (1998),151.
[8] DAS B.B., AMBIKA R., Chem. Phys. Lett., 370 (2003), 670.
[9] CHOWDARI B.V.R., PRAMODA KUMARI P., Solid State Ionics, 113 (1998),665.
[10] BIH L., OMARI E.L., REAU J.M., YACOUBI A., NADIRI A., HADDAD M., Mater. Lett., 50 (2001), 308.
[11] ELKHOLY M.M., El-MALLAWANY R.A., Mater. Chem. Phys., 40 (1995), 63.
[12] MOGUS-MILANKOVIC A., SANTIC A., KARABULUT M., DAY D.E., J. Non-Cryst. Solids, 330 (2003), 128.
[13] GOVINARAJU G., BASKARAN N., SHAHI K., MANORAVI P., Solid State Ionics, 76 (1995), 47.
[14] ARDELEAN I., Mod Phys Lett, 16 (2001), 523.
[15] KUNDU T.K., CHAKRAVORTY D.K., J. Mater Res., 14 (1999), 1069.
[16] DESOKY El., MOHAMED S.M., KASHIF I., J. Mater. Sci. Mater. Electr., 10 (1999), 279.
[17] FAROUK H M., SANAD A., J. Mater. Sci. Mater. Electr., 6 (1995), 393.
[18] YOKOKAWA T., SHIBATA M., OOKAWA M., J. Non-Cryst. Solids, 190 (1995), 226.
[19] KASHIF I., FAROUK H., ALY S.A., J. Mater. Sci. Mater. Electr., 2 (1991), 216.
[20] KAMINSKII A.A., *Crystalline Lasers: Physical Processes and Operating Schemes*, CRC Press, Boca Raton, 1996.
[21] ZANNONI E., CAVALLI G., BETTINELLI M., J. Phys. Chem. Solids, 60 (1999), 449.
[22] NAGESWARA RAO P., RAGHAVAIAH B.V., KRISHNA RAO D., VEERAIAH N., J. Mater. Chem. Phys., 91 (2005), 381.
[23] SRINIVASA Reddy M., VEERAIAH N., J. Phys. Chem. Solids, 67 (2006), 789.
[24] AHMAD M.M., HOGARTH C.A., KHAN M.N., J. Mater. Sci., 19 (1984), 4041.
[25] KHALIFA F.A., EL BATAL H.A., AZOOZ A., Ind. J. Pure Appl. Phys., 36 (1998), 314.
[26] GOVINDARAJ G., BASKARAN N., SHAHI K., MANORAVI P., Solid State Ionics, 76 (1995), 47.
[27] MACHIDA N., ECKERT H., Solid State Ionics, 107 (1998), 255.
[28] MUTHUPARI S., PRABAKAR S., RAO K.J., J. Phys. Chem. Solids, 57 (1996), 553.
[29] SELVARAJ U., RAO K.J., Chem. Phys., 123 (1988a), 141; J. Non-Cryst. Solids, 104 (1988), 300.
[30] HUI-FEN WU., LIN CHUNG-CHENG, SHEN J.P., Non-Cryst. Solids, 209 (1997),76.
[31] RAO J.L., NARENDRA G.L., LAKSMAN S.V.J., Polyhedron, 9 (1990), 1475.
[32] RAO P.N., RAGHAVAIAH B.V., RAO D.K., VEERAIAH N., J. Lumin., 117 (2006), 53.
[33] GOLGSTEIN A., CHIRIAC V., BECHERESCU D., J. Non-Cryst. Solids, 92 (1987), 271.
[34] BOUDLICH D., HADDAD M., KLIAVA J., J. Non-Cryst. Solids, 224 (1998), 151.
[35] BIH L., OMARI El., HADDAD M., REAU J.M., BOUDLICH D., YACOUBI A., NADIRI A., Solid State Ionics, 132 (2000), 71.
[36] SRINIVASA RAO G., VEERAIAH N., J. Solid State Chem., 166 (2002), 104.

[37] HADDAD M., NADIRI A., BIYADI A., ARCHIDI M.E., FOLGADO J.V., BELTRAN-PORT D., J. Alloys Comp., 188 (1992), 161.
[38] IORDANOVA R., DIMITROV V., KLISSURSKI D., J. Non-Cryst. Solids, 231 (1998), 227.
[39] KRISHNA MOHAN N., SAMBASIVA RAO K., GANDHI Y., VEERAIAH N., Physica B, 6 (2006), 166.
[40] DURGA D. K., VEERAIAH N., J. Mater. Sci., 36 (2001), 5625.
[41] RADHA KRISHNAN S., SRINIVAS R.S., Phys. Rev. B, 14 (1976), 6967.
[42] BÖTTCHER C.J.F., BORDWIJK P., *Theory of Electrical Polarization* (Part II), Elsevier, New York 1978.
[43] EL-DAMARAWI G., J. Phys. Cond. Matter., 7 (1995), 1557.
[44] MONTANI R.A., FRECHERO M.A., Solid State Ionics, 158 (2003), 327.
[45] AUSTIN I.G., MOTT N.F., Adv. Phys., 18 (1969), 657.
[46] NAGA RAJU G., SRINIVASA RAO N., VEERAIAH N., Physica B, 373 (2006), 297.
[47] VENKATESWARA RAO G., VEERAIAH N., Phys. Chem. Glasses, 43 (2002), 205.
[48] SAHAYA BASKARAN G., LITTLE FLOWER G., KRISHNA RAO D., VEERAIAH N., J. Alloys Comp., 431 (2007), 303.
[49] RAO A.V., LAXMIKANTH C., VEERAIAH N., J. Phys. Chem. Solids, 67 (2007), 2263.
[50] ELLIOT S.R., *Physics of Amorphous Materials*, Longman, Essex, 1990.
[51] BUTCHER P., HYDEN K.J., Phil. Mag., 36 (1997), 657.
[52] POLLAK M., Phil. Mag., 23 (1971), 579.
[53] TAREEV B., *Physics of Dielectric Materials*, Mir, Moscow, 1979.

Received 18 May 2007
Revised 28 August 2007

Materials Science-Poland, *Vol. 26*, *No. 3*, *2008*

Sinker electrical discharge machining of aluminium matrix composites

P. CICHOSZ*, P. KAROLCZAK

Institute of Production Engineering and Automatization, Wrocław University of Technology
Wybrzeże Wyspiańskiego 27, 50-370 Wrocław, Poland

Principal features of aluminium matrix composites are put forward. Emphasis is put on temperatures of melting and coefficients of heat conduction of matrix and reinforcement. The paper presents results of electrical discharge machining of aluminium matrix composites with particular attention given to thickness of the defected layer after machining. Influence of various machining parameters on the behaviour of saffil fibres and matrix material in the affected zone is presented. Scanning micrographs and roughness measurements are used to analyse surface finish following machining. The influence of used current parameters on the quality of surface layer after electrical discharge machining is discussed. The results for composite materials are compared with those for aluminum alloys.

Key words: *aluminium matrix composites; machining; spark erosion*

1. Introduction

Metal matrix composites (MMC) are increasingly popular as materials of choice for fabricating high-strength parts in such areas as aviation, aerospace, automotive industry, electrotechnology, sports and recreation [1]. At present, a large variety of composites are commercially available. The matrix can be metal, polymer or ceramics, and reinforcement can be of similar types in form of fibres, particles or powders. The investigation described in this paper was carried out on aluminium composite materials reinforced with ceramic Al_2O_3 fibres of the saffil type manufactured by ICI SAFFIL. Cast AlSi9Mg (AK9) alloy constituted the matrix The compositions and properties of the materials under under study are given in Tables 1–3. The presented method of fabricating parts with suitably arranged fibres worked out at the Institute of Production Engineering and Automation of the Wrocław University of Technology [2] consisted in preparing a fluid mixture of saffil fibres and silica cohesive agent. The solution was then filtered off, formed into a desired shape, dried and fired at a high temperature. The saffil brick was then placed at a given place of a mold, poured with a molten metal and squeeze cast. The casting was further subject to electrical discharge (ED) machining.

*Corresponding author, e-mail: piotr.cichosz@pwr.wroc.pl

Machining of composites is difficult [3–5]. Hard reinforcement induces high wear in cutting tools. Application of wear-resistant materials such as polycrystalline diamond may be limited by their prohibitive cost. Intricate shapes of workpieces may also render traditional material removal operations inapplicable. That is why EDM applied to shaping MMC parts is increasingly attracting attention of manufacturers and investigators [6–9].

Table 1. Chemical composition and properties of Al_2O_3 saffil fibres

Chemical composition [%]		Properties					
Al_2O_3	SiO_2	Fibre diameter [μm]	P [kg·m^{-3}]	R_m [MPa]	E [GPa]	Θ [deg]	λ [Ω/μK]
96	4	3	3300	2000	300	2320	29-30

Table 2. Approximate chemical composition of AlSi9Mg alloy [wt. %]

Si	Cu	Mg	Mn	Fe	Ti
9.5	< 0.05	0.35	< 0.1	< 0.18	0.15

Table 3. Minimum properties of AlSi9Mg alloy

$YS_{0.2}$ [MPa]	UTS [MPa]	A_{50mm} [%]	HB	Θ [deg]	λ [W/(m·K)]
190	230	2	75	600	150–170

EDM in MMCs poses many challenges due to the presence of two phases with completely different properties. A ductile matrix has a low melting point and a high thermal conductivity while the brittle reinforcement is characterized by a high melting point and low thermal conductivity. High thermal resistance of composites has an adverse effect on the efficiency of ED machining processes [6] and is one of those aspects that require a lot of investigative effort. The aim of the presented paper is to investigate applicability of sinker ED machining to shaping aluminium composites reinforced with saffil fibres.

2. Experimental

The experiments were conducted on an EDM 16 machine with an M1E electrolytic copper electrode and glifer dielectric fluid. The surfaces to be machined were ground prior to tests to ensure uniform initial conditions. The following three sets of current parameters were used: a) $U = 80$ V, $I_z = 0.8$ A, $I_r = 3$ A, b) $U = 80$ V, $I_z = 1$ A, $I_r = 5$ A, c) $U = 80$V, $I_z = 4$ A, $I_r = 40$ A, where I_z is the intensity of ignition, I_r – working intensity and U – voltage.

For the sake of comparison, the same conditions were used in EDM of reference AlSi9Mg alloy without saffil reinforcement. The ED machined surfaces were examined with optical and scanning microscopy. Surface roughness was evaluated using

a Taylor Hobson Form Talysurf 120L profilographometer. Mesohardness was measured using a LECO tester.

3. Sinker ED machining of pure Al alloy

Figure 1 shows a micrograph of the defect-affected layer in pure Al alloy produced by the sinker ED machining operation adopted in this study. Clearly visible are the heat-affected zone and a crater left by spark discharge. Microstructure of the alloy has been recast and fragmented. Finer microstructure resulted in higher values of mesohardness. In the areas of strong thermal influence it reached 130–147 HV and was by 65% higher than that of the bulk material. Depth of the said layer was strongly dependent upon machining parameters and varied from 20 to 120 μm. Surface roughness as determined by *Ra* was found to be approximately equal to 6 μm.

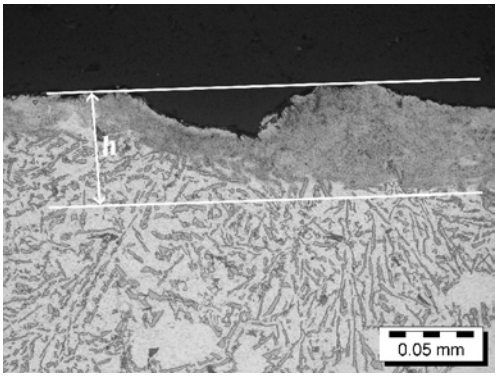

Fig. 1. Optical micrograph across the defect-affected layer of AlSi9Mg workpiece following the sinker EDM operation. Sinker EDM parameters: $U = 80$ V, $I_z = 1$ A, $I_r = 5$A, machining area size: 120 mm^2, $h \approx 60$ μm, $Ra = 6.17$ μm

4. Sinker ED machining of the composite

ED machining of the composite was done using three sets of current parameters listed in Sect. 2. The first set (a) with low currents is shown in action in Fig. 2.

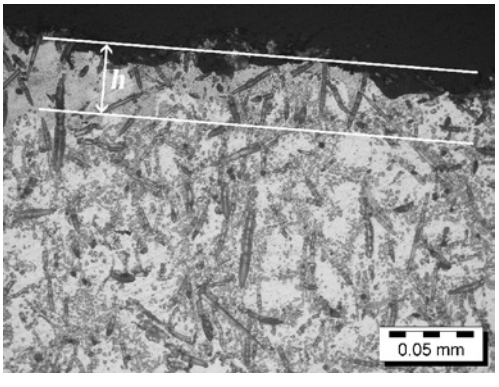

Fig. 2. Optical micrograph across the defect-affected layer of composite workpiece following the sinker EDM operation. Sinker EDM parameters: $U = 80$ V, $I_z = 0.8$ A, $I_r = 3$A, machining area size: 120 mm^2, $h \approx 30$ μm

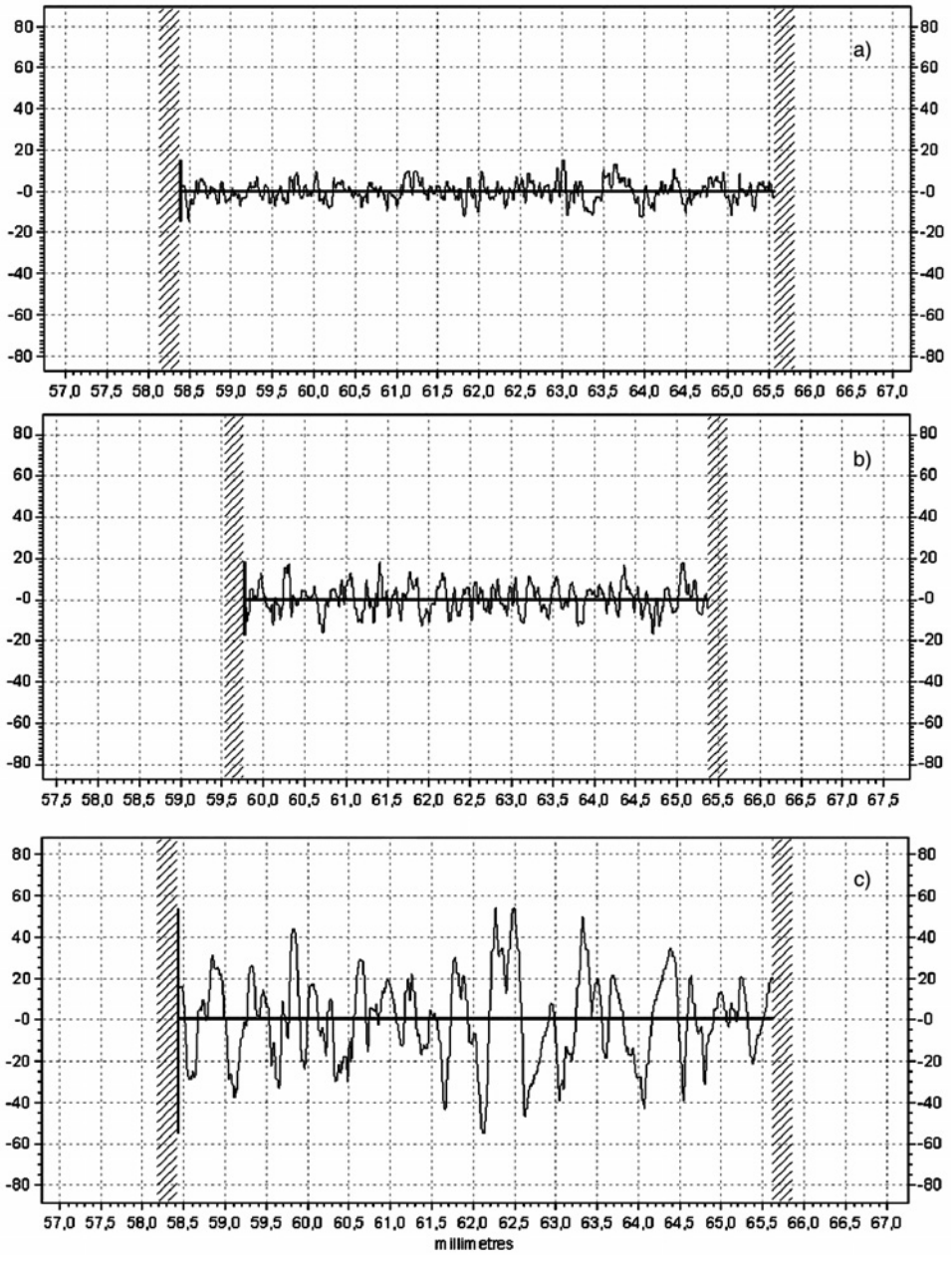

Fig. 3. Surface roughness profiles for a composite specimen following the sinker EDM operation: a) Ra = 3.55 μm, b) Ra = 5.1 μm, c) Ra = 17 μm

Depth of the heat-affected zone was equal to about 30 μm. Only mild metallurgical changes could be observed within that zone. The matrix was slightly recast and made finer. Ceramic fibres were generally left undamaged. Those directly affected by

spark discharges were degraded. Some fibres were found to stick out a few μm from the surface. Hardness of the zone (148–157 HV) was higher than that of the bulk material. Surface roughness was found to be Ra = 3.5–4 μm (Fig. 3).

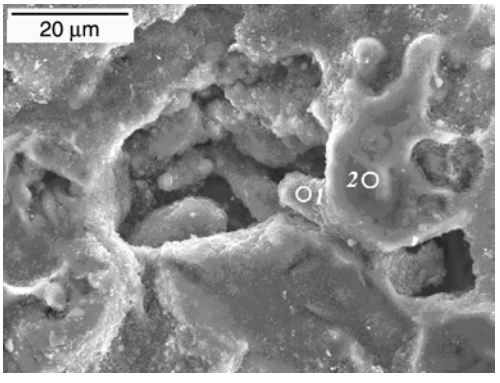

Fig. 4. Scanning micrograph of the ED machined composite surface; U = 80 V, I_z = 0.8A, I_r = 3 A

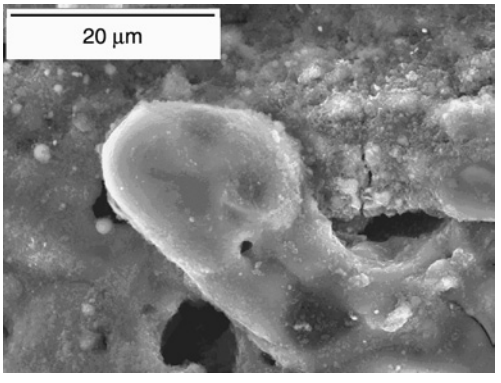

Fig. 5. Scanning micrograph of the ED machined composite surface; U = 80 V, I_z = 0.8A, I_r = 3 A

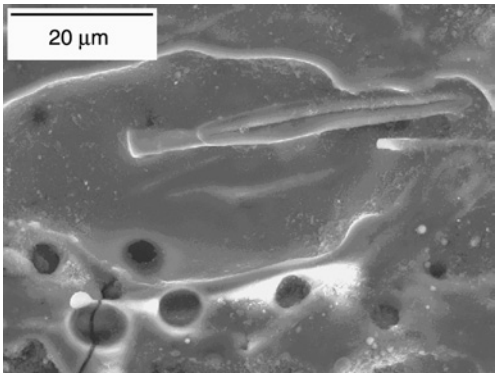

Fig. 6. Scanning micrograph of the ED machined composite surface; U = 80 V, I_z = 0.8 A, I_r = 3 A

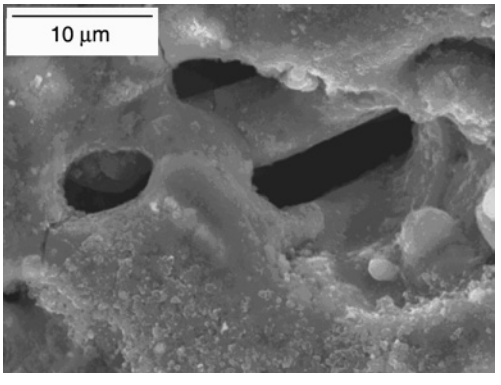

Fig. 7. Scanning micrograph of the ED machined composite surface; U = 80 V, I_z = 0.8 A, I_r = 3 A

Figure 4 shows the scanning micrograph of the composite surface machined with the parameters (a). Clearly visible are craters produced by spark discharges. Both the matrix and reinforcement are heavily recast. Few fibres were found undamaged (denoted by 1). At a place denoted by 2 there was a fibre-now molten up completely. Its presence was established by spectrometer examination of the surface targeted at oxygen.

Figure 5 shows another area of the surface machined with the parameters (a). A centrally placed object resembles a fibre. Chemical analysis determined that there is no oxygen at this place so it must be a peculiarity of solidification.

Figure 6 shows a rare case where saffil fibres did remain on the machined surface. There are three fibres visible with analytically confirmed high oxygen content. Numerous craters with smooth contours are the evidence that the area was melted to a high depth and the resulting long time of cooling helped the craters to be smoothed out.

A high-magnification scanning micrograph in Fig. 7 shows a single crater with an unmelted fragment of a thick (~5 μm) fibre. It was probably this large fibre volume that saved the fibre from being melted. By using higher current parameters (set (b)) a higher intensity of thermal action was achieved. The heat-affected zone has now a depth of about 70 μm (Fig. 8). Undamaged fibres no longer protrude from the surface. The overall surface finish has deteriorated and *Ra* has now risen to 5–6 μm (Fig. 3).

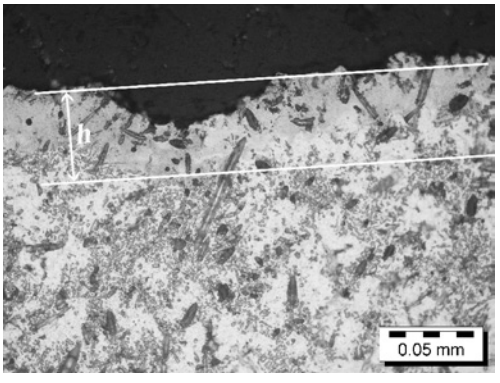

Fig. 8. Optical micrograph across the defect-affected layer of composite workpiece following the sinker EDM operation; sinker EDM parameters: $U = 80$ V, $I_z = 1$ A, $I_r = 5$ A, machining area size: 120 mm^2, $h \approx 70$ μm

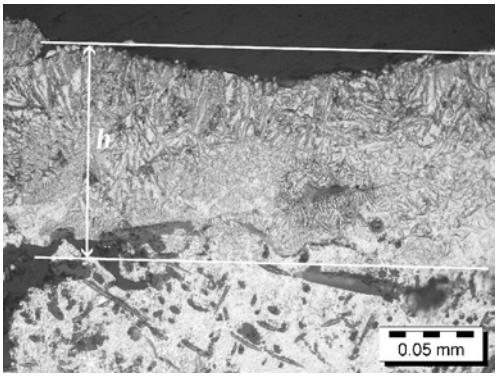

Fig. 9. Optical micrograph of the ED machined composite surface; Sinker EDM parameters: $U = 80$ V, $I_z = 4$A, $I_r = 40$ A, machining area size: 120 mm^2, $h \approx 120$ μm

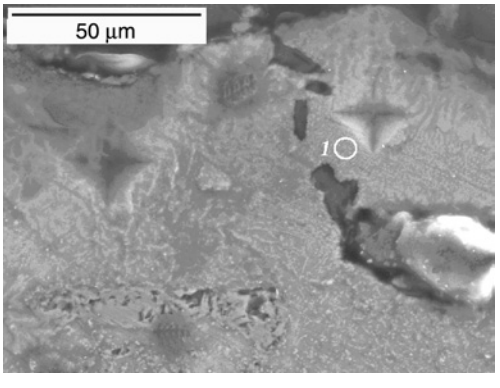

Fig. 10. Scanning micrograph of surface layer of the ED machined composite: $U = 80$ V, $I_z = 4$ A, $I_r = 40$ A

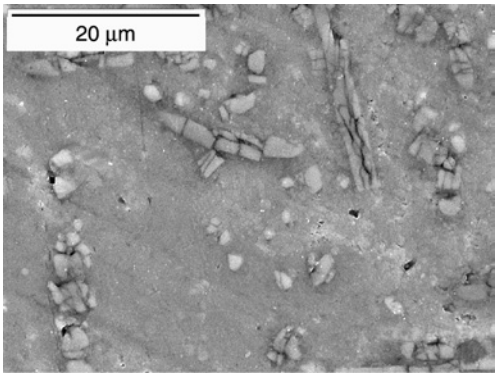

Fig. 11. Scanning micrograph of surface layer of the ED machined composite; $U = 80$ V, $I_z = 4$ A, $I_r = 40$ A

The third current parameters set (c) caused the biggest changes in the composite top layer. The depth of melting was now $h = 120$ μm. Numerous deep craters were noticed (Fig. 9). A new feature were blisters located just beneath the surface. They

frequently contained saffil fibres. The top composite layer crystallized in the direction perpendicular to the surface. Surface roughness was the worst of the three cases (Ra = 17 μm, Fig. 3). Optical examination of the recast layer produced by the set (c) current parameters revealed no undamaged fibres. Spectrometer probe examination detected areas with increased oxygen content attesting to the fibres being dissolved in the matrix and forming new Al–O compounds.

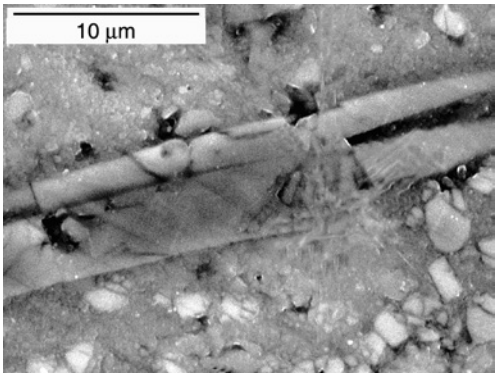

Fig. 12. Scanning micrograph of surface layer of the ED machined composite; U = 80V, I_z = 4 A, I_r = 40 A

Mesohardness of the recast layer was low: 113–130 HV. In some places the hardness reached 280–320 HV (area 1 in Fig. 10). These fibres were initially assumed to be molten fibres but the assumption turned out false as no higher oxygen content was detected. Those anomalies in hardness remain to be further investigated. Special attention was paid to fibres located just beneath the recast layer produced by set (c) (Fig. 11). The fibres are fragmented and broken, they must have been damaged by high energy of the pulses. The extent of damage decreases with increasing depth (Fig. 12).

4. Final remarks

The investigation showed that ED machining process parameters affect the condition of surface layer in machined aluminium MMCs. Low current parameters resulted in a thin layer with a recast structure of increased hardness. Reinforcing fibres were generally left undamaged, some of them protruding from the surface. Some fibres were melted down and then resolidified as featureless blobs.

Higher process parameters resulted in severe detrimental changes to the surface layer structure. Higher material removal rates produced a very rough finish with poor surface integrity (numerous craters and sub-surface blisters).

There is a need for working out optimized patterns of current density and frequency of sparks that would eliminate or reduce the extent of finishing operations necessary for removing the recast layer.

References

[1] SOBCZAK J., WOJCIECHOWSKI S., , Kompozyty (Composites), 2 (2002), 25 (in Polish).
[2] NAPLOCHA K., *Optimization of process variables in manufacturing the AK9 type materials reinforced with Al_2O_3 fibres*, Institute of Production Engineering and Automation, Wrocław University of Technology, Doctor Thesis, Wrocław 1999 (in Polish).
[3] JANKOWIAK M., KAWALEC M., KRÓL G., *Machining ability of cutting edges in turning Al_2O_3-particle reinforced Al alloys*, ZN Politechniki Rzeszowskiej, Mechanika 44, 1995, 133 (in Polish).
[4] CRONJAGER L., MEISTER D., *Machinability of fibre and particle-reinforced aluminium*, Annals of CIRP, 41 (1992), 63.
[5] TETI R., *Machining of composite materials*, Annals of CIRP, 51 (2002), 611.
[6] PEROŃCZYK J., BIAŁO D., Kompozyty (Composites) 1 (2001), 211 (in Polish).
[7] PEROŃCZYK J., BIAŁO D., Kompozyty (Composites) 3(2003), 366 (in Polish).
[8] TRZASKA M., PEROŃCZYK J., BIAŁO D., Kompozyty (Composites) 5 (2005), 51 (in Polish).
[9] WANG CH., YAN B., J. Mat. Proc. Techn., 12 (2000), 90.

Received 13 June 2007
Revised 15 October 2007

Materials Science-Poland, *Vol. 26*, *No. 3*, *2008*

Dielectric and structural characteristics of Sm doped $Ba_4La_{9.33}Ti_{18}O_{54}$ ceramics

S. BAHEL, S. BINDRA NARANG*

Department of Electronics Technology, Guru Nanak Dev University, Amritsar, Punjab, India

The microwave dielectric properties and structural variation of Sm doped $Ba_4La_{9.33}Ti_{18}O_{54}$ have been investigated. $Ba_4(La_{1-y}Sm_y)_{9.33}Ti_{18}O_{54}$, y = 0.0–0.7 ceramics were prepared by conventional solid state route. The electric permittivity and loss tangent were measured using a network analyzer in the frequency range of 0.3–3.0 GHz at room temperature. The loss tangent decreases significantly upon increasing Sm contents, along with a slight reduction in electric permittivity. A relatively good combination of dielectric properties was obtained for y = 0.5 (ε' = 83.3 and $\tan\delta$ = 0.021 at 3.0 GHz). X-ray diffraction and scanning electron microscopy were applied to investigate the microstructure and correlate it with microwave dielectric properties.

Key words: *ceramics; X-ray diffraction; scanning electron microscopy; electric permittivity; loss tangent*

1. Introduction

The latest development in mobile communication increased the need for good quality microwave dielectric ceramics to be used as resonators, band pass filters and duplexers. The ceramics required for these devices should have a high electric permittivity (ε') and a low dielectric loss (or loss tangent) or high quality factor (Q = 1/ $\tan\delta$). The ceramics based on a $BaO–R_2O_3–TiO_2$ (R = rare earth; Sm, Nd, Pr, La) ternary system has been extensively investigated [1–3]. In this system, $Ba_{6-3x}R_{8+2x}Ti_{18}O_{54}$ solid solutions showing high electric permittivity were discovered on the tie line joining $BaTiO_3$ and R_2TiO_5 composition [4]. The $Ba_{6-3x}R_{8+2x}Ti_{18}O_{54}$ solid solution shows a tungsten bronze-type structure with orthorhombic symmetry. The fundamental structural formula of this compound was reported [5] as $[R_{8+2x}Ba_{2-3x}V_x]_{A1}[Ba_4]_{A2}[V_4]_C Ti_{18}O_{54}$, where V is vacancy, A1-site is rhombic forming 2×2 perovskite block, while A2-site and *C*-site are pentagonal and trigonal ones, respectively. Three different cations with different diameters occupy different sites – the middle sized R ions

* Corresponding author, e-mail: sukhleen2@yahoo.com

mainly occupy A1-sites; the largest Ba ions occupy A2-sites and A1 sites and the smallest Ti ions alone occupy octahedral *B* sites. At $x = 2/3$, the R and Ba cations separately occupy A1 and A2 sites which leads to the highest *Q* value or the lowest loss tangent [5, 6]. Under special conditions of R = La and $x = 2/3$, the composition $Ba_4La_{9.33}Ti_{18}O_{54}$ exhibits the highest electric permittivity with the highest dielectric loss [5, 7].

The purpose of this paper is to reduce the loss without much change in electric permittivity. The Sm substitution in place of Nd has been shown [8–10] effective in reducing the loss of barium neodymium titanate (similar material). It attracted the attention and provided the motivation to study the effect of Sm doping on microwave dielectric properties of $Ba_4La_{9.33}Ti_{18}O_{54}$.

2. Experimental

Samples of $Ba_4(La_{1-y}Sm_y)_{9.33}Ti_{18}O_{54}$ with y = 0.0, 0.1, 0.3, 0.5 and 0.7 were synthesized by conventional solid state method from individual reagent grade oxide powders – BaO (99.5%), La_2O_3 (99.9%), Sm_2O_3 (99.9%) and TiO_2 (99.5%). Stoichiometric proportions of the raw materials were mixed in agate mortar for 12 h in methanol, dried and calcined at 1100 °C for 2 h. The calcined powders were ground again for 12 h and an organic binder, 3 wt. % PVA (poly (vinyl alcohol)), was added. These were then passed through a mesh and pressed to pellets of various shapes under the load of 98 kN. These pellets were then sintered at 1300 °C for 2h in air in a linearly programmable furnace. The sintered pellets were polished with fine emery paper to make the surfaces flat, smooth and parallel for measurements.

These samples were then characterized for various properties. X-ray powder diffraction (XRD) patterns were recorded with powders of sintered samples using Ni filtered CuK_α radiation in the 20–80° 2θ range (model PWQ 1729, Philips). From these patterns, lattice parameters were calculated by the least square method. The internal strain/fluctuation of *d*-spacing η was obtained from the following equation [5] as the grain size of the ceramics is sufficiently large:

$$\eta = \frac{\beta}{2\tan\theta} \tag{1}$$

where β is the full-width at half-maximum (FWHM) and is calculated using a computer program.

The bulk densities were measured by the liquid displacement method (Archimedes method) [11]. The micro-structural observation was carried out by scanning electron microscopy (model JSM 6100, JEOL Japan). The electric permittivity and loss tangent were measured by coaxial open ended probe method [12] using network analyzer (model 8714ET, Agilent Technologies) in the frequency range 0.3–3.0 GHz at room temperature.

3. Results and discussion

Figure 1 shows the XRD patterns of $Ba_4(La_{1-y}Sm_y)_{9.33}Ti_{18}O_{54}$ ceramics with various Sm contents. The patterns are identified with tungsten bronze-type compounds and match with the one reported for $Ba_4La_8Ti_{17}O_{50}$ (JCPDS file no 42-0419). All the peaks are indexed and there is no evidence of any secondary phase present for $y < 0.5$. However for $y = 0.7$, all peaks are assigned to tungsten bronze-type $BaSm_2Ti_4O_{12}$ structure (JCPDS file no 44-62). A small amount of a secondary phase, identified as $Ba_4La_8Ti_{17}O_{50}$, is also detected. All the solid solutions have the perovskite structure with an orthorhombic symmetry.

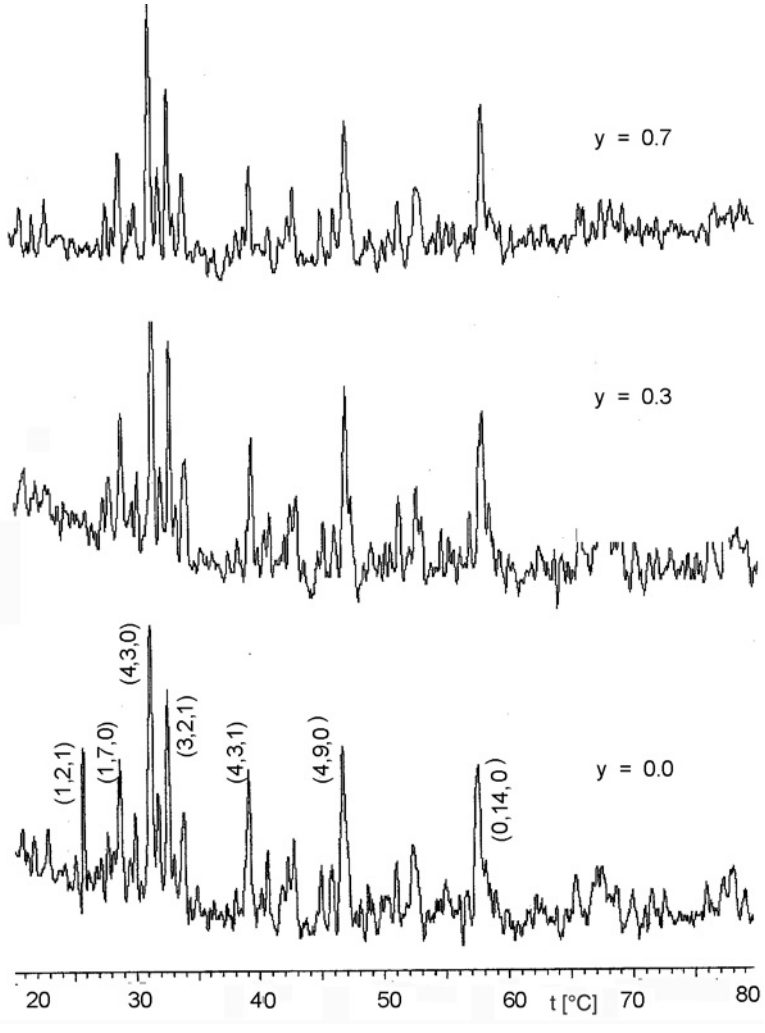

Fig. 1. X ray diffraction patterns for $Ba_4(La_{(1-y)}Sm_y)_{9.33}Ti_{18}O_{54}$

The lattice parameters for different Sm contents are given in Table 1. The variation of unit cell volume with increasing Sm contents is shown in Fig. 2.

Table 1. Variation of lattice parameters for different Sm contents

Composition y	a [Å]	b [Å]	c [Å]
0.0	12.33	22.41	3.87
0.1	12.32	22.38	3.85
0.3	12.31	22.35	3.85
0.5	12.26	22.18	3.81
0.7	12.19	22.12	3.78

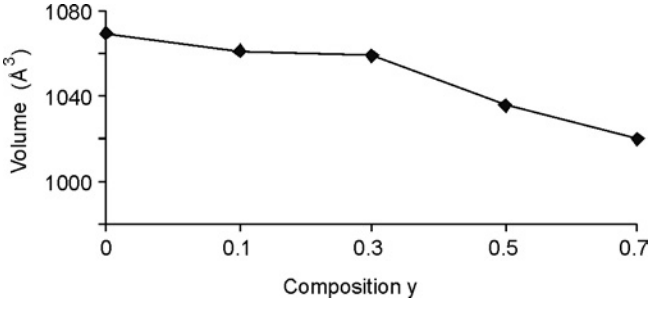

Fig. 2. Cell volumes for various Sm contents

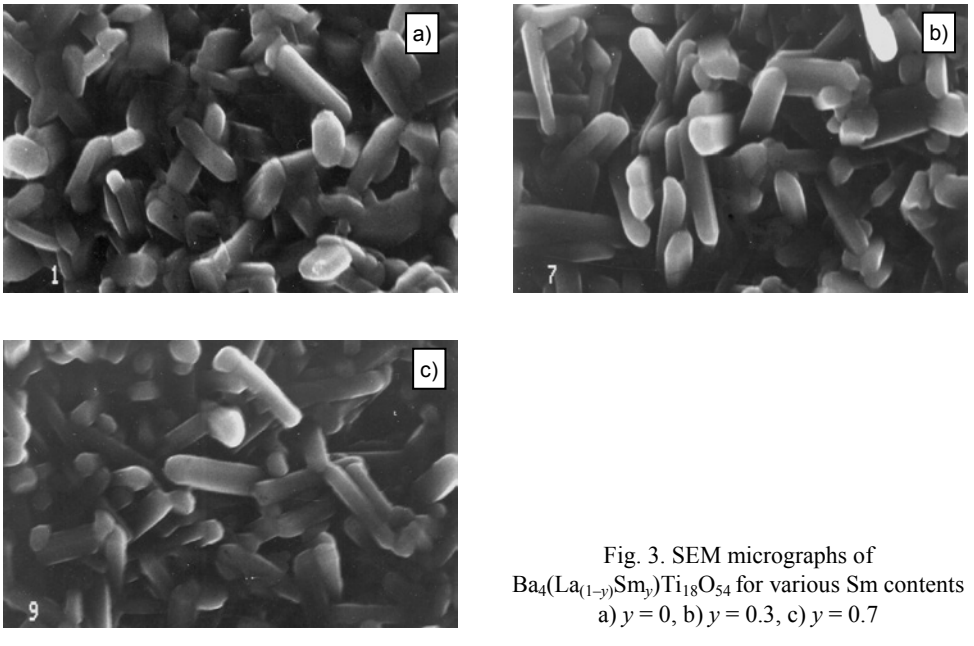

Fig. 3. SEM micrographs of $Ba_4(La_{(1-y)}Sm_y)Ti_{18}O_{54}$ for various Sm contents a) $y = 0$, b) $y = 0.3$, c) $y = 0.7$

The lattice parameters gradually decrease as the amount of Sm substitution for La increases with maximum change for *c*-axis and minimum for *a*-axis. However, with respect to changes per Å, the maximum change is 2.32% for *c*-axis, the minimum is 1.13% for *a*-axis and the change for *b*-axis is 1.29%. The change in lattice parameters could be attributed to the change in ionic radius between La and Sm ions. Shannon [13] reported the effective ionic radii for 12 co-ordinations as 1.36 Å and 1.24 Å for La and Sm ions, respectively. The difference of ionic radii directly affects the lattice parameters because a repetition of the rhombic and pentagonal sites stacked along *c*-axis brings out the length of lattice parameters.

The SEM micrographs of fractured surface of the sintered samples are shown in Fig. 3. The ceramics have a close microstructure with low porosity and closely packed hexagonal grain. It shows that the average grain size decreases slightly with increase in Sm contents.

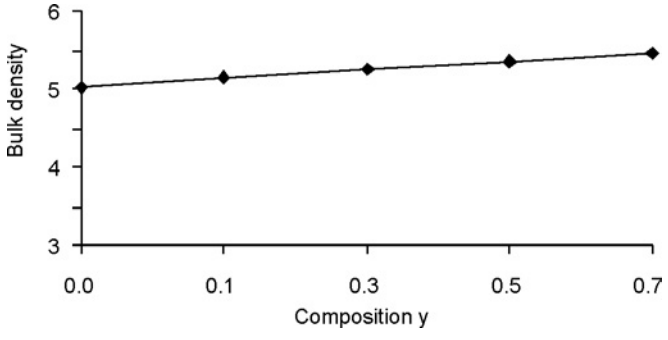

Fig. 4. Bulk densities (in g/cm^3) for various Sm contents

The bulk densities of $Ba_4(La_{1-y}Sm_y)_{9.33}Ti_{18}O_{54}$ ceramics as a function of increasing Sm contents are shown in Fig. 4. The ceramics have a high value of bulk density (> 5.0 g/cm^3) with a maximum of 5.45 g/ cm^3 for $y = 0.7$.

The electric permittivities and loss tangents of all the ceramics are shown in Figs. 5 and 6, respectively, in functions of frequency in 0.3–3.0 GHz region at room temperature. The electric permittivity decreases from 93.04 to 81.02 and loss tangent also decreases from 0.1659 to 0.012 at 3.0 GHz with increase in Sm contents. The dielectric properties of the solid solutions are highly influenced by the crystal structure. Table 1 shows that the lattice parameters decrease with increase in Sm substitution for La. This decrease in lattice parameters may lead to shrinkage of *B*-sites occupied by Ti ions, and then the displacement of the Ti ions from the centre of the octahedra becomes smaller and therefore the electric permittivity and dielectric loss decrease [14].

Moreover, the variation of electric permittivity is also dependent on the polarizability of R ion and it decreases with the decrease in its polarizability [5]. The decrease in the electric permittivity with increase in Sm substitution for La could also be due to the low polarizability of Sm (4.74 Å^3) as compared to La (6.03 Å^3) [15].

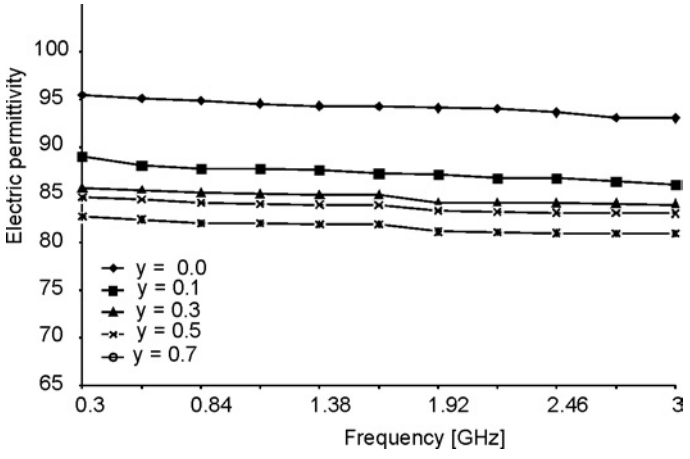

Fig. 5. Variation of electric permittivity with frequency for different Sm contents

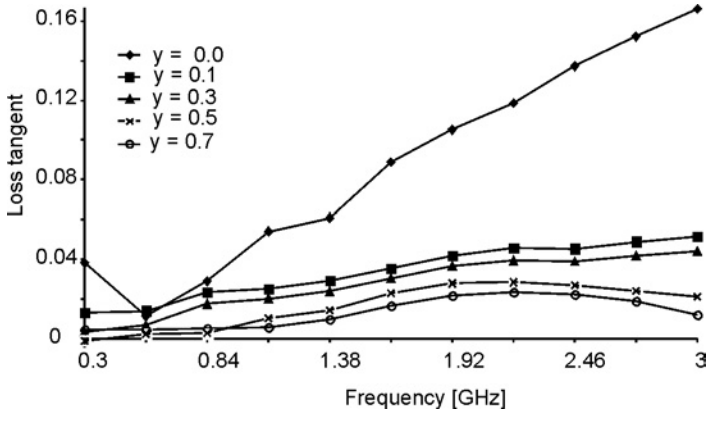

Fig. 6. Variation of loss tangent with frequency for different Sm contents

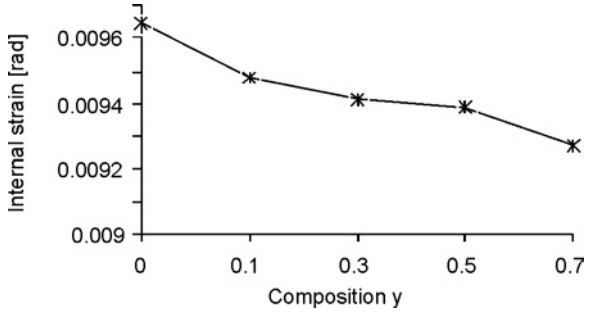

Fig. 7. Dependence of internal strain on Sm contents

Ohsato [5] had shown that the crystal structure with large size difference between Ba and R ions has the excellent quality factor as it has low internal strain. The variation of internal strain in fuction of different Sm contents is shown in Fig 7. With in-

crease in Sm substitution for La, the internal strain decreases and hence the loss tangent also decreases.

4. Conclusions

Microwave dielectric ceramics $Ba_4(La_{(1-y)}Sm_y)_{9.33}Ti_{18}O_{54}$ with y = 0.0–0.7 were synthesized using conventional mixed oxide route. These were then characterized for their dielectric and structural properties. The electric permittivities were 93.03–81.02 and loss tangents were 0.1659–0.012 as y = 0.0–0.7 at 3.0 GHz. It has been found that substitution of Sm results in reducing the tangent loss with a slight decrease in electric permittivity. The excellent microwave dielectric properties were obtained for y = 0.5 with electric permittivity 83.3 and loss tangent 0.021 at room temperature.

Acknowledgements

The authors would like to thank M.L. Sharma (SAIF, Punjab University, Chandigarh, India) for guiding SEM analysis and Gurvinderjit Singh (CAT, Indore, India) helping in analysis of XRD patterns.

References

[1] KOLAR D., STADLER Z., GABERSCEK S., SUVOROV D., Ber. dt. Keram. Ges., 55 (1978), 346.
[2] KOLAR D., GABERSCEK S., VOLAVSEK B., J. Solid. State Chem., 38 (1981), 158.
[3] KAUR D., NARANG S.B., SINGH K., J. Ceram. Proc. Res., 7 (2006), 31.
[4] OHSATO H., OHHASHI T., NISHIGAKI S., OKUDA T., SUMIYA K., SUZUKI S., Jpn. J. Appl. Phys., 32 (1993), 4323.
[5] OHSATO H., J. Eur. Ceram. Soc., 21 (2001), 2703.
[6] OHSATO H., IMAEDA M., Mater. Chem. Phys., 79 (2003), 208.
[7] NARANG S.B., KAUR D., BAHEL S., Mater. Lett., 60 (2006), 3179.
[8] LAFFEZ P., J. Mater. Sci., 30 (1995), 267.
[9] LI Y., CHEN X.M., J. Europ. Ceram. Soc., 22 (2002), 715.
[10] CHENG C.C., HSIEH T.E., LIN I-NAN, Mat. Chem. Phys., 79 (2003), 119.
[11] ANGADI B., JALI V.M., LAGARE M.T., KINI K.S., UMARJI A.M., Bull. Mater. Sci., 25 (2002), 191.
[12] CHEN L.F., ONG C.K., NEO C.P., VARADAN V.V., VARADAN V.K., *Microwave Electronics Measurement and Materials Characterization*, Wiley, New York, 2004.
[13] SHANONON R.D., Acta Cryst., 32A (1976), 751.
[14] OHSATO H., OHHASHI T., KATO H., NISHIGAKI S., OKUDA T., Jpn. J. Appl. Phys., 34 (1995), 187.
[15] SHANNON R.D., J. Appl. Phys., 73 (1993), 348.

Received 3 July 2007
Revised 13 November 2007

Materials Science-Poland, *Vol. 26*, *No. 3*, *2008*

Lifetime prediction in creep-fatigue environment

M. H. SABOUR[1*], R. B. BHAT[2]

[1] Department of Mechanical Engineering, Semnan University, Semnan, Iran

[2] Department of Mechanical and Industrial Engineering,
Concordia University, Montreal, Quebec, Canada

The creep-fatigue interaction has been studied and innovative mathematical models are proposed to predict the operating life of aircraft components, specifically gas turbine blades subject to creep-fatigue at high temperatures. The historical evolution of the creep-fatigue lifetime prediction is given in order to place the present study in the context. A literature review of the life estimation under creep-fatigue environment is presented.

Key words: *creep-fatigue; lifetime;, constitutive model*

1. Introduction

There is a general tendency towards more severe operating conditions, i.e. higher mechanical loadings and temperatures, in order to increase the efficiency of gas and steam turbines, internal combustion engines, heat exchangers, conventional and nuclear electric power generation equipment and other engineering components and devices. This trend has resulted in starting, growth and interaction of complex damaging processes within the materials of these devices. They can lead to the failure of a component and, consequently, of a whole structure, and thus limit their lifetime. Therefore, a safe assessment of lifetime is very important for the prevention of such failures which may have disastrous consequences; too conservative predictions, however, unnecessarily increase the cost of production and maintenance of such systems.

The blades operate in a damaging environment of high temperatures, centrifugal and gas pressure forces and thermal cycling. These conditions combine at every point in the blade to create an interaction between creep and thermo-mechanical fatigue damage. Because of stress redistribution due to the creep process, it is necessary to include a viscoelastic material model in the finite element analysis. Otherwise, over-conservative creep life predictions are estimated if only the initial elastic stresses are considered. In the current investigation, several aspects of lifetime prediction are of

[*]Corresponding author, e-mail: sabour_mh@yahoo.com

interest. They include the damage due to creep-fatigue interactions, modelling using FEM, and experimental validation. Many researchers have dealt with this issue over the years. The simulation studies on the life-limiting modes of failure, as well as estimating the expected lifetime of the blade, using the proposed models have been carried out. Although the scale model approach has been used for quite some time, the thermal scaling (scaled temperature in model and test, with consideration of its restrictions) has been used in this study for the first time.

Many investigators have examined creep-fatigue crack initiation [1–3] and propagation modes [1, 4–11] in general. Some of them focused on studying the effect of specific parameters such as hold time [12, 13] or creep stress effect [14], environment [5, 15], a new evidence of orientation [16, 17], geometry [18], and material parameters [19–21]. Some of them studied metallurgical problems [22] or discussed design rules [23]. In design field, some of them developed a system for assessment [24], used numerical method [25] or damage concept [26] for life prediction, or suggested their own constitutive model [27, 28]. Since it is easier, many of them used thermo-mechanical loading [29–32] for the tests. It was shown in the above studies that the origin of failure under low-cycle fatigue is mainly related to the geometrical discontinuities on the specimen surface and creep-fatigue-environment interactions may enhance the cracking problem. This fact shows the importance of the current study. In low cycle fatigue (LCF) tests, it has been reported that as the hold time is increased, the fatigue life decreases at a fixed test temperature, and the reason for life reduction is reported to be due to the creep effect of stress relaxation which makes an additional plastic strain enlarging the hysteresis loop during hold time. It is reported that creep mechanisms of stress relaxation being the main reasons for fatigue life reduction under creep-fatigue interactions, after a long enough hold time, are the same as that of the monotonic creep [33].

A significant reduction in fatigue life is observed with hold time in compression or in both tension and compression. The influence of tensile hold on fatigue life is more complicated. The mean stress develops during both tensile and compressive hold tests. The scanning electron microscopy (SEM) analysis of fracture surfaces shows that crack initiation and first stage of growth is transgranular but crack growth in a second stage is intergranular [34]. In fact, it has been noted that high-temperature tensile yield strength is an important parameter in studying high-temperature low cycle fatigue properties, crack growth in creep and the effect of cyclic loading on growth in creep-fatigue [10]. To date, there has been no “unified” approach with which the problem of fatigue crack growth at high temperature can be solved in a general manner.

The results show that mixed time and cycle dependent crack growth seems to be the dominant fatigue crack growth mode in the two powder metallurgy (PM) nickel alloys studied, whilst limited creep may be present at the crack tip, particularly under static and long dwell loading conditions [35]. Coffine [36] produced the first significant evidence to suggest that the oxidation is primarily responsible for high temperature low cycle fatigue damage. A variety of studies have been carried out on different alloys, especially directionally solidified superalloy Mar [37, 38], Inconel [39], Co-

base [40, 41], Cr-base [4, 42], Ti-base [43–45], and Al [46]. In the 300 series austenitic stainless steels, such as 304, 316 and 316L used in high temperature applications, many studies have been devoted to understand the creep-fatigue interaction behaviour by employing the hold-time tests [32–55]. It has been observed in these investigations that at relatively high temperatures, continuous cycling endurance is corrupted when a hold-period is included in the cycle. In general, the imposition of holds at tension peak strain tended to be more harmful than those imposed at compression peak strain. Further, there has been conflicting reports on the influence of the tension-hold duration on fatigue life. Hales [56] reported a continuous reduction in life with increase in the length of tension hold-time, while others [13, 57, 58] noted a saturation effect in the life reduction. The creep-fatigue effect in stainless steels is mainly recognized to be due to the inherent weakness of the grain boundaries which lend themselves to the formation of creep induced grain boundary voids that can enlarge into intergranular cavities and cracks [44]. It is acknowledged that the difference between small and long cracks is independent of environment [59]. Several damage rules have been suggested for estimating the cumulative damage under creep-fatigue conditions. The most common approach is based on linear superposition of fatigue and creep damage.

There are divergent opinions regarding which damage approach provides the best basis for life prediction. It is quite clear that a number of variables, such as test temperature, strain range, frequency, time and type of hold, waveform, ductility of the material, and damage characteristics, affect the fatigue life. The conclusions drawn in any investigation may therefore apply only to the envelope of material and test conditions used in that study. The validity of any damage approach has to be examined with reference to the material and service conditions relevant to a specific application.

2. Linear damage summation

The most common approach is based on linear superposition of fatigue and creep damage. Indeed, the mainstay of the present design procedures is the linear life-fraction rule, which forms the basis of the ASME Boiler and Pressure Vessel Code, Section III, Code Case N-47 [63]. This approach combines the damage summations of Robinson for creep [64] and of Miner for fatigue [65] as follows [66]:

$$\sum \frac{N}{N_f} + \sum \frac{t}{t_r} = D \tag{1}$$

where N/N_f is the cyclic portion of the life fraction, in which N is the number of cycles at a given strain range and N_f is the pure fatigue life at that strain range. The time-dependent creep-life fraction is t/t_r where t is the time at a given stress and temperature, and t_r, is the time to rupture at that stress and temperature. D is the cumulative damage index. Failure is presumed to occur when D = l. If Equation (1) were obeyed, a straight line of the type shown in Fig. 1 between the fatigue- and creep-life fractions

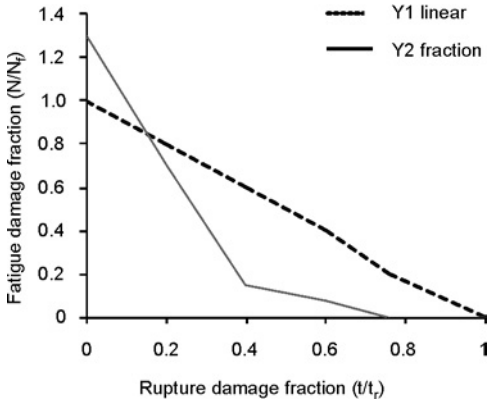

Fig. 1. Creep rupture/low cycle fatigue damage interaction curve for 1Cr–Mo-V rotor steel at 450 °C

would be expected. The life-fraction rule has no mechanistic basis. Its applicability is, therefore, material-dependent. Contrary to experience, it also assumes that tensile and compressive hold periods are equally damaging. The strain softening behaviour, which has been seen in many steels, and the effect of prior plasticity on subsequent creep are not taken into account. Use of virgin material ruptures life to compute creep-life fractions are, therefore, inaccurate. In spite of these limitations, the damage-summation method is very popular because it is easy to use and requires only standard S-N curves and stress-rupture curves.

3. Models of creep-fatigue interaction

As the blades operate at metal temperatures in excess of $0.4T_{\text{melt}}$ in kelvins, creep rupture is clearly a possible failure mode. Also, as the engine cycles through start-up and shut-down with each flight, the transient thermal and body loading stresses cause fatigue damage which can lead to ultimate failure. Thus it is possible to predict the relative amounts of creep and fatigue damage at each point in the blade at each moment of the cycle, which in turn depends upon knowing the stress and temperature conditions at each instant and at spatial point. At start-up, the thermal load was applied to the blade, resulting in a transient thermal stress response. These stresses often reached a maximum value $\sigma_{\max}$ before achieving a steady-state condition. It is therefore necessary to record this maximum stress value at each point over the blade and use it in the fatigue life calculation.

3.1. Model 1

The fluctuating stress can be considered as a varying stress in fatigue-creep model. Since the fluctuating stress is a combination of alternating and mean stresses, it can be

assumed that the part representing the static load can cause creep at elevated temperatures, whereas the alternating part is responsible for fatigue damage. To find the lifetime, the total damage is found by the following model.

3.1.1. Fatigue damage prediction

The Coffine–Manson formula can be applied in elasto-plastic material models. In the case of viscoelasticity, the modified Coffine–Manson formula will be used which includes energy dissipation ΔW as a failure criterion. The number of cycles to failure, N_f, can be calculated from the strain range $\Delta\varepsilon$ using the method of universal slopes. This method has the advantage of using material data obtainable from simple tensile tests. The equation combines the Coffine–Manson law given by

$$\frac{\Delta\varepsilon_p}{2} = \varepsilon_f' \left(2N_f\right)^c \tag{2}$$

where $\Delta\varepsilon_p$ is the plastic strain range, ε_f' is the fatigue ductility coefficient being some fraction (from 0.35 to 1) of the true fracture strain measured in the tension test

$$\varepsilon_f' = \ln\left(\frac{100}{100 - RA}\right)$$

RA is the area reduction [%] at a break, c is the fatigue ductility exponent ranging from about –0.5 to –0.7, N_f is the number of reversals (each cycle equals 2 reversals) and the Basquin law given by

$$\frac{\Delta\varepsilon_e}{2} = \frac{\sigma_f'}{E}\left(2N_f\right)^b \tag{3}$$

where $\Delta\varepsilon_e$ is the elastic strain range, σ_f' is the fatigue strength coefficient approximated by the true fracture stress, equal appromaxitely to s_{ut} + 50 (in units of ksi[*]), b is the fatigue strength exponent ranging from about –0.06 to –0.14, E is Young's modulus of elasticity. The final formula is given by:

$$\frac{\Delta\varepsilon_{\text{tot}}}{2} = \frac{\sigma_f'}{E}\left(2N_f\right)^b + \varepsilon_f' \left(2N_f\right)^c \tag{4}$$

The total strain range, $\Delta\varepsilon_{\text{tot}}$, can be found by the finite element analysis at each integration point in the model, and the coefficients and the exponents can be found by fatigue tests on the material. For instance, the values for Steel 4340 are

[*]1 ksi = 1.52×10^4 Pa.

$$\varepsilon_f' = 0.58, \quad c = 0.57, \quad b = -0.09, \quad \frac{\sigma_f'}{E} = 0.0062 \tag{5}$$

Using these values, the value of N_f (Eq. (4)), and consequently the fatigue damage parameter, D_f, may be calculated

$$D_f = \frac{n}{N_f} = \frac{t}{t_m N_f} \tag{6}$$

where: n is the number of cycles completed, t is the total analysis time, t_m is the flight duration (mission time),

3.1.2. Creep damage prediction

After the initial transient at start-up, the blade metal temperatures and stresses approach steady-state conditions. However, as these temperatures are typically higher than 40% of T_{melt} [K], creep occurs resulting in stress redistribution. It is therefore important to model the creep process throughout the life of the component. To find the creep damage, it is needed to find the rupture time. For this purpose, the Larson–Miller [67] relation can be used. From the Norton law one can write:

$$\dot{\varepsilon} = \frac{\varepsilon}{t_R} = A_1 \exp\left(-\frac{B_1}{T}\right) \tag{7}$$

From that the rupture time, t_R, is determined as

$$t_R = A_2 \exp\left(\frac{B_2}{T}\right) \tag{8}$$

Taking logarithms on both sides

$$\ln t_R = \ln A_2 + \frac{B_2}{T} = f(\sigma, T) \tag{9}$$

Assuming that $\ln A_2$ is a true constant and that B_2 varies with the stress, the equation can be rearranged to arrive at

$$B_2 = T\left(\ln t_R - \ln A_2\right) = T\left(C_1 + \ln t_R\right) \tag{10}$$

From the pure creep tests for each material, C can be found. For instance, for steel 4340, it equals to 16.65. The suggested value from the tests is $C_1 = 20$. Consequently, from Eq. (10):

$$\begin{aligned} &P = T\left(20 + \ln t_R\right) = f(\sigma, T) \\ &f(\sigma, T) = b_0 + b_1\left(\ln \sigma\right) + b_2\left(\ln \sigma\right)^2 + b_3\left(\ln \sigma\right)^3 \end{aligned} \tag{11}$$

Denoting $Y = \ln t_R$, and $X = \ln\sigma$, we have

$$y = \frac{1}{-17.2T + 460}\left(b_0 + b_1 X + b_2 X^2 + b_3 X^3\right) \tag{12}$$

where: t_R is the rupture time in h, T is temperature in °C, σ is von Mises effective stress inunits of ksi, and b_0, b_1, b_2, b_3 are material constants.

Once t_R is found, the creep damage parameter, D_c, is calculated according to the Robinson rule:

$$D_c = \sum_{i=1}^{N} (\frac{\Delta t}{t_R})_i \tag{13}$$

where Δt is the spend time in h, t_R – rupture time in h, i – number of load case.

The total damage parameter is:

$$D_{\text{tot}} = D_c + D_f = \sum_{i=1}^{N}\left(\frac{N}{N_f} + \frac{\Delta t}{t_R}\right)_i \tag{14}$$

The total damage parameter $D_{\text{tot}} \geq 1$ results in failure.

3.2. Model 2

Assuming that the creep behaviour is controlled by the mean stress (σ_m) and that the fatigue behaviour is controlled by the stress amplitude (σ_a), the two processes combine linearly to cause failure. This approach is similar to the development of the Goodman diagram except that instead of an intercept of ultimate stress (σ_u) on the σ_m axis, the intercept used is the creep-limited static stress (σ_{cr}) as shown in Fig. 2.

The creep-limited static stress corresponds either to the design limit on creep strain at the design life or to creep rupture at the design life, depending on which is the governing failure mode. Applying linear failure prediction rule, failure is predicted to occur under combined isothermal creep and fatigue if

$$\frac{\sigma_a}{S_f} + \frac{\sigma_m}{\sigma_{cr}} \geq 1 \tag{15}$$

where: σ_a – alternating stress, σ_m – mean stress, σ_{cr} – creep strength (creep stress for corresponding time to rupture), S_f – fatigue strength.

An elliptic relationship is also shown in Fig. 2. Failure is predicted to occur under combined isothermal creep and fatigue if

$$\left(\frac{\sigma_a}{S_f}\right)^2 + \left(\frac{\sigma_m}{\sigma_{cr}}\right)^2 \geq 1 \tag{16}$$

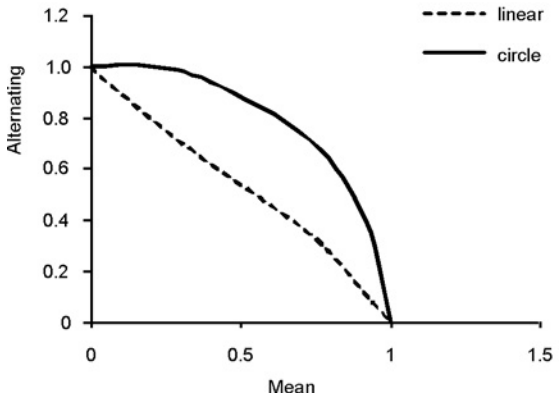

Fig. 2. Failure prediction diagram for combined creep and fatigue at constant temperature

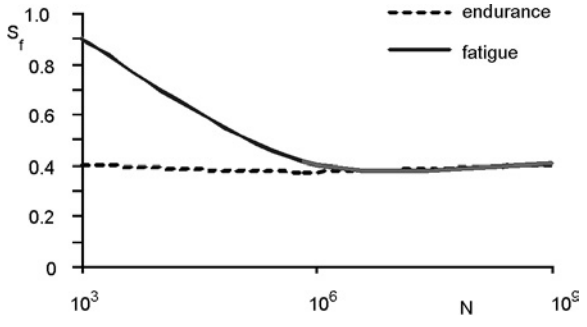

Fig. 3. Failure prediction diagram for creep and fatigue at constant temperature

From Equation (15), σ_a, σ_m and σ_{cr} are known, and S_f can be found. From Fig. 3, we note that:

$$\begin{aligned} &\text{if} \quad S_f > 0.9\sigma_{ut} \quad &&\text{then} \quad N < 10^3 \\ &\text{if} \quad 0.9\sigma_{ut} > S_f > S_e \quad &&\text{then} \quad N = N_{\text{diagram}} \\ &\text{if} \quad S_f < S_e \quad &&\text{then} \quad N > 10^6 \end{aligned} \tag{17}$$

3.3. Model 3

3.3.1. Fatigue damage

It is known that in case of pure fatigue, the damage can be defined as

$$D_f = \sum \frac{N_i}{N_{f_i}} \tag{18}$$

where: N – number of cycles at stress σ_i, N_{f_i} – number of cycles to failure at stress σ_i.

If the process occurs at a constant stress, σ, and constant T

$$D_f = \frac{N}{N_f} \tag{19}$$

where N is the number of cycles at stress a and temperature T, N_f is the number of cycles to failure at stress σ and temperature.

3.3.2. Creep damage

The creep damage under static load can be defined as

$$D_c = \sum \frac{t_i}{t_R} \tag{20}$$

where: t_i is the time spent at stress a and temperature T, t_R – rupture time at stress a, and temperature T and in with hold time for each stress σ, and temperature T_i

$$D_c = \sum \frac{(t_h)_i}{t_{R^i}} \tag{21}$$

where $(t_h)_i$ is the hold time at each temperature T_i. If the process occurs at constant stress, σ, and isothermal condition, T,

$$D_c = \frac{Nt_h}{t_R} \tag{22}$$

where N is the number of cycles with hold time at stress a and temperature T, t_h is the hold time at stress σ and temperature T, t_R is the rupture time at stress σ and temperature T.

3.3.3. Creep-fatigue damage

In creep-fatigue interaction, the total damage is the summation of fatigue damage and creep damage

$$D_t = D_f + D_c = \frac{N}{N_f} + \frac{Nt_h}{t_R} \tag{23}$$

When D_t =1, the failure occurs and hence

$$D_R = \frac{N_R}{N_f} + \frac{N_R t_h}{t_R} = 1 \tag{24}$$

where D_R is the damage at rupture. Consequently,

$$N_R = N_{SF}\left[\frac{1}{\frac{1}{N_f}+\frac{t_h}{t_R}}\right] \tag{25}$$

In Equation (25), N_{SF} is a safety factor which ranges from 0.1 to 1, t_h is known, t_R can be found from Larson-Miller relationship, Equation (12) or from pure creep tests, and N_f can be found from pure fatigue tests or from Eq. (5). Then the number of cycles to failure at creep-fatigue interaction, N_R, can be calculated. Knowing the number of cycles spent in combination of creep and fatigue, the present life status can be found:

$$L_r = 1 - \frac{N}{N_R} \tag{26}$$

where L_r is the remaining life. The remaining number of cycles can be easily calculated as

$$N_r = N_R - N \tag{27}$$

where N_r is the remaining number of cycles.

4. Mechanical testing

One of the most important facts in test is the load waveform. The waveforms shown schematically in Fig. 4 have been applied in the present study. The low-cycle fatigue tests were carried out under closed-loop true temperature control. The tests were performed between 40.04 MPa and 60.10 MPa for fatigue, and creep-fatigue but for the latter 5 s dwell time was applied and the tests were done at 800 °C. For all tests, the specimens with 228.6 mm gauge length and 12.7 mm diameter was used. For the creep test, the average constant stress of 50.07 MPa at 800 °C was applied.

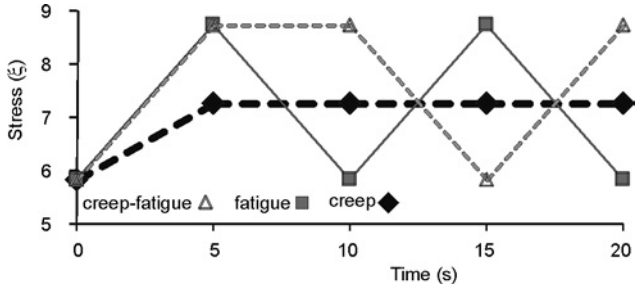

Fig. 4. Load waveform in mechanical testing

The specimen was heated at a temperature gradient along the gauge length not greater than ±2°. Test temperatures varying in the range from 800 °C to 1100 °C were

applied. Ninteen specimens were tested for pure fatigue, pure creep and creep-fatigue interaction, respectively, at various temperatures.

4.1. Test schedule for model 2

Equation (15) has been used to predict failure. Creep-limited static stress, σ_{cr}, in Eq. (15) corresponds either to the design limit on creep strain at the design life or to creep rupture at the design life, depending on which failure mode governs. For this purpose, the tabulated data of material creep test can be used. The following steps are taken:

1. The test temperature, T, is selected.
2. From the creep test data of the material based on design life, and the selected temperature at step 1 as the working temperature, the corresponding creep-limited static stress, σ_{cr} is selected. For instance the a_{cr} at 704.44 °C and for 100 000 h life, is equal to 289.58 MPa.
3. The mean stress, σ_m, and the alternating stress, σ_a, as components of cyclic load are selected.
4. Cyclic load is applied until break and the number of cycles to failure is counted.
5. S_f from Eq. (25) is calculated and the number of cycles to failure is found from Eq. (17).

4.2. Test schedule for model 3

From Equation (25), the following steps are taken:

1. Selecting the temperature, T, between 760 °C and 982.22 °C and the stress, σ, between 206.84 MPa and 275.79 MPa for the test.
2. Selecting the cycle frequency, f, for the fatigue test.
3. Running fatigue test and finding the number of cycles to failure, N_f.
4. Running the static isothermal creep test and finding the rupture time, t_R.
5. Selecting the hold time, t_h, for the cyclic creep test.
6. Running the cyclic creep test at the same frequency of the fatigue one, and finding the number of cycles to failure, N_R.
7. Calculating N_R from Eq. (24).
8. Repeating steps 1–7 for other samples. In the case of using of Eqs. (4) and (24) for fatigue and creep life, respectively, steps 3 and 4 can be ignored.

5. Test analysis

High-temperature strength data are often needed for conditions for which there is no experimental information. This is particularly true of long-time creep and stress-rupture data, where it is quite possible to find that the creep strength to give 1% de-

formation in 100 000 h (11.4 years) is required, although the alloy has been in existence for only 2 years.

Obviously, in such situations extrapolation of the data to long times is required. Reliable extrapolation of creep, creep-fatigue, and stress-rupture curves to longer times can be made only when it is certain that no structural changes occur in the region of extrapolation which would produce a change in the slope of the curve. Since structural changes generally occur in shorter times at higher temperatures, one way of checking on this point is to examine the log-stress-log-rupture life plot at a temperature several hundred degrees above the required temperature. For example, if in 1000 h no change in slope occurs in the curve at about 100 °C above the required temperature, extrapolation of the lower temperature curve as a straight line to 10 000 h is probably safe and extrapolation even to 100 000 h may be possible.

Certain useful techniques have been developed for approximating long-term behaviour based on a series of short-term tests. For instance, the data from creep tests may be cross plotted in a variety of different ways. The basic variables involved are stress, strain, time, temperature, and perhaps strain rate. Any two of these basic variables may be selected as plotting coordinates, with the remaining variables to be treated as parametric constants for a given curve.

One of the commonly used methods for extrapolating short-time creep and creep -fatigue data to long-term applications is the thermal acceleration method. As is a common way in linear viscoelasticity, creep testing guidelines usually dictate that test periods of less than 1% of the expected life are not deemed to give significant results. Tests extending to at least 10% of the expected life are preferred where feasible.

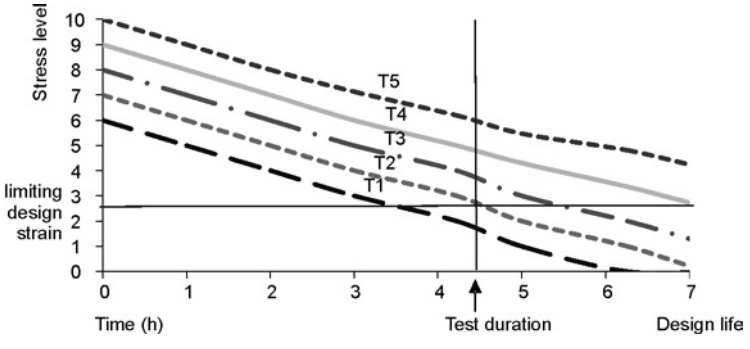

Fig. 5. Thermal acceleration method for creep testing

The thermal acceleration method involves laboratory testing at temperatures much higher than the actual service temperature expected. As shown in Fig. 5, the data are plotted as stress versus time for a family of constant temperatures where the creep strain produced is constant for the whole plot. It may be noted that stress rupture data may also be plotted in this way. As an aid in extrapolation of stress-rupture data several time–temperature parameters have been proposed for trading off temperature for time. The basic idea of these parameters is that they permit the prediction of long-time

rupture behaviour from the results of shorter time tests at higher temperatures at the same stress.

In our tests, we did both upscale and downscale temperature tests. In order to justify the scale model theory specifically in thermal downscaling, the scaled down temperature has been used for the model in comparison with the prototype. On the other hand, in order to run the creep and creep-fatigue test in a time shorter than the reality, tests at the upscale temperature have been carried out. More or less the same upscale force has been applied for the fatigue test to take shorter time than the real case. In the case of applying the real load, it may take ca. 6 months.

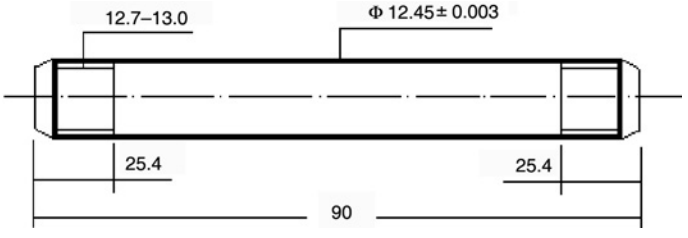

Fig. 6. Geometry of fatigue, creep,
and creep-fatigue specimen, steel 4340 (dimensions in mm)

Material for creep-fatigue tests was Steel 4340. The material and its chemical, physical, and mechanical properties are described in Tables 1–3, respectively. Figure 6 shows the geometry of a specimen used for the creep-fatigue tests.

Table 1. Chemical composition of steel 4340 (in wt. %)

C	Mn	P	S	Si	Cu	Ni	Cr	Mo	Al	V	N	Cd	Sn
0.4	0.75	0.008	0.029	0.26	0.03	1.72	0.87	0.23	0.021	0.001	0.0055	0.002	0.001

Table 2. Physical properties of steel 4340

A [%]	T_{melt} [°C]	ρ [kg/m^3]	α [μm/(m·°C)]	ΔL [%]	ν
36–43	1426.67	7.85×10^3	13.7	13.2	0.29

Table 3. Mechanical properties of steel 4340

S_y [MPa]	E [GPa]	S_{ut} [MPa]	BHN
710	195–205	825–1110	248

The apparatus used in this study was Gleeble-3500 (Fig. 7), a controlled electro-hydraulic thermal-fatigue testing machine with high-precision conduction heating and air-cooling functions [68].

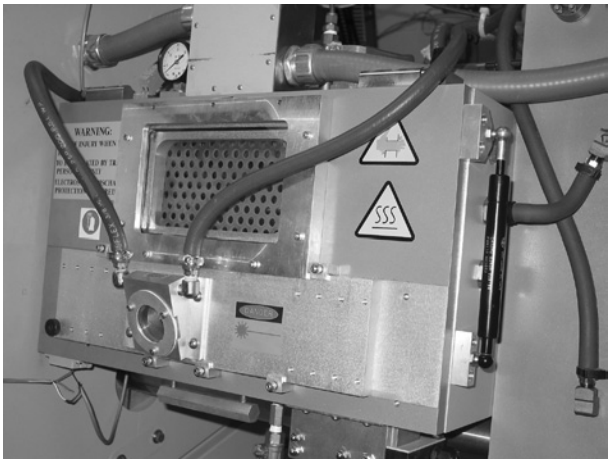

Fig. 7. Gleeble-3500 for various creep, fatigue and creep-fatigue tests
(with the courtesy of National Research Council (NRC) at Boucherville, Quebec)

For axial displacement measurement, Fastar-SP100 sensor from Data Instruments was used which is based on inductance variation. Temperature was measured with a 0.2 mm in diameter thermo-couples welded at the middle and both ends of the specimen. The temperature difference within the gauge length was not greater than ±2 °C to the set temperature throughout the duration of a test. In the creep-fatigue tests, force was computer-controlled by the same triangular waveform cycling. The same temperature was used for creep, and creep-fatigue tests, using the output of the thermocouple.

The waveforms shown in Fig. 4 were applied in the tests, and were done using the testing facilities at the National Research Council (NRC), Boucherville, Quebec S_f= 807.18 MPa, which is greater than $0.9S_{ut}$ = 742.5 MPa. It can be concluded that $N_f < 10^3$.

5.1. Test results

5.1.1. Model 1

For creep, four tests were carried out on a sample of steel 4340 90 mm long, 12.7 mm in diameter which was cleaned and annealed at 248 BHN. For creep test the waveform shown in Fig. 8 has been applied. Indeed we could just apply the temperature and the force of 6.31 KN which is equivalent to stress of 50.09 MPa (Fig. 9). The creep strains at various temperatures at a constant load (6.31 KN) are shown in Figs. 10–13.

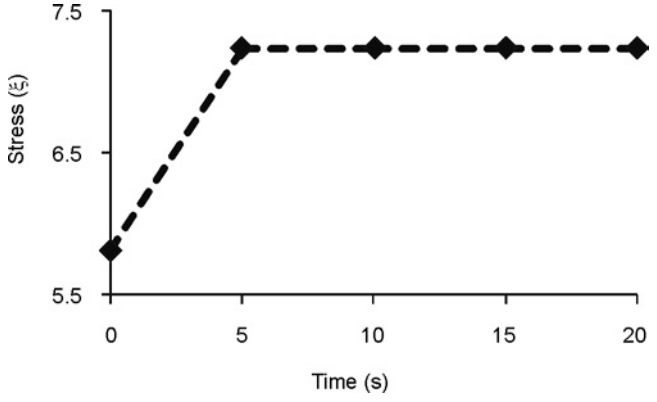

Fig. 8. Stress waveform for creep tests

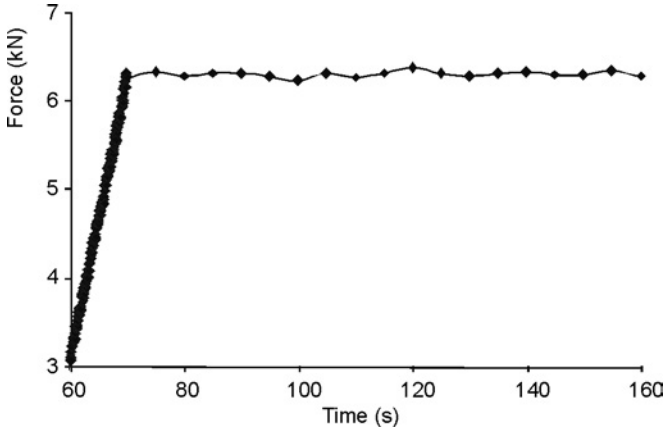

Fig. 9. Force waveform for creep tests

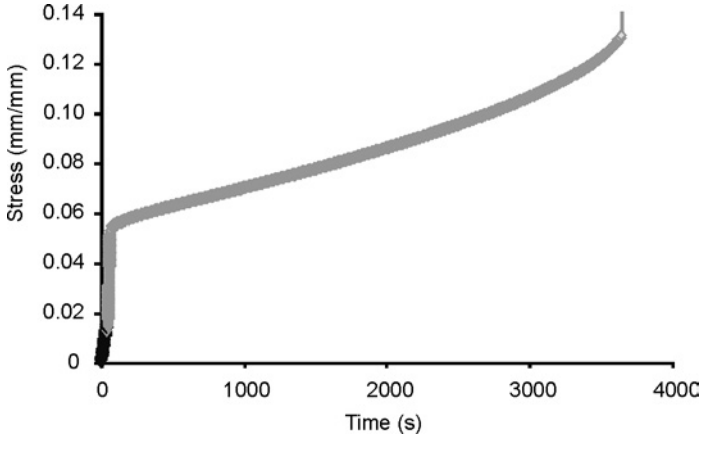

Fig. 10. Creep strain vs. time at 800 °C in creep test

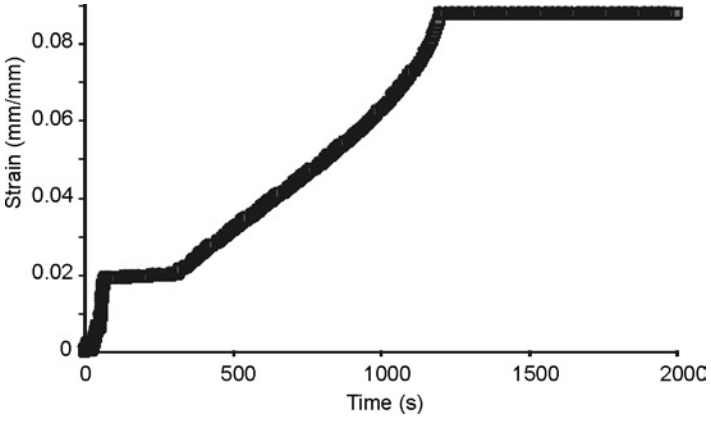

Fig. 11. Creep strain vs. time at 850 °C in creep test

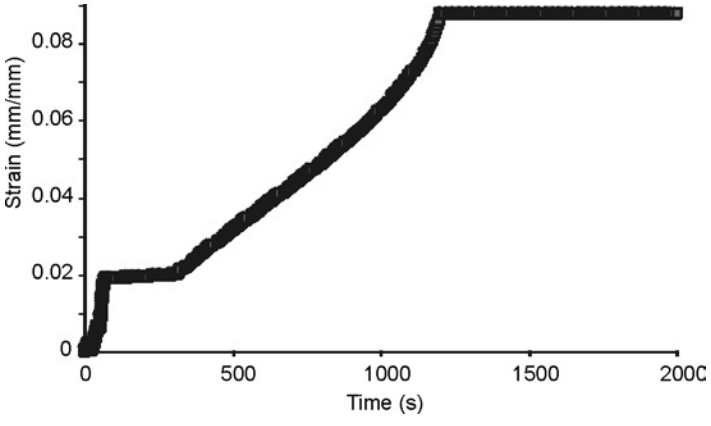

Fig. 12. Creep strain vs. time at 853 °C in creep test

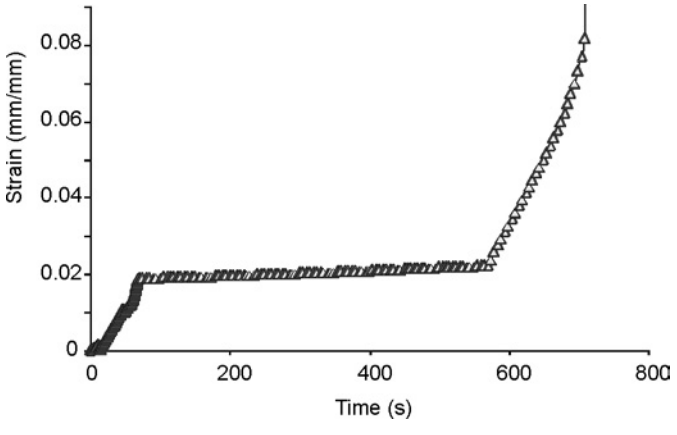

Fig. 13. Creep strain vs. time at 875 °C in creep test

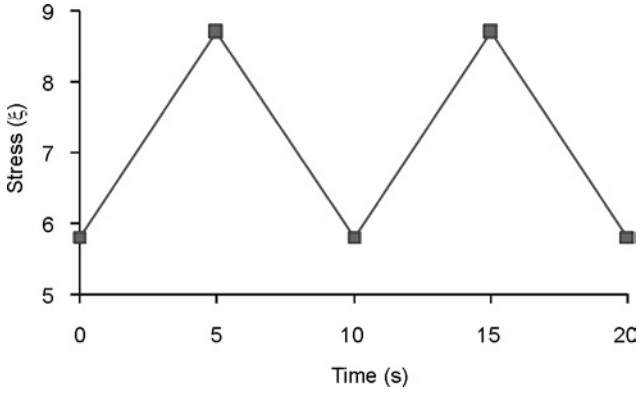

Fig. 14. Stress waveform for fatigue test

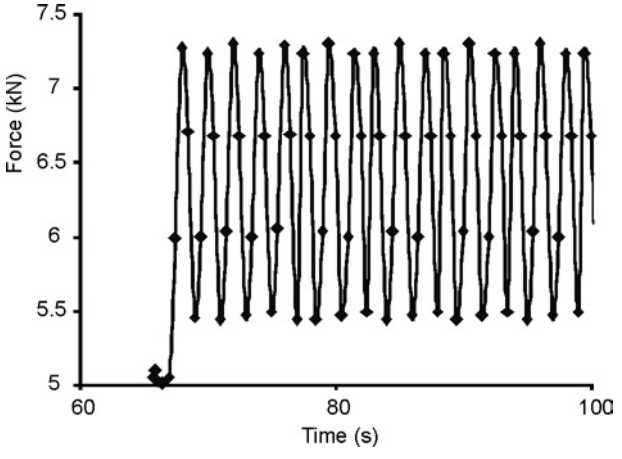

Fig. 15. Force waveform for fatigue test

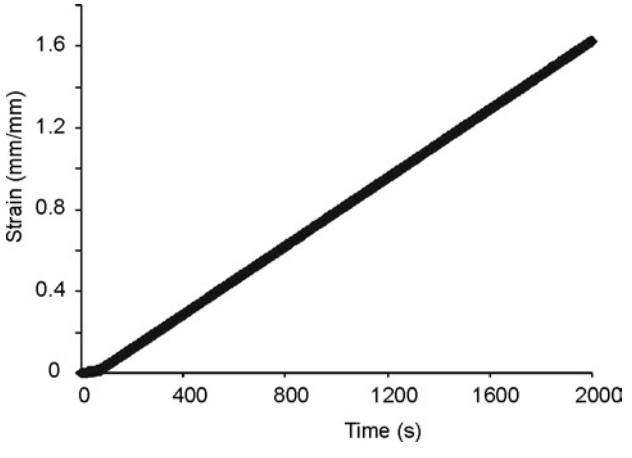

Fig. 16. Strain vs. time in fatigue test

For fatigue, a cyclic load (Fig. 14) was applied on a sample of steel 4340 of 12.7 mm in diameter, 90 mm long until break down. The minimum stress was 40.04 MPa and the maximum stress was 60.10 MPa. Practically we could apply force between 5.07 kN to 7.61 kN (Fig. 15). The total spend time was 2019.5 s and each cycle was 10 s but it took 66 s of preliminary time to start the cyclic load. Then taking the net time for the cyclic load, the number of reversals is obtained. Figure 16 shows the strain vs. time in the fatigue test.

Table 4. Creep test results for steel 4340

Test No.	T [°C]	t_R [s]
1	800	3645
2	850	1205
3	853	1125
4	875	715

Table 5. Creep, fatigue and total damages from model 1 and the test

Model	Creep damage D_c	Fatigue damage D_F	Total damage D_T
Model 1 (test data)	0.01372	0.02476	0.0384786
Model 1 (calculation data)	0.0135448	0.02619596	0.0275504
Test			0.03986

The test data has been used to find the total damage at creep-fatigue interaction. As an example, the damages at 50 s obtained from tests and from the models are shown in Table 5. For the test, cyclic load was applied on a sample of 12.7 mm in diameter 90 mm long steel 4340 until break down. The minimum stress was 40.04 MPa (5.81ξ) and the maximum stress was 60.10 MPa and the hold time was 5 s. The force and temperature were applied and the stress and strain were measured. Practically break down happened after 1254.5 s.

5.1.2. Model 2

Based on the Miners rule for fatigue failure, for the case that was tested we have: σ_a = 10.03 MPa, σ_m= 50.07 MPa, σ_{cr} for 800 °C and 1 h lifetime is 50.7 MPa, S_{ut}= 825 MPa, then $0.9S_{ut}$ = 742.5 MPa. Substituting these values in the Miners equation, we have

$$N_f = \frac{\text{Total spent time}}{\text{period of 1 cycle}} = \frac{1254.5}{15} = 83.6 \tag{28}$$

5.2.3. Model 3

From Equation (25) we have:

$$N_R = N_{SF} = \left[\frac{1}{\frac{1}{N_f} + \frac{t_h}{t_R}} \right] \tag{29}$$

For the case that was tested we have: $N_f = 195.35$, $N_{SF} = 0.54$, $t_h = 5$ s, $t_R = 3645$ s. Using Equation (25) ,the number of cycles to break for the steel 4340 was obtained as

$$N_R = 83.1951 \text{ cycles} \tag{30}$$

The present life status for instance after 50 s which is equivalent to 3.33 cycles, is

$$L_R = 1 - \frac{N}{N_R} = 1 - \frac{3.33}{83.1951} = 0.9599$$

Test result gives

$$N_R = \frac{1254.5}{15} = 83.6 \text{ cycles} \tag{31}$$

The present life status for instance after 50 s which is equivalent to 3.33 cycles, is

$$L_R = 1 - \frac{N}{N_R} = 1 - \frac{3.33}{83.6} = 0.9601 \tag{32}$$

6. Discussion and conclusions

Three constitutive models have been suggested. In the first model, the main idea is that the total damage can be used for break point of the components, and the damages due to creep and fatigue can be accumulated linearly. In this model, the creep model uses the Norton power law, Larson–Miller and Robinson rule approach, while the fatigue model combines the Miner rule and the universal slope method. The damages are calculated separately and the total damage is found by linear summation in order to find the lifetime.

In model 2, the fluctuating stress is considered as a varying stress in the fatigue -creep model. Since the fluctuating stress is a combination of alternating and mean

stress, it can be assumed that the mean part represents the static load which can cause creep at elevated temperatures, whereas the alternating part is responsible for fatigue damage. This model is an extension to the Goodman theory, except that instead of an intercept of ultimate stress (σ_U) on the σ_m axis, the intercept used is the creep-limited static stress (σ_{cr}).

In model 3, the approach for this model is that the creep-fatigue interaction can be considered as cyclic fatigue but with the hold time at maximum, minimum, or extreme stresses. This model has two strong points: 1) the required data can be used from pure creep and pure fatigue tests; 2) it has a safety factor (or a weakness factor) that is based on the material information and industrial experiences, between 0 and 1.

Out of three constitutive models, the first one is the most accurate and reasonable one, although the third one is the easiest one. The main weak point of the second one is that it gives just a range of the lifetime or lifecycle for the low frequency loads, and it cannot be accurate in that region. The weak point of the 3rd one is finding the safety factor accurately. It should be noted that more tests are needed to find the constants in universal slope equation. In the present study, the constants are taken from ASM handbook. For unknown materials, many more tests are needed to find those constants. In the present case, the result of the lifetime prediction in creep-fatigue interaction tests and the first constitutive model has quite reasonable and acceptable match. Three suitable models for predicting the lifetime were developed and studied. The finite element technique was used to study the component dynamic behaviour. Natural frequencies and mode shapes were obtained. The response and stress due to harmonic and centrifugal loading were also obtained. The analytical results were compared with those obtained from experiments.

References

[1] OHTANI R., KITAMURA T., TSUTSUMI M., MIKI H., Proc. Asian Pacific Conf. Fracture and Strength, Tsuchiura (Japan), 1993, pp. 151–156.
[2] EWALD J., SHENG S., Mater. High Temp., 15 (2003), 323.
[3] GRANACHER J., MAO T.S., FISCHER R., Mater. High Temp., 15 (2003), 331.
[4] MAILE K., KLENK A., GRANACHER J., SCHELLENBERG G., TRAMER M., Key Eng. Mater., 171–174 (2000), 85.
[5] KOTEKAZAWA R., Fatigue Fract. Eng. Mater. Struct., 16 (1993), 619.
[6] MICHEL D.J., THOMPSON A.W., Fatigue, 87 (1987), 1057.
[7] WANG S., CHI S., GENG G., Acta Metal. Sin., 20 (1984), 83.
[8] SADANANDA K., SHAHINIAN P., *Creep-Fatigue Crack Growth*, Appl. Sci. Publ., London, 1981, pp. 109–195.
[9] SHAHINIAN P., SADANANDA K., ASME, New York, 1976, pp. 365–390.
[10] GENG M. F., Mater. Sci. Eng., 257 (1998), 250.
[11] MARIE S., DELAVAL C., Intl. J. Press. Vess. Piping, 78 (2001), 847.
[12] GEMMA A.E., Eng. Fract. Mech., 11 (1979), 763.
[13] BRINKMAN C.R., KORTH G.E., BOBBINS R.R., Nucl. Techn., 16 (1972), 297.
[14] YAGI K., KUBO K., TANAKA C., J. Japan Soc. Mater. Sci., 28 (1979), 400.

[15] REIS E.E, RYDER R.H., *Creep-Fatigue Damage in OFHC Coolant Tubes for Plasma Facing Components*, Proc. 19th Symposium on Fusion Technology, 1996.
[16] BELLOWS R.S., TIEN J.K., Scripta Metall., 21 (1987), 653.
[17] RICHARD-FRANDSEN R., TIEN J.K., Scripta Metall., 18 (1984), 731.
[18] DUGGAN T.V., SABIN P., *The Effect of Geometry on Crack Formation, Advances in Research on the Strength and Fracture of Materials*, Proc. 4th International Conference on Fracture, New York, 1978, p. 285.
[19] BERMAN I., GANGADHARAN A.C., JAISINGH G.H., GUPTA G.D., J. Press. Vess. Techn., 98 (1976), 75.
[20] PARK Y.S., NAM S.W., AND HWANG S.K., Mater. Lett., 53 (2002), 392.
[21] HARDT, MAIER H.J, CHRIST H.J., Int. J. Fatigue, 21 (1999), 779.
[22] SALAM I., TAUQIR A., KHAN A.Q., Engineering Failure Analysis, 9 (2002), 335.
[23] BESTWICK R.D.W., BUCKTHORPE D.E., Fatigue Fract. Eng. Mater. Struct., 17 (1994), 849.
[24] HOLDSWORTH S.R., Nucl. Eng. Des., 188 (1999), 289.
[25] ZHANG G., RICHTER B., Fatigue Fract. Eng. Mater. Struct., 23 (2002), 499.
[26] LEMAITRE J., PLUMTREE A., Trans. ASME, 101 (1979), 284.
[27] SHI X.Q., WANG Z.P., ZHOU W., PANG H.L., YANG Q.J., J. Electr. Pack., 124 (2002), 850.
[28] RUBESA D., *Lifetime Prediction and Constitutive Modeling for Creep-Fatigue Interaction*, Bruder-Borntraeger, Berlin, 1996, p. 140.
[29] COLOMBO F., MASSEREY B., MAZZA E., HOLDSWORTH S., *Service-Like Thermo-Mechanical Fatigue Tester for the Lifetime Assessment of Turbine Components*, 9th Int. Conf. Mechanical Behavior of Materials, Geneva, Switzerland, 2003.
[30] HOLDSWORTH S.R., MAZZA E., AND JUNG A., *Creep-Fatigue Damage Development during Service-Cycle Thermo-Mechanical Fatigue Tests of ICrMoV Rotor Steel*, 9th Int. Conf. Mechanical Behavior of Materials, Geneva, Switzerland, 2003.
[31] CHARKALUK E., CONSTANTINESCU A., Mater. High Temp., 17 (2000), 373.
[32] YAO Q., QU J., WU S.X., J. Electr. Pack., 121 (1999), 196.
[33] JEONG C.Y., CHOI B.G., NAM S.W., Mater. Lett., 49 (2001), 20.
[34] CHEN L.J., YAO G., TIAN J.F., WANG Z.G., ZHAO H.Y., Int. J. Fatigue, 20 (1998), 543.
[35] TONG J., DALBY S., BYRNE J., HENDERSON M.B., HARDY M.C., Int. J. Fatigue, 23 (2001), 897.
[36] COFFINE L.F., Fatigue Elev. Temp., ASTM.520, 1973, 5–34.
[37] AGHION E., BAMBERGER M., BERKOVITS A., Israel J. Techn., 24 (1988), 225.
[38] OKADA M., TSUTSUMI M., KITAMURA T., OHTANI R., Fatigue Fract. Eng. Mater. Struct., 21 (1988), 751.
[39] VENKITESWARAN P. K., FERGUSON D. C., AND TAPLIN D.M.R., *Fatigue at Elevated Temperatures*, Proceedings of the Symposium, Philadelphia, PA, ASTM, 462–472, 1973.
[40] OHNAMI M., SAKANE M., Bull. Japan Soc. Mech. Eng., 21 (1978), 547.
[41] KOBURGER C.W, DUQUETTE D.J, STOLOFF N.S., Metall. Trans. A, Phys. Metall. Mater. Sci., 11 A (1980), 1107.
[42] PLUMTREE A., PERSSON N.G., *Creep-Fatigue Interaction in an Austenitic Fe-Ni-Cr Alloy at 600 °C*, Advances in Research on the Strength and Fracture of Materials, Proc. 4th Int. Conf. Fracture, Pergamon Press, New York, 1978, pp. 821–829.
[43] OHTANI R., KITAMURA T., ZHOU W., Int. J. Fatigue, 19 (1997), 185.
[44] SRINIVASAN V.S., NAGESHA A., VALSAN M., BHANU SANKARA RAO K., MANNAN S.L. SASTRY D.H., Int. J. Press. Vess. Piping, 76 (1999), 863.
[45] KORDISCH T., NOWACK H., Fatigue Fract. Eng. Mater. Struct., 21 (1998), 47.
[46] MASAKAZU O., HIROMICHI T., JUNNOSUKE M., Mater. Sci. Res. Int., 3 (1997), 56.
[47] MICHEL D.J., SMITH H.H., Acta Metall., 28 (1980), 999.
[48] WAREING J., TOMKINS B., *Creep-Fatigue Interaction Failure in Type 316 Stainless Steel, Advances in Research on the Strength and Fracture of Mater.*, Proc. 4th Int. Conf. Fracture, New York, Pergamon Press, 1978, 81.

[49] MAIYA P.S., MAJUMDAR S., Metallurgical Transactions A -Physical Metallurgy and Mater. Sci., 8A (1977), 1651.
[50] WAREING J., Metall. Trans. A, 8A (1977), 711.
[51] PLUMTREE A., Metal Sci., 11 (1977), 425.
[52] MILLER A., ASMS, Conf. Micromechanical Modeling of Flowand Fracture, ASME, Transactions, Series H- J. Eng. Mater. Techn., 98 (1976), 106.
[53] NAM S.W., Mater. Sci. Eng., 322 (2002), 64.
[54] ISOBE N., SAKURAI S., YORIKAW.A. M., IMOU K., TAKAHASHI Y., Int. J. Press. Vess. Piping, 77 (2000), 817.
[55] TAKAHASHI Y., OGATA T., TAKE K., Nucl. Eng. Des., 153 (1995), 235.
[56] HALES R., Fatigue Eng. Mater. Struct., 3 (1980), 339.
[57] WAREING J., Fatigue Eng. Mater. Struct., 4 (1981), 131.
[58] JASKE C., MINDLIN H., PERRIN J., ASTM, 520 (1973), 365.
[59] OKAZAKI M., YAMAZAKI Y., Int. J. Fatigue, 21 (1999), 79.
[60] ASME, Boiler and Pressure Vessel Code, Section III, Code Case N-47, 1974.
[61] ROBINSON E.L., ASME Trans., 160 (1938), 253.
[62] MINER M.A., J. Appl. Mech., 12 (1945), A159.
[63] TAIRA S., *Creep in Structures*, Academic Press, 1962, pp. 96–124.
[64] LARSON F.R., MILLER J., ASME Trans., 1952, 765–775.
[65] *Dynamic Systems*, Inc. P.O. Box 1234, Poestenkill, NY, 12140.

Received 13 February 2007
Revised 28 June 2008

Materials Science-Poland, *Vol. 26*, *No. 3*, *2008*

Orthorhombic to tetragonal phase transition and superconductivity in $Ba_2Cu_3O_4Cl_2$

M. S. DA LUZ*, C. A. M. DOS SANTOS, A. J. S. MACHADO

Escola de Engenharia de Lorena – USP, P.O. Box 116, Lorena – SP 12606-810, Brazil

The orthorhombic to tetragonal phase transition in $Ba_2Cu_3O_4Cl_2$ has been investigated. This transition was observed by X-ray powder diffractometry carried out in samples heat treated between 700 and 750 °C. Results of X-ray diffractograms simulation confirm the phase transition. *dc*-Magnetization measurements performed in SQUID showed the existence of a signal due to diamagnetism. The results suggest the existence of localized superconductivity and explain the different magnetic properties reported in the literature for the $Ba_2Cu_3O_4Cl_2$ compound.

Key words: *oxychloride; structural transition; diamagnetism*

1. Introduction

Copper oxyhalide compounds have received much attention in recent years because of their similar structures to high critical temperature (high-T_C) superconducting oxides. The discovery of superconductivity in $Sr_2CuO_2F_{2+\delta}$ [1] stimulated further effort in the area and many new copper oxyhalide systems have been fabricated [2]. Among them, $Ba_2Cu_3O_4Cl_2$ (Ba2342) is one of the most interesting materials. Ba2342 seems to be an insulator with a tetragonal structure (space group: *I*4*/mmm*) and lattice constants a = 5.517 Å and c = 13.808 Å. This compound crystallizes in a layered structure composed of Cu_3O_4, Ba and Cl layers [3]. The Cu_3O_4 layers contain two types of Cu sites: Cu_1 and Cu_{11} sites. The Cu_1 have an octahedral coordination with four square-planar oxygen ions in the basal plane, two chlorine ions at the apices, whereas the Cu_{11} ions are surrounded only by four square planar oxygen ions. On the other hand, it is known that the Cu_1 spin is antiferromagnetically ordered and Cu_{11} is paramagnetically ordered at room temperature [4, 5]. The competition between these magnetic effects is considered to result in the multi-steps magnetic transitions in this compound. Furthermore, two magnetic transitions were observed in Ba2342; one at

*Corresponding author, e-mail: luz@physics.montana.edu

$T \sim 330$ K (denoted by T_H) and another at $T \sim 30$ K (T_L) [6, 7]. Between T_H and T_L, the compound displays weak ferromagnetism. Noro et al. [8] studied the effect of the substitution of Cu for Ni and reported the disappearance of a weak ferromagnetic moment which decreased drastically by introducing a small amount of Ni as a dopant.

In contrast to the exposed above, diamagnetism and metal-like behaviour have been observed for the Ba2342 compound at low temperatures which suggest the existence of superconductivity in this compound as reported previously by some authors [9, 10]. In addition, some other copper oxyhalide compounds are superconductors. Another important aspect is that most of the high-T_c superconductors have crystalline structure containing Cu–O layers with CuO stoichiometry. In particular, $YBa_2Cu_3O_{7-\delta}$ shows a phase transition from tetragonal to orthorhombic structure, which occurs near 700 °C in an oxygen atmosphere [11]. The critical transition temperature depends on the oxygen partial pressure and occurs when the stoichiometry is near $YBa_2Cu_3O_{6.5}$. The highest superconducting transition temperature ($T_C \sim 90$ K) is only observed for the orthorhombic structure [11]. In addition, some other copper oxyhalide compounds are superconductors [1, 12, 13]. Also, high-pressure synthesis (at GPa) has been responsible for inducing superconductivity in $(Ca, K)_2CuO_2Cl_2$ ($T_C = 24$ K) [14] and $(Ca, Na)_2CaCu_2O_4Cl_2$ ($T_C = 49$ K) [15].

In this paper, results of X-ray powder diffractometry are reported which suggest the existence of an orthorhombic to tetragonal transition in the $Ba_2Cu_3O_4Cl_2$ compound. Magnetic measurements show a diamagnetic signal, and are in agreement with previous results: this suggests the existence of localized superconductivity in this compound [9, 10].

2. Experimental

Polycrystalline samples of $Ba_2Cu_3O_4Cl_2$ were prepared by the solid state diffusion method using $BaCO_3$, CuO and $BaCl_2 \cdot 2H_2O$ powders of high purity. The powders were mixed, ground, calcined at 700 °C for 24 h, pressed into pellets, sintered at 750 °C for 48 h followed by cooling to room temperature. In addition, the samples were heat treated at 700 °C. The samples were characterized by X-ray powder diffractometry (Rich. Seifert-ISO Debyeflex 1001) which was carefully indexed using the reference [16]. The X-ray diffraction intensity data of 2θ were collected from 10 to 50°. A step-scan mode was adopted with a scanning step of 0.02° (in 2θ) and duration of 2 s. The samples were also characterized by scanning electron microscopy (Jeol -JXA840) with energy dispersive spectrometry (EDS) in order to study the granular structures and grain compositions of the samples.

Using the Powder Cell software [16] to calculate lattice parameters and to simulate X-ray powder diffractograms (XRD), we were able to study the experimental X-ray diffractograms and the influence of the heat treatment on the crystalline structure of the $Ba_2Cu_3O_4Cl_2$ compound.

Magnetization measurements were performed using a quantum design superconducting quantum interference device (SQUID) magnetometer.

3. Results and discussion

Figure 1 shows the XRD for the $Ba_2Cu_3O_4Cl_2$ sample heat treated at 750 °C (a) and 700 °C (b). Both diffractograms display single phases, but a careful analysis of them shows the existence of distinct peaks for the sample heat treated at 750 °C, see for example 103 reflections in the insets. This result is an evidence for a phase transition from orthorhombic to tetragonal structure in the $Ba_2Cu_3O_4Cl_2$ compound. In order to confirm this phase transition we performed simulation for the tetragonal and orthorhombic X-ray diffractograms. We adopted the crystallographic parameters shown in tables 1 and 2 using the following space groups: *I4/mmm* and *Immm* for the tetragonal and orthorhombic, respectively. The orthorhombic symmetry (*Immm*) was chosen because it is a subgroup of *I4/mmm* and the atomic positions were based on the International Tables for Crystallography [16]. The lattice parameters were tested until the best agreement between experimental and simulated X-ray powder diffractograms was obtained.

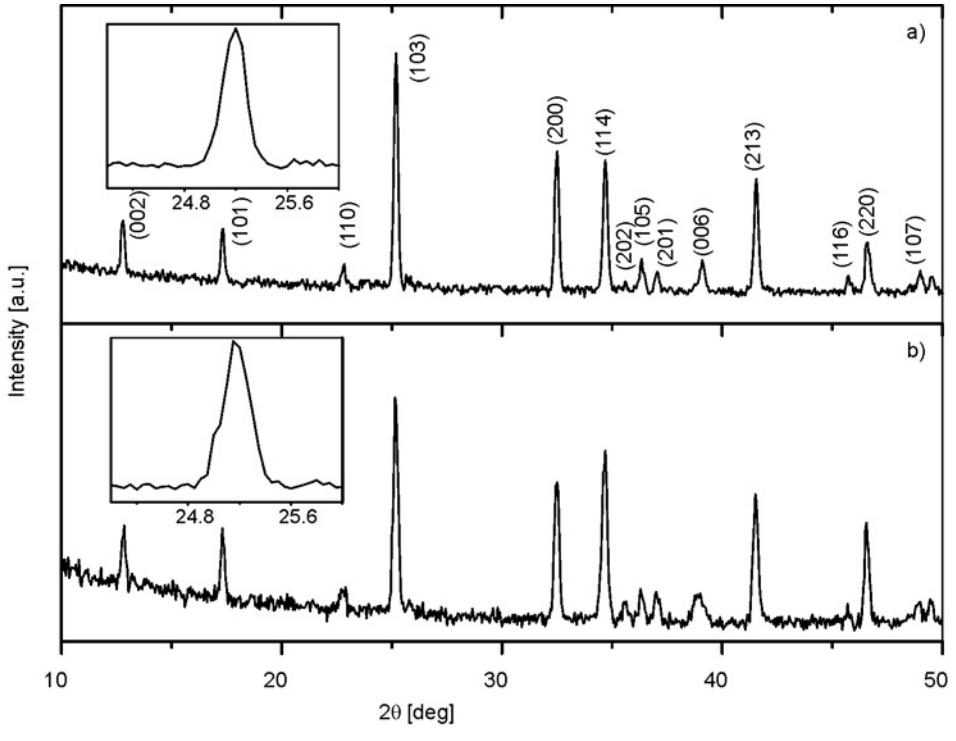

Fig. 1. Experimental diffractograms for the sample $Ba_2Cu_3O_4Cl_2$ heat treated at 750 °C (a) and 700 °C (b). Insets show 103 reflections

Table 1. Atomic positions for $Ba_2Cu_3O_4Cl_2$ with tetragonal (*I*4/*mmm*) and orthorhombic (*Immm*) symmetries [16]

Atom	*I*4/*mmm*	*I*/*mmm*	*x*	*y*	*z*
Ba	4e	4i	0.000	0.000	0.365
Cu1	4c	2d	0.000	0.500	0.000
Cu2	2a	2a	0.000	0.000	0.000
O	4d	4j	0.000	0.500	0.250
Cl	8h	4e	0.250	0.000	0.000

Table 2. Lattice parameters for $Ba_2Cu_3O_4Cl_2$ sample

Heat treatment temperature [°C]	Lattice parameters [Å]			Structure
	a	*b*	*c*	
750	5.5129	5.5129	13.8216	tetragonal
700	5.4902	5.5249	13.7925	orthorhombic

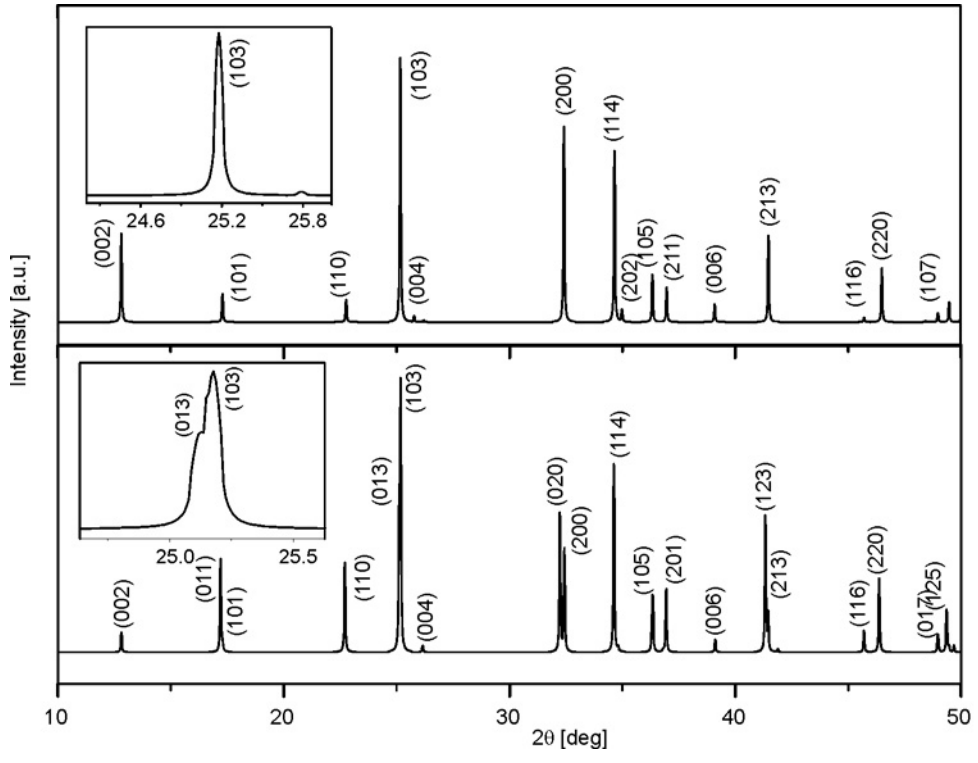

Fig. 2. Simulated X-ray powder diffractograms for the $Ba_2Cu_3O_4Cl_2$ with tetragonal (a) and orthorhombic (b) symmetries. Insets highlight the 103 simulated reflections

In Figure 2, we can observe that the result for the simulation of the tetragonal structure is in good agreement with the experimental X-ray powder diffractograms shown in Fig. 1. For the orthorhombic structure, we can see the appearance of double

peaks (see for example the inset of this figure and also 200 reflections) which is similar to the sample heat treated at 700 °C (Fig. 1b). The similarities between experimental and simulated diffractograms suggest that this oxychloride system has a phase transition from orthorhombic (*Immm*) to tetragonal (*I4/mmm*) structure. We have noted that the X-ray powder diffractograms have some similarities with those of $YBa_2Cu_3O_{7-\delta}$ ceramic superconductor which also shows a phase transition as a function of oxygen content [11]. Thus, the phase transition observed in this work could explain the appearance of the diamagnetic signal and different magnetic properties reported for the $Ba_2Cu_3O_4Cl_2$ compound [9, 10].

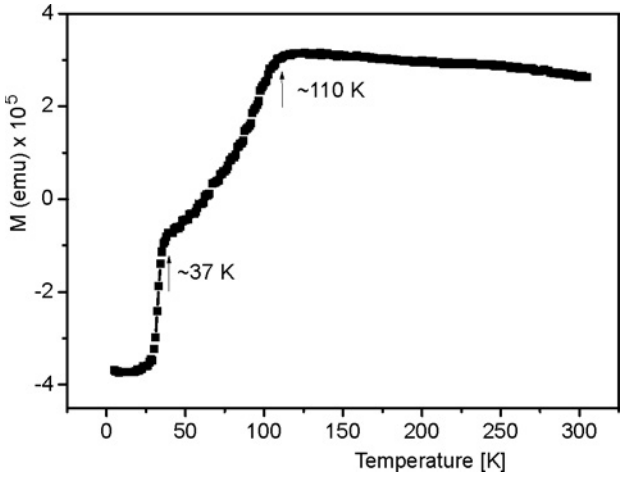

Fig. 3. Magnetic moment as a function of temperature
for a $Ba_2Cu_3O_4Cl_2$ sample heat treated for 72 h at 700 °C

Figure 3 illustrates the temperature dependence of the magnetic moment for a sample of $Ba_2Cu_3O_4Cl_2$ heat treated at 700 °C (with orthorhombic symmetry). The presence of diamagnetism can be unambiguously observed, and it is in agreement with results reported previously [9, 10]. Thus, our results are another indication of the existence of superconductivity in the $Ba_2Cu_3O_4Cl_2$ compound. We suggest that the orthorhombic phase can be responsible for the diamagnetic behaviour, but the superconductor volume in this system is small and it is probably related to the coexistence between orthorhombic and tetragonal phases. We speculate that the high pressure synthesis would be able to stabilize the orthorhombic phase and promote the appearance of superconductivity in $Ba_2Cu_3O_4Cl_2$.

4. Conclusion

This work reports heat treatment effects on the $Ba_2Cu_3O_4Cl_2$ samples. We have observed the formation of double peaks in the X-ray diffractograms of $Ba_2Cu_3O_4Cl_2$

samples heat treated at lower temperatures, which were interpreted as a consequence of a structural transition in this compound. Simulations of X-ray powder diffractograms confirm this idea and suggest that the phase transition is related to a change from orthorhombic to tetragonal structure. dc-Magnetization measurements performed in SQUID showed the existence of diamagnetism in the signal. The structural transition and the diamagnetism suggest the existence of superconductivity and can explain the different magnetic behaviors reported in the literature about the $Ba_2Cu_3O_4Cl_2$ compound.

Acknowledgements

This work has been supported by FAPESP (00/03610-4 and 97/11113-6) and by CNPq.

References

[1] AL-MAMOURI M., EDWARDS P.P., GREAVES C., SLASKI M., Nature, 369 (1994), 382.
[2] ADACHI S., TATSUKI T., TAMURA T., TANABE K., Chem. Mater., 10 (1998), 2860.
[3] VON KIPKA R., MULLER-BUSCHBAUM H.K., Z. Anorg. Allg. Chem., 419 (1976), 98.
[4] YAMADA K., SUZUKI N., AKIMITSU J., Physica B, 213–214 (1995), 191.
[5] RUCK K., ECKERT D., KRABBES G., WOLF M., MÜLLER K.-H., J. Solid State Chem., 141 (1998), 378.
[6] NORO S., HARADA H., YAMADAYA T., TADOKORO M., SUZUKI H., Mater. Sci. Eng. B, 25 (1994), 167.
[7] ITO T., YAMAGUCHI H., OKA K., Phys. Rev. B, 55 (1997), R684.
[8] NORO S., TUYUKI Y., NAKANO R., MAEDAI Y., Physica B, 322 (2002), 57.
[9] JINHUA Y., ZHIGANG Z., AKIYUKI M., Physica C, 341 (2000), 489.
[10] DA LUZ M.S., DOS SANTOS C.A.M., MACHADO A.J.S., FERREIRA B., Braz. J. Phys., 3 (2002), 744.
[11] JORGENSEN J.D., BENO M.A., HINKS D.G., SODERHOLM L., VOLIN K.J., HITTERMAN R.L., GRACE J.D., SCHULLER I.K., SEGRE C.U., ZHANG K., KLEEFISH M.S., Phys. Rev. B, 36 (1987), 3608.
[12] JIN C.Q., WU X.J., LAFFEZ P., TATSUKI T., TAMURA T., ADACHI S., YAMAUCHI H., KOSHIZUKA N., TANAKA S., Nature, 375 (1995), 301.
[13] CHE G.C., LIU G.D., REN Z.A., DONG C., CHEN H., NI Y.M., JIA S.L., ZHAO Z.X., Supercond. Sci. Technol., 15 (2002), 875.
[14] TATSUKI T., ADACHI S., ITOH M., TAMURA T., WU X.J., JIN C.Q., KOSHIZUKA N., TANABE K., Physica C, 255 (1995), 61.
[15] ZENITANI Y., INARI K., SAHODA S., UEHARA M., AKIMITSU J., KUBOTA N., AYABE M., Physica C, 248 (1995), 167.
[16] KRAUS W., NOLZE G., J. Appl. Cryst., 29 (1996), 301.

Received 6 July 2007
Revised 29 October 2007

Materials Science-Poland, *Vol. 26*, *No. 3*, *2008*

New magnetic Ni-Al hydrotalcite-like materials Synthesis and characterization

J. WANG*, J. YOU, P. YANG, C. ZHONG, Z. LI, M. ZHANG, X. JING

School of Material Science and Chemical Engineering, Key Laboratory of Science and Technology of Controllable Chemical Reactions, Harbin Engineering University, Harbin 150001, PR China

Novel magnetic Ni-Al hydrotalcite with Ni/Al molar ratio of 3 was synthesized by the hydrothermal method and co-precipitation. The obtained material was characterized in detail by thermogravimetric analysis – differential scanning calorimetry, X-ray diffraction (XRD), transmission electron microscopy (TEM), and vibrating sample magnetometry (VSM). XRD analysis indicated that a more well-crystallized hydrotalcite-like phase and higher thermal stability were present in the hydrothermally treated product than in that obtained by the conventional co-precipitation method. Well-defined flat particles were observed by TEM, and the (200) lattice plane (d = 0.21 nm) could be clearly seen in the HRTEM image. Furthermore, VSM results showed that the obtained material exhibited paramagnetism.

Key words: *hydrotalcite; magnetism; hydrothermal method; co-precipitation*

1. Introduction

Hydrotalcites (HTLcs) are commercially available and cheap solid bases; hydrotalcites and calcined hydrotalcites (normally referred to as mixed oxides) are highly active, selective catalysts and play an important role in many base-catalyzed reactions, such as Claisen–Schmidt condensations [1] and Knoevenagel condensations [2]. However, the problems of separation, recovery and pollution limit their industrial applications. The separation methods for these solid mixed oxides need extra equipment and treatments, which consume a great deal of energy and money. Therefore, it is essential to synthesize a novel solid base catalyst to extend the utility of catalysts and develop green routes. The drive to develop environmentally benign processes has led to a considerable increase in research activities both in academic and industrial sectors for the development of solid base catalysts. Based on the above consideration, Carja et al. [3] reported new magnetic layered structures which can be used as precursors for new

*Corresponding author, e-mail: zhqw1888@sohu.com

hybrid nanostructures such as aspirin-hydrotalcite-like anionic clays. Srikanth et al. [4] reported the synthesis of super-paramagnetic Fe_3O_4 nanoparticles recently. The presented Fe_3O_4 possesses uniform crystallite size (about 11 nm) and high-dispersion.

Co-precipitation is the most common method to synthesize HTLcs which is based on the reaction of a solution containing M^{II} and M^{III} metal cations in adequate proportions with an alkaline solution. However, the crystallinity of the obtained samples is strongly affected by the synthetic parameters such as the pH value, temperature, concentration of used solutions and others [5–7]. Hydrothermal synthesis is a well-known and established method to prepare transition metal oxides and other well-crystallized samples [8–10]. It is well-known that the catalytic performance of hydrotalcite is dramatically increased through the incorporation Ni into the hydrotalcite material. The formation of surface-enriched Ni in the hydrotalcite seems to be the main reason for its high catalytic performance [11].

In our present work, two methods have been used to obtain the magnetic Ni-Al hydrotalcites: one method is based on the direct co-precipitation synthesis by using Fe_3O_4 as magnetic core, the other one is based on the hydrothermal treatment by the introduction of Fe_3O_4 endowed Ni-Al HTLcs with magnetism which makes it possible to achieve the ease of recovery and recycling of HTLcs through an external rotating magnetic field. New results are reported for the first time, to the best of our knowledge. This novel magnetic Ni-Al HTLcs is expected to be used as a green catalyst, and thus solve the disadvantages as mentioned above.

2. Experimental

Synthesis. Magnetic nanoparticles were prepared by dissolving 0.01 mol of $FeSO_4$ and 0.01 mol of $Fe_2(SO_4)_3$ in water, under stirring at 45 ºC, and 20 wt. % of $NH_3{\cdot}H_2O$ were added dropwise together at a constant pH value of 10–11. The obtained material (Fe_3O_4) was recovered, washed several times with de-ionized water until the pH was neutral. The obtained Fe_3O_4 was preserved as a suspension.

An aqueous solution containing 17.45 g of $Ni(NO_3)_2{\cdot}6H_2O$ and 7.5 g of $Al(NO_3)_3{\cdot}9H_2O$ was added dropwise to Fe_3O_4 solution with Ni/Fe molar ratio equal to 50 under vigorous stirring. During the synthesis, the temperature was maintained at 60 °C and pH at about 11 by simultaneous addition of NaOH and Na_2CO_3 solution. The resulting mixture was transferred to an autoclave pressure vessel and hydrothermally treated at 200 °C for 10 h. When the autoclave temperature reached the room temperature, the product was removed, filtered, washed with distilled water to get netural pH, and dried at 80 °C for 24 h. The resulting sample was calcined at various temperatures between 200 °C and 900 °C for 5 h.

Magnetic Ni-Al HTLcs was also prepared by the direct co-precipitation method, in order to compare with the obtained hydrothermally treated sample. An aqueous solution containing $Ni(NO_3)_2{\cdot}6H_2O$ and $Al(NO_3)_3{\cdot}9H_2O$ was added dropwise to the above synthesized Fe_3O_4 solution with Co/Fe molar ratio equal to 50 under vigorous stirring.

During the whole synthesis, the temperature was maintained at 65 °C and the pH at about 10 by the simultaneous addition of NaOH and Na_2CO_3 solution. When enough reaction time had elapsed, the product was removed, filtered, washed with distilled water to get neutral pH, and dried at 80 °C for 24 h.

Characterization. Thermogravimetric analysis – differential scanning calorimetry (TG-DSC) of the as-synthesized sample was performed on a NEZSCH STA 409PC thermoanalyzer. The analysis was carried out in Ar atmosphere in the temperature range 40–600 °C with the heating rate of 10 °C/min. Powder X-ray diffraction (XRD) patterns were recorded on a Rigaku D/max-IIIB diffractometer using CuK_α radiation ($\lambda = 0.15406$ nm). Transmission electron microscopy (TEM) and high-resolution transmission electron microscopy (HRTEM) experiments were performed using a Philips CM 200 FEG electron microscope with an acceleration voltage of 200 kV. The samples were dispersed in ethanol. Carbon-coated copper grids were used as the sample holders. Magnetic hysteresis loops were measured using a vibrating sample magnetometer (VSM, JDAW-2000). For magnetization measurements, the powder was pressed strongly and fixed in a small cylindrical plastic boxes.

3. Results and discussion

3.1. TG-DSC studies

The TG-DSC curves of the magnetic Ni-Al HTLcs treated by hydrothermal method and co-precipitation method are shown in Fig. 1. Both the TG-DSC profiles of magnetic Ni-Al HTLcs exhibited two apparent endothermic events, and two distinc-

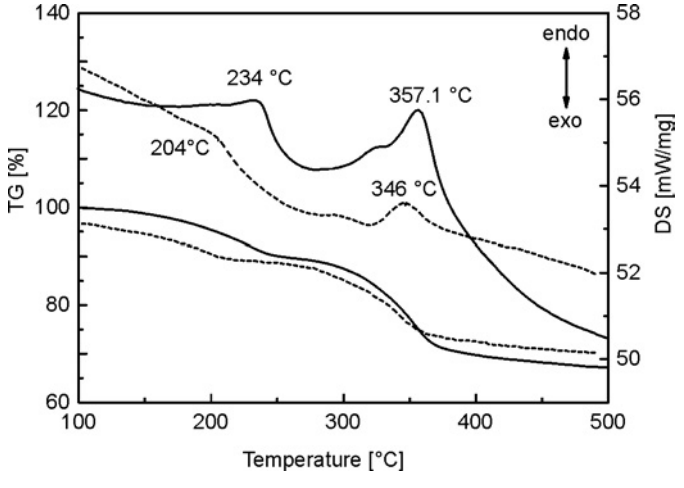

Fig. 1. TG-DSC curves of magnetic Ni-Al HTLcs synthesized by hydrothermal treatment (solid lines) and conventional co-precipitation (dashed lines)

tive steps of weight loss. The DSC profile of hydrothermally treated samples (solid lines) exhibited two apparent endothermic peaks at 234 and 357.1 °C, with a minor, broad endothermic peak at about 324 °C. This also can be proved by the TG curve, where two clear weight losses can be observed. At the first stage, the weight loss can be assigned to the loss of physically absorbed (surface) and interlayer water [12–14], in the diagram of TG curve, 8.44 % loss was observed. Based on this value, the water content was estimated to be 2.34 per chemical formula. The second one can be assigned to the loss of hydroxyl ions and removal of carbonate ions. Notably, the TG-DSC profiles for magnetic Ni-Al HTLcs synthesized by direct co-precipitation (broken lines) showed two apparent endothermic peaks at 204.1 °C and 346 °C, which was slightly lower than hydrothermal treatment showed. This indicated that the sample possessed high thermal stability which can be further demonstrated by the following XRD and TEM observations.

3.2. Powder X-ray diffraction XRD

The XRD patterns of magnetic Ni-Al HTLcs synthesized by hydrothermal method (A) and co-precipitation method (B) are shown in Fig. 2. In both samples, there appeared diffraction peaks corresponding to the layered double hydroxides structure. In concrete, the sharp symmetric reflections of the basal (003), (006) and (009) planes; broad, less intense and asymmetric reflections for the nonbasal (012), (015) and (018) planes were observed.

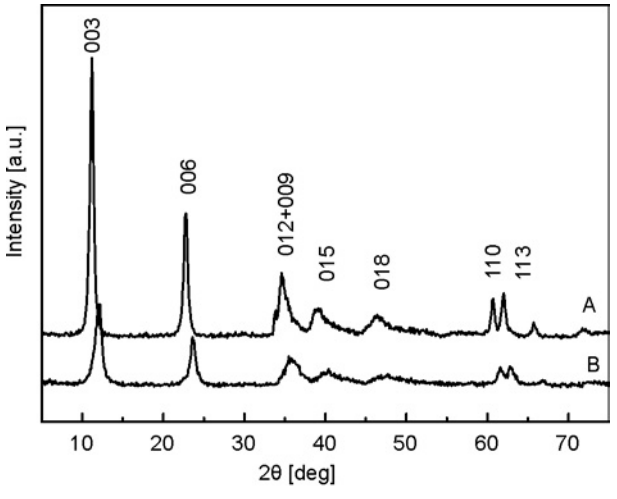

Fig. 2. XRD patterns of magnetic Ni-Al HTLcs synthesized
by hydrothermal treatment (A) and conventional co-precipitation (B)

At the same time, (009) and (012) reflections partially overlapped in the 2θ range of 33–37°. All of these features were characteristic of a typical hydrotalcite-like

phase [15]. No typical diffraction peak of iron oxides was observed for Fe-LDH sample, which showed that the magnetism (Fe_3O_4) was highly dispersed in the hydrotalcite structure. It should be noted that the hydrothermal treatment resulted in an increasing intensity of diffraction peaks. Furthermore, after the hydrothermal treatment, the typical XRD diffraction peaks shift to lower angles, which implied the increase of the interlayer spacing and growth of crystallites. The growth of crystallites can be explained: the amorphous part of the co-precipitated sample dissolves during hydrotalcite synthesis under hydrothermal conditions, which results in the increase of hydrotalcite content.

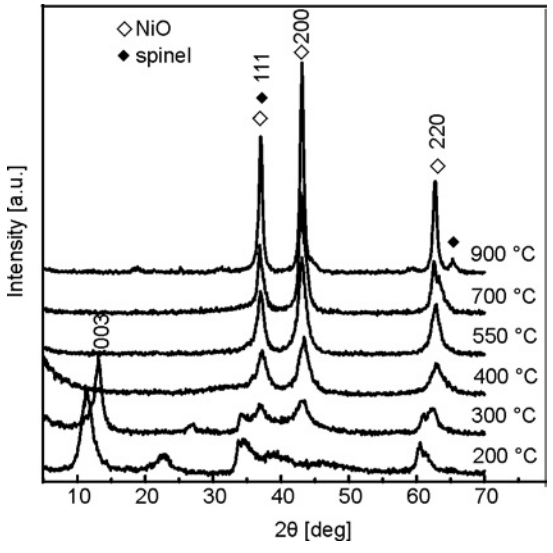

Fig. 3. XRD patterns of hydrothermally treated magnetic Ni-Al HTLcs calcined at various temperatures

In order to investigate the effect of calcination temperature on the structure of hydrothermally treated magnetic Ni-Al HTLcs, the samples calcined at various temperatures were characterized by XRD. As shown in Fig. 3, the presented XRD pattern of magnetic Ni-Al HTLcs calcined at 200 °C was similar to that of the dried sample obtained by hydrothermal treatment, which indicates the obtained calcined sample still possesses a layered double structure. However, the XRD diffraction peaks, especially for (003), of the calcined sample shifted to higher angles when the temperature was increased to 300 °C. The decomposition of the hydroxide layers and the removal of interlayer anions (carbonate) resulted in the decrease of the interlayer spacing, and thus the shift of XRD diffraction peaks which was consistent with the TG-DSC results. It should be noted that, at this temperature, the characteristic (200) peaks of NiO were evident. Further increase of the calcination temperature led to the complete decomposition of HTLcs and the formation of single oxide NiO (cubic structure, JCPDS 4-835). The (110), (200), and (200) diffraction peaks can be clearly seen in Fig. 3.

With the increase of calcination temperature, these diffraction peaks became more narrow and intense, which can be attributed to the growth of crystallites and improvement of crystallization. For the conventional Ni-Al HTLcs, $NiAl_2O_4$ was formed as a crystalline phase at 800 °C. However, for our obtained sample, even if the temperature was increased to 900 °C, the calcined sample can also possess the single NiO crystalline phase after thermal decomposition. This can be ascribed to the hydrothermal treatment and the introduction of Fe_3O_4 during the synthetic process. The Al^{3+} ions can either be incorporated in an amorphous nickel aluminate phase, or in a separate amorphous alumina phase [16]. Single NiO crystalline phase maintained at high temperature is particularly important for applications in catalysis and electrochemistry fields. Moreover, it exhibited spinel phase ($Ni_aFe_bAl_cO_d$) when the calcination temperature increased to 900 °C. Mixed oxides involving spinel as a basic catalyst can be used in multiform catalytic reactions.

3.3. Transmission electron microscopy (TEM)

The morphology of a hydrothermally treated magnetic Ni-Al HTLcs sample without calcination was investigated by TEM. The TEM images are shown in Fig. 4. The flat particle morphology was observed to be regular, and of hexagonal shape throughout. The grain boundaries were well defined and the platelet size was about 200 nm. A dissolution and re-crystallization of the smallest crystallites and amorphous parts during hydrothermal treatment should be responsible for the large particle size.

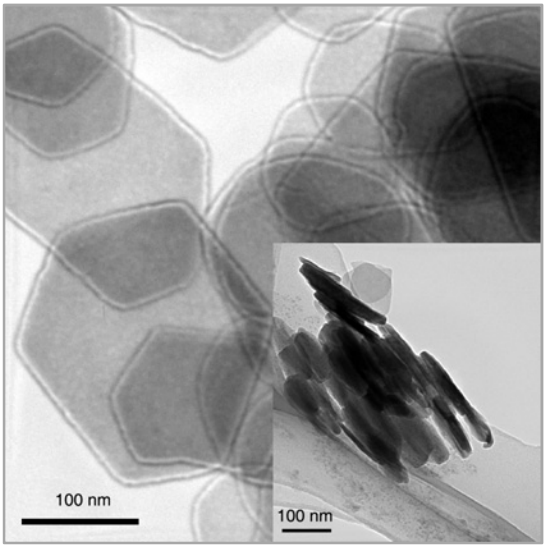

Fig. 4. TEM image of magnetic Ni-Al HTLcs without calcination

The increase in both crystallinity and crystallite size upon hydrothermal treatment was further confirmed by the XRD observations. No diffraction fringes were observed, although the sample was crystalline, as evidenced by the XRD pattern. However, it should be remembered that in the experimental conditions, necessary for TEM analysis, the samples were kept under high vacuum. Therefore, it seemed reasonable to assume that a deep dehydration and a partial loss of the layered structure occurred. The inset of Fig. 4 shows the profile of the sample. It can be clearly seen that the thin plates composed of layered structures and the thickness of the platelet was about 17 nm.

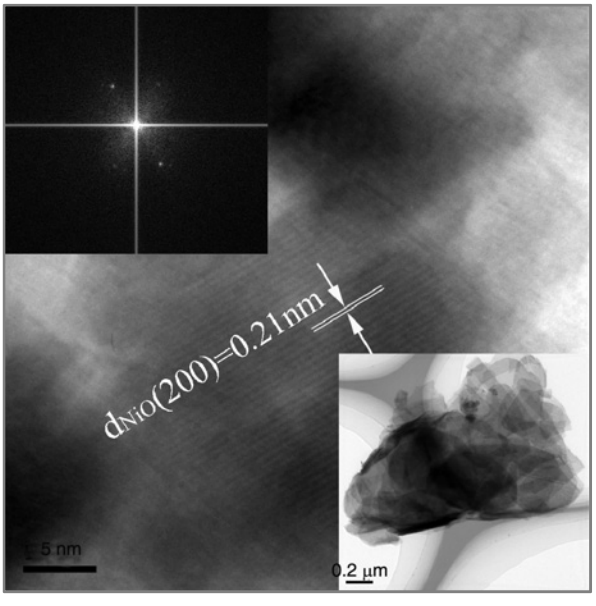

Fig. 5. TEM image and the corresponding Fourier diffractogram (inset) of magnetic Ni-Al HTLcs calcined at 300 °C

Figure 5 shows typical TEM images at various magnifications of hydrothermally treated magnetic Ni-Al HTLcs calcined at 300 °C. The micrograph at lower magnification (the inset of Fig. 5) clearly shows the structure of HTLcs that had been partly destroyed by calcination. The lattice fringes can be easily observed from the HRTEM image. The lattice fringe corresponding to (200) (d = 0.21 nm) crystallographic planes of NiO was presented in Fig. 5, which was consistent with the Fourier diffractograms shown in the inset of Fig. 5. The TEM observations were in good agreement with XRD results.

3.4. Vibrating sample magnetometry (VSM)

Figure 6 shows the hysteresis curves of hydrothermally treated magnetic Ni-Al HTLcs without calcination. The Ni/Fe molar ratio was 50. The magnetic properties,

such as saturation magnetization (M_s), remanent magnetization (M_r) and coercivity (H_c), are given in Table 1. The hysteresis curve of the hydrothermally treated magnetic Ni-Al HTLcs exhibited a paramagnetic behaviour (M_s = 2.09 emu/g and H_c = 0 Oe). It demonstrated that the obtained sample exhibited paramagnetism which can be attributed to the Fe_3O_4 particle with very small particle size [4]. However, the specific saturation magnetization decreased to 1.88 emu/g when the (FeO_x/Fe-HTLcs)

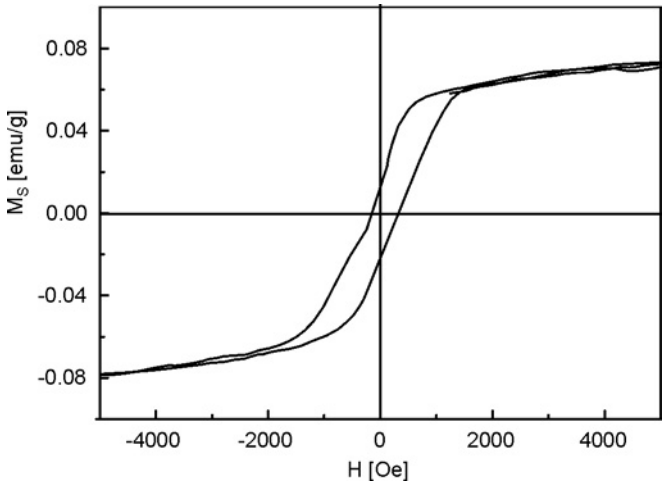

Fig. 6. Magnetic hyteresis curve of magnetic Ni-Al HTLcs without calcination

sample was calcined at 400 °C, which can be due to the change of magnetic valence. XRD pattern of the sample calcined at 400 °C showed metal oxide (NiO) formation, as shown in Fig. 3. Non-magnetic substances, such as NiO, may impede the magnetization orientation of the product and result in the decrease of the magnetism. From Table 1, it can be observed that the coercivity (H_c) of the sample calcined at 400 °C was 339 Oe. The increase in the H_c value was attributed to adhesion and growth of the crystal grains, which resulted in a change from paramagnetism to ferrous magnetism in the Ni-Al HTLcs.

Table 1. The magnetic capability of magnetic Ni-Al HTLcs
(Ni/Fe molar ratio equal to 50)

	Calcination temperature [°C]	
	0	400
M_s (emu/g)	2.09	1.88
M_r (emu/g)	0.37	0.37
M_r/M_s	0.178	0.198
j_{Hc} [Oe]	0	339

4. Conclusions

We introduced a simple synthesis route to prepare the magnetic Ni-Al HTLcs on the basis of the hydrothermal treatment method. The hydrothermally treated magnetic Ni-Al HTLcs presented higher thermal stabitlity in comparison with the sample in the absence of hydrothermal treatment. Furthermore, the obtained materials exhibited paramagnetism. This novel material has potential applications as a green catalyst or as a catalyst-support. We expect this novel synthetic method can be extended to the synthesis of other magnetic HTLcs.

Acknowledgement

We gratefully acknowledge the support of this research by the Key Technology R&D program of Heilongjiang Province (no.G202A423, no.TB06A05), and by the Science Fund for Young Scholar of Harbin City (no. 2004AFQXJ038).

References

[1] CLIMENT M.J., CORMA A., IBORRA S., PRIMO J., J. Catal., 151 (1995), 60.
[2] CORMA A., FORNÉS V., MARTIN-ARANDA R.M., REY F., J. Catal., 134 (1992), 58.
[3] CARJA G., CHIRIAC H., LUPU N., Magn J., Magn. Mater., 311 (2007), 26.
[4] GASS J., PODDAR P., ALMAND J., SRINATH S., SRIKANTH H., Adv. Funct. Mater., 16 (2006), 71.
[5] KOVANDA F., KOLOUŠEK D., CÍLOVÁ Z., HULÍNSKÝ V., Appl. Clay Sci., 28 (2005), 101.
[6] CARPENTIER J., LAMONIER J.F., SIFFERT S., ZHILINSKAYA E.A., ABOUKAÏS A., Appl. Catal. A, 234 (2002), 91.
[7] KUŚTROWSKI P., SULKOWSKA D., CHMIELARZ L., RAFALSKA-LASOCHA A., DUDEK B., DZIEMBAJ R., Microporous Mesoporous Mater., 78 (2005), 11.
[8] LABAJOS F.M., RIVES V., ULIBARRI M.A., J. Mater. Sci., 27 (1992), 1546.
[9] RAO M.M., REDDY B.R., JAYALAKSHMI M., JAYA V.S., SRIDHAR B., Mater. Res. Bull., 40 (2005), 347.
[10] KOOLI F., KOSUGE K., TSUNASHIMA A., J. Solid State Chem., 118 (1995), 285.
[11] JANA S.K., WU P., TATSUMI T., J. Catal., 240 (2006), 268.
[12] YUN S.K., PINNAVAIA T.J., Inorg. Chem., 35 (1996), 6853.
[13] KLOPROGGE J.T., HICKEY L., FROST R.L., J. Solid State Chem., 177 (2004), 4047.
[14] TAKEHIRA K., KAWABATA T., SHISHIDO S., MURAKAMI K., OHI T., SHORO D., HONDA M., TAKAKI K., J. Catal., 231 (2005), 92.
[15] XU Z.P., XU R., ZENG H.C., Nano. Lett., 1 (2001), 703.
[16] PÉREZ-RAMÍREZ J., MUL G., MOULIJN J.A., Vib. Spectr., 27 (2001), 75.

Received 8 July 2007
Revised 4 June 2008

Materials Science-Poland, *Vol. 26*, *No. 3*, *2008*

The effect of impact energy on the formation of nanocrystalline powders in Cu–50% Fe immiscible alloy systems

M. R. VAEZI[1*], S. H. MIR SHAH GHASSEMI[2], A. SHOKUHFAR[2]

[1]Advanced Materials Research Center, Materials and Energy Research Center, Karaj, Iran

[2]Advanced Materials and Nanotechnology Research Center, Department of Materials Science and Engineering, Faculty of Mechanical Engineering, K.N. Toosi University of Technology, Tehran, Iran

The study of mechanical alloying in the Cu–Fe system, as a model system for those with positive heats of mixing, has been investigated. The effects of impact force which pertains to ball-to-powder ratio, rotation speed and milling time, on the strain and grain size of final powders have been studied. The aim of this research was to find the optimum condition for mechanical alloying of Cu–Fe system by the automatic design and analysis of Taguchi experiments. X-ray diffraction (XRD) was used to analyze the effect of incoming energy on the diffusion rate.

Key words: *mechanical alloying; nanocrystalline; immiscible systems; diffusion; Taguchi design*

1. Introduction

Over the last three decades, powder processing by ball milling has attracted wide practical interest as it offers a simple but powerful way to synthesize non-equilibrium phases and microstructures from nanograin materials to extended solid solutions, amorphous phases [1–3], chemically disordered compounds [4–7], and nanocomposites [8, 9]. Mechanical alloying (MA) can be comparable with those methods accompanied by cold working (dislocation density about 10^{11} cm^{-2}). In MA, powders are entrapped between ball–ball and ball–wall and the impact force of the collision transfers to them. Therefore, powders undergo a severe plastic deformation, which causes a strain rate of 10 s^{-1} and, therefore, significantly enhances dislocation density. If two different kinds of powder particles are joined together and then flattened because of the impact force, they become like a lamellar composite (thickness ca. 0.1–0.5 μ), and

*Corresponding author, e-mail: vaezi9016@yahoo.com

the diffusion distance decreases. Another significant parameter which promotes diffusion during MA is the presence of new surfaces. Fracturing powders results in appearance of new surfaces which are clean, i.e. without oxide layers, and prepare good sites for atomic motion and diffusion. Mechanically alloyed powders also exhibit extension of equilibrium solid solubility limits, which is important in miscible systems [10, 11]. It becomes more significant in systems such as Cr–Cu [12], Ag–Cu, Cu–Fe [13], Cu–W [14, 15] and Al–Pb [16] which are immiscible at room temperature by using other methods and are partially or even fully soluble by using MA.

The Cu–Fe system does not form any intermetallic compounds and has negligible mutual solid solubility in equilibrium at temperatures below 700 °C because of the large positive enthalpy of mixing [17]. During MA, the energy of balls transfers to the entrapped powders and causes severe plastic deformation, thus enhancing density of dislocations and promotes the formation of excess vacancies [18]. On the other hand, pipe diffusion needs low temperature and high strain rate or stress which are provided by MA [19, 20]. These conditions together increase atomic diffusion and consequently lead to the formation of solid solutions of Cu(Fe). Although there exist lots of research work on the formation [21–23] and characterization [24–27] of the Cu–Fe immiscible system, there is no analytical viewpoint on the effect of milling parameters and mixed fraction of its mechanical alloying. Note that according to Jiang et. al. [25], mechanical alloying leads to the formation of single-phase solid solutions of up to 60 at. % Fe in Cu, and 20 at. % Cu in Fe but according to our research, based on XRD peak position and width changes, no detectable dissolution of Cu in Fe is observed. This research work addresses the optimum parameters to diffuse Fe in Cu, and also the effects of impact force on the strain and grain size of final powders in Cu–Fe systems have been studied. The Taguchi method is a scientifically rigorous mechanism for evaluating and implementing improvements in processes, materials, equipment, and facilities. These improvements are aimed at improving the desired characteristics and simultaneously reducing the number of defects by studying the key variables controlling the process and optimizing the procedures or design to yield the best results. In other word, Taguchi helps to design samples to find these optima and reduces the number of required samples and consequent tests.

2. Experimental

Mechanical alloying was performed in a high-energy ball milling Fritsch P-5 planetary mill using stainless steel containers and balls (15 mm in diameter). The 50% Cu–50% Fe alloy powders were produced by milling 3.2 g of copper powder (99.7% pure, <100 μm) and 2.8 g of iron powder (> 99% pure), both purchased from Merck. Stearic acid (1 wt. %) was added to the initial powders in order to prevent agglomeration. After milling, the powders were removed from the container. The milled samples were analyzed by X-ray diffraction (XRD) in a Siemens (D-500) diffractometer using CuK_α radiation (λ = 0.1540510 nm).We used an automatic design

and the analysis of Taguchi experiments to find the optimum parameter values. Three most significant factors including ball-to-powder ratio (BPR), time and speed were chosen. We assumed that arranging two levels for each of these factors can help to realize the values of most significant parameters. Therefore, the BPR values 10 and 20 have been chosen. For time and speed, levels of 10–20 h and 200–400 rpm realized to be the finest amounts. Based on 2-level control factors Taguchi offers L-4 design which is listed in Table 1. CF0 represents a mixture of unmilled elemental powders.

Table 1. Conditions and parameters of the experiment

Sample	BPR	Time [h]	Speed [rpm]
CF1	10	10	200
CF2	10	20	400
CF3	20	10	400
CF4	20	20	200

3. Results and discussion

XRD spectra of the milled samples are shown in Fig. 1. The diffraction Bragg peaks are broadened, shifted and reduced in intensity. Several factors such as decrease in crystalline size, internal strain and broadening, due to the X-ray machine itself, can be related to the peak broadening. We omit the third factor and investigate on the first two. Each sample has its own conditions (different BPR, speed and milling time) which cause the changes in peaks. Note that each of the selected parameters affects changes in peaks by its own power which can be analyzed employing Taguchi procedure. This power is a combination of impact factor (which pertains to BPR and speed) and milling time. On the other hand, it is clear that diffusion of Fe atoms in Cu lattice results in broadening of peaks. Diffusion of Fe atoms in Cu lattice leads to increase in the lattice constant. It means that the lattice parameter of Cu increases which leads to the reduction in degree of peaks. Although Fe and Cu have similar atomic radii, and mechanical alloying can promote the formation of both Fe(Cu) and Cu(Fe), based on XRD results (changes in width and position of (110) peak) and even considering atomic radius and melting temperature prove that atomic diffusion of Fe into Cu matrix and consequently formation of Cu(Fe) is more likely than Cu atoms to diffuse into Fe matrix.

Table 2 lists peak position, broadening values, relative crystallite sizes and lattice parameters of Cu. The crystallite size evolution for milled powders was determined by the Williamson–Hall method. The method is based on the broadening of the diffraction lines due to the strain and crystallite size. The Williamson–Hall equation is expressed as [28]:

$$\sqrt{(B_i^2 - B_0^2)}\cos\theta = \frac{0.89\lambda}{d} + S\sin\theta \tag{1}$$

where B_i is the full width at a half-maximum (FWHM) of the peaks of mechanically alloyed powders, B_0 the width at a half-maximum of peaks of unmilled powders, θ – the Bragg angle, λ the wavelength of X-ray, S the internal microstrain and d – crystallite size.

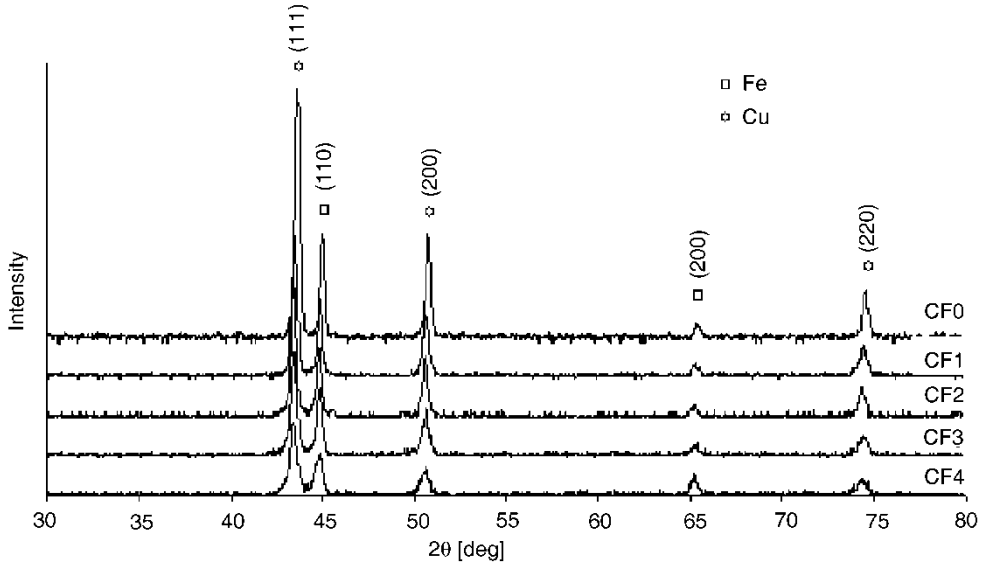

Fig. 1. XRD spectra of milled samples at various milling conditions

Table 2. Peak positions, width of (111) peak, microstrain and crystallite size of samples

Sample	2θ (111) [deg]	FWHM	Microstrain S	Crystallite size d [nm]	Lattice parameter [nm]
CF0	43.64	0.27	–	-	0.3588
CF1	43.50	0.32	–0.0017	42	0.3594
CF2	43.46	0.29	–0.0011	65	0.3592
CF3	43.50	0.36	–0.0024	30	0.3597
CF4	43.44	0.41	–0.0031	23	0.3599

A comparison of these values with each other shows that the shift of (111) peak is more significant in CF4, which means that its operating condition is the most significant. From Taguchi design and its analysis, it is clear that the important factors are BPR, speed and time, respectively.

According to Eq. (1), the crystallite size of samples can be calculated from the intercept of the straight line, whereas the values of microstrain can be obtained from the

slope of this line. Figure 2 illustrates the effect of milling condition on the microstrain and the crystallite size of samples. As shown in Fig. 2, the value of $\sqrt{(B_i^2 - B_0^2)}\cos\theta$ decreases linearly with sinθ. It is obvious that negative slope of these lines correlates to the compressive induced stress caused by ball collisions. The impact energy of balls has a direct relationship with their collision speed and their numbers (which create the

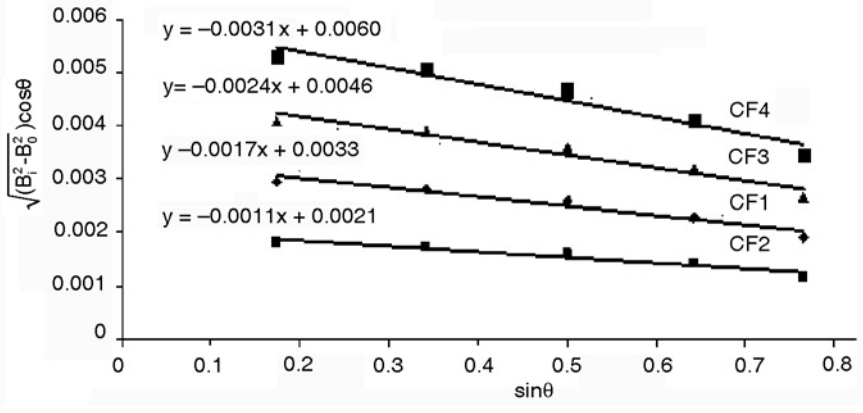

Fig. 2. Williamson-Hall plot: effect of milling parameters on microstrain and crystallite size

PBR factor). These factors, i.e. impact energy and milling time can explain the arrangement of the straight lines. The greater the impact energy, the higher is the induced strain. Another noticeable parameter is lattice parameter of Cu matrix. As listed in Table 2, and considering dissolution of Fe atoms in Cu lattice, substituting Fe atoms into Cu lattice result in increasing of the distance of Cu planes. Difference between Cu and Fe atomic radii causes this change. So as a result of Fe dissolution into Cu lattice, in addition to the effect of induced microstrain, lattice parameters change (Table 2). Taguchi design can estimate the optimum condition to achieve the least crystalline size which was the last sample. One can estimate that using BPR of 20, time of 20 h and speed of 200 rpm are the optimum parameters just like sample CF4. Although it might seem that increasing the speed could enhance the impact energy, it should be kept in mind that an increase above the criyical value leads to adhesion of balls to the wall of vials. Incidentally, at speeds higher than the critical value, there is no effective impact and collision, therefore energy of balls is not transferred to the powders. This fact can be seen in sample CF2. This sample was treated at a speed of 400 rpm, which is estimated to be over the critical value. As is explained about the impact energy, this sample has the least effective incoming energy. Another point which can be inferred about milling condition is that although mechanical alloying is a time-dependent process, optimizing other factors could help to improve the milling process and consequently decrease milling time dramatically. For example, although sample CF2 is milled for about 20 h due to deviation of other milling parameters from their optimum values, it has the least induced strain.

Each sample was milled at different milling times to investigate on the effect of these conditions on Fe fraction which diffused into Cu lattice. Kinetic of Fe dissolution into Cu lattice can be followed by the evolution of the (110) X-ray peak intensity of the unmixed Fe as a function of milling time. The obtained curves of the mixed fraction of Fe which are considered as the fraction transformed (Fig. 3) can be well described by the Johnson–Mehl–Avrami kinetics formalism in which the fraction transformed exhibits a time dependence of the following form [29, 30]:

$$X = 1 - \exp\left(-(kt)^n\right) \tag{2}$$

where n is the order of reaction or the Avrami parameter, X is the volume fraction transformed, t is the milling time and K is the rate constant.

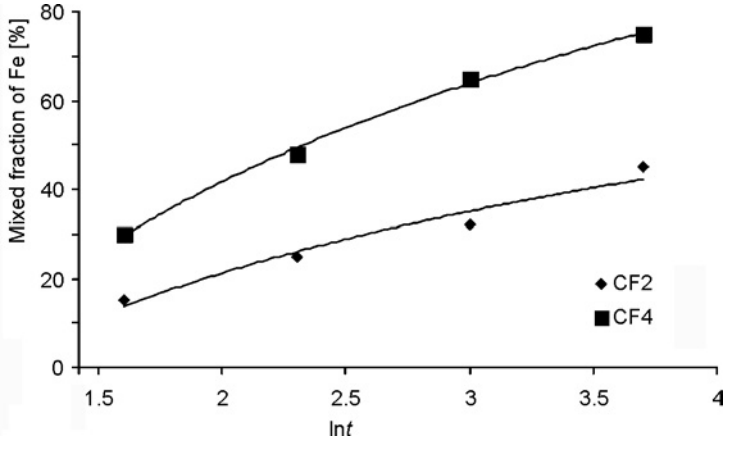

Fig. 3. Mixed fraction of Fe in function of ln$t$

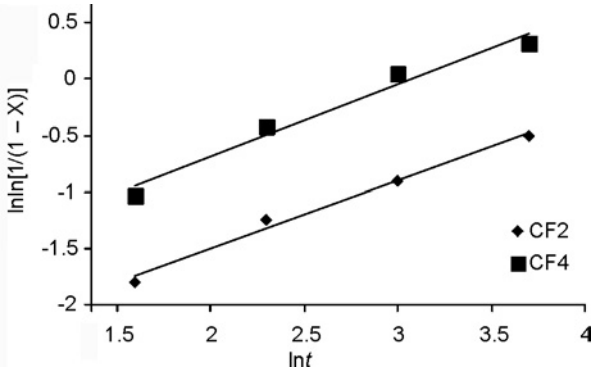

Fig. 4. Johnson–Mehl–Avrami plot in function of milling time

The kinetic parameters, n and k, can be deduced from the double logarithmic plot lnln(1/(1–X)) vs. ln$t$. These curves represent the amount of mixed fraction for the least

intensive and most intensive condition across milling time. As expected, milling with the most effective condition results in diffusion of more Fe atoms into Cu lattice for the same milling time. For instance, while less than 10% of Fe can diffuse into Cu lattice during the first 5 h of milling for CF2, up to 30% of Fe atoms diffuse into Cu lattice for CF4. Another point, the rate of solubility is higher for CF4 in comparison with other samples, which can be seen in Fig. 4. The obtained Avrami parameters $n_2 = 0.60$ and $n_4 = 0.64$ are quite small ($n < 1$) and differ significantly from those usually obtained for the nucleation and growth during the crystallization process.

These values are comparable to those obtained for transformation controlled by the diffusion at the interface and by the dislocation segregation. This might be correlated to the existence of a high density of dislocations and various types of defects induced by severe plastic deformations during milling [31, 32].

4. Conclusion

Ball-milled Cu–50 % Fe powdered mixture has been studied by X-ray diffraction. Using Taguchi design L-4 introduces 4 different samples which can estimate significant values of three most significant factors: BPR, time and speed among 2 levels. It predicts that using PBR of 20 and time of 20 hrs together with a speed of 200 rpm can reduce the crystalline size to the minimum achievable value, and increase microstrain to the highest available. One of the samples which was produced at these data shows a crystalline size of 23 nm and microstrain of 0.0031. Calculating the Avrami parameter proved how it is possible to enhance atomic diffusion by finding the best combination of milling conditions.

References

[1] SURYANARAYANA C., Prog. Mater. Sci., 46 (2001), 1.
[2] MURTY B.S., NAIK M.D., MOHAN R.M., RANGANATHAN S., Mater. Forum, 16 (1992), 19.
[3] SCHULTZ L., Mater. Sci. Eng., 97 (1988), 15.
[4] ERMAKOV A.E., YURCHIKOV E.E., ELSUKOV E.P., Fiz. Tverd. Tela, 4 (1982), 1947.
[5] ELSUKOV E.P., BARINOV V.A., GALAKHOV V.R., YURCHIKOV E.E., ERMAKOV A.E., Phys. Metals Metall., 55 (1983), 119.
[6] BAKKER H., ZHOU G.F., YANG H., Mater. Sci. Forum, 179–181 (1995), 47.
[7] JANG J.S.C., KOCH C.C., J. Mater. Res., 5 (1990), 498.
[8] YING D.Y., ZHANG D.L., Mater. Sci. Eng. A, 286 (2000), 152.
[9] DJEKOUN A., OTMANI A., BOUZABATA B., BECHIRI L., RANDRIANANTOANDRO N., GRENECHE J.M., Catalysis Today, 113 (2006), 235.
[10] ROJAS P.A., PEÑALOZA A., WÖRNER C.H., FERNÁNDEZ R., ZÚÑIGA A., J. Alloys Comp., 425 (2006), 334.
[11] SCHWARZ R.B., PETRICH R.R., SAW C.K., J. Non-Crystal. Solids, 76 (1985), 281.
[12] OGINO Y., YAMASAKI T., MURAYAMA S., SAKAI R., J. Non-Crystal. Solids, 117–118 (1990), 737.
[13] RAVISHANKAR N., ABINANDANAN T.A., CHATTOPADHYAY K., Mater. Sci. Eng. A, 304–306 (2001), 413.

[14] GAFFET E., LOUISON C., HARMELIN M., FAUDOT F., Mater. Sci. Eng. A, 134 (1991), 1380.
[15] ABOUD T., WEISS B.Z., CHAIM R., Nanostr. Mater., 6 (1995), 405.
[16] FANG F., ZENG M.Q., CHE X.Z., ZHU M., J. Alloys Comp., 340 (2002), 252.
[17] HUANG X., MASHIMO T., J. Alloys Comp., 288 (1999), 299.
[18] KRASNOWSKI M., KULIK T., Scripta Mater., 48 (2003), 1489.
[19] WU F., ISHEIM D., BELLON P., SEIDMAN D.N., Acta Mater., 54 (2006), 2606.
[20] DAS D., CHATTERJEE P.P., MANNA I., PABI S.K., Scripta Mater., 41 (1999), 861.
[21] HUANG X., MASHIMO T., J. Alloys Comp., 288 (1999), 299.
[22] WEI S., YAN W., LI Y., LIU W., FAN J., ZHANG X., Physica B, 305 (2001), 135.
[23] HUANG J.Y., JIANG J.Z., YASUDA H., MORI H., Phys. Rev. B, 58 (1998), 45.
[24] YANG Y., ZHU Y., LI Q., MA X., DONG Y., WANG G., WEI S., Physica B, 293 (2001), 249.
[25] JIANG J.Z., GENTE C., BORMANN R., Mater. Sci. Eng. A, 242 (1998), 268.
[26] GAFFET E., HARMELIN M., FAUDOT F., J. Alloys Comp., 194 (1993), 23.
[27] ORECCHINI A., SACCHETTI F., PETRILLO C., POSTORINO P., CONGEDUTI A., GIORGETTI CH., BAUDELET F., MAZZONE C.G., J. Alloys Comp., 424 (2006), 27.
[28] WILLIAMSON G.K., HALL W.H., Acta Metall., 1 (1953), 22.
[29] CHRISTIAN W., *The Theory of Transformations in Metals and Alloys*, Part I, 2nd Ed., Pergamon Press, Oxford, 1975.
[30] AVRAMI M., J. Chem. Phys., 9 (1941), 177.
[31] GUPTA R., GUPTA A., Mater. Sci. Eng. A, 304–306 (2001), 442.
[32] MOUMENI H., ALLEG S., GRENECHE J.M., J. Alloys Comp, 419 (2006), 140.

Received 22 August 2007
Revised 26 November 2007

Materials Science-Poland, *Vol. 26*, *No. 3*, *2008*

Optical characterization of nanoporous GaN through electroless wet chemical etching

L.S. CHUAH*, Z. HASSAN, H. ABU HASSAN

Nano-Optoelectronics Research and Technology Laboratory, School of Physics,
Universiti Sains Malaysia, 11800 Minden, Penang, Malaysia

High quality unintentionally doped n-type GaN layers were grown on Si(111) substrate, using AlN as the buffer layer, by radio frequency (RF) nitrogen molecular beam epitaxy. The present work reports on the photoluminescence (PL) studies of porous GaN prepared by ultraviolet assisted electrochemical etching in a solution of 2:1:1 HF:CH_3OH:H_2O_2 under illumination of an UV lamp with 500 W power for 10, 25 and 35 min. The optical properties of porous GaN samples were compared to the corresponding as-grown GaN. PL studies suggested that the porosity was capable of improving the lattice mismatch induced strain. Porosity induced PL intensity enhancement was found in nanoporous samples. The resulting nanoporous GaN displays blue-shifted PL spectra compared to the as-grown GaN. Appearance of the blue-shifted emission is correlated with the development of highly anisotropic structures in the morphology.

Key words: *photoluminescence; porous GaN; electrochemical etching; Si; RF-MBE*

1. Introduction

Porous semiconductors, especially porous silicon (PSi), exhibit properties absent in their crystalline counterparts [1]. Nonplanar structures developed by anodic etching can have specific surface areas as large as ca. 100 $m^2 \cdot g^{-1}$ [2], and quantum confinement coupled with the decreased efficiency of non-radiative recombination produce luminescence above the bulk band gap [3]. The high surface area, band gap shift, and efficient luminescence suggest uses of porous semiconductors in chemical and biochemical sensing [4, 5]. While PSi has attracted much attention, its thermal, chemical, and mechanical instability hinders its large scale application [6]. Interest in porous semiconductors as-growth templates arises from the pores acting as sinks for mismatch dislocations, accommodating elastic strain in heterostructures [7]. Since the discovery of light emitting porous silicon by Canham in 1990 [1], significant progress

*Corresponding author, e-mails: chuahleesiang@yahoo.com, zai@usm.my

has been made on the studies of the structural, optical as well as mechanical and electrical properties of porous silicon.

In the last decade, porous semiconductors have been widely studied, primarily due to the potential for intentional engineering of properties not readily obtained in the corresponding crystalline precursors, as well as the potential applications in optoelectronics, chemical and biochemical sensing. When porosity is formed, these materials exhibit various special optical features, for instance, a shift of band gap, luminescence intensity enhancement, as well as photoresponse improvement. Among porous semiconductors, porous silicon receives enormous attention and has been investigated most intensively; however the instability of physical properties has prevented it from large scale application. This leads to the development of other porous semiconductors, for instance, the conventional III–V compounds such as GaAs, GaP and InP; and the wide bandgap materials, such as GaN and SiC.

The research in porous GaN is strongly driven by its superior physical properties such as the mechanical, excellent thermal, and chemical stability, as well as the potential shift of the bandgap [8]. Moreover, it has been reported that porous GaN can be used as an intermediate layer for the reduction of substrate induced strain [9, 10]. Since bulk GaN in wafer size is not available, GaN thin film usually is grown on poor lattices and thermally mismatched foreign substrates, which will result in high residual stress and eventually lead to high density of structural defects. Research has also suggested that nanopatterned porous structures may serve as a template for nanoscale lateral epitaxial overgrowth [11]. In comparison, the study of porous GaN is still in the early stage, many fundamental properties are still not well understood.

Electroless etching is also called electrochemical oxidation without external bias. Metal-assisted electroless-chemical etching is an etching technique, developed recently, which is proven to be efficient in generating porous semiconductors (especially GaN). In this process, a discontinuous layer of Pt is deposited on the semiconductor surface before immersing into a solution containing CH_3OH, HF, and an oxidant, H_2O_2. Etching proceeds as the H_2O_2 is catalytically reduced at the surface of the Pt, thereby injecting mobile holes into the valence band. Similar to anodic etching, the holes will induce dangling bonds, and the dangling bonds will be attacked by nucleophilic species, resulting in material dissolution [12].

In this work, nanoporous GaN structures were formed from crystalline GaN on conducting Si substrate using metal-assisted UV electroless etching in $HF/CH_3OH/H_2O_2$. The optical properties of porous GaN samples were characterized by photoluminescence (PL) spectroscopy.

2. Experimental

The unintentionally doped n-type GaN film, grown on silicon (111) substrate, was used in this study. The film growth has been performed in a Veeco model Gen II MBE system, using standard effusion sources for evaporation of Al (6N5) and Ga (7N), and

nitrogen with 7N purity was channeled by RF source to generate reactive nitrogen species. The plasma was operated at typical nitrogen pressure of 1.5×10^{-5} Torr under the discharge power of 300 W. Prior to loading into the MBE chamber, the Si(111) wafers (resistivity < 0.02 Ω·cm, n-type) were cleaned by using a standard Radio Corporation of America (RCA) method. RCA cleaning, also known as standard cleaning (SC), has been widely used in the semiconductor industry for more than twenty years.

In the preparation chamber, the substrates were outgassed for 10 min at 400 °C prior to growth. In the growth chamber, Si substrate was heated at 750 °C, and a few monolayers of Ga were deposited on the substrate for the purpose of removing SiO_2 by formation of GaO_2. A RHEED reconstruction with prominent Kikuchi lines was then observed, that turned into clean Si(111) surfaces at 750 °C. To grow an AlN buffer layer, the substrate was heated up to 850°C. Both the Al and N shutters were opened simultaneously for 30 min. Subsequently, a GaN epilayer was grown on top of the buffer layer for 15 min, with substrate temperature set at 800 °C. The unintentionally doped n-type GaN film, grown on Si(111) substrate, was used in this study. The thickness of GaN film was about 0.6 μm, with a carrier concentration of 4×10^{19} cm^{-3}, as determined by the Hall effect measurement.

The wafer was then cleaved into few pieces. Prior to the metallization, the native oxide of the sample was removed in the 1:20 $NH_4OH:H_2O$ solution, followed by 1:50 $HF:H_2O$. Subsequently, boiling aqua regia (3:1 $HCl:HNO_3$) was used to etch and clean the sample. Porous GaN in this work was generated by Pt assisted electroless etching. Two narrow stripes of Pt with thickness of about 250 nm were deposited on the GaN sample by using a sputtering system. The samples were then etched in a solution of 2:1:1 $HF:CH_3OH:H_2O_2$ under illumination of a 500 W UV lamp for 10, 25 and 35 min. After chemical treatment, the samples were removed from the solution and rinsed with distilled water; this was followed by the removal of the residual Pt by ultrasonic cleaning.

The optical properties of as-grown and porous GaN samples were characterized by photoluminescence (PL). PL measurements were performed at room temperature by using a Jobin Yvon HR800UV system, which is an integrated confocal microphotoluminescence spectrometer. A He-Cd laser (325 nm) was used as an excitation source. For measurement, the incident laser power was 20 mW. To focus the laser on the sample surface, microscope objective lenses UV 40x was employed. The emitted light was dispersed by a double grating monochromator with 0.8 m focal length and equipped with a 1800 grove/mm holographic plane grating. Signals were detected by a Peltier cooled CCD array detector. Before the micro-PL measurement, a high quality single crystal silicon sample (with the zone-center-mode at 520.70 cm^{-1}) was used to calibrate the system. The full width at half-maximum (FWHM) of the Si Lorentzian peak width was ca. 3 cm^{-1}. The essential parameters (peak position and FWHM) of the PL peak were determined by using curve fitting software with Gaussian and Lorentzian models.

3. Results and discussion

The morphology of the as grown and porous GaN films was characterized by plan-view scanning electron micrographs (SEM). As seen in Fig. 1, the circular porous area is very uniform, with pore diameter in the 80–110 nm range. The etching duration has significant effect on the size and shape of the pores. For a 10 min sample, the pore sizes were observed to be around 70 to 80 nm. For a 25 min sample, the pore sizes were observed to be around 80 to 100 nm. For a 35 min sample, the pore sizes were observed to be around 100 to 110 nm. The size of the material between pores was found to be around 30–40 nm.

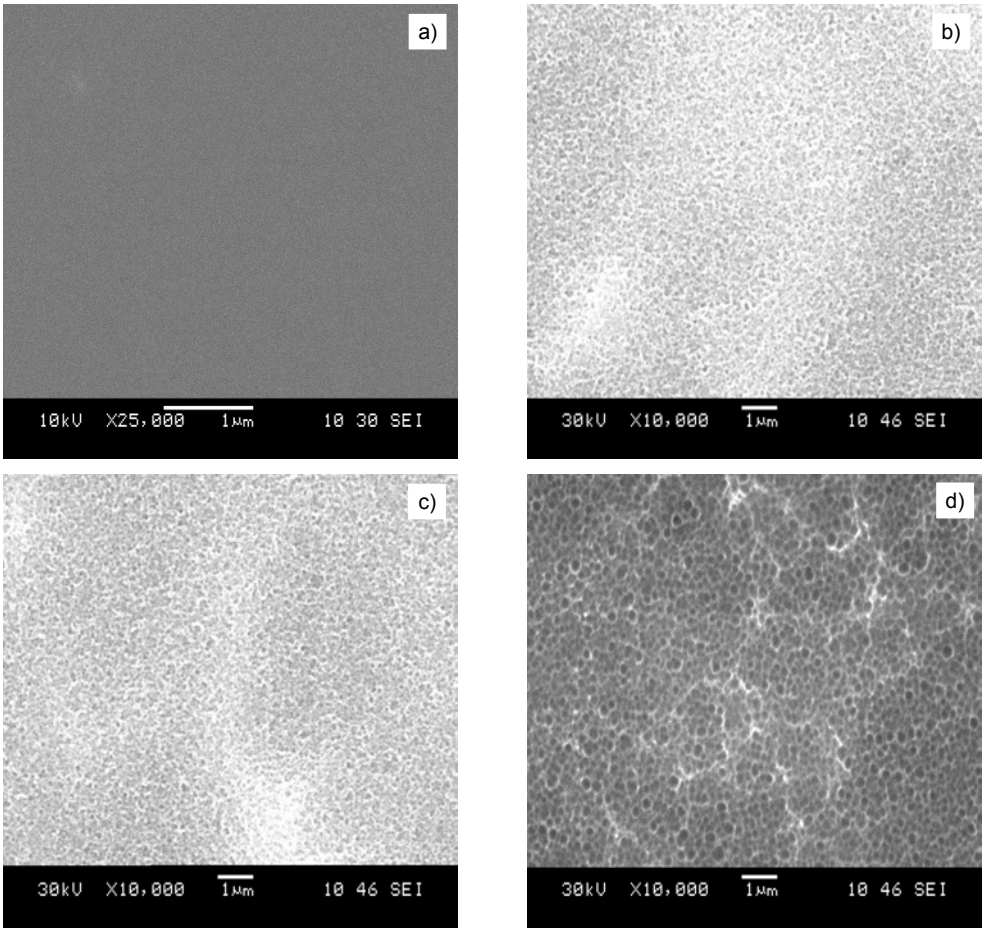

Fig. 1. SEM images of the samples: a) as-grown, b) etched for 10 min, c) etched for 25 min, d) etched for 35 min

Figure 2 illustrates the room temperature photoluminescence (PL) spectra of nanoporous GaN samples etched under different durations. The peak position, FWHM, peak shift

and the intensity of near band edge PL are given in Table 1. The spectra of the nanoporous GaN samples were observed to be blue-shifted relative to the spectra of

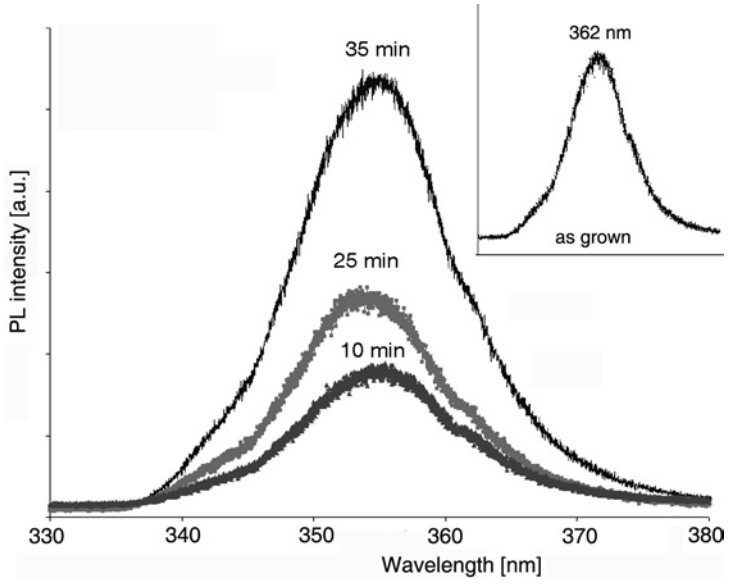

Fig. 2. The near band edge PL spectra of samples etched under various durations

the as-grown sample. Appearance of the blue-shifted PL emission is correlated with the development of highly anisotropic structures in the morphology. On the other hand, Yam et al. [13] claimed that porous GaN samples were observed to be PL red-shifted relative to the as-grown sample. Their finding was generally different from our result. Similar blue-shifted PL was also observed and reported by Adelmann et al. [14].

Table 1. The peak positions, FWHM, peak shift and the relative intensity of near band edge PL of different samples

Sample	Peak position [nm]	FWHM [nm]	Peak shift [nm]	Relative intensity
As-grown	362.01	6.8	-	1.00
10 min	357.63	8.5	1.4	1.20
25 min	356.50	8.8	2.0	1.64
35 min	358.13	9.9	3.1	1.80

Among the samples, there is little difference in the peak shift, and this indicates that the change of pore size has little influence on the degree of PL blue-shift. On the other hand, the PL intensity of the nanoporous samples is found to be increased. The amplification of the porosity-induced PL intensity could be explained by the reduction of surface pit density and extraction of strong PL by light scattering from the sidewalls

of the GaN crystallites [15], however, it could be also ascribed to the optical microcavity effect, which is inherent to porous GaN areas characterized by strong light scattering. It has been known that optical mode density could be altered by interference due to the optical environment [16], and this concept has long been applied in the fabrication of resonant cavity light emitting diodes in which the optical properties have been greatly enhanced [17].

The increase of the width of PL line of the porous samples, which is reflected in their FWHM, could be attributed to a relatively wide statistical size distribution of the pores. This shows that the luminescence spectrum of the nanoporous GaN is broader for the sample prepared under longer chemical etching time. The broad luminescence band of the porous GaN with the feature of the homogeneous line shape is explained by the recombination of localized excitons with strong phonon coupling.

4. Conclusion

We have used PL to characterize porous GaN samples fabricated by UV assisted electrochemical etching. PL measurements revealed that the near band edge peaks of all porous samples were blue-shifted, which was ascribed to the relaxation of the tensile stress in the porous samples. On the other hand, the PL intensities of the nanoporous samples are found to be increased. The amplification of the porosity-induced PL intensity could be explained by the reduction of surface pit density and reduction of strong PL by light scattering from the sidewalls of the GaN crystallites. The studies showed that porosity could influence the optical properties of the GaN.

Acknowledgement

The support from FRGS grant and Universiti Sains Malaysia is gratefully acknowledged. The authors would like to thank Mrs Ee Bee Choo for the SEM measurements.

References

[1] CANHAM L. T., Appl. Phys. Lett., 57 (1990), 1046.
[2] CULLIS A. G., CANHAM L. T., CALCOTT P. D. J., J. Appl. Phys., 82 (1997), 906.
[3] BRUS L., J. Phys. Chem., 98 (1994), 3572.
[4] SOHN H., LETANT S., SAILOR M. J., TROGLER W. C., J. Am. Chem. Soc., 122 (2000), 5393.
[5] LIN V.S.Y., MOTESHAREI K., DANCIL K.P.S., SAILOR M.J., GHADIRI M. R., Science, 278 (1997), 840.
[6] FAUCHET P.M., TSYBESKOV L., PENG C., DUTTAGUPTA S.P., BEHREN J.VON, KOSTOULAS Y., VANDYSHEV J.M.V., HIRSCHMAN K. D., IEEE J. Sel. Top. Quantum Electron., 1 (1995), 1126.
[7] SOLDATENKOV F.Y., ULIN V.P., YAKOVENKO A.A., FEDOROVA O.M., KONNIKOV S.G., KOROLKOV V. I., Tech. Phys. Lett., 25 (1999), 852.
[8] LI X., KIM Y-W, BOHN P.W., ADESIDA I., Appl. Phys. Lett., 80 (2002), 980.
[9] INOKI C.K., KUAN T.S., LEE C.D., SAGAR A., FEENSTRA R.M., Mater. Res. Soc. Symp. Proc, K1.3.1 (2002), 722.

[10] INOKI C.K., KUAN T.S., LEE C.D., SAGAR A., FEENSTRA R.M., KOLESKE D.D., DIAZ D.J., BOHN P.W., ADESIDA I., J. Electron. Mater., 32 (2003), 855.
[11] INOKI C.K., KUAN T.S., SAGAR A., LEE C.D., FEENSTRA R.M., KOLESKE D.D., DIAZ D.J., BOHN ADESIDA P.W., I., Phys. Stat. Sol. a, 11 (2003), 200.
[12] DIAZ D.J., WILLIAMSON T.J., ADESIDA I., BOHN P.W., J. Vac. Sci., Technol., B 20 (2002), 2375
[13] YAM F.K., HASSAN Z., NG S.S., Thin Solid Films 515 (2007), 3469.
[14] ADELMANN C., MARTINEZ-GUERRERO E., CHABUEL F., SIMON J., BATAILLOU B., MULA G., DANG L., PELEKANOS S., DAUDIN N.T., B., FEUILLET G., MARIETTE H., Mater. Sci. Eng., B 82 (2001), 212.
[15] VAJPEYI A.P., TRIPATHY S., CHUA S.J., FITZGERALD E.A., Physica E, 28 (2005), 141.
[16] BENISTY H., DE NEVE H., WEISBUCH C., IEEE J. Sel. Top. Quantum Electron., 34 (1998), 1612.
[17] SCHUBERT E. F., *Light-Emitting Diodes*, Cambridge University Press, Cambridge, 2003.

Received 19 September 2007
Revised 3 February 2008

Materials Science-Poland, *Vol. 26*, *No. 3*, *2008*

Dry sliding wear characteristics of 0.13 wt. % carbon steel

V.K. GUPTA[1*], S. RAY[2], O.P. PANDEY[3]

[1]Mechanical Engineering, University College of Engineering, Punjabi University, Patiala (Pb.) 147 002, India

[2]Department of Metallurgical and Materials Engineering, Indian Institute of Technology, Roorkee (U.A.) 247 667, India

[3]School of Physics and Material Science, Thapar University, Patiala (Pb.) 147 004, India

Wear characteristics of 0.13 wt. % plain carbon steel, heat treated under various conditions, were monitored on a standard pin-on-disk wear testing machine under the normal loads of 2.5, 4.5 and 5.5 kg and at a constant sliding velocity of 1 m/s. Weight loss of the specimen was measured at various time intervals to obtain wear rate. The variation in volume loss with sliding distance indicated the presence of run-in wear followed by steady state wear. The wear mechanism was found to be primarily oxidative in nature, which was confirmed by the analysis of worn surfaces and wear debris generated during sliding. Wear resistance was found to be dependent on the microstructure and morphology of the phases. The wear coefficients calculated for various heat-treated specimens revealed that the ferrite-coarse pearlite, ferrite-fine pearlite, ferrite-tempered martensite and ferrite martensite structures show the wear resistance in decreasing order.

Key words: steel; sliding wear; wear coefficient

1. Introduction

Plain carbon steels consisting of about four-fifths of the total tonnage of steel production, are economical compared to alloy steels. These are extensively used as structural components for many engineering applications. Among many failure modes associated with steel components, wear presents a unique challenge to the designer and the developer of mechanical components. Wear characteristics of steel components and their real life performance under various working environments have been the

[*]Corresponding author, e-mail: guptavk_70@yahoo.co.in

subject of numerous investigations [1–19]. Because so many variables are involved, such as load, sliding speed, test geometry, composition, hardness, environment etc., controversies over the understanding of wear mechanism still exist, as these parameters are interdependent variables. In addition to these variables, the type of microstructure also influences the wear resistance of steel. Although several investigations have demonstrated an improvement in wear resistance of steel through surface hardening treatments and surface alloying [20], very few studies have been done to correlate the wear properties of steel with its microstructure [2, 5–8, 10–17]. Wayne and Rice [2] have revealed the dependence of wear on microstructure and have concluded that the dual phase (DP) steel, consisting of hard martensite islands embedded in a relatively soft and ductile ferrite matrix, offers higher wear resistance than that observed in steel with spheroidal carbides. The wear resistance of DP steel was found to depend on the volume fraction of martensite. Similar observations have also been reported by Tyagi et al. [12]. Sawa and Rigney [5] have shown that the wear behaviour of DP steel also depends strongly on morphology (i.e., shape, size and distribution) of its martensite phase. Tyagi et al. [11] have found that ferrite–martensite structure exhibits higher wear resistance compared to ferrite–fine pearlite structure. In our earlier study [10] on wear behaviour of near eutectoid steel containing 0.86 wt. % carbon, it was observed that coarse pearlite structure possesses better wear resistance compared to fine pearlite and tempered martensite structure.

In the present investigation, an attempt is made to study the influence of microstructure in hypoeutectoid steel containing 0.13 wt. % of carbon on its wear characteristics under dry sliding condition at different loads and at a fixed sliding speed at room temperature, using a standard pin-on-disk wear testing machine. The idea of selecting this composition was to observe the variation in wear characteristics with variation in carbon contents and to compare the results with those of our earlier study for nearly eutectoid steel [10].

2. Experimental

Commercial grade steel containing C (0.13 wt. %), Mn (0.62 wt. %), Si (0.08 wt. %), P (0.048 wt. %) and S (0.035 wt. %) was used in the present investigation. The steel samples were subject to various heat treatment processes to attain variety of microstructures. The wear characteristics of heat-treated samples were investigated. The details of experimental procedures are described below.

Heat treatment of samples. In order to compare the results of our earlier study [10] samples of similar size, 30 mm long and 6.25 mm in diameter were cut from a steel bar. Four sets comprising three pins in each set were taken for carrying out heat treatment. All sets of samples were heated in a tubular furnace to 840 °C in the ($\alpha + \gamma$) region for a period of 40 min. These samples were covered with cast iron chips to avoid oxidation. After heating, three sets of samples were taken out of the furnace.

The first set was allowed to cool in air to develop ferrite-fine pearlite structure and the remaining two sets were directly quenched in water to develop dual phase microstructure containing martensite in a matrix of ferrite. Out of these two sets of water quenched samples, one set was further subject to high temperature tempering treatment at 640 °C for two hours followed by water quenching resulting in ferrite-tempered martensite structure. The fourth set was allowed to cool inside the furnace up to room temperature to attain ferrite-coarse pearlite structure. In the present study, the deviation from conventional normalising and annealing treatment by cooling from the intercritical annealing temperature range (i.e., $\alpha + \gamma$ region) was done to keep similar ferrite areas in the steel subject to various heat treatments. The bulk hardness of the heat-treated samples was measured at a load of 20 kg on calibrated Vickers hardness-testing machine using a diamond pyramid indenter, and is reported in Table 1.

Table 1. Hardness of 0.13 wt. % carbon steel heat treated under various conditions

Sample	VHN
Annealed	99
Normalized	108
Intercritically annealed and quenched	161
Intercritically annealed, quenched and tempered	134

Metallographic studies. The heat-treated samples were prepared for metallographic studies by grinding them on belt grinder driven by an electric motor. These samples were further polished up to 4/0 grade (~38 μm) of emery paper followed by cloth polishing using submicron size alumina paste. After polishing, the samples were etched with 2% nital and analysed under optical and scanning electron microscope. Volume fractions of phases present in samples were estimated by the point counting method [21]. Microhardness of phases present in the heat-treated samples was measured using 0.005 kg load on the Vickers scale, and is reported in Table 2.

Table 2. Microhardness (measured at 0.005 kg load) and volume fraction of phases in heat-treated samples

Sample	Phase present	Microhardness [VHN]	Volume fraction of the phase
Annealed	ferrite	174	0.84
	pearlite (coarse)	280	0.16
Normalized	ferrite	184	0.79
	pearlite (fine)	420	0.21
Intercritically annealed and quenched	ferrite	280	0.69
	martensite	552	0.31
Intercritically annealed, quenched and tempered	ferrite	195	0.80
	tempered martensite	276	0.20

Wear test. Wear tests were conducted using polished pin samples with flat surfaces in the contact region but rounded in the corner and cleaned with acetone to remove dust or grease from the surfaces. Dry sliding wear tests were carried out against the counterface of a hardened and polished disk made of EN-32 steel having HRC from 62 to 65 at a relative humidity of 50–70% at room temperature of 35 °C.

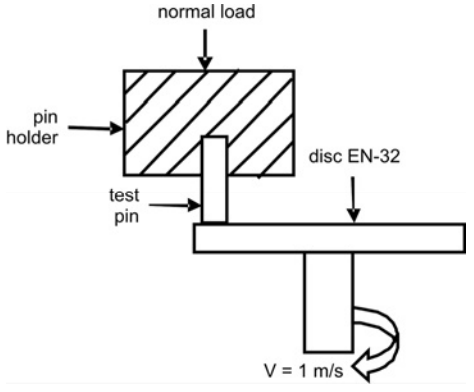

Fig. 1. Test geometry of Pin-on-disc wear testing machine

A sturdy pin-on-disk machine supplied by DUCOM, Bangalore (India), as shown schematically in Fig. 1, was used to carry out the wear tests. Pin weight losses were measured at various time intervals, using an electronic balance having an accuracy of 10^{-7} kg. Weight losses were converted to volume losses by dividing the weight by the density of steel. Initially, the weight loss of the pin was measured after every 2 min of sliding, for up to 16 min, and thereafter, at the intervals of 15 min for a total sliding period of 3 h. The tests were conducted at the loads of 2.5, 4.5 and 5.5 kg, and at a constant sliding velocity of 1 m/s. Each test at a given load and sliding velocity was repeated three times, with identical new samples on a fresh disk surface, and the average data for volume loss after each time interval were used for the analysis of wear rate. The wear debris obtained after the initial 16 min of sliding as well as after each test run were examined under SEM. The worn surfaces of the samples were also examined under SEM to know the wear mode of the worn surfaces.

3. Results and discussion

3.1. Microstructural characteristics of pin specimens

The microstructures of the heat-treated samples were examined under optical and scanning electron microscope. Figures 2a1 and 2a2 show the microstructure of the

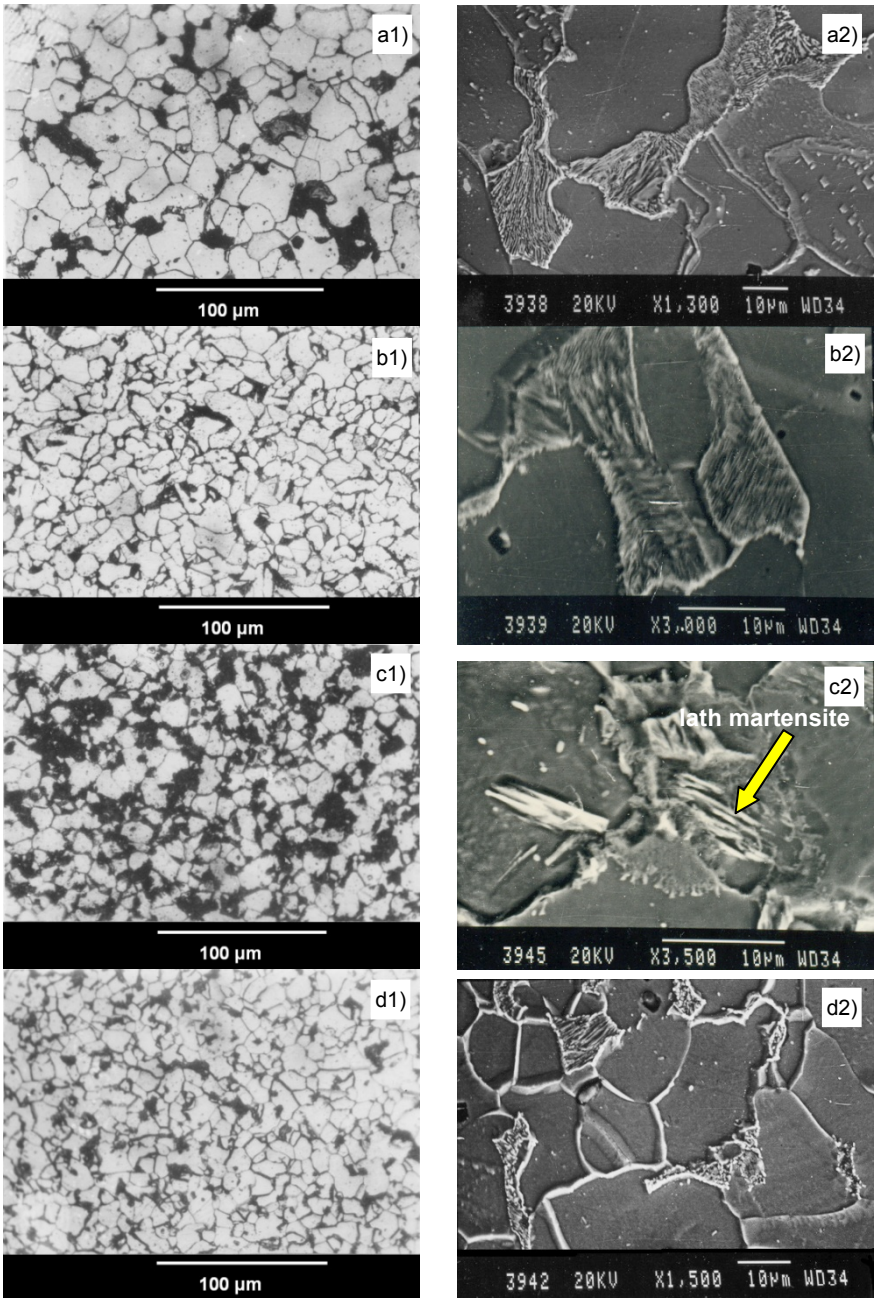

Fig. 2. Micrographs (1 – optical, 2 – SEM) of steel samples: a) annealed (AD), b) normalized (ND) c) intercritically annealed and quenched (IQ), d) intercritically annealed, quenched and tempered (IT)

annealed sample, revealing the presence of ferrite (bright areas) and of pearlite (dark areas). However, the structure of pearlite could be clearly seen in Fig. 2a2 at higher

magnification. The ferrite grain size is observed to vary from 10 to 20 μm. The volume fractions of ferrite and pearlite as observed from point counting method are 0.84 and 0.16, respectively. Figures 2b1 and 2b2 show the normalized ferrite-fine pearlite microstructures examined under optical microscope and SEM at various magnifications. The sample has bright areas of ferrite and dark areas of pearlite as observed at low magnification, but the pearlite could be resolved at a higher magnification in most of the areas. The volume fraction of pearlite is 0.21, as compared to 0.16 in the annealed sample. The ferrite grain size is observed in the 6–12 μm range, and is finer than that observed in the annealed sample. The ferrite–martensite microstructures of the sample intercritically annealed at 840 °C and quenched in water is shown in Figs. 2c1 and 2c2. Bright areas of ferrite and dark areas of martensite are evident in Fig. 2c1 but at higher magnification a coarser lath type of martensite could be observed inside the dark areas, Fig. 2c2. The microhardnesses of the dark and bright areas are found to be 552 VHN and 280 VHN, respectively (Table 2) which correspond to the hardness of martensite and ferrite in DP steel of similar composition [2]. The volume fractions of ferrite and martensite phases are 0.69 and 0.31, respectively. However, in some of the reports on steel containing higher carbon percentage, the hardness of martensite phase reported is on the higher side [11, 12]. This indicates that a complete transition of pearlite-austenite into martensite has not occurred, which is also evident in microstructures. Figures 2d1 and 2d2 show ferrite-tempered martensite microstructures of intercritically annealed and quenched samples followed by tempering at 640 °C for 2 h. It could be noticed that the volume fraction of dark etching martensite area has reduced to about 0.20 compared to that observed in the quenched sample, as is shown in Fig. 2c1. The microstructure observed under SEM, as shown in Fig. 2d2, clearly reveals tempered carbides in certain areas, but still there are some areas where one could observe lath martensite.

3.2. Wear characteristics

The dependences of cumulative wear volume on the sliding distance under various normal loads and at a fixed sliding velocity of 1 m/s are shown in Figs. 3a–d for annealed (AD), normalized (ND), intercritically annealed and quenched (IQ), and intercritically annealed, quenched and tempered (IT) steels, respectively.

The cumulative wear volume loss with the sliding distance under different normal loads of 2.5, 4.5 and 5.5 kg has demonstrated a sub-linear variation, with coefficients of correlation exceeding 0.975 at all normal loads for all the steel samples. However, the data can be analyzed on a linear scale using two separate stages of wear behaviour characterized by two different linear segments. The change in slope has been observed after first 4 to 7 experimental points (first stage run-in) with last point common between both the linear segments. Both the lines have been determined by the linear least squares fit. The slope of the line gives the wear rate. The procedure followed helps to establish the run-in period rate (first stage) separately from the long-term steady-state rate (second stage).

For AD steel, the first linear segment (run-in) is found to be steeper compared to the second linear segment (steady state). A similar variation has been observed for ND, IQ and IT steels, as shown in Figs. 3b–d, respectively. The two stage linear wear trend has also been reported by other investigators [2, 10–12, 22–26] in different steels.

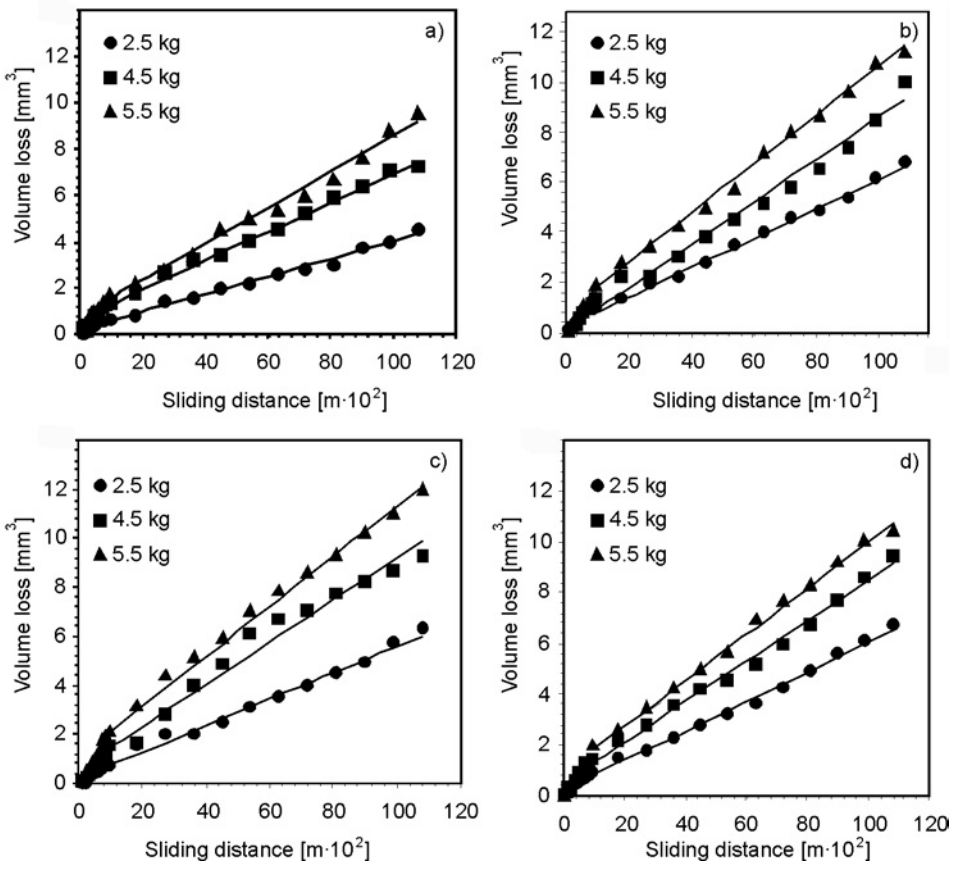

Fig. 3. Dependence of volume loss on the sliding distance for: a) AD, b) ND, c) IQ, d) IT steel specimen at various loads and a constant sliding velocity of 1 m/s

The wear rates of the samples at various loads have been determined from the slopes of the linear segments of Figs. 3a–d. Wear rates for both the linear segments are observed to increase almost linearly with load for all the heat-treated steel specimens, as shown in Figs. 4a, b. The observed linear variation of wear rate with load is indicative of Archard's wear law [10]. At a given load, the second linear segment shows a relatively lower wear rate compared to the first linear segment, for all the steel samples, as is evident from comparing Fig. 4a with 4b. Except for the load of 2.5 kg, the wear rate increases in the following order: AD, IT, ND and IQ for both the linear segments as shown in Figs. 4a, b. At a normal load of 2.5 kg, the wear rate corresponding

to first linear segment is relatively higher for ND steel compared to other steel specimens, which have almost equal values of wear rate, as shown in Fig. 4a. The wear rate corresponding to the second linear segment at a normal load of 2.5 kg is significantly lower in AD steel compared to those observed in other steel specimens (Fig. 4b). The steady state wear rate at a relatively lower load of 2.5 kg is almost similar in ND and IT steels but slightly higher than in IQ steel (Fig. 4b). Therefore, in terms of wear rates of both the segments ferrite–coarse pearlite structure is superior to ferrite–fine pearlite at all the loads. The ferrite-tempered martensite structure results in lower wear rates compared to the ferrite–martensite structure at higher loads of 4.5 and 5.5 kg. But, at a lower load of 2.5 kg, the ferrite-martensite structure has slightly lower wear rate in the second segment compared to the ferrite–tempered martensite structure, whereas in the first segments both the specimens have almost equal wear rates. At higher loads of 4.5 and 5.5 kg, the ferrite–tempered martensite appears to have an even better structure than ferrite–fine pearlite, in terms of wear rates of both the segments.

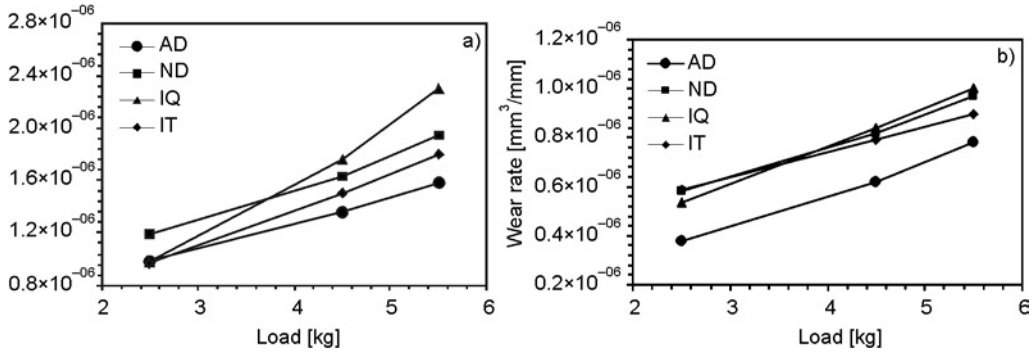

Fig. 4. Dependence of wear rate on load for heat-treated samples corresponding to: a) first linear segment, b) second linear segment

The wear coefficients have been obtained at different loads for AD, ND, IQ, and IT steels and are reported in Table 3. The wear coefficients are calculated using Archard's wear law

$$V = \frac{kWS}{3H}$$

where V is the volume loss in wear, W – the applied load, S – the sliding distance, H – the bulk hardness and k – the wear coefficient of the material [10]. The wear coefficients are estimated by dividing the wear rate (V/S) by the contact area (W/H), estimated from the applied load and indentation hardness, and multiplying the result by the geometrical factor of three. The first linear segment is observed to have a higher wear coefficient as compared to the second linear segment, for all the steel samples at different loads. Similar observations have also been made by some of the earlier investigators [10–12] on different steels.

Table 3. Wear coefficients corresponding to 1st (run-in) and 2nd (steady-state) segments

Sample	Linear segment	Wear coefficient ($k\times10^{-4}$) at loads of			Average ($k\times10^{-4}$)
		2.5 kg	4.5 kg	5.5 kg	
Annealed (AD)	1st	1.176	0.898	0.853	0.976
	2nd	0.451	0.409	0.421	0.427
Normalized (ND)	1st	1.545	1.174	1.149	1.289
	2nd	0.752	0.590	0.571	0.638
Intercritically annealed and quenched (IQ)	1st	1.891	1.890	2.020	1.934
	2nd	1.035	0.900	0.878	0.938
Intercritically annealed, quenched and tempered (IT)	1st	1.560	1.344	1.316	1.407
	2nd	0.942	0.705	0.654	0.767

3.3. Nature of wear surface and debris

Figures 5 and 6 show the SEM micrographs of the worn surfaces of the AD and IT steels, respectively, at different loads. The samples tested at low load of 2.5 kg are observed to be smooth, except for a few deep grooves as shown in Figs. 5(a) and 6(a), whereas at higher load of 5.5 kg worn surfaces are observed to have cracking, spalling, and thicker oxide cover, as shown in Figs. 5b and 6b. Therefore, it appears that

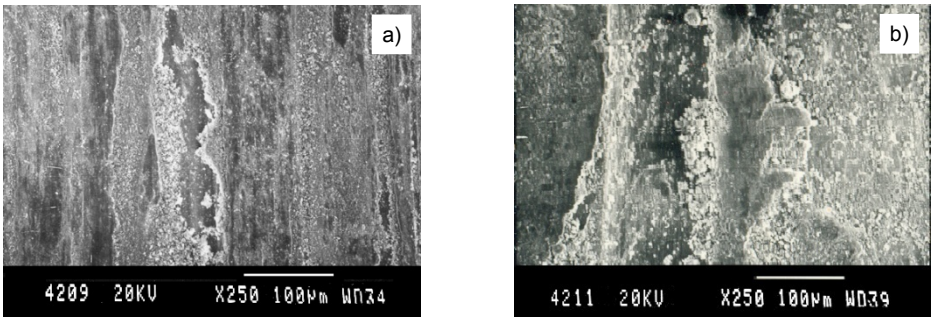

Fig. 5. SEM of worn surface of AD steel specimen tested at: a) 2.5 kg, b) 5.5 kg load

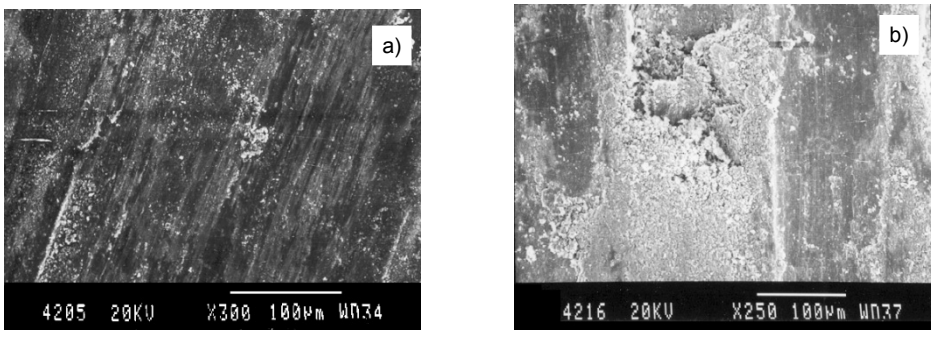

Fig. 6. SEM of worn surface of IT steel specimen tested at: a) 2.5 kg, b) 5.5 kg load

more oxide is generated at higher loads due to higher frictional heating, which leads to an increase in the temperature of the sliding surface. Glasscott et al. [23] in their study have also observed that oxide debris are generated during the process of wear which buildup progressively in the wear track as the contact pressure increases. During sliding, more and more oxide is produced, the metal–metal contact is reduced, thus lowering the wear rate, and leading to transition from severe to mild wear [9]. SEM micrographs of the worn surfaces also reveal the presence of scoring marks and areas of rough grooves in the direction of sliding. There are also a few craters seen in some areas where metallic particles have come into debris due to micro-welding or delamination, as shown in Fig. 5b. The adhesion effect is also visible at some places in Figs. 5b and 6b. In some samples, a flake-type morphological feature of the debris sticking to the surfaces is observed. These types of features have also been reported by other investigators [11, 27, 28]. The key features of all the tracks observed is that debris were observed to adhere at the worn surfaces in each specimen.

The wear debris collected for short sliding distances corresponding to the first linear segment have been compared under SEM with those obtained at long sliding distances corresponding to the second linear segment. A detailed analysis of all the debris collected for each sample corresponding to first and second linear segments have been performed. The common feature of the analysis performed for all the steel samples at each load corresponding to first linear segment indicates that oxidative wear is the dominating factor, as is evident from Fig. 7. The morphological features of the debris indicate that it is oxide in nature which is being formed in different stages, depending upon the availability of oxygen content. The reason for formation of oxide is that the surface gets exposed to atmosphere slowly as the load applied is relatively low.

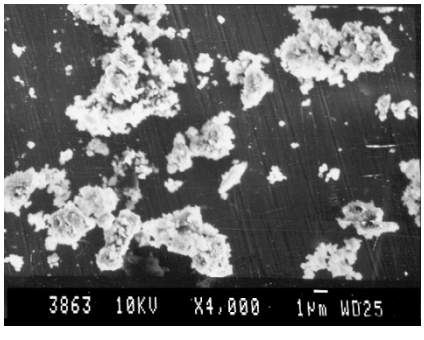

Fig. 7. SEM of wear debris corresponding to first linear segment for IQ steel specimen tested at 4.5 kg

As the load increases (corresponding to second linear segment), the volume fraction of the debris also increases. A detailed analysis of these wear debris have been done. Since the nature of debris corresponds to metallic and oxidative wear, thus only few micrographs have been presented for discussion (Figs. 8a–c). The samples tested at higher load in annealed conditions exhibit the features corresponding to metallic as well as oxidative wear (Fig. 8a). The flake type of morphology corresponds to metallic wear, whereas the round, rugged and coagulated features correspond to oxides. The

morphological features of the debris indicate that metal is removed from surface which gets oxidized during ploughing in the course of sliding. The ploughing marks are clearly visible on the surfaces of metallic debris (Fig. 8a).

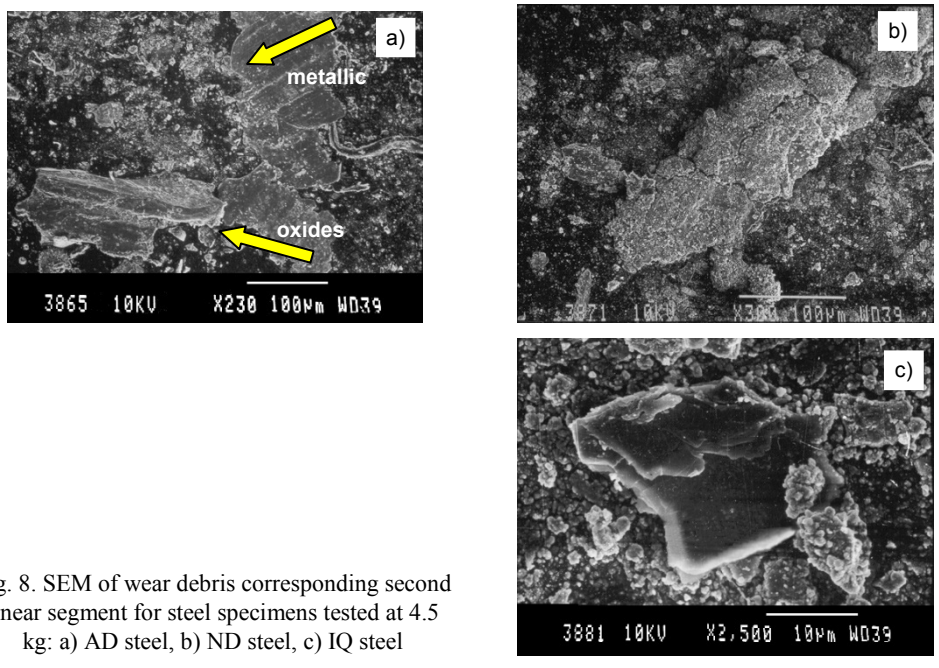

Fig. 8. SEM of wear debris corresponding second linear segment for steel specimens tested at 4.5 kg: a) AD steel, b) ND steel, c) IQ steel

Since annealed sample is very soft in nature, the metallic debris did not get oxidized so easily because of higher thermal conductivity of the phases present in it. The debris corresponding to normalized condition also indicates similar features (Fig. 8b). The loss of material due to the wear indicates that metallic debris get oxidized during sliding, as is evident from the micrograph shown in Fig. 8b. Fine cracks observed on the metallic surface of the debris further support our view that metal firstly comes out in the form of flakes, then it gets converted to oxides as the sliding distance increases. An important feature observed for debris obtained from IQ samples is that metallic wear dominates as compared to oxidative wear, as revealed from Fig. 8c. A typical morphological feature observed is that during the sliding, the debris get fragmented easily, leading to its transition to oxides at higher loads and higher sliding distances. The round spherical features of debris observed in Fig. 8c, which are partially oxidized, further supports this hypothesis. Since the loss of material in these steel samples is greater in comparison with other steel samples, it is obvious that some phases get easily detached from the matrix, as there is a vast difference between the coefficient of thermal expansion of ferrite and that of the martensite phase, which provides a conducive atmosphere for its easy detachment. At higher loads and higher sliding distances, the temperature of the worn samples increases, which leads to a higher wear rate, be-

cause of reasons stated above. The EDX analysis done for all these debris indicates the presence of iron as a major constituent, which is shown in Figs. 9a–d.

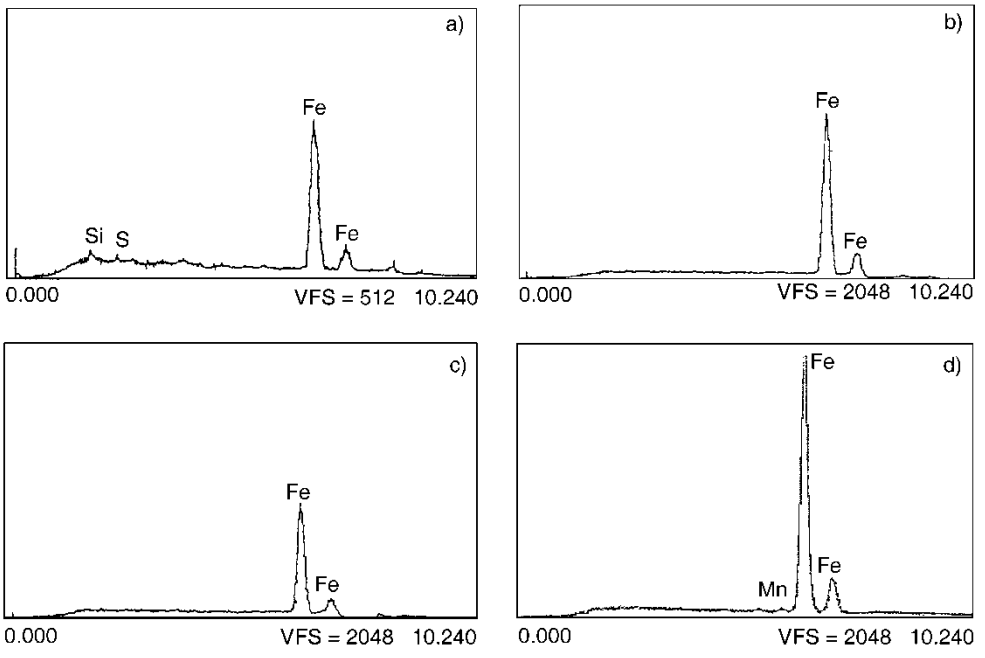

Fig. 9. EDX spectrum of wear debris for: a) AD steel tested at 3.5 kg load, b) ND steel tested at 3.5 kg load, c) IT steel tested at 3.5 kg load, and d) IT steel tested at 5.5 kg load.

Since the morphological features of first linear segment were oxidative in nature and those of second linear segments were primarily metallic in nature, it requires a further confirmation through X-ray diffraction (XRD) analysis. For this purpose, the debris obtained for different steel samples corresponding to first linear segment and second linear segment were separately mixed in a proper way and subject to XRD as presented in Figs. 10a, b for the first and second linear segments, respectively. The analysis indicates that all possible iron oxides (i.e., Fe_2O_3, FeO and Fe_3O_4) are present in debris corresponding to both the segments. Peaks of Fe were also observed in X-ray diffraction pattern.

The consistently higher rate of wear in the first linear segment as compared to that observed in the second linear segment, as shown in Figs. 4a, b, may be explained based on the initial surface roughness of the wearing steel samples. The surfaces of all the engineering components always possess some amount of roughness and have asperities. When a pair of these kinds of fresh surfaces is brought into contact and starts sliding relative to each other, mechanical, chemical, thermal and micro-structural changes begin to occur in and around the contact interface [29]. Due to contact at the asperities, the surfaces evolve to attain better conformity to each other at the end of the run-in stage. The wear in this stage occurs by the removal of high asperities, initial

oxide layers and surface contaminants. Consequently, the material loss and the wear rate are higher in the run-in stage of the wear. In the run-in stage, the oxidation of the surface begins and progresses with frictional heating generated during sliding. The transfer layer of oxide may thus begin to form in the run-in stage and evolves to the steady state, providing an extent of cover determined by the conditions of load, sliding velocity and environmental conditions. The transfer layer protects the underlying metal, and thus the wear rate decreases. The second stage of wear indicates a steady state with respect to (i) the evolution of mating surfaces to better conformity, (ii) the spread of oxide and compacted transfer layer, and (iii) the real area of contact [12]. Sawa and Rigney [5] have also noticed a lower wear rate for DP steels in the steady state as compared to that in the run-in stage.

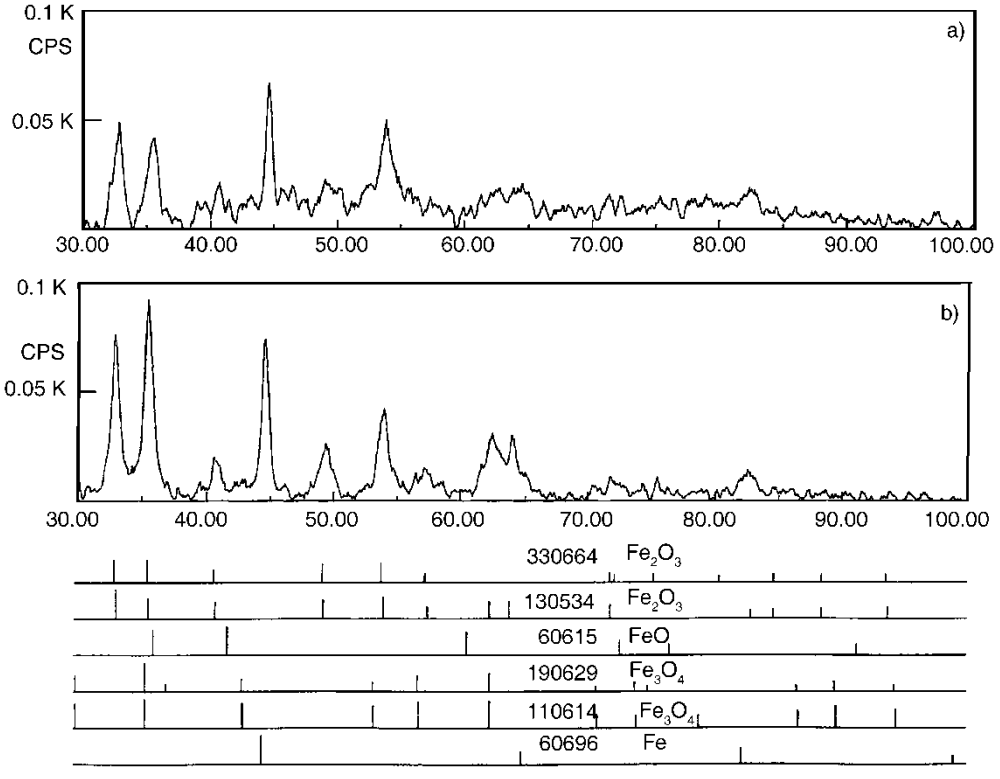

Fig. 10. X-ray diffraction of wear debris of steel samples corresponding to:
a) first linear segment, b) second linear segment

Based on the wear coefficient of both segments, the ferrite–coarse pearlite microstructure has the lowest wear coefficient and it increases in the following order: ferrite–fine pearlite, ferrite–tempered martensite and ferrite–martensite. From these results it appears that relatively coarser cementite plates in coarse pearlite are able to hold out better against sliding wear than the fine cementite plates in fine pearlite. The

masking of fine cementite plates by flow of ferrite could be a contributing factor to increased wear. Fine carbide particles in ferrite-tempere martensite structure are not able to hold out as well as fine cementite plates in fine pearlite. Ferrite-martensite structure appears to be the worst out of all the structures investigated. In spite of its greater hardness, its higher overall adhesion energy may have resulted in its higher wear, as it does not have any carbide in the structure.

The presence of a coarser cementite and cementite plates, as observed in AD and ND steels, rather than particles in IT steel, appears to contribute more wear resistance. The superiority of pearlitic structure over tempered martensitic structure, as observed in this investigation, is well supported by the earlier studies [6–8, 10, 30]. Though, some of the reports mention that higher volume fraction of martensite provides better wear resistance, they do not consider other structural features existing in the system [12, 14]. However, our study further strengthens our previous work carried out on steel with high carbon content [10]. Both the studies, namely the earlier work [10] as well as the present work, are on similar lines and exhibit better understanding with detailed analysis of structural features observed.

4. Conclusions

The present study carried out to determine the influence of microstructure and the morphology of phases in heat treated 0.13 wt. % carbon steel on the dry sliding behaviour against the counter-face of hardened steel has led to the following conclusions:

The volume loss in wear increases with sliding distance and could be described in terms of two linear segments. The wear rate in the first linear segment is higher than that in the second linear segment, which has been attributed to the run-in period in the first segment and progressive development of oxide cover in the second linear segment. The wear rate in both the linear segments increases with load, which is indicative of Archard's wear law.

The mechanism of wear is primarily oxidative, as revealed the analysis of worn surfaces and wear debris. In terms of wear rates of the both segments, ferrite–coarse pearlite structure is superior to ferrite–fine pearlite structure at all the loads. The ferrite–tempered martensite structure results in lower wear rates in both segments compared to ferrite–martensite structure, except at a lower load of 2.5 kg.

Based on the wear coefficients in the first and the second linear segments, the ferrite–coarse pearlite, ferrite–fine pearlite, ferrite–tempered martensite and ferrite–martensite structures in 0.13 wt. % carbon steel show the wear resistance in decreasing order.

References

[1] WELSH N.C., Phil. Trans. Royal Soc. London, A257-31 (1965), 51.
[2] WAYNE S.F., RICE S.L., Wear, 85 (1983), 93.
[3] LIM S.C., ASBY M.F., Acta. Metall., 35 (1987), 1.

[4] LIM S.C., ASBY M.F., BRUNTON J.H., Acta Metall., 35 (1987), 1343.
[5] SAWA M., RIGNEY D.A., Wear, 119 (1987), 369.
[6] PRASAD B.K., PRASAD S.V., Wear, 151 (1991), 1.
[7] WANG Y., PAN L., LEI T.C., Wear, 143 (1991), 57.
[8] GARNHAM J.E., BEYNON J.H., Wear, 157 (1992), 81.
[9] VENKATESHAN S., RIGNEY D, A., Wear, 153 (1992), 163.
[10] GUPTA V.K., PANDEY O.P., Indian J. Eng. Mater. Sci., 7 (2000), 354.
[11] TYAGI R., NATH S.K., RAY S., Metall. Mater. Trans., A32 (2001), 359.
[12] TYAGI R., NATH S.K., RAY S., Metall. Mater. Trans., A33 (2002), 3479.
[13] TYAGI R., NATH S.K., RAY S., Wear, 255 (2003), 327.
[14] TYAGI R., NATH S.K., RAY S., Mater. Sci. Tech., 20 (2004), 645.
[15] MOHAN S., PRAKASH V., PATHAK J.P., Wear, 252 (2002), 16.
[16] DENG S., SUN L., LI Z., Lubr. Eng., 4 (2005), 84.
[17] KAUL R., GANESH P., TIWARI P., NANDEKAR R.V., NATH A.K., J. Mater. Proc. Tech., 167 (2005), 83.
[18] AMAMOTO Y., GOTO H., Tribology Int., 39 (2006), 756.
[19] CESCHINIA L., PALOMBARINIA G., SAMBOGNAA G., FIRRAOB D., SCAVINOB G., UBERTALLIB G., Tribo. Int., 39 (2006), 748.
[20] BAYER R.G., *Mechanical Wear Prediction and Prevention*, Marcel Dekker, New York, 1994.
[21] DEHOFF R.T., RHINES F.N., *Materials Science and Engineering Series*, McGraw-Hill, New York, 1968
[22] CLAYTON P., Wear, 60 (1980), 75.
[23] GLASCOTT J., STOOT F.H., WOOD G.C., Wear, 97 (1984), 155.
[24] SMITH A.F., Wear, 110 (1986), 151.
[25] SMITH A.F., Wear, 123 (1988), 313.
[26] IWABUCHI A., HORI K., KUBOSAWA H., Wear, 128 (1988), 123.
[27] CLARKE J., SARKAR A.D., Wear, 69 (1981), 71.
[28] GLASSER W.A., Wear, 73 (1981), 371.
[29] BLAU P., Wear, 72 (1981), 55.
[30] KALOUSEK J., FEGRADO K.M., LAUFFR E.E., Wear, 105 (1985), 199.

Received 2 September 2007
Revised 7 December 2007

Materials Science-Poland, *Vol. 26*, *No. 3*, *2008*

Surface microstructure and specific surface area of pure and Na-substituted gyrolites

K. BALTAKYS[1*], R. SIAUCIUNAS[1], S. KITRYS[2]

[1]Department of Silicate Technology, Kaunas University of Technology, Radvilenu 19, LT – 50270 Kaunas, Lithuania

[2]Department of Physical Chemistry, Kaunas University of Technology, Radvilenu 19, LT – 50270 Kaunas, Lithuania

Pure gyrolite was synthesized within 32 h at 200 °C from a stoichiometric composition (the molar ratio CaO/SiO_2 was equal to 0.66 with water/solid ratio of the suspension equal to 10.0) of the initial CaO and $SiO_2 \cdot nH_2O$ mixture. Meanwhile, Na-substituted gyrolite was synthesized twice quicker – within 16 h at 200 °C. These compounds were characterized by XRD, STA, FT-IR, SEM/EDS and BET analysis. It was found that gyrolite is a mesoporous material. Its specific surface area S_{BET} = 143.15 m^2/g, the radius of dominant plate pores r_p = 80–90 Å, the calculated total pore volume ΣV_p = 0.661 cm^3/g. Gyrolite texture changes upon introducing Na^+ ions into its crystal structure: the specific surface area S_{BET} diminishes to 27.24 m^2/g, the radius of dominant cylindric pores r_p = 60–70 Å, the calculated total pore volume ΣV_p = 0.118 cm^3/g.

Key words: *gyrolite; Na-substituted gyrolite; pore size;* BET *equation*

1. Introduction

Calcium silicate hydrates are highly multiplex systems with over 30 stable phases. From a theoretical and practical points of view, the synthesis, properties and structure of the main calcium silicate hydrates (C–S–H(I), 1.13 nm tobermorite, xonotlite, α-C_2S hydrate and gyrolite have been analyzed in detail [1–16]. Majority of these compounds occur naturally or may be synthesized in the laboratory.

Recently, the interest in gyrolite has increased because of new possibilities of its application: it may be used to educe heavy metal ions and remove them from wastewaters [17]. Of specific interest is the purported ability of gyrolite to separate supercoiled plasmid, opencircular plasmid, and genomic DNA [18].

*Corresponding author, e-mail: kestutis.baltakys@ktu.lt

The structure, optical properties and chemistry of natural gyrolite were studied by Mackay and Taylor [19], Chalmers et al. [20], Gard et al. [21], Lachowski et al. [22], and others [23, 24]. However, their opinions differ. A full structural solution for gyrolite was proposed by Merlino [25]. Currently it is supposed that his proposed model of gyrolite crystal lattice precisely represents a real structure of this compound. Merlino showed that this phase structure is built up by the stacking of SiO_4 tetrahedral sheets (S_1, S_2, and $\overline{S}_2$, where S_2 and $\overline{S}_2$ are symmetry-related units) and CaO_6 octahedral sheets (O and $\overline{O}$, which are symmetry-related units). The $Si–O_4$ tetrahedra in the silicate sheets are linked by sharing three oxygen atoms to give a pseudo-hexagonal sheet structure with tetrahedral in six-membered rings. Each unit cell contains three distinct silicate sheets two of which (S_2 and $\overline{S}_2$) are symmetrically equivalent with the six-membered rings having four tetrahedra pointing one way and two the other; the third sheet (S_1) has alternate tetrahedral six-membered rings pointing in opposite directions. These sheets are linked by layers of Ca–(O, OH) polyhedra to build up a "complex layer" perpendicular to the *c* axis. The stacked complex layers ($\overline{S}_2$, $\overline{O}$, S_1OS_2) with composition $[Ca_7Si_{12}O_{30}(OH)_4]^{2-}$ are connected through interlayer sheets made by Ca^{2+} ions and water molecules (Fig. 1).

However, some properties (like sorption capacity) depend not only on the crystal lattice of the porous body but also on the surface microstructure and specific surface area, as well as dominant pore size and their differential distribution according to the radius in the compound. In the case of gyrolite crystal lattice, those properties usually depend on the proportion of crystalline (S_1, S_2, $\overline{S}_2$) and amorphous (X sheet) parts (Fig. 1). However, data presented in references about the texture of low-base compounds (C/S = 0.6–0.8) are not extensive and often controversial.

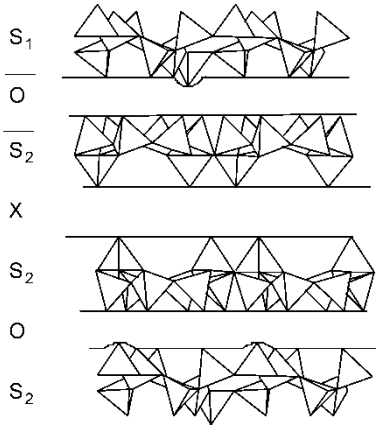

Fig. 1. Schematic drawing of the crystal structure of gyrolite as viewed along the *a* direction

The aim of this paper is to determine the gyrolite surface microstructure and specific surface area, as well as the dominant pore sizes and their differential distribution

according to the radius in this compound, crystal size and form, stability at low and high temperature and the influence of Na^+ ions on these properties.

2. Materials and methods

The following reagents were used as starting materials: fine-grained $SiO_2 \cdot nH_2O$ (Reachim, Russia, ignition losses 21.43%, specific surface area S_a = 1560 m²/kg by Blaine's); NaOH solutions (Reachim, Russia; c = 1.04 %); CaO (99.6 % Reachim, Russia) additionally was burned at 1000 ºC for 0.5 h.

The synthesis of gyrolite has been carried out in unstirred suspensions in vessels of stainless steel. Pure gyrolite was synthesized within 32 h at 200 °C from a stoichiometric composition (the molar ratio of CaO/SiO_2 was equal to 0.66 with water/solid ratio of the suspension equal to 10.0) of the initial CaO and $SiO_2 \cdot nH_2O$ mixture. Na-substituted gyrolite was synthesized within 16 h at 200 °C. The amount of NaOH, corresponding to 5% of Na_2O from the mass of dry materials, was added in the form of solution and additionally an appropriate quantity of water was added that water/solid ratio of the suspension kept equal to 10.0. These conditions of the syntheses were chosen according to previously published data [16]. The products of the syntheses were filtered, rinsed with ethyl alcohol to prevent carbonization of materials, dried at 50 ± 5 ºC and sieved through a sieve with a mesh width of 50 μm.

The specific surface area of the raw materials was determined by the Blaine's method with an air permeability apparatus (Model 7201, Toni Technik Baustoffprüfsysteme GmbH).

The X-ray powder diffraction data were collected with a DRON–6 X-ray diffractometer in the Bragg–Brentano geometry using Ni-filtered CuK_α radiation and a graphite monochromator, operating at 30 kV and emission current of 20 mA. The step-scan covered the angular range 2–60° (2θ) in steps of 2θ = 0.02°. The computer program X-fit [26] was used for diffraction profile refinement under the pseudoVoid function and for the description of the diffractional background under the 3rd degree of the Tchebyshev polynom.

Simultaneous thermal analysis (STA) (differential scanning calorimetry DSC and thermogravimetry (TG)) was carried out on a Netzsch instrument STA 409 PC at the heating rate of 15 °C/min, in the temperature range from 30 °C up to 1000 °C under an air atmosphere. The ceramic sample handlers and crucibles of Pt-Rh were used.

Scanning electron microscopy (SEM) (Oxford ISIS Leo 440 i) coupled with energy dispersive X-ray spectrometer (EDS) was performed using an accelerating voltage of 20 kV and a working distance of 10 mm for SEM observations and a 200 s accumulation time for EDS analyses.

FT-IR spectra have been carried out with a Perkin Elmer FT–IR Spectrum X system. Specimens were prepared by mixing 1 mg of the sample with 200 mg of KBr. The spectral analysis was performed in the range of 4000–400 cm^{-1} with the spectral

resolution of 1 cm^{-1}. The surface areas, total pore volumes and pore size distributions of the products of the syntheses were performed by a BET surface area analyzer "Quantasorb" (Quantachrome).

The specific surface area of gyrolite was calculated by the BET equation using the data of the lower part of N_2 adsorption isotherm ($0.05 < p/p_0 < 0.35$):

$$\frac{1}{X\left(\frac{p_0}{p}-1\right)} = \frac{C-1}{X_m C}\cdot\frac{p}{p_0}+\frac{1}{X_m C}$$

where X is the mass of adsorbate, adsorbed on the sample at relative pressure p/p_0, p – the partial pressure of adsorbate, p_0 – the saturated vapour pressure of adsorbate, X_m – the mass of adsorbate adsorbed at a coverage of one monolayer, C is a constant which is a function of the heat of the adsorbate condensation and heat of adsorption.

The BET equation yields a straight line when $1/X[(p_0/p) - 1]$ is plotted versus p/p_0. The slope of $(C - 1)/X_mC$ and the intercept of $1/X_mC$ was used to determine X_m and C: slope $S = (C - 1)/X_mC$ and intercept $I = 1/X_mC$. Solving for X_m yields $X_m = 1/(S + I)$. BET plot is usually found to be linear in the range $p/p_0 = 0.05$–0.35. The total surface area of the sample S_t was determined from the equation $S_t = X_m N A_{cs}/M$, where M is the molecular mass of the adsorbate, N – Avogadro's constant, A_{cs} – the cross-sectional area occupied by each nitrogen molecule (16.2×10^{-20} m^2). The specific surface area was given by the equation $S_{BET} = S_t/m$, where m is the mass of gyrolite sample. The total pore volumes and pore size distributions were calculated according to the corrected Kelvin equation and Orr et al. scheme [27, 28] based on the entire N_2 desorption isotherm at 77 K. The Kelvin equation relates the depression of the adsorbate vapour pressure to the radius of a capillary filled with adsorbate:

$$\ln\frac{p}{p_0} = -2\,\frac{\gamma V_m \cos\theta}{R\,T\,r_k}$$

where p is the saturated vapour pressure in equilibrium with the adsorbate condensed in a capillary or a pore, p_0 – the normal adsorbate saturated vapour pressure, γ – the surface tension of nitrogen at its boiling point, V_m – the molar volume of liquid nitrogen, θ – the wetting angle (usually taken 0° hence $\cos\theta = 1$), R – the gas constant, T – the absolute temperature, and r_K the Kelvin radius of pore. When N_2 is used as the adsorbate, the Kelvin equation can be rearranged

$$r_k = \frac{4.146}{\lg\frac{p_0}{p}}$$

The Kelvin radius r_K is not the actual pore radius because some adsorption takes place on the wall of the pore prior to the occurrence of condensation in the pore. During desorption, an adsorbed layer remains on the wall when evaporation takes place.

Therefore, the true pore radius r_p was calculated from the equation $r_p = r_K + t$, where t is the thickness of the adsorbed layer, calculated according to the Halsey equation [27]:

$$t = 3.54\left[\frac{5}{\ln\frac{p_0}{p}}\right]^{1/3}$$

where 3.54 is the thickness of one adsorbed nitrogen layer. If the pores are assumed to be cylindrical and if the relative pressure is changed from $(p/p_0)_2$ to $(p/p_0)_1$, the pores between radii r_2 and r_1 will empty ($p_2 < p_1$, $r_2 < r_1$). When p_2 is lowered to p_1, the thickness of the adsorbed film on previously emptied pores changes from t_2 to t_1. The volume of liquid (V_L) evaporated due to emptying of pores and the decrease in thickness of adsorbed layers in previously empty pores was calculated by the following equation:

$$V_L = \pi\left(\overline{r}_p - t_2\right)^2 L + (t_2 - t_1)\sum A$$

where $\overline{r}_p$ is the average pore radius in the interval r_2 to r_1, L – the total length of all pores in the range from r_2 to r_1, A – the area of adsorbed film remaining in the pores after the evaporation out of the pores has occurred. The mean volume of pores with $\overline{r}_p$ is $V_p = \pi\overline{r}_p^2 L$. Then

$$V_p = \left(\frac{\overline{r}_p}{\overline{r}_p - t_2}\right)^2 V_L - \left(\frac{\overline{r}_p}{\overline{r}_p - t_2}\right)^2 (t_2 - t_1)\sum A$$

substituting $r_p = r_K + t$:

$$V_p = \left(\frac{\overline{r}_p}{\overline{r}_K}\right)^2 \left(V_L - \Delta t\sum A\right)$$

The volume of liquid desorbed in any interval of desorption isotherm is related to the volume of gas by the equation: ΔV_L (cm^3) = $\Delta V_{gas}(1.54 \times 10^{-3})$. For cylinders, A is given by

$$A = \frac{2\Delta V_p}{\overline{r}_p} \times 10^4 \quad [\mathrm{m}^2]$$

with V_p in cm^3 and r_p in Å.

The analysis of the desorption isotherms was completed when ($\Delta t\Sigma A$) exceeded ΔV_L because the desorbed gas originates from the adsorbed layer rather than from

evaporation of the liquid from inside the pores. ΣA is the cumulative surface area and is obtained by summing A in each radius interval.

The shapes of natural pores are usually non-uniform. Their complicated shapes for calculation purposes are usually approximated by selected geometrical models. Among many models (slit-like, ink-bottle, conical, globular, etc.) the most frequently used is the cylindrical pore model. Moreover, gyrolite has a plate-like crystal structure. It is thus conceivable that slit-like (plates) pores will dominate in the gyrolite crystal lattice. For the calculations of slit-like pores we used the following equation:

$$\bar{d}_p = r_K + 2t; \qquad V_p = \frac{\bar{d}_p}{r_K}\left(\Delta V_L - 2\Delta t \sum A\right); \qquad A = \frac{2V_p}{d_p}$$

where $\bar{d}_p$ is the distance between two plates (in Å).

3. Results and discussion

Our preliminary investigation focused on the synthesis and characterization of pure gyrolite (without any additives) and Na-substituted gyrolite. The results of XRD

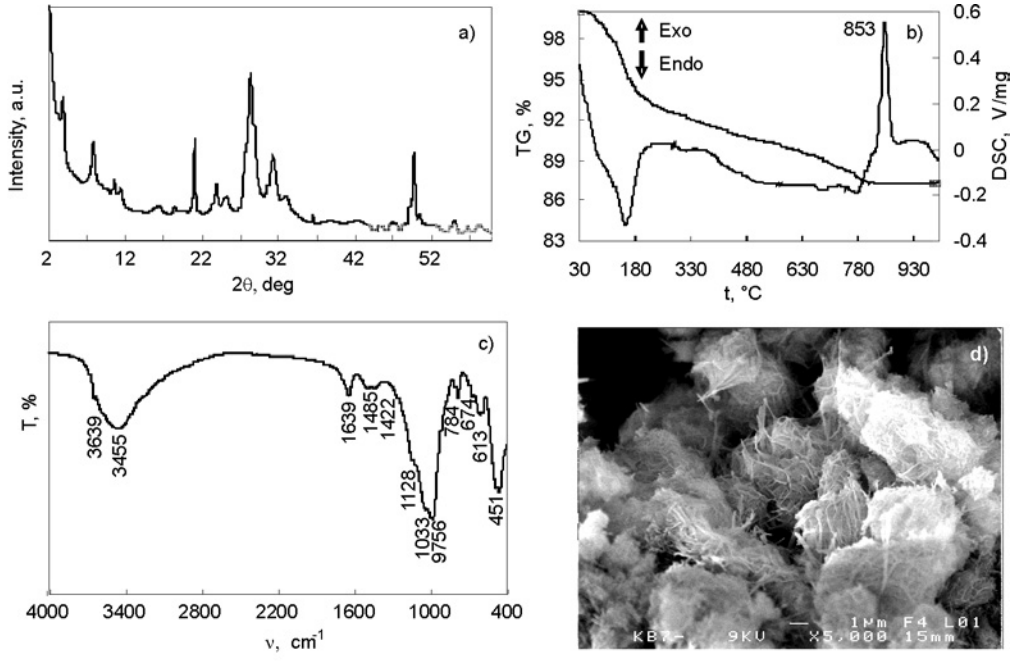

Fig. 2. X-ray diffraction pattern (a), DSC–TG curve (b), FT-IR spectrum (c) and SEM micrograph (d) of pure gyrolite. Duration of the hydrothermal synthesis at 200 °C equals 32 h

studies confirmed that in the $CaO–SiO_2 \cdot nH_2O–H_2O$ system within 32 h at 200 °C pure gyrolite was formed, whereas in the samples doped with 5% Na_2O within 16 h at 200 °C only Na-substituted gyrolite was found. An intensive peak with the *d* spacing of 2.2 nm is attributed to gyrolite, i.e. this diffraction reflection is not characteristic of other calcium silicate hydrates. Moreover, in the X-ray diffraction pattern, the peaks which are also typical of gyrolite have been identified (*d* spacings – 1.1262; 0.8371; 0.4197; 0.3732; 0.3511; 0.2803; 0.2141 nm, Fig. 2a). It should be noted that the mentioned properties of gyrolite are slightly altered by Na^+ ions inserted into crystal lattice of the former compound: the main basal reflection *d* spacing increases to 2.324 nm in X-ray diffraction pattern (Fig. 3a).

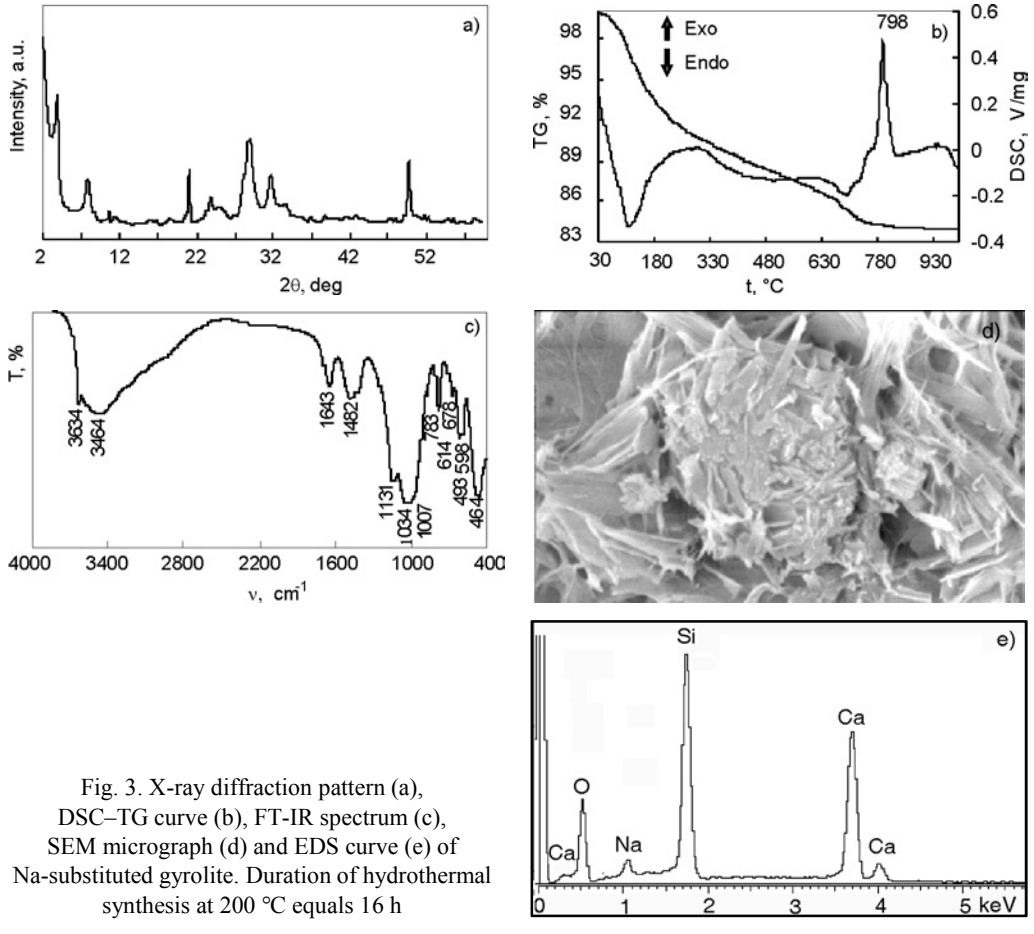

Fig. 3. X-ray diffraction pattern (a), DSC–TG curve (b), FT-IR spectrum (c), SEM micrograph (d) and EDS curve (e) of Na-substituted gyrolite. Duration of hydrothermal synthesis at 200 °C equals 16 h

On the DSC curve, only two thermal effects corresponding to gyrolite are visible. A broad endothermic peak appearing in the temperature range of 137–143 °C is related to the loss of physisorbed and interlayer water from the crystal structure of gyrolite. The other exothermic peak is associated with recrystallization of this compound

into wollastonite (Fig. 2b). This step is accompanied by a complete destruction of the gyrolite structure. In the case of Na-substituted gyrolite, in DSC curve the shape of wollastonite formation peak changes and moves to lower temperature (Fig. 3b, exothermic peak at 798 °C). The findings of SEM also confirmed the formation of gyrolite in the synthesis products. The SEM photos show that plate Na-substituted gyrolite crystals are much larger than those of pure gyrolite (Figs. 2d, 3d). EDS analysis proved the presence of sodium (~ 3 %) in the crystal structure of gyrolite (Fig. 3e). All of these findings have been confirmed by the FT-IR spectroscopy data, which can be used to distinguish gyrolite from other calcium silicate hydrates [29]. A sharp peak near 3635 cm^{-1} is visible only in the gyrolite spectrum (Figs. 2c, 3c). Its presence proves that clearly distinguished OH positions exist in the structure of gyrolite connected only with Ca atoms and not influenced by hydrogen bridge links. A wide band near 3446 cm^{-1} means the opposite –molecular water forms hydrogen bridge links in the interlayers. The bands in the range of 1634 cm^{-1} are assigned to $\delta(H_2O)$ vibrations and confirm this presumption. Vibrational modes for gyrolite and Na-substituted gyrolite are presented in the Table 1.

Table 1. Vibrational modes for gyrolite and Na-substituted gyrolite

Bend assigment	Band position (wavenumber), cm^{-1}	
	Gyrolite	Na-substituted gyrolite
δ(O–Si–O)	451	464
	492	493
δ(Si–O–Si)	596	598
ν(OH–)?	613	614
ν_s(Si–O–Si)	674	678
	784	783
ν(O–Si–)	975	
ν_{as}(Si–O–Si) from Q^3	1033	1007
	1128	1034
		1131
$\nu(C–O_3^{2-})$	1422	1482
	1485	
δH_2O(bending)	1639	1643
ν(OH^-)	3455	3464
	3639	3634

To evaluate the stability of gyrolite structure at low temperatures and to estimate the influence of the adsorbed water vapour (adsorbate) on the structure of its crystal lattice, gyrolite samples were saturated with water vapour, i.e. kept in desiccator for 60 h under various relative pressures (p/p_0 = 1; 0.877; 0.753; 0.56; 0.355). Then each sample was frozen in liquid nitrogen (–197 °C) for 15 min and then heated to room temperature (20 °C). X-ray diffraction patterns obtained after these experiments show that there was essentially no change in the structure of gyrolite (Fig. 4).

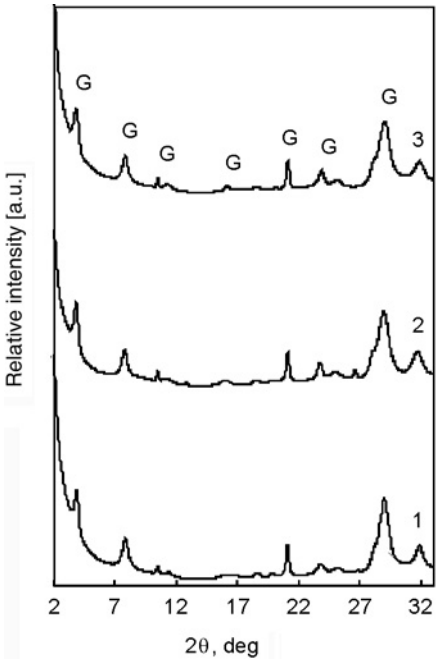

Fig. 4. X-ray diffraction patterns of gyrolite subject to water vapour adsorption: 1 – pure gyrolite; 2 – saturated (60 h) with water vapour under $p/p_0 = 1$; 3 – saturated (60 h) with water vapour under $p/p_0 = 1$, frozen in liquid nitrogen (–197 °C) during 15 min and heated to room temperature; G – gyrolite

Therefore, it can be stated that a stable monomolecular layer of adsorbed N_2 is formed on the surface of the gyrolite pores, and the calculations of the specific surface are reliable. The line prominence ratios R^2 are equal to 0.9866 for gyrolite and 0.9969 for Na-substituted gyrolite (Table 2).

Table 2. Parameters of the BET equation of gyrolite and Na-substituted gyrolite

Adsorbent	Parameters of BET equation		X_m, g	S_{BET}, m^2/g	C_{BET}	R^2
	S	I				
Gyrolite	4117.4	6.54	0.00024	143.15	637	0.987
Na-substituted gyrolite	8136.8	6.20	0.00012	27.24	1034	0.997

S_{BET} significantly decreases after introducing Na^+ ions into the crystal lattice of gyrolite. It equals 143.15 m^2/g, and diminishes to 27.24 m^2/g after 5% of Na_2O has been added to primary mixtures. These findings once more prove the influence of Na^+ ions on the synthesis processes of gyrolite when bigger particles are formed and at the same time the specific surface area decreases.

The value of C_{BET} constant proves that the structure of gyrolite crystals consists of disorder sheets (gel inserts, i.e., it has no firm frame). It is already known that C_{BET} values range from 50 to 200, higher values indicating a possibility of chemisorption of N_2 at 77 K or an unstable structure of the analysed materials. The highest $C_{BET} = 1034$ was obtained when Na^+ ions were introduced into the gyrolite structure. The volume of gyrolite pores and distribution of their radii were calculated based on the isotherms

of N_2 adsorption–desorption (Figs. 5, 6). The isotherms are characteristic of mesopore materials. Isotherms have a clear bend (point A). Micropore sorbents do not have a point A in the $0.05 \le p/p_0 \le 0.30$ range. A characteristic feature of the isotherms in gyrolite is hysteresis: desorption curves in Fig. 5 are shifted "to the left" with respect to the adsorption isotherms. This is characteristic of mesopore solid bodies when diameters of pores vary from 15 to 500 Å.

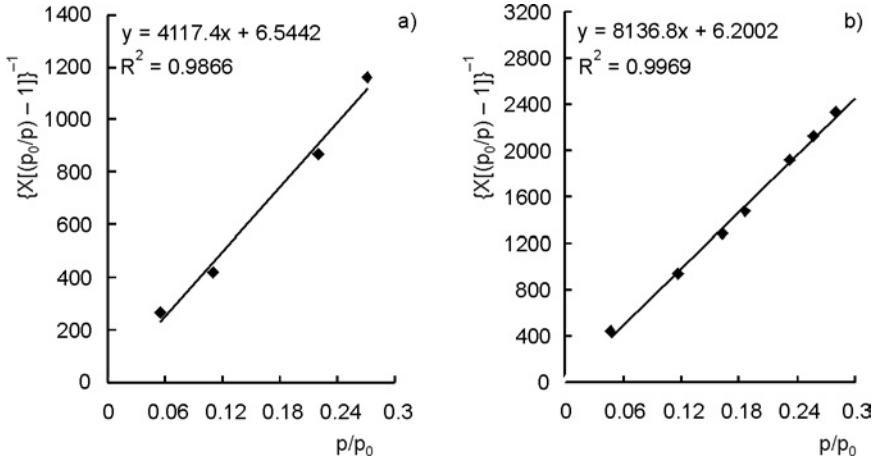

Fig. 5. BET isotherms of N_2 adsorption of gyrolite (a) and Na-substituted gyrolite (b) at 77 K

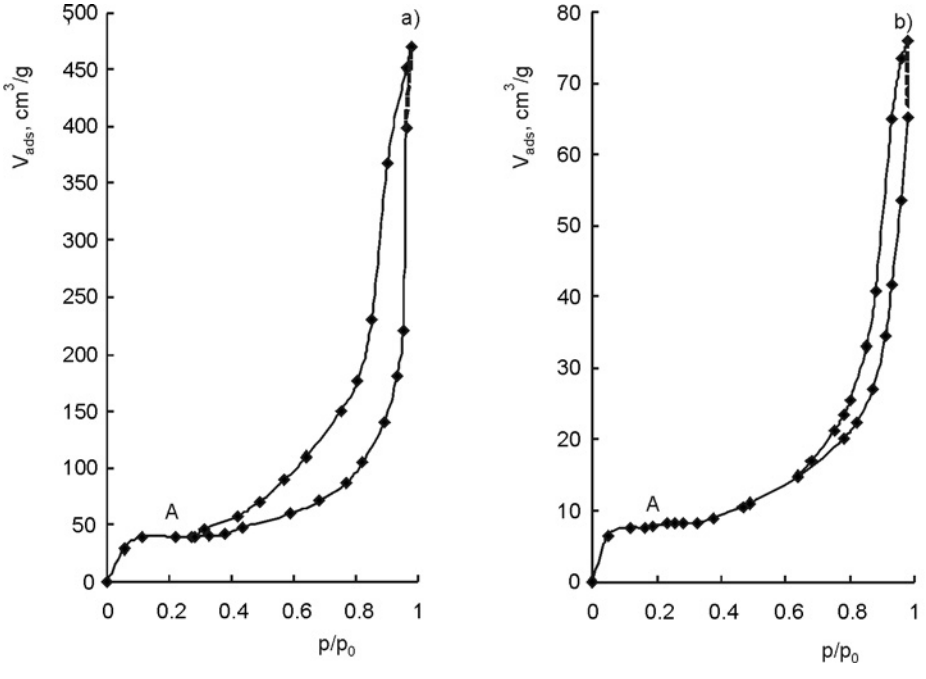

Fig. 6. Isotherms of N_2 adsorption–desorption of gyrolite (a) and Na-substituted gyrolite (b) at 77 K

According to the IUPAC classification, isotherms of pure gyrolite correspond to the case when pores are formed between parallel crystal plates (H3 type), adsorption and desorption coincide in the area of low p/p_0 amounting to about 0.30 and the isotherm of desorption has a refraction. And, on the contrary, after introducing Na^+ ions, the isotherm of hysteresis becomes characteristic of pores having a cylindrical or open tubular form. In this case, adsorption and desorption coincide in the area of $p/p_0 \approx 0.70$ and the hysteresis is narrow. It can be cautiously assumed that Na^+ ions are spread between the silicate layers of the crystal lattice of gyrolite. A possible formation of hydrogen bridge links in the X-interlayer of Na-substituted gyrolite structure is presented in Fig. 7.

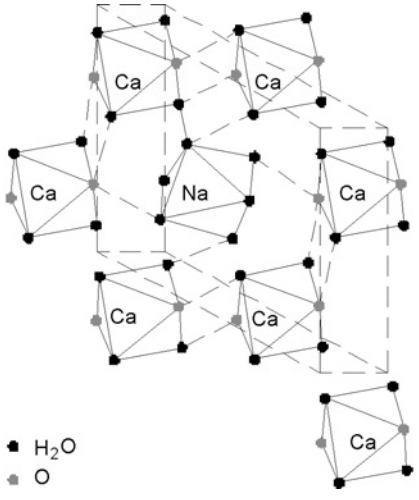

Fig. 7. Formation of hydrogen bridge links in the X-interlayer of Na-substituted gyrolite structure

The distribution of pore diameters is calculated according to the common model of a dominating form of pores. The most suitable model of pore distribution is the one whose experimentally defined S_{BET} value is the closest to the value of the calculated specific surface ΣA. Therefore, the distribution of pores to the diameters was calculated according to two models (cylindrical pores and pores between parallel plates). To calculate the distribution of pores of the pure gyrolite to the diameters the most suitable model is when pores are formed of parallel pores (the measured $S_{BET} = 143.15$ m^2/g, the calculated $\Sigma A = 157.71$ m^2/g). In this case, S_{BET} and ΣA differ by only 9.23%. In the case of cylindrical pore model S_{BET} and ΣA differed by over than 52.57%.

It is accepted that the model is the right one when this difference does not exceed 20% (compare $S_{BET} = 143.15$ m^2/g, and $\Sigma A = 272.77$ m^2/g). The dominating pores of the pure gyrolite are of about 8–9 nm in diameter, the total pore volume ΣV_p is 0.661 cm^3/g. Meanwhile, the more suitable model of cylindrical pores is for Na-substituted gyrolite because the measured $S_{BET} = 27.24$ m^2/g, and the calculated $\Sigma A = 30.25$ m^2/g. In this case, the diameters of the dominating pores are ranging from 6 to 7 nm, and the pore volume significantly decreases compared to the pure gyrolite and equals 0.12 cm^3/g.

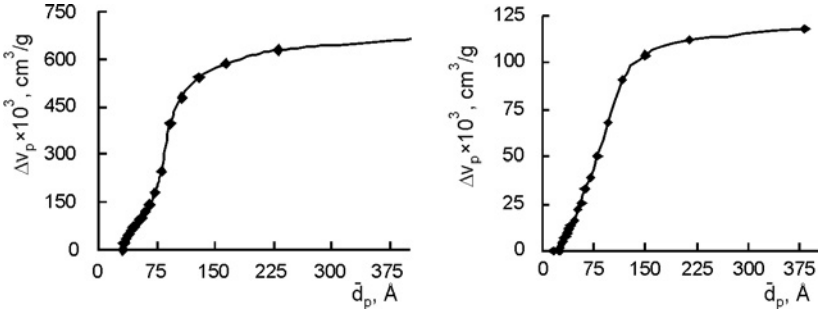

Fig. 8. Total pore volumes of gyrolite (a) and Na-substituted gyrolite (b)

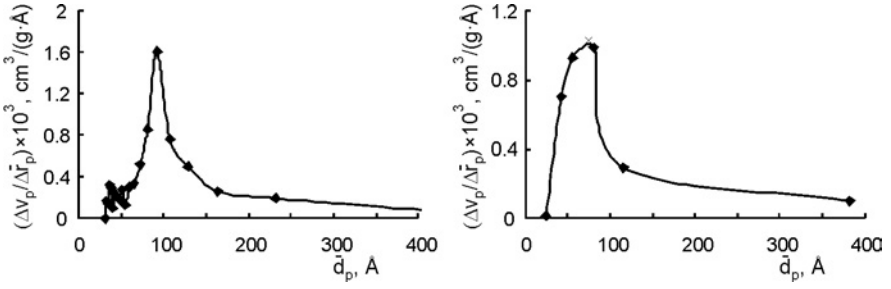

Fig. 9. Differential distributions of volume pore sizes of gyrolite (a) and Na-substituted gyrolite (b)

The results of the analysis of the specific surface confirmed the data obtained by other researchers [30]. Nocun-Wczelik also states that gyrolite is a mesopore compound and its S_{BET} varies depending on the synthesis conditions, additions used, etc. Thus, pure gyrolite satisfies the main requirements for adsorbents (i.e., high specific surface, smoothness, particles of a proper size, mechanical resistance to high pressure) and can be used as an adsorbent and/or chemisorbent. Besides, addition of Na_2O to the primary mixture allows one to alter the size of the particles, the specific surface area, the total pore volume, the differential pore distribution to the radii.

4. Conclusions

The properties of gyrolite are slightly altered by introducing Na^+ ions into its crystal lattice: the main basal reflection *d* spacing increases to 2.324 nm in the X-ray diffraction pattern; the wollastonite formation peak in DSC curve shifts to lower temperatures.

It was found that crystal structure of gyrolite is stable under water vapour pressure at low temperature (in liquid nitrogen, –197 °C) is. It was found that gyrolite is a mesoporous material. Its specific surface area S_{BET} = 143.15 m^2/g, the radius of dominant plate pores r_p = 80–90 Å, the calculated total pore volume ΣV_p = 0.661 cm^3/g. The gyrolite texture changes when Na^+ ions are introduced into the crystal structure: its specific surface area

becomes S_{BET} = 27.24 m^2/g, the radius of dominant cylindric pores r_p = 60–70 Å, the calculated total pore volume ΣV_p = 0.118 cm^3/g.

References

[1] TAYLOR H.F.W., Adv. Cem. Based Mater., 1 (1993), 38.
[2] TAYLOR H.F.W., Cem. Concr. Res., 23 (1993), 995.
[3] ZADOV A.E., N.V.CHUKANOV, ORGANOVA N.I., BELAKOVSKY D.I., FEDOROV A.V., KARTASHOV P.M., KUZMINA O.V., LITZAREV M.A., MOKHOV A.V., LOSKUTOV A.B., FINKO V.I., Proc. Russian Mineralogical Society, 124 (1995), 36.
[4] VIEHLAND D., YUAN L.J., XU Z., CONG X.D., KIRKPATRICK R.J., J. Am. Cer. Soc., 80 (1997), 3012.
[5] SASAKI K., MASUDA T., ISHIDA H., MITSUDA T., J. Am. Cer. Soc., 79 (1996), 1569.
[6] KIRKPATRICK R.J., YARGER J.L., MCMILLAN P.F., YU P., CONG X.D., Adv. Cem. Based Mater., 5 (1997), 93.
[7] YANAGISAWA K., FENG Q., YAMASAKI N., J. Mater. Sci. Lett., 16 (1997), 889.
[8] HEJNY C., ARMBRUSTER T., *Structure modelling and identification of xonotlite polytypes*, [in:] Proc. 6th International Congress on Applied Mineralogy, 2000, pp. 795–797.
[9] SHAW S., HENDERSON C.M.B., CLARK S.M., Chem. Geol., 167 (2000), 129.
[10] KALOUSEK G.L., MITSUDA T., TAYLOR H.F.W., Cem. Concr. Res., 7 (1977), 305.
[11] YANO T., URABE K., IKAWA H., TERAUSHI T., ISHZAWA N., UDAGAWA S., Acta Cryst., 49 (1993), 1555.
[12] GEORGESCU M., TIPAN J., BADANOIU A., CRISAN D., DRAGAN I., Cem. Concr. Comp., 22 (2000), 315.
[13] MARSH R.E., Acta Cryst., 50 (1994), 996.
[14] BALTAKYS K., ŠIAUČIŪNAS R., BALTUŠNIKAS A., Chem. Techn., 1 (2004), 45.
[15] ŠTEVULA L., PETROVIČ J., Cem. Concr. Res., 13 (1983), 684.
[16] ŠIAUČIŪNAS R., BALTAKYS K., Cem. Concr. Res., 34 (2004), 2029.
[17] MIYAKE M., IWAYA M., SUZUKI T., J. Am. Cer. Soc., 73 (1990), 3524.
[18] WINTERS M.A., RICHTER J.D., SAGAR S.L., LEE A.L., LANDEI R.J., Biotechnol. Prog., 19 (2003), 440.
[19] MACKAY A.L., TAYLOR H.F.W., Mineral. Mag., 30 (1953), 80.
[20] CHALMERS R.A., FARMER V.C., HARKER R.I., KELLY S., TAYLOR H.F.W., Mineral. Mag., 33 (1964), 821.
[21] GARD J.A., MITSUDA T., TAYLOR H.F.W., Mineral. Mag., 40 (1975), 325.
[22] LACHOWSKI E.E., MURRAY L.W., TAYLOR H.F.W., Mineral. Mag., 43 (1979), 333.
[23] SHAW S., HENDERSON C.M.B., CLARK S.M., Am. Mineral., 87 (2002), 533.
[24] JAUBERTHIE R., TEMIMI M., LAQUERBE M., Cem. Concr. Res., 26 (1996), 1335.
[25] MERLINO S., Mineral. Mag., 52 (1988), 377.
[26] CHEARY R.W., COELHO A.A., *Programs XFIT and FOURYA, deposited in CCP14 Powder Diffraction Library*, Engineering and Physical Sciences Research Council, Daresbury Laboratory, Warrington, England, (1996) (http://www.ccp14.ac.uk/tutorial/xfit-95/xfit.htm).
[27] GREG S., SING K., *Adsorption, Specific Area, Porosity*, Moscow, Mir, 1984 (in Russian).
[28] ORR C., DALLA VALLE J.M., *Fine Particle Measurements*, MacMillan, New York, 1959.
[29] GARBEV K., PhD Dissertation, Faculty of Geology and Geography, University St. Kliment Ohridski, Sofia, 2004.
[30] NOCUN-WCZELIK W., Cem. Concr. Res., 27 (1997), 83.

Received 20 September 2007
Revised 19 November 2007

Materials Science-Poland, Vol. 26, No. 3, 2008

Studies of conductivity in mixed alkali vanadotellurite glasses

M. PRASHANT KUMAR, T. SANKARAPPA*

Department of Physics, Gulbarga University, Gulbarga 585 106, Karnataka, India

A set of novel mixed alkali vanadotellurite glasses $(V_2O_5)_{0.25}(Li_2O)_{0.25}(K_2O)_x(TeO_2)_{1-x}$ ($0.05 \geq x \leq 0.30$) have been investigated for density and dc conductivity in the temperature range from 380 K to 480 K. The density exhibited a minimum, and molar volume showed a maximum at $x = 0.20$. Conductivity data have been analyzed in the light of Mott's small polaron hopping model and high temperature activation energy values have been determined. The conductivity and activation energy also passed through a minimum and maximum, respectively, at $x = 0.20$. This result has been attributed to the mixed alkali effect. The strength of mixed alkali effect has been estimated. It is for the first time that vanadotellurite glasses are shown to exhibit mixed alkali effect. Various physical and polaron hopping parameters have been determined and discussed.

Key words: *glass; tellurite glass; bulk density; conductivity; mixed alkali effect*

1. Introduction

The electrical conductivity in glasses doped with transition metal ions (TMI) have always been observed to be semiconducting type and that was due to the polaron hopping between multivalent states of TMI [1–3]. Glasses containing Li^+, Ag^+, Cu^+ and Na^+ ions exhibit significant ionic conductivity at ordinary temperatures. An interesting aspect of electrical conduction in ionic glasses is the so called mixed alkali effect (MAE). Mixed alkali doped glasses exhibit lower electrical conductivity compared to that of single alkali composition, for the same total ionic concentrations [4–7]. A general understanding of ion transport in glasses is based on the assumption that cations jump from one position to another similar one while the negatively charged centres remain fixed in position in the glass matrix [7]. The mixed alkali effect has not been completely understood mainly due to the difficulty to determine the conduction pathways for the mobile ions [8]. Ion conducting glasses have technological applications for electrochemical devices such as solid-oxide fuel cells, solid state batteries or

*Corresponding author, e-mail: sankarappa@rediffmail.com

chemical sensors [9]. MAE has been observed in different physical properties of silicate, borate, germanate and tellurite glasses [10, 11]. MAE has been observed in terms of electrical conductivity and thermal properties in sodium–rubidium–borate glasses [11]. In particular, MAE in terms of glass transition temperature and electrical conductivity has been observed in K_2O-Na_2O-TeO_2 systems [12]. El-Damrawi [13] investigated MAE in Ag and Na doped tellurite and phosphotellurite glasses. Li–Na–Te glasses have been explored for thermal properties and MAE has been reported in terms of specific heat capacity and glass transition temperature [14]. Li–Rb doped phosphate glasses have been investigated for electrical conductivity and pointed out that the strength of MAE depends on the sizes of the alkali ions [15]. Various theoretical models such as Mott's small polaron hopping (SPH), variable range hopping (VRH) [16–19] and Greaves VRH models [20, 21] have been used to explain temperature dependence of conductivity in glasses. There are no reports on physical properties of the glass systems containing both alkali and transition metal ions.

In the present paper, we report the results of investigations of bulk density at room temperature and dc conductivity in function of temperature in the glass systems; $(V_2O_5)_{0.25}(Li_2O)_{0.25}(K_2O)_x(TeO_2)_{1-x}$, x = 0.05, 0.10, 0.15, 0.20, 0.25 and 0.30, labelled as MA1, MA2, MA3, MA4, MA5 and MA6. The objective of the present investigation is to study the electrical conductivity in a glass system wherein both TMI and two different alkali ions are present and in terms of the possibility of occurrence of MAE in these systems.

Vanadium oxide (V_2O_5) can also act as glass former. In the present systems, its content is fixed at mole fractions equal to 0.25. In few samples its content is comparable with the main glass former, TiO_2 and therefore V_2O_5 in these systems may play the roles of network former or network modifier or both. No special experiment or analysis has been conducted to ascertain exactly the role of V_2O_5. However, it is often quoted that vanadium exists in two different valence states that is, V^{4+} and V^{5+}. The existence of two different oxidation states paves the way for polaron conduction in the glasses.

2. Experimental

The glass samples were prepared by the melt-quenching technique using the analytical grade V_2O_5, Li_2CO_3, K_2CO_3 and TeO_2 (Sigma-Aldrich). The well ground mixture of chemicals in appropriate weight ratios was taken in porcelain crucible and melted in a muffle furnace at a constant temperature in the range 1200–1300 K for 1 h. The melts were quickly quenched to room temperature and the random pieces of samples were collected. In order to relieve the mechanical stresses, the samples were annealed at 525 K. Glassy nature of the samples was confirmed by X-ray diffraction studies.

It is possible that corrosive melts at high temperatures can attack the porcelain made crucibles. However, there are numerous reports wherein the glasses were pre-

pared at the temperature ranges operated here [22, 23], and no chemical analysis of the samples was carried out and the set compositions were assumed. Due to unavailability of the facilities and expertise no chemical analysis has been performed of the present glasses and the set compositions are taken for granted. Moreover, the integrity of our porcelain crucibles after quenching the melt was observed to be intact.

Densities at room temperature were measured by following the Archimedes principle using a sensitive single pan balance (Sartorius). Carbon tetrachloride, CCl_4 (density = 1.595 g/cm^3) was used as an immersion liquid. The uncertainty on density was estimated to be ±0.026 g/cm^3.

Samples (4±0.04) mm thick of cross sectional areas ranging from (30±0.30) mm^2 to (50±0.50) mm^2 were cut for dc conductivity measurements and the silver electrodes were painted on two major surfaces of the samples. Conductivities in the temperature range 300–525 K were measured by the two probe method. The currents and voltages were measured using a digital nanoammeter and a multimeter to the accuracy of ±0.1nA and ±10mV, respectively. The temperature of the sample was measured to the accuracy of ±1 K using a chromel-alumel thermocouple and a digital microvoltmeter. To verify the reproducibility and minimize errors, the experiment was repeated and data collected over several experiments has been averaged. The conductivity was determined from the equation: $\sigma = t/RA$, where t is the thickness, R is the resistance and A is the cross sectional area of the sample.

The errors on conductivity, $\Delta\sigma$, were estimated taking into account errors on the measured thickness, Δt, areas, ΔA, voltages, ΔV, and currents, ΔI. The estimated errors on conductivity were found to lie in the range 4–5%.

The ionic conductivity is often measured by the ac impedance spectroscopy to avoid the polarization effects on the sample–contact interfaces. However, there are numerous reports in which the ionic conductivity has been measured using the dc method [2, 3, 24–26]. Since ions Li^+ and K^+ incorporated into the glass network are lighter ones and in many instances the ionic conductivity has been detected by the dc method, we have adopted the dc technique to measure ionic conductivity of the present glasses. To avoid initial polarizations, if any, the current measurements were actually started after about 30 s of keeping constant voltage across the sample. The resistance measurements were repeated several times to check the reproducibility of the data.

3. Results

3.1. Density and molar volume

The density of the present glasses was found to be in the range of 2.24 to 3.22 g·cm^{-3} (Table 1).

Table 1. Physical properties of Li_2O and K_2O doped vanadotellurite glasses

Glass compositions in mole fractions				$\rho \pm 0.026$ [g·cm^{-3}]	$V_m \pm 0.450$ [cm^3·mol^{-1}]	$N \pm 0.04$ [10^{21}cm^{-3}]	$R \pm 0.01$ [nm]	$\sigma \times 10^{-6}$ [ohm^{-1}·m^{-1}] at 450 K
V_2O_5	Li_2O	K_2O	TeO_2					
0.25	0.25	0.05	0.45	3.220	40.891	5.331	0.572	6.23±0.09
0.25	0.25	0.10	0.40	2.895	45.112	4.793	0.593	4.31±0.06
0.25	0.25	0.15	0.35	2.462	52.612	4.076	0.626	2.45±0.10
0.25	0.25	0.20	0.30	2.236	57.451	3.702	0.646	1.16±0.09
0.25	0.25	0.25	0.25	2.368	53.796	3.920	0.634	2.25±0.12
0.25	0.25	0.30	0.20	2.748	45.968	4.549	0.604	8.68±0.06

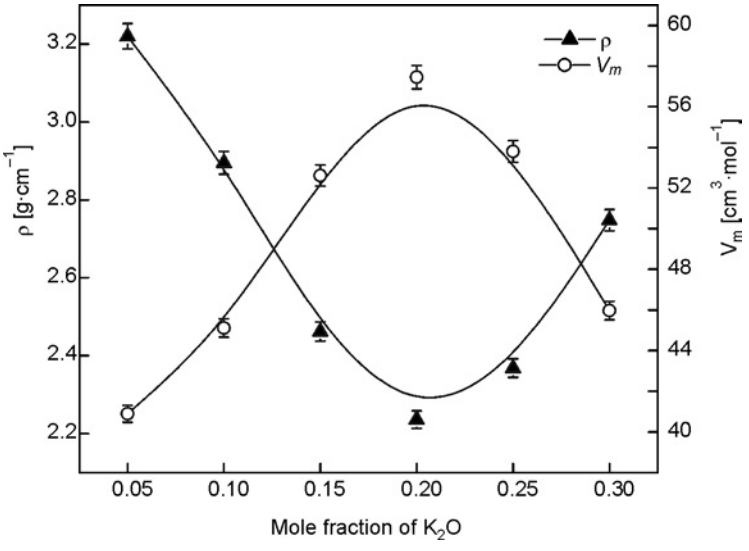

Fig. 1. Compositional dependence of bulk density and molar volume. The solid lines are guides to the eye

The density decreased with K_2O content up to 0.20 mole fraction and increased for further doping of K_2O (Fig. 1). The molar volume, V_m, was calculated from the density data using the relation $V_m = M/\rho$ [27], where M is the molecular weight of the glass which is given as

$$M = 0.25M_{V_2O_5} + 0.25M_{Li_2O} + xM_{K_2O} + (0.5 - x)M_{TeO_2}$$

The values of V_m were found to be in the range 40.89–57.45 cm^3·mol^{-1} and increased continuously with increase in K_2O up to 0.20 mole fraction and decreased for further increase in K_2O (Fig. 1).

The vanadium ion density, N [27] was estimated using the relation

$$N = 2\left(\left(\frac{\rho m_{V_2O_5}}{M_{V_2O_5}}\right)N_A\right)$$

where ρ is the density of the glass, $m_{V_2O_5}$ is the mole fraction of V_2O_5, $M_{V_2O_5}$ is molecular weight of V_2O_5 and N_A is the Avogadro number. The calculated values of N are presented in Table 1. The error on N values was estimated using the relation

$$\Delta N = \left(\frac{2N_A m_{V_2O_5}}{M_{V_2O_5}}\right)\Delta\rho$$

and was found to be $\pm 0.01\times 10^{21}$.

3.2. dc conductivity

In the studied temperature range, the measured conductivities were found in the range from 10^{-5} to 10^{-8} $ohm^{-1}\cdot m^{-1}$ being in agreement with the reported dc conductivities in alkali ions doped similar and other glass systems [2, 9–15]. The temperature dependence of dc conductivity was observed to be of a semiconductor type. The conductivity decreased monotonously with increase in concentration of alkali ions up to the 0.20 mol fraction of K_2O and then it increased for further increase in total alkali concentration. The initial decrease and then increase in conductivity with K_2O content is believed to be due to mixed alkali effect and this is discussed elaborately in the following section.

4. Discussion

4.1. Density and molar volume

The variation of density and molar volume with alkali concentration in the present glasses indicate that the glass network becomes continuously loose packed up to 0.20 mol fraction of K_2O and shows a sign of tight packing of network for further doping of the second alkali [28–30]. The monotonous increase in V_m with the addition of second alkali up to 0.20 mol fraction of K_2O reveals no significant change in the topology of glass network in the studied systems [30]. However, the observed increase in V_m with further addition of K_2O above 0.20 mol fraction may be a sign for change in the structure and the topology of the glass network. The composition dependence of bulk density, in the present glasses, suggests the occurrence of mixed alkali effect.

No structural investigations have been conducted on the present glasses and no structural information on mixed alkali vanadotellurite glasses is available in the litera-

ture, either. However, structural aspect of single and mixed alkali tellurite glasses has been reported [12, 31], where it was concluded that in these systems non-bridging oxygen ions (NBOs) exist. The NBOs number increases with the increase of second alkali and their concentration becomes maximum at the composition corresponding to conductivity minimum. This may be the case in the present glass systems also.

4.2. dc conductivity

According to Mott's small polaron hopping model (SPH) [16, 17], the electrical conductivity in non-adiabatic regime is expressed as,

$$\sigma = \frac{\sigma_0}{T}\exp\left(-W/k_B T\right)$$

where W is the activation energy and σ_0 is the pre-exponential factor given as

$$\sigma_0 = \nu_0 N e^2 R^2 C(1-C)\exp(-2\alpha R)/k_B$$

where, $\nu_o = \theta_D k_B/h$ is the optical phonon frequency [32], $\theta_D = 2T_D$, is the Debye temperature, N is the concentration of TMI, R is mean spacing between the TMI given as $R = N^{-1/3}$, α is the tunnelling factor and C is the fraction of reduced TMI concentration to that of total TMI concentration. The estimated values of N, R, θ_D and ν_0 for the present glasses are presented in Table 1. The errors on R were calculated using the formula $\Delta R = (\Delta N/3N^{4/3})$.

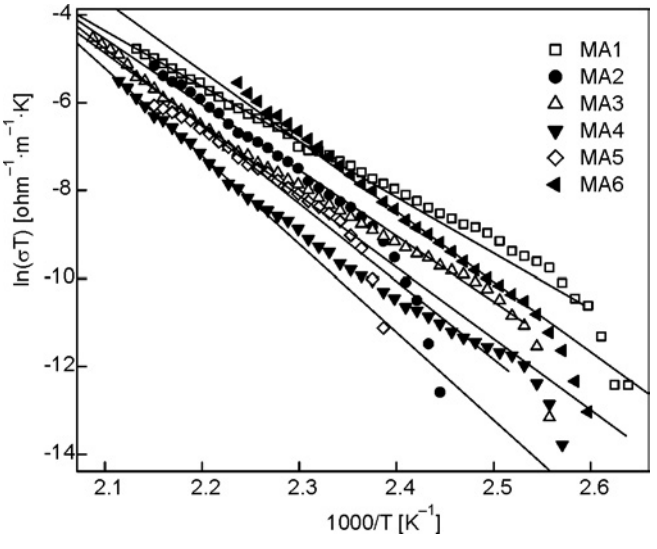

Fig. 2. Temperature dependences of dc conductivity in MA glasses.
The solid lines are least square linear fits to the data

According to Eq. (1), the plots of $\ln(\sigma T)$ vs. $(1/T)$ were made for the present glasses and they are shown in Fig. 2. The dependences were found to be linear at high temperatures and non-linear at low temperatures. The precise values $\theta_D/2$ were not determined due to larger uncertainties in the measured conductivities at lower temperatures. The general behaviour of the curves is observed to be similar to that reported for alkali doped vanadophosphate [2], vanadotellurite and phosphotellurite glasses [10–13]. The least square lines were fit to the data corresponding to high temperatures. The best fit of $\ln\sigma$ vs. $1/T$ gave r^2 from 0.9992 to 0.9996 (r is the correlation coefficient). From the slopes of the lines, the activation energies, W, were determined (Table 2). The W values for the present glasses were found to lie between 1.091 eV and 1.638 eV. These values are in close agreement with those reported in literature [2, 9–13]. The computational errors on activation energies were estimated as per $\Delta W = (\Delta\text{slope})k_B$ and they are found to lie within ±0.002 eV. The activation energies of the present glasses are in near agreement with mixed alkali borate glasses [4, 5], phosphate glasses [2, 33] and tellurite glasses [10–13].

Table 2. Polaron hopping parameters for MA glasses

Glass	$W \pm 0.002$ [eV]	$WH \pm 0.01$ [eV]	$\varepsilon_p \pm 0.002$	$r_p \pm 0.004$ [nm]	J ± 0.001 [eV]	$N(E_f)$ [10^{21} $eV^{-1}\cdot m^{-3}$]	$\gamma_p \pm 0.01$
MA1	1.091	0.651	0.99	0.231	0.122	1.17	21.00
MA2	1.289	0.770	0.81	0.239	0.121	0.89	24.81
MA3	1.522	0.909	0.65	0.252	0.119	0.64	29.29
MA4	1.638	0.978	0.59	0.261	0.118	0.54	31.52
MA5	1.487	0.888	0.66	0.256	0.119	0.63	28.61
MA6	1.377	0.822	0.75	0.243	0.120	0.73	26.50

The variation of activation energy W, and conductivity σ at 450 K in function of mole fraction of second alkali content K_2O are plotted in Fig. 3. From Figure 3 it can be observed that the conductivity decreases with the increase of K_2O content and reaches minimum at 0.2 mole fraction and increases for further increase of K_2O content. On the other hand, the activation energy W increases with the increase of K_2O content and reaches maximum at 0.2 mole fraction and decreases for further increase of K_2O content. The conductivity going through minimum and activation energy passing through maximum at 0.2 mole fraction of the second alkali content is due to mixed alkali effect taking place in MA glasses.

The dynamic structure model (DSM) and matrix mediated coupling (MMC) have been mainly used to discuss the observed results. In addition to DSM and MMC, there exists a number of structural models or views which have been proposed to explain the dynamics of diffusion of alkali ions in glasses [8, 12, 34]. There is no single model which can explain MAE in all types of glasses and our presently studied systems are special and complicated ones as they contain both TMI and mixed alkali ions. In these systems, the second alkali ions were introduced at the cost of TeO_2 and therefore no

models have been invoked to analyze the observed MAE in the present systems. In the TMI and alkali doped glasses, the conductivity is due to both polarons and alkali ions. Polaron hopping between TMI sites of different oxidation or valency gives rise to electronic conductivity and ionic movement interstitially leads to ionic conductivity.

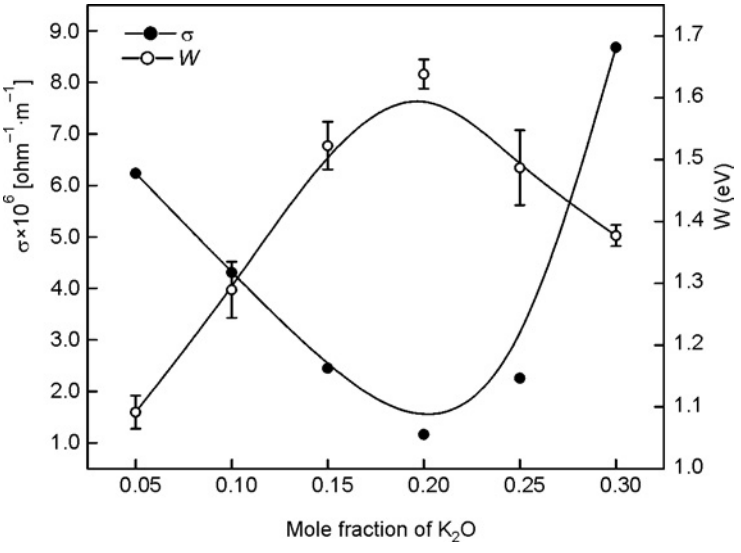

Fig. 3. Compositional dependence of the high temperature activation energy and conductivity at 450 K. The solid lines are guides to eye

Bazian et al. [35, 36] proposed an explanation for the phenomenon of mixed electronic-ionic conduction in oxide glasses. In the glasses where both ions and polarons coexist there must be some interaction between them. The argument goes as follows: mobile electrons or polarons formed by the capture of the moving electrons by TMI of low valency (V^{4+} in the case of vanadium) are attracted by the oppositely charged cations (Li^+ and K^+). This so formed cation–polaron pair tends to move together as a neutral entity. Then the migration of these pairs does not involve any net displacement of charge so this process does not contribute to the electrical conductivity. These authors compared this phenomenon with that of interaction assumed or explanation of the so called mixed alkali effect. So, in the present systems the number of polaron-ion pairs may increase upon increasing K_2O content and that in turn decreases the total conductivity. The conductivity reaches minimum when polaron–ion number reaches a possible maximum. There is another explanation due to Jayasinghe et al. [37], where the continuous blocking of electronic paths with the addition of ionic content is proposed.

The strength of MAE, $\Delta \ln \sigma_{dc}$, has been estimated [6] from

$$\Delta \ln \sigma_{dc} = \ln \sigma_{dc\ \mathrm{lin}} - \ln \sigma_{dc\ \mathrm{min}}$$

where $\ln\sigma_{dc\ \mathrm{lin}}$ represents logarithm of conductivity on the linear interpolated line between two end points in $\ln\sigma$ vs. x plot, which correspond to x for the minimum conductivity (x stands for mole fraction of K_2O). The term $\ln\sigma_{\mathrm{dc\ min}}$ represents the logarithm of the minimum experimental value of conductivity. The estimated value of $\Delta\ln\sigma_{dc}$ for the present glasses is 2.02 and this is in the range of values reported for other binary alkali glass systems [6].

4.3. Parameters associated with polaron hopping

Considering a strong electron-phonon interaction, Austin and Mott [17] proposed that

$$W = W_H + \frac{W_D}{2} \quad \text{for} \quad T > \frac{\theta_D}{2}$$

$$W \approx W_D \quad \text{for} \quad T < \frac{\theta_D}{4}$$

where W_H is the polaron hopping energy and W_D is the disorder energy arising from the energy difference of the neighbours between two hopping sites.

Polaron hopping energy W_H was calculated using the formula [38]:

$$W_H = \frac{W_p}{2} = \frac{e^2}{4\varepsilon_p}\left(r_p^{-1} - R^{-1}\right)$$

Where W_p is the polaron binding energy, ε_p is the effective electric permittivity, which can be determined from the relation, $\varepsilon_p = e^2/4Wr_p$ [16] and the small polaron radius, $r_p = (1/2)(\pi/6N)^{1/3}$ [39]. The estimated values of W_H, ε_p and r_p, are listed in Table 2 and they are comparable with reported values for other similar glasses [1–3, 38]. The errors on W_H and r_p were calculated to be ±0.01 eV and ±0.004 nm, respectively.

In the SPH model, the polaron bandwidth J, which is a measure of electron wavefunction overlap on adjacent sites, is given by [32, 40]

$$J > \left(\frac{2kTW_H}{\pi}\right)^{1/4}\left(\frac{h\nu_0}{\pi}\right)^{1/2} \quad \text{for adiabatic SPH}$$

$$J < \left(\frac{2kTW_H}{\pi}\right)^{1/4}\left(\frac{h\nu_0}{\pi}\right)^{1/2} \quad \text{for non-adiabatic SPH}$$

The polaron bandwidths were calculated from the relation $J = J_0\exp(-\alpha R)$, where $J_0 = W_{H(\mathrm{min})}/4$ [39]. The calculated values of J are listed in Table 2. The value of α was taken from the literature quoted for TMI doped glasses ($\alpha = 20\ \mathrm{nm}^{-1}$) [32]. From Table 2, it can be noted that J for all the glasses satisfies the condition for non-adiabatic

conduction given in Eq. (6) and Holstein's condition, i.e., $J < W_H/3$ [41]. The dependences of J, ε_p and $N(E_F)$ on K_2O content are similar, that is they decrease up to 0.20 mole fraction and increase for further increase of K_2O content.

The densities of states, $N(E_F)$, near the Fermi level were calculated [38] from:

$$J \approx \frac{e^3 N(E_F)^{1/2}}{\varepsilon_p^{3/2}}$$

The estimated values of $N(E_F)$ are shown in Table 2 and they are of the order of 10^{21} $eV^{-1}\cdot m^{-3}$. These $N(E_F)$ values are in agreement with the reported values for many TMI doped glasses [38]. The values of the small polaron coupling constant γ_p, which is a measure of electron-phonon interaction, were calculated using the relation $\gamma_p = 2W_H/h\nu_o$ [16,38] and shown in Table 2. The nature of variation of W_H, r_p and γ_p with K_2O content is same as W that is, they increase up to 0.20 mole fraction and decrease for further increase in K_2O content. The γ_p behaviour reveals that the electron-phonon interaction becomes stronger with increase in K_2O concentration, which in turn decreases the electronic contribution to the total electrical conductivity. For higher concentrations of K_2O, γ_p decreases and hence the increase in electrical conductivity was observed.

5. Conclusion

A set of mixed alkali vanadotellurite glasses prepared by melt quench technique was subjected to room temperature density and dc conductivity studies. The density decreased up to 0.20 mole fraction of K_2O and increased for further increase in K_2O content. This is attributed to the structural changes taking place in the glasses at 0.20 mole fraction of K_2O.

The electrical conductivity and activation energy passed through minimum and maximum, respectively, at 0.20 mole fraction of second alkali (K_2O) content. This must be due to mixed alkali effect. The estimated strength of mixed alkali effect agrees with the results reported for other glasses. In view of the absence of any universal theory to explain mixed alkali effect, no theoretical model has been invoked to describe mixed alkali effect in the present glasses. It is concluded that the observed effect is due to interaction of alkali ions among themselves and their interaction with the remaining glass network offered by V_2O_5–TeO_2. It is for the first time that vanadotellurite glasses are shown to be exhibiting mixed alkali effect.

Acknowledgement

One of the authors, M. Prashant Kumar acknowledges the financial assistance from UGC, India in the form of Rajiv Gandhi National Fellowship.

References

[1] MOGUS-MILANKOVIC A., DAY D.E., SANTIC B., Phys. Chem. Glasses, 40 (1999), 69.
[2] DEVIDAS G.B., SANKARAPPA T., COUGULE B.K., PRASAD G., J. Non-Cryst. Solids, 353 (2007), 426.
[3] GOHAR I.A., MOUSTAFA Y.M., MEGAHED A.A., MANSOUR E., Phys. Chem. Glasses, 39 (1998) 56.
[4] GAO Y., CRAMER C., Phys. Chem. Glasses, 46 (2005), 182.
[5] GAO Y., CRAMER C., Solid State Ionics, 176 (2005), 921.
[6] GAO Y., CRAMER C., Solid State Ionics, 176 (2005), 2279.
[7] ARPAD W.I., VOSS S., MEHRER H., J. Non-Cryst. Solids, 333 (2004), 231.
[8] SWENSON J., ADAMS S., Phys. Rev. Lett., 90 (2003), 15.
[9] BERKEMEIER F., VOSS S., IMRE A.W., MEHRER H., J. Non-Cryst. Solids, 351 (2005), 3816.
[10] ROYCHOUDHURY P., BATABYAL S.K., PAUL A., BASU C., J. Appl. Phys., 92 (2002), 3530.
[11] IMRE A.W., VOSS S., MEHRER H., J. Non-Cryst. Solids, 333 (2004), 231.
[12] BAHGAT A.A., ABOU-ZEID Y.M., Phys. Chem. Glasses, 42 (2001), 371.
[13] EL-DAMRAWI G., Phys. Chem. Glasses, 42 (2001), 56.
[14] KOMATSU T., NOGUCHI T., J. Am. Ceram. Soc., 80 (1997), 1327.
[15] KARLSSON C., MANDANICI A., MATIC A., SWENSON J., BORJESSON L., Phys. Rev. B, 68 (2003), 064202.
[16] MOTT N.F., J. Non-Cryst. Solids, 01 (1968), 01.
[17] AUSTIN I.G., MOTT N.F., Adv. Phys., 18 (1969), 41.
[18] EL-DESOKY M.M., KASHIF I., Phys. Stat. Sol. (a), 194 (2002), 89.
[19] SEN S., GHOSH A., Phys. Rev. B, 60 (1999), 15143.
[20] MOTT N.F., Philos. Mag., 19 (1969), 835.
[21] GREAVES G.N., J. Non-Cryst. Solids, 11 (1973), 727.
[22] HARISH BHAT M., KANDAVEL M., GANGULI M., RAO K.J., Bul. Mater. Res., 27 (2004), 189.
[23] MOHAMMED M.I., ABD-ALLAH K.H., HASSAAN M.Y., Egypt. J. Solids, 27 (2004), 299.
[24] EL-HOFY M., HAGER I.Z., Phys. Stat. Sol. (a), 199 (2003), 448.
[25] AL-SHAHRANI A., AL-HAJRY A., EL-DESOKY M.M., Phys. Stat. Sol. (a), 200 (2003), 378.
[26] BATAL F.H., ASHOUR A.H., Mater. Chem. Phys., 77 (2002), 677.
[27] MANSOUR E., EL-DAMRAWI G., EL-MAKSOUD S., MOUSTAFA Y., DOWEIDAR H., Phys. Chem. Glasses, 43 (2002), 80.
[28] SEN S., GHOSH A., J. Mater. Sci., 15 (2000), 995.
[29] SEN S., GHOSH A., J. Non-Cryst. Solids, 258 (1999), 29.
[30] EL-DESOKY M .M., J. Non-Cryst. Solids, 351 (2005), 3139.
[31] EL-DAMRAWI G., MANSOUR E., Phys. Chem. Glasses, 45 (2004), 192.
[32] SAKATA H., SEGA K., CHAUDHARI B.K., Phy. Rev. B, 60 (1999), 3230.
[33] MOGUSMILANKOVIC A., SANTIC B., DAY D.E., RAY C.S., J. Non-Cryst. Solids, 283 (2001), 119.
[34] CRAMER C., BRUKLAUS S., RATAI E., GAO Y., Phys. Rev. Lett., 91 (2003), 26.
[35] BAZAN J.C., DUFFY J.A., INGRAM M.D., MALLACE M.R., Solid State Ionics, 86– 88 (1996) 497.
[36] MURAWSKI L., BARCZYNSKI R.J., Solid State Ionics, 176 (2005), 2145.
[37] JAYASINGHE G.D.L.K., DISSANAYAKE M.A.K.L., BANDARANAYAKE P.W.S.K., SOUQUET J.L., FOSCALLO D., Solid State Ionics, 121 (1999), 19.
[38] PAL M., HIROTA K., TSUJIGAMI Y., SAKATA H., J. Phys. D: Appl. Phys., 34 (2001), 459.
[39] SEGA K., KURODA Y., SAKATA H., J. Mater. Sci., 33 (1998), 138.
[40] SAYER M., MANSINGH A., Phys. Rev. B, 06 (1972), 4629.
[41] EMIN D., HOLSTEIN T., Ann. Phys., 53 (1969), 439.

Received 7 September 2007
Revised 17 November 2007

Materials Science-Poland, Vol. 26, No. 3, 2008

Structural, optical, electrical and magnetic properties of sol-gel derived $Zn_{1-x-y}Co_xAl_yO$ films

M. SHARMA, R. M. MEHRA*

Department of Electronic Science, University of Delhi, South Campus, New Delhi 110021, India

A detailed study has been presented of optical, electrical, structural and magnetic properties of $Zn_{1-x}Co_xO$ ($0 < x \leq 0.25$) films co-doped with 1 at. % of Al. The polycrystalline films have been synthesized on Corning glass 7059 substrates by the sol-gel technique using spin coating. Highly preferential *c*-axis oriented films have been obtained at the annealing temperature of 600 °C. The lattice constant *d* of *c*-axis wurtzite $Zn_{1-x-y}Co_xAl_yO$ obeys Vegard's law for ($0 < x \leq 0.25$). The inclusion of Al in ZnO is highly beneficial for the magnetism in ZnO because it enhances the free electron density. Optical spectra measurements reveal that band gap energy exhibits a blue shift upon increasing Co concentration. A positive magnetoresistance for Co doped ZnO and negative magnetoresistance for ZnO without cobalt at 77 K has been observed. The ferromagnetic behaviour has been confirmed by measurements using superconducting quantum interference device. The coercive field and the remanence increase with increase in Co content.

Key words: *sol-gel; ZnO:Co; dilute magnetic semiconductor; hysteresis*

1. Introduction

An exciting possibility to utilize both the charge and spin character of an electron to develop spintronic devices such as spin field effect transistors (FETs) and spin light emitting transistors (LEDs) [1, 2] has led to extensive search for materials in which semiconducting properties can be integrated with magnetic properties. These materials are categorized as dilute magnetic semiconductors (DMSs) which are fabricated by introducing small fractions of transition metals (TMs) into host (non magnetic) semiconductors, e.g., III–V [3] and II–VI compounds [4]. The essential requirement for achieving practical spintronic devices is efficient electrical injection of spin-polarized carriers [5]. The material should be capable of transporting the carriers with high transmission efficiency in the host semiconductor.

*Corresponding author, e-mail: rammehra2003@yahoo.com

These key aspects of spin injection, spin dependent transport manipulation and detection form the basis for current research and future technology [3]. Low power consumption of these devices has the advantage of resulting in high packing densities for memory elements [6]. Thus from industrial application point of view it is important for DMS to be an efficient conductor and ferromagnetic at room temperature. In 1998, Ohno [7] reported existence of ferromagnetic behaviour in Mn doped GaAs with the Curie temperature T_c of 100 K. Unfortunately, the highest T_c reported to date was 172 K [8]. This caused researchers to search for other material systems.

Recent studies have identified wide band gap semiconductors including GaN and ZnO systems as promising materials for spintronics applications [9]. From the point of view of industrial application (opto- and magnetoelectronics) ZnO with exciton binding energy of 63 meV and 3.3 eV bandgap has many attractive aspects such as low cost, abundance, and, in addition, it is environmentally friendly [10]. Moreover, it is transparent to visible light and has a higher TM solubility. Dietl et al. [11] made theoretical predictions for room temperature ferromagnetism (RTFM) in heavily doped p-type ZnO alloy. Since p-type ZnO is difficult to fabricate [10], much work has been pursued on n-type ZnO with various TM dopants. Co was chosen as its ionic radius matches to that of Zn^{2+} ion resulting in high solubility [12]. Al is a good co-dopant as it is an adequate electron donor and has no d electrons to interfere with magnetic ordering. Early experimental work has provided mixed and even contradicting results. In one of the studies of doping various TMs into ZnO by Ueda et al. [13] highly conducting n-type Co doped ZnO displayed room temperature ferromagnetism. Research studies [14–16] confirmed these findings. Other studies found that ferromagnetism is extrinsic in nature and arises from nanoclusters and secondary magnetic phases [17–19].

We need to study $Zn_{1-x-y}Co_xAl_yO$ system in detail to understand its structural, electrical and optical properties as they play an important role in promoting ferromagnetism (FM) and in determining the origin of ferromagnetism. We have grown thin films of $Zn_{1-x-y}Co_xAl_yO$ on Corning glass substrate by sol-gel process with high pH sol. Sol -gel technique has advantages in fabricating DMS sample because the mole fractions can be controlled accurately and samples with various compositions can be easily obtained.

2. Experimental

The precursor sols were prepared from zinc acetate dihydrate $Zn(CH_3COO)_2{\cdot}2H_2O$ (Merck Extra Pure Chemical Ind. Ltd, India, purity 99.95%)), methanol (AR, Merck Chemicals, India) and monoethanolamine [MEA] (Merck, India). Cobalt acetate hexahydrate $Co(CH_3COO)_2.6H_2O$ (AR, Merck Chemical Ind. Ltd, India, purity 99.9%) was introduced as a dopant in at. % varying from 5 to 25. Aluminium chloride $AlCl_3$ (Merck, India) was also introduced into the sol in 1 at. %. pH of the solution was 9 with MEA/ZnAc weight ratio as 1. The obtained mixture was stirred using magnetic stirrer for about 60 min to obtain clear homogeneous solution. Microscopic Corning glass (7059) slide substrates were cleaned ultrasonically, first in acetone and then sub-

sequently in methanol for 10 min each. They were further cleaned with deionised water for 20 min and finally dried in nitrogen atmosphere. The clear solutions were used after 48 h for spin coating. The spinning speed and time were optimized to 3000 rpm and 20 s, respectively, to ensure that each spun layer is thin enough to ensure simultaneous evaporation of all solvent, thus preventing cracking of the films. The wet films were kept to hydrolyze in air at room temperature for 5 min, and then were dried at 300 °C for next 10 min. The drying process removes the residual organic solvents and organic groups in the deposited gel film and converts the organic precursor film into a dense inorganic film. An approximate thickness of 15 nm was obtained for each spin. The above process of coating and drying was repeated several times to increase the film thickness and to get the desired thickness. Finally the deposited films were annealed in air in the temperature range of 400–600 °C for 1 h. A slow cooling rate was maintained to avoid the possibility of stress in the films as expected in rapid cooling.

Crystallite phase and orientation were evaluated by the X-ray diffraction method (XRD, Philips PW 1830 Geiger counter diffractometer, PW 3710) using a monochromatized X-ray beam with nickel-filtered CuK_α radiation (λ = 1.54 Å) operating at 40 kV and 20 mA. A continuous scan mode was used to collect 2θ data from 20° to 50°, with a 0.02 sample pitch and 3 deg/min scan rate. The compositions of Co and Al doped ZnO films were determined by the elemental dispersion analysis using X-ray (EDAX) measurements (SEM, LEO 435VP, UK). Average surface roughness R_a and crystallite size were measured by the atomic force microscopy (Burleigh-SPI 3700). Images were recorded via a multimode scanning probe microscope (Digital Instruments). We have used a contact mode with the constant force method (the force between the sample surface and the tip was kept constant by a feedback system while the surface beneath the tip was scanned). The thicknesses of the films were determined by SANTEC ellipsometry and it was found to lie in the range of 200 nm. Optical characterization was performed in the wavelength range of 250–1000 nm using a Solidspec UV-3700 spectrophotometer. The electrical conductivity σ and magnetoresistance were measured by the van der Pauw technique. Contacts for transport measurement were made by pressed indium. The sign of the Hall coefficient confirmed the n-type conduction of the films. The magnetic properties of the sample were characterized using commercial superconducting quantum interference device SQUID (Quantum Design, USA) magnetometer.

3. Results and discussion

3.1. Chemical analysis on $Zn_{0.94}Co_{0.05}Al_{0.01}O$ thin film (EDAX)

Composition analysis of $Zn_{0.94}Co_{0.05}Al_{0.01}O$ film is shown in Fig. 1. The film annealed at 600 °C for 1 h in air atmosphere showed the presence of zinc, cobalt and aluminium. No other impurity was found within the EDAX detection limit.

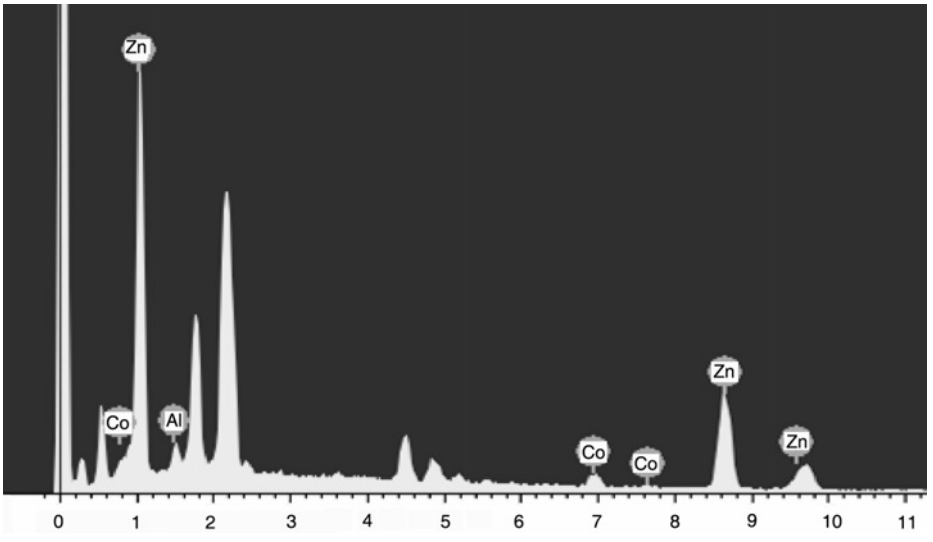

Fig. 1. Energy dispersive X-ray analysis spectrum of $Zn_{0.94}Co_{0.05}Al_{0.01}O$ film annealed at 600 °C

3.2. Structural analysis

Figure 2 shows the XRD patterns of $Zn_{0.95}Co_{0.05}Al_{0.01}O$ in function of annealing temperature T_a. It shows an evidence of polycrystalline structure with (100), (002) and (101) peaks. Upon increase of T_a from 400 °C to 600 °C, the intensity of (002) reflection peak increases. The film grown at 600 °C exhibits a highly *c*-axis preferential growth.

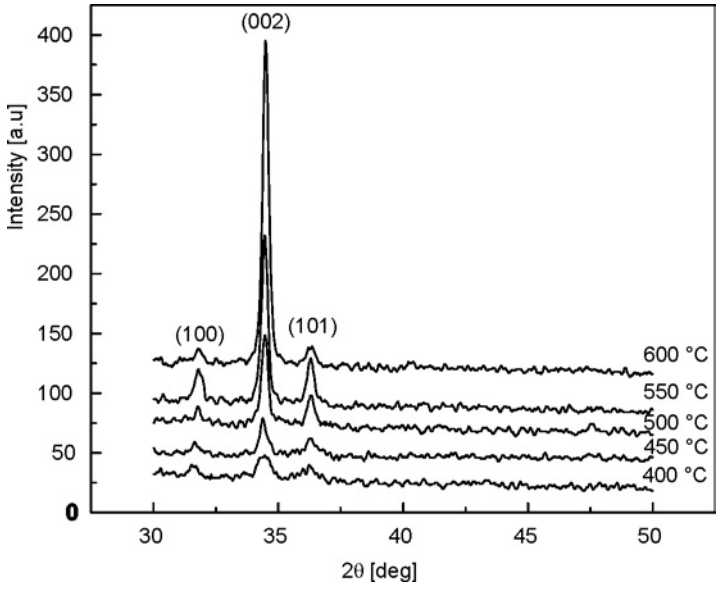

Fig. 2. X-ray diffraction patterns of $Zn_{0.94}Co_{0.05}Al_{0.01}O$ films grown at various temperatures

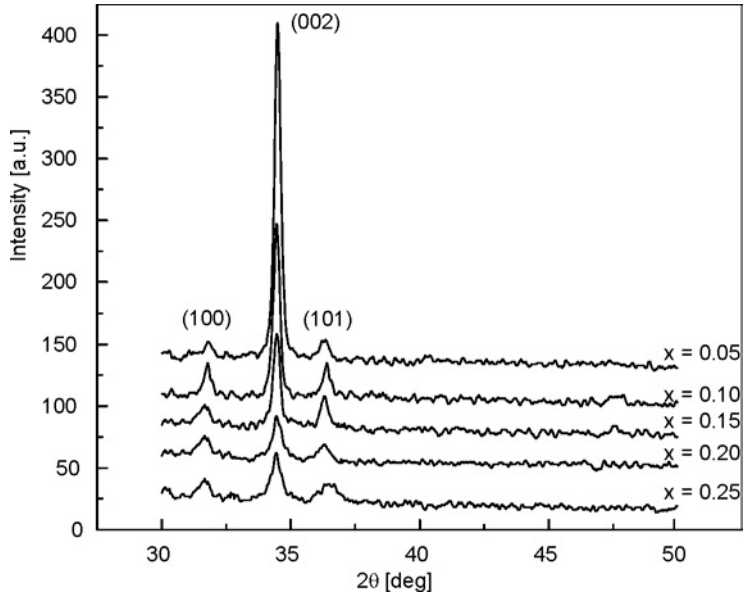

Fig. 3. X-ray diffraction patterns of $Zn_{1-x-y}Co_xAl_yO$ (x = 0.05–0.25, y = 0.01) films annealed at 600 °C

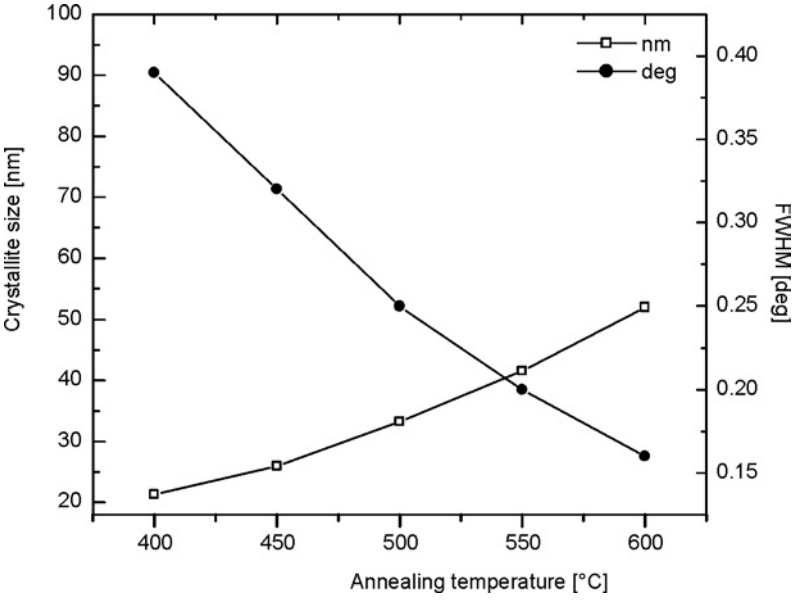

Fig. 4. Dependence of annealing temperature on crystallite size and full width half maximum (FWHM)

Figure 3 shows the X-ray diffraction patterns of the $Zn_{1-x}Co_xO$:Al films annealed at the optimized temperature (600 °C) with various Co concentrations x (0.05–0.25).

The films exhibit a dominant peak at $2\theta = 34.43°$ corresponding to the (002) plane of ZnO, and other peaks corresponding to (100) and (101) indicating the polycrystalline nature of the films. It is seen from the figure that the relative intensity of the (002) peak decreases with increasing Co dopant concentration. No peaks corresponding to either (111) peak Co (44.217) or 400 peak Co_2O_4 (44.74) or (400) peak Co_3O_4 (44.81) appear in the diffraction pattern of the samples, suggesting that Co is incorporated well at the Zn lattice site in the hexagonal wurtzite structure of ZnO. (102) peak for ZnO (47.539) is observed in some samples. We do not exclude the possibility of formation of clusters small enough not to be detected by XRD. Crystallite size was calculated from the Scherrer's equation [20] based on the (002) plane. It is observed in Fig. 4 that the full width half maximum (FWHM) decreases and crystallite size increases with the increase in annealing temperature. The values of crystallite sizes at various T_a are listed in Table 1.

Table 1. Crystallite sizes (t) determined from XRD data and AFM images for $Zn_{0.94}Co_{0.05}Al_{0.01}O$ films at various annealing temperatures (T_a)

T_a [°C]	t [nm]	
	XRD	AFM
450	25.9	20
500	33.2	35
550	41.5	49
600	51.9	59

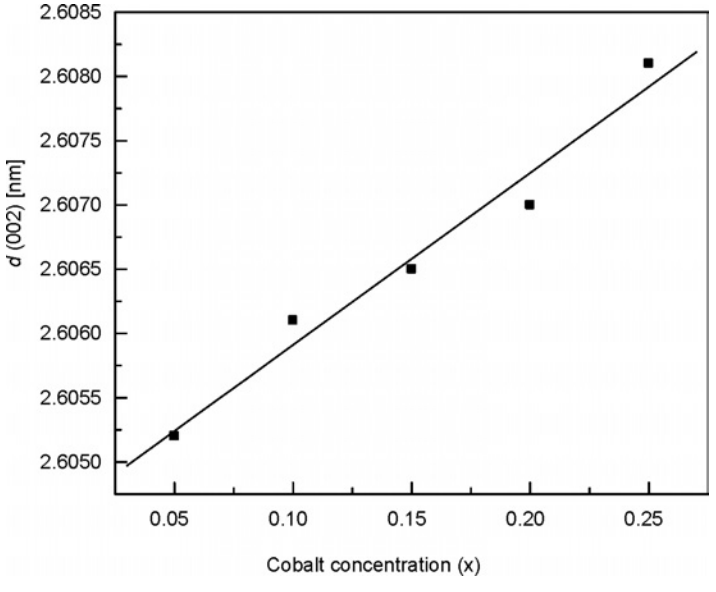

Fig. 5. Dependence of c-axis lattice constants (d(002) values) on Co content in $Zn_{1-x}Co_xO$:Al films

The interplanar spacing *d* in the direction of *c* axis (002) in function of Co content is shown in Fig. 5. It is seen from the figure that the *d* values increase upon increase of the Co content up to 25% in accordance with Vegard's law. Thus up to 25% Co lies within solubility limit of substitution. Cobalt exists in the divalent state, and high solubility of Co is attributed to the ionic radius of Co^{2+} (72 pm) being similar to that of Zn^{2+} (74 pm) in the tetrahedral coordinated structure. Ueda et al. [13] showed a similar dependence of *d* on Co concentration for PLD grown ZnO films co-doped with Co and 1% of Al.

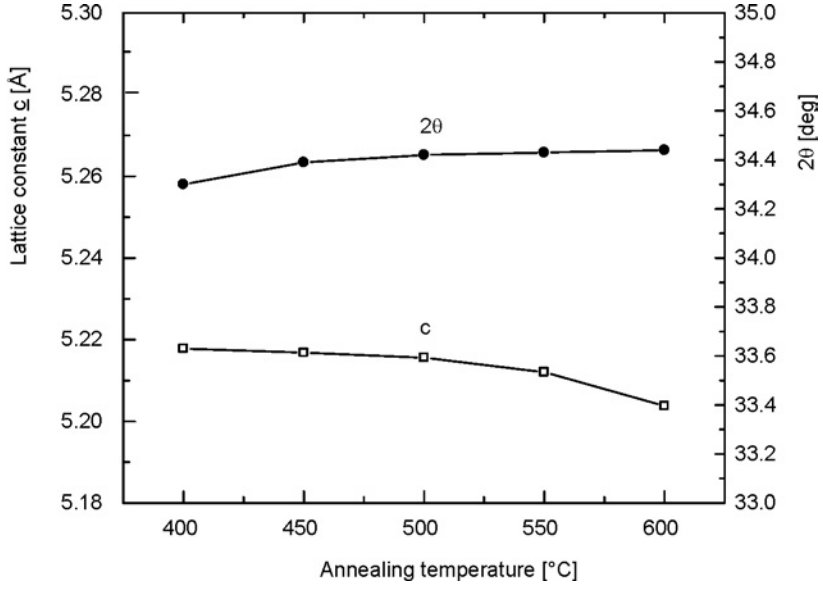

Fig. 6. Effect of annealing temperature on the lattice constant *c* and diffraction angle 2θ of (002) peak of $Zn_{0.94}Co_{0.05}Al_{0.01}O$ films

Figure 6 shows the variation of the diffraction angle 2θ of (002) peak and lattice constant *c* with the annealing temperature. A shift in the (002) peak 2θ position to a slightly higher value is observed with the increase in the annealing temperature and it approaches near to the powder value of 34.44° at 600 °C. It is important to note that the value of the *c* lattice parameter for the as deposited $Zn_{0.95}Co_{0.05}O$:Al films is large in comparison to unstressed bulk value of 5.207 Å [12]. This is consistent with other works reporting increase of the *c* axis lattice constant with increase in Co concentration in doped ZnO films [13]. A large value of the lattice constant for the as grown and annealed compared to the unstressed powder value shows that the unit cell is elongated along the *c* axis, and compressive forces act in the plane of the film. This indicates a reduction in the tensile stress with annealing, which may be due to the large coefficient of linear expansion of films in comparison with the glass substrate with increase in the annealing temperature. The higher value of *c* at 400 °C shows that the unit cell is elongated along the *c* axis, and compressive forces act in the plane of the films.

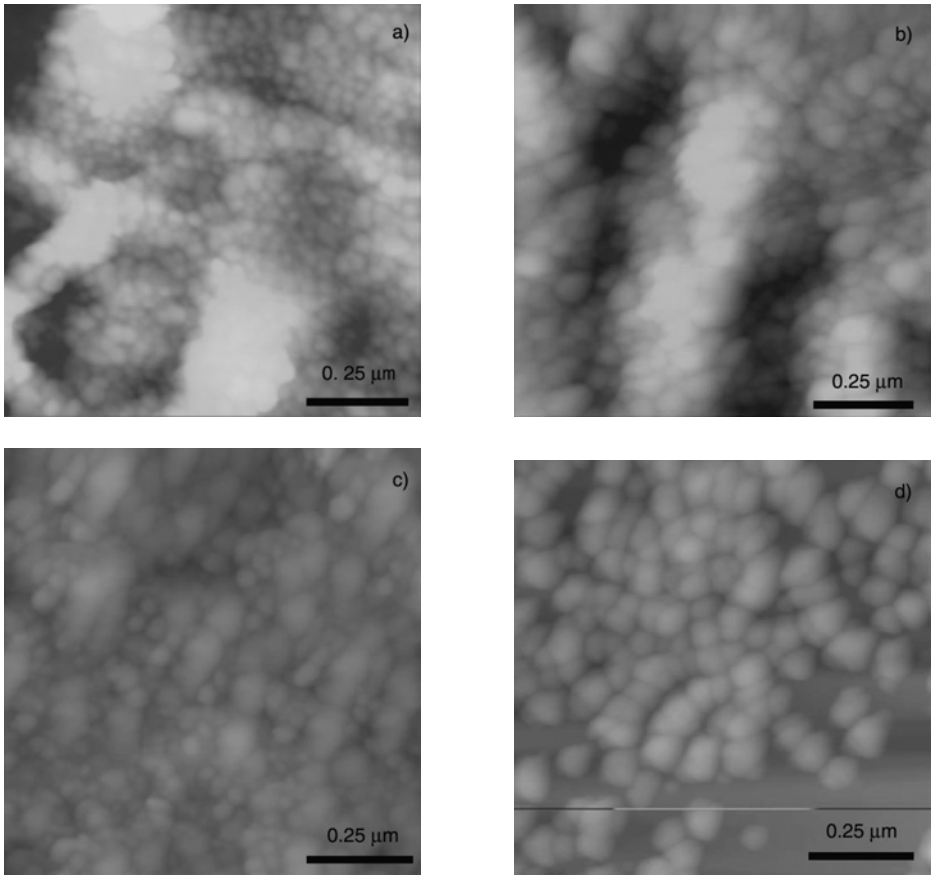

Fig. 7. AFM images of $Zn_{0.94}Co_{0.05}Al_{0.01}O$ films annealed at: a) 450 °C, b) 500 °C, c) 550 °C, d) 600 °C

Figure 7 shows the AFM graphs of the surfaces of deposited films for Co dopant concentration $x = 0.05$, annealed at various temperatures. The formation of a fine surface having uniformly distributed grains and gradual increase in grain size is clearly observed in films annealed at a higher temperature of 600 °C. The minimum average roughness 5 nm, which was obtained for the film grown at 600 °C, originates from the craters between the grain boundaries and the contribution of the substrate roughness to the first layer of the film. These values of grain size are also listed in Table 1. It is seen from the table that the value of grain size correspond well with the values obtained from XRD measurements by the Scherrer–Warren formula

$$t = \frac{0.94\lambda}{\beta \cos\theta}$$

where t is the crystallite size in nm, λ is wavelength in nm, β is the FWHM of the (002) peak and θ is the angle of the (002) peak.

3.3. Transmittance

Figure 8 shows optical transmission spectra of $Zn_{1-x-y}Co_xAl_yO$ films annealed at 600 °C and recorded in the wavelength region of 300–1000 nm for various Co contents

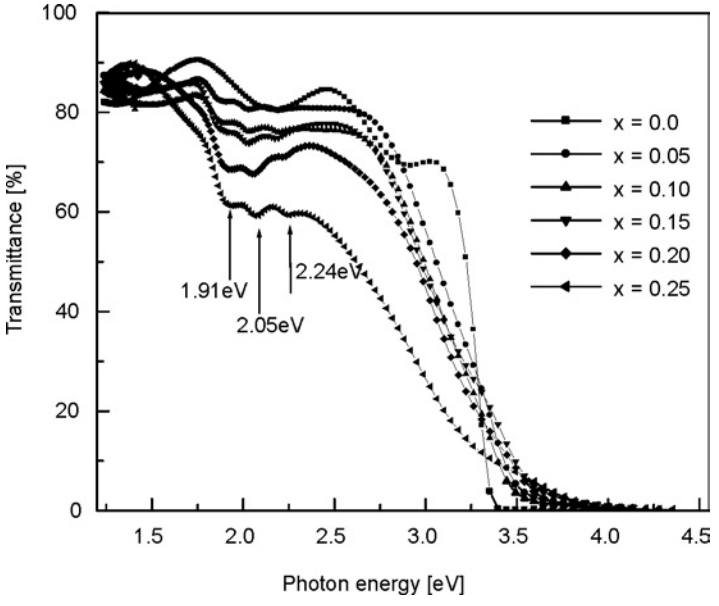

Fig. 8. Optical transmission spectra of sol-gel deposited $Zn_{1-x}Co_xO$:Al films recorded at room temperature for various Co contents x and 1 at. % of Al

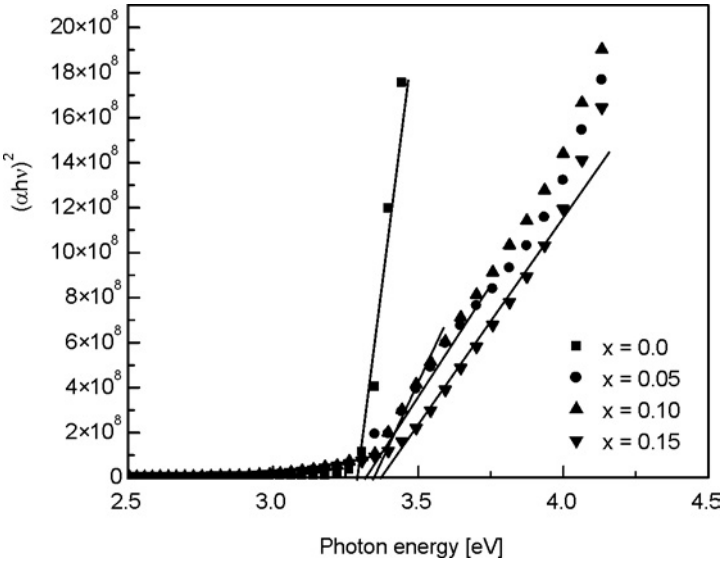

Fig. 9. Optical absorption spectra of $Zn_{1-x}Co_xO$:Al films

x = (0–0.25). The transmission is found to be maximum for the sample without Co and decreases with the increase in Co concentration. The fundamental edge for thin films is located at 3.26 eV. The decrease in optical transmission is associated with the loss of light due to (i) oxygen vacancies and (ii) scattering at grain boundaries. The increase in scattering centres due to increased number of grain boundaries with an increase in Co dopant content may be responsible for the loss of transmission. A decrease in grain size and thereby increase in grain boundaries in $Zn_{1-x-y}Co_xAl_yO$ film upon increasing Co concentration has been observed. We attribute absorption bands at about 1.9, 2.05, 2.24 eV to the d-d transitions of tetrahedral coordinated Co^{2+} which are assigned to $^4A_2(F) \rightarrow {}^2E(G)$, $^4A_2(F) \rightarrow {}^4T_1(P)$, $^4A_2(F) \rightarrow {}^2A_1(G)$, transitions in the high spin state of $Co^{2+}(3d^7)$, respectively [17]. The figure shows clearly that intensities of the absorption bands increase with Co content, indicating consistent incorporation of Co^{2+} ions into ZnO lattice in the valence state of 2+ by the sol-gel process.

The band gap energy E_g was determined by using formula the $(\alpha h\nu)^2 = B(E - E_g)$ and plotting the curves $(\alpha h\nu)^2$ vs. E, where α is the absorption coefficient, E is the photon energy and B is a constant. These curves are shown in Fig. 9.

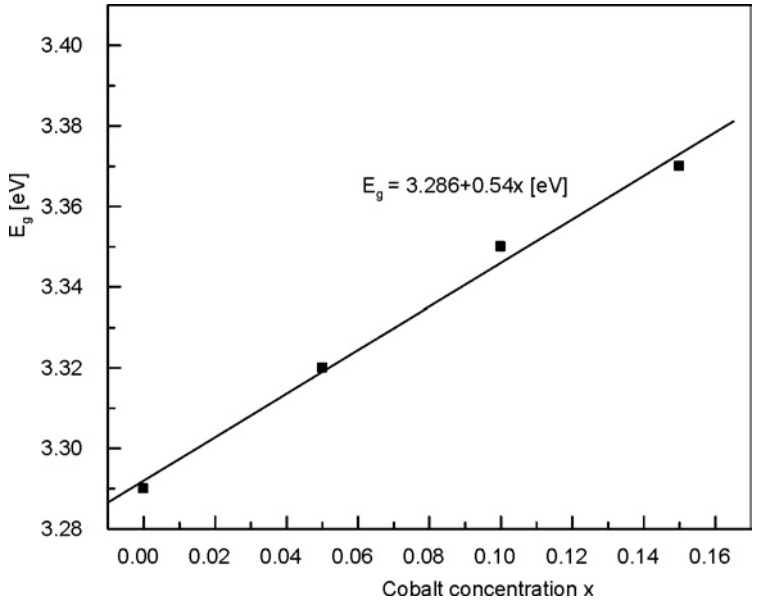

Fig. 10. Dependence of band gap (E_g) of $Zn_{1-x}Co_xO$:Al films on the Co content

Figure 10 shows dependence of E_g on the Co content. The variation of E_g with Co content was found to follow the relationship $E_g = (3.286 + 0.54x)$ eV. It means that the extrapolated value 3.286 eV of the band gap for $x = 0$ corresponds to the undoped ZnO films. A characteristic difference in the absorption edge has been observed with Co incorporation in ZnO. The sharp absorption edge observed for pure ZnO sample at 3.18 eV was found to start shifting vigorously with an increase in Co concentration.

This blue shift in the optical band gap is also observed in ZnMnO [21], ZnMgO [22]. Kim et al. [17] also showed similar blue shift in PLD deposited $Zn_{1-x}Co_xO$ films. He showed variation of E_g with x up to 30% of Co content.

3.4. Electrical properties

The influence of the annealing temperature from 400 °C to 600 °C on the resistivity ρ, carrier concentration n and Hall mobility μ_H of $Zn_{1-x-y}Co_xAl_yO$ films containing 5 at. % of Co with 0 and 1 at. % of Al is shown in Figs 11 and 12, respectively. It is seen from the figures that the carrier concentration has increased as a result of Al doping. This increase is attributed to the substitutional doping of Al^{3+} at Zn^{2+} sites creating one extra free electron in the conduction band [23]. The major conduction was confirmed to be n-type by the Hall measurements and films exhibited semiconducting behaviour. The resistivity is found to decrease with increasing T_a. The decrease in resistivity with higher temperature is due to an improvement in crystallinity.

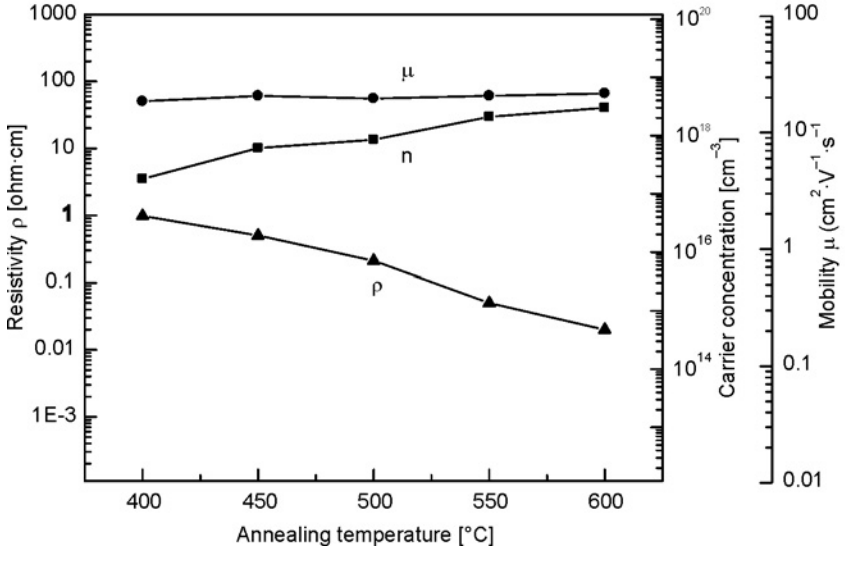

Fig. 11. Resistivity, electron concentration, and Hall mobility in function of annealing temperature for $Zn_{1-x-y}Co_xAl_yO$ ($x = 0.05$, $y = 0$)

The mobility is found to increase upon increasing T_a, which is also due to improvement in the crystalline structure. Figure 12 shows that the value of mobility ranges from 17 to 43.5 cm^2/(V·s) [13]. The carrier concentration is found to increase with increase in T_a. The maximum carrier concentration obtained was 10^{21} cm^{-3} at 600 °C for $Zn_{0.94}Co_{0.05}Al_{0.01}O$. The increase in grain size means a decrease in grain boundaries (lesser scattering area) and pores in the annealed films as compared to the as deposited films. Thus the number of electron trap states reduces and hence the car-

rier concentration increases. Xu et al. [12] declared carrier concentration to vary from 10^{20} to 10^{21} cm^{-3}) for ZnO films co-doped with 5% Co and 1% Al by PLD.

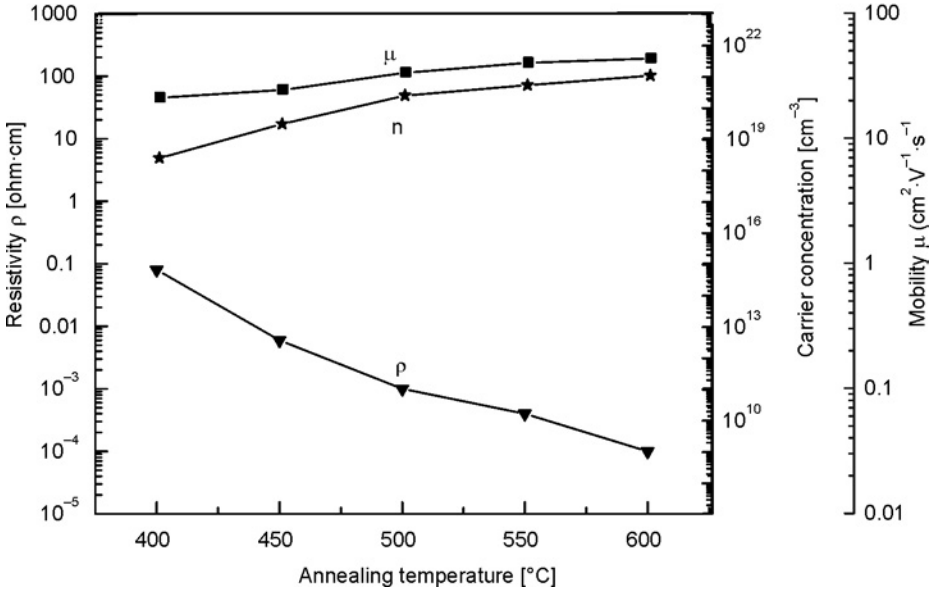

Fig. 12. Resistivity, electron concentration, and Hall mobility in function of annealing temperature for $Zn_{1-x-y}Co_xAl_yO$ (x = 0.05, y = 0.01)

3.5. Magnetic properties

Figure 13 shows magnetoresistance (MR) at 77 K with magnetic field applied perpendicular to the film plane. MR helps to reveal the nature of fundamental exchange coupling in the DMS. It can be explained in terms of three different competitive mechanisms such as sp-d exchange [24], weak localization [25], spin disorder scattering [26]. Negative MR is due to scattering of spin polarized charge carriers at isolated magnetic impurities. Positive MR can be well understood by the dominance of sp-d exchange interaction over the weak localization effect and spin disorder scattering with increase in Co content.

Films without Co give negative MR as the applied field will align the spins and thus reduce the scattering. Positive MR is seen in Co doped ZnO films. It was found that positive MR increases with increase in Co content.

The magnetic properties were measured with a SQUID magnetometer at room temperature for $Zn_{1-x}Co_xAl_{1-x-y}O$ (x = 0, 0.05, 0.10, 0.15) films. The magnetic field is applied parallel to the film plane. Diamagnetic and/or paramagnetic signals of the glass substrate were detected. Figures 14 and 15 show hysteresis loops for various concentrations of Co. The ferromagnetism is clearly shown by the coercivity and remanence. The remanence of the films for higher concentrations is higher than for

lower concentrations of Co. The coercive field for x = 0.15 was 10 mT and the estimated saturation magnetization was 8×10^{-9}Am^2 from the field dependence of magneti-

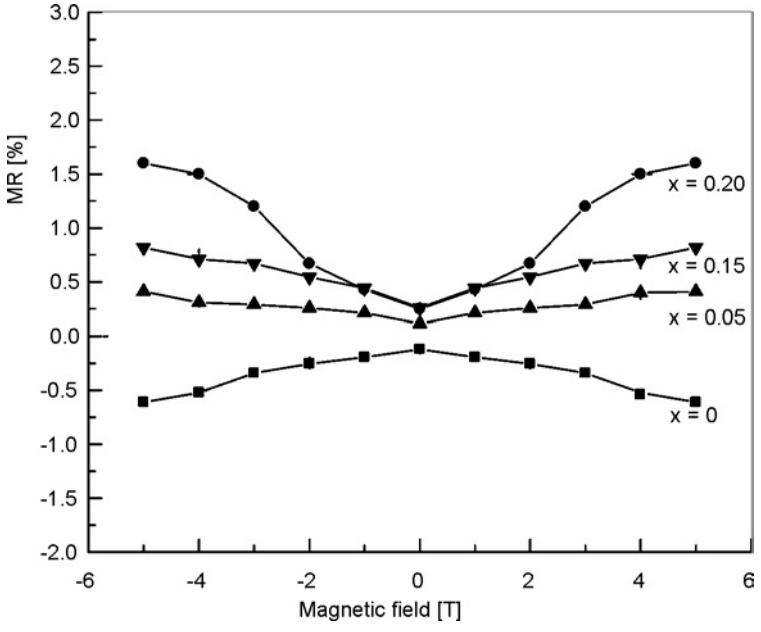

Fig. 13. Magnetoresistance curves for various concentrations of Co at 77 K

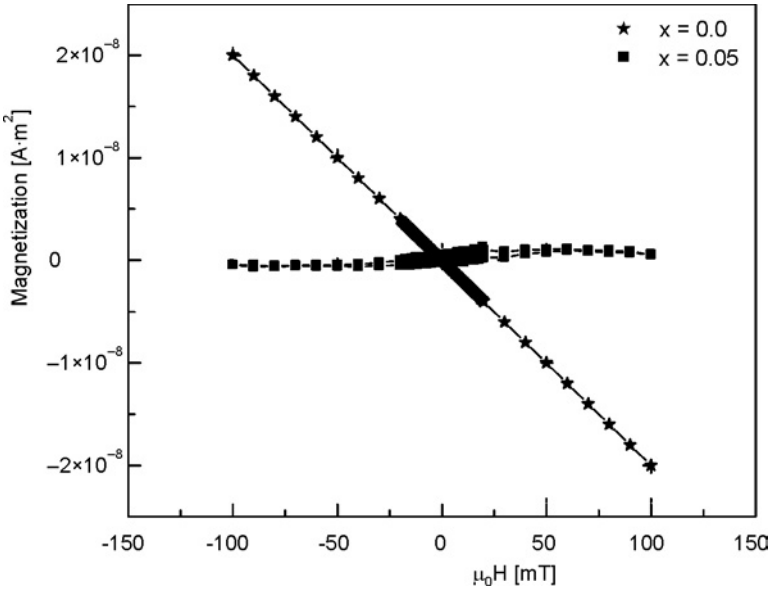

Fig. 14. Magnetization curves measured in plane
for $Zn_{1-x}Co_xO$:Al films (x = 0.0 and 0.05)

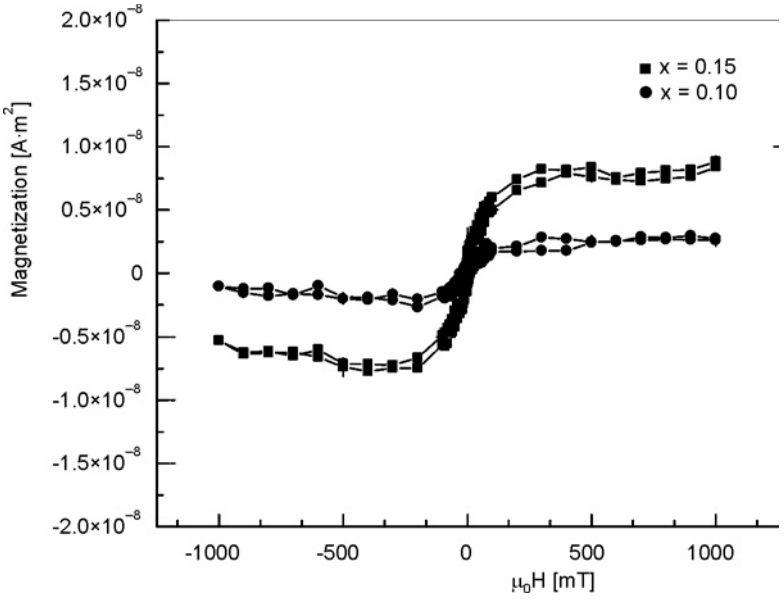

Fig. 15. Magnetization curves measured in plane for $Zn_{1-x}Co_xO$:Al films (x = 0.1 and 0.15)

zation (M–H) curve. The saturation field was around 284 mT. In absence of Co dopant, ZnO film exhibits diamagnetic behaviour and Co doped films exhibits hysteresis loops.

4. Conclusion

$Zn_{1-x}Co_xO$ ($0 < x \leq 0.25$) films with 1 at. % of Al doping on Corning glass have been prepared by the sol-gel process. XRD and UV-VIS-NIR spectroscopy results confirm the substitutional doping of Co in the ZnO wurtzite lattice. High conductivity and good transparency were obtained for $Zn_{0.94}Co_{0.05}Al_{0.01}O$ film annealed at 600 °C. The observed positive MR is the representative of DMS nature of the Co doped films. SQUID measurements have further confirmed the ferromagnetic nature of these films. The coercivity and remanence of the films are found to increase with Co concentration.

Acknowledgements

The authors are grateful to Dr. Stephen Weyeneth of the Physics Institute, University of Zürich, Switzerland for the SQUID measurements and discussion. The financial support from the DST, New Delhi for the Solidspec 3700 UV-VIS-NIR spectrophotometer is also gratefully acknowledged.

References

[1] WOLF S.A., AWSCHALOM D.D., BUHRMAN R.A., DAUGHTON J.M., VON MOLNAR S., ROUKES M.L., CHTCHELKANOVA A.Y., TREGER D.M., Science, 294 (2001), 1488.
[2] PRINZ G.A., Science, 282 (1998), 1660.
[3] PEARTON S.J., ABERNATHY C.R., OVERBERG M.E., THALER G.T., NORTON D.P., THEODOROPOULOU N., HEBARD A.F., PARK Y.D., REN F., KIM J., BOATNER L.A., J. Appl. Phys., 93 (2003), 8979.
[4] PRELLIER W., FOUCHET A., MERCEY B., J. Phys. Condes.Matter, 15 (2003), R1583.
[5] *Spin Electronics*, M. Ziese, M.J. Thornton (Eds.), Springer, Berlin, 2001.
[6] BUHRMAN R., WTEC Spin Electronics Workshop, Washington, DC, 2 Nov. 2001 (Viewgraphs from the presentation are available at http://www.wtec.org/spin/views/buhrman/index.htm).
[7] OHNO H., Science, 281 (1998), 951.
[8] NAJMUL A.M., SUGAHARA S., TANAKA M., Phys. Rev., B67 (2003), 241308.
[9] YANG S.G., PAKHOMOV A.B.,.HUNG S.T, WONG C.Y., IEEE Trans. Magn., 37 (2002), 2877.
[10] SATO K., KATYAMA-YOSHIDA H., Jpn. J. Appl. Phys., 40 (2001), L334.
[11] DIETL T., OHNO H., MATSUKURA F, CUBERT J, FERRAND D., Science, 287 (2000), 1019.
[12] XU X.H., BLYTHE H.J., ZIESE M., BEHAN A.J., NEAL J.R., MOKHTARI A., IBRAHIM R.M., FOX A.M., GEHRING G. A., New J. Phys., 8 (2006), 135.
[13] UEDA K., TABATA H., KAWAI T., Appl. Phys. Lett., 79 (2001), 988.
[14] HYEON-JUN LEE, SE-YOUNG JEONG, CHAE RYONG CHO, CHUL HONG PARK, Appl. Phys. Lett., 81 (2002), 4020.
[15] CHO W.K., CHOO Y.M, KIM H., KIM D., IHM Y., Appl. Phys. Lett., 80 (2002), 3358.
[16] RAMACHANDRAN S., TIWARI A., NARAYAN J., Appl. Phys. Lett., 84 (2004), 5255.
[17] KIM J.H., KIM H., KIM D., IHM Y. E. AND CHO W.K., J. Appl. Phys., 92 (2002), 6066.
[18] PARK J.H., KIM M.G., JANG H.M., RYU S., KIM Y.M., Appl. Phys. Lett., 84 (2004), 1338.
[19] BELGHAZI Y., SCHMERBER G., COLIS S., REHSPRINGER J.L., DINIA A., BERRADA A., Appl. Phys. Lett., 89 (2006), 122504.
[20] CULLITY B.D., *Elements of X-Ray Diffraction*, Addison-Wesley, Reading, MA, 1978.
[21] FUKUMURA T., JIN Z., OHTOMO A., KOINUMA H., KAWASAKI M., Appl. Phys. Lett., 75 (1999), 3366.
[22] OHTOMO A., KAWASAKI M., KOIDA T., MARUBUCHI K., SEGAWO Y., Appl. Phys. Lett., 72 (1998), 2466.
[23] SAGAR P., KUMAR M., MEHRA R.M., Mater. Sci.-Poland, 23 (2005), 685.
[24] SAWICKI M., DIETL T., KOSSUT J., IGALSON J., WOJTOWICZ T., PLESIEWICZ W., Phys. Rev. Lett., 56 (1986), 508.
[25] PIKUS F.G., PIKUS G.E., Solid State Commun., 100 (1996), 95.
[26] TOYOZAWA Y., J. Phys. Soc. Japan, 17 (1962), 986.

Received 25 September 2007
Revised 19 November 2007

Materials Science-Poland, Vol. 26, No. 3, 2008

Effect of Ni addition on the microstructures of melt-spun CuCr ribbons

M. YU[1], Y. WANG[1], Y. WANG[1, 2*], Z. SUN[2]

[1]Institute of Materials Science and Technology, Taiyuan University of Science and Technology, Taiyuan 030024. P. R. China

[2]School of Science, Xi'an Jiaotong University, Xi'an 710049, P. R. China

The microstructures and resistivities of melt-spun Cu75Cr25 and Cu(75–*x*)Cr25Ni*x* (*x* = 1 or 3 wt. %) ribbons were studied. The size of the Cr-rich phase from liquid phase separation in the Cu75Cr25 microstructure can be decreased from the micrometer-scale to about 250 nm by using melt spinning. After annealing at 600 °C for 3 h, the resistivity of Cu75Cr25 ribbon can meet the needs of contact. On the melt-spun base, alloying by Ni could further decrease the size of the Cr-rich phase from 250 nm to about 150 nm. However, when the Ni content is higher than or equal to 3%, the resistivity of annealed Cu75–*x*Cr25Ni*x* ($x \geq 3$) ribbons is too high to be used by the medium-voltage vacuum interrupters. For nano-grained CuCr alloys, its lower arc chopping current is advantageous to the use of contact and the circuitry protect, its long arc trace route and high velocity of spot direction motion could mitigate the partial ablate of cathode surface and the lifetime of contact could be prolonged.

Key words: *microstructure; CuCr alloys; contact, melt spinning; resistivity*

1. Introduction

The contact material based on CuCr alloys containing 20–50 wt. % of Cr has been widely investigated because it is a dominating contact material used in medium-voltage vacuum interrupters. To improve its electric properties, refining the Cr-rich phase in its microstructure is an important subject [1–4].

Melt spinning is nowadays the most common method of rapid solidification. It is capable of refining the microstructure, extending the solid solubility limits, forming a metastable phase, etc. A number of studies [5–12] have been undertaken to investigate the microstructures of rapidly solidified metals. However, it has not been well used in the research of refining the microstructure of CuCr alloys containing ca. 20–50

*Corresponding author, e-mail: Wyheyj@163.com

wt. % of Cr. In these alloys, the liquid phase separation of undercooled CuCr melts will occur in a rapid solidification process. In this paper, the abbreviation Cu*x*Cr*y*Ni*z* will stand for the composition of an alloy containing *x*, *y* and *z* wt. % of Cu, Cr and Ni, respectively. Although the liquid phase separation is disadvantageous to refine the Cr-rich phase, its size can be still decreased to about 300 nm in the microstructure of Cu70Cr30 alloys by melt-spinning with about 10^6 K/s cooling rate [13–16]. Besides rapid solidification, alloying is another general way to refine the microstructure of alloys, so a little work has been done on the influence of Ni addition to the microstructure of melt-spun Cu75Cr25 alloys.

2. Experimental

Pure (> 99.95%) Cu, Cr and Ni were used to prepare CuCrNi alloys by the arc-melting technique. 10 g of the material was inserted into a quartz tube. When the material was heated by high frequency induction to the required temperature, the ribbon was prepared by liquid quenching on a single roller melt spinning under the pressure of 0.5 atm Ar. The velocity of the cooling roller was 33 m/s, the calculated cooling rate of ribbon was about 10^6 K/s. The dimensions of prepared ribbons were about 3 mm wide and 25–40 μm thick. Under this condition, the maximal undercooling of ribbon was about 400–450 K [7, 11].

Some melt-spun ribbons were annealed in a vacuum furnace at 600 °C for 3 h. The microstructures of samples were analyzed by a Hitachi H-800 transmission electron microscope (TEM). The foil specimen for TEM was prepared by a twin-jet thinning device. The resistivity of ribbon was measured by the four point probe method.

3. Results

3.1. The microstructures of melt-spun Cu75Cr25 ribbons

The microstructure of a melt-spun Cu75Cr25 ribbon is shown in Fig. 1a. A spherical particle marked by an arrow is the Cr-rich phase from liquid phase separation [13]. The diameters of the Cr-rich phases in Fig. 1a are about 250 nm. By increasing the cooling rate, the size of the Cr-rich phase from liquid phase separation in the melt-spun Cu75Cr25 microstructure can be refined from the micron-scale to nanoscale [13]. After annealing at 600 °C for 3 h, the Cr-rich phase from liquid phase separation did not obviously grow up; the diameters of the Cr-rich phase in Fig. 1b are still about 250 nm. The result indicates that the Cr-rich phase in the melt-spun Cu75Cr25 microstructure have a good invariance. Even if the material is repeatedly heated by arc in the work process of contact, the melt-spun Cu75Cr25 microstructure would not transform obviously which is advantageous to keep the electric properties of a contact. On

the other hand, by contrasting Fig.1a and Fig.1b, the precipitates come forth in the Cu matrix after annealing which mainly causes that the resistivity of Cu75Cr25 ribbons decreases from 16.43 μΩ·cm in the melt-spun state to about 4.53 μΩ·cm in the annealed state (The resistivity of contact should be lower than 5μΩ·cm [3, 4]).

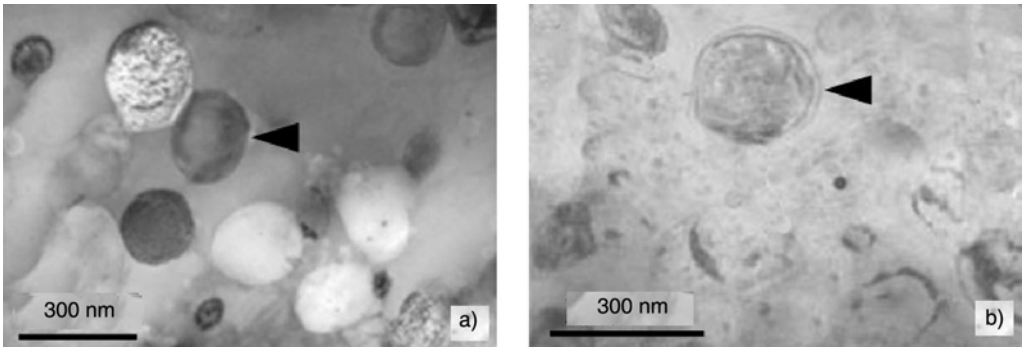

Fig. 1. The microstructure of melt-spun Cu75Cr25; ribbons: a) as-quenched,
b) annealed at 600 °C for 3 h. The arrows point to the Cr-rich phase from liquid phase separation

3.2. The microstructures of melt-spun Cu74Cr25Ni1 ribbons

Figure 2a shows the microstructure of a melt-spun Cu74Cr25Ni1 ribbon. The diameter of the Cr-rich phase marked by an arrow is about 200 nm (i.e., is smaller than 250 nm). On the melt-spun base, alloying by 1 wt. % of Ni could further decrease the size of the Cr-rich phase from liquid phase separation. After addition of Ni, the microstructure of Cu75Cr25 alloys is not changed; the diameters of the Cr-rich phase in Fig. 2b are also about 200 nm after annealing at 600 °C for 3 h. Adding 1% of Ni results in that the resistivity of annealed Cu74Cr25Ni1 ribbon is increased to 4.96 μΩ·cm. The reason for the increase of resistivity may be that the concentration of the solute in Cu phase was increased by Ni addition.

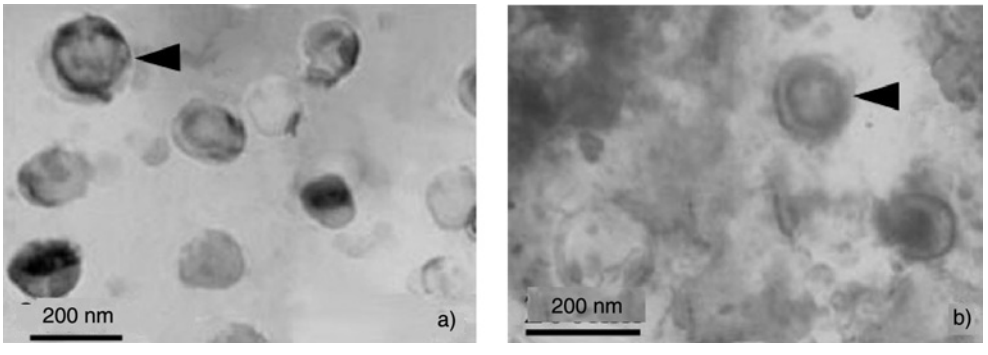

Fig. 2. The microstructure of melt-spun Cu74Cr25Ni1 ribbons: a) as-quenched,
b) annealed at 600 °C for 3 h. The arrows show the Cr-rich phase from liquid phase separation

3.3. The microstructures of melt-spun Cu72Cr25Ni3 ribbons

The microstructure of melt-spun Cu72Cr25Ni3 ribbon is shown in Fig. 3a. The Cr-rich phase from liquid phase separation in Fig. 3a is refined to the size smaller than 150 nm. When the ribbon was annealed at 600 °C for 3 h, the Cr-rich phase in Fig. 3b did not grow up much. Upon increase of Ni content in Cu75Cr25 alloys, the alloying effect becomes more remarkable. However, the resistivity of annealed Cu72Cr25Ni3 ribbons is about 13 μΩ·cm, which may be too high to be used by the medium-voltage vacuum interrupters.

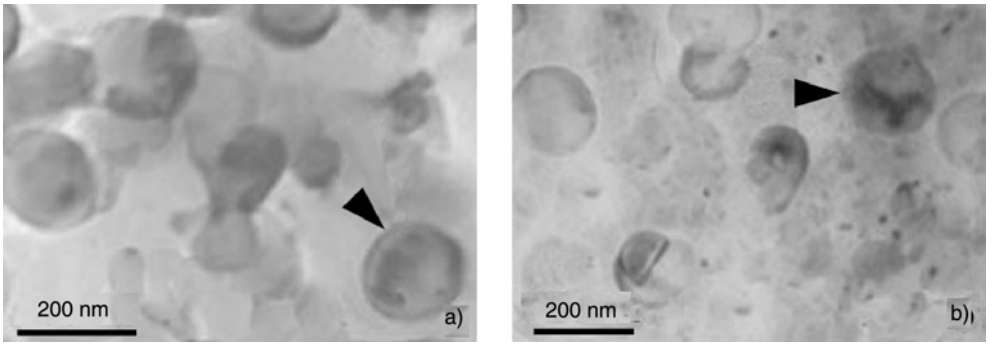

Fig. 3. The microstructure of melt-spun Cu72Cr25Ni3 ribbons: a) as-quenched, b) annealed at 600 °C for 3 h. The arrows show the Cr-rich phase from liquid phase separation

4. Discussion

The arc chopping current of a CuCr contact is an important parameter determining its applicability in service. The arc between electrodes will gradually crush out and the current in a circuit will become smaller and smaller when a breaker is turned off. The current in the circuit is called the arc chopping current when the arc crushes out completely, but the current does not descend to zero. The arc chopping current will arouse an overvoltage by the inductance in a circuit. The overvoltage is very disadvantageous to the electric system. In general, the higher the vapour pressure of contact materials, the lower is the arc chopping current.

The arc chopping currents of melt-spun Cu75Cr25 and Cu74Cr25Ni1 are 1.8 A and 1.6 A, respectively, much lower than that of coarse-grained Cu75Cr25 alloys, 3.6 A. The interfacial energy in nano-grained CuCr alloys is higher than that in coarse-grained CuCr ones, thus the vapour pressure of nano-grained CuCr alloys is also higher than that of coarse-grained CuCr alloys, which results in that the nano-grained CuCr alloys have a lower arc chopping current.

The arc spot stays in a small area with a diameter not exceeding 1 mm on the surface of a coarse-grained Cu75Cr25 cathode. For nano-grained CuCr alloys, the trace of arc spot is in a sub-direction which is different with the random walk pattern of

coarse-grained Cu75Cr25 cathode, the arc trace route is about 3 mm long and the velocity of spot direction motion is about 60 m/s [2] which could mitigate partial ablation of the cathode surface and the lifetime of contact may be prolonged. The trace of arc spot and its effects on the contact characteristics have been studied in detail by Yang [2]. In a word, the decrease of sizes of the Cr-rich phase in the microstructure of Cu75Cr25 alloys could improve the electric properties of its contact.

5. Conclusions

By using melt spinning, the size of the Cr-rich phase from liquid phase separation in the Cu75Cr25 microstructure can be decreased from the micron-scale to about 250 nm, which reveals that by increasing the cooling rate of the solidification process, the microstructure of Cu75Cr25 alloy can be markedly refined. After annealing at 600 °C for 3 h, the resistivity of Cu75Cr25 ribbon can meet the technical needs for a contact.

On the melt-spun base, alloying by Ni could further decrease the size of the Cr-rich phase from liquid phase separation, and the higher Ni addition, the smaller becomes the size of the Cr-rich phase. However, when the Ni addition is higher than or equal to 3 wt. %, the resistivity of annealed Cu72Cr25Ni3 ribbons is too high to be used by the medium-voltage vacuum interrupters.

For nano-grained CuCr alloys, its lower arc chopping current is advantageous for the use of contact and the circuitry protect, its long arc trace route and high velocity of spot direction motion could mitigate a partial ablation of the cathode surface and the lifetime of contact could be prolonged.

Acknowledgement

The authors would like to thank the National Science Foundation of China (grant 50371066) for their financial support.

Reference

[1] ZHIMAO YANG, QIULI ZHANG, QINGFENG WANG, CHENGYU ZHANG, BINGJUN DING, Vacuum, 81 (2006), 545.
[2] ZHIMAO YANG, QIULI ZHANG, CHENGYU ZHANG, YUE SUN, BINGJUN DING, Phys. Lett. A, 353 (2006), 98.
[3] RIEDER W.F., SCHUSSEK M., GLATZLE W., KNY E., IEEE Trans. CHMT, 12 (1989), 273.
[4] WANG Y., DING B., IEEE Trans. CPMT, 22 (1999), 467.
[5] TENWICK M.J., DAVIES H.A., Mater. Sci. Eng., 98 (1988), 543.
[6] ZHONGHUA ZHANG, XIUFANG BIAN, YAN WANG, XIANGFA LIU, J. Mater. Sci., 37 (2002), 4473.
[7] MASLOV V.V., NOSENKO V.K., J. Mater. Sci., 37 (2002), 4663.
[8] TIANYI CHENG, LÖSER W., LEONHARDT M., J. Mater. Sci., 33 (1998), 4365.
[9] ZHANG LIN, WU YOUSHI, BIAN XIUFANG, XING ZHINA, J. Mater. Sci. Lett., 18 (1999), 1969.
[10] NAGARAJAN R., MANJINI S., CHATTOPADHYAY K., AOKI K., J. Mater. Sci., 32 (1997), 6021.
[11] FENG LIU, GENCANG YANG, XUEFENG GUO, J. Mater. Sci., 36 (2001), 3607.

[12] COOPER K.P., JONES H.N., J. Mater. Sci., 36 (2001), 5315.
[13] YOUHONG WANG, XIAOPING SONG, ZHANBO SUN, XUAN ZHOU, JUAN GUO, Mater. Sci.-Poland, 25 (2007), 199.
[14] YOUHONG WANG, ZHANBO SUN, XUAN ZHOU, SONG XIAOPING, Rare Metal Mater. Eng., 35 (2006), 1289.
[15] SUN ZHANBO, WANG YOUHONG, GUO JUAN, Trans. Nonferrous Metals Soc. China, 16 (2006), 998.
[16] WANG YOUHONG, SUN ZHANBO, SONG XIAOPING, Chinese J. Nonferrous Metals, 15 (2005), 1045.

Received 23 December 2006
Revised 28 April 2008

Materials Science-Poland, Vol. 26, No. 3, 2008

First-principles plane-wave pseudopotential method calculations for Cu alloying Mg_2Ni hydride

J. ZHANG[1, 2], D.W. ZHOU[1*], P. PENG[2], J.S. LIU[2]

[1]State Key Laboratory of Advanced Design and Manufacturing for Vehicle Body, Hunan University, Changsha 410082, China 1

[2]College of Materials Science and Engineering, Hunan University, Changsha 410082, China 2

Energetics and electronic structures have been calculated based on the first-principles plane-wave pseudopotential method for Cu alloying Mg_2Ni phases and the corresponding hydrides. These calculations show that the $Mg_2Ni(II)''_{1-x}Cu_x$ (x = 1/3) phase has the highest structural stability and Cu alloying Mg_2Ni hydride benefits the improvement of the dehydrogenating properties of the system, which is also well explained through the density of states (DOS) and the charge distributions of Mg_2Ni phases and Mg_2Ni hydrides with and without Cu alloying.

Key words: *Mg_2Ni phase; heat of formation; plane-wave pseudopotential theory; dehydrogenating properties; electronic structure*

1. Introduction

Magnesium and its alloys have been considered the most promising hydrogen storage materials due to their high hydrogen storage capacity, light weight and low cost. However, a slow hydriding and dehydrogenating kinetics and high dissociation temperature limit their practical application for hydrogen storage. In recent years, Mg_2Ni (A_2B)-type hydrogen storage alloys have been extensively researched as potential candidates for Ni/MH cathode materials. To improve the hydriding and dehydrogenating kinetics of Mg_2Ni alloy, partial component substitution has been confirmed to be an efficient method. For example, a partial substitution of Al, V, Ti, Zr for Mg at A positions [1–3] or Cu, V, Fe, Co, Mn, Cr for Ni at B positions [4–7] in Mg_2Ni phase will reduce the structural stability of the hydride (Mg_2NiH_4) and decrease its dissociation temperature. Among these substitutions, the corresponding $Mg_2Ni_{1-x}Cu_xH_4$ ($x \leq 0.4$)

* Corresponding author, e-mail: ZDWe_mail@yahoo.com.cn

hydride with the partial substitution of Cu for Ni at B positions in Mg_2Ni phase has excellent dehydrogenating properties.

Nowadays, considerable experimental and theoretical investigations have been performed on studying the dehydrogenating properties of Cu alloying Mg_2Ni hydride. Dehouche et al. [5] found that the heat of formation (53.2 kJ/mol) of the Mg_2Ni hydride with Cu alloying is decreased compared to that of the hydride without Cu alloying (64.5 kJ/mol), meanwhile, the dissociation temperature of the system is reduced significantly. Simicic et al. [6] synthesized $Mg_2Ni_{0.75}Cu_{0.25}$ and $Mg_2Ni_{0.6}Cu_{0.4}$ alloys by mechanical milling of Mg_2Ni with different contents of Cu, which remarkably improves hydriding and dehydrogenating kinetics of pure Mg_2Ni at low temperature below 473 K. Yang. et al. [7] fabricated $Mg_2Ni_{0.75}M_{0.25}$ (M = Ti, Cr, Mn, Fe, Co, Ni, Cu and Zn) alloys by milling diffusion method. They found that the structural stability, dissociation enthalpy and dissociation temperature of the corresponding hydrides are all decreased with the increasing unit volume of these alloys, and the effect of Cu on Mg_2Ni hydride is proved to be the most promising. All above experiments have been focused on destabilizing the phase structure of Mg_2Ni hydride by Cu alloying to decrease the dissociation temperature of this system. Whereas, due to the complexity of crystal structure for Mg_2Ni hydride (Mg_2NiH_4) and the uncertainty of Cu occupying sites in Mg_2Ni phase, it becomes difficult for the dehydrogenating properties of Cu alloying Mg_2Ni hydride to be further experimentally investigated. Garcia et al. [8] calculated the electronic structure of the Mg_2Ni hydride (Mg_2NiH_4) by the *ab initio* method. They determined the occupying sites of H atoms in the structure, and then, the bonding types of different atoms were deduced according to the charge distributions in Mg_2NiH_4. They suggested that the $[NiH_4]^{4-}$ anion exists in the form of covalent bonding interaction between H and Ni, while there are electrovalent bonding interaction between $[NiH_4]^{4-}$ anion and Mg^{2+} cation. Therefore, Mg_2NiH_4 with the antifluorite structure possesses a relatively stable phase structure. Takahashi et al. [9] calculated the electronic structure of Mg_2NiH_6 cluster model alloyed by 3d transition metal elements M (M = V, Cr, Fe, Co, Cu, Zn) by using DV-Xα method. It was found that the bonding interaction between Ni and H is stronger than that between Mg and H, and the stability of the hydride directly lies on the bonding interactions between Ni and Mg, Ni and H. After the partial substitution of different alloying elements M for Ni, it was noted that the reduced structural stability of the Mg_2Ni hydride can be ascribed to the weakened bonding interaction between M and Mg. In addition, the negative heat of formation of the system with the substitution of Cu for Ni is the smallest, which means that the Cu substitution makes the hydride become the most unstable. Recently, Jasen et al. [10] calculated the electronic properties of Mg_2NiH_4 monoclinic phase by using a density functional approach. It was concluded that the hydrogen atoms present a bonding much more developed with Ni than with Mg in the hydride from the electronic density and overlap populations analyses. Since Mg_2NiH_4 is also a stable compound under normal conditions, it is essential to decrease the stability of the

hydride by transition metal (Cu) alloying to produce a suitable material for practical hydrogen storage.

The most stable phase structure of Cu alloying Mg_2Ni has not been detected so far and the electronic structures of the hydrides with and without Cu alloying have not been well studied from the energy point of view to illuminate the electronic mechanism of improved dehydrogenating properties. Grounded on the previous work, first-principles plane-wave pseudopotential method based on density functional theory is used to systematically investigate the energetics and electronic structures of Cu alloying Mg_2Ni phases and their hydrides in the present work, some new results are expected to be the theoretical guidance for designing the advanced Ni/MH battery materials.

2. Models and method of computation

The Mg_2Ni phase has the A_2B type structure as shown in Fig. 1a. The lattice parameters of its unit cell are a = 0.5219 nm and c = 1.3293 nm with the space group $P6222$ (NO.180) [6]. The atomic coordinates in the unit cell are: +6Mg(I): (0.5, 0, z) z = 1/9, +6Mg(II): (x, 2x, 0) x = 1/6, +3Ni(I): (0, 0, 1/6), +3Ni(II): (0, 0.5, 1/6).

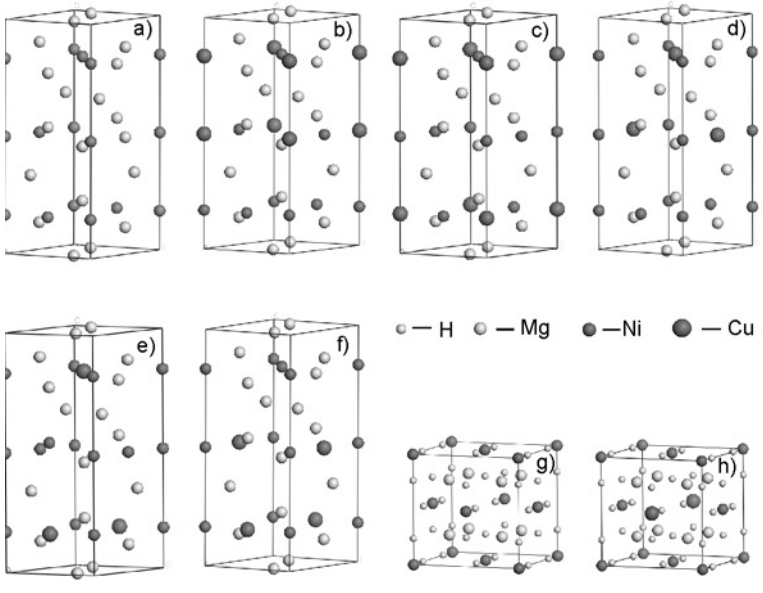

Fig. 1. Models used in calculations: a) crystal structure of Mg_2Ni, b) cell of $Mg_2Ni(I)_{1-x}Cu_x$, c) cell of $Mg_2Ni(I)'_{1-x}Cu_x$, d) cell of $Mg_2Ni(II)_{1-x}Cu_x$, e) cell of $Mg_2Ni(II)'_{1-x}Cu_x$, f) cell of $Mg_2Ni(II)''_{1-x}Cu_x$, g) cell structure of Mg_2NiH_4, h) cell of $Mg_2Ni_{1-x}Cu_xH_4$

Considering the cell character of Mg_2Ni phase and computational cost, the cell models of $Mg_2Ni_{1-x}Cu_x$ (x = 1/3) have been constituted by substituting two Cu atoms

for two Ni atoms. To determine the most stable positions of two Cu atoms in $Mg_2Ni_{1-x}Cu_x$ (x = 1/3) cell, five possible models have been designed as shown in Figs. 1b–f. If the two different sites of Ni(I) atoms are occupied by two Cu atoms, there will be two possible cases: $Mg_2Ni(I)_{1-x}Cu_x$ and $Mg_2Ni(I)'_{1-x}Cu_x$ as shown in Fig.1(b) and (c); If the two different sites of Ni(II) atoms are occupied by two Cu atoms, there will be three possible cases: $Mg_2Ni(II)_{1-x}Cu_x$, $Mg_2Ni(II)\ )'_{1-x}Cu_x$ and $Mg_2Ni(II)\ )''_{1-x}Cu_x$ as shown in Figs. 1d–f. To evaluate the dehydrogenating properties of Cu alloying Mg_2Ni hydride, the cell models of Mg_2NiH_4 [8] and $Mg_2Ni_{1-x}Cu_xH_4$ (x = 1/4) are constituted as shown in Figs. 1g and 1h. The lattice parameters of Mg_2NiH_4 are $a = b = c$ = 0.6507 nm with the space group *Fm*3*m* (NO.225). The positions of atoms are +4Ni (0, 0, 0), +8Mg (0.25, 0.25, 0.25) and +16H (x, 0, z), (0, x, –z), (–x, 0, z), (0, –x, –z), x = 0.2379, z = 0, respectively.

Cambridge serial total energy package (CASTEP) [11], the first-principles plane-wave pseudopotential method based on the density functional theory is used in this work. CASTEP uses a plane-wave basis set for the expansion of the single-particle Kohn–Sham wave functions, and pseudopotential to describe the computationally expensive electron–iron interaction in which the exchange-correlation energy by the generalized gradient approximation (GGA) of Perdew is adopted for all elements in our models by adopting the Perdew–Burke–Ernzerhof parameters [12]. Ultrasoft pseudopotential [13] represented in a reciprocal space is used. In the present calculations, the cutoff energy of atomic wave functions (PWs), E_{cut}, is set at 310 eV. A finite basis set correction and the Pulay scheme of density mixing [14, 15] are applied for the evaluation of the energy and stress. The atomic orbits used are: Mg $2p^6 3s^2$, Ni $3d^8 4s^2$, Cu $3d^{10} 4s^1$, and H $1s^1$. All atomic positions in Cu alloying Mg_2Ni models and the inner atomic positions in Cu alloying Mg_2Ni hydride model have been relaxed according to the total energy and force by using the Broyden–Flecher–Goldfarb–Shanno (BFGS) scheme [16] and their lattice parameters are well tested as shown in Table 1; the experimental cell structure and lattice constant for Mg_2NiH_4 are directly adopted without geometry optimization. The calculations of total energies and electronic structures for all the models are followed by cell optimization with self-consistent-field (SCF) tolerance of 2.0×10^{-6} eV/atom, RMs force of 0.5 eV/nm, stress of 0.1 GPa, and displacement of 2.0×10^{-4} nm.

3. Results and discussion

3.1. Stable structure of Cu alloying Mg_2Ni phase

Commonly, as an important index, the heat of formation (ΔH) is used for evaluating the structural stability of alloys with the same constituent elements but different types of structures, i.e., the bigger the negative heat of formation, the more stable is the corresponding alloy [17]. Hence, ΔH of Mg_2Ni and all $Mg_2Ni_{1-x}Cu_x$ cells (Figs. 1a–f) per atom is calculated by using the following formula [18, 19]:

$$\Delta H = \frac{1}{18}\left(E_{\text{tot}} - 12E_{\text{solid}}^{\text{Mg}} - (6-x)E_{\text{solid}}^{\text{Ni}} - xE_{\text{solid}}^{\text{Cu}}\right) \quad (1)$$

where E_{tot} refers to the total energy of the cell at the equilibrium lattice constant, $E_{\text{solid}}^{\text{Mg}}$, $E_{\text{solid}}^{\text{Ni}}$ and $E_{\text{solid}}^{\text{Cu}}$ are single atomic energies of *hcp*-Mg, *fcc*-Ni, *fcc*-Cu in solid states, respectively, x refers to the numbers of the alloying Cu atoms. In this paper, when the single atomic energies are calculated, the same pseudopotential with $Mg_2Ni_{1-x}Cu_x$ cell models is adopted. We calculate single atomic energies by the following method. First, the energy of a pure metal crystal in the solid state is calculated, then the energy is divided by the number which means the amounts of atoms involved in the crystal, and the result of the calculation is just the energy of a single atom of pure metal. The calculated energies of Mg, Ni and Cu atoms for the considered systems are –977.87 eV, –1356.19 eV, –1352.67 eV, respectively. The calculated heats of formation of Mg_2Ni, $Mg_2Ni(I)_{1-x}Cu_x$, $Mg_2Ni(I)'_{1-x}Cu_x$, $Mg_2Ni(II)_{1-x}Cu_x$, $Mg_2Ni(II)'_{1-x}Cu_x$, $Mg_2Ni(II)''_{1-x}Cu_x$ are listed in Table 1.

Table 1. Equilibrium lattice constants, cell volume, total energies and formation heat of crystal models

Model	Lattice parameter [nm]			Cell volume [nm^3]	Total energy [eV]		ΔH [$kJ \cdot mol^{-1}$]
	a	*b*	*c*		Crystal cell	Primitive cell	
Mg_2Ni	0.5202	0.5202	1.3254	0.3133	–19876.9837	–3312.8306	–28.97
Mg_2Ni [6]	0.5219	0.5219	1.2930	0.3136	–	–	–13 [20]
$Mg_2Ni(I)_{1-x}Cu_x$	0.5160	0.5224	1.3456	0.3176	–19869.4309	–3311.5718	–26.26
$Mg_2Ni(I)'_{1-x}Cu_x$	0.5220	0.5153	1.3463	0.3173	–19869.4709	–3311.5785	–26.47
$Mg_2Ni(II)_{1-x}Cu_x$	0.5168	0.5238	1.3416	0.3183	–19869.3637	–3311.5606	–25.90
$Mg_2Ni(II)'_{1-x}Cu_x$	0.5231	0.5167	1.3431	0.3184	–19869.3643	–3311.5607	–25.90
$Mg_2Ni(II)''_{1-x}Cu_x$	0.5183	0.5183	1.3425	0.3185	–19869.4908	–3311.5818	–26.58
Mg_2NiH_4	0.6507	0.6507	0.6507	0.2755	–13506.5860	–3376.6465	–
$Mg_2Ni_{1-x}Cu_xH_4$	0.6507	0.6507	0.6507	0.2755	–13501.5611	–3375.3903	–

In the present work, the calculated heat of formation of Mg_2Ni is –28.97 kJ/mol, being a little different from the experimental value (–13 kJ/mol) [20]. If the thermodynamic effect on crystal structure is considered, the present calculation should be in good agreement with the experimental result. Further analysis was done, and it was found that the heat of formation of Cu alloying Mg_2Ni phase is all negative, which means that the structures of these phases can exist and be stable [17]. Since the negative heat of formation for $Mg_2Ni(II)''_{1-x}Cu_x$ (x = 1/3) system is the biggest among the five substitutions when two Cu atoms occupying the two sites at (0, 0.5, 0.16667) and (0.5, 0, 0.5) of Ni (II) atoms as shown in Fig. 1f, it can be concluded that this kind of structure has the highest structural stability. Due to the limitation of actual experimental conditions, it is difficult to detect the precise sites occupied by Cu atoms in Cu alloying Mg_2Ni systems. The results calculated in this paper cannot be compared with the experimental data but these new results are expected to be a theoretical guidance for designing the advanced Ni/MH battery materials.

3.2. Dehydrogenating properties of Cu alloying Mg_2Ni hydride phase

Dehouche et al. [5] found experimentally that the heat of formation of Cu alloying Mg_2Ni hydride and its phase structural stability are both decreased compared with that of pure Mg_2Ni hydride system, which benefits improving the dehydrogenating properties of this system. Simicic et al. [6] solved the problem of slow kinetics of pure Mg_2Ni at low temperature by substituting Cu for Ni which remarkably destabilizes the phase structure of the Mg_2Ni hydride (Mg_2NiH_4). To further understand the experimental phenomenon, the dehydrogenating reaction heat (Q) of the Mg_2Ni hydride systems with and without Cu alloying is calculated from the chemical reaction view, respectively, in addition, the Cu alloying effect on dehydrogenating properties of the Mg_2Ni hydride will also be well investigated.

The equation of hydriding/dehydrogenating reaction of Mg_2Ni system with and without Cu alloying can be written as:

$$Mg_2Ni_{1-x}Cu_x + 2H_2 \longleftrightarrow Mg_2Ni_{1-x}Cu_xH_4 \tag{2}$$

The energy of this system itself will be changed during the hydriding/dehydrogenating: commonly, the hydriding is exothermic, while the dehydrogenating is endothermic. Hence, as far as the Cu alloying Mg_2Ni system is concerned, the change of the energy before and after hydriding/dehydrogenating reaction can be expressed as:

$$E_{\text{tot}}(Mg_2Ni_{1-x}Cu_x) + 2E_{\text{tot}}(H_2) = E_{\text{tot}}(Mg_2Ni_{1-x}Cu_xH_4) + Q \tag{3}$$

where $E_{\text{tot}}(Mg_2Ni_{1-x}Cu_x)$, $E_{\text{tot}}(Mg_2Ni_{1-x}Cu_xH_4)$ refer to the total energy of the $Mg_2Ni_{1-x}Cu_x$ system before and after hydriding, respectively, $E_{\text{tot}}(H_2)$ is the energy of a gaseous hydrogen molecule, and Q refers to the heat absorbed for dehydrogenating (or released for hydriding). From Eq. (3), it can be seen that whether the dehydrogenating reaction is easy, mainly depends on the value of Q, i.e., the smaller the value of Q, the less the heat to absorb for dehydrogenating is, and then, the easier the dehydrogenating reaction of this hydride system becomes.

Based on the above analysis, the heat of dehydrogenating reaction of Mg_2Ni hydrides with and without Cu alloying is calculated by using the following equations:

$$Q_{\text{Ni}} = -[E_{\text{tot}}(Mg_2NiH_4) - E_{\text{tot}}(Mg_2Ni) - 2E_{\text{tot}}(H_2)] \tag{4}$$

$$Q_{\text{Cu}} = -[E_{\text{tot}}(Mg_2Ni_{1-x}Cu_xH_4) - E_{\text{tot}}(Mg_2Ni_{1-x}Cu_x) - 2E_{\text{tot}}(H_2)] \tag{5}$$

where Q_{Ni}, Q_{Cu} refer to the heat of dehydrogenating reaction of Mg_2Ni hydrides with and without Cu alloying, respectively. The calculated values of $E_{\text{tot}}(Mg_2NiH_4)$, $E_{\text{tot}}(Mg_2Ni_{1-x}Cu_xH_4)$, $E_{\text{tot}}(Mg_2Ni)$ and $E_{\text{tot}}(Mg_2Ni_{1-x}Cu_x)$ are –3376.65 eV, –3375.39 eV, –3312.8306 eV, –3311.5818 eV, respectively. The total energy of H_2 ($E_{\text{tot}}(H_2)$ takes | –2.320Ry (≈ –31.5652196848 eV) [21]. Hence, from Eqs. (4) and (5), it can be found that the calculated values of Q_{Ni} and Q_{Cu} are 33.07kJ/(mol H_2) and 13.56 kJ/(mol H_2),

respectively. The dehydrogenating reaction heat to be absorbed for the Cu alloying Mg_2Ni hydride system is significantly decreased compared with that before Cu alloying, which means that the Mg_2Ni hydride becomes unstable after Cu alloying, and the dehydrogenating properties of this system are improved markedly. Based on this, the experimental phenomenon reported by Dehouche [5] and Simicic [6] can also be well interpreted based on the present calculated results.

3.3. Density of states

An analysis of total and partial density of states (DOS) of $Mg_2Ni_{1-x}Cu_x$ cell models with five various structures is performed to understand the electronic structure mechanism of the most stable phase structure for Cu alloying Mg_2Ni systems. It is found that there is little difference in the bonding peaks at various energy ranges of valence electrons in these structures. As far as the crystals with the same constituent Cu at. % but different types of structures are concerned, a conclusion about relative stability is often derived from comparison of the values of their density of states at the Fermi level $N(E_F)$, i.e., the lower the $N(E_F)$, the more stable is the corresponding phase structure [22]. To verify the criterion in the case of $Mg_2Ni_{1-x}Cu_x$ compounds, the calculated values of $N(E_F)$ of $Mg_2Ni_{1-x}Cu_x$ with five different types of structures are presented in Fig. 2.

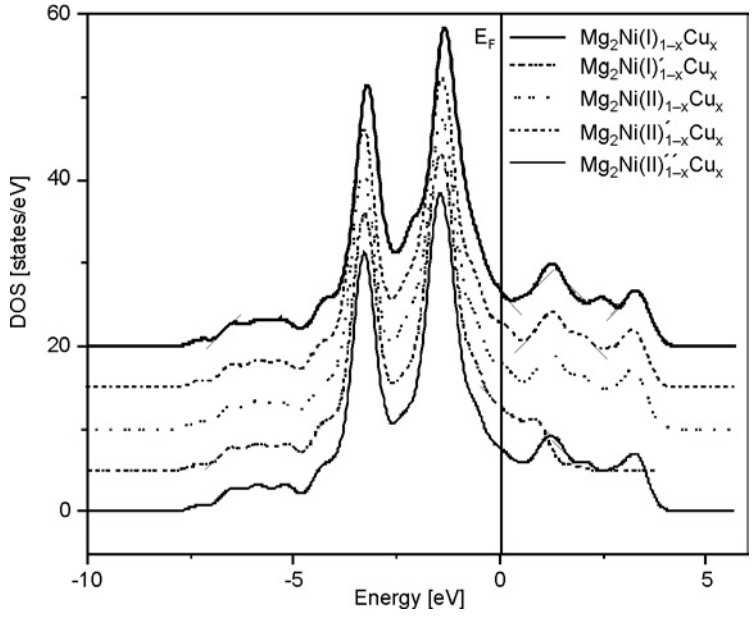

Fig. 2. Total DOS of Cu alloying Mg_2Ni phase around E_F.
The curves have been vertically displaced

The $N(E_F)$ values of five computational models in the order of Fig. 1d, 1e, 1b, 1c and 1f are 8.04702 electrons/eV, 7.94366 electrons/eV, 7.67374 electrons/eV, 7.65078

electrons/eV, 6.65797 electrons/eV, respectively. It is found that the decreasing order of the $N(E_F)$ values is in good agreement with the increasing order of the negative heat of formation of the computational models as shown in Fig. 3, which means that the $N(E_F)$ value of the $Mg_2Ni(II)''_{1-x}Cu_x$ (x = 1/3) phase structure is the lowest in Cu alloying Mg_2Ni systems and this structure is the most stable.

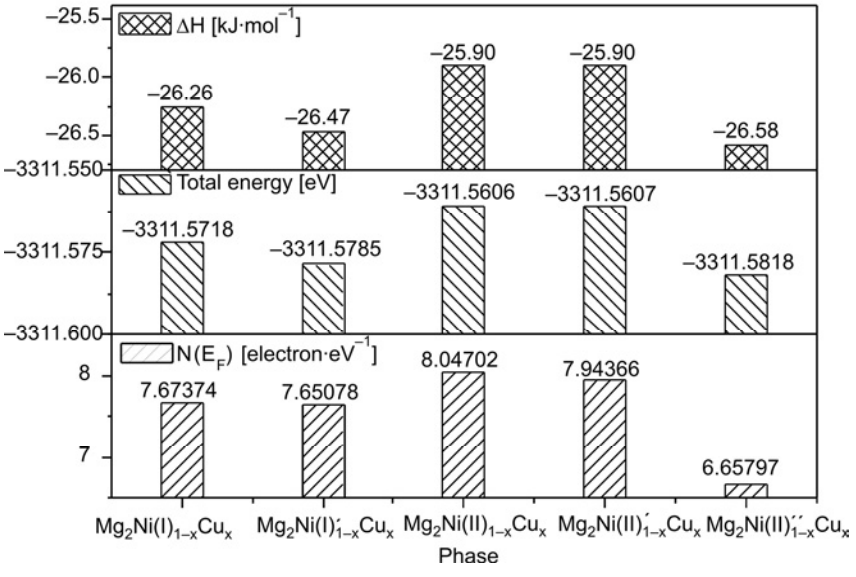

Fig. 3. $N(E_F)$, total energy and heat of formation in Cu alloying Mg_2Ni phase

A further analysis of total and partial density of states (DOS) of Mg_2Ni hydride with and without Cu alloying is also done to understand the Cu alloying effect on dehydrogenating properties of Mg_2Ni hydride. The total and partial DOSs of Mg_2NiH_4 and $Mg_2Ni_{1-x}Cu_xH_4$ (x = 1/4) cell are plotted in Figs. 4a and b. It is found that the main bonding peaks of Mg_2NiH_4 are located at the energy range from the Fermi energy (E_F) to –11 eV (Fig. 4a). The bonding peak between E_F and –2 eV mainly originates from the contribution of valence electrons of Mg(s) and Mg(p) as well as a few Ni(d) and H(s) orbits. The bonding peak between –4 eV and –2 eV results from the bonding of valence electrons of Mg(s), Mg(p), Ni(d) and a few H(s). The bonding peak between –7 eV and –4 eV is the interaction of Ni (d) and H(s) as well as a few Mg(s) and Mg (p) electrons. The bonding peak between –11 eV and –7 eV is caused by Mg(s), H(s) and a few Ni(s). After Cu alloying, the energy range of the main bonding peaks is not markedly changed (Fig. 4b), which is still from E_F to –11 eV, but there is a new bonding peak appearing at the energy range between –5 eV and –4 eV. The heights of the main bonding peaks originating from the contribution of valence electrons of Mg, Ni and H orbits are all decreased compared with that before Cu alloying. For example, the height of the peak between –4 eV and –2 eV is decreased from 29.16 electronic states/eV before Cu alloying to 22.30 electronic states/eV after Cu alloying.

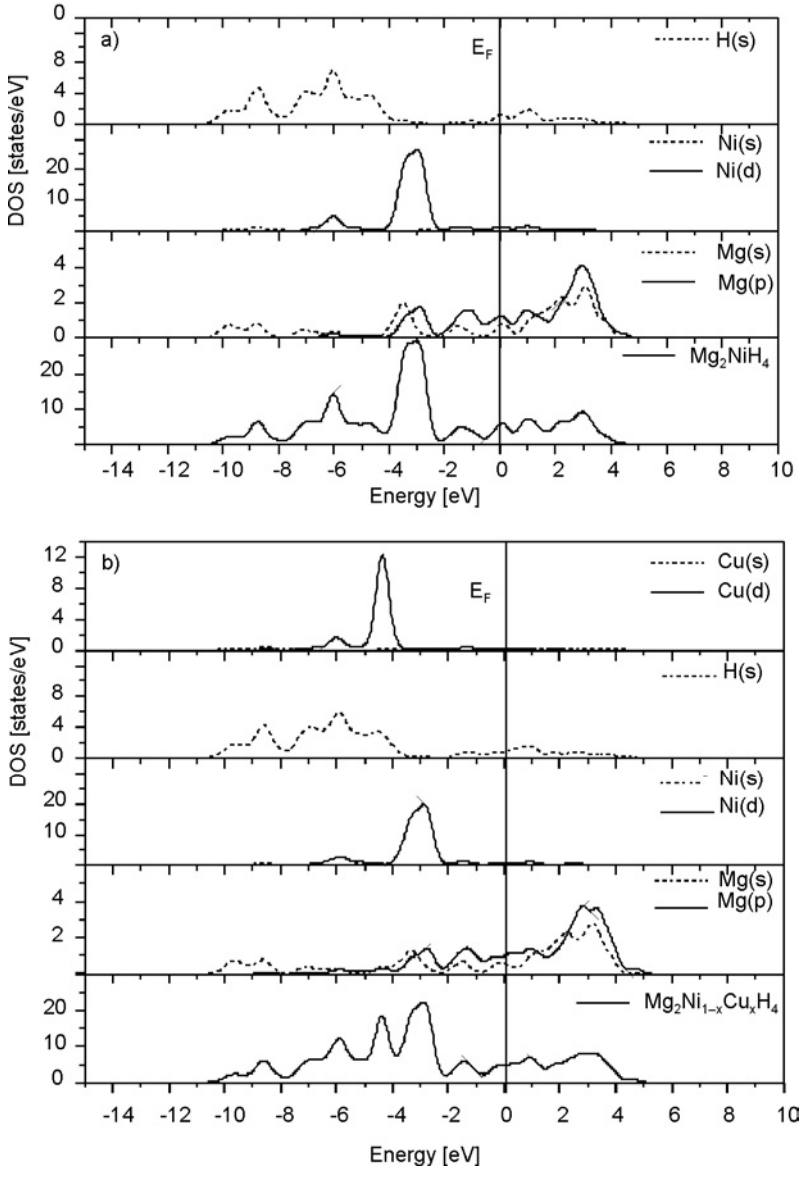

Fig. 4. Total and partial DOS of alloying Mg_2NiH_4 (a) and $Mg_2Ni_{1-x}Cu_xH_4$ (b)

The height of the peak between –7 eV and –5 eV is decreased from 14.13 electronic states/eV before Cu alloying to 12.22 electronic states/eV after Cu alloying. The height of the peak between –11 eV and –8 eV is decreased from 6.57 electronic states/eV before Cu alloying to 2.37 electronic states/eV after Cu alloying. Based on the analysis above, it is found that there are fewer bonding electrons in Cu alloying Mg_2Ni hydride than in pure Mg_2NiH_4. The fewer the bonding electron numbers, the weaker are the charge interactions, and fewer electrons in low energy range far below

the Fermi level will lead to reduce the structural stability of the corresponding system [23, 24]. Hence, when Ni atoms are partially substituted by Cu atoms in Mg_2NiH_4, the structural stability of the hydride will be reduced and the dehydrogenating reaction will become easier, which benefits in improving the dehydrogenating properties of the Mg_2Ni hydride system.

3.4. Electron density

The total valence electron density contour plots of $(1\bar{1}0)$ planes of Mg_2Ni hydrides before and after Cu alloying are presented in Figs. 5a, b, respectively.

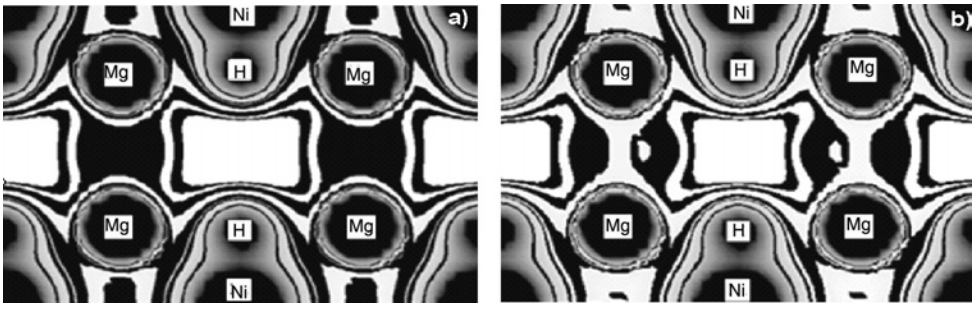

Fig. 5. Charge distribution on $(1\bar{1}0)$ planes of Mg_2NiH_4 (a) and $Mg_2Ni_{1-x}Cu_xH_4$ (b)

It can be seen that there is a strong bonding between Ni and H in Mg_2NiH_4 cell, while there are weakened bonding interactions between Mg and H, Ni and Mg (Fig. 5a). Takahashi [9] and Jasen [10] found that the bonding interaction between Ni and H atoms is stronger than that between Mg and H, which is in good agreement with our results. After Cu alloying, due to the addition of Cu, the bonding interactions between Ni and Mg, Ni and H are both slightly reduced (Fig. 5b) which will benefit in reducing the structural stability, decreasing the heat of dehydrogenating and markedly improving the dehydrogenating properties of Mg_2Ni hydride system.

4. Conclusions

Based on calculations of negative heat of formation of Cu alloying Mg_2Ni phases, it can be seen that the $Mg_2Ni(II)''_{1-x}Cu_x$ (x = 1/3) phase structure is the most stable among the five substitutions when two Cu atoms occupy two sites at (0, 0.5, 0.16667) and (0.5, 0, 0.5) of Ni(II) atoms.

From the calculated results of the dehydrogenating reaction heat of Cu alloying Mg_2Ni hydride, it results that the heat of dehydrogenating reaction is remarkably decreased compared with that without Cu alloying, which benefits in improving its dehydrogenating properties.

After comparing the density of states (DOS) and the charge distributions of Mg_2Ni and Mg_2NiH_4 with and without Cu alloying, it is found that the main reason for the Mg_2Ni (II)$''_{1-x}Cu_x$ (x = 1/3) with the most stable phase structure should be ascribed to the lowest $N(E_F)$ value at the Fermi level in this system compared with that of other substitutions. The improved dehydrogenating properties of Mg_2Ni hydride system with Cu alloying mainly originates from the weakened bonding between Mg and Ni, Ni and H as well as the decreasing of bonding electron numbers in low energy range below the Fermi level.

Acknowledgements

The work was supported by the PhD Programs Foundation of Ministry of Education of China (20020530012).

References

[1] KOHNO T., KANDA M., J. Electrochem. Soc., 144 (1997), 2384.
[2] ZHANG Y.S., YANG H.B., YUAN H.T., YANG E.D., ZHOU Z.X., SONG D.Y., J. Alloys Comp., 269 (1998), 278.
[3] LIANG G., HUOT J., BOILY S., VANNESTE A., SCHULZ R., J. Alloys Comp., 282 (1999), 286.
[4] ZALUSKI L., ZALUSKA A., TESSIER P., STROM-OLSEN J.O., SCHULZ R., J. Alloys Comp., 217 (1995), 295.
[5] DEHOUCHE Z., JIAOZANDRY R., GOYETTE J., BOSE T.K., J. Alloys Comp., 288 (1999), 269.
[6] SIMICIC M.V., ZDUJIC M., DIMITRIJEVIC R., NIKOLIC-BUJANOVIC L., POPOVIC N.H., J. Power Sources, 158 (2006), 730.
[7] YANG H., YUAN H., JI J., SUN H., ZHOU Z., ZHANG Y., J. Alloys Comp., 330–332 (2002), 640.
[8] GARCIA G.N., ABRIATA J.P., SOFO J.O., Phys. Rev. B., 59 (1999), 11746.
[9] TAKAHASHI Y., YUKAWA H., MORINAGA M., J. Alloys Comp., 242 (1996), 98.
[10] JASEN P.V., GONZÁLES E.A., BRIZVELA G., NAGEL O.A., GONZÁLES G.A., Juan A., Int. J. Hydrogen En., 32 (2007), 4943.
[11] SEGALL M.D., LINDAN P.L.D., PROBERT M.J., PICKARD C.J., HASNIP P.J., CLARK S.J., PAYNE M.C., J. Phys.: Condens. Matter, 14 (2002), 2717.
[12] MARLO M., MILMAN V., Phys. Rev. B., 62 (2000), 2899.
[13] VANDERBILT D., Phys. Rev. B., 41 (1990), 7892.
[14] FRANCIS G.P., PAYNE M.C., J. Phys.: Condens. Matter, 2 (1990), 4395.
[15] HAMMER B., HANSEN L.B., NØRSKOV J.K., Phys. Rev. B., 59 (1999), 7413.
[16] MONKHORST H.J., PACK J.D., Phys. Rev. B., 13 (1976), 5188.
[17] SONG Y., GUO Z.X., YANG R., LI D., Acta Mater., 49 (2001), 1647.
[18] MEDVEDEVA M.I.,GORNOSTYREV Y.N., NOVIKOV D.L., Acta Mater., 46 (1998), 3433.
[19] SAHU B.R., Mater. Sci. Eng. B., (49) 1997, 74.
[20] NGOK T., TKHAI V.F., Non-Ferrous Met. Res., 12 (1984), 161.
[21] NAKAMURA H., NGUYEN-MANH D., PETTFFOR D.G., J. Alloys Comp., 281 (1998), 81.
[22] FU C.L., WANG X.D., YE Y.Y., HO K.M., Intermetallics, 7 (1999), 179.
[23] NYLEN J., GARCIA F.J., MOSEL B.D., POTTGEN R., HAUSSERMANN U., Solid State Sci., 6 (2004),147.
[24] VAKHNEY A.G., YARESKO A.N., ANTONOV V.N., NEMOSHKALENKO V.V., Int. J. Hydrogen En., 26 (2001), 453.

Received 12 October 2007
Revised 30 November 2007

Materials Science-Poland, Vol. 26, No. 3, 2008

Electronic structure and magnetic properties of $Ce_2Pd_{1-x}Co_xSi_3$ and $Ce_2Pd_{1-x}Fe_xSi$*

G. KOZŁOWSKI[1], A. JEZIERSKI[2**]

[1]Faculty of Technical Physics, Poznań University of Technology,
ul. Nieszawska 13A, 60-965 Poznań, Poland

[2]Institute of Molecular Physics, Polish Academy of Sciences,
M. Smoluchowskiego 17, 60-179 Poznań, Poland

Electronic and magnetic properties of $Ce_2Pd_{1-x}Co_xSi_3$ and $Ce_2Pd_{1-x}Fe_xSi_3$ alloys have been calculated by the TB LMTO-ASA method. The spin polarized calculations indicate that the magnetic moment of $Ce_2Pd_{1-x}Co_xSi_3$ decreases upon the increase of the concentration x but for $Ce_2Pd_{0.5}Fe_{0.5}Si_3$ the value of the magnetic moment has a minimum.

Key words: *electronic structure; LMTO; magnetic moment; intermetallic compounds*

1. Introduction

The intermetallic Ce_2TSi_3 compounds have been studied experimentally in the last years [1–5]. Ce_2TSi_3 systems with T = (Co, Fe) crystallizes into hexagonal crystal structures described by the space group *P*6/*mmm* (No. 191). The positions of atoms are listed in Table 1. Magnetic measurements [1] suggested a reduction of the cerium moment for systems with high Co content. Ce_2PdSi_3 was reported to exhibit the Kondo effect [2] and classified as a heavy fermion system with a strong anisotropic magnetic behaviour [3]. In this work, we present the effect of substitution of Co and Fe in Ce_2PdSi_3 on its electronic and magnetic properties.

2. Method of calculations

The electronic and magnetic properties were calculated by ab-initio spin-polarized Tight Binding Linear Muffin Tin Orbital (TB LMTO) method in the atomic spheres

---

*Presented at the Conference of the Scientific Network "New Materials for Magnetoelectronics – MAG-EL-MAT 2007", Będlewo near Poznań, 7–10 May, 2007.

**Corresponding author, e-mail: andrzej.jezierski@ifmpan.poznan.pl

approximation (ASA) [6]. The exchange correlation potential was assumed according to von Barth and Hedin [7]. We apply a scalar-relativistic approximation for the band electrons and the fully-relativistic approximation for the frozen core electrons. The values of the atomic spheres' radii were chosen in such a way that the sum of volumes of all atomic spheres was the same as the volume of the unit cell. The calculations were performed for the experimental lattice parameters [1] listed in Table 2. The number of *k*-points in the irreducible Brillouin zone changed from 340 to 370 depending on the symmetry of the system.

Table 1. Nonequivalent atomic positions in Ce_2PdSi_3

Atom	Wyckoff site	*x*	*y*	*z*
Ce(1)	1a	0	0	0
Ce(2)	3f	0.5	0	0
Pd	2d	0.3333	0.6666	0.5
Si	6m	0.1702	0.3403	0.5

Table 2. Lattice parameters and the space groups of $Ce_2Co_xPd_{1-x}Si_3$ and $Ce_2Fe_xPd_{1-x}Si_3$

Material	*a* [Å]	*c* [Å]	Space group
Ce_2PdSi_3	8.2631	4.2830	*P*6/*mmm*
$Ce_2Co_xPd_{1-x}Si_3$			
$x = 0.25$	8.2241	4.2678	*P*2*mm*
$x = 0.5$	8.1869	4.2494	*Pcmm*
$x = 0.75$	8.1460	4.2297	*P*2*mm*
$x = 1$	8.1040	4.1970	*P*6/*mmm*
$Ce_2Fe_xPd_{1-x}Si_3$			
$x = 0.25$	8.2414	4.2674	*P*2*mm*
$x = 0.5$	8.2229	4.2520	*P*2*mm*
$x = 0.75$	8.1956	4.2431	*P*6/*mmm*
$x = 1$	8.1240	4.2120	*P*6/*mmm*

The calculations were performed for the supercell model ($Ce_8T_4Si_{12}$). In the supercell model, we had four positions of transition metal and we changed the concentration of impurity with the step of 0.25. The electronic and magnetic properties were calculated for the various distributions of Pd and Co(Fe) atoms in the supercell. From all possible arrangements of Pd and Co(Fe) atoms, one with a minimum total energy was chosen for further calculations.

3. Results and discussion

In Figure 1a, we present the total density of states (DOS) and the partial density of states (PDOS) of ferromagnetic Ce_2PdSi_3. The density of states consists of three regions. The bands situated at the bottom of the energy scale were occupied by 3s states

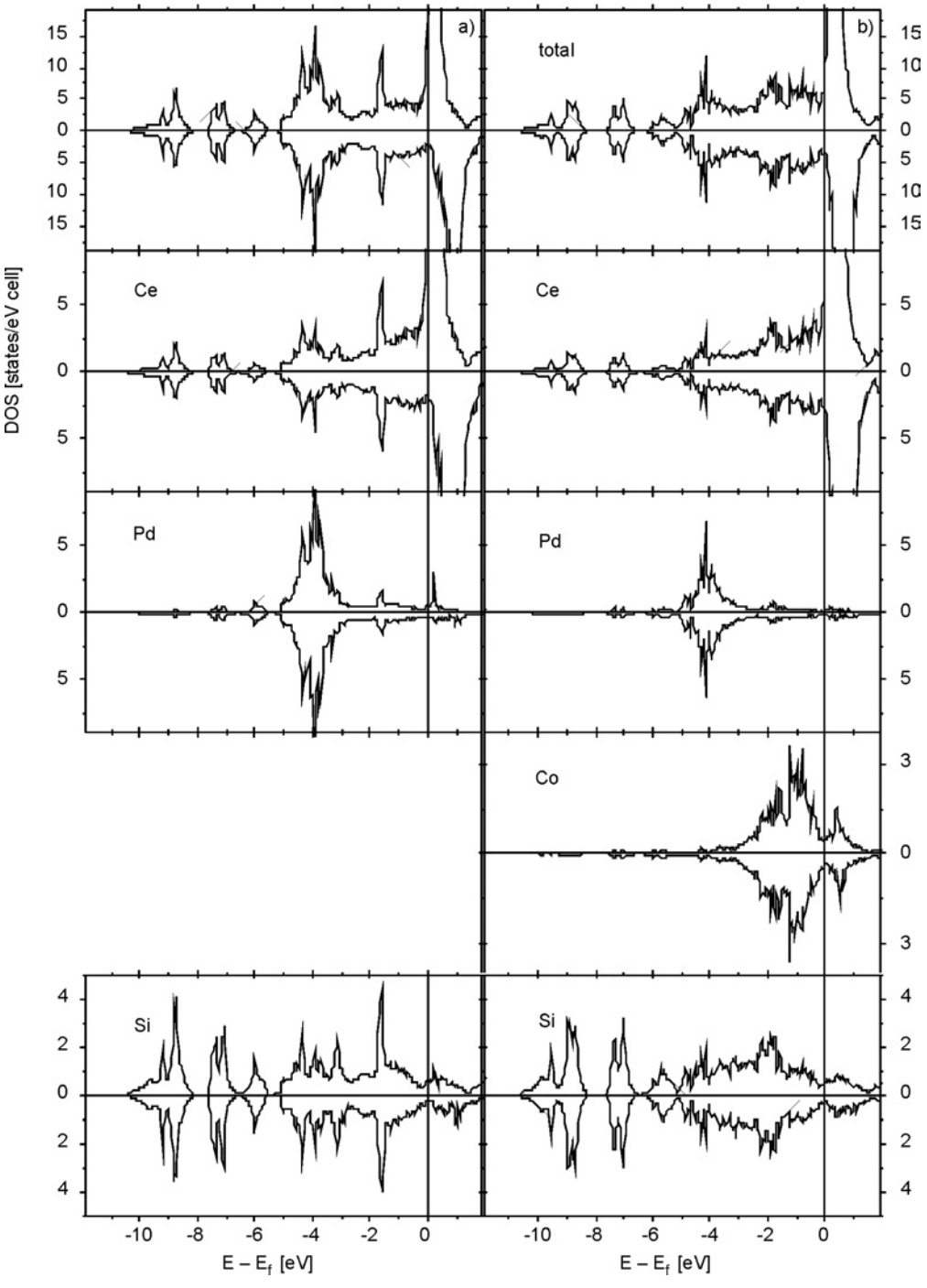

Fig. 1. Total and partial densities of states of: a) Ce_2PdSi_3, b) $Ce_2Pd_{0.5}Co_{0.5}Si_3$

of Si. The bottom of valence band is dominated by 4d states of Pd which hybridize with 3p states of Si. 4f states of Ce are located near the Fermi level and give the main contribution to the density at the Fermi level. The total DOS at Fermi energy is estimated as 19.19 (states/eV f.u.) The magnetic moment of Ce_2PdSi_3 obtained from the spin-polarized self-consistent calculations is $2.12\mu_B$ (Table 3).

Table 3. Magnetic moment on cerium [μ_B] in $Ce_2Pd_{1-x}Co_xSi_3$ and $Ce_2Pd_{1-x}Fe_xSi_3$

Material	Magnetic moment on cerium [μ_B]				Total magnetic moment [μ_B]
	Ce	Ce1	Ce2	Ce3	
Ce_2PdSi_3	0.58	–	–	0.48	2.12
$Ce_2Pd_{1-x}Co_xSi_3$					
$x = 0.25$	0.58/0.6	0.41/0.42	–	0.14/0.15	1.46
$x = 0.5$	0.57	0.33	0.11	0.03	0.91
$x = 0.75$	–	0.22/0.3	0.05/0.08	–0.06/–0.09	0.31
$x = 1$	–	–	0	0	0
$Ce_2Pd_{1-x}Fe_xSi_3$					
$x = 0.25$	0.6/0.56	–0.62	–	0.11/0.13	0.85
$x = 0.5$	0.39	0.39	0.39	0.39	0.15
$x = 0.75$	–	–0.5/–0.52	–0.54	0.3/0.41	0.71
$x = 1$	–	–	0	0	0

In Figure1b we plotted the total and partial densities of states of $Ce_2Pd_{0.5}Co_{0.5}Si_3$. The substitution of Co by Pd leads to a change of the total density of states particularly near the Fermi energy. Co 3d states are located below the Fermi energy and we observed a strong hybridization between 4f Ce and 3d Co states. The local disorder and hybridization lead to the change of the shape of cerium density of states.

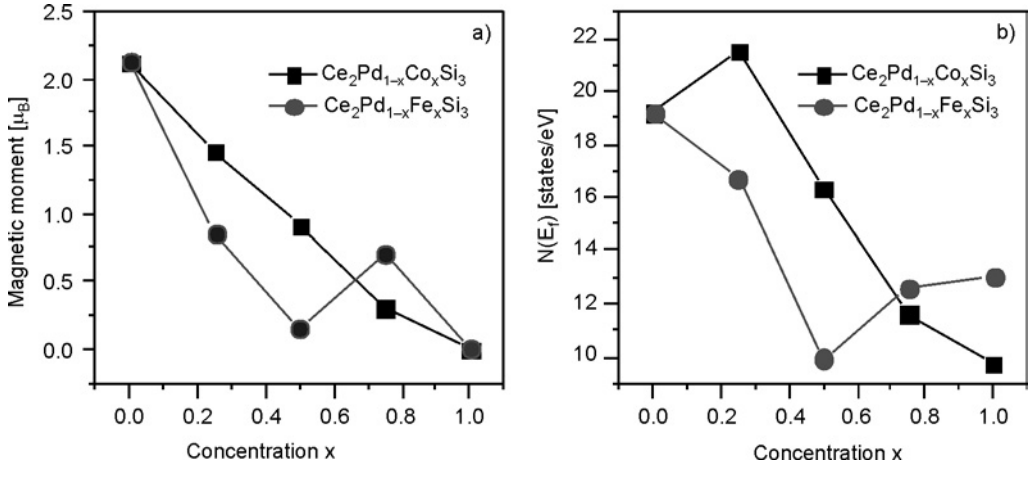

Fig. 2. Dependence of the total magnetic moment (a) and the density of states at the Fermi level $N(E_f)$ (b) on the concentration x for $Ce_2Pd_{1-x}Co_xSi_3$ and $Ce_2Pd_{1-x}Fe_xSi_3$

The dependences of the total magnetic moment on concentration in $Ce_2Pd_{1-x}Co_xSi_3$ and $Ce_2Pd_{1-x}Fe_xSi_3$ are presented in Fig. 2a. The total magnetic moment in $Ce_2Pd_{1-x}Co_xSi_3$ decreases upon increase of cobalt concentration. In $Ce_2Pd_{1-x}Fe_xSi_3$ we observe a similar dependence up to $x = 0.5$ but for $x = 0.75$ the total magnetic moment increases. In Table 3, we presented the values of the total magnetic moment on cerium atoms, that strongly depended on the local environment. The dependences of the densities of states at the Fermi level $N(E_f)$ on concentration x for $Ce_2Pd_{1-x}Co_xSi_3$ and $Ce_2Pd_{1-x}Fe_xSi_3$ alloys is presented in Fig. 2b. We observe different dependences of $N(E_f)$ on concentration x for both systems. The value of $N(E_f)$ in $Ce_2Pd_{1-x}Co_xSi_3$ decreases in the range $0.25 < x < 1.0$, however in $Ce_2Pd_{1-x}Fe_xSi_3$ alloys the value of $N(E_f)$ decreases up to $x = 0.5$ and then increases.

4. Conclusion

Ab-intio spin-polarized TB LMTO calculations have shown that substitution of palladium atom by cobalt or iron atoms changed electronic and magnetic properties of $Ce_2Pd_{1-x}Co_xSi_3$ and $Ce_2Pd_{1-x}Fe_xSi_3$ systems. Our calculations indicated that the total magnetic moment decreased upon increasing the Co and Fe concentration up to 50%, what was in a good agreement with experimental observation. For $Ce_2Pd_{1-x}Fe_xSi_3$, the density of states at the Fermi level $N(E_f)$ decreases till $x = 0.5$ and then increases up to Ce_2FeSi_3.

Acknowledgements

This work was supported by funds for sciences in years 2007–2010 as a research project.

References

[1] GORDON R.A.,WARREN C.J., ALEXANDER M.G., DISALVO F.J., PÖTTGEN R., J. Alloys Comp., 248 (1997), 24.
[2] MALLIK R., SAMPATHKUMARAN E.V., J. Magn. Magn. Mater., 164, (1996), L13.
[3] SAHA S.R., SUGAWARA H., MATSUDA T.D., AOKI Y., SATO H., SAMPATHKUMARAN E.V. Phys. Rev. B, 62 (2000), 425.
[4] MAJUMDAR S., SAMPATHKUMARAN E.V., J. Magn. Magn. Mater., 223 (2001), 247.
[5] WAWRZYNSKA E., KELLER L., SAMPATHKUMARAN E.V., SZYTUŁA A., J. Alloys Comp., 373 (2004), 73.
[6] ANDERSEN O.K., JEPSEN O., Phys. Rev. Lett., 53 (1984), 2571.
[7] VON BARTH U., HEDIN L., J. Phys. C, 5 (1972), 1629.

Received 10 May 2007
Revised 21 January 2008

Materials Science-Poland, Vol. 26, No. 3, 2008

Orbital Kondo anomaly and channel mixing effects in a double quantum dot*

D. SZTENKIEL**, R. ŚWIRKOWICZ

Faculty of Physics, Warsaw University of Technology, ul. Koszykowa 75, 00-662 Warsaw, Poland

A system consisting of two quantum dots connected to separate reservoirs is studied and electron transport properties are investigated in the Kondo regime with use of the non-equilibrium Green function technique based on the method of equation of motion. As the orbital quantum number is conserved during tunnelling processes when each dot is attached to its own leads, the orbital SU(2) Kondo effect is observed. It is shown that the mixing between the leads strongly modifies transport properties leading to a considerable suppression of the Kondo resonance.

Key words: *double quantum dot; Kondo effect*

1. Introduction

Electronic transport through quantum dot (QD) system has been intensely investigated during the last years. Fano-like features [1–3], Kondo resonance [4, 5] as well as interference effects [6] have been studied. It is well known that spin fluctuations can lead to the Kondo effect at a sufficiently low temperature. However, the Kondo resonance can also arise from the orbital degeneracy when a real spin degree of freedom is not taken into account [7–10]. The existence of the orbital or pseudo-spin Kondo resonance was first reported by Wilhelm et al. [7] in a double quantum dots (DQD) system with each dot connected to its own left and right electrodes. In this case, two degenerate states of DQD play the role of the pseudo-spin. The effect was also observed in a system with a parallel geometry in the presence of interdot coupling and anisotropy [8]. Quantum fluctuations between the orbital and spin degrees of freedom lead to SU(4) Kondo anomaly and the effect has been recently observed in a carbon nanotube quantum dot [9] as well as in vertical semiconductor QDs [10].The highly symmetric

---

*Presented at the Conference of the Scientific Network "New Materials for Magnetoelectronics – MAG-EL-MAT 2007", Będlewo near Poznań, 7–10 May, 2007.

**Corresponding author, e-mail: DSZ@poczta.fm

SU(4) Kondo was also studied theoretically with use of variety of techniques [11–17]. For example, in the work by Lim et al., the transition from the SU(4) symmetry to a SU(2)-Kondo was investigated in dependence on the mixing between channels and/or asymmetry [17].

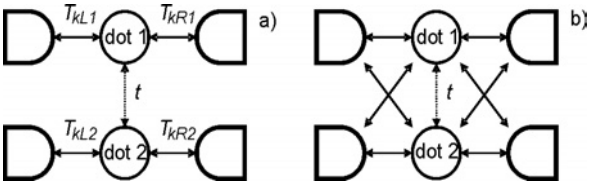

Fig. 1. Schematic diagram of the system: a) $\alpha = 0$, b) $\alpha \neq 0$

In this work, we study a DQD system consisting of two equivalent single-level dots, each coupled to left and right leads (Fig. 1). The electronic transport is theoretically studied by means of the non-equilibrium Green function and the equation of motion method. We focus on the orbital (pseudo-spin) Kondo effect. In contrast to the spin Kondo effect, two degenerate states of DQD play the role of the pseudo-spin. In this case the up and down pseudo-spins are related to an extra electron in the first (up) or second (down) dot. Tunnelling processes in which the orbital quantum number (pseudo-spin) is conserved can lead to the orbital Kondo effect (Fig. 1a). In the experiment, this conservation of the pseudo-spin quantum number is not obvious and some cross coupling may take place. The mixing between channels takes place when it is possible for electron to tunnel coherently from one dot via the reservoirs to another one (Fig. 1b). The maximal cross coupling is realized if quantum dots are attached to a single common lead.

2. Model

We model the system by the two-impurity Anderson Hamiltonian, which can be written as

$$H = H_L + H_R + H_{DQD} + H_T \tag{1}$$

Here

$$H_\beta = \sum_k \varepsilon_{k\beta} a_{k\beta}^+ a_{k\beta}$$

with $\beta = L,R$ describes the non-interacting left ($\beta = L$) and right ($\beta = R$) reservoirs. $a_{k\beta}^+$ ($a_{k\beta}$) creates (annihilates) an electron in the state k with energy $\varepsilon_{k\beta}$ in lead β. The term H_{DQD} corresponds to the two-dot region and is written as

$$H_{DQD} = \sum_{i=1,2} E_i d_i^+ d_i + t(d_1^+ d_2 + d_2^+ d_1) + U d_1^+ d_1 d_2^+ d_2 \tag{2}$$

d_i^+ (d_i) creates (annihilates) an electron in the dot i (i = 1, 2) with energy E_i and t describes the interdot hopping between dots. The interdot electron interactions are taken into account in a form of Hubbard-like term with the correlation parameter U. In this paper, we neglect on-site Coulomb repulsions and consider only empty or singly occupied states in each quantum dot. The last term in Hamiltonian (1):

$$H_T = \sum_{\substack{k,i=1,2 \\ \beta=L,R}} (T_{k\beta i} a_{k\beta}^+ d_i + T_{k\beta i}^* d_i^+ a_{k\beta})$$

accounts for the tunnelling between the dots and reservoirs. $T_{k\beta i}$ are the tunnelling matrix elements which are related to the tunnelling rates by

$$\Gamma_{ii'}^{\beta} = 2\pi \sum_k T_{k\beta i} T_{k\beta i'}^* \delta(\varepsilon - \varepsilon_{k\beta})$$

In this work, $\Gamma_{ii'}$ are assumed to be independent of energy, constant within the electron band and zero otherwise. The exchange of electrons between the dots through the attached electrodes is determined by the parameter α, where $\alpha = \Gamma_{i-i}^{\beta} / \Gamma_{ii}^{\beta}$. The term Γ_{i-i}^{β} describes the tunnelling processes in which the orbital quantum number is not conserved. α = 0 corresponds to the case of no mixing between two separated electrodes, whereas for α = 1 quantum dots are coupled to a single common left and right reservoirs.

The non-equilibrium Green function formalism is introduced to describe transport properties of the system. The retarded G^r and advanced G^a Green functions are calculated with use of the equation of the motion method. In this work, we consider temperatures comparable to the Kondo temperature so high-order GFs are truncated using the decoupling procedure proposed by Meir [18]. Such an approximation is reasonable in the temperature range where the Kondo effect takes place. Finally, in the limit of infinite U ($U \to \infty$) GFs can be written in the following matrix which form corresponds to the Dyson equation

$$\hat{G}(\varepsilon) = [\hat{I} - \hat{g}(\varepsilon)\hat{\Sigma}(\varepsilon)]^{-1} \hat{g}(\varepsilon)$$

where $\hat{\Sigma}(\varepsilon)$ describes the self-energy of interacting system and is given by (for more details see Ref [19])

$$\hat{\Sigma}(\varepsilon) = \hat{g}(\varepsilon)^{-1} - \hat{\tilde{n}}^{-1} \hat{g}(\varepsilon)^{-1} + \hat{\tilde{n}}^{-1} (\hat{\Sigma}_0 + \hat{\tilde{\Sigma}}(\varepsilon) + \hat{T}) \tag{3}$$

with $T_{ii'} = \delta_{i-i'} t$, $\tilde{n}_{ii} = 1 - < d_{-i}^+ d_{-i} >$, $\tilde{n}_{i-i} = < d_{-i}^+ d_i >$. The term $g_{ii'} = \delta_{ii'} (\varepsilon - E_i)^{-1}$ describes GF of an uncoupled double quantum dot in the absence of any interaction and $\hat{\Sigma}_0$ is the self-energy of non-interacting system, whereas

$$\tilde{\Sigma}_{ii}(\varepsilon) = \sum_{k,\beta} \frac{|T_{k\beta-i}|^2}{\varepsilon - \varepsilon_{k\beta}} f_\beta(\varepsilon_{k\beta}) + \sum_{k,\beta} \frac{2t^2 \left(|T_{k\beta i}|^2 + |T_{k\beta-i}|^2 \right) f_\beta(\varepsilon_{k\beta})}{(\varepsilon - \varepsilon_{k\beta}) \left[(\varepsilon - \varepsilon_{k\beta})^2 - 4t^2 \right]} - \sum_{k,\beta} \frac{2t\, T_{k\beta i}^* T_{k\beta-i}}{(\varepsilon - \varepsilon_{k\beta})^2 - 4t^2} f_\beta(\varepsilon_{k\beta}) \tag{4}$$

$$\tilde{\Sigma}_{i-i}(\varepsilon) = -\sum_{k,\beta} \frac{T^*_{k\beta i} T_{k\beta-i}}{\varepsilon - \varepsilon_{k\beta}} f_\beta(\varepsilon_{k\beta}) + \sum_{k,\beta} \frac{t\left(\left|T_{k\beta i}\right|^2 + \left|T_{k\beta-i}\right|^2\right)}{\left(\varepsilon - \varepsilon_{k\beta}\right)^2 - 4t^2} f_\beta(\varepsilon_{k\beta}) - \sum_{k,\beta} \frac{4t^2 T^*_{k\beta i} T_{k\beta-i} f_\beta(\varepsilon_{k\beta})}{\left(\varepsilon - \varepsilon_{k\beta}\right)\left[\left(\varepsilon - \varepsilon_{k\beta}\right)^2 - 4t^2\right]} \tag{5}$$

The mean values $< d_i^+ d_{i'} >= -i\int \frac{d\varepsilon}{2\pi} G^<_{i'i}$ are calculated self-consistently. To do this, we obtain the lesser GF $G^<$ with use of Keldysh equation $\hat{G}^< = \hat{G}^r \hat{\Sigma}^< \hat{G}^a$ with the self-energy $\hat{\Sigma}^<$ determined from the Ng ansatz [20] with $\hat{\Sigma}^< = \hat{\Sigma}_0^< (\hat{\Sigma}_0^r - \hat{\Sigma}_0^a)^{-1} (\hat{\Sigma}^r - \hat{\Sigma}^a)$ and $\Sigma_0^< = i(\hat{\Gamma}^L f_L + \hat{\Gamma}^R f_R)$, where $f(\varepsilon)$ is the Fermi–Dirac distribution function for the lead β. Finally, the current flowing from the lead β can be calculated according to the formula derived by Meir[18]

$$I^\beta = i\frac{2e}{\hbar} Tr \int \frac{dE}{2\pi} \hat{\Gamma}^\beta(\varepsilon)\left\{\hat{G}^<(\varepsilon) + f_\beta(\varepsilon)\left[\hat{G}^r(\varepsilon) - \hat{G}^a(\varepsilon)\right]\right\} \tag{6}$$

3. Results and discussion

We analyze the symmetric system with

$$\Gamma^L_{11} = \Gamma^L_{22} = \Gamma^R_{11} = \Gamma^R_{22}$$

Moreover, in order to normalize the total tunnelling rate, we assume

$$\hat{\Gamma}^L = \hat{\Gamma}^R = \frac{\Gamma}{1+\alpha}\begin{pmatrix} 1 & \alpha \\ \alpha & 1 \end{pmatrix}$$

where Γ represents the tunnelling coupling and is treated here as the energy unit. Calculations are performed for $kT = 0.01\Gamma$, $U \to \infty$, equal level positions $E_1 = E_2 = E_0$ and square electron band of width $D = 500\Gamma$.

First, we consider the system with dots coupled capacitively, so there is no direct tunnelling between dots and $t = 0$ is assumed. Figure 2 shows the density of states (DOS) and the transmission in the Kondo regime ($E_0 = -4\Gamma$) calculated for several values of α. When $\alpha = 0$, we can see a well defined Kondo peak in DOS pinned at the Fermi energy of the leads (the peak is well presented in the inset). With increase of mixing between channels, the peak becomes strongly asymmetric and DOS is considerably suppressed for energies higher than E_F.

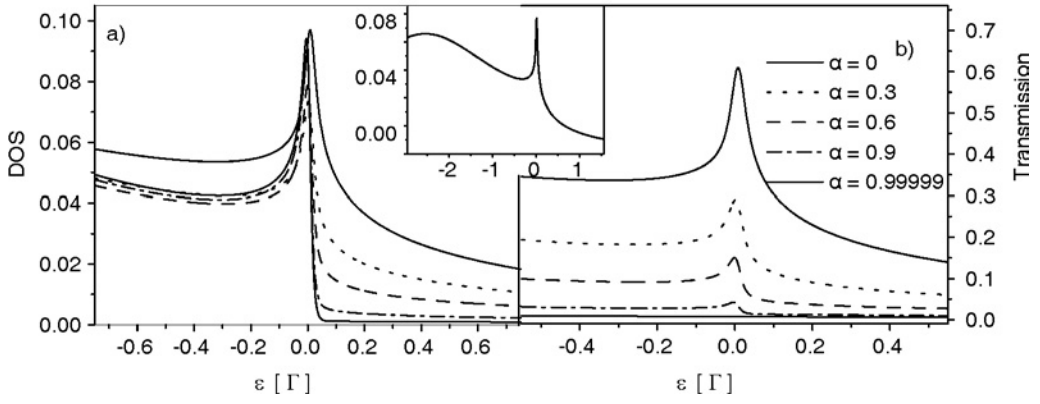

Fig. 2. Density of states and transmission for various cross-coupling parameters α and $E_0 = 4\Gamma$, $t = 0$

Next, the influence of mixing between leads on the transmission is investigated. We can see that the peak in transmission is the highest when no mixing between channels is taken into account. The peak intensity decreases with increasing cross-coupling (α). In such a situation, transport of electrons between the dots through the reservoirs is possible, what breaks the conservation of the pseudo-spin. The peak completely disappears when α approaches unity, $\alpha \approx 1$ (single common electrode for both quantum dots). Tunnelling electrons lose information about their pseudo-spin orientation and the orbital Kondo effect is destroyed. It is important to emphasize that the orbital Kondo vanishes only for the totally symmetric coupling of each leads to both dots.

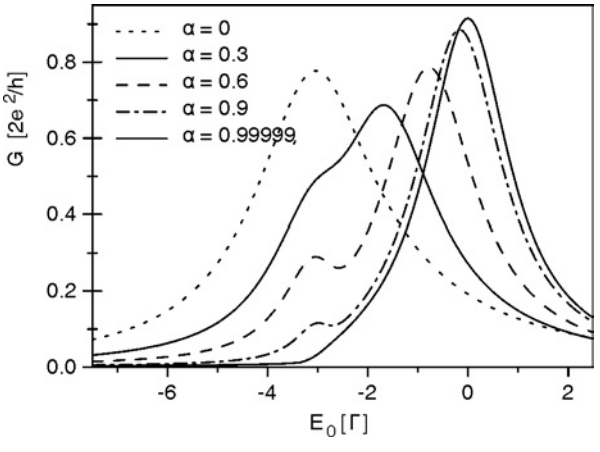

Fig. 3. The linear conductance in function of the dot level position E_0 for indicated values of α and $t = 0$

An influence of mixing on the linear conductance G is presented in Fig. 3 in which spectra calculated for various values of α are plotted. Results presented in Fig. 3 well confirm the conclusion that channel mixing effects suppress the orbital Kondo reso-

nance. With no cross-coupling between leads taken into account ($\alpha = 0$), the conductance is maximal in the Kondo regime, as expected. For $\alpha \neq 0$, the conductance shows a small cusp apart from the main peak. With increase of channel mixing parameter α, the position of the cusp remains constant and corresponds to the Kondo regime, while the maximum moves towards higher energies. First, we focus on the Kondo regime. The mixing violates the conservation of the pseudo-spin and Kondo effect is destroyed gradually. Indeed, with increase of α the side peak becomes narrower and its intensity decreases considerably. At the same time, the right maximum becomes higher and is shifted toward the Fermi energy of electrodes $E_F = 0$. For $\alpha \approx 1$ there is only one maximum and the shape of the conductance curve resembles very well the one obtained with use of standard Hartree–Fock approximation where no Kondo effect is expected.

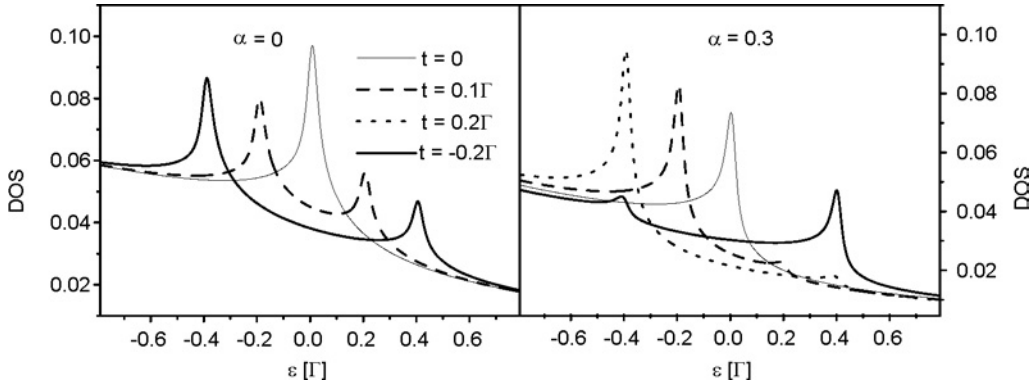

Fig. 4. Densities of states (DOS) in the Kondo regime ($E_0 = -4\Gamma$) calculated for indicated values of α and tunnelling rate t

Next, the influence of tunnelling coupling between dots on the Kondo anomaly is analyzed. Densities of states are plotted in Fig. 4 for indicated values of tunnelling rate t and the parameter α. When interdot coupling is taken into account, the Kondo peak becomes split into two components centred at $\varepsilon = \pm 2t$, what also leads to the suppression of the effect. It is worth mentioning that the interdot tunnelling t affects the orbital Kondo resonance in similar way as a magnetic field does for the spin Kondo. For $\alpha \neq 0$, no peaks practically appear at $\varepsilon = 2t$ and the curves have an asymmetric shape. Only for $\alpha = 0$ results are identical for negative and positive values of the interdot coupling ($t = 0.2\Gamma$ and $t = -0.2\Gamma$).

The differential conductance ($G_{\mathrm{diff}} = dI/dV$) calculated for several values of interdot tunnelling t and α is presented in Fig. 5. For the system with energy levels of both dots aligned, the results are fully symmetric with respect to the bias reversal. For $t = 0$ there is a pronounced zero-bias maximum which intensity strongly decreases when mixing effects become important (compare results presented for $\alpha = 0$ and $\alpha = 0.3$). When interdot tunnelling effects are included, the peak splits into two components

centred at $eV = \pm 2t$. This result is in good qualitative agreement with experimental data [8]. With increase of cross-coupling α the differential conductance drops, peak intensity is lower but their positions remain unchanged.

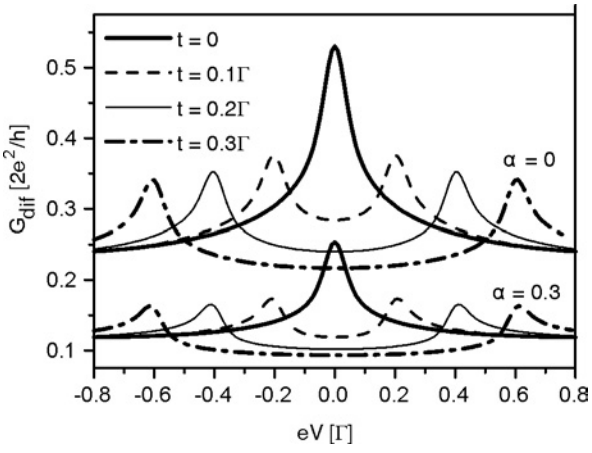

Fig. 5. Bias dependence of differential conductance for indicated values of t, $E_0 = -4\Gamma$, $\alpha = 0$ (upper curves) and $\alpha = 0.3$ (lower curves)

4. Conclusions

We have analyzed the electron transport though the system in the Kondo regime in a presence of channel mixing effects. The orbital Kondo phenomenon has been studied when α changes from 0 with no mixing to 1 with maximum mixing what corresponds to both dots coupled to common left and right reservoirs. The zero-bias Kondo anomaly in the differential conductance is obtained for $t = 0$. With increase of α, the Kondo effect is gradually destroyed and intensity of the Kondo peak is lowered. A strong suppression of the linear conductance G in the Kondo regime due to channel mixing effects is also obtained. For maximum mixing, the system corresponds to DQDs in parallel configuration with orbital Kondo effect destroyed. Therefore, the linear conductance shows only a peak in a the vicinity of the Fermi level in the leads. A presence of the tunnelling coupling between dots leads to a splitting of the Kondo anomaly and to additional suppression of the effect.

References

[1] JOHNSON A.C., MARCUS C.M., HANSON M.P., GOSSARD A.C., Phys. Rev. Lett., 93 (2004), 106803.
[2] RUSHFORTH A.W., SMITH C.G., FARRER I., RITCHIE D.A., JONES G.A., ANDERSON D., PEPPER M., Phys. Rev. B, 73 (2006), 081305.
[3] LADRON DE GUEVARA M.L., CLARO F., ORELLANA P.A., Phys. Rev. B, 67 (2003), 195335.

[4] GOLDHABER-GORDON D., SHTRIKMAN H., MAHALU D., ABUSCH-MAGDER D., MEIRAV U., KASTNER M.A., Nature, 391 (1998), 156.
[5] GORES J., GOLDHABER-GORDON D., HEEMEYER S., KASTNER M.A., SHTRIKMAN H., MAHALU D., MEIRAV U., Phys. Rev. B, 62 (2000), 2188.
[6] KOBAYASHI K., AIKAWA H., KATSUMOTO S., IYE Y., Phys. Rev. Lett., 88 (2002), 256806.
[7] WILHELM U., SCHMID J., WEIS J., VON KLITZING K., Physica E, 14 (2002), 385.
[8] HOLLEITNER A.W., CHUDNOVSKIY A., PFANNKUCHE D., EBERL K., BLICK R.H., Phys. Rev. B, 70 (2004), 075204
[9] JARILLO-HERRERO P., KONG J., VAN DER ZANT H.S.J., DEKKER C., KOUWENHOVEN L.P., DE FRANCESCHI S., Phys. Rev. Lett., 94 (2005), 156802.
[10] SASAKI S., AMAHA S., ASAKAWA N., ETO M., TARUCHA S., Phys. Rev. Lett 93 (2004), 017205; TOKURA Y., SASAKI S., AUSTING D.G., TARUCHA S., Physica B, 298 (2001), 260.
[11] SATO T., ETO M., Physica E, 29 (2005), 652.
[12] LE HUR K., SIMON P., BORDA L., Phys. Rev. B, 69 (2004), 045326.
[13] LÓPEZ R., SÁNCHEZ D., LEE M., CHOI M-S., SIMON P., LE HUR K., Phys. Rev. B, 71 (2005), 115312.
[14] LE HUR K., SIMON P., LOSS D., Phys. Rev. B, 75 (2007), 035332.
[15] GALPIN M.R.,.LOGAN D.E., KRISHNAMURTHY H.R., Phys. Rev. Lett., 94 (2005), 186406.
[16] ZARAND G., BRATAAS A., GOLDHABER-GORDON D., Solid State Comm., 126 (2003), 463; BORDA L., ZARAND G., HOFSTETTER W., HALPERIN B.I., VON DELFT J., Phys. Rev. Lett., 90 (2003), 026602.
[17] LIM J.S., CHOI M-S., CHOI M.Y., LÓPEZ R., AGUADO R., Phys. Rev. B, 74 (2006), 205119.
[18] MEIR Y., WINGREEN N.S., LEE P.A., Phys. Rev. Lett., 70 (1993), 2601.
[19] SZTENKIEL D., SWIRKOWICZ R., J. Phys: Cond. Matter, to be published.
[20] NG T.K., LEE P.A., Phys. Rev. Lett., 61 (1988), 1768.

Received 10 May 2007
Revised 21 January 2008

Materials Science-Poland, *Vol. 26*, *No. 3*, *2008*

Spin-polarized transport through two quantum dots Interference and Coulomb correlation effects*

P. TROCHA[1*], J. BARNAŚ[1,2]

[1]Department of Physics, Adam Mickiewicz University, ul. Umułtowska 85, 61-614 Poznań, Poland

[2]Institute of Molecular Physics, Polish Academy of Sciences, ul. Smoluchowskiego 17, 60-179 Poznań, Poland

Electronic transport through two single-level quantum dots attached in parallel to ferromagnetic leads has been analyzed theoretically. The intra-dot Coulomb correlation was taken into account, while the inter-dot hopping and Coulomb repulsion have been neglected. The dots, however, may interact *via* the external leads when the off-diagonal elements of the coupling matrix do not vanish. Conductance and tunnel magnetoresistance associated with the magnetization rotation from antiparallel to parallel configurations are calculated by the non-equilibrium Green function technique. The relevant Green functions are derived from the appropriate equation of motion in the Hartree–Fock approximation. We focus on the interference effects due to nonzero off-diagonal elements of the coupling matrix.

Key words*: quantum dot; tunnel magnetoresistance; quantum interference*

1. Introduction

Owing to a recent progress in nanotechnology, it is now possible to attach quantum dots (QDs) to magnetic/nonmagnetic electrodes (leads) and investigate spin and charge transport through the dots. This, in turn, leads to a significant theoretical activity aimed at understanding details of electronic transport through single QDs as well as through the arrays of dots [1–8]. In this paper, we consider electronic transport through two QDs which are coupled in parallel to two external ferromagnetic leads. The inter-dot hopping and inter-dot Coulomb interaction are neglected, while the intra-dot electron correlations are taken into account. The two quantum dots interact with the ferromagnetic leads, and the corresponding interaction matrix includes both diagonal and off-diagonal elements. The latter are of particular interest here as they give rise to indirect interaction of the dots and lead to some interference effects.

---

*Presented at the Conference of the Scientific Network "New Materials for Magnetoelectronics – MAG-EL-MAT 2007", Będlewo near Poznań, 7–10 May, 2007.

**Corresponding author, e-mail: piotrtroch@o2.pl

Transport characteristics of the system in the linear response regime are calculated using the Green function formalism [9–14]. Since the systems with Coulomb interaction cannot be treated exactly, we applied the Hartree–Fock decoupling scheme to calculate the higher order Green functions from the corresponding equations of motion. The average values of the occupation numbers (which enter the expressions for the Green functions) and the Green functions have been calculated self-consistently. In section 2, we briefly describe the model as well as the theoretical method. Numerical results and their discussion are presented in section 3, whereas summary and final conclusions – in section 4.

2. Model and method

We consider two single-level quantum dots attached to ferromagnetic leads with collinear (parallel or antiparallel) magnetic moments. The system is described by the-Hamiltonian of the general form:

$$H = H_{\text{leads}} + H_{DQD} + H_{\text{tunnel}}$$

The first term, H_{leads}, describes the left (L) and right (R) electrodes in the non-interacting quasi-particle approximation:

$$H_{\text{leads}} = H_L + H_R \quad \text{with} \quad H_\alpha = \sum_{\mathbf{k}\sigma} \varepsilon_{\mathbf{k}\alpha\sigma} c^+_{\mathbf{k}\alpha\sigma} c_{\mathbf{k}\alpha\sigma} \quad \text{for } \alpha = L, R \text{ (for } \alpha = L, R)$$

The second term describes the two quantum dots

$$H_{DQD} = \sum_{i\sigma} \varepsilon_{i\sigma} d^+_{i\sigma} d_{i\sigma} + \sum_i U_i n_{i\sigma} n_{i\bar{\sigma}}$$

where $\varepsilon_{i\sigma}$ is the energy of the ith dot bare level, $n_{i\sigma} \equiv d^+_{i\sigma} d_{i\sigma}$ is the particle number operator, and U_i denotes the corresponding Coulomb integral. The last term of the Hamiltonian, H_{tunnel}, describes electron tunneling from the leads to dots (and *vice versa*)

$$H_{\text{tunnel}} = \sum_{\mathbf{k}\alpha} \sum_{i\sigma} V^\alpha_{i\mathbf{k}\sigma} c^+_{\mathbf{k}\alpha\sigma} d_{i\sigma} + hc$$

where $V^\alpha_{i\mathbf{k}\sigma}$ are the relevant matrix elements. Coupling of the dots to external leads can be parameterized in terms of

$$\Gamma^\alpha_{ij\sigma}(\varepsilon) = 2\pi \sum_{\mathbf{k}} V^\alpha_{i\mathbf{k}\sigma} V^{\alpha *}_{j\mathbf{k}\sigma} \delta(\varepsilon - \varepsilon_{\mathbf{k}\alpha\sigma})$$

We assume that the matrix elements $\Gamma^\alpha_{ij\sigma}(\varepsilon)$ are constant within the energy band, $\Gamma^\alpha_{ij\sigma}(\varepsilon) = \Gamma^\alpha_{ij\sigma} = \text{const}$ for $\varepsilon \in \langle -D, D \rangle$, and $\Gamma^\alpha_{ij\sigma}(\varepsilon) = 0$ otherwise (here 2D is the electron bandwidth).

When the matrix elements $V^{\alpha}_{i\mathbf{k}\sigma}$ can be assumed real and constant, the coupling matrix $\mathbf{\Gamma}^{\alpha}_{\sigma}$ can be written in the form,

$$\mathbf{\Gamma}^{\alpha}_{\sigma} = \begin{pmatrix} \Gamma^{\alpha}_{11\sigma} & \sqrt{\Gamma^{\alpha}_{11\sigma}\Gamma^{\alpha}_{22\sigma}} \\ \sqrt{\Gamma^{\alpha}_{11\sigma}\Gamma^{\alpha}_{22\sigma}} & \Gamma^{\alpha}_{22\sigma} \end{pmatrix}$$

The above form of $\mathbf{\Gamma}^{\alpha}_{\sigma}$ corresponds to the case of maximum off-diagonal elements. In a general case, however, the off-diagonal matrix elements can be significantly reduced in comparison to those given in the equation, or even can be totally suppressed due to complete destructive interference. To include these effects, we introduce a prefactor $q \in \langle 0,1 \rangle$ in the off-diagonal matrix elements. Moreover, the off-diagonal elements can be complex in a general case. Here, however, we assume them real. Thus, in the parallel magnetic configuration one can write:

$$\Gamma^{L}_{11\sigma} = \Gamma_0(1 \pm p_L), \qquad \Gamma^{L}_{22\sigma} = \alpha\Gamma_0(1 \pm p_L), \qquad \Gamma^{L}_{12\sigma} = \Gamma^{L}_{21\sigma} = q\Gamma_0\sqrt{\alpha}(1 \pm p_L)$$
$$\Gamma^{R}_{11\sigma} = \gamma\alpha\Gamma_0(1 \pm p_R), \qquad \Gamma^{R}_{12\sigma} = \Gamma^{R}_{21\sigma} = q\gamma\Gamma_0\sqrt{\alpha}(1 \pm p_R), \qquad \Gamma^{R}_{22\sigma} = \gamma\Gamma_0(1 \pm p_R)$$

for $\sigma = \uparrow$ (upper sign) and $\sigma = \downarrow$ (lower sign). Here, p_α is the polarization strength of the α-th lead, γ_0 is a constant, the factor α takes into account a difference in the coupling strengths of a given electrode to the two dots, whereas γ describes asymmetry in the coupling of the dots to the left and right leads. Similar formula can be written for antiparallel configuration.

Electric current J flowing through the system can be determined from the following formula [13, 14]:

$$J = \sum_{\sigma} J_{\sigma}$$
$$= \frac{ie}{2\hbar}\sum_{\sigma}\int \frac{d\varepsilon}{2\pi} Tr\left\{\left[\mathbf{\Gamma}^{L}_{\sigma} - \mathbf{\Gamma}^{R}_{\sigma}\right]\mathbf{G}^{<}_{\sigma}(\varepsilon) + \left[f_L(\varepsilon)\mathbf{\Gamma}^{L}_{\sigma} - f_R(\varepsilon)\mathbf{\Gamma}^{R}_{\sigma}\right]\left[\mathbf{G}^{r}_{\sigma}(\varepsilon) - \mathbf{G}^{a}_{\sigma}(\varepsilon)\right]\right\},$$

where

$$f_\alpha(\varepsilon) = \left[\exp\left(\frac{\varepsilon - \mu_\alpha}{k_B T}\right) + 1\right]^{-1}$$

is the Fermi–Dirac distribution function for the α-th lead, whereas $\mathbf{G}^{<}_{\sigma}(\varepsilon)$ and $\mathbf{G}^{r(a)}_{\sigma}(\varepsilon)$ are the Fourier transforms of the lesser and retarded (advanced) Green functions of the dots. To calculate the Green functions $\mathbf{G}^{r(a)}_{\sigma}(\varepsilon)$, we write the corresponding equation of motion and apply the Hartrtee–Fock decoupling scheme for higher order Green functions. In turn, the lesser Green function $G^{<}_{ij\sigma}(\varepsilon)$ has been calculated

from the corresponding equation of motion, with the higher order Green functions calculated on taking into account the Langreth theorem [14] and the Hartree–Fock decoupling scheme assumed when calculating $\mathbf{G}_{\sigma}^{r(a)}(\varepsilon)$. Details of the calculations will be presented elsewhere. We only note that these formulas include the expectation values $\langle n_{i\sigma}\rangle$, $\langle d_{i\bar{\sigma}}^{+} c_{k\alpha\bar{\sigma}}\rangle$ and $\langle c_{k\alpha\sigma}^{+} d_{i\bar{\sigma}}\rangle$, which can be determined taking into account the identities:

$$\langle n_{i\sigma}\rangle = -i\int \frac{d\varepsilon}{2\pi} G_{ii\sigma}^{<}(\varepsilon)$$

$$\langle d_{i\bar{\sigma}}^{+} c_{k\alpha\bar{\sigma}}\rangle = -i\int \frac{d\varepsilon}{2\pi} \langle\langle c_{k\alpha\sigma} \mid d_{j\sigma}^{+}\rangle\rangle^{<}$$

and a similar one for $\langle c_{k\alpha\sigma}^{+} d_{i\bar{\sigma}}\rangle$. The averages $\langle n_{i\sigma}\rangle$, $\langle d_{i\bar{\sigma}}^{+} c_{k\alpha\bar{\sigma}}\rangle$, $\langle c_{k\alpha\sigma}^{+} d_{i\bar{\sigma}}\rangle$ and the Green functions have been determined self-consistently.

3. Numerical results

Using the formulas derived above, one can calculate numerically the current, conductance, and tunnel magnetoresistance. The latter quantity describes the change in the system resistance when magnetic configuration of the system varies from antiparallel to parallel, and is described quantitatively by the ratio $(R_{AP} - R_P)/R_P$, where R_{AP} and R_P are the resistances in the antiparallel and parallel magnetic configurations, respectively. In the following discussion, we assume spin degenerate and equal bare dot levels, $\varepsilon_i\sigma = \varepsilon_0$ (for i = 1, 2 and $\sigma = \uparrow,\downarrow$). We also assume the same spin polarization of both leads ($p_L = p_R = p$ = 0.4), the same intra-dot Coulomb parameters for both dots ($U_1 = U_2 = U$), and left-right symmetry of the coupling (γ = 1). We also note that energy in this paper is measured in the units of γ_0, and that the numerical results are valid for temperatures above the corresponding Kondo temperature.

Let us consider first the case of nonmagnetic electrodes and U = 0. Figure 1 shows the linear conductance (per spin) in function of the dots' level position, calculated for two different values of the parameter α and two limiting values of the parameter q. For q = 1 (maximum off-diagonal elements of $\mathbf{\Gamma}_{\sigma}^{\alpha}$) and $\alpha \neq 1$ (in our case α = 0.15), the conductance has a dip when the bare dot levels cross the Fermi level of the leads. The dip is a consequence of destructive quantum interference of electron waves transmitted through the two effective levels of the DQD system, i.e. through the dot levels renormalized due to their interaction *via* the electrodes (owing to non-zero off-diagonal elements of the matrix $\mathbf{\Gamma}_{\sigma}^{\alpha}$). The dip, however, disappears when α = 1, but the conductance maximum does not reach $2e^2/h$ as it does for the totally decoupled dots (q = 0 and α = 1). It is also worth noting that the width of the peak for q = 1 and α = 1 is

two times higher than that for totally decoupled dots, and is of the order of $4\gamma_0$. The dip also disappears when $q = 0$, independently of the value of the parameter α.

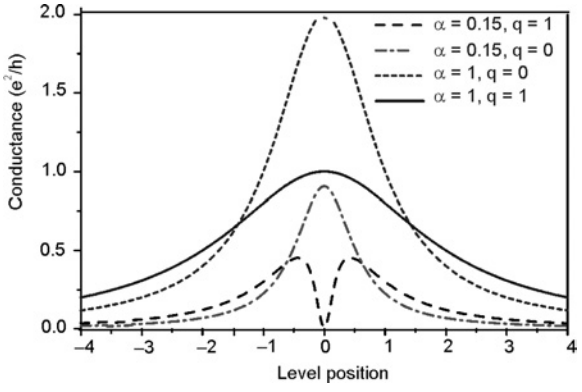

Fig.1. Linear conductance per spin in function of the position of bare dot levels (ε_0), calculated for indicated values of the parameters α and q and for $p = 0$, $U = 0$ and $k_BT = 0.01$. The energy is measured in the units of Γ_0

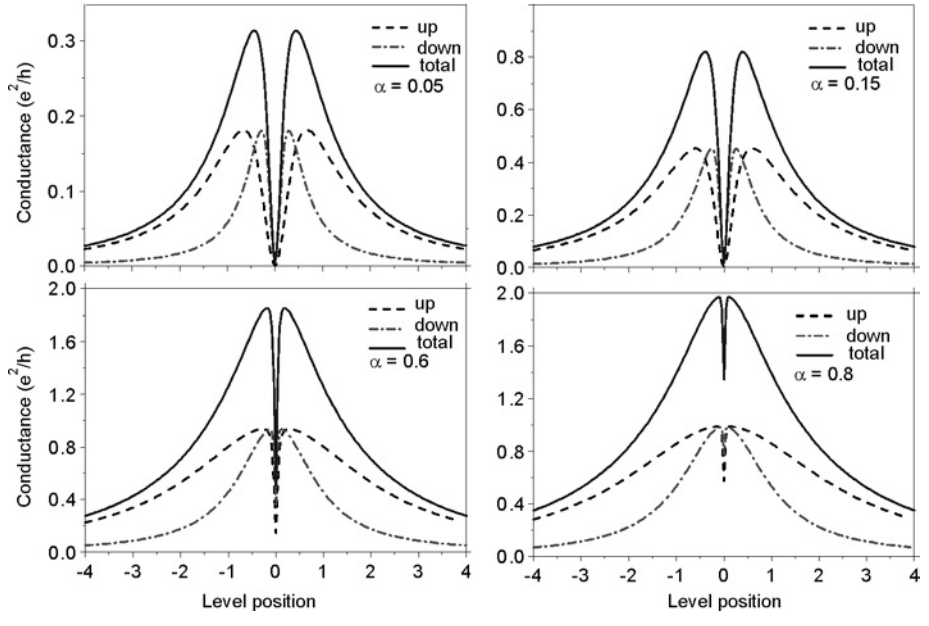

Fig. 2. Linear conductance for parallel magnetic configuration (total and for both spin channels) in function of the position of the dot levels (ε_0), calculated for indicated values of the parameter α and for $q = 1$, $p = 0.4$, $U = 0$, and $k_BT = 0.01$. The energy is measured in the units of Γ_0

In Figure 2, we show the linear conductance (total and for both spin channels) in the situation when the QDs are coupled to ferromagnetic leads, calculated for indicated values of the parameter α and for $q = 1$. The dip in the conductance emerges

when α departs from 1 ($\alpha < 1$), and increases with decreasing α. However, the conductance also decreases with decreasing α and disappears for $\alpha = 0$ (the dots are then coupled to one lead only and transport is suppressed). Thus, the conductance dip appears when there is an asymmetry in the coupling of a given electrode to the two dots, but only if the off-diagonal coupling elements are non-zero ($q > 0$).

Consider now the influence of the Coulomb interaction on the interference effects described above. First, the Coulomb interaction leads to splitting of the structure from Fig. 2. As a result, Coulomb counterparts of the spectra from Fig. 2 appear on their negative energy side, with characteristic gaps between the two parts of the spectra, as shown in Fig. 3. It is also worth to note that the Coulomb interaction generally breaks the symmetry of the spectra. Such symmetry is clearly seen in Fig. 2, but is absent in Fig. 3, particularly for α close to 1.

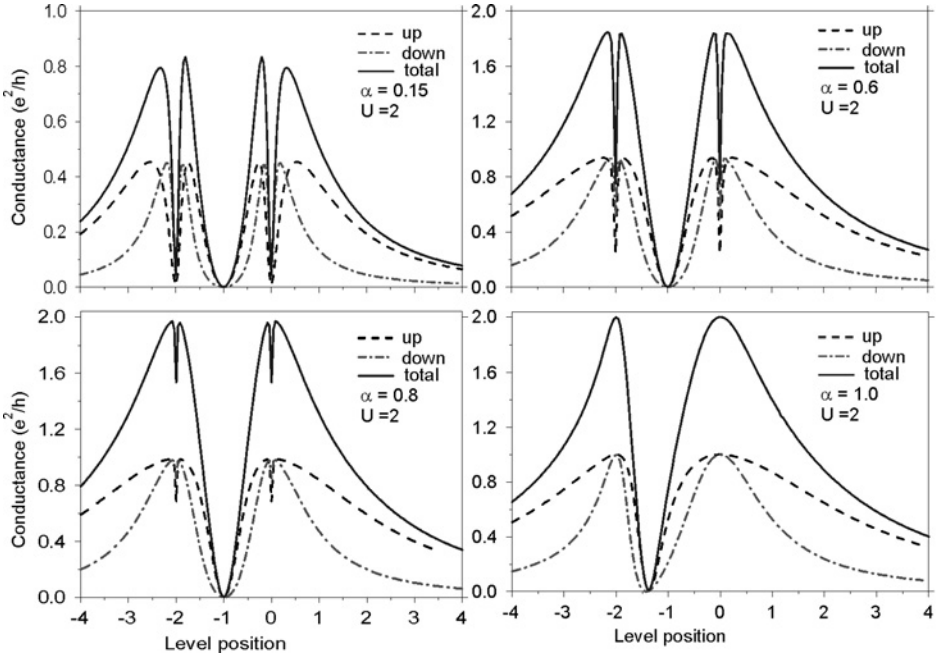

Fig. 3. Linear conductance for parallel magnetic configuration (total and for both spin channels) in function of the position of the dot levels (ε_0), calculated for indicated values of the parameters α and U, and for $q = 1$, $p = 0.4$, and $k_B T = 0.01$. The energy is measured in the units of Γ_0

The spectra shown in Fig. 3 are for a relatively large value of U ($U = 2$). The Coulomb counterparts are then well separated from the main spectra and the gap between them is well defined. The situation is more complex when the parameter U is smaller, as shown in Fig. 4. The four-peak structure is still present for $U = 0.6$, but only three peaks survive for $U = 0.2$ (see Fig. 4a).

Linear conductance in the parallel configuration is different from that in the antiparallel one. This leads to a nonzero tunnel magnetoresistance (TMR), shown in Fig. 5

for indicated values of the Coulomb parameter U. When the dots' levels are well above or well below the Fermi level of the leads, TMR tends to the Julliere value,

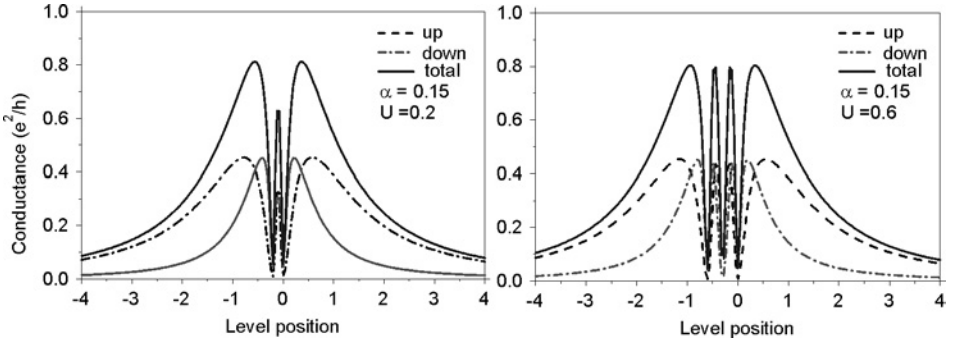

Fig. 4. Linear conductance for parallel magnetic configuration (total and for both spin channels) in function of the position of the dot levels (ε_0), calculated for indicated values of the parameters α and U, and for $q = 1$, $p = 0.4$, and $k_BT = 0.01$. The energy is measured in the units of Γ_0.

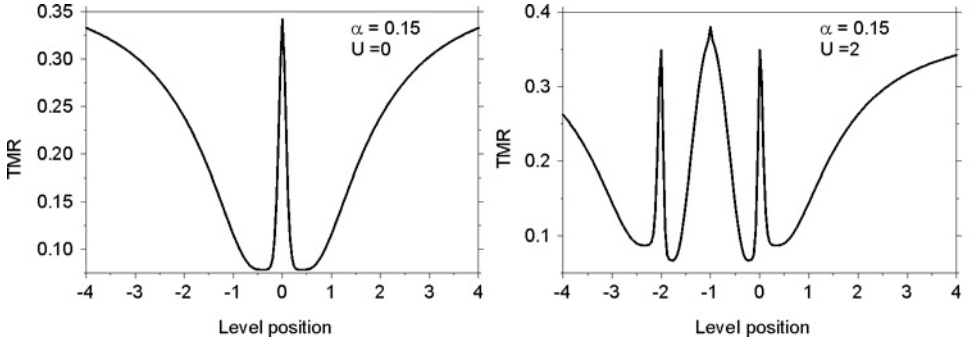

Fig. 5. TMR in the linear response regime in function of the level position (ε_0) calculated for indicated values of the parameter U, $p = 0.4$, $k_BT = 0.01$

$2p^2/(1-p)^2$, observed in planar magnetic junctions with the same ferromagnetic electrodes. When the dot levels approach the Fermi energy, the situation becomes more complex and TMR displays new features, as for instance some enhancement (peaks) and/or suppression (dips) seen in Fig.5. This is particularly seen for $U>0$, where the number of peaks and dips in TMR is larger than for $U = 0$.

4. Summary and conclusions

We considered transport through two quantum dots attached in parallel to two ferromagnetic leads. The dots do not interact directly, however, they can interact indirectly *via* the leads provided the off-diagonal elements of the coupling matrix are nonzero. We have found a splitting in the conductance peak for $U = 0$, which is a result of

quantum interference. Apart from this, we have shown that including Coulomb correlations leads to splitting of the spectra and additional Coulomb counterparts to the main spectra appear, with characteristic Coulomb gaps between.

The influence of quantum interference and Coulomb correlation on TMR was also analyzed and we found some additional features of the magnetoresistance. These new features follow from the interplay of Coulomb interaction and quantum interference.

Acknowledgement

This work, as a part of the European Science Foundation EUROCORES Programme SPINTRA, was supported by funds from the Ministry of Science and Higher Education as a research project in years 2006–2009 and the EC Sixth Framework Programme, under Contract N. ERAS-CT-2003-980409. One of the authors (PT) also acknowledges support from the MAGELMAT network.

References

[1] LANDRÓN DE GUEVARA M.L., CLARO F., ORELLANA P.A., Phys. Rev. B, 67 (2003), 195335.
[2] LU H., LÜ R., ZHU B.-F., cond-mat/0511101, J. Phys.: Condens. Matter, 18 (2006), 8961.
[3] DING G.-H., KIM C.K., NAHM K., Phys. Rev. B, 71 (2005), 205313.
[4] BULKA B.R., KOSTYRKO T., Phys. Rev. B, 70 (2004), 205333.
[5] TROCHA P., BARNAŚ J., phys. stat. sol. (c), 3 (2006), 113.
[6] TROCHA P., BARNA Ś J., phys. stat. sol. (b), 244 (2007), 2553.
[7] TROCHA P., BARNA Ś J., Mater. Sci.-Poland, 25 (2007), 545.
[8] WYSOCKI A., BARNAŚ J., Acta Phys. Superfic., 9 (2006), 177.
[9] TANAKA Y., KAWAKAMI N., Phys. Rev. B, 72 (2005), 085304.
[10] ŚWIRKOWICZ R., WILCZYŃSKI M., BARNAŚ J., J. Phys. Condens. Matter, 18 (2006), 2291.
[11] WEYMANN I., BARNAŚ J., KÖNIG J., MARTINEK J., SCHÖN G., Phys. Rev. B, 72 (2005), 113301.
[12] RUDZIŃSKI W., BARNAŚ J., ŚWIRKOWICZ R., WILCZYŃSKI M., Phys. Rev. B, 71 (2005), 205307.
[13] MEIR Y., WINGREEN N. S., Phys. Rev. Lett., 68 (1992), 2512.
[14] JAUHO A.-P., WINGREEN N.S., MEIR Y., Phys. Rev. B, 50 (1994), 5528.

Received 10 May 2007
Revised 21 January 2008

Materials Science-Poland, *Vol. 26*, *No. 3*, *2008*

Theoretical analysis of transport in ferromagnetic single -electron transistors in the sequential tunnelling regime*

J. WIŚNIEWSKA**, I. WEYMANN

Institute of Physics, Adam Mickiewicz University, ul. Umułtowska 85, 61-614 Poznań, Poland

Spin-dependent transport properties of a single-electron transistor have been analysed, whose two external electrodes and the central part (island) are ferromagnetic. Based on the real-time diagrammatic technique, all transport contributions have been calculated up to the first order in the coupling strength between the island and the leads – this comprises a sequential tunnelling. Relevant occupation probabilities of different charge states are determined from the generalized master equation in the Liouville space. Assuming that spin relaxation processes on the island are sufficiently fast to neglect spin accumulation, we analyze electric current flowing through the system in the parallel and antiparallel magnetic configurations, as well as the resulting tunnel magnetoresistance. We show that transport characteristics of ferromagnetic single-electron transistors exhibit a strong dependence on the magnetic configuration of the system. Furthermore, we also demonstrate that the bias dependence of both the differential conductance and tunnel magnetoresistance displays an oscillatory-like behaviour resulting from single-electron charging effects.

Key words: *ferromagnetic single-electron transistor; spin-dependent transport; real-time diagrammatic technique*

1. Introduction

We consider spin-dependent transport properties of a ferromagnetic single-electron transistor (FM SET) whose two external electrodes as well as the central electrode (island) are ferromagnetic. Based on the real-time diagrammatic technique [1–3], we analyze spin-dependent transport in the sequential tunnelling regime. In this transport regime, if the applied bias voltage is above a certain threshold voltage, the current flows due to consecutive, uncorrelated single-electron tunnelling events. On the other hand, if the applied transport voltage is below the threshold voltage, the current is exponentially suppressed due to the Coulomb interaction which prevents further tunnelling and gives rise to the Coulomb blockade effect. Apart from the Coulomb block-

---

*Presented at the Conference of the Scientific Network "New Materials for Magnetoelectronics – MAG-EL-MAT 2007", Będlewo near Poznań, 7–10 May, 2007.

**Corresponding author, e-mail: justyw@amu.edu.pl

ade phenomena, charging with single electrons leads to the so-called Coulomb staircase characteristics of the current versus the bias voltage as well as the sawtooth-like dependence of the current on the gate voltage Coulomb oscillations [4]. In addition, if the electrodes are ferromagnetic, one finds further interesting effects, resulting from the interplay of the single-electron charging and spin-dependence of tunnelling processes such as oscillations of tunnel magnetoresistance (TMR), spin accumulation, etc. [5–8].

Assuming that the spin relaxation processes on the island are sufficiently fast to neglect the effects of spin accumulation, we have analyzed the bias and gate voltage dependence of the electric current and differential conductance of FM SET in the parallel and antiparallel magnetic configurations as well as the resulting TMR effect. We show that the TMR exhibits an oscillatory-like behaviour on the bias voltage, while it changes periodically with the gate voltage.

In Section 2, we define the model and present its theoretical description. Section 3 contains general results calculated with the aid of the real-time diagrammatic technique and discussion. Summary is given in Section 4.

2. Model and theoretical description

A scheme of a ferromagnetic single-electron transistor considered in the paper is shown in Fig. 1. It consists of a mesoscopic metallic island coupled by tunnelling junctions to two external electrodes, as well as to an external nonmagnetic gate voltage. Both the island and the leads are assumed to be built of ferromagnetic materials. It is also assumed that the system can be in two different magnetic configurations: the parallel and antiparallel ones. In the parallel configuration, all the magnetizations are aligned, whereas in the antiparallel configuration the magnetization of the island is antiparallel to magnetic moments of the leads (Fig. 1).

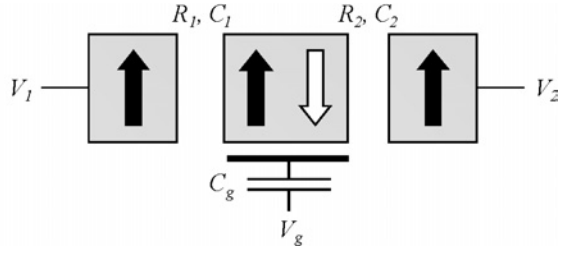

Fig. 1. A scheme of the ferromagnetic single-electron transistor consisting of two ferromagnetic external electrodes and a ferromagnetic island between them, while the gate is nonmagnetic. It is assumed that the system can be either in parallel or antiparallel magnetic configuration. The parameters are as indicated in the figure

The tunnelling of electrons through small metallic island in ferromagnetic single -electron transistor reveals, associated with low capacitance of the junctions, a strong dependence on the charging energy of the system given by [4]

$$E_{ch}(N,V) = \frac{\left(Ne - C_1V_1 - C_2V_2 - C_gV_g\right)^2}{2C} \tag{1}$$

where e is the electron charge, N denotes the number of excess electrons occupying the island, $C = C_1 + C_2 + C_g$ is the total capacitance of the island, C_1 and C_2 are the capacitances of the first and second junctions, while C_g denotes the gate capacitance. When the charging energy is larger than the thermal energy, transport characteristics reveal the effects associated with discreteness of charge, such as Coulomb blockade, Coulomb oscillations, etc. [4]. Furthermore, if the transparency of tunnel barriers is low and the resistance of a single barrier is much higher than the quantum resistance, $R_Q = h/e^2$, transport through the system is dominated by incoherent, sequential tunnelling processes, when the electrons are transferred through the system one by one. This transport regime can be described in the lowest-order perturbation with respect to the coupling strength of the island to the leads. Moreover, we also note that this transport regime is relevant to many current experiments [9]. In this analysis we assume that spin relaxation processes on the island are sufficiently fast to neglect spin accumulation on the island. We also assume that the system is symmetrically biased, $V_1 = -V_2 = V/2$.

In order to determine the transport characteristics, we employ a diagrammatic technique in a real time [1–3] to identify processes of sequential tunnelling in the FM SET. This technique consists in a systematic perturbation expansion of the density matrix elements and the current operator with respect to the coupling between the island and the leads. The transport properties of the system are governed by the time evolution of the density matrix, which is usually visualized graphically as a sequence of irreducible diagrams on the Keldysh contour [1–3]. Each diagram has a certain number of tunnelling lines, which indicate respective tunnelling processes between the island and the leads. Since we consider only the first-order processes, the diagrams in the sequential tunnelling approximation have only one tunnelling line, corresponding to a sequential tunnelling event. Each tunnelling line gives the golden-rule rate

$$\alpha_r^{\pm,\sigma}(\omega) = \pm\alpha_0^{r,\sigma}\frac{\omega - \mu_r}{e^{\pm\beta(\omega-\mu_r)} - 1}, \tag{2}$$

where

$$\alpha_0^{r,\sigma} = \frac{h}{4\pi^2e^2}\frac{1}{R_{r,\sigma}} = \frac{R_Q}{4\pi^2R_{r,\sigma}}$$

$R_{r,\sigma}$ denotes spin-dependent resistance of the r = 1, 2 junction, ω is the energy of tunnelling lines in diagrams, μ_r denotes the electrochemical potential of the electrode r, and $\beta = 1/k_BT$. The sign of $\alpha_r^{\pm,\sigma}(\omega)$ depends on the direction of tunnelling line (+ for lines directed backward or – for lines directed forward with respect to the closed time path in diagram).

Because we consider only the spin-conserving tunnelling processes and collinear magnetic configurations of the system, the density matrix of the system is diagonal; its elements, P_χ, correspond then to the probability of finding the system in a certain state χ in charge space. The relevant probabilities in a stationary state can be found by using the following master-like equation [1–3]

$$0 = \sum_{\chi'} P_{\chi'} \Sigma_{\chi'\chi} \tag{3}$$

where the object needed as an input is the Laplace transform of the generalized transition rate $\Sigma_{\chi',\chi}(t',t)$ from a state χ' (initial charge state of a diagram) at time t' to state χ (final charge state of a diagram) at time t. This rate is the sum over all irreducible diagrams [1–3] contributing to the transport through the FM SET and corresponds to the self-energy of the Dyson equation for the full propagator of the system. The value of any first-order diagram is added to the appropriate matrix element of the self-energy matrix $\Sigma_{\chi',\chi}$. The self-energies can be defined as

$$\Sigma_{\chi',\chi}(t',t) = \sum_r \left\{ \Sigma^{r+}_{\chi',\chi}(t',t) + \Sigma^{r-}_{\chi',\chi}(t',t) \right\} \tag{4}$$

here $\Sigma^{r+}_{\chi',\chi}$ includes all those diagrams which contribute to $\Sigma_{\chi',\chi}$ with the rightmost vertex on the upper propagator and rightmost contraction line describing tunnelling out of electrode through junction r, as well as diagrams with rightmost vertex on the lower propagator and the rightmost process describing tunnelling into lead r; $\Sigma^{r-}_{\chi',\chi}$ is given by summing correspondingly the rest of diagrams. For the case of FM SET and in the sequential tunnelling regime, we get

$$\Sigma_{\chi,\chi} = -\Sigma_{\chi,\chi-1} - \Sigma_{\chi,\chi+1} = -2\pi i \sum_{r,\sigma} \alpha_r^{-,\sigma}\left(E_\chi - E_{\chi-1}\right) - 2\pi i \sum_r \alpha_r^{+,\sigma}\left(E_{\chi+1} - E_\chi\right) \tag{5}$$

Having determined the respective first-order self-energies, one can calculate both the occupation probabilities of the island as well as the sequential current flowing through the system. The stationary current flowing through the barrier r is given by [1–3]

$$I_r = -\frac{ie}{\hbar} \sum_{\chi,\chi'} P_{\chi'} \Sigma^{r+}_{\chi',\chi} = \frac{ie}{\hbar} \sum_{\chi,\chi'} P_{\chi'} \Sigma^{r-}_{\chi',\chi} \tag{6}$$

3. Results and discussion

Using Equation (6) one can calculate the current flowing through the system in the parallel and antiparallel magnetic configurations. Due to the spin dependence of the diagrams, the current flowing in the parallel configuration I_p is generally larger than

the current flowing through the system in the antiparallel configuration I_{ap}. This difference gives rise to a nonzero tunnel magnetoresistance (TMR) effect. The TMR is defined as [5, 10]:

$$TMR = \frac{I_p}{I_{ap}} - 1 \tag{7}$$

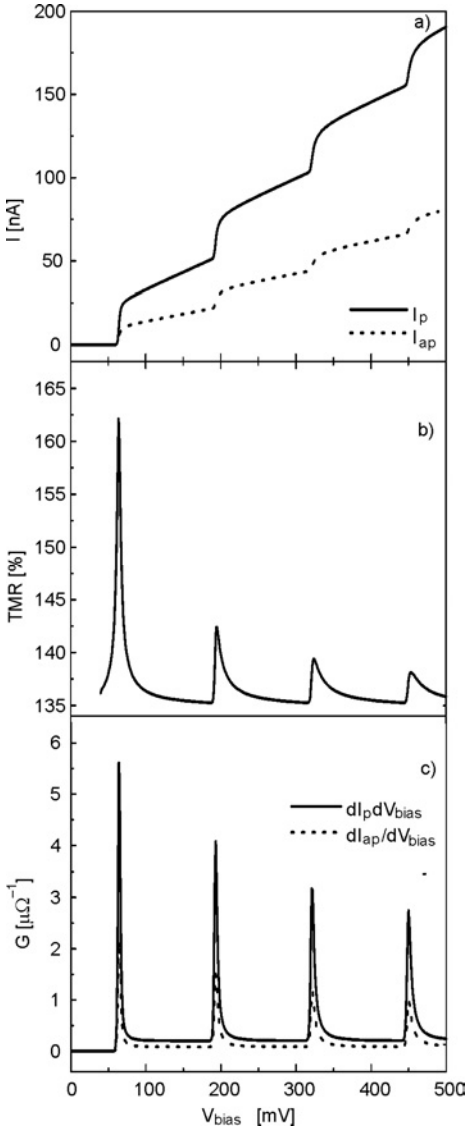

Fig. 2. The bias voltage dependence of electric current (a), differential conductance (c) in the parallel and anti-parallel magnetic configurations, as well as the resulting TMR (b). The parameters assumed in numerical calculations are: $C_1 = C_2 = 1$ aF, $C_g = 0.5$ aF, $T = 4.2$ K and $V_g = 0$, while the barrier resistances: $R_1^{p,+} = 20000R_Q$, $R_1^{p,-} = 100R_Q$, $R_2^{p,+} = 20R_Q$, $R_2^{p,-} = 0.5R_Q$, whereas $R_r^{ap} = \sqrt{R_r^{p,+}R_r^{p,-}}$ for $r = 1.2$

In the following, we present and discuss results of our numerical calculations of transport characteristics of FM SET. In Figure 2a, we show the current flowing through the system as a function of the bias voltage for both parallel and antiparallel magnetic configurations.

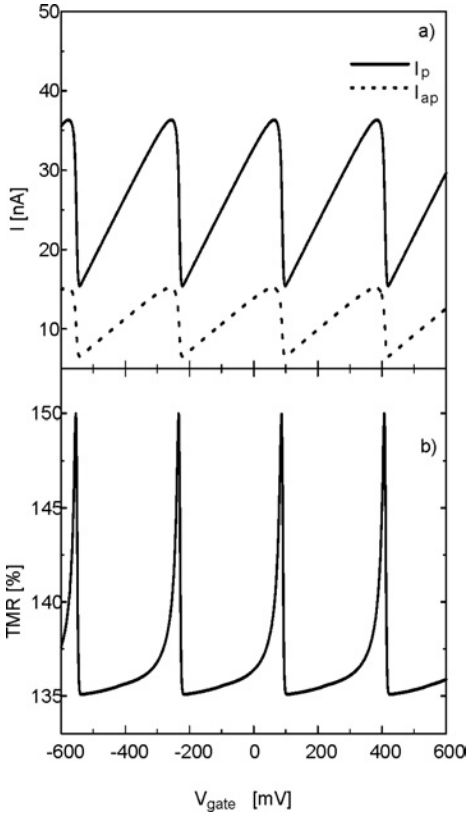

Fig. 3. The electric current (a) and TMR (b) in function of the gate voltage, calculated for the bias voltage $V = 50$ mV. The other parameters are the same as in Fig. 2

First of all, one can see that the sequential current is blocked for small bias voltages – this is the Coulomb blockade effect. When the transport voltage is above the threshold voltage, transport is allowed and electrons can tunnel one by one through the system. By increasing the bias voltage further, additional charge states start participating in transport, which leads to the so-called Coulomb staircase I–V characteristic. The occurrence of additional charge states in the energy window provided by transport voltage is also visible in the bias dependence of the differential conductance. Each time a next step in the I–V curve appears, there is a peak in differential conductance. This is shown in Fig. 2c. Furthermore, as one can see from Fig. 2a, the current flowing through the system in the parallel configuration is larger than that in the antiparallel one. This results from the fact that in the antiparallel configuration the majority (minority) electrons of the leads tunnel to the minority (majority) electron band of the island, which effectively leads to the suppression of current, as compared to the paral-

lel configuration. This difference gives rise to TMR which is shown in Fig. 2b. The bias dependence of the TMR displays characteristic peaks for voltages corresponding to consecutive steps in the *I–V* curves (Fig. 2a). This leads to an oscillatory-like dependence of the TMR on the bias voltage. Moreover, it is interesting to note that the amplitude of these oscillations decreases with increasing the transport voltage. The oscillations of TMR with the bias voltage are a result of the interplay of spin-dependent tunnelling and single-electron charging effects.

In addition, in Figure 3, we present the gate voltage dependence of the current in the parallel and antiparallel configurations as well as the TMR. By sweeping the gate voltage, one changes the number of excess electrons on the island. Each time additional single electron is allowed to tunnel to the island, there is an enhancement of the current. This leads to the sawtooth-like oscillations of the current. This effect is visible in both magnetic configurations as it does not result from ferromagnetism of electrodes but is associated with single-electron charging phenomena. The gate voltage dependence of the TMR is shown in Fig. 3b. Similarly as the current, the gate voltage dependence of the TMR also displays characteristic oscillations. This effect may be of importance in future magnetoelectronic devices, as be changing the gate voltage one can tune the magnitude of the TMR effect.

4. Conclusions

Theoretical analysis has been carried out of transport properties of the ferromagnetic single-electron transistor consisting of an ferromagnetic island and two ferromagnetic external electrodes. The considerations were based on the real-time diagrammatic technique. By evaluating the contributions coming from different first order diagrams, we determined the current flowing through the FM SET for arbitrary transport and gate voltages. It has been shown that all the transport characteristics, i.e. the current, TMR and differential conductance, strongly depend on the magnetic configuration of the system and reveal the effects associated with the Coulomb blockade, as well as the Coulomb staircase and Coulomb oscillations.

We believe that the present analysis will be a good starting point to extend the considerations to include the higher-order contributions, e.g., due to co-tunnelling processes. This would enable one to study the transport properties of FM SETs also in the Coulomb blockade regime.

Acknowledgements

We acknowledge discussions with J. Barnaś. This work was supported by funds of the Polish Ministry of Science and Higher Education as the research project for years 2006–2009.

References

[1] SCHOELLER H., SCHÖN G., Phys. Rev. B, 50 (1994), 18436.
[2] KÖNIG J., SCHOELLER H., SCHÖN G., Phys. Rev. B, 58 (1998), 7882.
[3] KUBALA B., JOHANSSON G., KÖNIG J., PHYS. Rev. B, 73 (2006), 165316.
[4] *Single Charge Tunnelling*, NATO Advanced Study Institute, Series B: Physics, Vol. 294, H. Grabert, M.H. Devoret (Eds.), Plenum, New York, 1992.
[5] BARNAŚ J., FERT A., Phys. Rev. Lett.,80 (1998), 1058.
[6] MARTINEK J., BARNAŚ J., MAEKAWA S., SCHOELLER H., SCHÖN G., Phys. Rev. B, 66 (2002), 014402.
[7] WEYMANN I., BARNAŚ J., phys. stat. sol. (b), 236 (2003), 651.
[8] WIŚNIEWSKA J, WEYMANN I., BARNAŚ J., Mol. Phys. Rep., 40 (2004), 187.
[9] YAKUSHIJI K., ERNULT F., IMAMURA H., YAMANE K., MITANI S., TAKANASHI K., TAKAHASHI S., MAEKAWA S., FUJIMMORI H., Nature Mater., 4 (2005), 57.
[10] JULLIERE M., Phys. Lett. A, 54 (1975), 225.

Received 10 May 2007
Revised 21 January 2008

Materials Science-Poland, *Vol. 26*, *No. 3*, *2008*

Electronic properties of $ThCu_5Sn$ and $ThCu_5In$ compounds*

M. WERWIŃSKI**, A. SZAJEK

Institute of Molecular Physics, Polish Academy of Sciences,
ul. M. Smoluchowskiego 17, 60-179, Poznań, Poland

$ThCu_5In$ and $ThCu_5Sn$ alloys crystallize in an orthorhombic $CeCu_5Au$-type structure with the *Pnma* space group. *Ab-initio* band structure calculations have been performed based on the full-potential local-orbital (FPLO) method. The calculated densities of electronic states are used to obtain photoemission spectra. The spectra of valence bands are predominated by 3d electrons located on Cu atoms.

Key words: *actinide compounds; electronic structure; photoemission spectra*

1. Introduction

Uranium compounds have recently attracted attention because of many interesting properties such as the Pauli paramagnetism, spin fluctuations, heavy fermions, magnetic ordering, or superconductivity. Many of these properties are related to the uranium 5f electrons which show an intermediate character between the localized 4f electron system and itinerant character of 3d electrons. The role of 5f electrons is important in actinides and the question is if they are localized or itinerant or perhaps the two configurations coexist giving rise to a new character of the electronic structure, referred to as the duality of the behaviour of 5f electrons. It is very useful to compare properties of isostructural systems with and without 5f electrons treating the systems with thorium as reference ones. Results of investigations of the electronic structure of UCu_5M (M = In, Sn) have recently been published [1, 2]. X-ray phase analyses of annealed and as-cast $ThCu_5In$ and $ThCu_5Sn$ alloys indicated that they are isostructural and that their structure is similar to that of UCu_5In(Sn) ($CeCu_5Au$ type structure being an ordered variant of the $CeCu_6$ type, space group *Pnma*) [3, 4]. The aim of this paper is to calculate the band structure of $ThCu_5In$(Sn) employing the *ab-initio* method.

---

*Presented at the Conference of the Scientific Network "New Materials for Magnetoelectronics – MAG-EL-MAT 2007", Będlewo near Poznań, 7–10 May, 2007.

**Corresponding author, e-mail: werwinski@ifmpan.poznan.pl

2. Method of calculations and results

In order to study electronic structure of the $ThCu_5M$ compounds (M = In, Sn), we used the full-potential local-orbital (FPLO) method [5] based on the local spin density approximation (LSDA) [6]. The fully-relativistic mode was used in the calculations. The calculations were carried out for the orthorhombic structure with 28 atoms per unit cell (four formula units, see Fig. 1 and Table 1) and experimental values of the lattice constants [3]: a = 8.305 Å, b = 5.068 Å, c = 10.600 Å, for $ThCu_5In$, and a = 8.286 Å, b = 5.080 Å, c = 10.554 Å for $ThCu_5Sn$.

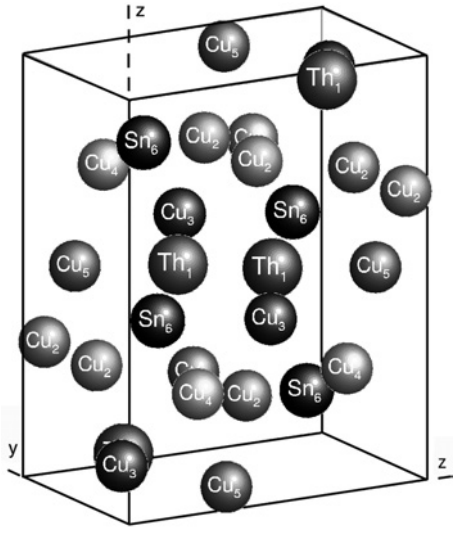

Fig. 1. Crystallographic structure of the $ThCu_5M$ (M = In, Sn) compounds

Table 1. Atomic positions [3] and the site projected densities of electronic states (DOS) at the Fermi level[a]

Atom	Position	DOS [states/(eV atom)]
Th(4c)	0.2538, 0.2500, 0.5600 0.2530, 0.2500, 0.5579	0.834 0.877
Cu1(8d)	0.0683, 0.5011, 0.3115 0.0699, 0.5020, 0.3116	0.309 0.306
Cu2(4c)	0.0583, 0.2500, 0.1037 0.0638, 0.2500, 0.1029	0.322 0.292
Cu3(4c)	0.3186, 0.2500, 0.2454 0.3195, 0.2500, 0.2460	0.305 0.263
Cu4(4c)	0.4144, 0.2500, 0.0162 0.4159, 0.2500, 0.0174	0.331 0.341
In(4c)	0.1397, 0.2500, 0.8604	0.324
Sn(4c)	0.1381, 0.2500, 0.8582	0.200

[a]The upper coordinates for Th and Cu atoms describe positions for $ThCu_5In$ cell and the lower for $ThCu_5Sn$ one.

For the calculations we assumed the following configurations of atoms: core (1s ... 5p electrons) + semi core (5d6s) + valence electrons (6p7s7p6d5f) for Th atoms, core (1s ... 2p electrons) + semi core (3s3p) + valence electrons (4s4p3d) for Cu atoms, and core (1s ... 3p electrons) + semi core (3d4s) + valence electrons (4p5s5p4d) for In and Sn atoms. The calculations were performed for the reciprocal space mesh containing 343 points within the irreducible wedge of the Brillouin zone using the tetrahedron method [7] for integrations. The LSDA exchange-correlation potential was assumed in the form proposed by Perdew and Wang [8]. The self consistent criterion was equal to 10^{-8} Ry for the total energy.

The theoretical X-ray photoemission spectra (XPS) were obtained from the calculated densities of electronic states (DOS) convoluted by Gaussian with a half-width equal to 0.3 eV and scaled using the proper photoelectronic cross sections for partial states [9].

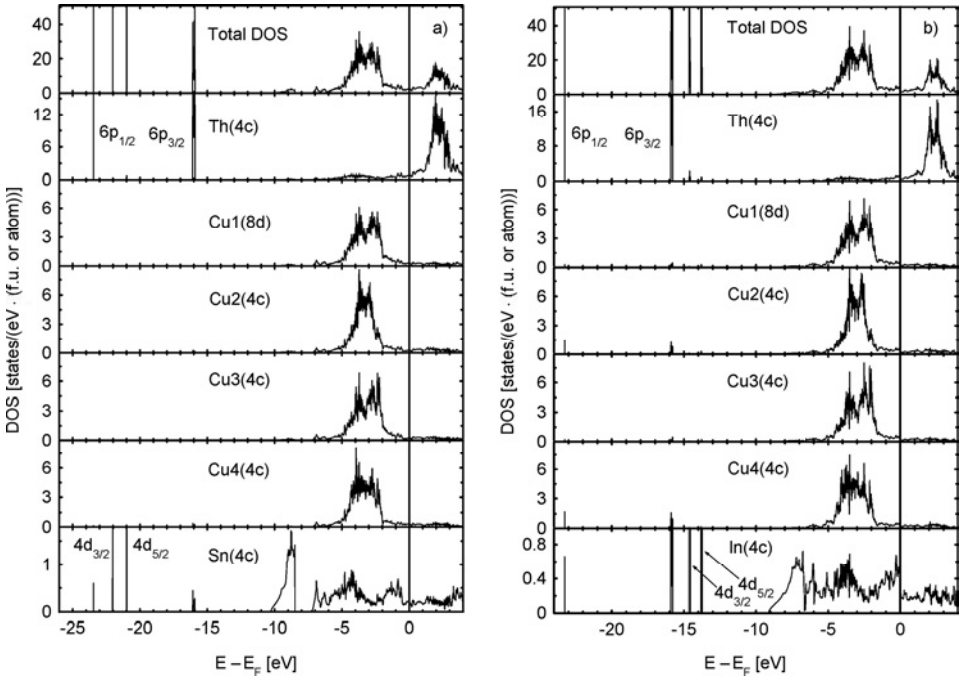

Fig. 2. Total and local DOS plots for the a) $ThCu_5Sn$, b) $ThCu_5In$ compounds

The DOS plots are presented in Fig. 2. Most of bands which form the valence bands for $ThCu_5M$ systems are located between about –10 eV and the Fermi level. The valence bands are formed mainly by Cu(3d) electrons located between –5 and –1 eV. The bottoms of valence bands are formed by Sn(4s) and In(4s) electrons. In the case of $ThCu_5Sn$, Sn(4s) electrons and the main part of valence band are separated by the gap of about 1.2 eV wide. Below the valence bands, we observe very narrow and tall peaks formed by flat bands occupied by the Th(6p), In(4d) and Sn(4d) electrons. The total

DOS at the Fermi level is equal to 2.73 and 2.59 states/(eV·f.u.) for $ThCu_5In$ and $ThCu_5Sn$, respectively. This means that the Sommerfeld coefficients in the linear term of the specific heat are equal to 6.43 and 6.10 mJ/(mol·K^2). These values are close to that obtained for $ThIn_3$, 5.28 mJ/(mol·K^2) [10]. The contributions provided by particular atoms are collected in Table 1. The Cu atoms provide about 40% and single thorium atom about 30% contribution to the total DOS at the Fermi level. The Th(6p) electrons for $ThCu_5In$ are slightly moved toward binding energies higher than in the case of $ThCu_5Sn$ one, conserving similar spin-orbit splitting (see Figs. 2 and 3).

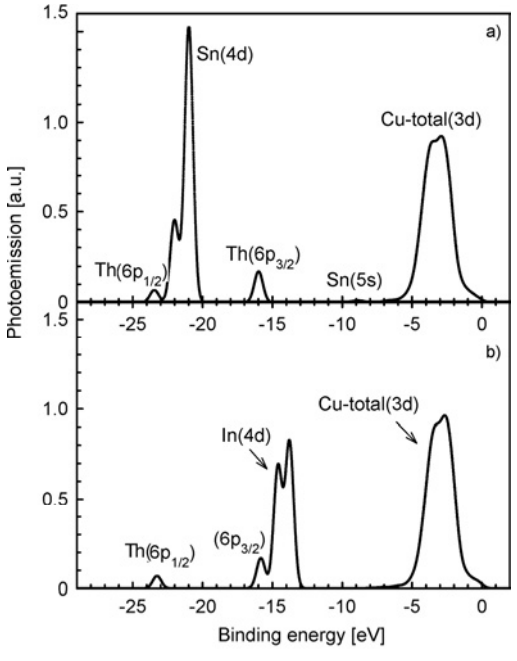

Fig. 3. X-ray photoemission spectra calculated for: a) $ThCu_5Sn$, b) $ThCu_5In$; δ = 0.3 eV

A larger difference exists for 4d electrons on Sn and In atoms. The positions of the peaks are quite different, and smaller spin-orbit splitting gives single two-peak bands in the photoemission spectra. In both cases the calculated spin-orbit splitting is similar to the experimental one.

Acknowledgements

This work was supported by funds for science in years 2007-2010 as a research project.

References

[1] CHEŁKOWSKA G., MORKOWSKI J.A., SZAJEK A., TROĆ R., J. Phys.: Condens. Matter, 14 (2002), 3199.
[2] CHEŁKOWSKA G., MORKOWSKI J.A., SZAJEK A., TROĆ R., Phil. Mag., B 82 (2002), 1893.
[3] ZAREMBA V., HLUKHYY V., STĘPIEŃ-DAMM J., TROĆ R., J. Alloys Compd., 321 (2001), 97.
[4] ZAREMBA V., STĘPIEŃ-DAMM J., TROĆ R., KACZOROWSKI D., J. Alloys Compd., 280 (1998), 196.

[5] KOEPERNIK K., ESCHRIG H., Phys. Rev. B, 59 (1999), 1743.
[6] OPAHLE I., KOEPERNIK K., ESCHRIG H., Phys. Rev. B, 60 (1999), 14035.
[7] BLÖCHL P., JEPSEN O., ANDERSEN O.K., Phys. Rev. B, 49 (1994), 16223.
[8] PERDEW J.P., WANG Y., Phys. Rev. B, 45 (1992), 13244.
[9] YEH J.J., LINDAU I., At. Data Nucl. Data Tables, 32 (1985), 1.
[10] MATSUDA T.D., HAGA Y., IKEDA S., SHISHIDO H., SETTAI R., HARIMA H., ONUKI Y., J. Phys. Soc. Jpn., 74 (2005), 3276.

Received 10 May 2007
Revised 21 January 2008

Materials Science-Poland, *Vol. 26*, *No. 3*, *2008*

Electronic structure of CePdAl Experiment and calculations*

W. GŁOGOWSKI, J. GORAUS, A. ŚLEBARSKI**

Institute of Physics, University of Silesia, 40-007 Katowice, Poland

CePdAl exhibits an antiferromagnetic phase below T_N = 2.7 K; its physical properties are typical of heavy fermion compounds (specific heat coefficient $\gamma \equiv C/T$ = 270 mJ/(mol·K^2)). The triangular coordination symmetry of the magnetic Ce ions gives rise to geometrical frustration and leads to an incommensurate antiferromagnetic structure below T_N, showing a coexistence of ordered and frustrated Ce moments. The purpose of this work was to discuss electronic structure of CePdAl and its influence on the geometrical frustration in the Kagomé-like lattice and the Kondo effect in CePdAl. We present the results of the X-ray diffraction analysis and the XPS Ce 3d core and valence band spectra. We also present the spin-polarized band structure calculations for CePdAl, using the LAPW method.

Key words: *strongly correlated electron systems; electronic structure*

1. Introduction

Our investigations of CePdAl have been carried out as part of the investigations of the $CeRh_{1-x}Pd_xAl$ compounds. It is of interest to examine in detail the effect of the increasing number of conduction electrons in solid solutions of $CeRh_{1-x}Pd_xAl$ on changes in the metallic ground state properties across the series.

CePdAl is a heavy fermion (HF) antiferromagnet with T_N = 2.7 K [1] with ZrNiAl type crystal structure [2, 3] where Ce atoms form a Kagomé-like lattice in the *c* plane. According to the neutron diffraction studies [4], the magnetic structure of CePdAl is incommensurate and Ce atoms located on the crystallographic 3f site exhibit a coexistence of ordered moments (2/3) and disordered moments (1/3). Reasons are effects of geometrical frustration [4] and/or the interplay of Kondo screening and exchange interaction [5]. These disordered moments are paramagnetic down to 30 mK, as was con-

---

*Presented at the Conference of the Scientific Network "New Materials for Magnetoelectronics – MAG-EL-MAT 2007", Będlewo near Poznań, 7–10 May, 2007.

**Corresponding author, e-mail: slebar@us.edu.pl

firmed by recent NMR measurements [6]. Considerations of the group theoretical symmetry analysis also confirmed that for frustrated Ce atoms (1/3 in 3f atomic sites) any magnetic moment parallel to the magnetically easy *c* axis is forbidden by symmetry [4].

It is also worth noting that antiferromagnetic order in CePdAl disappears above 1.1 Gpa [7] which suggests a quantum phase transition. CePdAl is well described by the phase diagram proposed by Doniach [8] in the $T_N P$ plane, with a maximum of T_N at about 0.75 GPa [9]. This behaviour suggests large value of $\rho(\mathcal{E}_F)J_{fc}$, where J_{fc} is the strength of exchange interaction between f electron and conduction electrons and ρ is the density of states (DOS) at the Fermi level, and in result location of this compound near the maximum in the Doniach diagram.

In this work, we present results of calculations of electronic structure which suggest a weak magnetic ground state of CePdAl and strong interatomic hybridization between Ce f states and Pd d states in the *c* plane. From the Ce 3d XPS spectra we estimated the value of the onsite hybridization energy V_{fc} between the f electrons and the conduction states. A simple analysis gives $\rho(\mathcal{E}_F)J_{fc} \approx 0.3$ eV which is quite large and well supports the T_N vs. P experimental data.

2. Experimental

CePdAl has been prepared by arc melting and then annealed at 800 °C for 3 weeks. The crystal structure of the sample was found to be hexagonal of the ZrNiAl -type (space group $P\bar{6}2m$). The X-ray photoelectron spectroscopy spectra (XPS) were obtained with monochromatized Al K_α radiation using a PHI 5700 ESCA spectrometer. From the survey spectra we found that there was neither carbon nor oxygen contamination. The electronic structure was computed for experimental lattice parameters using FP-LAPW (Wien2k) code, with GGA96 type gradient corrections [10]. The calculations were performed with spin-polarization and relativistic effects taken into account.

3. Results and discussion

In Figure 1, we present numerical calculations of the electronic density of states (total LAPW DOS) of CePdAl. Also shown in the figure, for comparison, are the XPS valence band (VB) spectra subtracted by a background, calculated by means of a Tougaard algorithm [11]. The characteristic features in the XPS VB spectrum are in good agreement with the calculated total DOS. The total DOS decomposes into three clearly separated parts. A band located in the binding energy range of 0–2 eV consists mainly of the Ce f states (see Fig. 2). A part of the VB which extends from ca. 2 eV and 4.5 eV is composed mainly of Pd d states, while the Al s states become dominant of the total DOS between 5 eV and ca. 8 eV. In band structure calculations the 4f elec-

trons are treated as band electrons. The calculated electronic specific heat coefficient $\gamma = 1/3\pi^2\rho(\mathcal{E}_F)k_B^2 \approx 22$ mJ/(mol·K)^2 is about 1/3 of the γ_0 obtained from the linear dependence of C/T on T^2 at $T = 0$.

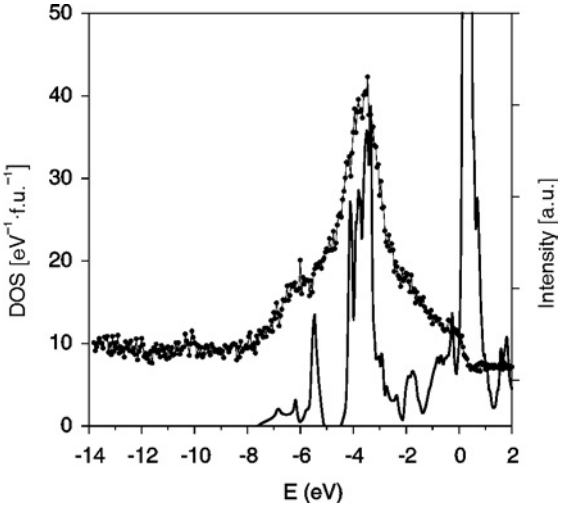

Fig. 1. LAPW total DOS calculated for CePdAl, and measured XPS valence bands corrected by the backgrounds (points)

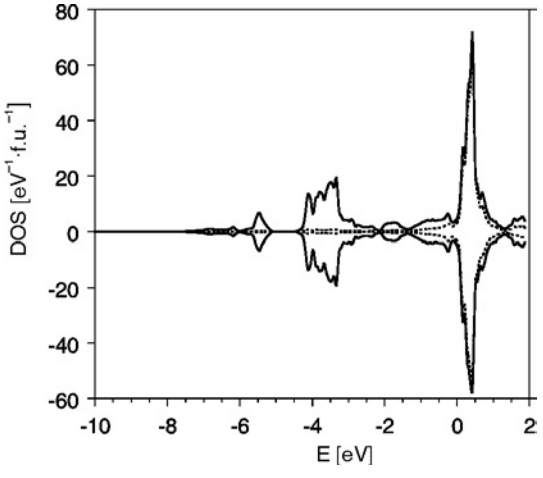

Fig. 2. The total DOS for both spin directions for the magnetic ground state (solid line). The Ce states in eV^{-1} per Ce atom are shown too (dotted line)

It is generally accepted that at low temperatures a narrow band of heavy electrons gives rise to the large electronic specific heat coefficient γ, and originates from the renormalized hybridization of the conduction band (c) states with the atomic f states. The strength of the fc exchange interaction can be turned by either the composition or pressure, and results in a competition between the intrasite Kondo and intersite Rud-

erman–Kittel–Kasuya–Yosida (RKKY) interactions. The first such model of the HF was proposed by Doniach [8], who examined the one-dimensional Kondo lattice and obtained the magnetic ground state with a simple phase diagram, which displays the magnetic ordering temperature T_{RKKY} in function of $\rho(\mathcal{E}_F)J_{fc}$, where $J_{sf} \sim V_{fc}^2/(\mathcal{E}_F - E_f)$, with E_f being the location of the f level in the band. This simple diagram describes often well the magnetic → nonmagnetic ground state transformation observed for many Ce compounds. CePdSb is the first Ce compound where the pressure dependence of T_{RKKY} is well explained by this diagram [12]. Recently [13], we have obtained the hybridization energy $V_{fc} \approx 82$ meV from the Ce 3d XPS spectra based on the Gunnarsson–Schönhammer theoretical method [14]. According to the Anderson model, $J_{sf} \approx 0.03$ eV, if E_f is about 0.24 eV (see Fig. 2). We can obtain $\rho(\mathcal{E}_F)J_{fc} \approx 0.3$ which locates CePdAl on the left side near the maximum in the T_N–$\rho(\mathcal{E}_F)J_{fc}$ diagram, in agreement to Ref. [9].

The diagram, however, due to its simplicity does not explain the character of the low temperature magnetic ground state. Also, it does not account for the f electron itineracy observed in many compounds. Doradziński and Spałek (DS) [15] discussed the magnetic phases in the periodic Anderson model and determined the conditions under which there appears a stable Fermi liquid state with a small antiferromagnetic moment of f electrons, largely compensated by the conduction electrons. In DS model, the stability of paramagnetic vs. magnetic ground state in the Kondo lattice limit is strongly dependent on the on-site hybridization magnitude V_{fc}, the bare f level position, the number conduction electrons and finally, on the intrasite f–f interaction U. Basing on our XPS data and calculations, the DS phase diagram on the V_{fc}–n_e plane (n_e is the total number of electrons per site) well describes CePdAl as an antiferromagnetic Kondo lattice compound.

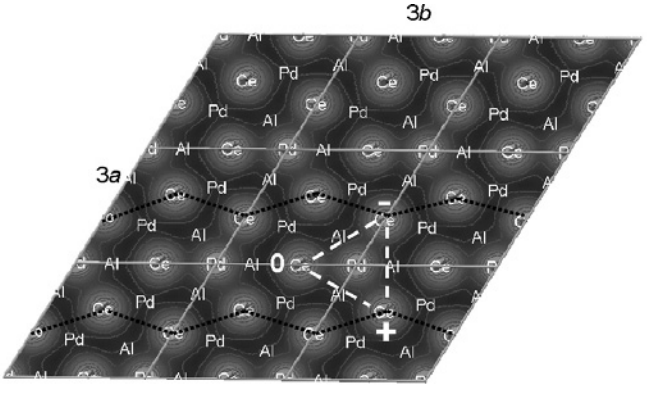

Fig. 3. The charge density distribution in the c plane. +, – and 0 represent Ce ions with antiferromagnetic orientation of the magnetic moments (+, –), and paramagnetic frustrated Ce ions (0); the figure shows 9 unit cells

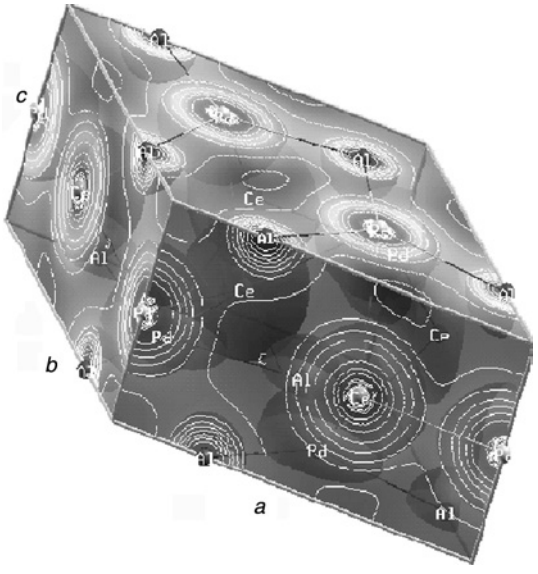

Fig. 4. The charge density distribution in the unit cell of CePdAl.
The planes *a*, *b* and *c* show the charge contours

In Figures 3 and 4 we present the charge densities distributed in the plane *c*, perpendicular to the *z* axis (Fig. 3) and in the planes *a* and *b*, respectively. In Fig. 3 the Ce magnetic moments (+, –) with antiferromagnetic orientation (see Ref. [4]) provoke the frustration of the third Ce ion (0) in Kagomé-like lattice. Pd atoms are located in center of this lattice and are strongly hybridized with Ce due to fd hybridization. The fd hybridization stabilizes the magnetic structure of CePdAl and could decide about the magnetic properties of this compound under external pressure. In CePdAl the fp hybridization is negligible.

In conclusion, we calculated the DOS of CePdAl, which was compared to the XPS VB spectra. The agreement is good. Based on the electronic structure calculations and the XPS spectra (VB XPS, Ce 4d XPS) we determined the hybridization energy V_{fc} between the Ce 4f and conduction electrons, occupation number of the f shell, $n_f = 1$, and the exchange coupling strength J_{fc}. In the Kondo lattice, the Kondo effect and the RKKY magnetic interaction are competing with each other depending on the value of $\rho(\mathcal{E}_F)J_{fc}$ (the Kondo interaction $T_K \sim \exp(-1/\rho(\mathcal{E}_F)J_{fc})$ and $T_{\mathrm{RKKY}} \sim \rho(\mathcal{E}_F)J_{fc}^2$), we found CePdAl located in the T_{RKKY}–$\rho(\mathcal{E}_F)J_{fc}$ diagram close to the maximum of T_{RKKY} at $\rho(\mathcal{E}_F)J_{fc} \approx 0.3$. Our calculations show strong interatomic hybridization effect between Ce f and Pd d states which seems to be important in formation of the ground state properties of CePdAl.

Acknowledgements

The authors thank for financial support from Projects No. 1 P03B 052 28, No. 1 P03B 094 30, and No. N202 038 31/1805 of the Ministry of Science and Higher Education.

References

[1] KITAZAWA H., MATSUSHITA A., MATSUMOTO T., SUZUKI T., Physica B, 199–200 (1994), 28.
[2] HULLIGER F., J. Alloys Comp., 196 (1993), 225.
[3] XUE B., SCHWER H., HULLIGER F., Acta Cryst. C, 50 (1994), 338.
[4] DÖNNI A., EHLERS G., MALETTA H., FISCHER P., KITAZAWA H., ZOLLIKER M., J. Phys.: Condens Matter., 8 (1996), 11213.
[5] NUNEZ-REGUEIRO M.D., LACROIX C., CANALS B., Physica C, 282–287 (1997), 1885.
[6] KAMIOKA K., OYAMADA A., HASHI K., MAEGAWA S., GOTO T., KITAZAWA H., ISIKAWA Y., Physica B, 259–261 (1999), 121.
[7] HANE S., GOTO T., ABE T., ISIKAWA Y., Physica B, 281–282 (2000), 391.
[8] DONIACH S., Physica B, 91 (1977), 231.
[9] TANG J., MATSUSHITA A., KITAZAWA H., MATSUMOTO T., Physica B, 217 (1996), 97.
[10] BLAHA P., SCHWARZ K., MADSEN G.K.H., KVASNICKA D., LUITZ J., *WIEN2k, An Augmented Plane Wave + Local Orbitals Program for Calculatin Crystal Properties*, Karlheinz Schwarz, Techn. Universität Wien, Austria, 2001. ISBN 3-9501031-1-2; PERDEW J.P., BURKE K., ERNZERHOF M., Phys. Rev. Lett., 77 (1996), 3865.
[11] TOUGAARD S., SIGMUND P., Phys. Rev. B, 25 (1982), 4452.
[12] CORNELIUS A.L., GANGOPADHYAY A.K., SCHILLING J., ASSMUS W., Phys. Rev. B, 55 (1997), 14109.
[13] GŁOGOWSKI W., ŚLEBARSKI A., Mater. Sci.-Poland, 24 (2006), 551.
[14] FUGGLE J.C., HILLEBRECHT F.U., ZOLNIEREK Z., LÄSSER R., FREIBURG CH., GUNNARSSON O., SCHÖNHAMMER K., Phys. Rev. B, 27 (1983), 7330.
[15] DORADZIŃSKI R., SPAŁEK J., Phys. Rev. B, 56 (1997), R14239; ibid. 58 (1998), 3239; for a brief review see: SPAŁEK J., DORADZIŃSKI R., [in:] *Magnetism and Electronic Correlations in Local-Moment Systems: Rare Earth Elements and Compounds*, M. Donath, P.A. Dowben, W. Nolting, World Scientific, New Jersey, 1998), p. 387; Acta Phys. Polon. A, 96 (1999), 677; 97 (2000), 71.

Received 10 May 2007
Revised 21 January 2008

Materials Science-Poland, *Vol. 26*, *No. 3*, *2008*

Specular and diffuse X-ray reflectivity study of surfactant mediated Co/Cu multilayers*

M. MARSZAŁEK[1**], M. KĄC[1], M. KRUPIŃSKI[2], A. POLIT[1], Y. ZABILA[1]

[1]The H. Niewodniczański Institute of Nuclear Physics, Polish Academy of Sciences, ul. Radzikowskiego 152, 31-342 Cracow, Poland

[2]AGH University of Science and Technology, ul. Mickiewicza 30, 30-059 Cracow, Poland

The application of X-ray techniques for studies of the interface structure of Co/Cu multilayers has been presented with a pre-deposited ultrathin film of Bi and Pb. The [Co(1 nm)/Cu(2 nm)] multilayers were thermally evaporated at very low deposition rates with a small amount of Bi and Pb surfactant (about 0.2 ML) introduced at each Cu layer. The structure of Co/Cu multilayers with added surfactant has been studied using low-angle specular and nonspecular X-ray reflectivity. In all studied specimens, the off-specular reflectivity replicates some of the features of specular reflectivity. The presence in diffuse spectra of a Bragg peak due to coherent scattering, as well as visible finite thickness clearly indicates a high degree of conformality and interface roughness replication in the surfactant mediated Co/Cu multilayers. X-ray reflectivity as well as X-ray diffuse scattering measurements showed a distinct variation in the structure of the multilayers with introduction of surfactant which leads to well-ordered periodic structures with small roughness.

Key words: *surfactant; surface segregation; Co/Cu multilayers; Auger electron spectroscopy; X-ray reflection; bismuth; lead*

1. Introduction

The discovery of the giant magnetoresistive (GMR) effect in magnetic multilayers which contain alternate layers of a magnetic element and a non-magnetic element as the basic building blocks offers a route to small bit size random access memories. In applications for magnetic storage devices, Co/Cu multilayers [1] form one of the most promising materials because of a very large GMR effect even at room temperature [2]. However, a wide variation of results for Co/Cu multilayers has been observed, due to the fact that the magnetic transition metals tend to agglomerate over the noble metals

---

*Presented at the Conference of the Scientific Network "New Materials for Magnetoelectronics – MAG-EL-MAT 2007", Będlewo near Poznań, 7–10 May, 2007.

**Corresponding author, e-mail: e-mail: Marta.Marszalek@ifj.edu.pl

because the surface free energy of Cu is significantly lower [3] than that of Co [4]. As a result, Co agglomerates rather than wets the Cu surface. It is also known that, in addition, noble atoms segregate out onto the transition metal surface, giving rise to intermixing across the interface. This results in multilayers with rough, diffuse, and intermixed interfaces which influence the magnetotransport properties. The strength of the antiferromagnetic coupling between the layers depends on the spacer thickness and can be disrupted by significant interface roughness. Therefore, smooth layer morphology is required for many modern electronic devices, and one promising approach that has been pursued to obtain heterostructures with atomically sharp interfaces is through the use of surface modifiers known as surfactants [5, 6]. Using this approach, if an adsorbed species or surfactant is present at the surface prior to the deposition of an overlayer, the balance of free energies can be drastically altered inducing 2-dimensional growth of thin films in conditions not favourable for such growth. Low-surface-energy elements are used as surfactants so that they can continuously segregate to the surface during deposition and no impurities are introduced into the growing film. The surfactant-mediated growth technique provides a good way to fabricate the films with desired, atomically smooth interfaces. It was originally introduced in semiconductor superlattice growth good results were also obtained, however, in polycrystalline spin valve and multilayers deposition [7–9]. In this paper, we present the application of X-ray technique for investigation of the effect of a pre-deposited Bi and Pb surfactants on the interface structure of Co/Cu multilayers.

2. Experimental

Sample preparation and characterization were done in an ultrahigh-vacuum system at pressures about 10^{-8} Pa. Si(100) wafers, covered with native SiO_2, were ultrasonically cleaned in organic solvents and rinsed in deionized water. Co/Cu multilayers with 10 repetitions of [Co/Cu/surfactant] trilayers have been obtained by sequential thermal evaporation of Co, Cu and Bi or Pb surfactant at the rates between 0.05 and 0.5 ML/min, and the thicknesses of Co (1 nm) and Cu (2 nm) correspond to the second maximum of the oscillating thickness dependence of magnetoresistance. The surfactants were introduced in very small amounts, about 0.2 ML, at each interface of the Co/Cu bilayers before Co deposition. Our earlier results [10] showed that addition of surfactant at each Co/Cu bilayer has better effect on the quality of the interface structure than for the case of its repetition at every second bilayer. Reference samples with the same number of Co/Cu bilayer repetitions were deposited without the introduction of surfactants. During deposition, the sample was kept at room temperature. Chemical composition of successive Co and Cu layers was monitored during growth after deposition of the individual elements by the Auger electron spectroscopy (AES). Low energy electron diffraction (LEED) measurements, performed simultaneously, did not show any distinct features associated with an ordered structure, indicating the polycrystalline structure of the samples. After deposition, the sample structure was investi-

gated *ex-situ* by X-ray reflectometry (XRR) performed with a Philips X'Pert MRD Pro diffractometer. CuK_α radiation operated at 40 kV and 30 mA was converted to a parallel beam by an incident beam optics with 0.03125° divergence slit and a diffracted beam parallel plate collimator with equatorial acceptance of 0.18°. The 0.04 rad. Soller slits were used on both, incident and diffracted beams. A programmable beam attenuator was used to reduce radiation intensity by a specific factor at small angles.The axial width of the incident beam was restricted by incident beam mask to 5 mm for all measurements.

Three types of scans in coplanar geometry were recorded: specular θ–2θ (Q_z) reflectivity scans, transverse ω rocking scans in which only the transverse component of the scattering vector varies, and offset scans, with the reciprocal space direction parallel to a θ–2θ scan, but offset by some amount in Q_z.

3. Results and discussion

X-ray reflectivity spectra of $[Co/Cu/surfactant]_{10}$ multilayers are shown in Fig. 1. The spectra of $[Co/Cu/surfactant]_{10}$ multilayers with Bi and Pb demonstrate well-defined Kiessig fringes, a similar fall-off of intensity with increasing angle, and well-resolved Bragg peak indicating that the bilayer thickness is conserved through the whole sample. The spectrum of a Co/Cu multilayer without surfactant shows that both finite-size peaks as well as superlattice reflections have smaller amplitude. Low angle specular X-ray reflectivity is sensitive only to the vertical structure of the multilayers averaged over horizontal dimensions of sample surface, and can provide information about the thicknesses, electronic densities of layers and the roughnesses characterized by the standard deviation of the height fluctuations of the interfaces [see for example [11]]. The increase in surface and interface roughness gives a lower reflectivity and smearing and broadening of the fringes. The detailed analysis of experimental data was done with simulation program REFLECTIVITY of Panalytical which applies the Parratt formalism for reflectivity [12]. The software allows the fitting of thickness t, rms roughness σ_{rms} and density d for groups or individual adjacent layers. Since a reliable refinement of multilayer system requires the minimum number of variable layer parameters, the best result was obtained by modeling the sample as the sum of the following contributions with common parameters for each group: the first Co/Cu bilayer close to substrate surface $(Co/Cu)_1$, followed by 8 repetitions of Co/Cu bilayers $(Co/Cu)_8$ and finally the Co/Cu-surfactant alloy bilayer, as observed in Auger spectra [13], or Co/Cu bilayer in case of multilayers prepared without surfactant. A good agreement was found between nominal and estimated Co and Cu thicknesses. The densities of Co and Cu films differed by no more than 10% from bulk density values. The fitted interface roughnesses for each component of this model are shown in Fig. 2. It is seen that the multilayer with surfactants had roughness of the order of 1–2 ML, but the multilayer without them had much larger roughness and strongly mixed interfaces, the result confirmed by a very small Bragg peak.

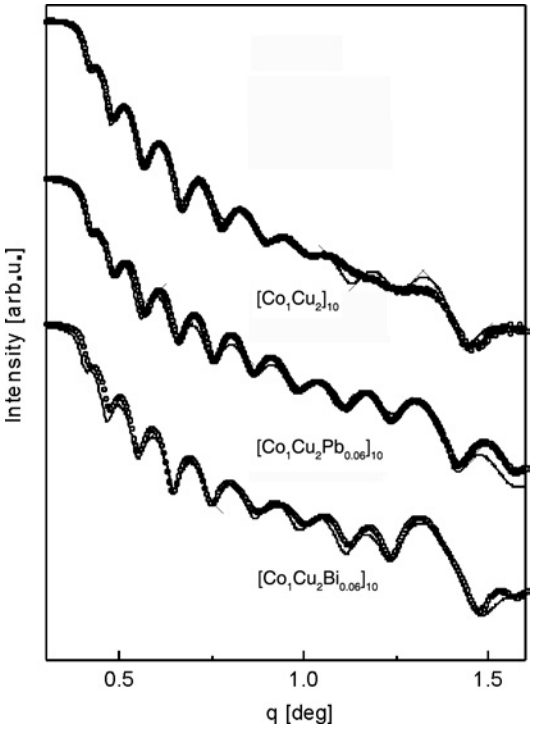

Fig. 1. Low-angle X-ray reflectivity data for $[CoCuBi]_{10}$ and $[CoCuPb]_{10}$ multilayers in comparison with $[CoCu]_{10}$. Theoretical fits to the specular reflectivity data are also shown (continuous lines)

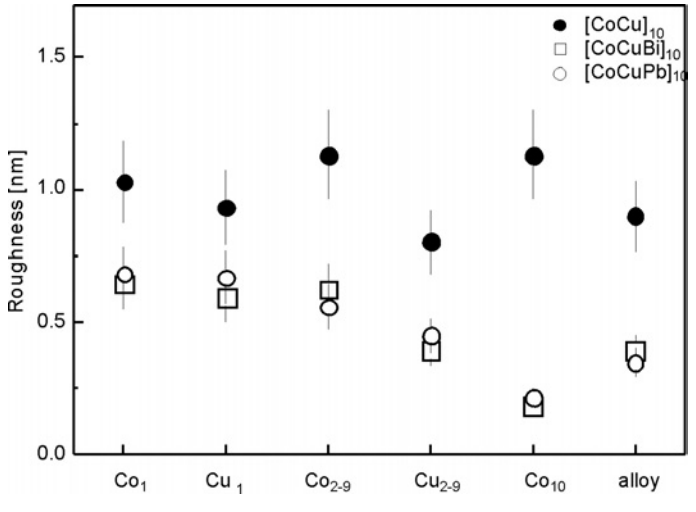

Fig. 2. The rms roughness σ_{rms} for $[Co/Cu]_{10}$ multilayers, with and without surfactant in function of film position in the multilayer system according to the model described in text

The specular XRR curves give no information on how roughness is correlated. Determination of the degree of roughness correlation requires looking at the diffuse scattering. Scans made in the slightly offset Q_z direction show the diffuse scattering resulting from correlated interfaces. For fully uncorrelated interfaces, the diffuse scattering along the Q_z direction is featureless and much lower in intensity than the specular scattering. For fully correlated interfacial roughness, the diffuse scattering is an exponentially modulated copy of the specular scattering. The replication of finite thickness oscillations in the offset scans and the diffuse scattering in the vicinity of the superlattice Bragg peaks with essentially the same shape as in specular scans is indicative of the increased layer to layer correlation of the roughness of the films.

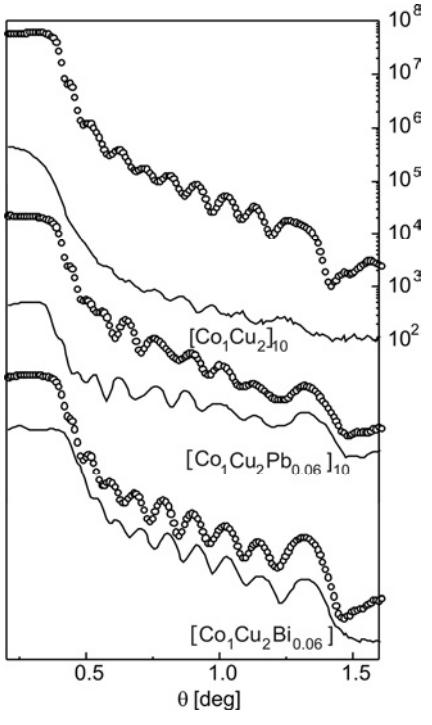

Fig. 3. The X-ray specular reflectivity and off-specular reflectivity scans (lines) of $[Co/Cu]_{10}$ multilayers prepared with and without surfactants. All spectra are drawn in the same logarithmic scale. For the clarity of the figure the scale is only marked for the top two lines

Specular and offset (offset angle $\Delta\varpi = 0.1°$) scans of Co/Cu multilayers shown in Fig. 3 exhibit the replication of the features from specular to diffuse for Co/Cu multilayers prepared with Pb and In, however, reference Co/Cu system without surfactant shows no replication. The presence of Bragg peak due to coherent scattering, as well as visible finite thickness clearly indicates a high degree of conformality and interface roughness replication in the surfactant mediated Co/Cu multilayers.

Transverse ω rocking scans provide information on the lateral length scale or in-plane correlation length of the film. The rocking curves measured at the Q_z position of the multilayer Bragg peaks are dependent on the sum of the correlated and uncorrelated roughness. Outside the Bragg peaks only the uncorrelated roughness is observed.

Consequently, measuring the diffuse scattering on and off Bragg peaks allows us to distinguish the correlated and uncorrelated roughness. If the roughness is highly correlated, there will be a different curvature of Q_x scans on and off the Bragg position.

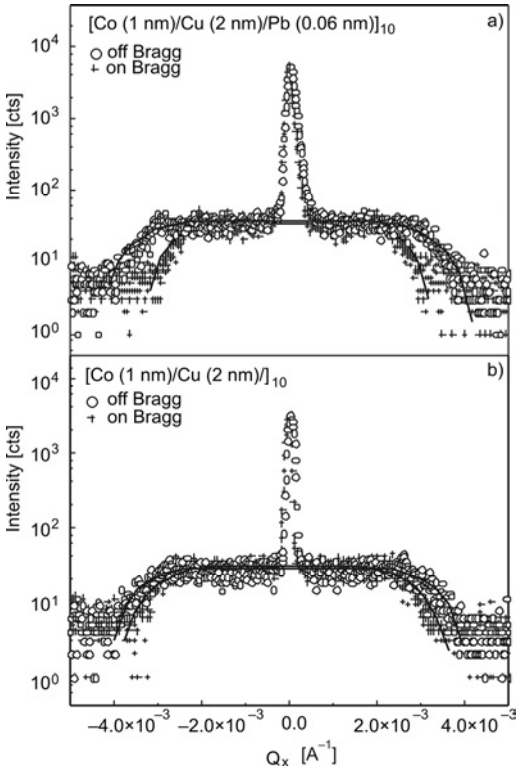

Fig. 4. X-ray rocking scans of $[Co/Cu]_{10}$ multilayer (a) with Pb surfactant compared with $[Co/Cu]_{10}$ multilayer reference sample (b). The spectra are plotted for the scattering angle corresponding to the first Bragg peak (cross symbols) and for the preceding intensity maximum (circles), determined from specular spectra in Fig. 1

Examples of rocking scans taken on and off the Bragg peak position for Co/Cu multilayers with and without surfactant, consisting of narrow resolution-limited specular and broad diffuse components, together with simple approximation [14] of the spectra curvature are shown in Fig. 4. Again we observed that for the Co/Cu multilayers grown with surfactant, the curvature is different on and off the Bragg peak positions, confirming an enhanced degree of correlation, whereas for the reference Co/Cu system curvature is essentially the same. The correlated vertical roughness σ_c was estimated from the ratio of the integrated specular and diffuse components [15] and it is equal 0.3 and 0.45 nm for reference Co/Cu and surfactant assisted Co/Cu multilayers, respectively. However, the precise determination of correlated and uncorrelated roughness as well as the lateral correlation length requires more experimental work, and careful examination of spectra taking into account the effect of instrumental resolution, which is of particular importance in the analysis of the diffuse scattering. The distorted wave Born approximation (DWBA) including different aspects of instrument broadening can be used for detailed analysis of diffuse scattering spectra and this work will be performed in the future.

4. Conclusions

The evolution of roughness and roughness correlation in polycrystalline Co/Cu multilayers grown with assistance of Bi and Pb surfactants has been studied using combined X-ray scattering techniques. X-ray reflectivity and X-ray diffuse scattering spectra show a distinct variation in the structure of the multilayer interface under the influence of surfactant. The structure of Co/Cu multilayers with Bi and Pb deposited at the bilayer interface demonstrated that use of surfactants in growth processes smoothes the interfaces between Co and Cu, and increases the layer-to-layer correlation, leading to the creation of flatter interfaces and films with homogeneous thicknesses. In contrast, the roughness of pure Co/Cu multilayer interfaces is significantly larger, and the periodicity of the bilayer stack is not well conserved. The conformal nature of the roughness in surfactant assisted Co/Cu multilayers was confirmed by the presence of coherent scattering in the diffuse spectra. A careful analysis of data with DBWA will also bring the value of lateral correlation length which can be very useful for determination of energy barrier relations on the surface.

Acknowledgements

This work was supported partially by the research grant of the Ministry of Science and Higher Education under contract No. N507 080 32/2310. The authors acknowledge the support of Polish Scientific Network MANAR.

References

[1] PARKIN S.S.S., LI Z.G., SMITH D.J., Appl. Phys. Lett., 58 (1991), 2710.
[2] MARROWS C.H., WISER N., HICKEY B.J., HASE T.P.A., TANNER B.K., J. Phys.: Cond. Matter, 11 (1999), 81.
[3] GAY J.G., SMITH J.R., RICHTER R., ARLINGHAUS F.J., WAGONER R.H., J. Vac. Sci. Technol. A, 2 (1984), 931.
[4] MEZEY L.Z., GIBER J., Jpn. J. Appl. Phys., 21 (1982), 1569.
[5] STEIGERWALD D.A., JACOB I., EGELHOFF W.F. Jr., Surface Sci., 202 (1988), 472.
[6] EGELHOFF W.F. Jr., [in:] *Ultrathin Magnetic Structures I: An Introduction to Electronic, Magnetic, and Structural Properties*, J. A. C. Bland, B. Heinrich (Eds.). Springer, Berlin, 1994.
[7] AN YUKAI, ZHANG HONGDI, DAI BO, MAI ZHENHONG, CAI JIANWANG, WU ZHONGHUA, J. Appl. Phys.,100 (2006), 023516.
[8] EGELHOFF W.F., Jr., CHEN P.J., POWELL C.J., STILES M.D., MCMICHAEL R.D., J. Appl. Phys., 79 (1996), 2491.
[9] ZOU W., WADLEY H.N.G., ZHOU X.W., JOHNSON R.A., BROWNELL D., Phys. Rev. B, 64 (2001), 174418.
[10] MARSZAŁEK M., BÖLLING O., JAWORSKI J., KĄC M., KRUK R., TOKMAN V., SULKIO-CLEFF B., phys. stat. sol. (c), 1 (2004), 3239.
[11] GIBAUD A., HAZRA S., Current Sci., 78 (2000), 1467.
[12] PARRATT L.G., Phys. Rev., 95 (1954), 359.
[13] MARSZALEK M., POLIT A., TOKMAN V., ZABILA Y., PROTSENKO I., Surface Sci., 601 (2007), 4454.
[14] STOEV K., SAKURAI K., Rigaku J., 14 (1997), 22.
[15] SAVAGE D.E., KLEINER J., SCHIMKE N., PHANG Y.-H., JANKOWSKI T., JACOBS J., KARIOTIS R., LAGALLY M. G., J. Appl. Phys., 69 (1991), 1411.

Received 10 May 2007
Revised 21 January 2008

Materials Science-Poland, *Vol. 26*, *No. 3*, *2008*

3d metallic layers electrochemically deposited from nearly nonaqueous electrolyte*

W. OLSZEWSKI[1**], K. SZYMAŃSKI[1], M. BIERNACKA[1], R. SOBIECKI[2]

[1]Faculty of Physics, University of Białystok, ul. Lipowa 41, 15-424 Białystok, Poland

[2]Faculty of Materials Science and Engineering, Warsaw University of Technology, ul. Wołoska 141, 02-507 Warszawa, Poland

A method of electroplating shiny layers of Fe, Co, Ni, Cu and Zn from universal type of electrolyte has been reported. At the beginning of the process, the electrolyte consists only of dimethylketone and inorganic acid. Since the electrolyte contains small amount of reactive species, layers with thickness of 400 nm can be formed and removed out of an electrolytic cell. Magnetic properties of the Fe layer have been reported.

Key words: *electrodeposition; nonaqueous electrolyte*

1. Introduction

Electrodeposition of metallic layers has a wide range of technical applications. Processes of 3d metallic layer deposition are particularly important for electronics [1]. For example, we quote copper electrodeposition, known as the damascene process [2] used in chip production, or 3d magnetic layers used in magnetoresistive sensors [3]. Aqueous electrolytes are commonly used for metallic layers deposition. Usually electrolyte includes many substances for achieving a good quality of the deposited layer – a strong adhesion to the substrate and a flat surface. Thus multicomponent electrolytes are designed for rather limited compositions of the deposited layers. Nonaqueous electrolytes are used in electrodeposition of chemically reactive metallic layers like rare earths, aluminum or alkaline metals. The aim of this contribution was to demonstrate a new type of electrolyte which is almost nonaqueous and under similar condi-

---

*Presented at the Conference of the Scientific Network "New Materials for Magnetoelectronics – MAG-EL-MAT 2007", Będlewo near Poznań, 7–10 May, 2007.

**Corresponding author, e-mail: wojtek@alpha.uwb.edu.pl

tions metallic layers of a few different 3d elements could be deposited. Some features of the deposited layers and the method of deposition have been presented.

2. The process of deposition

The electrolyte was composed of 95% dimethylketone and 5% ($HCl + H_2O$). Electrodeposits were obtained at room temperature on one side of the cathode discs (substrate) with the approximate surface area of 4 cm^2. Before electrodeposition, the substrates were mechanically polished.

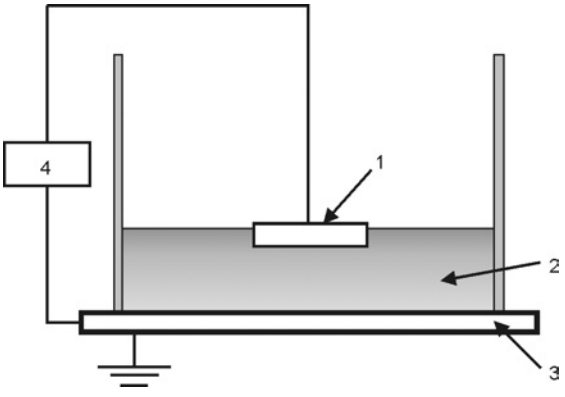

Fig. 1. The scheme of the electrochemical cell: 1 – anode, 2 – electrolyte, 3 – substrate, 4 – DC current source

The scheme of the electrochemical cell is shown in Fig. 1. The substrate was placed at the bottom of the cell. The anode was made of the element to be deposited. Approximately 5 cm^3 of electrolyte was used. Part of the anode was dissolved using DC current. After some time, concentration of ions in the electrolyte was self-adjusted and the process of deposition was performed. The density of cathodic current was stabilized to 5 mA/cm^2. The total time of the deposition was about 20 min. Under the same current conditions and nearly the same initial composition of the electrolyte, we were able to deposit shiny layers of five different elements: Fe, Co, Ni, Cu and Zn. Examples of Co layer deposited on Cu substrate and Cu layer deposited on Fe substrate are shown in Fig. 2.

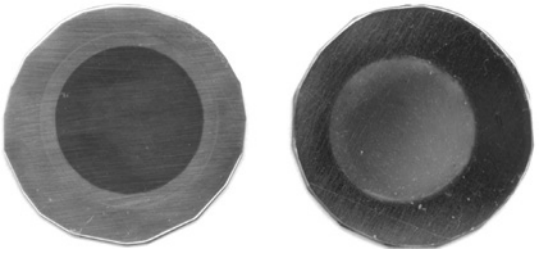

Fig. 2. Co layer on Cu substrate and Cu layer on Fe substrate obtained from nearly nonaqueous electrolyte

Small concentration of reactive HCl species does not result in fast corrosion of the deposited layers. Thus it is easy to safely remove smooth and shiny layer from the electrolytic cell.

3. Scanning electron microscopy results

To perform SEM measurements, samples were cut to pieces with the surface area of 1 cm^2. The pieces were covered by thermohardened resin and polished with emery paper and diamond powder suspension with decreasing gradation.

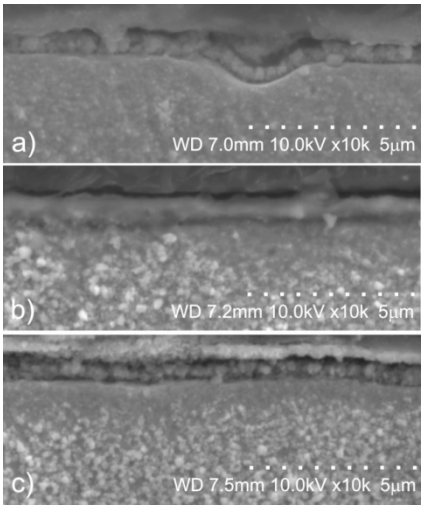

Fig. 3. The microstructure of the electrodeposited layers:
a) Co, b) Ni, c) Fe on the Cu substrate

The deposited layers of Fe, Co, and Ni obtained on Cu substrate were examined using the scanning electron microscopy with a beam size of approximately 1 μm. The microstructure of cross-sections of the layers are presented in Fig. 3. SEM measurements indicate that obtained layers are about 400 nm thick. Specific feature of the electrodeposition process is shown in Fig. 3a, where grove in the Cu substrate is covered by the Co layer of a uniform thickness.

4. Features of the process

Typical cation concentrations in electrolytes used are about 0.2–1.5 mol/dm^3 [4–6]. In the case of electrolyte used in our experiment, the cation concentration during the deposition process was about 0.03 mol/dm^3, over ten times smaller than typical concentrations used in electrodeposition processes. Low concentration of ions in the

electrolyte is the apparent advantage of the method. It reduces costs of the process, especially in case of noble or expensive metals. The process can by used for deposition of layers of isotopically enriched samples. Another advantage of small ion concentrations is its potential applications in technologies of radioactive sources preparation. As an example, we quote ^{57}Co deposition which is used in Mössbauer spectroscopy [7]. We have found that small amount of water present in the electrolyte is essential for the deposition of metallic layers. The role of water molecules is, however, unclear.

5. Mössbauer measurements

The deposited Fe layer on Cu substrate was examined using the conversion electron Mössbauer spectroscopy (CEMS) with two geometries: the wave vector of photon **k** was perpendicular or almost parallel (approximately 2°) to the layer plane. Obtained CEMS spectra are shown in Fig. 4.

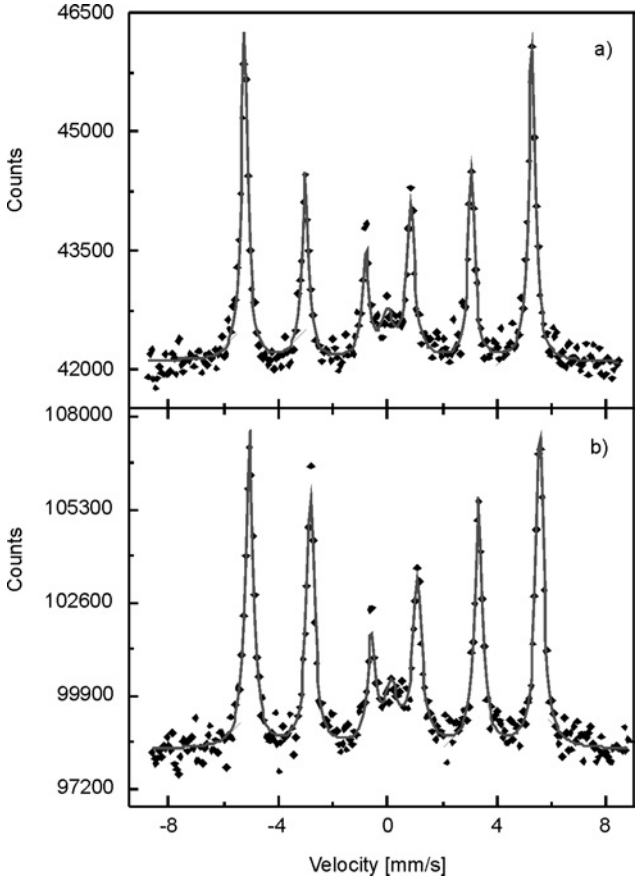

Fig. 4. The CEMS spectrum of an iron layer deposited on Cu and measured with **k** vector: a) perpendicular, b) almost parallel to the sample surface

Ratio of the intensities of the spectral lines observed in CEMS experiment depends on angle ϑ between directions of the **k** vector and the hyperfine magnetic field:

$$I_1:I_2:I_3:I_4:I_5:I_6 = 3(1+\cos^2\vartheta):4\sin^2\vartheta:(1+\cos^2\vartheta):(1+\cos^2\vartheta):4\sin^2\vartheta:3(1+\cos^2\vartheta) \quad (1)$$

It follows from Eq. (1) that in the case of magnetic moments arranged perpendicularly to the sample plane, $I_2/I_3 = 0$ for the **k** vector perpendicular to the surface, while $I_2/I_3 = 4$ for **k** parallel to the sample plane. In case of magnetic moments arranged in the sample plane, $I_2/I_3 = 4$ for **k** perpendicular while $I_2/I_3 = 4/3$ for **k** parallel to the surface. The Zeeman sextet and the doublet were fitted to the spectra. The obtained I_2/I_3 ratio is (1.73±0.04) for measurement with **k** vector perpendicular to the layer plane. This ratio increases to the value of (2.34±0.06) for measurement with low incidence angle. This indicates that magnetic moments have small preferential orientation, perpendicular to the sample plane.

6. Magnetization measurements

The magnetization measurements were carried out with the use of Vibrating Sample Magnetometer (VSM) model 7300 Lake Shore. Obtained magnetization curves

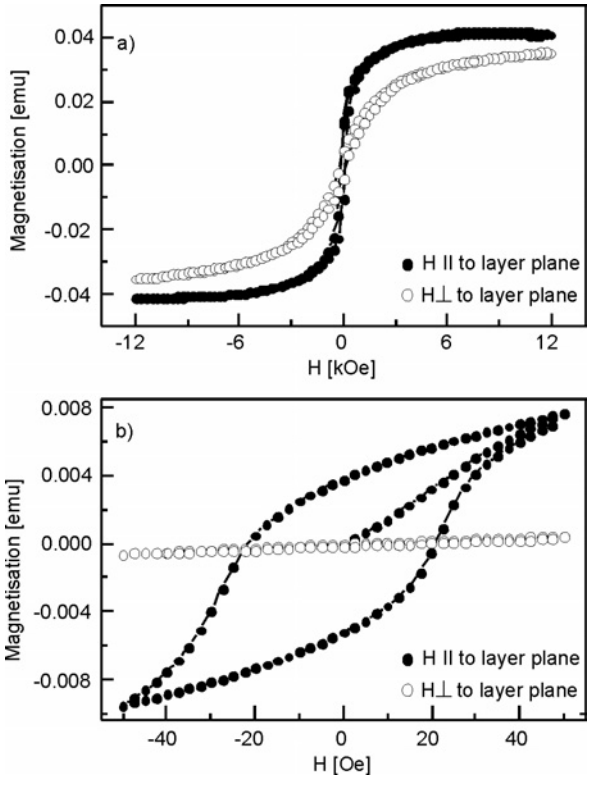

Fig. 5. Magnetization curves for Fe layer deposited on Cu substrate

measured at room temperature in strong (up to 12 kOe) and weak (up to 50 Oe) external magnetic field are shown in Figs. 5a and 5b, respectively. The shape of magnetization curves indicates that the Fe layer deposited on Cu substrate has an easy-plane type of magnetic anisotropy.

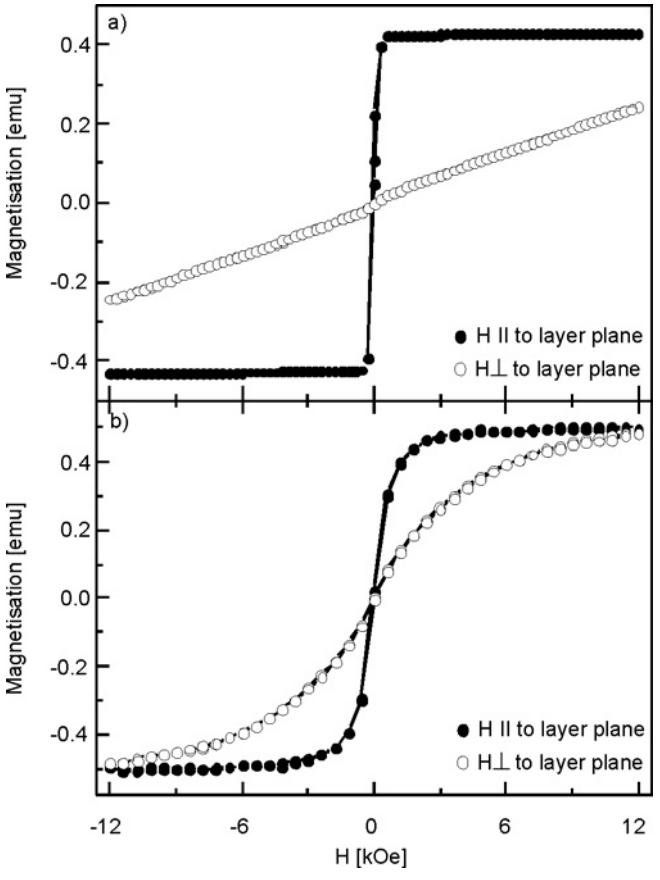

Fig. 6. Magnetization curves for: a) Fe foil, b) iron powder sample oriented in external magnetic field perpendicular to the sample plane

Two additional test samples with different types of magnetic anisotropies have been prepared. The first one was a pellet with the diameter of 1 cm, 1 mm thick, containing nonmagnetic filler (Li_2CO_3) and iron powder with the particle size about few micrometers. The iron particles and the filler were mixed with a two-component resin and exposed to magnetic field of about 1 T until solidification of the liquid components occurred. The magnetic field was perpendicular to the pellet plane. The procedure resulted in a preferred orientation of elongated iron particles [8]. The second test sample was pure iron foil of the thickness about 10 μm, rolled and annealed (900 °C for 1 h). Results of magnetization measurements are shown in Figs. 6a and 6b, respectively.

7. Discussion

CEMS measurements indicate that the magnetic moments are oriented in preferred direction, on average perpendicular to the sample plane. Magnetization measurements show that the deposited layer has rather an easy-plane type of anisotropy. However, the magnetization curves are substantially different from those measured for layer of magnetically soft material with clear shape anisotropy. Indeed, Fe foil is fully saturated in the magnetic field as small as 100 Oe (Fig. 6a) while the deposited layer saturates at the field as large as 6 kOe (Fig. 5a). Thus the in-plane magnetization processes in the deposited layer are strongly hindered. The possible reason for such behaviour is the presence of structural defects formed during the layer growth. Some inhomogeneities of the image of the Fe layer can be recognized in Fig. 3c. The magnetization curves (Fig. 5a) are similar to the magnetization curves of a pellet containing field oriented Fe particles (Fig. 6b). These similarities strongly suggest that there is a small perpendicular anisotropy in the deposited layer. The conclusion is in a full agreement with results of our CEMS observation. Details of the growth induced anisotropy are under investigation.

8. Conclusions

Nearly nonaqueous bath for deposition of the shiny metal layers has been reported. At the initial stage, the electrolyte does not contain cations of the deposited element. During the electrodeposition cation concentrations are much smaller than in typical electrolytes. We show that the same initial composition and the same current density is used for deposition of various 3d metals. Estimated thicknesses of the layers are of about 400 nm. Mössbauer measurements indicate that magnetic moments are preferentially oriented perpendicular to the film plane. Magnetization data of the deposited layer and the test samples were compared. It was concluded that small perpendicular anisotropy is present in the Fe layer deposited on the Cu substrate.

Acknowledgements

The authors wish to express their gratitude to T. Borowski of the Faculty of Materials Science and Engineering, Warsaw University of Technology, for technical support during the SEM measurements.

References

[1] MIKHAYLOVA M., KIM D.K., TOPRAK M. and MUHAMMAD M., Mat. Res. Soc. Symp. Proc., 750 (2003), 51.
[2] DATTA M., Electrochem. Acta, 48 (2003), 2975.
[3] GOMEZ E., PELLICER E., DUCH M., ESTEVE J., VALLES E., Electrochem. Acta, 51 (2006), 3214.
[4] PANDA B., DAS S.C., Hydrometallurgy, 59 (2001), 55.
[5] CHI-CHANG HU, YAU-RUEN WU, Mater. Chem. Phys., 82 (2003), 588.

[6] MYUNG N.V., PARK D.-Y., URGILES D.E., GEORGE T., Electrochem. Acta, 49 (2004), 4397.
[7] STEPHEN J., Nucl. Instr. Meth., 26 (1964), 269.
[8] OLSZEWSKI W., SZYMAŃSKI K., SATUŁA D., DOBRZYŃSKI L., Nukleonika, 52 (2007), S17.

Received 10 May 2007
Revised 21 January 2008

Materials Science-Poland, *Vol. 26*, *No. 3*, *2008*

Magnetic properties of silicon crystals implanted with manganese*

V. OSINNIY[1**], A. MISIUK[2], M. SZOT[1], K. ŚWIĄTEK[1], J. BĄK-MISIUK[1], A. BARCZ[2], W. JUNG[2], M. PRUJSZCZYK[2] AND T. STORY[1]

[1]Institute of Physics, Polish Academy of Sciences, al. Lotników 32/46, 02-668 Warsaw, Poland

[2]Institute of Electron Technology, al. Lotników 46, 02-668 Warsaw, Poland

The influence of thermal treatment on magnetic properties of Si/Mn crystals grown by the Czochralski and by floating zone methods and implanted with Mn^+ ions was studied by the SQUID magnetometry and electron spin resonance. Depending on thermal and hydrostatic pressure annealing conditions, three groups of Si/Mn samples were found: samples with only ferromagnetic phase, samples with ferromagnetic and paramagnetic contributions, and diamagnetic samples. The Curie temperature of ferromagnetic phase exceeds room temperature. The ESR and SQUID measurements suggest that Si/Mn implanted layer is magnetically inhomogeneous.

Key words: *ferromagnetic semiconductor; silicon; implantation*

1. Introduction

Utilizing the spin of electron in semiconductor devices opens new field of potential applications in high-speed and low-power spintronic devices [1, 2]. One of the main research directions in this field concerns ferromagnetic semiconductors created by appropriate magnetic and electrical doping of classical semiconductor materials. Particularly important is the search for ferromagnetism in Si – the most important material of electronic industry – for which theoretical models suggest the carrier concentration induced ferromagnetism to exist above room temperature. Nowadays, numerous groups investigate the magnetic properties of silicon structures doped by magnetic ions, prepared by various evaporation methods [3] or implantation [4, 5]. Recent examination of Si implanted with Mn^+ ions indicated an appearance of ferromagnetic

---

*Presented at the Conference of the Scientific Network "New Materials for Magnetoelectronics – MAG-EL-MAT 2007", Będlewo near Poznań, 7–10 May, 2007.

**Corresponding author, e-mail: osinn@ifpan.edu.pl

phase after implantation process with the estimated Curie temperature over 400 both K in n-type and in p-type materials [4]. The authors suggested that the ferromagnetic exchange is carrier mediated. In this paper, we report on experimental studies of the magnetic properties of silicon crystals implanted with Mn ions and subject to various thermal and hydrostatic pressure treatment regimes.

2. Experimental

The investigated Si/Mn structures were prepared by implantation of Mn^+ ions at energy $E = 160$ keV with the dose $D = 10^{16}$ cm^{-2} into two types of Si crystals. The first group – silicon wafers grown by Czochralski method (CzSi/Mn) – exhibited p-type conductivity with hole concentration $p = 10^{15}$ cm^{-3} and interstitial oxygen concentration $c_O = 9\times10^{17}$ cm^{-3}. The other group of Si crystals, fabricated by floating zone method (FzSi/Mn), was characterized by n-type conductivity with electron concentration $n = 10^{14}$ cm^{-3} and oxygen content $c_O = 1.5\times10^{17}$ cm^{-3}. The implantation process for CzSi crystals was carried out without substrate heating with silicon wafer temperature $T_S \leq 340$ K. In the case of FzSi structures, the wafer was heated and the implantation was done at $T_S = 610$ K. Subsequently, the Si/Mn samples were annealed in Ar atmosphere for $t \leq 10$ h under hydrostatic pressure $HP \leq 1.1$ GPa in a broad temperature range $540 \leq T_A \leq 1400$ K [6].

The crystal structure of Si/Mn was investigated by X-ray diffraction (reciprocal space mapping, XRRSM) and photoluminescence (PL) methods. The Mn depth profiles were measured by the secondary ion mass spectrometry (SIMS). The carrier concentration on the implanted and on the back (non-implanted) sides was controlled by electrical impedance measurements and calculated based on current–voltage (*I–V)* and capacitance–voltage (*C–V*) characteristics of the Schottky barrier junction Hg–Si.

The temperature and magnetic field dependence of magnetization was studied using a SQUID magnetometer in a broad temperature range (5–300 K) in the magnetic field up to 800 Oe. Only for a few samples, the investigation was performed at higher magnetic fields in order to reach magnetization saturation. For all investigated samples the weak magnetic signal was recorded with the maximum signal detected in Si/Mn about $(5–10)\times10^{-6}$ emu (measurement error equals 5×10^{-7} emu). The temperature and angle dependences of the electron spin resonance (ESR) spectra were measured by an X-band (9.4 GHz) Bruker spectrometer in the temperature range 2–300 K.

3. Results and discussion

Based on the PL measurements and the X-ray diffraction analysis, one may conclude that the crystal structure of CzSi/Mn prepared by implantation at $T < 340$ K is strongly disordered due to atomic displacements after implantation. The crystal structure of FzSi/Mn is more ordered with a well defined layered geometry. The PL mea-

surements of the samples also indicate the presence of numerous point defects and dislocations. The results of SIMS measurements are presented in Fig. 1. Projected range of the distribution of implanted Mn ions equals 140±50 nm with the width of distribution of about 100 nm. The thermal treatment of CzSi/Mn at temperature below 670 K has practically no effect on Mn distribution while the annealing at higher temperature shifts the Mn ions distribution towards the surface (Fig. 1). This Mn redistribution effect only weakly depends on the hydrostatic pressure. After the thermal treatment of FzSi/Mn structures, the profile of Mn distribution in Si wafer practically does not change.

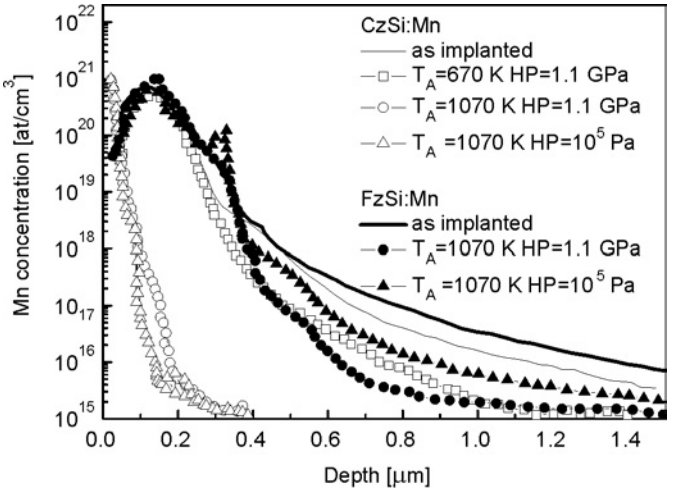

Fig. 1. Depth profiles of Mn in CzSi/Mn and FzSi/Mn samples, as implanted and annealed for 1 h at the temperature and under hydrostatic pressure conditions indicated in the figure

The electrical measurements were performed on implanted and on back sides of CzSi/Mn and FzSi/Mn structures annealed at 720 K for 10 h. Mn^+ implantation produces both donors and acceptors – the implanted CzSi/Mn samples are p-type while FzSi/Mn ones are n-type. After annealing the CzSi/Mn samples exhibiting higher oxygen concentration, a change of the type of conductivity to n-type was found. The carrier concentration on the implanted side is of the order of $n = 10^{16}$–10^{17} cm^{-3} for the CzSi/Mn sample and $n = 10^{14}$–10^{16} cm^{-3} for FzSi/Mn sample. Such a low carrier concentration puts in question the free carrier origin of ferromagnetic coupling between Mn ions in implanted Si/Mn layers. For instance, in the well known ferromagnetic semiconductors, in which ferromagnetic coupling between Mn ions is induced by free carriers ($Pb_{1-x-y}Sn_yMn_xTe$ and $Ga_{1-x}Mn_xAs$) the threshold carrier concentration is about 10^{20} cm^{-3}.

Based on the SQUID magnetization measurements, the Si/Mn samples can be divided into three groups. The samples from the first group exhibit ferromagnetic behaviour with the ferromagnetic hysteresis loop almost temperature independent in a broad temperature range. Magnetization of these samples remains practically con-

stant up to the room temperature, which indicates the Curie temperature exceeding room temperature in these materials (Fig. 2a). Assuming that Mn ions with $S = 5/2$ magnetic moment create magnetically homogeneous 100 nm thick implanted layer of $Si_{1-x}Mn_x$, the amount of ferromagnetic Mn ions corresponds to $x = 0.5$ at. %. The magnetic behaviour of the samples from the second group is characterized by the presence of both ferromagnetic and paramagnetic contributions (Fig. 2b). In order to describe the temperature dependence of magnetization, three contributions were taken

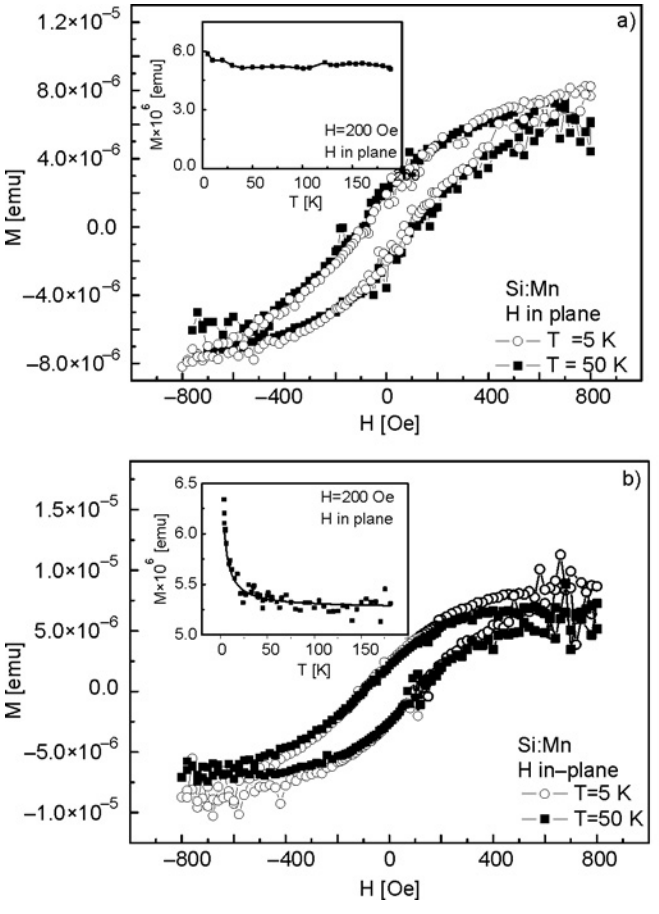

Fig. 2. Ferromagnetic hysteresis loops at various temperatures for samples from the first (a) and the second (b) groups. The insets show the temperature dependence of magnetization. The solid line presents the Curie-Weiss law fit

into account: diamagnetic (Si crystal), as well as paramagnetic and ferromagnetic phases of Si/Mn. Based on the Curie–Weiss law fitting, the amount of paramagnetic Mn ions can be evaluated as corresponding to $x = 1.5$ at. %. The samples from the third group show diamagnetic properties, which suggests that most of Mn ions are incorporated in Si matrix in a magnetically inactive form. In the case of FzSi/Mn

structures, the thermal treatment conditions have been determined for which all samples exhibit the ferromagnetic ordering (275 °C $\leq T_A \leq$ 450 °C, other parameters being of lesser importance). For CzSi/Mn structures, reliable establishing of such technological conditions failed. The main conclusion of the thermal treatments is that heating of a silicon wafer during implantation process enables fabrication of a more magnetically predictable structure. Below certain temperature of post growth treatment, the FzSi/Mn structures remain with evident ferromagnetic contribution plus more or less strong paramagnetic contribution. In order to decrease the contribution of ferromagnetism in these structures, higher temperatures during the post growth treatment are needed. In the non-heated CzSi/Mn structure, the magnetic distribution of Mn ions is more chaotic so any thermal treatment conditions cannot guarantee obtaining a Si/Mn structure with ferromagnetic ordering.

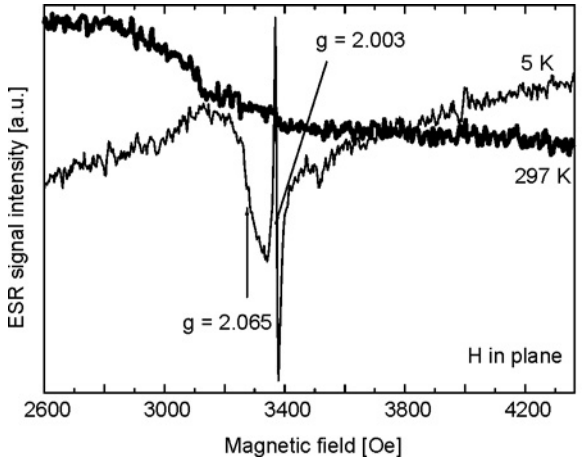

Fig. 3. X-band ESR spectra of FzSi/Mn crystal. The arrows point to two main resonance lines identified by their *g* factors

The ESR measurements revealed in Si/Mn samples at low temperatures the main resonance line with the *g* factor equal 2.003 (Fig. 3). We tentatively assign this very narrow ESR line to unpaired spins of electrons of lattice defects in Si (e.g., dangling bonds) or in SiO_2 [7, 8]. The broader line with the *g* factor equal to 2.065 which also is visible in the ESR spectrum cannot be assigned to single Mn ions but rather to magnetic Mn–Si nanoparticles. As this weak resonance overlaps with background signal from the quartz sample holder, we are unable to make any definite conclusion about Mn-related ESR signal in Si/Mn implanted structures. From the ESR measurements, we can clearly conclude that a small ferromagnetic contribution observed in SQUID measurements does not originate from any ultra thin continuous ferromagnetic layer. The ESR spectra of Si/Mn reveal neither the angular dependence due to shape anisotropy nor temperature dependence characteristic of ferromagnetic resonance. This conclusion supports the idea of Mn–Si nanoparticles enriched with Mn as a micro-

scopic origin of ferromagnetic properties of Si/Mn. Such objects have been observed by TEM investigations of Si implanted with Mn [9] which revealed regions with bands of dislocations and stacking faults along with a variety of Mn-rich nanoparticles and silicides [10].

Additionally, we performed a series of reference magnetic measurements of Si crystals implanted with other magnetic ions (Cr and V) and non-magnetic ions (Si and He). For Si implanted with Si only diamagnetic properties were observed. In the case of magnetic ions implantation, we observed a ferromagnetic behaviour of the investigated samples. Surprisingly, also Si crystals implanted with He ions show a certain small ferromagnetic contribution. This suggests that the possibility of appearance of ferromagnetism may not necessarily be connected with the presence of magnetic ions. Some authors observed the ferromagnetic properties in Si structures without any magnetic ions [11]. They explain the appearance of ferromagnetic ordering by unpaired spins of the dangling bonds. Therefore, the origin of ferromagnetism in Si crystals implanted with Mn^+ ions needs further investigations with a careful examination of possible contamination of Si/Mn structures with magnetic ions during the implantation process.

4. Conclusions

The magnetic properties of Si crystals implanted with Mn were experimentally studied by the SQUID magnetometry and the ESR. The implanted Si/Mn samples can be divided in three groups: samples with dominating ferromagnetic phase (Curie temperature exceeds room temperature), samples with ferromagnetic and paramagnetic phases coexisting and diamagnetic samples. Technological regimes of thermal treatment of FzSi/Mn structures exhibiting the ferromagnetic ordering were determined. The analysis of SQUID and ESR measurements indicate the absence of magnetically homogeneous thin ferromagnetic Si/Mn layer but rather point to the import role of Si-Mn nanoparticles and cooperative effect of unpaired spins of electrons of various crystal defects.

References

[1] DIETL T., OHNO H., MATSUKURA F., CIBERT J., FERRAND D., Science, 287 (2000), 1019.
[2] DIETL T., Semicond. Sci. Technol., 17 (2002), 377.
[3] NAKAYAMA H., OHTA H., KULATOV E., Thin Solid Films 395 (2001), 230.
[4] BOLDUC M., AWO-AFFOUDA C., STOLLENWERK A., HUANG M.B., RAMOS, F.G. AGNELLO G., LABELLA V.P., Phys. Rev. B, 71 (2005), 033302.
[5] MISIUK A., BAK-MISIUK J., SURMA B., OSINNIY W., SZOT M., STORY T., JAGIELSKI J., J. Alloys Comp., 423 (2006), 201.
[6] MISIUK A., Mater. Phys. Mech., 1 (2000), 119.
[7] WARREN W.L., POINTDEXTER E.H., OFFENBERG M., MULLER-WARMUTH W., J. Electrochem. Soc., 139 (1992), 872.

[8] TOMOZEIU N., VAN FAASEN E.E., ARNOLDBIK W.M., VREDENBERG A.M., HABRAKEN F.H.P.M., Thin Solid Films, 420–421 (2002), 382.
[9] DUNN K.A., THIEL B.L., RAMOS F.G., HUANG M.B., AWO-AFFOUDA C., BOLDUC M., LABELLA V., Microsc. Microanal., 11 (2005) 1720.
[10] GOTTLIEB U., SULPICE A., LAMBERT-ANDRON B., LABORDE O., J. Alloys Comp., 361 (2003), 13.
[11] DUBROCA T., HACK J., HUMMEL R.E., ANGERHOFER A., Appl. Phys. Lett., 88 (2006), 182504.

Received 10 May 2007
Revised 21 January 2008

Materials Science-Poland, *Vol. 26*, *No. 3*, *2008*

XPS study of $RNiSb_2$ (R = Pr, Nd)*

A. SZYTUŁA[1**], B. PENC[1], A. JEZIERSKI[2]

[1]M. Smoluchowski Institute of Physics, Jagiellonian University,
ul. Reymonta 4, 30-059 Cracow, Poland

[2]Institute of Molecular Physics, Polish Academy of Sciences,
ul. M. Smoluchowskiego 17, 60-179 Poznań, Poland

The electronic structure of the ternary $RNiSb_2$ (R = Pr, Nd) compounds, which crystallize in the tetragonal primitive $ZrCuSi_2$-type structure, was studied by the X-ray photoemission spectroscopy. The R3d core-levels and the valence bands were investigated. The results for the $PrNiSb_2$ valence band are compared with the previously calculated density of states. The obtained results indicate that the valence bands are mainly determined by the Ni3d band. The analysis of the XPS spectra of $R3d_{5/2}$ and $R3d_{3/2}$ based on the Gunnarsson–Schönhammer model gives the hybridization of the 4f orbitals with the conduction band. The experimental data concerning the valence band of these compounds are compared with the calculations based on the KKR-CPA method. The calculated data for the room temperature (paramagnetic region) give the peaks corresponding to the R4f states at the Fermi level E_F = 0. A different distribution of the peaks corresponding to the Ni3d states is observed. For $PrNiSb_2$ three peaks at 2.0, 2.3 and 3.5 eV are observed while for $NdNiSb_2$ a broad maximum between 5.0 and 8.0 eV is visible. The experimental data for $PrNiSb_2$ are in good agreement with the calculated ones while those for $NdNiSb_2$ are not.

Key words: *electronic structure; rare earth intermetallics; photoemission spectroscopy*

1. Introduction

The compounds $RNiSb_2$ (R = Pr, Nd) crystallize in the tetragonal $ZrCuSi_2$-type structure (space group $P4/nmm$) [1, 2]. The atoms are located in the following positions: R atoms in 2(*c*): ¼, ¼, z_R, Ni atoms in 2(*a*): ¾,¼, 0 and 2(*c*): ¼, ¼, z_{Ni} and Sb atoms in 2(*b*): ¾, ¼, ½ and 2(*c*): ¼, ¼, z_{Sb}. Magnetic and neutron diffraction measurements give the Néel temperatures of 6.3 K for R = Pr and 2.3 K for R = Nd, re-

---

*Presented at the Conference of the Scientific Network "New Materials for Magnetoelectronics – MAG-EL-MAT 2007", Będlewo near Poznań, 7–10 May, 2007.

**Corresponding author, e-mail: szytula@if.uj.edu.pl

spectively [3]. The neutron diffraction data at $T = 1.45$ K give the values of the magnetic moments lower than the free R^{3+} ions values.

In the course of systematic research of ternary rare earth intermetallic compounds we present the results of the photoemission measurements of $RNiSb_2$ compounds, where R = Pr and Nd. The XPS valence band spectra are compared with electronic structure calculations. Based on these results, the electronic structures of the compounds have been determined.

2. Experiment and results

All experiments were carried out on sintered pellets in vacuum. The XPS spectra were collected at room temperature using the Leybold LHS10 electron photoemission spectrometer with the MgK_α ($h\nu = 1253.6$ eV) and AlK_α ($h\nu = 1486.6$ eV) radiation in vacuum of about 10^{-9} mbar. The total energy resolution of the spectrometer with a hemispherical energy analyzer was about 0.75 eV for Ag3d. Binding energies were referred to the Fermi level ($E_F = 0$). The spectrometer was calibrated using the $Cu2p_{3/2}$ (932.5 eV), $Ag3d_{5/2}$ (368.1 eV) and $Au4f_{7/2}$ (84.0 eV) core-level photoemission spectra. Surfaces of the samples were mechanically cleaned by scraping with a diamond file in a preparation chamber under high vacuum (10^{-9} mbar) and then were moved immediately into the analysis chamber. This procedure was repeated until the C1s and O1s core-level peaks were negligibly small or were not changing after further scrapings. Such a cleaning procedure was performed before each XPS measurement. The Shirley method [4] was used to subtract background and the experimental spectra prepared in this way were numerically fitted using the 80% Gaussian and 20% Lorentzian model.

The electronic structure was calculated using the KKR–CPA method [5, 6]. The band structure was calculated using the specx (KKR–CPA) programme with the correlation – exchange potential proposed by Vosko et al. [7, 8]. Calculations were performed in the semi-relativistic treatment of the core level based on the available data on the crystal structure of $RNiSb_2$ (R = Pr, Nd): $a = 0.43674$ nm, $c = 0.9699$ nm, $z_R = 0.7635$, $z_{Ni} = 0.39$, $z_{Sb} = 0.125$ for R = Pr and $a = 0.45674$ nm, $c = 0.9629$ nm, $z_R = 0.7604$, $z_{Ni} = 0.38$, $z_{Sb} = 0.1345$ for R = Nd with the respective occupation numbers: 1 for R in 2*c*, $1 - n_{Ni}$ and n_{Ni} in 2*a* and 2*c* and 1 for Sb in 2*b* and 2*c*. The value of n_{Ni} is equal to 0.162 for R = Pr and 0.103 for R = Nd.

The calculated total density of states for $RNiSb_2$ (R = Pr, Nd) is shown in Fig. 1. The 4f level of Pr in $PrNiSb_2$ and of Nd in $NdNiSb_2$ gives high intensity peaks near the Fermi level. The observed distribution of the peaks corresponding to the Ni3d states is different: for $NdNiSb_2$ a broad maximum between 5.0 and 8.0 eV is visible. The data for the Pr compound are in good agreement with the previous calculations [9]. For $PrNiSb_2$ three peaks at 2.0, 2.3 and 3.5 eV are observed.

Materials Science-Poland

an
Interdisciplinary Journal of
Physics, Chemistry and
Technology of Materials

Vol. 26, No. 3, 2008

ISSN 0137-1339
Index No. 375675

Wrocław
University
of Technology

PMS SOCIETY

CENTRE OF
ADVANCED MATERIALS AND
NANOTECHNOLOGY

Wrocław University of Technology
Centre of Advanced Materials and Nanotechnology

Materials Science-Poland

Vol. 26 • No. 3 • 2008

Oficyna Wydawnicza Politechniki Wrocławskiej

Materials Science is an interdisciplinary journal devoted to experimental and theoretical research into the synthesis, structure, properties and applications of materials.

Among the materials of interest are:

- glasses and ceramics
- sol-gel materials
- photoactive materials (including materials for nonlinear optics)
- laser materials
- photonic crystals
- semiconductor micro- and nanostructures
- piezo-, pyro- and ferroelectric materials
- high-T_c superconductors
- magnetic materials
- molecular materials (including polymers) for use in electronics and photonics
- novel solid phases
- other novel and unconventional materials

The broad spectrum of the areas of interest reflects the interdisciplinary nature of materials research. Papers covering the modelling of materials, their synthesis and characterisation, physicochemical aspects of their fabrication, properties and applications are welcome. In addition to regular papers, the journal features issues containing conference papers, as well as special issues on key topics in materials science.

Materials Science is published under the auspices of the Centre of Advanced Materials and Nanotechnology of the Wrocław University of Technology, in collaboration with the Institute of Low Temperatures and Structural Research of the Polish Academy of Sciences and the Wrocław University of Economics.

All accepted papers are placed on the Web page of the journal and are available at the address:
http://MaterialsScience.pwr.wroc.pl

Materials Science is abstracted/indexed in: Chemical Abstracts, Materials Science Citation Index, Science Citation Index Expanded.

The Journal is supported by the State Committee for Scientific Research

Printed in Poland

Drukarnia Oficyny Wydawniczej Politechniki Wrocławskiej
Zam. nr 621/2008.

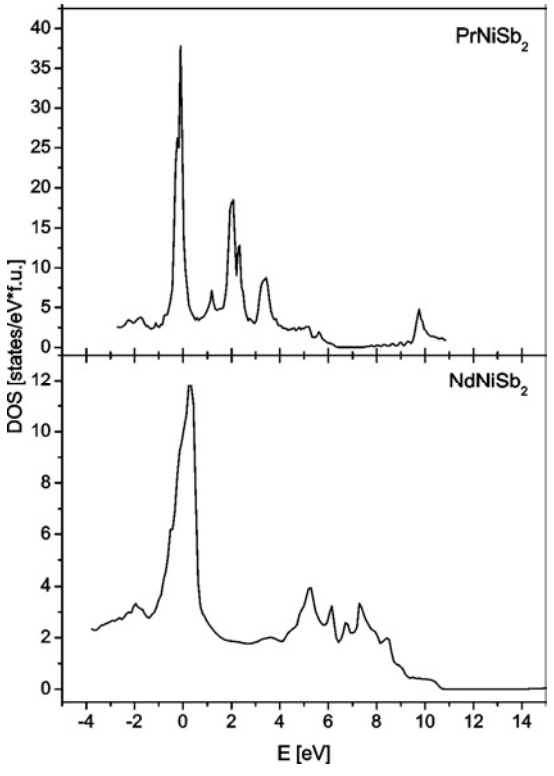

Fig. 1. Calculated electronic density of states for paramagnetic $RNiSb_2$ (R = Pr, Nd)

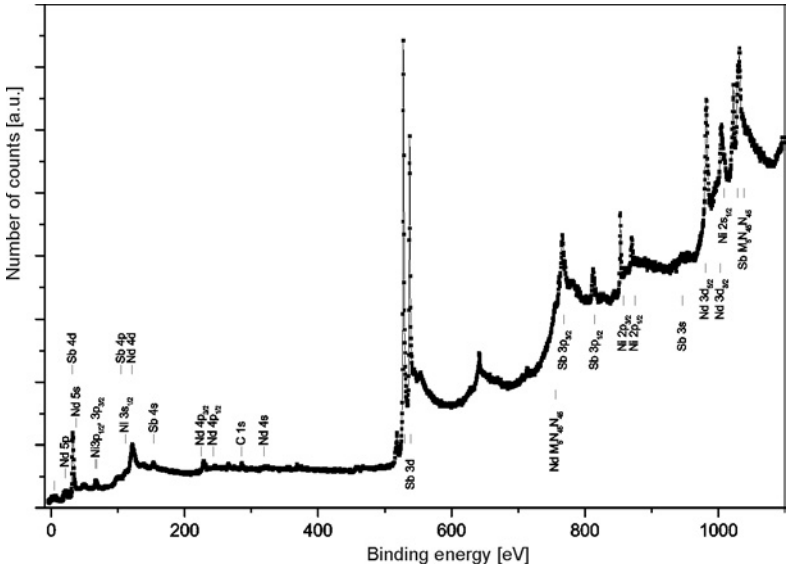

Fig. 2. XPS MgK_α spectrum of $NdNiSb_2$ (with the core-level lines) in a wide binding energy range from 0 to 1100 eV

Figure 2 shows the XPS spectrum of the $NdNiSb_2$ compound in a wide binding energy range of 0–1100 eV. The binding energies are related to the Fermi level ($E_F = 0$).

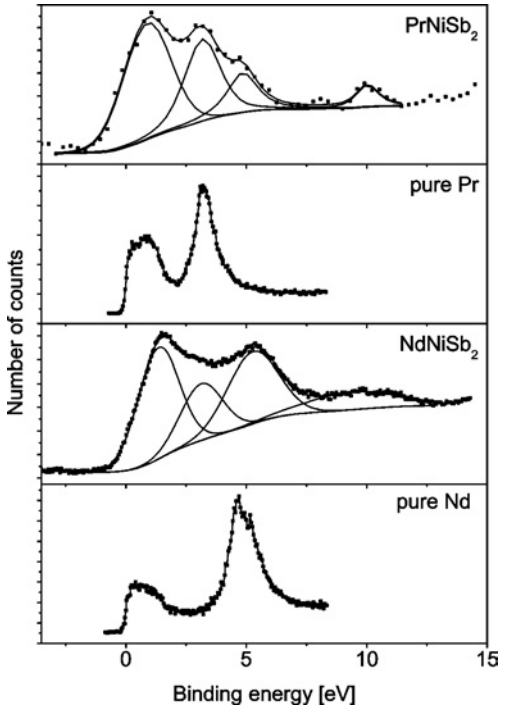

Fig. 3. XPS spectrum of valence band of $RNiSb_2$ (R = Pr, Nd) and the appropriate spectrum for metallic Pr and Nd

The XPS valence bands (VB) of $RNiSb_2$ (R = Pr, Nd) compounds and metallic Pr and Nd are presented in Fig. 3. In both $RNiSb_2$ spectra three peaks in the region between 0 and 7.5 eV and next at 10 eV are observed. Comparing the data for the investigated compounds and metallic rare earth elements with the calculations makes possible to give the interpretation of the measured spectra. The two peaks at 1.1 and 3.2 eV for $PrNiSb_2$ and 1.5 and 3.2 eV for $NdNiSb_2$ correspond to the Ni 3d states and the peak near 10 eV corresponds to the Sb 3s states. The peak connected with Pr 4f states in the $PrNiSb_2$ spectrum coincides with the second peak of the Ni 3d states at 3.2 eV. The peak of Nd 4f states in $NdNiSb_2$ spectrum is at 5.2 eV and is shifted to higher energies with respect to the metallic Nd (4.7 eV). The low intensity peak at 5.0 eV in $PrNiSb_2$ is probably connected with the oxygen impurity.

Figure 4 shows the Pr and Nd 3d XPS spectra of both investigated compounds. The high intensity peaks at 933.4 and 953.5 eV in $PrNiSb_2$ and 981.8 and 1004.6 eV in $NdNiSb_2$ correspond to the $R3d_{5/2}$ and $R3d_{3/2}$ levels. The structure of these spectra has been interpreted in terms of the Gunnarsson–Schönhammer theory [10]. The spin-orbit

splitting corresponds to the spectral structure of the 3d XPS peaks. This splitting is equal to 20.1 eV for R = Pr and 22.8 eV for R = Nd. At low-binding-energy side of the $3d_{5/2}$ and $3d_{3/2}$ main lines the shake down satellites (at 929.0 and 948.8 eV for $PrNiSb_2$ and 978.3 and 1000.7 eV for $NdNiSb_2$) are observed which is known to account for the screened $Pr3d^94f^3$ and $Nd3d^94f^4$ final states [11]. The additional peaks at 925.1 and 945.4 eV for $PrNiSb_2$ and 973.5 and 996.1 eV for $NdNiSb_2$ are connected with the line corresponding to the parasite radiation ($K_{\alpha 3}$, $K_{\alpha 4}$). The peak at 964.7 eV in $PrNiSb_2$ is connected with the Pr Auger signal expected at this energy. The additional small intensity peaks at 983.7 and 1008.5 eV (Δ_{S-O} = 24.7 eV) correspond probably to the Nd atoms in the second site or to an impurity.

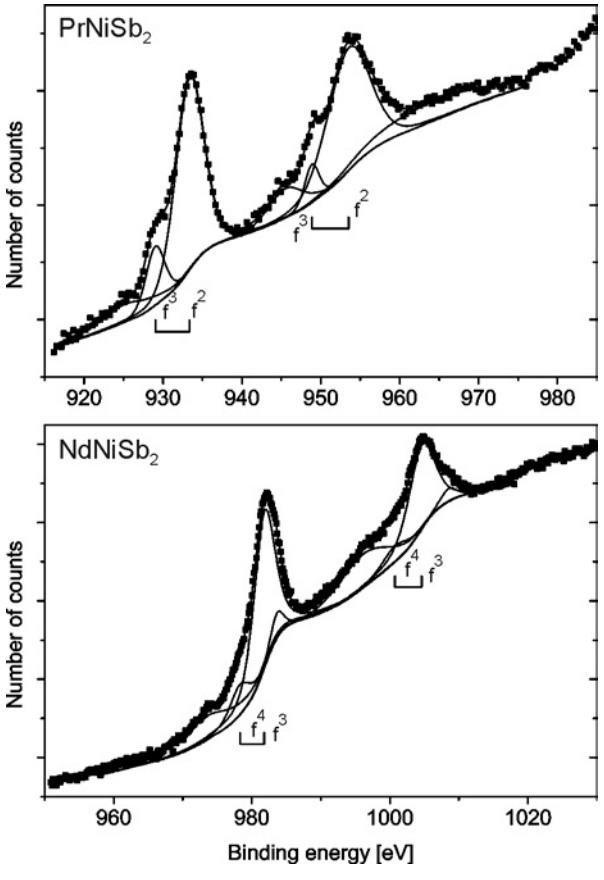

Fig. 4. X-ray photoemission spectra of $R3d_{5/2}$ and $R3d_{3/2}$ electron states of R = Pr, Nd in $RNiSb_2$ (R = Pr, Nd). The deconvolution of the spectra is shown. The strokes indicate the positions of the convoluted peaks (see the main text)

The energies and the relative intensities of R3d XPS peaks obtained as parameters which correspond to the final states in the fitting procedure are collected in Table 1. The separation of the peaks was based on the Doniach–Šunjić theory [12] which gives

the intensity ratio $r = I(f^{n+1})/[I(f^n) + I(f^{n+1})]$. The relation between the r values and Δ parameters were calculated only for R = La and Ce [11]. The results [13] indicate that it is possible to estimate the values of Δ for R = Pr and Nd, based on this relation. However, the evaluated results are only qualitative. The coupling parameter Δ is defined as $\pi V^2 \rho_{max}$, where ρ_{max} is the maximum of the density of conduction states and V is the hybridization. The r values are 0.17 for $PrNiSb_2$ and 0.164 for $NdNiSb_2$ which corresponds to the hybridization energies of 82.5 and 80.5 meV, respectively.

Table 1. Binding energies (E) and relative intensities (I)
of R3d XPS peaks for $PrNiSb_2$ and $NdNiSb_2$.
All energies are given in eV and related to the Fermi energy level ($E_F = 0$)

Compound	$3d_{5/2}$	$3d_{3/2}$
$PrNiSb_2$		
E [eV]	925.1, 929.0, 933.4	945.4, 948.8, 953.5, 964,7
I	18.7, 20.2, 100	18.3, 13.5, 66.7, 36.4
$NdNiSb_2$		
E [eV]	973.5, 978.3, 981.8, 983.7	996.1, 1000.7, 1004.6, 1008.5
I	47.2, 19.6, 100, 9.4	42.4, 13.1, 66.7, 6.3

The data for $PrNiSb_2$ and $PrNi_{1.8}Sb_2$ give the values of r equal to 0.24 and 0.28 and the corresponding Δ values of 120 and 140 meV, respectively [14].

The $Ni2p_{3/2}$ peak in both compounds is observed at 853.0 eV below the Fermi level and has two additional satellites: 853.5 and 861.0 eV. These satellites have been observed in Ni metal, $TbNi_2Ge_2$ and Fe_2NiAl [15], $SmNi_2B$ [16] and U_2Ni_2In [17]. The existence of the satellites may suggest that the Ni 3d band is not completely filled [16, 18]. Because the intensity of the peaks in both compounds is smaller than that for the pure Ni metal one expects the Ni magnetic moment to vanish. This is in good agreement with the neutron diffraction data, which give no evidence for any magnetic moment localized on the Ni atoms [3].

3. Concluding remarks

The XPS spectra of $RNiSb_2$ (R = Pr, Nd) at room temperature and calculations of their electronic structure have been presented. The analysis of the $R3d_{5/2}$ and $R3d_{3/2}$ states indicates that the hybridization of the 4f and conduction states in both compounds is smaller than in $PrNi_{2-x}Sb_2$ ($\Delta \approx 120$, 140 meV) [14]. This result suggests strong localization of the R4f states in the $RNiSb_2$ (R = Pr, Nd) compounds. The analysis of the valence bands shows that Ni 3d peaks are close to the Fermi level, from which could be concluded that these states are mostly occupied. The XPS data give R4f states at 3.2 eV for Pr in $PrNiSb_2$ and 4.6 eV Nd in $NdNiSb_2$. These results suggest the hybridization of the R4f states and Ni 3d states which probably influence the

values of the rare earth magnetic moments. The calculated value of the magnetic moment localized on praseodymium in $PrNiSb_2$, equal to $1.95\mu_B$ [9], is close to the experimental value ($1.88\mu_B$) [3]. Comparing our data for $PrNiSb_2$ with those presented in the work [19] for pure Pr and the oxides PrO_2 and Pr_2O_3 one can say that the effect of oxidation in our sample is small. Existence of a small oxygen impurity influences the intensity of the Pr3d-f^3 state and the value of the coupling parameter Δ that means that the obtained results are only quantitative.

The results presented in the paper give the explanation of the magnetic properties of the $RNiSb_2$ (R = Pr, Nd) compounds. The hybridization of Pr4f and Ni3d states cause the decrease of the value of the rare earth magnetic moment whereas small hybridization of Pr4f state with the conduction electron results in the low values of the Néel temperature. Similar properties are observed in the RAg_2Ge_2 (R = Pr, Nd) compounds which order at 12 K (R = Pr) and 2.0 K (R = Nd) and are characterized by low hybridization energies equal to 41 meV (R = Pr) and 71 meV (R = Nd) [20].

References

[1] PANKEVICH YU.V., PECHARSKIY V.K., BODAK O.I., Metally, 5 (1983), 227 (in Russian).
[2] SOLOGUB O., HIEBL K., ROGL P., NOËL H., BODAK O., J. Alloys Comp., 210 (1994), 153.
[3] ANDRÉ G., BOURÉE F., OLEŚ A., PENC B., SIKORA W., SZYTUŁA A., ZYGMUNT A., J. Alloys Comp., 255 (1997), 31.
[4] SHIRLEY D.A., Phys. Rev. B, 5 (1972), 391.
[5] AKAI H., DEDERICHS P. P., J. Phys. C, 18 (1985), 2355.
[6] KOTANI T., AKAI H., Phys. Rev. B, 54 (1996), 16502.
[7] VOSKO S.H., WILK L., NUSSAIR M., Can J. Phys., 58 (1980), 1200.
[8] VOSKO S.H., WILK L., Phys. Rev. B, 22 (1980), 3812.
[9] JEZIERSKI A., J. Magn. Magn. Mater., 241 (2002), 63.
[10] GUNNARSSON O., SCHÖNHAMMER K., Phys. Rev. B, 28 (1983), 4315.
[11] FUGGLE J.C., HILLEBRECHT F.U., ŻOŁNIEREK Z., LÄSSER R., FREIBURG CH., GUNNARSSON O., SCHÖNHAMMER K., Phys. Rev. B, 27 (1983), 7330.
[12] DONIACH S., ŠUNJIĆ M., J. Phys. C, 3 (1970), 285.
[13] CRECELIUS G., WERTHEIM G.K., BUSCHANAN D.N.E., Phys. Rev. B, 18 (1978), 6519.
[14] ŚLEBARSKI A., JEZIERSKI A., ZYGMUNT A., NEUMANN M., MÄHL S., BORSTEL G., J. Magn. Magn. Mater., 159 (1996), 179.
[15] GUZIK A., TALIK E., KUZNIETZ M., J. Magn. Magn. Mater., 272-276 (2004), e589.
[16] HONG N.M., THUY N.P., SCHANDY G., HOLUBAR T., HILSCHER G., FRANSE J.J.M., J. Appl. Phys., 73 (1993), 5698.
[17] SZYTUŁA A., JEZIERSKI A., WINIARSKI A., PENC B., Tran V.H., J. Phys.: Condens. Matter, 18 (2006), 1.
[18] TOLIŃSKI T., CHEŁKOWSKA G., KOWALCZYK A., Solid State Commun., 122 (2002), 145.
[19] LÜTKEHOFF S., NEUMANN M., ŚLEBARSKI A., Phys. Rev. B, 52 (1995), 13808.
[20] SZYTUŁA A., BAŁANDA M., KACZOROWSKI D., BARAN S., GONDEK Ł., HERNANDEZ-VELASCO J., STÜSSER N., WAWRZYŃSKA E., Intermetallics, 14 (2006), 315.

Received 10 May 2007
Revised 21 January 2008

Materials Science-Poland, *Vol. 26*, *No. 3*, *2008*

Investigation on optimum corrosion protection potential of Al alloy in marine environment*

SEONG-JONG KIM**, SEOK-KI JANG, JEONG-IL KIM

Mokpo Maritime University, Mokpo City, Jeonnam, 530-729, Republic of Korea

The Al alloy is environmental friendly, easy to recycle, and provides a high added value to fishing boats. We report a number of electrochemical experiments undertaken to determine the optimum conditions for protecting 5083 Al alloy in seawater. The current density in the cathodic polarization increased with the potential shifts to a more negative value. Current densities in –1.8 V to –2.4 V increased abruptly with any shift toward the active direction. On shifting in more anodic and cathodic directions outside the range from –1.4 V to –0.7 V, the current density increased suddenly. It was concluded that this potential range offered optimal protection potential.

Key words: *Al alloy; fishing boat; electrochemical experiments; optimum protection potential*

1. Introduction

Fibre-reinforced polymer (FRP) ships used with small boats for fishing pose numerous problems from both the environmental and recycling perspectives. In particular, no methods exist to dispose of these ships at the end of their service. Al alloy is environmental friendly, easy to recycle, and provides a high added value to fishing boats. Aluminum craft require less fuel. Developed nations have shown an increasing interest in utilizing Al alloys in ships since environmental restrictions on scrapping FRP ships have become stronger. The specific strength of Al ships is higher than that of steel ships [1]. Ships constructed with 5000-series Al alloy suffer little or no corrosion in the marine environment.

In this paper, we report a number of electrochemical experiments undertaken to determine the optimum conditions for protecting 5083F (Al–Mg alloy) in seawater.

---

*The paper presented at the 9th Symposium on "Reactivity of Metastable Materials, 2007 EMRS Fall Meeting", Warsaw, 17–21 September, 2007.

**Corresponding author, e-mail: kimji@mmu.ac.kr

2. Experimental

For the electrochemical experiments, the 5083F specimen (Al-Mg alloy, Si 0.090%, Fe 0.289%, Cu 0.018%, Mn 0.589%, Mg 4.449%, Cr 0.076%, Zn 0.005%, Ti 0.009%, Al balance, tensile strength 319.2 MPA, yield strength 154.8 MPa, elongation 23.7%) was mounted in an epoxy resin so as to leave an exposed area of 100 mm^2 that was polished with #600 emery paper. Each specimen was carefully degreased with acetone and distilled water. The electrochemical apparatus consisted of a Pt coil as the counter electrode and an Ag/AgCl reference electrode. Anodic polarization experiments were executed from an open circuit potential to the range of –0.5–3.0 V in seawater. Cathodic polarization experiments were undertaken from open circuit potential to –2.0 V. In potentiostatic experiments, a variety of polarization potentials in seawater were applied for 1200 s and evaluated in terms of the variations of current density remaining after 1200 s at a given applied potential.

3. Results and discussion

The anodic polarization curve for 5083F specimen in seawater is shown in Fig. 1. The 5083 Al alloy is most widely used because it is both strong and resistant to corrosion in the seawater environment. The current densities from open circuit potential to –0.5V for 5083F alloy were abruptly increased. The current density at the potential range above –0.5 V shows a very high value. The passivity phenomenon of 5083F Al alloy was not observed by a continuous increase in current density.

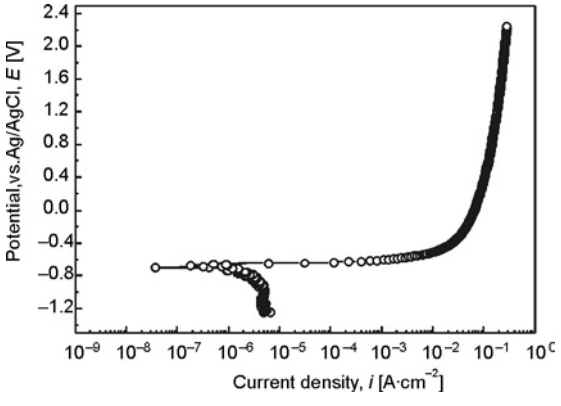

Fig. 1. Anodic polarization curve of 5083F in sea water

Figure 2 presents time dependences of current densities obtained from the potentiostatic experiment at anodic applied potentials of 5083F alloy in seawater. A variation in the current density was observed over the entire 1200 s of the experiment in the range from –0.80 V to ca. –0.60 V, but the values remained low. The current densities at –0.80, –0.70, and –0.60 V after 1200 s were 1.2×10^{-6}, 8.5×10^{-6}, and 7.0×10^{-3} A/cm^2, respectively. The current densities at applied potential from –0.50 V to ca.

–0.20 V remained constant from the earliest stages of the experimental run. The current densities for potentials of –0.20 and –0.50 V behaved in a similar manner to that during anodic polarization, gradually increasing over the initial stages. As the potential increased from 0 to 0.8 V and then to 1.6 V, the current density after 1200 s increased.

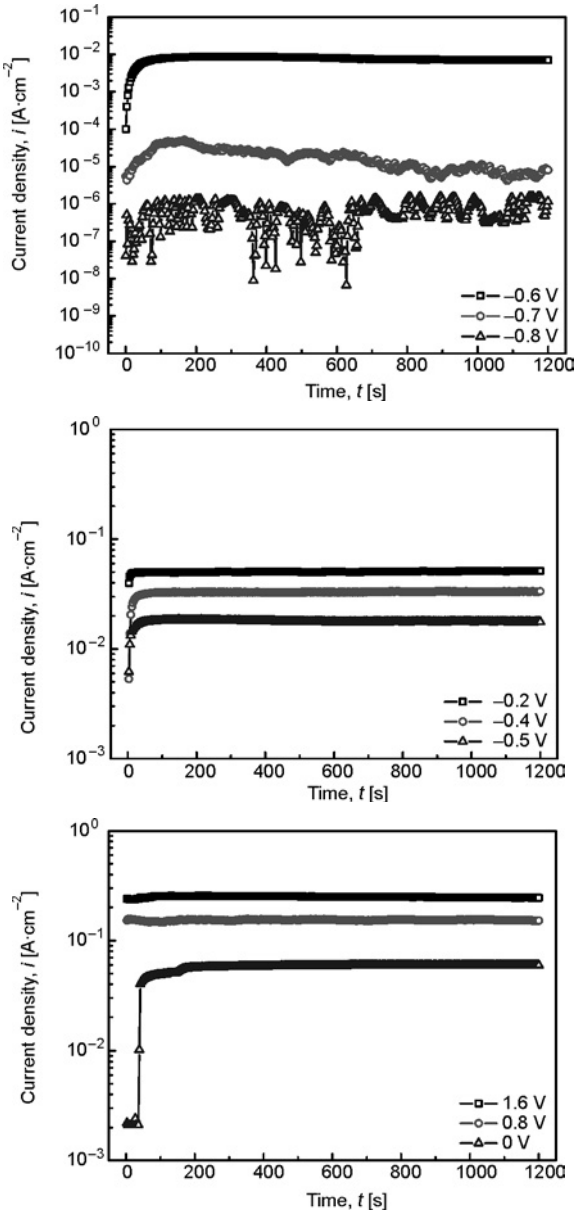

Fig. 2. Time-current density curves during 1200 s at anodic potential for 5083F in sea water

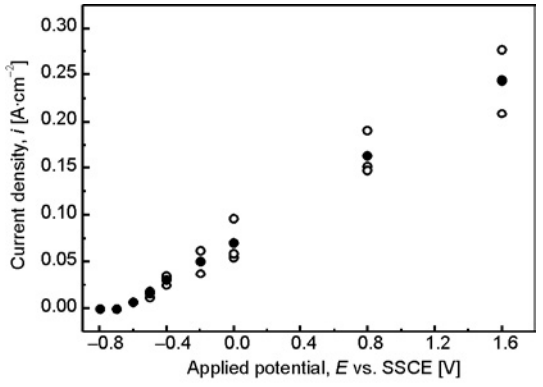

Fig. 3. Current densities after potentiostatic experiment during 1200 s for 5083F

Figure 3 compares the current densities obtained in the potentiostatic experiments after 1200 s for all 5083F specimens analyzed at various anodic potentials in seawater. Each potentiostatic experimental run was executed several times, with the black circles representing the mean values under various conditions. The current densities in the range from –0.8 V to –0.7 V show very low values in all experimental runs. At –0.6 V, the current density increased slightly. Above –0.6 V, the current densities increased in a straight line with increasing potential. Corrosion can similarly occur when hydrogen is generated at appropriate potentials in both acidic and alkaline solutions as shown in the *E*–pH diagram for Al [2]. The behaviour of Al in seawater (approximately pH 8.0) differs from that of Al in neutral solutions.

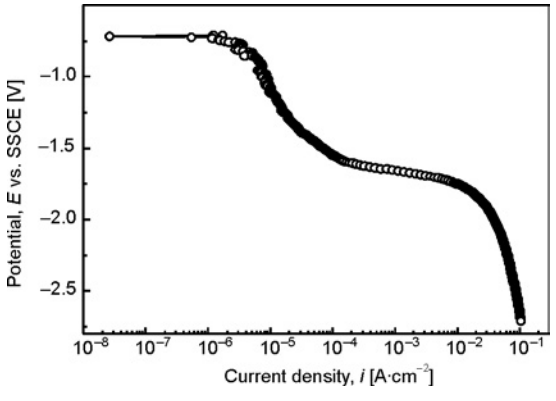

Fig. 4. Cathodic polarization curves in sea water

Figure 4 presents the result of cathodic polarization experiment for 5083F specimen in seawater. The polarization for 5083F Al alloys shows the effects of concentration polarization ($O_2 + 2H_2O + 4e^- \rightarrow 4OH^-$) and activation polarization ($2H_2O + 2e \rightarrow H_2 + 2OH^-$). The turning point between the concentration polarization due to oxy-

gen reduction and the activation polarization due to hydrogen gas generation is the limit potential which determines the corrosion protection potential. The current density in anodic polarization is higher than that of dissolved oxygen reduction during cathodic polarization. This implies that from the economical point of view cathodic protection is more beneficial than the anodic one. The current density at the corrosion protection potential of metal, which has a potential range corresponding to the concen-

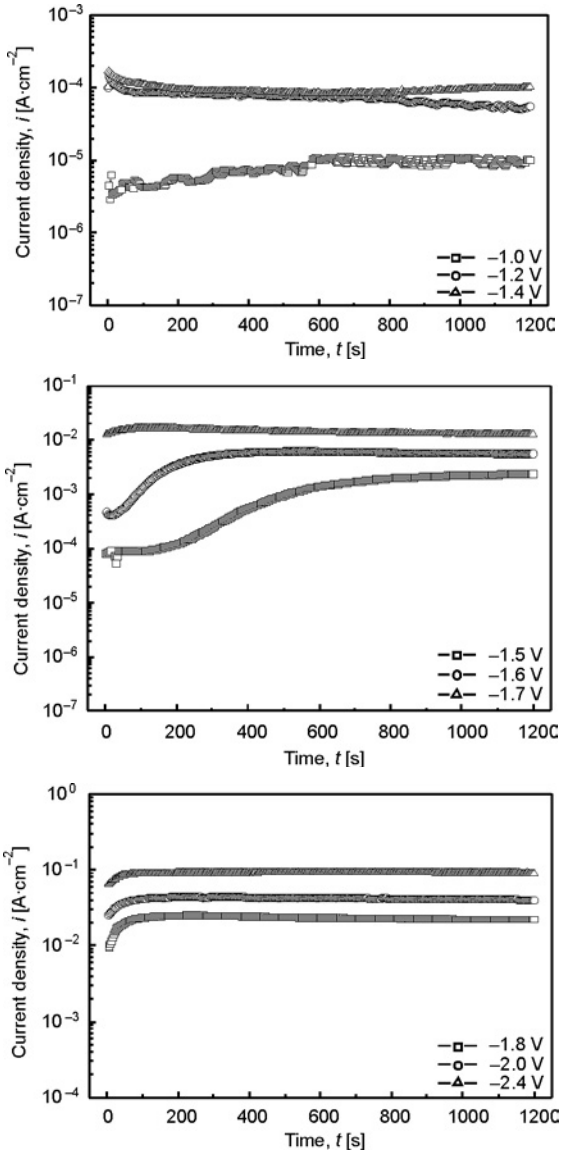

Fig. 5. Time–current density curves during 1200 s at cathodic potential for 5083F in sea water

tration polarization of the cathodic polarization curve, is very important. The limit protection potential (hydrogen embrittlement generation potential) at cathodic polarization of this Al alloy is –1.64 V.

In Figure 5, time dependences of current densities obtained from the potentiostatic experiment at cathodic potentials applied to 5083F alloy in seawater. The results were obtained at applied potentials of –1.4 V to –1.0 V, a potential range that includes that of dissolved oxygen reduction, i.e., that within the protection potential range. Current densities in the range from –1.4 V to –1.0 V showed stable values at early stages. All current densities tended to be low. In the range from –1.7 V to –1.5 V, spanning the changeover from concentration polarization to activation polarization, the current density increased with the potential shifts to a more negative value. This potential range corresponded to the generation of atomic hydrogen ($H^+ + e \rightarrow H$) or the production of molecular hydrogen from atomic hydrogen ($H^+ + e + H \rightarrow H_2$, $H^+ + H \rightarrow H_2$). The upshot was acceleration of activation polarization and an increase in current density. We concluded that atomic hydrogen affected the potential at which the changeover occurred. In the range from –2.4 V to –1.8 V, the current density increased with an increase in negative potential and the increase in current density was linear, with activation polarization intensifying the generation of hydrogen due to cathodic polarization that could be seen by the unaided eye. The effect of atomic hydrogen was smaller than that of molecular hydrogen. In investigations on hydrogen embrittlement in high-strength steel [3, 4], the point at which the changeover takes place from concentration polarization to activation polarization is at approximately –1.0 V (SCE). The current density for the potential at which hydrogen is generated during cathodic polarization increased abruptly. The potential of –0.9 V (SCE) in high-strength steel can also be included in the range at which concentration polarization occurs because the reaction involves the reduction of dissolved oxygen. However, hydrogen embrittlement can also occur at –0.9 V when atomic hydrogen is present. The changeover point for 5083F Al alloy appears at approximately –1.64 V. A comparison of the current densities measured for 5083F alloy in seawater at the conclusion of 1200 s is shown in Fig. 6 at various cathodic potentials.

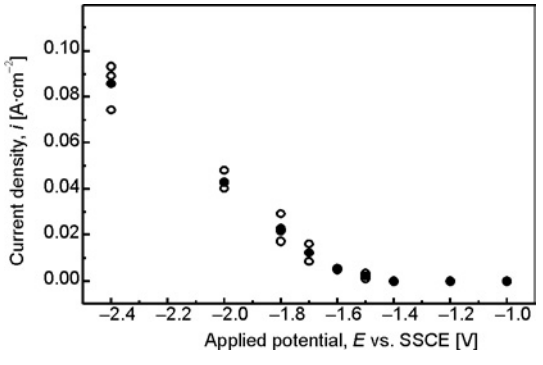

Fig. 6. Comparison of current density

The potential range between –1.4 V and –1.0 V during cathodic polarization showed a low current density applicable to protection. At –1.5 V, the effects of atomic hydrogen are seen in a slightly elevated current density. The potential range from –1.7 V to – 1.5 V corresponded to the changeover, and was affected by the presence of both atomic hydrogen and molecular hydrogen. We concluded, however, that effects on the current density from atomic hydrogen were small. Current densities in the range from –2.4 V to –1.8 V increased abruptly with any shift toward the negative direction and it seems likely that their high current densities reflected the presence of molecular hydrogen. This was the same trend observed in cathodic polarization. In the potential range from –0.7 V to –1.4 V, current densities were low and gave an estimate of the viable protection potential range. The current density increased suddenly when the applied potential shifted beyond the protection potential range in either the anodic or cathodic directions. The optimum protection potential in the potential range from –1.4 V to –0.7 V for 5083F alloy was obtained, when current densities were very low. According to the criteria for cathodic protection given by England (CP 1021) [5], the protection potential of Al is from –0.85 V to –1.1 V(SSCE), with pitting not occurring at a cathodic polarized potential of about 0.15 V compared to the open circuit potential. The current densities in all experiments undertaken to ascertain electrochemical properties returned very low values in the potential range in that effects on the current density from atomic which concentration polarization by dissolved oxygen reduction occurs.

4. Conclusions

Cathodic polarization results in concentration polarization by dissolved oxygen reduction and activation polarization as a result of hydrogen generation. The changeover occurs at –1.64 V (SSCE) in 5083F Al alloy. Current densities increase suddenly in both anodic and cathodic directions beyond the potential range of –1.4 V to –0.7 V. Consequently, optimum protection occurs in the potential range of –1.4 V V to –0.7 V.

References

[1] KANG B.Y., CHO J.H., Kor. J. Weld. Soc., 22 (2004), 39.
[2] POURBAIX M., *Atlas of electrochemical equilibria*, NACE, (1974), 168
[3] KIM S.J., MOON K.M., Met. Mater. Int., 8 (2002), 395.
[4] KIM S.J., OKIDO M., MOON K.M., Surf. Coat. Techn., 169–170 (2003), 163.
[5] JEON D.H., *Control of corrosion and protection*, 316, Il-Joong Publ. Co., 1985.

Received 10 September 2007

Materials Science-Poland, *Vol. 26*, *No. 3*, *2008*

Structure and properties of the multilayers produced on Inconel 600 by the PACVD method with the participation of trimethylaluminum vapours*

R. SITEK[1**], K. SIKORSKI[1], J. SOBCZAK[2], T. WIERZCHOŃ[1]

[1]Faculty of Materials Science and Engineering, Warsaw University of Technology, ul. Wołoska 141, 02-507 Warsaw, Poland

[2]Institute of Physical Chemistry, Polish Academy of Sciences, ul. Kasprzaka 44/52, 01-224 Warsaw, Poland

The paper presents the results of examinations of the structure and properties of Al_2O_3 + Ni_3Al + Ni(Cr, Fe, Al) + Cr-Ni + Cr_7C_3 multilayers produced on nickel alloys by the plasma assisted chemical vapour deposition method with the participation of trimethylaluminum vapours in gaseous atmosphere. The layers have a high surface hardness of about $1200HV_{0.05}$, and high heat and frictional wear resistance. In order to find a correlation between the structure of the multilayers and their properties, the following examinations have been executed: phase analysis by XRD and surface analysis by XPS, analysis of microstructure by optical and scanning electron microscopes as well as X-ray microanalyser, micro-hardness measurements, corrosion and frictional wear resistance testing.

Key words: *PACVD process; multilayers; Inconel 600; XPS*

1. Introduction

Creep-resistant austenitic nickel alloys belong to the group of materials widely used in industry for manufacturing turbine blades, sparking plug, compressor blades, exhaust reheater chambers, and nozzles of gas turbines, missile engines, and jet engines [1–5]. Owing to their high corrosion resistance, they find application in fabricating components of various chemical and petrochemical installations [5]. Heat-resistant nickel alloys can be exploited within the temperature range from 850 °C to 1250 °C [2]. As well known, the efficiency of an engine increases with temperature.

---

*The paper presented at the 9th Symposium on "Reactivity of Metastable Materials, 2007 EMRS Fall Meeting", Warsaw, 17–21 September, 2007.

**Corresponding author, e-mail: rsitek@inmat.pw.edu.pl

The temperature of gases in front of a turbine reaches the value of 1400 °C, thus, it should be lowered by cooling with air supplied partially from the compressor [3]. Another disadvantage of the nickel alloys is their poor resistance to frictional wear [6], which also restricts their application range. The materials alternative to the nickel super-alloys seem to be the intermetallic phases of the Ni–Al system which in the first place are lighter than the conventional nickel alloys and in addition show better resistance to oxidation and much better to frictional wear. A method of obviating the drawbacks of nickel super-alloys is to produce Ni–Al intermetallic layers on their surface using surface engineering techniques, which are highly economic and permit producing surface layers with a precisely specified chemical composition and the performance properties tailored to a given purpose [7].

In the present experiments Ni–Al intermetallic-based surface layers were obtained on Inconel 600 by subjecting the alloy to the plasma assisted chemical vapour deposition (PACVD) treatment with the participation of the trimethylaluminum metallorganic compound. In result of applying a thermo-chemical process, composite layers of σ-Al_2O_3 + Ni_3Al + Ni(Cr, Fe, Al) + Cr_7C_3 + Cr-Ni were obtained. The layers thus obtained show a good resistance to frictional wear and to corrosion. The properties of these layers chiefly depend on their phase compositions and the distribution of the individual phases between them.

2. Experimental

The chemical composition of the Inconel 600 samples used in the experiments is given in Table 1.

Table 1. Chemical composition of Inconel 600

Element	Mn	Cr	Fe	Si	Ti	Co	Al	Cu	C	Ni
Concentration [wt. %]	0.21	15.24	8.50	0.42	0.23	0.19	0.18	0.17	0.08	balance

The surface layers were produced on the Inconel 600 alloy using a glow discharge assisted PACVD process carried out in three stages realized in a single technological cycle, which was achieved by varying the chemical composition of the gaseous atmosphere and the process temperature. The initial stage was conducted at 400 °C with the atmosphere containing $Al(CH_3)_3$ vapours + hydrogen. The next stage, carried out at 550 °C, involved oxidation realized by introducing air (ca. 2 vol. %) into the reactive atmosphere. In the final stage, involving controlled diffusion processes, the treated samples were heated in an argon atmosphere at 850 °C. The phase composition of the obtained surface layer was analyzed in a Brucker D8 Discover diffractometer using CuK_α radiation in the 2θ range 20–100°, with the incidence angle of X rays, ω, ranging between 3° and 11°. The metallographic samples were prepared by cutting the

rods perpendicular to their surfaces, grinding with abrasive grades and finally polishing using polishing wheels and diamond pastes. Then the samples were etched with a reagent of the composition: 3g $FeCl_3$ + 10 cm^3 HCl + 90 cm^3 C_2H_5OH and observed under an Olympus IX70 optical microscope at the magnification of 1500×.

The chemical compositions of the surface layers were examined with a Cameca Semprobe SU-30 X-ray microanalyzer. The XPS spectra were recorded at various depths from the surface using a MICROLAB-350 (Thermo VG Scientific) spectrometer equipped with an X-ray radiation source. The analysis utilized the X-rays radiated by the Al Kα anode (1486.6 eV) operated at a power of 300 W (15 kV, 20 mA). The survey spectrum was recorded by scanning the energy range from 0 to 1350 eV at steps of 1 eV and pass energy of the spherical sector analyzer of 150 eV. The spectra of the individual C1s, O1s, Ti2p, N1s, Cr2p and Al2p regions were recorded at steps of 0.2 eV with the analyzer pass energy of 50 eV. The sample surface was bombarded with the Ar^+ ions supplied by an EX-05 ion gun and the spectra were recorded in function of the sputtering time proportional to the depth from the surface. The Ar^+ ions employed had energy of 3 keV and the magnitude of the ionic current was 1 μA. The spectra thus obtained were processed using the Avantage v.3.54 program (Thermo VG Scientific). The spectra were smoothed, the satellites due to the non-monochromatic radiation beam were removed, and the non-linear background was subtracted. The peaks were fitted using the shape of the synthetic peak constructed based on the Gauss and Lorentz shapes in a proportion of 70/30 (±5). Quantitative XPS analysis was executed on a layer surface before sputtering and on particular surfaces of layers after sputtering times of 10 335 s and 22 950 s. Fractures of the layers were examined by using a Hitachi S-3500N scanning electron microscope. The microhardness of the surface layers was measured by the Vickers method in a ZWICK Materialprüfung 3212002 hardness tester under the load of 50 G.

The examination of the corrosion resistance by the potentiodynamic method was performed in a NaCl + Na_2SO_4 solution (which simulated acidic rainfall of pH = 5.8) using a minicell installed on the sample surface. The cell was filled with an electrolyte, the rest potential (E_{ocp}) was determined and then the variation of the polarization current versus polarization potential was recorded and plotted. The polarization potential was varied from 300 mV (which was shifted towards the cathode potential by more than E_{ocp} value) to the anodic potential at the rate of 1 mV/s. All the potentials were referred to the potential of an Hg/HgO electrode. The intersection of the cathodic and anodic branches of the polarization curves indicated the magnitude of the corrosion current density $i_{corr.}$. The effect of the surface layers on the corrosion resistance of the material was evaluated based on the shift of the rest potential E_{ocp} determined for the modified surfaces with respect to the substrate potential, and also by calculating the protection degree using the formula (1).

$$\beta = \left(1 - \frac{i_{corr}^{w}}{i_{corr}^{p}}\right) \times 100\% \tag{1}$$

where: i_{corr}^{p} is the corrosion rate of the uncovered substrate, and i_{corr}^{w} is the corrosion rate observed in the material protected by the multi-component layer.

The frictional wear resistance of the layers was measured by the three rollers + taper method, and their adhesion to the substrate was examined using a Revetest device (CSEM Co). The loading rate was 100 N/min, the load ranged from 0 to 100 N, the sample feed rate was 10 mm/min and the acoustic emission sensitivity was 20.

3. Results

An X-ray phase and TEM [7, 8] analysis show that the layers produced by the PACVD method, carried out in a (H_2 + Ar) reactive atmosphere with the participation of the $Al(CH_3)_3$ metallorganic compound, are composite layers of the σ-Al_2O_3 + Ni_3Al + Ni(Cr,Fe,Al) + Cr_7C_3 + Cr-Ni type.

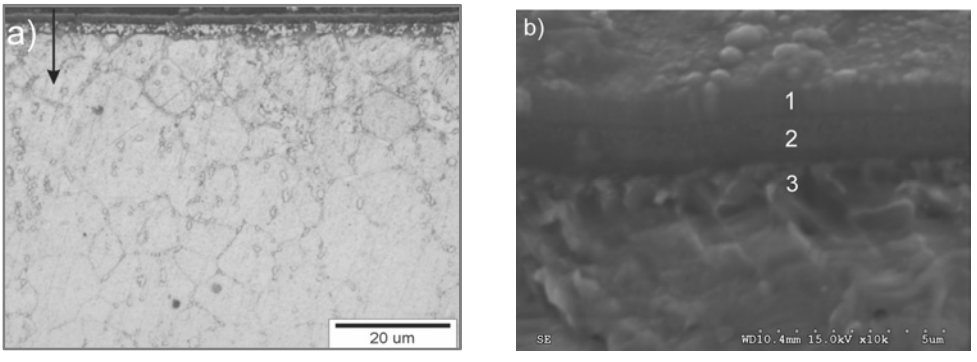

Fig. 1. Microstructure of a composite layer of the σ-Al_2O_3 + Ni_3Al + Ni(Cr, Fe, Al) + Cr_7C_3 + Cr-Ni type produced on the Inconel 600 by the PACVD method (a) and their fracture (b)

An image of the microstructure of the layer thus obtained is shown in Fig. 1a. The layer has a complex structure and is about 5 μm thick, which has been confirmed by the fractographic measurements (Fig. 1b). The layer appears to be composed of three zones.

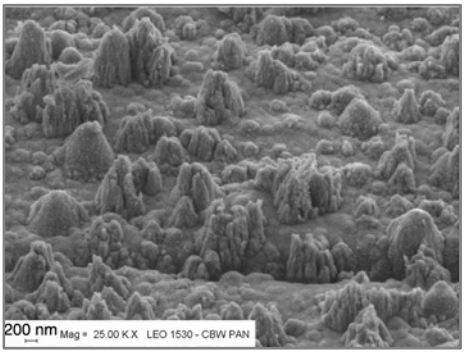

Fig. 2. Morphology of the surface of the σ-Al_2O_3 + Ni_3Al + Ni(Cr, Fe, Al) + $Cr0_7C_3$ 0+ Cr-Ni type layer produced by the PACVD method

The morphology of the surface of the layer is shown in Fig. 2. As can be seen, the layer has a finegrained structure. The fact that the grains are elongated suggests that the layer has grown in the columnar way. Its surface hardness is high, namely $1200HV_{0.05}$, which is indicative of an aluminum oxide film being present on the surface (the hardness of the substrate material is $220HV_{0.05}$).

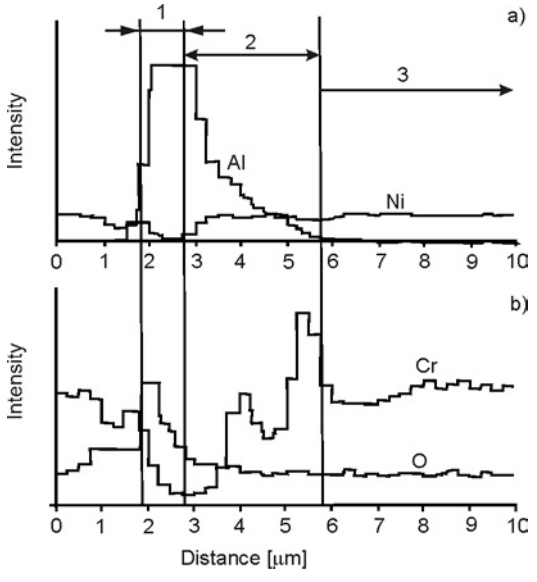

Fig. 3. Linear distribution of elements: a) Al and Ni, b) Cr and O on the cross-section of the composite layer; 1 – outer zone Al_2O_3, 2 – intermediate zone $Al_2O_3 + Ni_3Al + Ni$ (Cr, Fe, Al), 3 – substrate Inconel 600

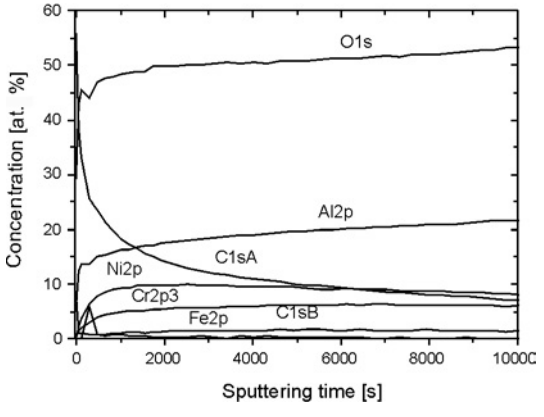

Fig. 4. Concentration profiles of elements in the outer layer (1) from the XPS analysis

Figure 3 shows the linear distribution of the elements identified on a cross-section of the sample obtained by X-ray microanalysis along the line shown in Fig. 1a. This distribution evidently shows that the layers are diffusively bound with the substrate (Fig. 3a). The increased concentration of chromium observed in the layer at a certain

depth (Fig. 3b) has already been explained by the formation of carbides in this zone [7, 8]. The outer zone of the aluminum oxide forms as a result of glow discharge assisted oxidizing (Fig. 3). Figure 4 shows the results of XPS examination of the outer zone of the layer. Detailed results of the analysis are given in Table 2.

Table 2. Concentration of elements *c* [at. %] and binding energies *E* of their compounds [eV] after ionic etching of various durations

Process	Ni $2p_{3/2}$		Fe $2p_{3/2}$		Cr $2p_{3/2}$		O1s		N1s		C1s		Al2p		Ti $2p_{3/2}$	
	E	*c*	*E*	*c*	*E*	*c*	*E*	*c*	*E*	*c*	*E*	*c*	*E*	at.%	*E*	*c*
Before etching	855.2	0.3	712.5	0.1	576.7	0.5	533.3	6.4	399.9	0.9	288.4	4.1	73.4	5.6	461.2	0.2
	852.9	0.2	710.8	0.4			531.8	17.1			286.3	9.9				
							530.3	8.9			284.6	44.9				
After 10 335 s Ar+	855.2	1.7	709.0	1.0	576.3	1.7	532.00	50.0	397.3	0.8	287.3	0.5	74.7	21.8	459.6	0.2
	852.9	7.5	707.0	2.3	574.3	2.8					285.9	1.6			456.6	0.1
											284.6	5.3				
											283.2	0.8				
After 22 950 s Ar+	854.9	0.7	711.4	1.3	577.6	0.8	532.29	52.6	397.6	1.0	288.39	0.2	74.9	25.3	462.0	0.1
	853.00	4.4	709.3	0.5	576.2	0.6					286.3	1.2				
			707.2	1.7	574.4	2.0					284.6	5.1				
											282.7	2.2				

Nickel present on the surface in trace amounts is much more visible at greater depths. Both on the surface and in the interior of the layer, it occurs in two basic states: as metallic nickel with binding energy of 852.92±0.1eV, and as NiO with its characteristic binding energy of 855±0.15 eV [9] (Fig. 5).

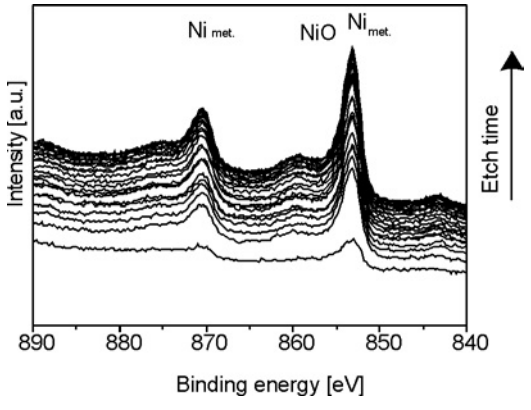

Fig. 5. XPS spectrum of the Ni2p region

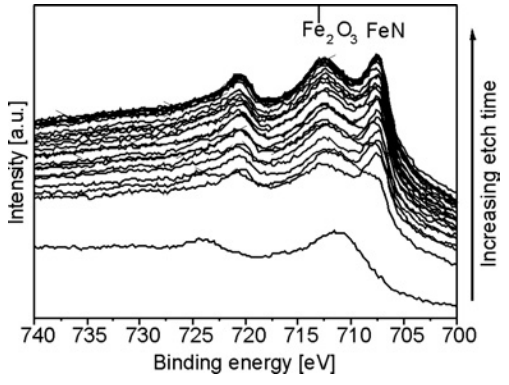

Fig. 6. XPS spectrum of the Fe2p3/2 region

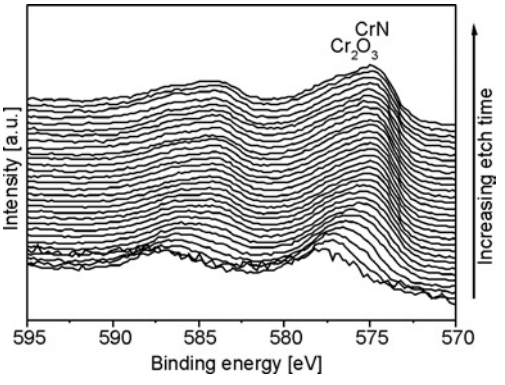

Fig. 7. XPS spectrum of the Cr2p region

Iron, occurring on the surface chiefly in the Fe_2O_3 form with binding energy of 710.8 eV, deeper in the layer also occurs in its metallic form with binding energy of about 707–708 eV (Fig. 6). Judging from the half-width of its peak, which in deeper zones of the layer is of the order of 2.4–2.6 eV, we cannot exclude that other iron compounds are also present, such as Fe-Ni with binding energy of 706.7 eV or Fe_3C with binding energy of 708.1 eV [10, 11]. Another broad peak visible in the Fe2p region corresponds to the binding energy of about 713 eV, which is above the value taken to be characteristic of the Fe_2O_3 type oxides, and should be ascribed rather to a satellite peak associated with the 'shake up' effect characteristic of the paramagnetic states of iron: Fe^{+2} and Fe^{+3} [9].

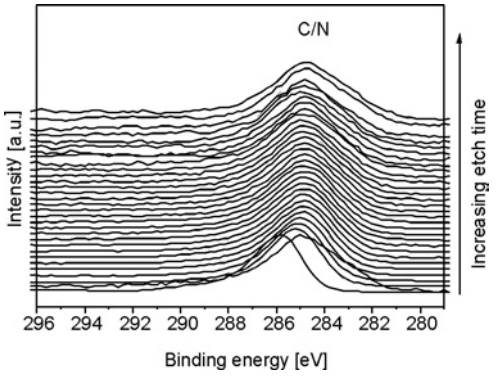

Fig. 8. XPS spectrum of the C1s region

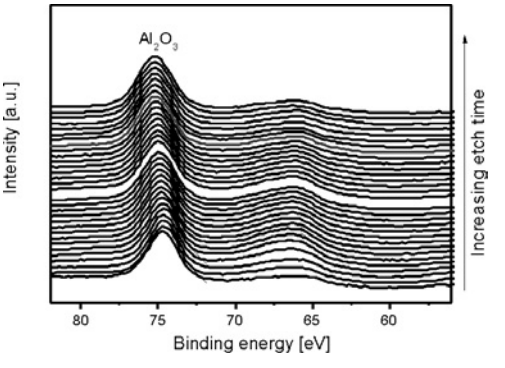

Fig. 9. XPS spectrum of the Al2p-Ni3p region

Chromium which, on the surface, occurs as the Cr^{3+} oxide with the binding energy of 576.6 eV [12], deeper in the layer is represented by a peak of the binding energy of about 575 eV (Fig. 7). A precise identification of this peak by XPS is not possible, since the peaks ascribed to the Cr-N bonds and the peaks due to the Cr-C bonds overlap one another [13–17]. The presence of carbides is confirmed by the clear broadening of the carbon peak towards lower energies, which can be seen in Fig. 8 in deeper

regions of the layer, and in the results of the TEM analysis described in [7, 8]. The only element which does not change its state in deeper zones of the layer is aluminum with binding energy of the Al2p peak equal to about 74.7 eV which is characteristic of the Al_2O_3 phase (Fig. 9).

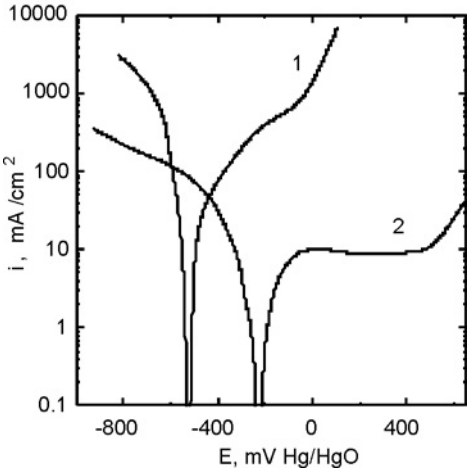

Fig. 10. Anodic polarization curves obtained for : 1 – untreated, 2 – PACVD-treated Inconel 600 immersed in an NaCl + Na_2SO_4 solution (simulating acidic rainfalls with pH = 5.8)

Table 3. Results of corrosion examinations

Material	E_{ocp} mV, Hg/HgO	$E_{corr.}$ mV, Hg/HgO	i_{corr} μA/cm^2	$i_{passive}$ μA/cm^2	Anticorrosion protection degree, β %
Inconel 600 (substrate)	–170	–460	1,5	–	–
Inconel 600 covered with the multilayer	–50	–240	<0,1	10	99

Corrosion examinations (Fig. 10, Table 3) performed in a NaCl + Na_2SO_4 solution (which simulated acidic rainfall of pH = 5.8) using the potentiodynamic method have shown that the σ-Al_2O_3 + Ni_3Al + Ni(Cr, Fe, Al) + Cr_7C_3 + Cr-Ni type composite layer formed on the Inconel 600 alloy improves the corrosion resistance of the alloy. This can be inferred from the facts that, in the alloy with the surface composite layer, the open circuit potential (E_{ocp}) and the corrosion potential ($E_{corr.}$) are shifted more towards the anodic potential and the corrosion current density $i_{corr.}$ is considerably lower (at $i_{corr.}$=10 μA, the anodic curve shows the passive state). The very high degree of anti-corrosive protection ensured by the composite layer is achieved thanks to its tightness (no cracks developed through the layer to the substrate).

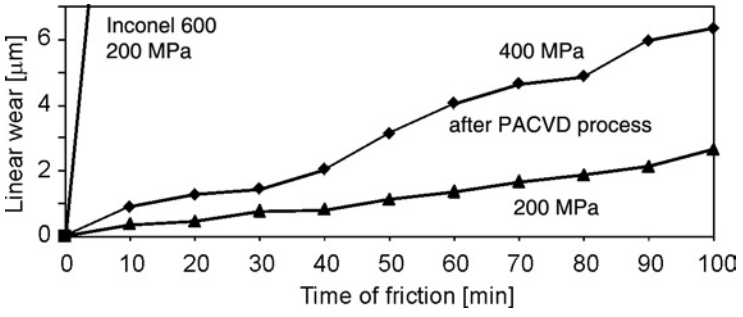

Fig. 11. Linear wear of an σ-Al_2O_3 + Ni_3Al + Ni(Cr, Fe, Al) + Cr_7C_3 + Cr-Ni type composite layer in function of friction time compared to the wear observed in the Inconel 600 alloy

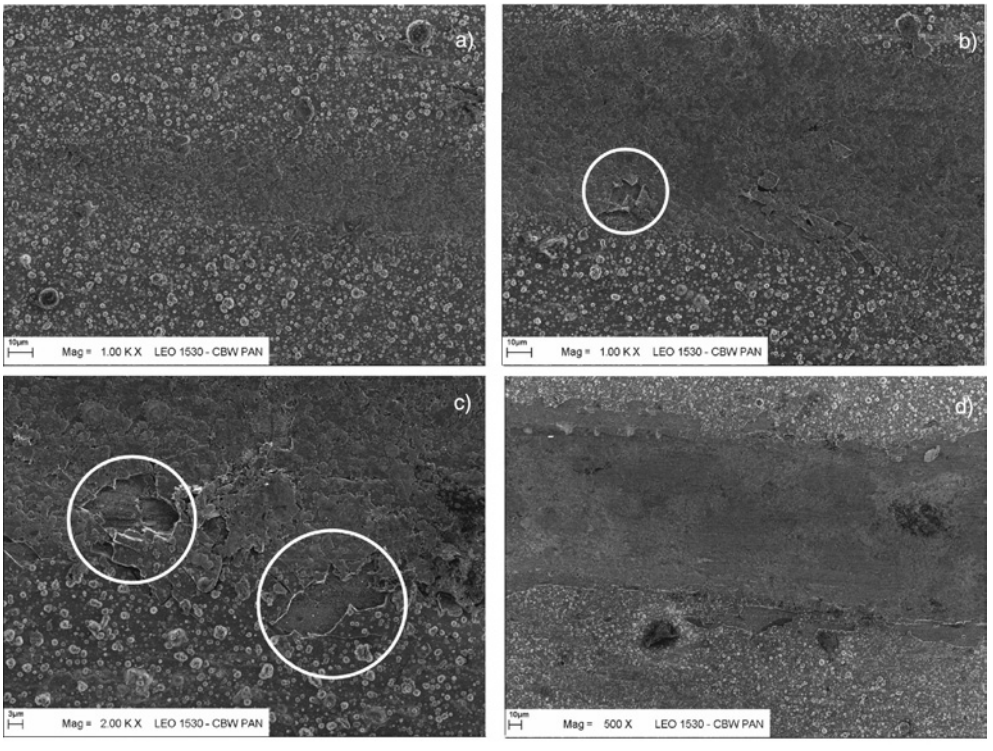

Fig. 12. Surface of an σ-Al_2O_3 + Ni_3Al + Ni(Cr, Fe, Al) + Cr_7C_3 + Cr-Ni type composite layer after the scratch test: a) initial stage of the test, b) *Lc* = 3.57 N, indenter cutting path 0.35 mm, c) *Lc* = 7.27 N, indenter cutting path 0.7 mm, d) *Lc* = 42.96 N, indenter cutting path 0.5 mm

The presence of the Al_2O_3 surface zone and of sublayers composed of Ni-Al intermetallic phases greatly improves the frictional wear resistance of Inconel 600 (Fig. 11). Untreated Inconel 600 examined under the load of 200 MPa is seized as early as after 10 min of the test, whereas the alloy covered with the multi-component

composite layer does not undergo seizure during the entire friction test, i.e. 100 min, even when higher loads of 200 and 400 MPa are applied. The results of the scratch test (Fig. 12) have shown that despite its complex structure, the layer adheres well to the substrate, which is an important performance property. At the initial stage of the indenter penetration, we can only see abrasion (Fig. 12a). The first single splinters are observed at the critical force Lc = 3.57 N at an indenter cutting path of 0.35 mm (Fig. 12b). Numerous splinters occur at Lc = 7.27 N after the indenter runs a cutting path of 0.7 mm (Fig. 12c), and finally the break-through of the ayer is observed at Lc = 42.96 N after a cutting path of 5 mm (Fig. 12d). It should however be noted that the layers are relatively thin with the thickness of the outer Al_2O_3 ceramic zone not exceeding 1 μm. Moreover, although the ceramic is very hard and resistant to compression, its tensile strength is not very high.

4. Conclusions

When applied to an Inconel 600 substrate, the PACVD process carried out with the participation of the $Al(CH_3)_3$ metallorganic compound yields a multi-component composite layer of the σ-Al_2O_3 + Ni_3Al + Ni(Cr,Fe,Al) + Cr_7C_3 + Cr-Ni type during a single technological cycle. The layer can be produced on Inconel 600 alloy parts with complicated shapes.

The layers thus obtained have a high hardness, due to the outer Al_2O_3 ceramic zone which also ensures their enhanced corrosion resistance,

The diffusion character of the individual sub-layers guarantees their good adherence to the Inconel 600 substrate and improve the tribological and mechanical properties.

Acknowledgement

Surface characterizations were performed using a Microlab 350 located at the Physical Chemistry of Materials Center of the Institute of Physical Chemistry, Polish Academy of Sciences and of the Faculty of Materials Science and Engineering at Warsaw University of Technology.

References

[1] KENNEDY L.R., THOMAS M., Adv. Mater. Processes, 149 (1996), 33.
[2] MIKUŁOWSKI B., Stopy żaroodporne i żarowytrzymałe, Wydawnictwa AGH, Kraków 1997.
[3] GODZIMIRSKI J., Technika i Eksploatacja, 5 (2006), 52 (in Polish).
[4] EZUGWU O.E., Int. J. Machine Tools Manuf., 45 (2005), 1353.
[5] DOBRZAŃSKI L., Podstawy nauki o materiałach i metaloznawstwo, WNT, Gliwice Warszawa 2002.
[6] DONG-GOO KIM, YOUNG-ZE LEE., Wear, 250 (2001), 673.
[7] TACIKOWSKI M., SŁOMA J., WOŹNIAK M., WIERZCHOŃ T., Intermetallics, 14 (2006), 123.
[8] TACIKOWSKI M., SITEK R., SIKORSKI K., WIERZCHOŃ T. (in critical review in Intermetallics).
[9] NIST X-ray Photoelectron Spectroscopy Database 20, Version 3.4, http://srdata.nist.gov/xps/.
[10] GONTIJO L.C., MACHADO R., MIOLA E.J., CASTELETTI L.C., NASCENTE, Surf. Coatings Technol., 183 (2004), 10.

[11] BONNET F., ROPITAL F., LECOUR P., ESPINAT D., HUIBAN Y., GENGEMBRE L., BERTHIER Y., MARCUS P., Surf. Interf. Analysis, 34 (2002), 418.
[12] GROHMANN I., KEMNITZ E., LIPPITZ A., Surf. Interf. Analysis, 23 (1995) 887.
[13] DETROYE M., RENIERS F., BESS-HERMAN C., VAREECKEN J., Appl. Surf. Sci., 144–145 (1999), 78.
[14] GROUDEVA-ZOTOVA S., VITCHEV R.G., Surf. Interf. Analysis, 30 (2000), 544.
[15] LIPPITZ A., HÜBERT TH., Surf. Coatings Technol., 200 (2005) 250.
[16] FIGUEROA C.A., ALVAREZ F., J. Appl. Phys., 97 (2005), 103528.
[17] RIVERE J.P., CAHOREAU M., MEHEUST P., J. Appl. Phys., 91 (2002), 6361.

Received 25 February 2008

Materials Science-Poland, *Vol. 26*, *No. 3*, *2008*

A new idea of the influence of solid materials on kinetics of chemical reactions

C. K. KAJDAS[1, 2], A. KULCZYCKI[1*]

[1]Institute for Fuels and Renewable Energy, ul. Jagiellońska 55, 03-301 Warsaw, Poland

[2]Warsaw University of Technology, Institute of Chemistry in Płock, ul. Łukasiewicza 17, 09-400 Płock, Poland

The mechanism of heterogeneous catalysis is still under discussion. There is no clear theory which explains the mechanism of influence of materials on the rate of chemical reactions. All existing theories assume that specific materials, catalysts, decrease activation energy E_a. We hypothesize that for standard and catalyzed heterogeneous reactions the same E_a (real activation energy) is needed to trigger reaction processes. We propose that the difference between E_a and apparent activation energy (E_{app}) can be presented as catalytic reaction activation energy (E_c). This hypothesis is based on the so-called α_i model considering tribochemistry, work function, thermionic emission, and the negative ion–radical action mechanism. The proposed model assumes that mechanical work done on a solid material is accumulated in this material and then emitted as electrons and/or photons to the space in which the reaction takes place. The developed model includes a specific angle γ at which the reaction can be initiated, when the stream of energy e_γ equals some 3–5 eV. Energy emitted by the surface as pulses of 3–5 eV can reach the value of E_a and trigger a heterogeneous catalytic process. The catalyst emits pulses of a high density energy flux and at the angle γ the value of emitted energy is equal to the real activation energy E_a.

Key words: *tribology; heterogeneous catalysis; activation energy*

1. The model

The accepted definition of a catalyst [1] is that it is a substance that increases the rate at which a chemical system approaches equilibrium, without being consumed in the process; catalysis is the phenomenon of a catalyst in action while the catalyst lowers the activation energy. The transition state along a reaction path is the point of maximum free energy, where bond-making and bond-breaking are balanced. Heterogeneous catalysis accelerates the movement of atoms on the passage through the tran-

*Corresponding author, e-mail: akulczycki@ipieo.pl

sition state; it provides the link between reactants and products on a reaction pathway which involves simultaneous motion of several to very many atoms [2]. It has been emphasized that predictability of the outcome of catalytic reactions depends critically on the understanding of their molecular mechanisms. The mechanism of protective layer formation by lubricants in space near solid materials during a tribological process was recently analyzed by using the so called α_i method [3]. The principle of the α_i method (model) was presented in detail by Kulczycki [4]. The model can be applied to tribological systems in which the mechanical work done can be treated as input and dissipated energy – predominantly heat – as output. The functional input–output relation may also be related to tribochemical reactions which are known to proceed much faster than thermochemical ones. On the other hand, one may compare tribochemical reactions with heterogeneous catalytic reactions [5].

The kinetics of tribochemical reactions depends on conditions of the tribological process, and as a result, it is necessary to find more than one function of the mechanism of a tribochemical reaction. For example, one function can be related to the mechanics of a tribological process, the other one to its chemical reactions. It was assumed that the relationship between these functions makes it possible to analyze the mechanism of a tribological process on a "basic level". Two functions have been taken into account: $f(y)$ and $\phi(y)$. It was assumed that in the both functions y is the only state variable. For transition from a state $y = a$ to a state $y = b$, the following is considered

$$\alpha_i = \frac{\dfrac{f(b) - f(a)}{\phi(b) - \phi(a)}}{\dfrac{f'(b)}{\phi'(b)}} \tag{1}$$

In the above equation, f' and ϕ' are load derivatives of the corresponding functions, and the value of a (describing the initial state) should be constant.

One of the possibilities is to describe the tribological process using thermodynamic relationships. Thus, $f(y)$ can be work L done on a tribological system during the test, up to a critical stage of the tribological system (seizure, weld) and $\phi(y)$ can be internal energy change Δu. Then Eq. (1) can be written as follows:

$$\alpha_i = \frac{L - L_0}{\Delta u - \Delta u_0} \frac{d\Delta u}{dL}, \qquad L = \mu P v t \tag{2}$$

where μ is the friction coefficient, v – speed, t – time, P – a critical value of the applied load (test result: seizure load, weld load) but it is difficult to define Δu. Equation (2) can be rewritten as

$$a_i = (L - L_0)C, \quad C = \frac{\dfrac{d\Delta u}{dL}}{\Delta u - \Delta u_0} \tag{3}$$

C is a function of P and for a number of different lubricating additives/reagents (obtained several different values of the critical applied load) its value is constant. Concluding, C should be a harmonic function of P, described by the following equation:

$$C = B\exp\left(\frac{k_1}{P}\right)\cos(k_2 P + k_3) \tag{4a}$$

or

$$C = Bk_4 P^2 \cos\left(\frac{k_5}{P}\right) \tag{4b}$$

where: k_1, k_2, k_3, k_4, k_5 are constant parameters, B is a function of energy of the dimension [energy]$^{-1}$. The exponential part of the above equation can be connected with the kinetics of chemical/tribochemical reactions by the Arrhenius equation, relating the reaction rate constant k with temperature

$$k = A\exp\left(-\frac{E_a}{RT}\right) \tag{5}$$

where E_a is the activation energy of a given chemical/tribochemical reaction and the average temperature T for the tribological system may be combined with the load P applied in the tribological process and properties of solid materials using the Rowe dependence [6]

$$T = T_b + \mu P^{0.5} D \tag{6}$$

Hence

$$k = A\exp\left(-\frac{E_a}{R(T_b + \mu P^{0.5} D)}\right) \tag{7}$$

where A is the pre-exponential (frequency) factor, T_b is ambient temperature of lubricant during the tribological process, and D is a constant whose value is characteristic of a given kind of solid material. The trigonometric part of the expression can be connected with emission of energy by metal/solid body (catalyst) surface. The stream of energy emitted by the surface depends on the angle γ related to the normal direction to solid body surface and can be expressed by

$$e_\gamma = e_0 \cos\gamma \tag{8}$$

Consequently

$$B = \frac{e_0 St}{\left(R\left(T_b + \mu P^{0,5} D\right)\right)^2} \tag{9}$$

where S is the area of active sites which emit energy, t stands for time of energy emission by the active sites, and C can be described by the following dependence

$$C = \frac{\left(A\exp\left(\frac{E_a}{R\left(T_b + \mu P^{0.5} D\right)}\right) e_0 \cos\left(k_2 P + k_3\right)\right) St}{R\left(T_b + \mu P^{0.5} D\right)^2} \tag{10}$$

Thus

$$kC = A\exp\left(-\frac{E_a}{R\left(T_b + \mu P^{0.5} D\right)}\right), \quad C = \frac{\left(e_0 \cos\left(k_2 P + k_3\right)\right) St}{R\left(T_b + \mu P^{0.5} D\right)^2} \tag{11}$$

Analysis of the mathematical model in relation to empirical results of studies of tribological processes leads to the conclusion resulting in a new idea of the mechanism of catalytic processes.

The model and, especially, the C value (see Fig. 1), combines the energy E_a delivered to molecules from the energy stream (E/t). Considering the energy delivered to molecules for each reaction, should be noted that:

- A critical rate of triboreactions is reached at a temperature or, equivalently, under a load for which the value of E_a is the same for different reactants in the case of the same mechanism of triboreactions; E_a is not a function of T nor P.
- k, under critical conditions, is connected with the energy emitted by the solid at a specific angle γ.
- The critical rate of triboreactions depends on energy emitted by the solid body.
- The distribution of the energy emitted by the solid body (catalyst) is controlled by the angle of emission

$$e_\gamma = e_0 \cos\gamma \tag{12}$$

where γ is a function of P and depends on the stream of energy introduced into the tribological system, e_0 is the density of the energy flux in the perpendicular direction to the solid body surface.

The value of the angle γ depends on the system energy flux. The critical state of a tribological system appears in conditions resulting in destruction of the protective film. As has been observed that for different reactants, the critical rate of reaction leading to protective layer destruction was achieved for different values of energy flux

into the system (different values of applied load P). The same value of C obtained for different reactants and different densities of streams of energy introduced into the system (characteristic of each reactant) leads to the conclusion that the same critical rate of destruction reaction was achieved and thus for each reactant a different angle γ is connected with the critical rate of reaction.

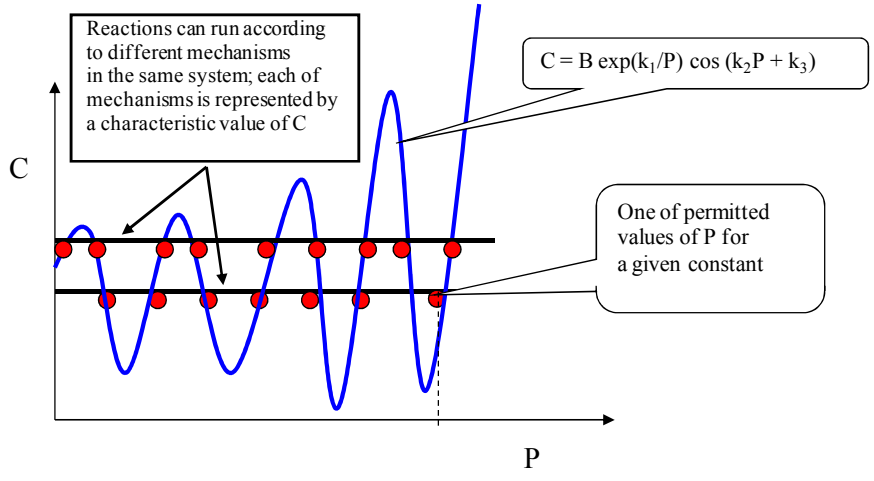

Fig. 1. Relation between the parameter C and the applied load P characteristic of the critical state of a tribological system (seizure or weld load); a given constant value of C can be obtained for a number of P values

Consequently, for each reactant there is a specific value of the energy flux density (e_γ) emitted by the solid/catalyst and the value of activation energy E_a is constant. Accordingly, it is possible to say that: (i) E_a is constant for a given type of reaction and the critical rate of reaction depends not only on the energy quantity added to reactants but on the density of the introduced energy stream (time of the tribological process is constant for each load); (ii) the catalyst emits pulses of energy flux of high density and at an angle γ the value of emitted in short time energy is equal to activation energy E_a; (iii) the catalyst collects energy introduced into the system and emits it as pulses of the high energy density flux, thereby initiating the reaction or increasing its rate. Figures 2 and 3 present schematically this approach.

The parameter C is constant for a given mechanism of reaction. For different mechanisms, different values of C are obtained. Consequently, for each mechanism of reaction (triboreaction) the critical rate of reaction can be achieved only under certain values of energy stream introduced into the system (T or P). For each of these values, relation between the rate constant calculated for temperature T in the friction area and stream of energy emitted by the solid equal to or higher than E_a is constant for a given mechanism of reaction. For another mechanism, this relation changes. It results from analysis of the mathematical model that it is feasible to say that the tribocatalytic effect is observed due to accumulation of energy (introduced into the system as mechan-

ical work) in the solid and the emitted as short time pulses of energy of a high density. Emission of energy by a solid is controlled by the angle of emission.

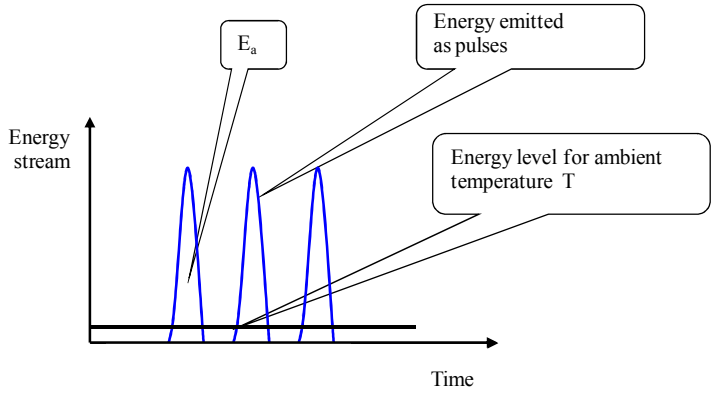

Fig. 2. A general idea of the action mechanism of a heterogeneous catalyst: a part of low energy stream (of the order of RT, i.e. less than E_a) , introduced into a solid catalyst is emitted by the catalyst as stream of high energy pulses

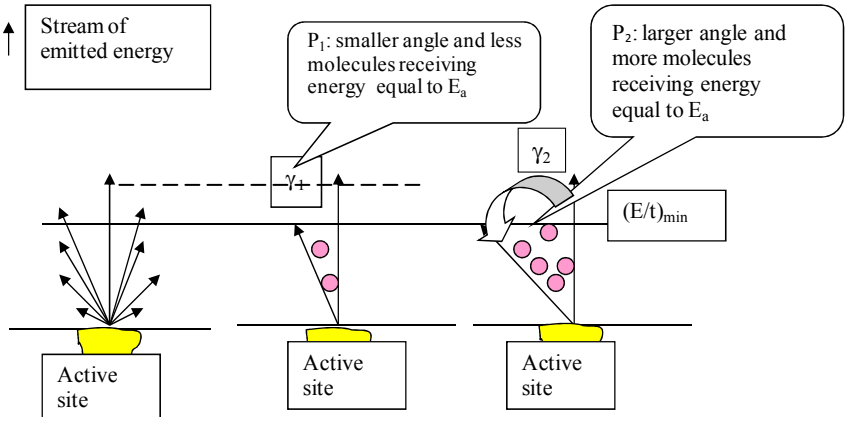

Fig. 3. Illustration of the main concept of the model; stream of the energy emitted by the catalyst depends on the angle γ, hence the number of molecules receiving energy equal to E_a depends on γ

2. Work function and thermionic emission

A promoter chemically modifies a catalyst but is not a catalyst itself. Vayenas at al. [7] described the electrochemical modification of metal catalyst surfaces and presented continuous *in situ* variations and monitoring of the amount of the promoter. Theoretical studies performed by Joyner and Pendry [8] demonstrate that short-range effects dominate, significantly affecting bonding to surface atoms only within a range

of less than 0.5 nm, in contrast with the new results of Vayenas et al. [7]. The short range effect, depending on the character of specific surface sites, and long-range electronic interactions, were recently discussed by Pittchard [9, 10]. It has been shown that both sodium and potassium, used as promoters, significantly decrease work functions of catalysts.

Given a small temperature range in which kinetic studies are carried out, it is reasonable to assume the activation energy as being independent of temperature [11]. Similarly, under a wide range of practical conditions, the weak temperature dependence of the pre-exponential factor is negligible compared to the temperature dependence of the exponential term. A thermal model of temperature rise developed by Vick et al. [12] for sliding contact was used to predict the temperature rise over the surface. The predicted temperature rise [13] along with the bulk temperature of the material was used in the Richardson–Dushman equation:

$$J = AT^2 \exp\left(-\frac{\phi}{k_B T}\right) \tag{13}$$

where J is the current density, $A = 4\pi mek_b^2/h^3 = 120$ A/(cm^2·K^2) is the Richardson constant, ϕ is the work function, m and e are the electron mass and electro charge, respectively, h and k_B are the Planck constant and Boltzmann constant, respectively.

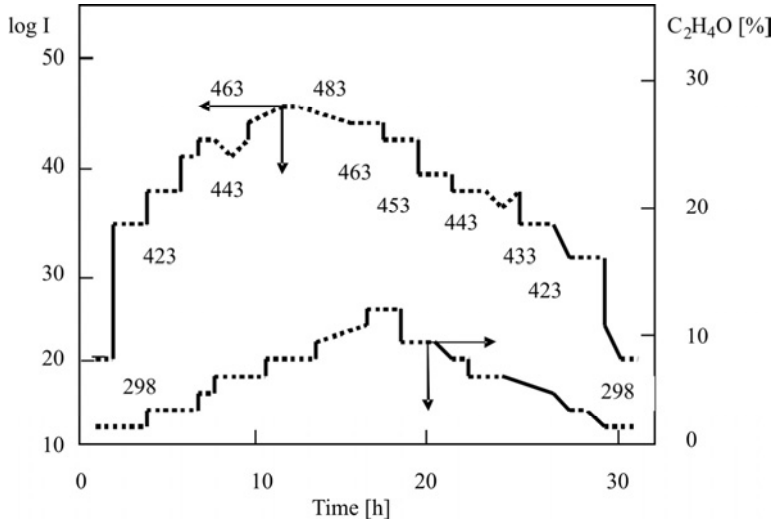

Fig. 4. Effect of temperature on the exoelectron emission rate (emission intensity, expressed in the logarithmic scale) and the formation rate of ethylene oxide (proportional to its amount in the product mixture, expressed in mol. %). The numbers near the upper curve denote temperatures of the system, expressed in K; after Ref. [15]

Park and Somorjai [14] demonstrated that exothermic catalytic reactions induce electronic excitation at metal surfaces, leading to the production of energetic hot elec-

trons. They monitored the flow of hot electrons for several hours using two types of metal –semiconductor Schottky diodes, Pt/TiO_2 or Pt/GaN, during the platinum catalyzed oxidation of carbon monoxide. The thickness of the Pt film used as the catalyst was 5 nm, less than the electron mean free path, resulting in the ballistic transport of hot electrons through the metal. The experiments indicated that chemical energy of the exothermic catalytic reaction was directly converted into hot electron flux in the catalytic nanodiode. Recently, Vick et al. [13] evidenced that high local temperatures generated by friction of the contacts between rubbing surfaces can activate the emission of electrons.

Actually, it is well known and acknowledged that heterogeneous catalytic reactions take place at centres where the electron exchange in the catalyst–substrate system is favoured and that electron emission arises from centres at the surface where electrons are weakly bound. At this point, it is to emphasize that thermally stimulated electron emission occurs in the same range of temperatures as that typical of heterogeneous catalysis [15], as depicted in Fig. 4.

3. The negative ion–radical action mechanism (NIRAM) applied to specific tribochemical and catalytic reactions

The kinetics of tribochemical reactions is different from the kinetics of thermochemical ones. Similar differences arise from the comparison of regular thermochemical heterogeneous reactions and heterogeneous catalytic reactions The difference relates to the initiation steps of these reactions. The NIRAM approach was put forward in order to explain the mechanism of tribochemical reactions and has been successfully applied to account for specific tribochemical reactions [16]. Reactions are said to be initiated by low-energy electrons (exoelectrons) emitted under boundary friction conditions [16]. The emitted electrons interact with molecules in the contact area, which then dissociate forming negative ions and radicals or a negative ion–radicals. Considering the NIRAM approach and the NIRAM-HSAB (hard and soft acids and bases) concept [17] it is possible to look for similarities and differences between tribochemistry and catalysis [5].

Typical physical phenomena evolving from wear processes comprise increased contact temperature and triboemission. Emitted low energy electrons can initiate tribochemical reactions which govern tribological processes by forming anti-wear films. Important research in the field of triboemission was carried out by Nakayama et al. [18] who used a Faraday-cup type assembly to detect bursts of electric current – either charged particle emission or surface charge variation – from scratching diamonds on metals and insulators. Kim et al. [19] investigated photon emission, electron emission intensities, and electron kinetic energy from reciprocating scratching of MgO with diamond. Molina et al. [21, 22] characterised triboemission of electrons from several solids. For the cases of diamond-on-alumina and diamond-on-sapphire, energy spectrometry showed that a large fraction of the triboemitted negative charges were of low energy (e.g., 1–5 eV). This finding was of importance because in the NIRAM ap-

proach it was hypothesized that the energy of triboelectrons to initiate tribochemical reaction should be 1–4 eV [16].

NIRAM comprises the following major stages:

(i) low-energy electron emission and creation of positively charged spots, generally on the top of asperities;

(ii) action of the emitted electrons with the lubricant molecules causing the formation of negative ions and radicals on the rubbing surfaces;

(iii) reaction of negative ions with metal surfaces, and other reactions such as free radical reactions, forming an organometallic (or inorganic) film which protects the rubbing surfaces from wear;

(iv) if the shear strength is high, chemical bonds of organometallic compounds are cleaved resulting in formation of inorganic films and further radicals.

(v) eventual destruction of protective layer caused by wear, followed by electron emission and subsequent formation of a new protective film according to the stages (i) through (iv).

In summary, the initiation reaction process is due to tribo-emitted low-energy electrons combined with temperature flash. Specific intermediate reactive species for both tribochemical reactions and some heterogeneous catalytic reactions are formed by the same mechanism mostly governed by the NIRAM approach. The same is due to catalysis and tribocatalysis [5]. The chemically stimulated exoelectron emission occurs continuously from silver catalyst during partial oxidation of ethylene and the emission rate is proportional to the rate of ethylene oxide formation [15]. Generation of fresh surface sites forms a real bridge between physics and chemistry of the wear processes leading to microscopic aspects of a wide variety of wear mechanisms. These mechanisms are often connected with tribochemical reactions that are initiated by the surface enlargement effects. Experimental details on wear and chemical reactions are presented in Ref. [22]. Typical physical phenomena initiated by wear processes include high temperature and triboemission.

4. Conclusions

The model put forward in this paper attempts to correlate mechanical work performed on a solid with its catalytic activity. The tribological system contains fluid reagents and a solid (a specific material). The material plays the role of catalyst (tribocatalyst). The mechanical work done on the system is transformed to internal energy increase. The internal energy is distributed into a liquid/fluid phase bringing about ambient temperature increase (T_b), and is accumulated in the solid. The energy accumulated in the solid is emitted from its surface as pulses of electrons and/or photons. There is a specific angle γ at which the reaction can reach a critical rate or may be initiated, e.g., when e_γ equals some 3–5 eV. The energy accumulated in the liquid phase is insufficient to overcome the threshold of the real activation energy E_a. The energy emitted by surface as pulses of 3–5 eV can reach the value of E_a and the tribo-

reaction process starts to proceed or reaches the critical rate. Based on the discussion concerning the α_i model, thermionic emission, and the NIRAM approach we conclude that for both thermochemical heterogeneous reactions and catalyzed heterogeneous processes, the same activation energy (E_a value) is needed to initiate the reaction process. The fact that triboreactions take place and the critical rate of triboreactions is reached under different conditions (load, temperature) for different reactants cannot be explained by decreasing of activation energy (E_a) by the solid catalyst because E_a is not a function of P.

In summary, it should be emphasized that the activation energy is constant for a given type of reaction and the reaction onset depends not only on the energy quantity added to reactants but on density of the introduced energy stream. The catalyst emits pulses of energy flux of high density and at an angle γ the value of emitted energy is equal to real activation energy E_a.

Acknowledgement

We wish to thank Professor Krzysztof J. Kurzydłowski for valuable comments and suggestions concerning this paper.

References

[1] BOND G.C., *Heterogeneous Catalysis: Principles and Applications*, 2nd Ed., Clarendon Press, Oxford, 1987.
[2] KLIER K., Topics Catal., 18 (2004), 141.
[3] KULCZYCKI A., KAJDAS C., Lubr. Sci. 6 (1994), 161.
[4] KULCZYCKI A., Wear, 103 (1985), 67.
[5] KAJDAS C., Proc. 2nd World Tribology Congress Tribology 2001, F. Franek, W.J. Bartz, A. Pauschitz (Eds.), The Austrian Tribology Society, Vienna 2001, pp. 39–41.
[6] Rowe C.N., ASLE Trans., 9 (1966), 100.
[7] VAYENAS C.G., BABELIS S., LADAS N., Nature, 343 (1990), 625.
[8] JOYNER R.W., PENDRY J.B., Catal. Lett., 1 (1988), 1.
[9] PITTCHARD J., Nature 343 (1990), 592.
[10] MARKERT K., WANDELT K., Surface Sci., 159 (1985), 24.
[11] *IUPAC Compendium of Chemical Terminology*, 2nd Ed., Blackwell Sci. Publ., Cambridge (1997).
[12] VICK B., FUREY M.J., FOO S.J., Numer. Heat Transfer A: Appl., 20 (1991), 19.
[13] VICK B., FUREY M.J., KAJDAS C., Tribol. Lett., 13 (2002), 147.
[14] PARK J.Y., SOMORJAI G.A., J. Vac. Sci. Technol. B: Microelect. Nanom. Struct., 24 (2006), 1967.
[15] SATO N., SEO M., J. Catal., 24 (1972), 224.
[16] KAJDAS C., Lubr. Sci., 6 (1994), 203.
[17] KAJDAS C., Proc. Internat. Tribology Conf., Yokohama 1995, Satellite Forum on Tribochemistry, JST, Tokyo 1995, pp. 31–35.
[18] NAKAYAMA K., HASHIMOTO H., SUSUKI T., J. Phys. D: Appl. Phys., 25 (1992), 303.
[19] KIM M., LANGFORD SC., DICKINSON J.T., Tribol. Lett., 1 (1995), 147.
[20] MOLINA G.J., FUREY M.J., RITTER A.L., KAJDAS C., Wear, 249 (2001), 214.
[21] MOLINA G.J., *Triboemission From Ceramics: Charge Intensity and Energy Distribution Characterizations*, PhD Dissertation, Virginia Tech., Blacksburg (VA), USA (2000).
[22] HIRATSUKA K., KAJDAS C., *Tribology. Science and Application*, CUN PAN, Warsaw (2004), pp. 71–90.

Received 11 August 2008

Contents

S. Prasad, K. Prasad, S.N. Choudhary, T.P. Sinha, Electrical properties of $0.90Pb[(Mg,Zn)_{1/3}Ta_{2/3}]O_3$ $-0.10PbTiO_3$ relaxor 475

Tian Tian, Xiao Xiu-Feng, She Hou-De, Liu Rong-Fang, Biomimetic growth of apatite on titania nanotube arrays fabricated by titanium anodization in NH_4F/H_2SO_4 electrolyte 487

X. Liujie, R. Cardoso, J. P. Davim, Modelling of tribological behaviours of composite PEEK -CF30 using BP neural networks 495

Z. Zhou, L. Chen, Morphology expression and proliferation of human osteoblasts on bioactive glass scaffolds 505

H. S. Zhuang, H. L. Xia, T. Zhang, D. C. Xiao, Synthesis, characterization, and visible-light photocatalytic activity of Fe_2O_3/SnO_2 nanocomposites 517

P. Syam Prasad, V. Ravi Kumar, G. Naga Raju, N. Veeraiah, Influence of nickel ions on dielectric and other physical properties of $PbO–MoO_3–B_2O_3$ glass system 527

P. Cichosz, P. Karolczak, Sinker electrical discharge machining of aluminium matrix composites. 547

S. Bahel, S. B. Narang, Dielectric and structural characteristics of Sm doped $Ba_4La_{9.33}Ti_{18}O_{54}$ ceramics 555

M. H. Sabour, R. B. Bhat, Lifetime prediction in creep-fatigue environment 563

M. S. da Luz, C. A. M. dos Santos, A. J. S. Machado, Orthorhombic to tetragonal phase transition and superconductivity in $Ba_2Cu_3O_4Cl_2$ 585

J. Wang, J.You, P. Yang, C. Zhong, Z. Li, M. Zhang, X. Jing, New magnetic Ni-Al hydrotalcite-like materials Synthesis and characterization 591

M. R. Vaezi, S. H. Mir Shah Ghassemi, A. Shokuhfar, The effect of impact energy on the formation of nanocrystalline powders in Cu–50% Fe immiscible alloy systems 601

L.S. Chuah, Z. Hassan, H. Abu Hassan, Optical characterization of nanoporous GaN through electroless wet chemical etching 609

V.K. Gupta, S. Ray, O.P. Pandey, Dry sliding wear characteristics of 0.13 wt. % carbon steel 617

K. Baltakys, R. Siauciunas, S. Kitrys, Surface microstructure and specific surface area of pure and Na-substituted gyrolites 633

M. Prashant Kumar, T. Sankarappa, Studies of conductivity in mixed alkali vanadotellurite glasses 647

M. Sharma, R. M. Mehra, Structural, optical, electrical and magnetic properties of sol-gel derived $Zn_{1-x-y}Co_xAl_yO$ films 659

M. Yu, Y. Wang, Y. Wang, Z. Sun, Effect of Ni addition on the microstructures of melt-spun CuCr ribbons 675

J. Zhang, D.W. Zhou, P. Peng, J.S. Liu, First-principles plane-wave pseudopotential method calculations for Cu alloying Mg_2Ni hydride 681

Conference of the Scientific Network "New Materials for Magnetoelectronics – MAG-EL-MAT 2007", Będlewo near Poznań, 7–10 May, 2007

G. Kozłowski, A. Jezierski, Electronic structure and magnetic properties of $Ce_2Pd_{1-x}Co_xSi_3$ and $Ce_2Pd_{1-x}Fe_xSi$ 693

D. Sztenkiel, R. Świrkowicz, Orbital Kondo anomaly and channel mixing effects in a double quantum dot 699

P. Trocha, J. Barnaś, Spin-polarized transport through two quantum dots Interference and Coulomb correlation effects 707

J. Wiśniewska, I. Weymann, Theoretical analysis of transport in ferromagnetic single-electron transistors in the sequential tunnelling regime 715

M. Werwiński, A. Szajek, Electronic properties of $ThCu_5Sn$ and $ThCu_5In$ compounds 723
W. Głogowski, J. Goraus, A. Ślebarski, Electronic structure of CePdAl. Experiment and calculations 729
M. Marszałek, M. Kąc, M. Krupiński, A. Polit, Y. Zabila, Specular and diffuse X-ray reflectivity study of surfactant mediated Co/Cu multilayers 735
W. Olszewski, K. Szymański, M. Biernacka, R. Sobiecki, 3d metallic layers electrochemically deposited from nearly nonaquaeous electrolyte 743
V. Osinniy, A. Misiuk, M. Szot, K. Świątek, J. Bąk-Misiuk, A. Barcz, W. Jung, M. Prujszczyk, T. Story, Magnetic properties of silicon crystals implanted with manganese 751
A. Szytuła, B. Penc, A. Jezierski, XPS study of $RNiSb_2$ (R = Pr, Nd) 759

9th Symposium on Reactivity of Metastable Materials, 2007 EMRS Fall Meeting, Warsaw, 17–21 September, 2007

R. Sitek, K. Sikorski, J. Sobczak, T. Wierzchoń, Structure and properties of the multilayers produced on Inconel 600 by PACVD method with the participation of trimethylaluminum vapours 767
Seong-Jong Kim, Seok-Ki Jang, Jeong-Il Kim, Investigation on optimum corrosion protection potential of Al alloy in marine environment 779

Regular paper

C. K. Kajdas, A. Kulczycki, A new idea of the influence of solid materials on kinetics of chemical reactions 787

GUIDELINES FOR AUTHORS

Manuscripts can be sent by conventional mail or by e-mail. Submission of a manuscript to *Materials Science-Poland* implies that it is not being considered for the publication elsewhere, and the authors have a necessary authorization to publish the material contained in the paper. **The manuscripts should conform to the formal standards of the Journal which may be found in the first issue of each volume and on the web page.**

Authors are encouraged to submit electronic versions of the manuscript by e-mail, to the address of the Journal. A single PDF file should be sent, containing text, references, figures, tables etc. Alternatively, the authors can submit the manuscript by conventional mail, sending a CD with the PDF file mentioned above, to the Editor-in-Chief at his address given below.

Each submitted manuscript will be reviewed, the final decision concerning its acceptance resting with the editors. Upon acceptance, the corresponding author will be requested to submit the following material (via e-mail or by conventional mail, on CD)

- A DOC or RTF file containing the final version of the text, references, tables and figure captions. The content of the file should be identical with that of the hard copy, and should exactly match the version seen and accepted be the referee(s).
- File(s) in appropriate formats containing figures. The required formats of the drawings (plots, schemes of technological processes) must be vector files such as XLS, OPJ, cdr (Excel, Origin, CorelDraw) which may also be exported as EPS, EMF or WMF files. Drawings submitted in tiff or jpg formats (bitmaps, raster graphics), even if exported as EPS, EMF or WMF files, will not be accepted. **Bitmaps are acceptable only in the case of photographs.** The photographs (only in grayscale) should have the resolution not lower than 300 dpi (estimated for the size in which they are expected to be reproduced).
- A PDF file containing the complete manuscript (text, literature, tables, figures, etc). The file should be carefully checked as it will serve as a hard copy in case of doubts. **The contents of the PDF file should exactly match the material in other files.**

Irrespective of whether the final version is submitted by e-mail or by conventional mail, the authors should also send **via conventional mail** a signed copy of the Copyright Transfer Agreement (available on the web page of the Journal).

For detailed information consult the first issue of each volume or the web page of the Journal.

The mail should be addressed to:

Professor Juliusz Sworakowski
Editor-in-Chief, Materials Science-Poland
Politechnika Wrocławska, W-3
Wybrzeże Wyspiańskiego 27
50-370 Wrocław, Poland

Electronic correspondence should be sent to: MatSci@pwr.wroc.pl
Web page of Materials Science-Poland: www.MaterialsScience.pwr.wroc.pl

The Publisher reserves the right to make necessary alterations to the text. Each corresponding author will be supplied with one free copy of the journal. Orders for additional offprints can be placed with the Publisher.

Subscription of "Materials Science-Poland" can be ordered via "RUCH" S.A., O.K.D.P.
Conditions and actual prices can be found at:
http://www.ruch.pol.pl

Subscription orders together with the copy of payment confirmation should be addressed to:
"RUCH" S.A., O.K.D.P.
Subscription Department and Foreign Co-operation
Jana Kazimierza 31/33
Pl 01-248 Warszawa

Single issues may be ordered at:
Oficyna Wydawnicza Politechniki Wrocławskiej
Wybrzeże Wyspiańskiego 27
Pl 50-370 Wrocław
oficwyd@pwr.wroc.pl

CHZ "Ars Polona" S.A.
Obrońców 25
Pl 03-933 Warszawa
arspolona@arspolona.com.pl